

1. The first step in the process is to identify the problem or issue that needs to be addressed. This involves gathering information and understanding the context of the problem.

AD \_\_\_\_\_

## FLUCTUATING CONCENTRATIONS IN ATMOSPHERIC DISPERSION

**G. E. DeVuall, D. F. Brown and W. E. Dunn**  
**Department of Mechanical and Industrial Engineering**  
**University of Illinois at Urbana-Champaign**  
**Urbana, IL 61801**  
**217-333-3832**

**A. J. Policastro**  
**Environmental Impact and Information Sciences Division**  
**Argonne National Laboratory**  
**9700 South Cass Avenue**  
**Argonne, IL 60439**  
**708-972-3235**

DTIC  
ELECTE  
MAR 04 1992

U. S. ARMY MEDICAL RESEARCH AND DEVELOPMENT COMMAND  
Fort Detrick, Frederick, MD 21702-5012

**Contracting Officer's Representative: Major John Young**  
**Health Effects Research Division**  
**U. S. ARMY BIOMEDICAL RESEARCH AND DEVELOPMENT LABORATORY**  
**Fort Detrick, Frederick, MD 21702-5010**

**The findings in this report are not to be construed as an official Department of the Army position unless so designated by other authorized documents.**

**92-05323**



## NOTICE

### Disclaimer

The findings in this report are not to be construed as an official Department of the Army position unless so designated by other authorized documents.

### Disposition

Destroy this report when it is no longer needed. Do not return it to the originator.

Unclassified

SECURITY CLASSIFICATION OF THIS PAGE

## REPORT DOCUMENTATION PAGE

Form Approved  
OMB No. 0704-0188

1. REPORT SECURITY CLASSIFICATION Unclassified		1b. RESTRICTIVE MARKINGS	
2. SECURITY CLASSIFICATION AUTHORITY		3. DISTRIBUTION / AVAILABILITY OF REPORT Approved for public release; distribution unlimited	
b. DECLASSIFICATION / DOWNGRADING SCHEDULE			
4. PERFORMING ORGANIZATION REPORT NUMBER(S)		5. MONITORING ORGANIZATION REPORT NUMBER(S)	
6a. NAME OF PERFORMING ORGANIZATION Argonne National Laboratory	6b. OFFICE SYMBOL (If applicable)	7a. NAME OF MONITORING ORGANIZATION	
c. ADDRESS (City, State, and ZIP Code) 9700 South Cass Avenue Argonne, IL 60439		7b. ADDRESS (City, State, and ZIP Code)	
8a. NAME OF FUNDING / SPONSORING ORGANIZATION U.S. Army Medical Research and Development Command	8b. OFFICE SYMBOL (If applicable)	9. PROCUREMENT INSTRUMENT IDENTIFICATION NUMBER 90PP0819	
c. ADDRESS (City, State, and ZIP Code) Fort Detrick Frederick, Maryland 21702-5012		10. SOURCE OF FUNDING NUMBERS	
		PROGRAM ELEMENT NO. 62720A	PROJECT NO. 3E1- 62720A835
		TASK NO. CA	WORK UNIT ACCESSION NO. 291
1. TITLE (Include Security Classification) (U) Assessment and Computerized Modeling of the Environmental Deposition of Military Smokes			
2. PERSONAL AUTHOR(S) G. E. DeVaul, D. F. Brown, W. E. Dunn and A. J. Policastro			
3a. TYPE OF REPORT Final	13b. TIME COVERED FROM 7/1/90 TO 9/30/90	14. DATE OF REPORT (Year, Month, Day) October 5, 1990	15. PAGE COUNT 438
6. SUPPLEMENTARY NOTATION Subtitle: Fluctuating Concentrations in Atmospheric Dispersion			
7. COSATI CODES		18. SUBJECT TERMS (Continue on reverse if necessary and identify by block number)	
FIELD	GROUP	SUB-GROUP	
04	01		
07	03		
		RA 3, smoke, screening smoke, obscuring smoke, hexachloroethane, gas chromatography	
9. ABSTRACT (Continue on reverse if necessary and identify by block number) This report presents the average and instantaneous concentration measurements from a series of atmospheric dispersion experiments conducted under both stable and unstable atmospheric conditions. The experiments were undertaken at two different sites over both flat and complex terrain. Fog oil and hexachloroethane (HC) chemical smoke were the surface-level point aerosols used in these experiments. Depending on the site and atmospheric conditions, measurements of concentration at points along crosswind transects were taken over time periods of an hour at distances from 25m to 3000m from the source. These measurements included both aerosol photometer records for instantaneous concentration data and aspirated filter cassettes for average concentration data. The data taken in these tests compare well with developed models for both the mean and variance in concentration. Intermittency is important at all locations, with positive concentrations recorded in the mean plume centerline only 20% to 50% of the time. Concentration fluctuation intensity ranges from 2 near the plume centerline to over 20 at the plume edge. Point histograms are shown to agree with the exponential distribution for $c > 0$ . Spectra for the concentration data show an inertial-convective subrange with a 5/3-power law versus frequency behavior. Integral time scales at individual points are relatively constant within tests and are equal to the mean duration of episodes or bursts with $c > 0$ . The probability distribution of individual burst durations at each sampler shows an exponential distribution.			
10. DISTRIBUTION/AVAILABILITY OF ABSTRACT <input type="checkbox"/> UNCLASSIFIED/UNLIMITED <input checked="" type="checkbox"/> SAME AS RPT. <input type="checkbox"/> DTIC USERS		21. ABSTRACT SECURITY CLASSIFICATION Unclassified	
12a. NAME OF RESPONSIBLE INDIVIDUAL Mary Frances Bostian		22b. TELEPHONE (Include Area Code) 301-663-7325	22c. OFFICE SYMBOL SGRD-RMI-S

D FORM 1473, JUN 86

Previous editions are obsolete.

SECURITY CLASSIFICATION OF THIS PAGE

UN

## FOREWORD

Opinions, interpretations, conclusions and recommendations are those of the author and are not necessarily endorsed by the U.S. Army.

\_\_\_\_\_ Where copyrighted material is quoted, permission has been obtained to use such material.

\_\_\_\_\_ Where material from documents designated for limited distribution is quoted, permission has been obtained to use the material.

\_\_\_\_\_ Citations of commercial organizations and trade names in this report do not constitute an official Department of the Army endorsement or approval of the products or services of these organizations.

\_\_\_\_\_ In conducting research using animals, the investigator(s) adhered to the "Guide for the Care and Use of Laboratory Animals," prepared by the Committee on Care and Use of Laboratory Animals of the Institute of Laboratory Animal Resources, National Research Council (NIH Publication No. 86-23, Revised 1985).

\_\_\_\_\_ For the protection of human subjects, the investigator(s) have adhered to policies of applicable Federal Law 45CFR46.

A. J. Policastro/wed 10/5/90  
PI Signature Date

Accession For	
NTIS GRA&I	<input checked="checked" type="checkbox"/>
DTIC TAB	<input type="checkbox"/>
Unannounced	<input type="checkbox"/>
Justification	
By	
Distribution/	
Availability Codes	
Dist	Avail and/or Special
A-1	



## EXECUTIVE SUMMARY

Most studies of atmospheric dispersion have focused on long-term average concentrations for pollution and hazard assessment. More recent work has included modeling of instantaneous or short-term concentrations. Instantaneous values of concentration can vary considerably from the long-term averages. Modeling methods for these instantaneous concentrations are not well developed because of the lack of good experimental data.

This report presents the average and instantaneous concentration measurements from a series of atmospheric dispersion experiments conducted under both unstable and stable meteorological conditions. The experiments were undertaken at two different sites, over both flat and complex terrain. Two types of surface-level point aerosol sources were used. One is a fog-oil smoke and the other is a hexachloroethane (HC) chemical smoke. Measurements of concentration at points along crosswind transects were taken over time periods of an hour at distances up to several kilometers from the source. These measurements included both aerosol photometer records for assessment of instantaneous concentration fields and aspirated filters for assessment of mean concentrations.

The flat-terrain site was located at Camp Atterbury, Indiana. Wind measurements were made from a 10-m micrometeorological tower near the center of the test grid and at the source location. Upper-level air measurements were taken from National Climatic Data Center records made at Peoria, Illinois and Dayton, Ohio. Both mean dosage and real-time data were recorded along crosswind transects at distances from 50 m to 450 m from the source.

The second set of dispersion tests were carried out at a site near Red Bluff, California. Two sampling grids were used due to the nature of the terrain and windfield. The daytime tests included crosswind concentration measurements at distances from 25 m to 250 m downwind from the source in a relatively flat area of the test site. Nighttime tests included crosswind measurement of concentration data at distances from 25 m to 3000 m downwind from a second source location in a winding valley. Surface-level wind instrumentation at this site included 14 surface stations, a 30-m micrometeorological tower, and 2 sonic anemometers. Measurement of upper-level winds were obtained from balloon soundings at the site.

The average concentration data appear to be consistent and valid, showing favorable agreement with both Gaussian-plume and mixed-layer mean concentration models. The real-time data show that concentration intermittency is important at all locations, and that positive concentrations ( $c > 0$ ) are present on the mean plume centerline only 20% to 70% of the time. Concentration fluctuation intensity ranges from 2 near the plume centerline to greater than 20 at the plume edge. Point concentration histograms are shown to agree with the exponential distribution for  $c > 0$ .

Spectra of the concentration data show an inertial-convective subrange with a  $5/3$ -power law versus frequency behavior. Integral time scales of the concentration records at all individual sampling points are approximately constant within a test and are equal to the mean duration of episodes or bursts with  $c > 0$ . The probability distribution of individual burst durations at each sampler shows an exponential distribution.

## **ACKNOWLEDGEMENT**

The authors wish to thank the staff of the Atterbury Reserve Forces Training Center for their assistance in the Atterbury-87 field study. We also wish to acknowledge the contributions of the many organizations which participated in the AMADEUS dispersion experiments in California

The contributions of Dr. James C. Liljegren and Mr. Daniel Maloney were especially noteworthy. Their efforts in the field and subsequent data analysis were vital to the acquisition, assessment and understanding of the data.

We also wish to thank Major John Young and Major David Parmer of the U. S. Army Biomedical Research and Development Laboratory for their important role in shaping the project. It is through their efforts that our involvement in the AMADEUS experiments was made possible. Moreover, their many helpful suggestions and insightful comments added enormously to the success of our effort.

## TABLE OF CONTENTS

	<u>Page</u>
EXECUTIVE SUMMARY .....	1
ACKNOWLEDGEMENT.....	3
TABLE OF CONTENTS.....	4
LIST OF FIGURES .....	7
LIST OF TABLES .....	14
NOMENCLATURE .....	16
1.0 INTRODUCTION.....	22
2.0 PREVIOUS WORK IN DISPERSION AND ATMOSPHERIC TURBULENCE.....	27
2.1 Review of Experiments and Dispersion Modeling in the Atmosphere.....	27
2.1.1 Mean Concentrations .....	28
2.1.2 Fluctuating Concentrations .....	32
2.2 The Atmosphere.....	38
2.3 The Atmospheric Boundary Layer.....	42
2.3.1 Unstable Boundary Layer.....	44
2.3.2 Stable Boundary Layer.....	44
2.3.3 Velocity and Temperature Scaling in the Atmospheric Boundary Layer .....	46
3.0 THE THEORY OF TURBULENT DISPERSION.....	58
3.1 Brownian Diffusion .....	59
3.1.1 The Diffusion Equation and the Langevin Equation .....	59
3.1.2 Relating the Stochastic Theory and the Diffusion Equation.....	61
3.1.3 General Solutions of the Diffusion Equation .....	63
3.2 Turbulent Dispersion .....	64
3.2.1 Mean Concentrations in Turbulent Dispersion .....	65
3.2.2 Mean Dispersion in Anisotropic Flow.....	72
3.3 Models of Mean Dispersion .....	75
3.3.1 Cross Wind Integrated Concentration in the Surface Layer.....	77
3.3.2 Lateral Width Calculations.....	80
3.3.3 Lagrangian Integral Scales in Turbulent Dispersion .....	80
3.4 Fluctuating Concentrations .....	81
3.4.1 Theory of Relative Cloud Dispersion.....	82
3.4.2 Relative Dispersion Modeling Results.....	88
3.4.3 Relative Dispersion Measurements .....	90
3.4.4 Peak to Mean Ratios Found from the Relative Dispersion Analysis.....	91

	<u>Page</u>
3.5 Concentration Fluctuations at a Point.....	92
3.5.1 Variance in Concentration at a Point.....	92
3.5.2 Probability Density Function of Concentration of a Point .....	99
3.5.3 Concentration Exceedance .....	104
4.0 METEOROLOGICAL INSTRUMENTATION AND MEASUREMENTS.....	109
4.1 The Camp Atterbury Site.....	109
4.1.1 The Sampling Grid at Camp Atterbury.....	109
4.1.2 Meteorological Instrumentation at Camp Atterbury.....	112
4.1.3 Meteorological Parameters and Scaling Variables.....	113
4.2 The Meadowbrook Site .....	139
4.2.1 Meadowbrook Meteorology .....	139
4.2.2 Meadowbrook Tests under Unstable Meteorological Conditions .....	144
4.2.3 Meadowbrook Tests under Stable Meteorological Conditions .....	166
5.0 SAMPLING, ANALYSIS, AND CHARACTERIZATION OF SMOKE.....	185
5.1 Mean Dosage Sampling Equipment.....	185
5.2 Aerosol Measurements and Collection .....	186
5.2.1 Aerosol Particle Size Measurement Instrumentation.....	186
5.2.2 Aerosol Particle Size Distributions.....	190
5.3 Fog-oil Smoke .....	194
5.3.1 Source Characteristics and Measurements .....	194
5.3.2 Analysis Methods for the Mean Dosage Samples of Fog Oil Smoke.....	196
5.3.3 Fog Oil Mean Concentration Error Analysis.....	211
5.4 HC Smoke Analysis.....	223
5.4.1 Source Characteristics and Chemical Constituents of the HC Smoke .....	223
5.4.2 Analysis Method for HC Smoke .....	230
5.4.3 HC Smoke Analysis Errors.....	234
5.4.4 HC Smoke Field Sample Analysis Errors .....	239
5.5 Real-Time Concentration Measurement Instruments .....	239
5.5.1 Types of Real-Time Measurement Instruments .....	241
5.5.2 Design, Construction, and Refinement of an Aerosol Photometer.....	243
6.0 EXPERIMENTAL RESULTS AND ANALYSIS .....	254
6.1 Camp Atterbury Fog Oil Smoke Data Analysis .....	254
6.1.1 Mean Concentration Data .....	254
6.1.2 Standard Deviation in Concentration .....	270
6.1.3 The Concentration Probability Distribution.....	274
6.1.4 Spatial Correlations of the Instantaneous Concentration Measurements .....	280
6.1.5 Autocorrelations and Spectra of the Concentration Records.....	282
6.1.6 Concentration Exceedance .....	292

	<u>Page</u>
6.2 Camp Atterbury HC Smoke Data Analysis .....	295
6.2.1 Mean Concentrations .....	306
6.2.2 Fluctuations in Concentration .....	312
6.2.3 Correlations and Spectra .....	312
6.2.4 Concentration Exceedance .....	320
6.3 Meadowbrook Fog-oil Dispersion Tests in Unstable Atmospheric Conditions ...	320
6.3.1 Mean Concentrations .....	325
6.3.2 Fluctuations in Concentration .....	336
6.3.3 Correlations and Spectra .....	336
6.3.4 Concentration Exceedance .....	350
6.4 Stable Meadowbrook Data .....	350
6.4.1 Mean Concentration Data .....	357
6.4.2 Fluctuating Concentration Data .....	373
6.4.3 Spectra of the Concentration Fluctuations .....	386
6.4.4 Concentration Exceedance .....	386
7.0 EXAMINATION OF THE PRECISION IN THE DATA-MODEL COMPARISONS .....	401
7.1 Mean Concentrations .....	401
7.1.1 The Field of Mean Concentration .....	401
7.1.2 Mean Plume Dimensions and Parameters .....	404
7.2 Fluctuating Concentrations .....	408
7.2.1 Intermittency and the Standard Deviation in Concentration .....	408
7.2.2 Temporal Measures of the Concentration Fluctuations .....	411
7.3 Standard Deviation in Time Averaged Mean Concentrations .....	415
7.4 Confidence Level Predictions .....	416
7.5 Empirical Concentration Model Summary .....	419
8.0 CONCLUSIONS .....	422
8.1 Meteorology and Mean Concentration Measurements .....	422
8.1.1 Camp Atterbury Dispersion Measurements .....	422
8.1.2 Meadowbrook Dispersion Measurements .....	423
8.2 Fluctuating Concentration Measurements .....	423
REFERENCES .....	426

## LIST OF FIGURES

<u>Figure</u>	<u>Page</u>
1.1 Time series of data from a real time concentration measurement .....	23
1.2 Comparison of mean concentration field to the instantaneous concentration field .....	25
2.1 Time scales in atmospheric turbulence for sources and sinks of turbulent kinetic energy .....	40
2.2 Spectra of the horizontal wind speed .....	41
2.3 Nomagram for scaling in the idealized unstable atmospheric boundary layer .....	45
2.4 Nomagrams for scaling in the idealized stable atmospheric boundary layer ..	47
3.1 An example of the step and delta functions for a record of concentration at a point .....	106
4.1 Topographical map of the Camp Atterbury dispersion site .....	110
4.2 Long term meteorological data from Camp Atterbury .....	111
4.3 Mean velocity profiles from Camp Atterbury meteorological data .....	116
4.4 Mean temperature profiles from Camp Atterbury meteorological data .....	117
4.5 Vertical standard deviation of velocity measured on the 10-m meteorological tower .....	119
4.6 Standard deviations in u-component velocity for the Camp Atterbury meteorological data .....	124
4.7 Standard deviations in v-component velocity for the Camp Atterbury meteorological data .....	125
4.8 Standard deviations in w-component velocity for the Camp Atterbury meteorological data .....	126
4.9 Spectra of the wind data from Camp Atterbury .....	127
4.10 Integral scales for the Camp Atterbury meteorological data .....	136
4.11 Topographical map of the Meadowbrook dispersion site .....	141
4.12 Vegetation types for the Meadowbrook test site .....	142
4.13 Vegetation height for the Meadowbrook test site .....	143

<u>Figure</u>	<u>Page</u>
4.14 Long term records of wind direction for the Meadowbrook meteorological towers .....	145
4.15 Long term wind velocity records for the Meadowbrook meteorological towers .....	147
4.16 Long term temperature records for the Meadowbrook meteorological towers .....	149
4.17 Wind vector map for the unstable dispersion tests .....	151
4.18 Distribution of the bulk Richardson number over the dispersion site for the unstable dispersion tests .....	156
4.19 Potential temperature profiles for the unstable dispersion tests.....	162
4.20 Standard deviations in u-component velocity for the Meadowbrook 30-m meteorological tower data .....	167
4.21 Standard deviations in v-component velocity for the Meadowbrook 30-m meteorological tower data .....	168
4.22 Standard deviations in w-component velocity for the Meadowbrook 30-m meteorological tower data .....	169
4.23 Wind vector map for the stable dispersion tests .....	170
4.24 Distribution of the bulk Richardson number over the dispersion site for the stable dispersion tests .....	177
5.1 Schematic of a inertial impaction stage for a aerosol particle separator .....	187
5.2 Impactor cutoff curves.....	189
5.3 Particle size distributions for fog-oil smoke measured in the Camp Atterbury field tests .....	192
5.4 Particle size distributions for HC smoke measured in the Camp Atterbury field tests .....	192
5.5 Diagram of the US Army M3A4 fog-oil smoke generator .....	195
5.6 Plots of release rates and exit temperatures for the fog-oil smoke generator at Camp Atterbury.....	197
5.7 Gas chromatograph schematic.....	206
5.8 A chromatogram of fog-oil overlayed with a chromatogram of a series of n-paraffin oils.....	210



<u>Figure</u>		<u>Page</u>
5.9	Velocity versus particle stopping distance and Stokes number for fog-oil smoke aerosol .....	215
5.10	Minimum mass concentrations of n-paraffins required for saturated vapor to exist at atmospheric pressure .....	218
5.11	Partitioning of vapor and aerosol in a fog-oil smoke sample .....	219
5.12	Oil losses for several methods of filter storage .....	222
5.13	Ratio of standard deviation to variance for average mean concentrations measured by multiple filters on the same sampling mast .....	224
5.14	Release rates and exit temperatures for single HC smoke pots .....	226
5.15	Releases rates versus time for the HC smoke dispersion tests at Camp Atterbury .....	228
5.16	A chromatogram of HC smoke vapor .....	235
5.17	Velocity versus particle stopping distance and Stokes number for HC aerosol smoke .....	238
5.18	Ratio of standard deviation to variance for mean HC smoke concentrations measured by multiple filters on the same sampling mast .....	240
5.19	Mechanical diagram of the aerosol photometer .....	245
5.20	Normalized spectral response of a silicon photodetector and light output of a tungsten bulb .....	246
5.21	Light scattering for fog-oil smoke and HC smoke using a tungsten-filament bulb with a silicon detector .....	248
5.22	Detector electronics for the aerosol photometer.....	250
5.23	Frequency response for the aerosol photometer electronics .....	252
5.24	Temporal response for the aerosol photometer .....	253
6.1	Sampler and source locations for the fog-oil smoke dispersion tests at Camp Atterbury .....	255
6.2	Profiles of fog-oil concentration measured along the sampling transects in the Camp Atterbury dispersion tests .....	256
6.3	Estimated plume widths for the fog-oil dispersion tests at Camp Atterbury as compared with model results .....	266
6.4	Cross wind integrated concentrations versus travel time for the fog-oil tests at Camp Atterbury.....	268

<u>Figure</u>		<u>Page</u>
6.5	Mixed-layer scaling for the crosswind integrated ground level concentrations for the fog-oil tests at Camp Atterbury.....	269
6.6	Mixed-layer scaling for the time averaged plume widths measured in the Camp Atterbury fog-oil dispersion tests.....	271
6.7	Normalized crosswind profile of mean concentration for the Camp Atterbury fog-oil dispersion tests .....	272
6.8	Standard deviation in concentration normalized by the centerline mean concentration for the Camp Atterbury fog-oil dispersion tests .....	273
6.9	Crosswind profile of the fluctuation intensity of concentration for the fog-oil tests at Camp Atterbury.....	275
6.10	A comparison of the histograms in concentration with the exponential distribution for the fog-oil tests at Camp Atterbury .....	276
6.11	Crosswind intermittency for the Camp Atterbury fog-oil dispersion tests ....	281
6.12	Cross correlation coefficients for the data taken in the Camp Atterbury fog-oil dispersion experiments .....	283
6.13	Joint intermittency for the data taken in the Camp Atterbury fog-oil dispersion experiments .....	284
6.14	Structure function for the concentration data taken in the Camp Atterbury fog-oil dispersion experiments .....	285
6.15	The root mean square plume width about its relative centerline for the fog-oil dispersion tests at Camp Atterbury.....	286
6.16	Spectra of the concentration variance for the fog-oil tests at Camp Atterbury .....	288
6.17	Ensemble averaged spectra of the concentration fluctuations measured in the Camp Atterbury fog-oil dispersion tests .....	293
6.18	Duration of bursts in concentration with $c > 0$ , versus the integral scale in concentration for the Camp Atterbury fog-oil dispersion tests.....	294
6.19	Histogram of time intervals for which the concentration exceeds zero .....	296
6.20	The crosswind distribution of intervals between smoke event starts for the fog-oil smoke tests at Camp Atterbury .....	299
6.21	Sampler and source locations for the HC smoke dispersion tests at Camp Atterbury .....	300
6.22	Profiles of zinc concentration in the HC smoke dispersion experiments at Camp Atterbury .....	301

<u>Figure</u>	<u>Page</u>
6.23 A model-data comparison for the HC smoke concentration measurements taken in the Camp Atterbury dispersion tests .....	307
6.24 Estimated plume widths for the HC smoke dispersion tests at Camp Atterbury as compared with a model.....	309
6.25 Mixed-layer scaling for the crosswind integrated ground level concentrations measured in the Camp Atterbury HC dispersion tests .....	310
6.26 Normalized crosswind profile of the mean concentration for the Camp Atterbury HC smoke dispersion tests.....	311
6.27 Crosswind profile of the fluctuation intensity of concentration for the HC smoke tests at Camp Atterbury .....	313
6.28 Crosswind intermittency for the Camp Atterbury HC smoke dispersion tests .....	314
6.29 A comparison of the histograms in concentration with the exponential distribution for the HC smoke tests at Camp Atterbury .....	315
6.30 Spectra of the concentration variance for the HC smoke tests at Camp Atterbury .....	317
6.31 Ensemble averaged spectra of the concentration fluctuations measured in the HC smoke dispersion tests at Camp Atterbury.....	319
6.32 Duration of bursts in concentration with $c > 0$ , versus the integral scale in concentration for the Camp Atterbury HC smoke dispersion tests.....	321
6.33 Histogram of time intervals for which the concentration exceeds zero for the HC smoke dispersion tests at Camp Atterbury.....	322
6.34 The crosswind distribution of intervals between smoke event starts for the HC smoke tests at Camp Atterbury .....	324
6.35 Terrain, instrument locations, and vegetation for the daytime unstable Meadowbrook dispersion site .....	326
6.36 Measured wind vectors over the test duration for the daytime unstable dispersion tests at the Meadowbrook site .....	327
6.37 Profiles of fog-oil concentration measured along the sampling transects in the daytime unstable Meadowbrook dispersion tests .....	328
6.38 Estimated plume widths for the fog-oil dispersion tests at Meadowbrook in daytime unstable conditions as compared with model results.....	333
6.39 Mixed-layer scaling using the free convection limit for the cross wind integrated ground level concentrations measured in the daytime unstable fog-oil dispersion tests at the Meadowbrook site.....	334

<u>Figure</u>		<u>Page</u>
6.40	Mixed-layer scaling using the for the time averaged plume widths measured in the daytime unstable fog-oil dispersion tests at the Meadowbrook site .....	335
6.41	Normalized crosswind profile of mean concentration for the daytime unstable Meadowbrook dispersion tests.....	337
6.42	Crosswind profile of the standard deviation in concentration normalized by the centerline mean concentration for the daytime unstable Meadowbrook dispersion tests .....	338
6.43	Crosswind profile of fluctuation intensity of concentration for the daytime unstable dispersion tests at the Meadowbrook site.....	339
6.44	A comparison of the histograms in concentration with the exponential distribution for the HC smoke tests at Camp Atterbury .....	340
6.45	Crosswind intermittency for the daytime unstable Meadowbrook dispersion tests .....	345
6.46	Spectra of the concentration variance for the HC smoke tests at Camp Atterbury .....	346
6.47	Ensemble averaged spectra of the concentration fluctuations measured in the unstable Meadowbrook dispersion tests .....	347
6.48	Duration of bursts in concentration with $c > 0$ , versus the integral scale in concentration for the unstable Meadowbrook smoke dispersion tests .....	351
6.49	Histogram of time intervals for which the concentration exceeds zero for the unstable Meadowbrook smoke dispersion tests.....	352
6.50	The crosswind distribution of intervals between smoke event starts for the unstable Meadowbrook smoke dispersion tests .....	355
6.51	Map of the sampler locations for the Meadowbrook stable dispersion tests ..	356
6.52	The near-source sampling transects for the stable Meadowbrook dispersion tests .....	358
6.53	Source wind vectors for the stable dispersion tests at Meadowbrook .....	359
6.54	Elevation of samplers along the sampling transects for the stable dispersion grid at the Meadowbrook site.....	360
6.55	Profiles of fog-oil concentration measured along the sampling transects for the stable Meadowbrook dispersion tests .....	361
6.56	Wind speeds along the smoke plume path for the fog-oil dispersion tests at Meadowbrook .....	374

<u>Figure</u>		<u>Page</u>
6.57	Crosswind integrated concentration versus downwind distance for the stable dispersion tests at Meadowbrook.....	375
6.58	Estimated plume widths for the stable dispersion tests at Meadowbrook as compared with model predictions .....	376
6.59	Normalized crosswind profile of mean concentration for the stable fog-oil dispersion tests at Meadowbrook .....	377
6.60	Crosswind profile of the standard deviation in concentration normalized by the centerline mean concentration for the stable Meadowbrook dispersion tests .....	378
6.61	Crosswind profile of fluctuation intensity of concentration for the stable Meadowbrook dispersion tests .....	379
6.62	A comparison of the histograms in concentration with the exponential distribution for the HC smoke tests at Camp Atterbury .....	380
6.63	Crosswind intermittency for the stable Meadowbrook dispersion tests .....	387
6.64	Concentration spectra for the stable Meadowbrook dispersion tests.....	388
6.65	Duration of bursts in concentration with $c > 0$ , versus the integral scale in concentration for the stable Meadowbrook smoke dispersion tests .....	393
6.66	Histogram of time intervals for which the concentration exceeds zero for the stable Meadowbrook dispersion tests .....	394
7.1	The ratio of predicted to measured cross wind integrated concentration using the Gaussian plume model.....	406
7.2	The ratio of predicted to measured cross wind integrated concentration using the mixed-layer scaling model.....	407
7.3	Stability parameter $z_i/L$ versus the integral scale of concentration.....	413
7.4	Levels of concentration for which $P(c) = 0.99$ from the data as compared with model predictions .....	417

## LIST OF TABLES

<u>Table</u>	<u>Page</u>
2.1 Scales of motion in the atmosphere .....	38
4.1 Meteorological scaling values for the Camp Atterbury dispersion tests .....	118
4.2 Inversion heights for the Camp Atterbury tests.....	122
4.3 Meteorological surface-layer scaling parameters for the unstable Meadowbrook dispersion tests .....	161
4.4 Inversion heights estimated for the unstable Meadowbrook dispersion tests .....	166
4.5 Meteorological scaling parameters for the unstable Meadowbrook dispersion tests .....	184
5.1 Cut Sizes for the California Measurements PC-2 cascade impactor.....	188
5.2 Measured particle size parameters for the lognormal distribution .....	193
5.3 Calculated particle diameters for fog-oil smoke and HC smoke using the Hatch-Choate equations for the lognormal distribution.....	193
5.4 Mass release rates for the fog-oil smoke generator.....	204
5.5 Key parameters of gas chromatography method used to analyze fog-oil smoke vapor samples .....	208
5.6 Approximate fog-oil molecular weight distribution .....	211
5.7 Flow meter corrections for the sampling filters.....	212
5.8 Settling velocities for the fog-oil smoke aerosol.....	216
5.9 Composition of unburned HC smoke mixture.....	225
5.10 Gaseous combustion products of HC smoke.....	225
5.11 Ratio of zinc to aluminum in HC smoke .....	227
5.12 Mass releases and mean release rates for HC smoke tests .....	230
5.13 Average composition of the HC smoke aerosol .....	232
5.14 Key parameters of gas chromatography method used to analyze HC smoke vapor samples.....	233
5.15 Ratio of zinc concentration to that of the identified organic vapor compound.....	234

<u>Table</u>	<u>Page</u>
5.16 Flow meter corrections for the sampling filters.....	236
5.17 Settling velocities for HC smoke aerosol.....	239
6.1 Average integral scales of the concentration fluctuations for the Camp Atterbury fog-oil dispersion tests .....	292
6.2 Average integral scales of the concentration fluctuations for the HC dispersion tests at Camp Atterbury.....	312
6.3 Average integral scales of the concentration fluctuations for the unstable Meadowbrook dispersion tests .....	350
7.1 Model-data correlation coefficients for mean concentrations in the unstable dispersion tests.....	402
7.2 Comparison of models to mean concentration data on a point by point basis .....	403
7.3 Plume width model-data comparison .....	405
7.4 Mixed-layer scaling comparison of model and data values.....	405
7.5 Gaussian plume shape scaling.....	409
7.6 Concentration fluctuation intensity.....	410
7.7 Intermittency errors and conditionally averaged data ratios .....	411
7.8 Comparison of the integral scale and the mean burst durations.....	414
7.9 Errors in the mean concentrations measured in the dispersion tests.....	415
7.10 Errors in the ratio of measured to predicted $c_{99}$ for the dispersion tests.....	419

## NOMENCLATURE

<u>Symbol</u>	<u>Meaning</u>
$c$	Mass concentration
$c_\xi$	Concentration level at which $P(c_\xi) = \xi$
$C_p$	Specific heat of air
$C_D$	Drag coefficient
$C_y$	Dimensionless crosswind integrated concentration, $\bar{c}_y z_i \bar{u}_x / q$
$c_i$	Centroid of concentration field
$\bar{c}_s$	Conditional mean concentration, $\bar{c}/I$
$\bar{c}_y$	Crosswind integrated concentration
$d_{ij}$	Standard deviation tensor of concentration field
$d_p$	Diameter of an aerosol particle
$d_g$	Geometric mean of a particle size distribution
$\hat{d}$	Mode of a count particle size distribution (most frequently occurring diameter)
$\bar{d}$	Count mean diameter of a particle size distribution
$\bar{d}_{50}$	Count median diameter of a particle size distribution, (equal to $d_g$ for a lognormal distribution)
$d_m$	Diameter of average mass for a particle size distribution, (that diameter, when multiplied by the total number of particles, gives the total mass)
$\bar{d}_{m50}$	Mass median diameter for a particle size distribution, (50% point of the mass weighted distribution)
$\bar{d}_{mm}$	Mass mean diameter of a particle size distribution
$dW_t$	Gaussian white noise
$E(\kappa)$	Turbulent kinetic energy spectrum, $\kappa^2 = \kappa_x^2 + \kappa_y^2 + \kappa_z^2$
$f$	Dimensionless frequency $nz/\bar{u}_x$
$f_i$	Dimensionless frequency $nz_i/\bar{u}_x$
$F$	Surface-layer velocity function, $\bar{u}/u_*$



<u>Symbol</u>	<u>Meaning</u>
$G$	Surface-layer temperature function, $(T(z)-T_0)/T_*$
$g$	Gravitational constant
$g, g_i$	Instantaneous center of mass of a concentration field
$H$	Surface heat flux
$h$	Boundary layer height
$I$	Concentration intermittency
$I$	Light intensity
$i_\parallel, i_\perp$	Intensity of scattered light parallel and perpendicular, respectively, to a scattering element
$L$	Monin-Obukhov length
$N$	Dissipation rate of concentration variance
$N$	Integer count index, total number of steps or particles
$n$	Frequency
$p(x)$	Probability density function of random variable $x$
$P(x)$	Probability distribution of random variable $x$
$P$	Pressure
$Pr$	Prandtl number, $\nu/\alpha$
$Q_0$	Kinematic heat flux
$Q$	Volumetric flow rate
$q$	Mass release rate
$r$	Radial coordinate direction
$Re$	Reynolds number
$Re_p$	Reynolds number of an aerosol particle
$Ri$	Gradient Richardson number
$Ri_B$	Bulk Richardson number
$R_{ij}$	Autocorrelation function for velocity $i = u, v, w$

<u>Symbol</u>	<u>Meaning</u>
$R_{cc}$	Autocorrelation function for concentration
$s$	Vertical concentration distribution shape parameter exponent
$S_{ii}(n)$	One-dimensional single-sided spectra of velocity, $i = u, v, w$
$S_{cc}(n)$	One-dimensional single-sided spectra of concentration fluctuation
$Sc$	Schmidt number
$St$	Stokes number
$T$	Temperature
$T$	Total averaging time or test duration
$T_*$	Surface-layer temperature parameter
$T_0$	Temperature at height $z_0$
$t, t', t''$	Time
$t_0$	Initial time
$t_L$	Lagrangian integral time scale
$t_E$	Eulerian integral time scale
$u, v, w$	Velocity components in the mean flow direction, the crosswind flow direction, and the vertical direction respectively
$u_i$	Eulerian velocity component, $i = x, y, z$
$\tilde{u}$	Concentration weighted mean velocity
$v_i$	Lagrangian particle velocity, $i = x, y, z$
$v_s$	Settling velocity of an aerosol particle
$W_t$	Weiner process
$x, x', x''$	Spatial position vector $(x, y, z)$
$X, X_i$	Particle displacement
$X$	Dimensionless downwind distance, $(w_s/z_i)/(x/\bar{u}_x)$
$Y, Y_i$	Lagrangian particle position
$x, y, z$	Rectangular coordinates in the mean flow direction, the crosswind flow direction, and the vertical direction respectively

<u>Symbol</u>	<u>Meaning</u>
$u_*$	Friction velocity
$w_*$	Convective velocity scale
$z_i$	Inversion height in the unstable boundary layer
$z_0$	Roughness height
$z_s$	Source height
$Z_s$	Dimensionless source height, $z_s/z_i$
$\bar{z}$	Concentration weighted mean plume height
$\alpha$	Thermal diffusivity
$\alpha$	Concentration fluctuation intensity, $\sigma_c / \bar{c}$
$\alpha, \alpha_1$	Coefficients for inertial subrange scaling of the turbulent velocity spectra
$\mathcal{A}$	Random particle acceleration
$\beta, \beta_1$	Coefficients for inertial-convective scaling of the turbulent scalar spectra
$\beta$	Relaxation time constant for an aerosol particle
$\mathcal{D}$	Mass diffusivity
$\Delta x$	Increment in $x$
$\delta$	Direc delta function
$\delta$	Initial source size
$d\omega_t$	Random forcing function
$\epsilon$	Dissipation rate of turbulent kinetic energy
$f$	Coriolis parameter
$\zeta_{ij}$	Relative separation tensor for two particles
$\phi_m, \phi_h$	Dimensionless momentum and sensible heat flux gradient functions in the surface layer
$\psi_m, \psi_h$	Dimensionless momentum and temperature profile functions in the surface layer
$\phi$	Elevation angle
$\Psi(x y), \psi(x y)$	Transition probability density function of $x$ given $y$

<u>Symbol</u>	<u>Meaning</u>
$\mathcal{R}$	Gas constant
$\phi_\epsilon$	Dimensionless dissipation rate using surface boundary layer scaling
$\psi_\epsilon$	Dimensionless dissipation rate using mixed boundary layer scaling
$\phi, \varphi$	Characteristic functions for probability density functions
$\Lambda$	Local scaling parameter in the stable boundary layer
$k$	von Karman constant
$\kappa$	Wavenumber
$\mathcal{K}_i$	Mass eddy diffusivity
$\hbar$	Plank's constant
$\ell$	Integral length scale
$\ell_E$	Eulerian integral length scale
$\ell_L$	Lagrangian integral length scale
$\lambda$	Rate parameter for a series of randomly distributed events
$\lambda$	Average rate of occurrence of single events $c > c_{\text{limit}}$ in a concentration record
$\lambda_u$	Inverse of the average continuous period with $c > c_{\text{limit}}$ in a concentration record
$\lambda_d$	Inverse of the average continuous period with $c < c_{\text{limit}}$ in a concentration record
$\lambda_{BV}$	Brunt-Vaisala frequency in stably stratified fluid
$\mu$	Viscosity coefficient
$\sigma_i$	Standard deviation in plume concentration distribution, $i = x, y, z$
$\sigma_i$	Standard deviation in velocity, $i = u, v, w$
$\sigma_{i,r}$	Standard deviation in plume concentration distribution with respect to the relative plume centroid $i = x, y, z$
$\sigma_{i,g}$	Standard deviation in the center of mass trajectories for an ensemble of concentration fields.
$\sigma_g$	Geometric standard deviation

<u>Symbol</u>	<u>Meaning</u>
$\sigma_r$	Standard deviation in the plume concentration distribution in radial coordinate system
$\sigma_c$	Standard deviation of instantaneous concentration at point
$\sigma_{c,s}$	Conditional standard deviation in concentration
$\sigma_e$	Standard deviation in the estimate of mean concentration at a point
$\Sigma_{ij}$	Relative particle dispersion tensor with respect to an instantaneous center of mass
$\nu$	Kinematic viscosity
$\mathcal{V}$	Sampling volume
$\mu$	Geometric mean
$\eta$	Kolmogorov length scale
$u$	Kolmogorov velocity scale
$\theta$	Potential temperature
$\theta$	Horizontal angle
$\rho$	Density
$\rho_f$	Density of fluid
$\rho_p$	Density of an aerosol particle
$\rho_{12}$	Correlation coefficient of random variables 1 and 2
$\mathcal{R}$	Gas constant
$\tau_c$	Integral time scale of the concentration fluctuations
$\tau_{ii}$	Shear stress tensor $i = x, y, z$

#### Miscellaneous Symbols

$\bar{\phantom{x}}$ (overbar)	Indicates time average
$\prime$ (prime)	Indicates fluctuating quantity
$\langle \phantom{x} \rangle$ (bracket)	Indicates ensemble average

## 1. INTRODUCTION

Most methods of study and modeling of atmospheric dispersion have focused on slowly varying mean concentrations for pollution and hazard assessment. The purpose of this technical report is to alternatively focus on the turbulent fluctuations and intermittency in concentrations using experimental measurements and probabilistic models.

Deliberate release of military smoke presents some unique opportunities for the study of atmospheric dispersion modeling. In many cases, smoke releases are characterized as being short term events with high concentration levels. Brief exposure to airborne materials, even at low concentrations, can be hazardous depending on the toxicity potential of the substance involved. The evaluation of concentration fluctuations can be effectively and collectively applied to industrial settings where releases of hazardous materials can occur and when explosive limits, often as low as 1%, can lead to accidents. Additionally, establishing confidence limits in mean concentration predictions and measurements requires higher order moments of the concentration field. These confidence limits are significant because of the high fluctuation intensity of concentration records and the long correlation times in atmospheric flows.

We can: (i) find a better physical description of dispersion in the atmosphere by studying the fluctuating concentrations. The probabilistic approach used in this report allows different types of releases, such as continuous plumes or instantaneous puffs of material to be treated in a similar manner and (ii) provide a means for estimating nonlinear effects of concentration in more complex situations. One effect of importance is radiational heat transfer and light propagation through a cloud. Another is in estimating mass balances of greenhouse gases in the atmosphere. Transpiration of greenhouse gases such as  $\text{CO}_2$  by plants is a highly nonlinear function of concentration.

Intermittency in concentration is defined as the fraction of time that smoke is present at a fixed point in space. A real-time record of concentration measured downwind from a small surface level smoke source is shown in Figure 1.1. This measurement was taken near the centerline of the smoke plume and is characteristic of real-time concentration measurements. A great deal of intermittency and fluctuation in concentration is present in these data demonstrating the significance of intermittency in our measurements and that average measurements alone are insufficient for describing short-term behavior. The importance of higher order statistics is further accentuated when considering that the standard deviation of the signal is of the same order as the mean, and the peak level is nearly an order of magnitude larger than the mean. Measurements taken near the edges of a plume typically exhibit much lower intermittency than shown in Figure 1.1 and can have standard deviations may be up to an order of magnitude larger than the mean.

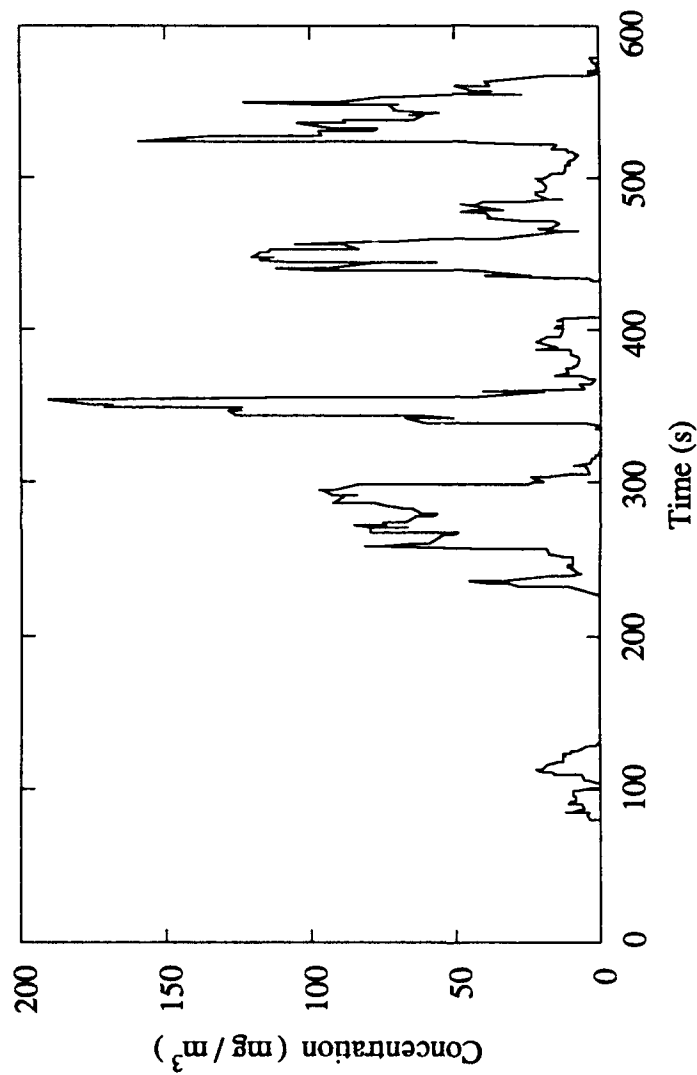


Figure 1.1 Real time concentration measurement taken with an aerosol photometer. This instrument was located 160-m downwind from a hexachloroethane (HC) smoke pot near the mean plume centerline, and data were recorded at frequency of 1 Hz. These data are from a HC test on August 1, 1986 at Camp Atterbury, Indiana over nearly flat terrain.

Most dispersion models only predict average concentrations. This average, which is taken over a period ranging from 10 minutes to an hour depending on the application, smooths the random fluctuations in the instantaneous plume. A comparison of instantaneous and time-weighted average concentration isopleths is shown in Figure 1.2. In this figure the instantaneous plume outline is supplied by an aerial photograph taken during a highly convective daytime release. The mean concentration isopleth is calculated for the same test from time-weighted average data. Although average predictions of concentration show a smooth isopleth of concentration, the visible outline of the instantaneous plume in this figure exhibits no such behavior.

The topics in this report are a subset of many possible atmospheric dispersion scenarios. This subset includes experimental tests and simple analytical models for a steady surface-level point source of a passively dispersing aerosol. Such dispersion can be considered to be the mixing of 'marked' fluid into clean fluid. The dispersion is measured over periods of up to an hour, at distances to several kilometers from the source. The wind conditions in these tests may be considered quasi-stationary and a well developed theory is used for scaling the atmospheric boundary layer.

Results of this investigation show the field of concentration variance can be predicted using a source and transport of the concentration variance similar to that for the mean field. The probability distribution of concentration at a single point in the flow is shown to follow an exponential distribution for the fraction of time that marked fluid is present at the sampling point, with an explicit intermittency, or fraction of time that marked fluid is present, at a given sampler. For mean concentrations, the variance in concentration, and the intermittency, a self-similar crosswind scaling is shown to apply and empirical models are developed to predict these quantities at ground level.

The experimental data in this report come from two sets of field dispersion experiments. The tests were conducted in nearly flat terrain near Camp Atterbury, Indiana and at the Meadowbrook Site, a mountainous area 20 miles east of Red Bluff, California. All releases were at ground level from a single smoke generator, with up to 50 sampling locations in crosswind lines at distances from the source of 50 m to 3000 m, depending on the site and the atmospheric conditions. Measurements were made of wind conditions at two locations for the Atterbury tests and up to 14 locations for the Meadowbrook tests. Instruments and methods were developed for measuring and recording the field of mean concentration and fluctuating concentration for both a fog-oil smoke and a hexachloroethane generated smoke in these tests.

The data taken in these trials comprise over 12 hours of dispersion data taken in 18 tests. Of these tests, 12 are suitable for detailed analysis. Meteorological conditions varied from highly convective daytime conditions to stable nighttime conditions. This data has been very helpful in improving the understanding of the physics of turbulent dispersion as well as the modeling of



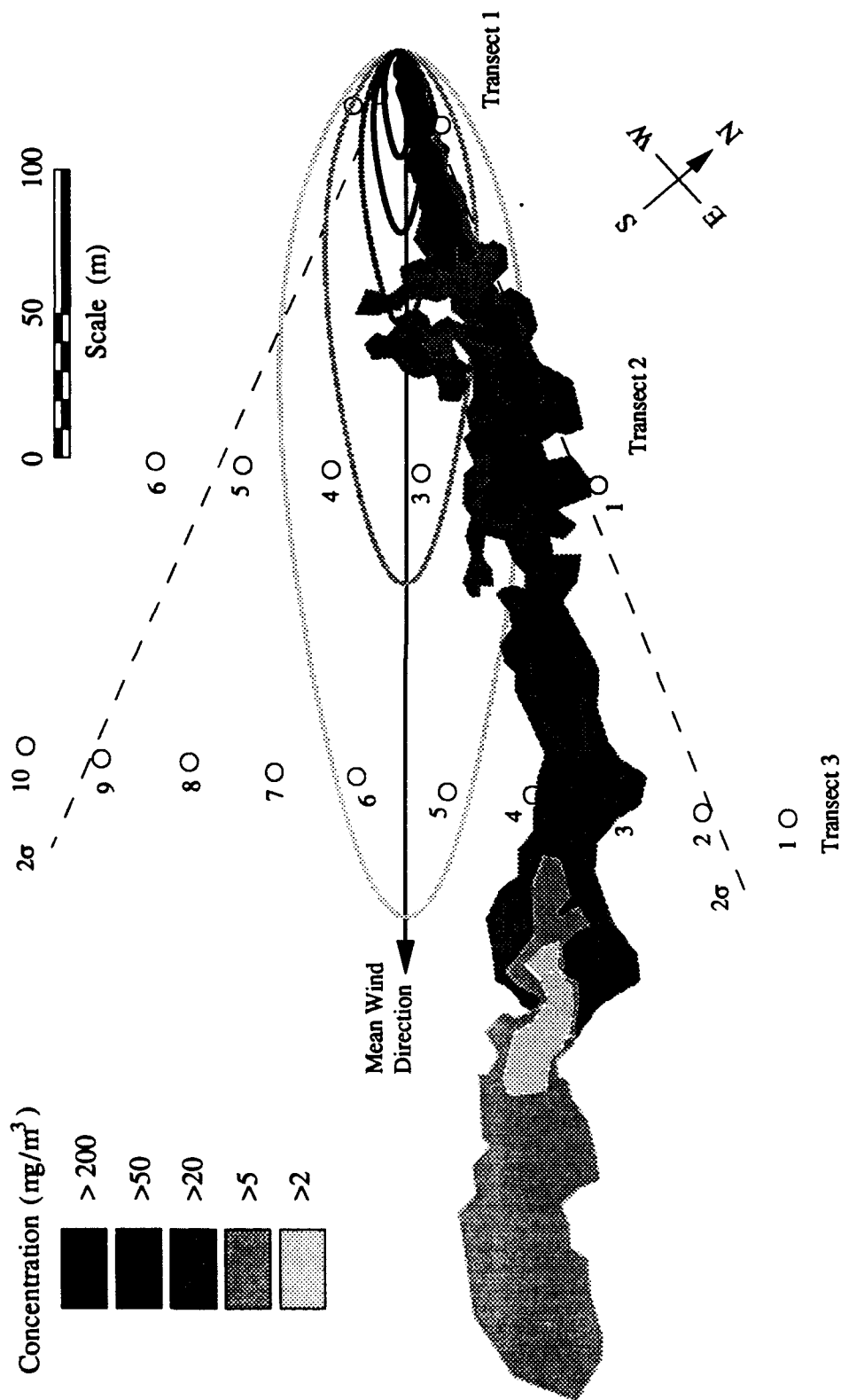


Figure 1.2 Comparison of mean concentration field to the instantaneous concentration field. These data are from Test 0926871 at the Meadowbrook unstable dispersion site. Isopleths of the average concentration field are determined from a fit to the average surface level concentration measurements and are shown as elliptical lines. The instantaneous profile is derived from an aerial photograph and is shown as a filled outline. Grays in the plume photograph are calibrated against instantaneous surface level concentration measurements.

concentration fluctuations. It is among the most complete set of data available which includes measurements of real-time tracer concentrations, source release rate data, and detailed meteorological measurements.

The following chapters of this report begin with a review of current practices in atmospheric dispersion modeling, a review of previously acquired data sets, and a discussion of the atmospheric boundary layer in Chapter 2. The theory of turbulent dispersion for both mean and fluctuating concentration fields is covered in Chapter 3. This includes a review of existing theory and a presentation of new material as it pertains to the modeling of concentration fluctuations. Descriptions of the meteorology and site characteristics are given in Chapter 4, followed by a summary of instrument descriptions and experimental analysis techniques in Chapter 5. Results and comparison of the dispersion experiments with theory are given in Chapter 6. These results are divided into sections covering the different sites and source types within a group of tests. An error analysis of the data and a summary of applicable models are covered in Chapter 7, with conclusions given in Chapter 8.

## **2. PREVIOUS WORK IN DISPERSION AND ATMOSPHERIC TURBULENCE**

### **2.1 Review of Experiments and Dispersion Modeling in the Atmosphere**

In atmospheric dispersion, most efforts are directed toward estimating means in concentration over specified periods. These averages may usually be assumed stationary for time periods less than an hour due to the presence of a gap in the turbulent energy spectra for a one-hour time period as later discussed in Section 2.2. Dispersion model inputs consist of time averaged meteorological variables and source parameters. Results are given in terms of a deterministic field of mean concentration which is constant within the averaging period but may vary in time and space with a changing time series of one-hour averaged model inputs.

Mean concentrations are not well represented by these models. For example Nieuwstadt (1980a) calculated a time series of one-hour average SO<sub>2</sub> concentrations at 30 receptor locations in a Netherlands industrial area using a Gaussian plume model. Comparison with measured values gave average correlation coefficients for each receptor in the range 0.03 to 0.39 with an overall average of 0.26. Liu and Moore (1984) also found very poor agreement between data and Gaussian model predictions for a time series of one-hour average SO<sub>2</sub> concentrations measured near Kinkaid, Illinois. They concluded that the model inputs of source strength and meteorological measurements were without skill in improving the concentration estimates.

These examples illustrate the general failure of the Gaussian model in predicting concentration. This poor agreement can be due to a bias in the model. It may also be due to insufficient meteorological or source strength data. Lamb (1984) shows the accuracy in dispersion predictions decreases with increasing distance from the source and the proximity of the meteorological measurements. This problem in accuracy arises from the fluctuations inherent in turbulent flow. No error estimate in mean concentration is provided in this type of dispersion model.

Some of the shortcomings in deterministic models have been addressed through purely statistical models derived from a series of concentration measurements. For air quality or hazard assessment, the average concentration is not as great a concern as is estimating exceedance limits or the probability density function of concentration. For air quality assessment, concentration data sets have been used to determine statistical models for concentration distributions. Larsen (1969, 1974) shows that urban pollutant concentrations are distributed approximately lognormally for all averaging times greater than an hour. Hunt (1972) and Phinney and Newman (1972) estimate the precision in fitting data sets to the lognormal distribution. Taylor et al. (1986) and Jakeman et al. (1986) investigate statistical techniques for applying other probability distributions to concentration data sets. All of the distributions are positively skewed.

These types of statistical models of concentration are based entirely on experimental measurements and requires that the time series of data is stationary. Their primary use is in estimating confidence limits for exceeding a given concentration, estimating maximum values from limited data sets, and extrapolating expected average concentrations for different sampling periods. They often neglect any causal relations such as that represented by meteorological parameters, source strengths and locations, removal mechanisms, and seasonal variations. Improvement in this type of model may incorporate some of the causal effects used in deterministic models (Jakeman et al., 1983) or may model the seasonal or diurnal behavior of a nonstationary data set (North et al., 1984).

In our effort we are ultimately concerned with the improvement of the existing models. This goal, however, entails the collection of experimental measurements which are required for the assessment of atmospheric effects as well as model calibration. We need to include more predicted information so that, in addition to the mean concentration, the full probability density function of concentration is represented within the stationary one-hour averaged period. This will allow consistent prediction of short-term (less than one hour) exceedance levels and allow calculation of error limits on averaged mean concentrations.

Exceedance levels or concentration distributions for time periods greater than 1 hr may be found using statistical distributions of meteorological and source data in combination with the short-term distribution of concentration statistics. Information on multiple sources may be obtained by superposition. This approach can allow conditional effects of meteorology and source strength on concentration levels at given locations to be examined.

### **2.1.1 Mean Concentrations**

#### **Modeling Distributions of Mean Concentration**

The body of literature for prediction of mean concentrations in the atmosphere is extensive. Excellent reviews are given by Pasquill (1974), Pasquill and Smith (1983), Randerson (1984), Panofsky and Dutton (1984), and Hanna et al. (1982). There are three basic approaches to modeling the mean concentration distribution. These include statistical methods, gradient transfer or  $\mathcal{K}$  theory, and similarity theory.

The statistical approach for turbulent dispersion was introduced by Taylor (1921) in relating Eulerian velocity statistics to the Lagrangian statistics of elements of marked fluid in homogeneous turbulence. This theory shows that far from a source the average plume growth  $\sigma_y(t)$  is proportional to  $t^{1/2}$  where  $t$  is travel time. Near the source (in the region where fluid motion is correlated),  $\sigma_y(t)$  is proportional to  $t$ . The travel time is often approximated by  $t = x/\bar{u}_x$  where  $x$  is the downstream distance and  $\bar{u}_x$  is the mean wind speed.

Sutton (1947a) used the statistical approach and  $\mathcal{K}$ -theory in a point-source atmospheric dispersion model with a Gaussian concentration distribution normal to the mean wind and a power-law decay with distance from the source. For a ground-level source and a reflective boundary, the ground-level concentration for the Gaussian plume model is written (see Csanady, 1973)

$$\bar{c}(x,y) = \frac{q}{\pi \sigma_y \sigma_z \bar{u}_x} \exp\left(-\frac{y^2}{2 \sigma_y^2}\right) \quad (2.1)$$

where  $q$  is the source strength. The plume widths in the horizontal and vertical coordinates respectively are  $\sigma_y$  and  $\sigma_z$ . These are often fitted from empirical measurements. Batchelor (1949) shows that a Gaussian crosswind distribution is found for mean concentrations in a dispersing plume for reasons which vary with the distance from the source. Near the source the velocity distributions have a Gaussian distribution and the pollutant is carried in the direction of this velocity. Farther from the source, the velocity fluctuations become independent of one another and the distribution will approach a Gaussian form from consideration of the central limit theorem (see Papoulis, 1965) and symmetry about the plume axis.

Many present day models are based on the Gaussian approach. Draxler (1976) and Gryning et al. (1987) give empirical forms for the dispersion parameters  $\sigma_y$  and  $\sigma_z$  used in this model. These equations asymptotically match the plume growth expected from Taylor's theory. Because of inhomogeneity in the atmospheric boundary layer, dispersion in the vertical direction is not always well represented by a Gaussian plume.

Gradient transfer methods have been most successful in predicting the vertical distributions of concentration close to the surface boundary. In this region the scale of the concentration gradient is greater than the size of the dispersing fluctuations in velocity. Solutions have been primarily examined through  $\mathcal{K}$ -theory models using numerical solution or analytical solutions obtained for power law approximations to  $\mathcal{K}$ . Mean concentration profiles from a surface-level source may be summarized using an equation of the form

$$c(z) = \mathcal{A} \exp\left(-\mathcal{B} \frac{y^n}{\sigma_z^n}\right) \quad (2.2)$$

and the exponent  $n$  determines the profile shape. If  $n = 2$  the distribution follows a Gaussian profile. Gryning et al. (1987) gives an exponential distribution with  $n = 1$  for neutral flow far from the source and  $n = 3$  as an asymptotic limit for stable flow. The coefficients  $\mathcal{A}$  and  $\mathcal{B}$  are examined by van Ulden (1978) and Nieuwstadt and van Ulden (1978) in a comparison with atmospheric dispersion data.

In an alternate examination of dispersion near the surface, Venkatram (1988) relates plume behavior due to velocity shear through a reexamination of Taylor's statistical approach. Also of use very near the surface are similarity solutions in which surface boundary layer parameters are used in scaling concentration measurements (Pasquill and Smith, 1983).

In unstable atmospheric conditions, mean concentration distributions are strongly affected by the vertical anisotropy of thermal plumes and downward subsidence. Deardorff (1970a) found a atmospheric convective velocity scale which also applies in Rayleigh convection. Similarity results for atmospheric dispersion using this parameter and the boundary layer height are given by Nieuwstadt (1980b) and Briggs (1985). These solutions compare favorably with laboratory measurements of dispersion in Rayleigh convection by Deardorff and Willis (1975).

Modeling in unstable flow may also be based on the statistical approach. Monte-Carlo simulations of Lagrangian particle motion have been particularly successful in this regard. Durbin (1983) gives an introduction to stochastic dispersion modeling and relates the theory for dispersion in a homogeneous field given by Batchelor (1949) to anisotropic conditions. Thomson (1984), van Dop et al. (1985) and Sawford (1986) investigate closure approximations for Lagrangian particle motion in anisotropic turbulent flow. Liljegren (1989) presents an extensive review of statistical methods and implements the Monte-Carlo dispersion model for convective dispersion in the atmosphere.

### **Experimental Work in Measuring Mean Concentration Distributions**

Experiments are necessary in estimating dispersion parameters and in determining the accuracy of the modeling approaches for mean concentrations. The most productive studies of atmospheric dispersion have focused on releasing a tracer gas or aerosol into the atmosphere and measuring the downwind concentration at given positions and times. In all cases this includes measurements of meteorological conditions, the source strength, and time-averaged downwind concentrations. The more extensive test series have focused on dispersion in flat and uniform terrain. In interpreting results from these experiments it is assumed that the tracer material is conserved and not lost by deposition on the ground or through chemical reactions.

According to Pasquill (1974), the first quantitative experiments in atmospheric dispersion began in 1923 on Salisbury Plain near Porton, Wilshire, England. Aerosols used in these experiments included smoke screens, dye-stuff, and arsenic compounds. Gases included chlorine, phosgene, and sulphur dioxide. Crosswind profiles of averaged concentrations were measured at distances up to 300 m from a point source. For distances between 300 m and 1000 m, the analysis focused on peak concentrations. Results of this work include estimates of the cloud dimensions in neutral conditions. Cloud size is also related to measurements of turbulence. Results from

dispersion tests at Porton for the period from 1932 to 1938 are summarized by Sutton (1947b) and form the basis for his Gaussian plume model.

Dispersion tests conducted at the Round Hill Field Station of the Massachusetts Institute of Technology and in Project Prairie Grass during the period from 1954 to 1957 used more sensitive detection methods for specific tracers and better meteorological instrumentation than the earlier Porton experiments. The Prairie Grass tests were conducted over flat terrain near O'Neil, Nebraska in 1956 and are summarized by Barad (1958) and Haugen (1959). This series of tests consisted of a total of 70 experiments conducted in July and August, 1956. Crosswind concentrations of a ground-level SO<sub>2</sub> tracer dispersed from a point source were measured over a 10-min averaging time at downwind distances of 50 m, 100 m, 300 m, 400 m, and 800 m. Wind fluctuations in the horizontal and vertical were measured using fast-response instruments.

Ramsdell et al. (1985) summarizes a series of over 300 dispersion experiments carried out at the Hanford site near Richland, Washington during the period from 1959 to 1974. The test area at Hanford is relatively flat with a 30 m variation in elevation within 1 km of the source. Vegetation consists of 1 to 2 m high sagebrush and steppe grasses. Up to 1000 ground-level samples per experiment were taken in these dispersion tests. The main sampling grid included transects at distances from 400 m to 12800 m. Meteorological instrumentation was mounted on a 122-m tower near the center of the site and on a 25-m tower at the source location.

Aerosol tracers used in the Hanford experiments include zinc-sulfide, fluorescein, and rhodamine dye. These were collected using filter samples with analysis based on the fluorescent properties of the material as discussed by Leighton et al. (1965). Tracer gases included krypton-85 and xenon-133. Detection methods for these radioactive tracers are described by Nickola (1971) and Ludwick et al. (1968) for the krypton-85 gas and Eggleton and Thompson (1961) for the xenon-133 gas.

Selections of data from the Porton, Hanford, and O'Neil data have been used in finding plume parameters and in validation of a wide variety of mean-concentration dispersion models. These have been supplemented by a number of less extensive dispersion studies intended to improve prediction methods in more complicated situations.

Several studies have been undertaken in gently rolling terrain and in study of nocturnal drainage flow in mountain-valley systems. These have limited application to our measurements at the Meadowbrook test site under the same conditions. Pasquill and Smith (1983) summarize many of these dispersion experiments.

### 2.1.2 Fluctuating Concentrations

In investigating concentration fluctuations we are mainly concerned with fluctuations within our one-hour stationary averaging period. Concentrations at a Eulerian point  $x$  with respect to the source can be represented through

$$c(x,t) = \bar{c}(x,t) + c'(x,t) \quad (2.3)$$

and the problem is to characterize  $c(x,t)$  in terms of a probability distribution  $P(c)$  or in terms of means and higher order moments such as the variance. We write the probability distribution  $P(c)$  as

$$P(c) = \int_{-\infty}^c p(c) dc = \text{PROB} [ c(x,t) \leq c ] \quad (2.4)$$

and  $p(c)$  is the probability density function. A separate problem is in determining the average dimensions of the instantaneous cloud.

#### Probability Density Functions of Concentration

An important feature found in dispersion from a point source is the intermittency. Intermittency is the fraction of time for which  $c > 0$  at a given sampler location. This is a different situation than that found for urban concentration distributions which are often fitted using the lognormal distribution. Csanady (1967), Barry (1971) and Hanna (1984b) have all proposed a Poisson-like distribution or exponential distribution with an explicit intermittency factor for fitting concentration histograms from a point source. From derivations given in Section 3.5.2 of this report we show this distribution is given by

$$P(c) = 1 - I \exp \left( - I \frac{c}{\bar{c}} \right) \quad (2.5)$$

where  $I$  is the intermittency or fraction of time the material is present at the sampler, and  $\bar{c}$  is the mean concentration at this point. It fits measurements of concentration distributions in the atmosphere from Jones (1979, 1983) and Hanna (1984a,b). Both experiments used a small source and instruments which were fast enough to capture most of the turbulent fluctuations in concentration. This two parameter distribution is fully characterized by the mean and the variance and predicting both would be sufficient for determining the full probability density function of concentration at a point.



## **The Variance in Concentration**

Distribution of concentration variance downwind from a small source has been examined using various methods. Murthy and Csanady (1971) and Csanady (1973) use a transport equation for concentration variance which is based on the conservation equations. Durbin (1980) uses statistical methods which require following the Lagrangian motion of two correlated particles. Both techniques result in a Gaussian crosswind distribution of variance for small sources, and a profile of fluctuation intensity  $\sigma/\bar{c}$  which is a minimum on the plume axis and increases toward the plume edge. Both methods show the centerline value of  $\sigma/\bar{c}$  depends only on the ratio of source size to the Lagrangian turbulent integral scale.

## **Experimental Work in Measuring Concentration Fluctuations**

In investigating concentration fluctuations we need temporal records of concentration taken with fast response instruments at fixed positions relative to the source. To apply an ergodic hypothesis, we require a steady, continuous source and we require stationary atmospheric conditions. Multiple samplers are required for fully analyzing the field of concentration in the atmosphere. The available data which meet this criteria are very limited in scope.

Hanna (1984b) has analyzed data from a U.S. Army dispersion experiment at Elgin Air Force Base, Florida. These data are taken from two tests, each approximately 10 minutes in duration. A fog-oil smoke generator was used in creating a continuous smoke plume with an initial size of 10 cm. At a transect approximately 100 m downwind from the source, 1-s average concentrations were measured along a line using aerosol photometers.

The mean crosswind profile for these data is approximately Gaussian in shape. From the real time records of concentration, the intermittency, or fraction of time that smoke is present, is only 0.5 to 0.6 at the mean plume centerline and 0.1 at a crosswind position of  $2\sigma_y$ . The probability density for each sample follows the exponential distribution for the fraction of time that smoke is present. The fluctuation intensity  $\sigma/\bar{c}$  at the plume centerline is 1.3 and increases to 5 at a crosswind position of  $2\sigma_y$ .

The continuous release  $\text{Kr}^{85}$  experiments conducted as part of the Hanford dispersion tests are discussed by Nickola (1971) and Ludwick et al. (1968). In these tests data from 63 samplers was collected on two crosswind transects at a downwind distance of 200 m and 800 m. The data are averaged over 34.4 s sampling periods which removes some of the higher frequency fluctuations and biases the intermittency. The total test durations are from ten to twenty minutes.

Ramsdell and Hinds (1971) present an analysis of four of these tests. Fluctuation intensity  $\sigma/\bar{c}$  in these tests is a strong function of crosswind position  $\sigma_y$ , but not a strong function of

distance from the source. This intensity varies from  $\sigma_c/\bar{c} = 1.4$  at  $y/\sigma_y = 0$  to  $\sigma_c/\bar{c} = 3.0$  at  $y/\sigma_y = 2.0$ . Intermittency varies from 0.65 at  $y/\sigma_y = 0$  to 0.2 at the plume edge. Some effects of the time-averaged smoothing of the data are also investigated.

In another dispersion experiment, Jones (1979, 1983) has used a negative-ion generator with a size of 1 cm and a single detector for fast 100 Hz measurements of concentration fluctuations in the atmosphere. Three experiments were conducted. In each experiment, the detector was positioned at distances of 2 m, 5 m, 10 m, and 15 m from the source and operated for 45 minutes. Intermittencies in these tests varied from 0.1 at the closest distance to 0.02 at 15 m. This intermittency is much smaller than found in the atmospheric tests discussed by Hanna (1984b) and may be a function of the different source sizes in the two studies. Our rescaling of the probability distributions of concentration given in these papers shows they follow the exponential probability distribution given in Eq. 2.5.

Other published investigations of concentration fluctuations in simple geometries are limited to dispersion in laboratory flows. These may be divided into two groups. One group considers dispersion into extended regions of turbulent flow such as in a boundary layer or in grid turbulence. The second group is concerned with concentration and mixing in flows such as jets or wakes.

Fackrell (1980) describes a method of measuring concentration fluctuations in methane using a modified flame ionization detector and a propane tracer. A frequency response of 300 Hz is claimed for this method and measurements of concentration spectra with a  $-5/3$  inertial convective subrange are shown.

Robins and Fackrell (1979) and Fackrell and Robins (1982a,b) use this detector to study dispersion from a ground-level point source in a wind tunnel boundary layer over a rough surface. This is intended to simulate a 1:2000 model of the neutral atmospheric boundary layer. A self-preserving form for the mean profiles in the horizontal and vertical is seen. The fluctuation intensity  $\sigma_c/\bar{c}$  is also approximately self-preserving in the crosswind and vertical planes. The centerline values vary from  $\sigma_c/\bar{c} = 0.53$  to 0.35 in the range  $0 < x/h < 20$  ( $h$  is the boundary layer height) and is insensitive to a range of source sizes. Cross stream values of  $\sigma_c/\bar{c}$  approach 2 at the plume edges. In the vertical plane the concentration variance has an elevated maximum and decreases near the surface. The intermittency is one at the surface centerline and decreases with crosswind distance and distance from the surface. The probability distribution of concentration is nearly Gaussian near the surface plume centerline and approaches an exponential form near the plume edges.

These wind tunnel dispersion results have lower values of  $\sigma_c/\bar{c}$  than the comparable atmospheric measurements. They also do not show the effect of intermittency at the plume centerline.

Wilson et al. (1982, 1985) attributes this difference to the low frequency variation in wind direction which is found in the atmosphere but is absent from the wind tunnel studies.

Becker et al. (1967) describes a light scattering method for quantifying smoke concentration in laboratory flows at frequencies of up to 10 kHz. Experimental results are discussed by Becker et al. (1966) for dispersion from a small source in the core region of a turbulent pipe flow. The mean profile and concentration variance was found to follow a self-preserving profile when scaled by the plume width  $\sigma_r$ . The fluctuation intensity increased from near  $\sigma_c/\bar{c} = 1.0$  at  $r/\sigma_r = 0$  to  $\sigma_c/\bar{c} = 5$  at the plume edge and was not a strong function of distance from the source.

Gad-el-Hak and Morton (1979) studied dispersion of smoke from a point source downstream from grid turbulence using a laser light scattering technique. This method was used at frequencies up to 5000 Hz. Self preserving forms were found for the mean and variance in concentration as a function of radial position  $r/\sigma_r$ . The concentration fluctuation intensity increased from 0.4 at the plume centerline up to 2.0 near  $r/\sigma_r = 2.0$ . The intermittency was unity for  $r/\sigma_r < 1.0$  but decreased at greater crosswind distances.

Dispersion in single-length-scale flows includes measurement of scalar fields of temperature or concentration in a jet or wake. This is different from the previous cases because the turbulent region is limited by the width of the jet or wake. Freymuth and Uberoi (1973) measured the temperature wake behind a heated sphere. Turbulent jet measurements have been made by Shaughnessy and Morton (1977) and Becker et al. (1967) using an aerosol smoke and an light scattering detection technique. Measurements in a methane jet using Raman spectroscopy were made by Birch et al. (1978).

In all these cases, a self preserving region for the jet or wake concentration profile was found. Centerline scalar fluctuation intensity varied from 0.2 to 0.5. An off-axis maximum in scalar variance is found. This is located near the position of maximum mean scalar gradient. Intermittency on the axis of symmetry for these experiments was always unity and decreased with off-axis position. Probability distributions of concentration measured by Birch (1978) varied from a near Gaussian profile near the jet centerline to an exponential distribution with an explicit intermittency closer to the edge of the jet.

### **Spectral Behavior of Concentration Variance**

The spectral behavior of scalars such as concentration and temperature variance at high frequencies is similar to the behavior of velocity spectra in high Reynolds number flow. A theory for the smallest scales of motion associated with velocity fluctuations in turbulence was developed by A. N. Kolmogorov in 1941. This theory postulates a universal spectral function for turbulent kinetic energy. In this small-scale range the velocity structure is locally isotropic, or independent

of orientation, and depends only on the rate at which energy reaches the small scales  $\epsilon = \overline{v(\partial u_i/\partial x_j + \partial u_j/\partial x_i)^2}$  and the kinematic viscosity  $\nu$  of the fluid. Scales of length  $\eta = (\nu/\epsilon)^{1/4}$ , and velocity  $v = (\nu\epsilon)^{1/4}$  and time  $t = (\nu/\epsilon)^{1/2}$  formed with these two quantities are called the Kolmogorov microscales.

The power spectra of turbulent kinetic energy in these small scale ranges (the size distribution of eddies) follows a universal function when nondimensionalized by the Kolmogorov microscales. If the range of eddy sizes is large, Kolmogorov also suggests the existence of a subrange in which there is neither viscous dissipation, nor energy input from the mean flow, but only inertial interaction between eddies. In this inertial subrange, the kinetic energy spectrum  $E(\kappa)$  must be independent of viscosity, since dissipation is negligible, and the spectra must match with the equilibrium spectra at small viscous wavenumbers. Using the definition of  $\eta$  and  $v$  this gives

$$E(\kappa) = v^2 \eta \alpha [\eta \kappa]^{-5/3} = \alpha \epsilon^{2/3} \kappa^{-5/3} \quad (2.6)$$

so the power spectrum exhibits a  $-5/3$  power law behavior for wavenumbers in the inertial subrange. The one-dimensional single-sided velocity spectra  $S_{uu}$  in the mean flow direction will follow the same dimensional arguments to give

$$S_{uu}(\kappa) = \alpha_1 \epsilon^{2/3} \kappa^{-5/3} \quad (2.7)$$

Measurements of  $S_{uu}$  may be related to the kinetic energy spectra in the inertial subrange using  $\alpha_1 = (55/18)\alpha$  from Batchelor (1953, Eq.3.4.18). Using equations valid for homogeneous turbulence (see Panofsky and Dutton, 1984, p.97), we have the relation  $S_{vv}(\kappa) = S_{ww}(\kappa) = (4/3)S_{uu}(\kappa)$ . Gibson and Schwartz (1963) have found the constant  $\alpha$  to be  $1.34 \pm 0.06$  from analysis of grid turbulence data from several different authors.

Scalar spectra of concentration (and temperature) will exhibit an inertial-convective range if the Reynolds number is large enough for an inertial subrange to exist for the kinetic energy spectra. From Corrsin (1951) the concentration spectra are scaled as

$$E_c(\kappa) = \beta N \epsilon^{-1/3} \kappa^{-5/3} \quad (2.8)$$

where  $N = \overline{\mathcal{D}(\partial c/\partial x_i)(\partial c/\partial x_i)}$  the dissipation rate of concentration variance and  $\beta$  is a proportionality constant (see Tennekes and Lumley, 1972). This inertial-convective subrange is independent of the dissipation scales  $\nu$  and  $\mathcal{D}$ . A similar expression for the one-dimensional concentration spectra may also be written with a different coefficient  $\beta_1$  following the notation for velocity spectra. Gibson and Schwarz (1963) have measured the spectra of concentration in grid turbulence which follows the  $-5/3$  power law scaling. At higher frequencies where the effect of dissipation is evident, the exact shape of the spectra depends on the Schmidt number  $Sc = \nu/\mathcal{D}$  for concentration

or the Prandtl number  $Pr = \nu/\alpha$  for temperature. This equilibrium range of the scalar spectra is discussed by Batchelor (1959).

In addition to the universal high frequency behavior of concentration spectra, there is a lower frequency behavior which depends on the geometry of the flow. This latter subject has not been well investigated previously; one intent of the present study is to quantify this behavior for dispersion from a point source in the atmosphere.

### **Relative Dispersion**

A problem of dispersion which is closely related to concentration fluctuations is the concept of relative dispersion, where the concern is in following an expanding cluster of particles or puff of pollutant in a Lagrangian coordinate system. Examination of the dispersion with respect to the centroid of the puff requires consideration of correlated motion within the cluster. Many of the same statistical techniques for examining relative dispersion have application in examining concentration fluctuations as shown by Durbin (1980).

In the Eulerian frame of reference and considering only stationary meteorological conditions, instantaneous puff behavior is directly related to the behavior of a continuous plume released from the same source. In both cases the average probability of an element of pollutant leaving the source and arriving at a given sampling location is the same. This average probability represents a mean concentration normalized by the the source strength of either the continuous plume or the sum of many individual puffs.

Predictions of puff sizes about a moving centroid are based on the average behavior of many individual puffs. This average size is much smaller than the average width of a continuous plume release from the same source because the wandering component of the plume is removed in the averaging about the puff centroid. Experiments in measuring relative dispersion have used either fast moving sampling probes which traverse the plume or photographs of a visible plume. In both types of measurements the instantaneous profile is ensemble averaged about a moving plume centroid. Smith and Hay (1961) and Michelson (1983) have found  $\sigma_{y,r} \approx 0.2 \sigma_y$  for a range of dispersion distances near a small source. The value  $\sigma_y$  is the plume width with respect to fixed centroid, although  $\sigma_{y,r}$  is the width with respect to the moving center of mass.

It is possible to define fluctuating concentrations with respect to the relative plume centroid. Murthy and Csanady (1971) describe an experimental test of relative diffusion in Lake Huron. Fluorescent dye is dispersed in an underwater current. Fluorometers measured crosswind profiles of the downwind plume which were then ensemble averaged with respect to a moving plume centroid. The mean profile in these experiments is nearly Gaussian and the profile of  $\sigma/\bar{c}$  appears to follow a universal profile scaling using  $y/\sigma_{y,r}$ . Centerline values of  $\sigma/\bar{c} = 0.3$  were found.

This increased near the edge of the plume. No measurements of the absolute plume location or width were made.

## 2.2 The Atmosphere

As a prelude to a discussion of the theory of atmospheric dispersion, we require a discussion of flow and turbulence in the atmosphere. The earth's atmosphere consists of a 100-km deep envelope of gases and vapors which surround the planet. All of the weather on the earth is contained in the lowest 20 km of this layer. Flow in the lower atmosphere is nearly always turbulent.

The earth receives radiant energy from the sun, which heats the earth and the atmosphere. Varying latitudes, different rates of absorption of energy over different land surfaces, oceans, and the reflection of energy from constantly moving clouds causes the solar heating to vary over the planet surface. Global and local winds result from this differential rate of heating, carrying colder, higher density air toward warmer, lower density regions. Coriolis forces from the earth's rotation and geographic features on the surface modify the atmospheric flow.

The transport of water vapor and thermal energy through the atmosphere and the mixing of these by turbulence is a major factor in the weather. This transport and mixing results in local conditions of clouds, precipitation, or clear weather. This, in turn, will affect the larger wind patterns through variations in local solar heating rates.

As in all turbulent flows, various scales of motion exist in the atmosphere. These scales of motion may range from global patterns down to local and instantaneous fluctuations in wind speed and direction. Division of these scales of motion is shown in Table 2.1 which is drawn from Stern, et al. (1973).

Table 2.1 Scales of motion in the atmosphere

Name	Time scale	Horizontal scale	Vertical scale
Microscale	1 second - 1 hour	1mm - 1 km	1mm - 10 m
Mesoscale	1 hour - 12 hour	1 km - 100 km	10 m - 1 km
Macroscale	12 hour - 1 week	100 km - hemisphere	1 km - 20 km

Different mechanisms are responsible for maintaining turbulent motion in each of the above ranges in scale (Randerson, 1984). In the macroscale region, instabilities are caused by the latitudinal variation in solar heating. Mesoscale turbulence may be caused by the latent heat release in cloud formation, flow over topographical features such as cities or islands, and from flow over

surfaces which vary in surface character, such as in coastal areas or mountains. In the microscale region, unstable flow is caused by horizontal and turbulent wind shear, surface roughness, and thermal instability. A nomogram of these sources of turbulent motion and their scales are shown in Figure 2.1.

The instability and turbulence in the microscale region are fairly well characterized, being dominated by thermal stratification and ground-induced mechanical turbulence. During periods of overcast weather, buoyancy forces in the atmosphere may be small. Any turbulence near the surface is caused by mechanical friction at the ground surface and the atmosphere is considered to be neutrally stable. Under clearer conditions during the day the surface is warmed by solar radiation which results in an unstable stratification of the atmosphere near the surface. At night under clear skies the surface cools due to heat loss to the night sky. This results in a stable atmospheric stratification.

The solar heat flux to the surface varies with the time of day. This changes the degree of instability in the atmosphere, so that it is considered a non-stationary system. Time-averaged means and moments in non-stationary systems appear to depend on the size of the averaging interval and also fluctuate from sample to sample. This is known as the "drift of the mean" and violates necessary assumptions for stationary flow (Kampé de Fériet, 1974).

This effect can be circumvented according to Monin and Yaglom (1971 v.1, p. 419-421), if averages are taken for specified synoptic conditions (i.e., specified "weather"), for a specified season, and a specified time of day. The averages must be taken over an interval considerably longer than the characteristic period of the large eddies in the flow for relatively stable averages to be obtained.

In the surface layer of the atmosphere over uniform terrain these eddies have time scales on the order of tens of seconds so that ten to twenty minute averages (of wind and temperature, for example) will be relatively stable. When the averaging period is extended to more than several hours, the mean values again exhibit fluctuations due to long period variations in synoptic conditions.

An illustration of this spectral gap is given in Figure 2.2 using two sample spectra of a long-term record of horizontal wind speed. These data are taken from van der Hoven (1957) and our measurements at Camp Atterbury. The magnitude of the kinetic energy is influenced by the sampling height, but is similar in shape for both cases. A gap in the spectra is shown at a frequency equivalent to a time duration near 1 hr. A similar gap is found in measurements by Walker (1965), Kaimal et al. (1976), and Højstrup (1982). This gap is responsible for the validity of assuming stationary conditions in the microscale. It does not occur for all synoptic conditions. Exceptions include the periods when or during which weather fronts or storms are passing through the area, or rapid transition periods such as those that exist just after dawn or at dusk.

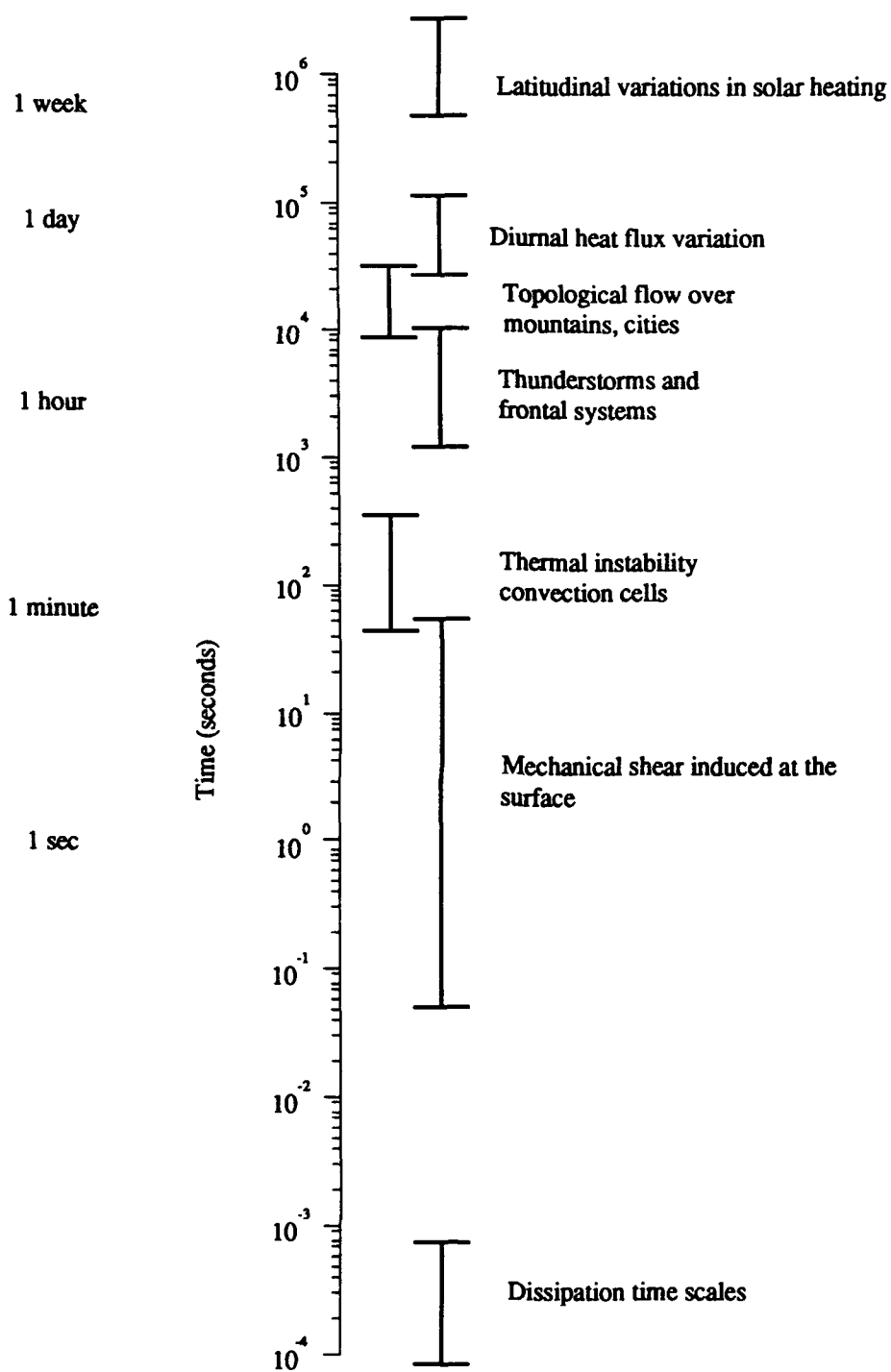


Figure 2.1 Time scales in atmospheric turbulence for sources and sinks of turbulent energy.



— Spectrum of the horizontal wind speed at an average height of 100 m above the ground. From Van der Hoven (1957).

..... Spectrum of the horizontal wind speed from surface layer measurements at 10 m. This data is from our Camp Atterbury measurements and National Climatic Data Center 1 hour surface station measurements at Indianapolis, Peoria, Dayton, Evansville, and Louisville.

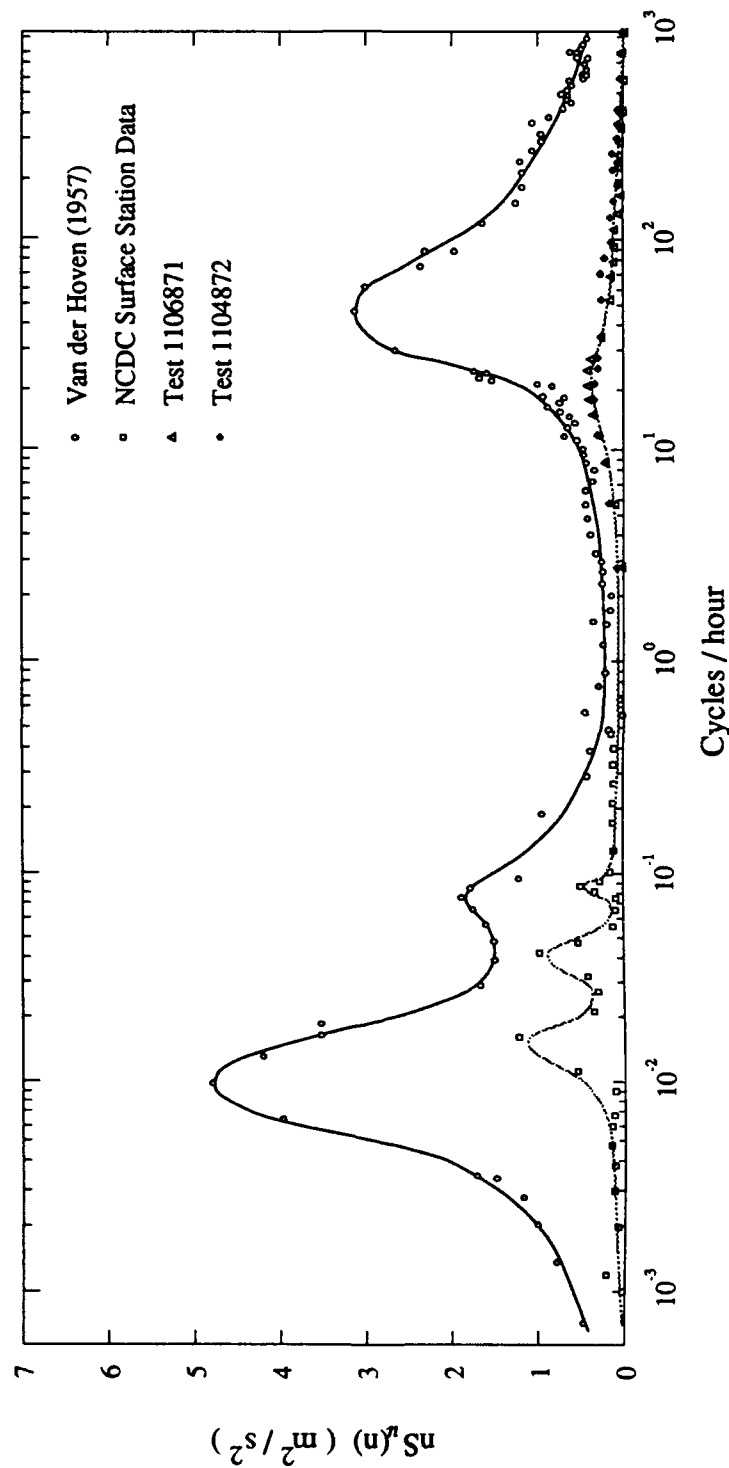


Figure 2.2 Spectra of the horizontal wind speed. This plot shows the mesoscale gap in energy which permits the quasi-stationary analysis. The vertical scale is linear.

## 2.3 The Atmospheric Boundary Layer

A boundary layer exists in the atmosphere above the surface for a wide variety of meteorological conditions. This boundary layer may be due to mechanical drag at the surface or due to convective mixing above the surface.

Since most sources of pollutants in the atmosphere are contained within the atmospheric boundary layer (including our own ground level tracer sources), predicting the dispersion of pollutants requires an understanding of the behavior of the wind within this layer. This includes a knowledge of both the mean and fluctuating wind components, as well as the variables and parameters which affect the behavior of the wind.

In the atmosphere, the boundary-layer depth varies with time throughout the day and night. It may range from several meters to several kilometers in height. The free stream velocity above the layer is driven by a balance of pressure and Coriolis forces in a geostrophic flow. In periods other than at dawn or dusk, or near mesoscale events such as thunderstorms or weather fronts, conditions can often be taken to be approximately stationary over time periods of tens of minutes to several hours, and a simple steady-state boundary-layer analysis is possible.

The vertical temperature gradient is an important indicator in the atmospheric boundary layer. Because temperature alone is not a measure of the potential energy of a parcel of air, the potential temperature, defined by

$$\theta = T \left( \frac{P_{00}}{P} \right)^{\kappa/C_p} \quad (2.9)$$

is often used (Panofsky and Dutton, 1984). The values of  $T$  and  $P$  are measured at the same height, and  $P_{00} = 1000$  mb by definition. The potential temperature would be the temperature achieved in bringing the parcel of air to 1000 mb in an isentropic process. The approximation

$$\theta = T(z_0) + \frac{g}{C_p} [z - z_0] \quad (2.10)$$

is sometimes used in finding the potential temperature. Near the surface this gives an adiabatic lapse rate of  $-0.0098$  K/m.

With both turbulence and thermal gradients present in the atmosphere, the Reynolds number  $Re = u'l/\nu$ , and the Richardson number

$$Ri = \frac{(g/\theta)(\partial\theta/\partial z)}{(\partial\bar{u}_x/\partial z)^2} \quad (2.11)$$

are both important dimensionless parameters. Turbulent flow in the atmosphere yields very large Reynolds numbers. In the definition of  $Re$  we have used the fluctuating velocity  $u'$  and the turbulent integral scale  $l$  as scaling values, along with the kinematic viscosity  $\nu$ . The Richardson number requires the buoyancy parameter  $g/\theta$ , and the vertical gradients in potential temperature ( $\partial\theta/\partial z$ ) and mean velocity ( $\partial\bar{u}_x/\partial z$ ).

The Richardson number is associated with buoyancy effects in the flow and is an important indicator for the presence of turbulent flow. For  $Ri < 0.21$  flow is generally turbulent. The Richardson number is a function of height from the surface. Several other scaling parameters are used to more completely quantify the turbulence near the ground. One of these is the Monin-Obhukhov length  $L$ . This is approximately given by  $Ri = z/L$  in the unstable surface layer according to Golder (1972).

For cases in which the buoyancy effects are negligible and  $d\theta/dz = 0$ , conditions in the atmosphere are neutral. Neutral conditions occur most often on very overcast days or nights in higher latitudes. Much more common are conditions of unstable flow, which occur for vertical temperature gradients which decrease at a greater rate than for neutral conditions, and stable conditions for which the opposite is true.

In clear weather during daylight hours, most of the warming of the atmosphere occurs at the ground, which is heated by radiation from the sun. This results in an unstable stratification of the atmosphere near the ground, a negative Richardson number, and a convective boundary layer. The warm, more buoyant air at ground level rises, and cooler air at higher levels replaces the displaced warm air. This results in a constant churning of the atmosphere with very good mixing rates of pollutants, tracers, and contaminants throughout the mixing layer.

Conversely, on clear nights the ground cools much faster than the atmosphere due to radiational exchange between the ground and the sky. This results in a stable stratification of air. Turbulence from mechanical friction at the surface is suppressed, and the mixing rates of contaminants in the atmosphere are greatly reduced.

For the atmosphere, in stationary conditions and over flat uniform terrain, the state of the boundary layer can be characterized by a bulk stability parameter  $h/L$ , where  $h$  is the depth of the boundary layer and  $L$  is the Monin-Obhukhov length. The Monin-Obhukhov length  $L$  is the ratio of the mechanically generated turbulent energy to that produced by buoyancy. The magnitude of  $L$  indicates the approximate height below which shear generated turbulence dominates the flow.

The boundary layer height  $h$  is the total depth over which momentum or energy are transferred. In near-neutral conditions with  $h/L \sim 0$ , we have  $h = \mathcal{A}u_* / f$ , where  $f$  is the Coriolis parameter and the proportionality constant  $\mathcal{A}$  is in the range of 0.15 to 0.25 according to Panofsky and Dutton (1984). In unstable conditions Deardorff (1972) shows that  $u_* / f$  is not a controlling

parameter for  $h/L < -1.5$  and the boundary layer height is usually well defined by a temperature inversion at  $h = z_i$  which is called the mixing height. In stable conditions for which  $h/L > 0$  the boundary layer height may be taken as the height above which  $Ri > 0.21$ .

### 2.3.1 Unstable Boundary Layer

A nomogram for the various scaling regions in the unstable boundary layer over flat, uniform terrain is reproduced in Figure 2.3, which is based on several plots from Olesen et al. (1984) and Holtslag and Nieuwstadt (1986). This logarithmic plot indicates the various scaling regions for unstable ( $h/L < 0$ ) flow, along with pertinent parameters in each of the regions, which will be discussed in the following sections. The unstable atmospheric boundary layer is fairly well characterized and has been extensively studied. The diagonal lines in the figure indicate constant values of  $h/L$ . For a particular  $h/L$ , the changing scaling regimes for different levels of height  $z$  within the boundary layer are found along the given  $h/L$  line. Most quantities in the boundary layer will scale with the indicated quantities within each regime. The regions in this nomogram include the surface layer, the near neutral upper layer, the mixed layer, the convective matching layer, and the entrainment layer. Scaling parameters for these regions will be discussed in later sections.

In the convective boundary layer, time scales are on the order of  $(z_i/w_*)$ , which for typical atmospheric conditions is about five minutes. This convective time scale is much less than the time scale of the diurnal variations in the boundary conditions imposed by the inversion height  $z_i$ , the surface heat flux  $H$ , or changes in the geostrophic pressure field. With this ratio of time scales, the boundary layer structure quickly adjusts to changing boundary conditions and a quasi-steady state exists, according to Kaimal et al. (1976).

### 2.3.2 Stable Boundary Layer

Stable boundary layers develop over land due to nocturnal cooling of the ground. In the early development of this layer, beginning at dusk over land, buoyancy forces suppress the turbulence generated due to shear at the ground, and limit the momentum transfer between the surface and upper levels of air. This creates a stagnant layer at the ground. With continued evolution of the boundary layer, the vertical velocity gradient increases to a point of instability, and a resultant mixing of the cooler ground level air through a greater depth of the atmosphere occurs. Part of the instability is due to restoring buoyancy forces, so that wave motion is supported and coexists with the turbulent fluctuations. In an ideal situation without shear and a constant (potential) temperature gradient with height, this wavelength is determined by

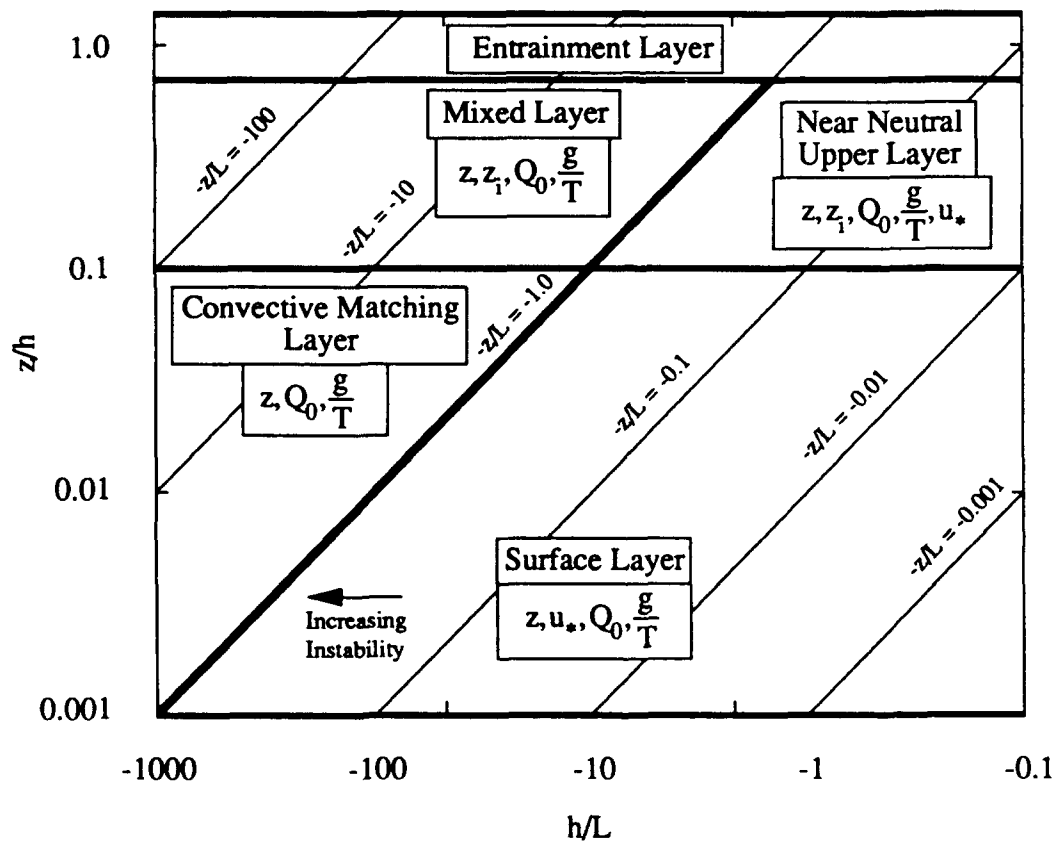


Figure 2.3 Nomogram for scaling in the idealized unstable atmospheric boundary layer. Notation, scaling regimes, and parameters are discussed in the text. Division of the scaling regions in the above graph is fairly arbitrary and may be subject to other interpretations.

$$\lambda_{BV} = \left( \frac{g}{T} \frac{dT}{dz} \right)^{1/2} \quad (2.12)$$

which is the Brunt-Vaisala frequency (see Pasquill and Smith, 1983). This is related to the Richardson number through

$$Ri = \frac{\lambda_{BV}^2}{\left( \frac{\partial u}{\partial z} \right)^2} \quad (2.13)$$

Occasionally, in higher level boundary layer measurements, a dominant wavelength is measured which corresponds to the Brunt-Vaisala frequency found using a bulk temperature gradient. Closer to the ground where wind shear and a changing temperature gradient exist,  $\lambda_{BV}$  can vary considerably with height.

The behavior of the stable boundary layer throughout its depth is poorly understood in comparison with the unstable boundary layer. Some regions of the stable layer can be intermittent, with alternating periods of turbulent air from below and smooth laminar air from above arriving at a given height. The evolution of the stable boundary layer is very slow, without a true steady state ever being reached. Zeeman (1979) states that the evolution time scale of the stable boundary layer is often longer than the duration of the stable nighttime regime, so that the present state of a nocturnal boundary layer depends on past development. Models of the stable layer are usually qualitative in nature due to the lack of confirming experimental data, especially in the upper levels of the atmosphere.

A nomagram for the scaling in the idealized stable boundary layer is given in Figure 2.4. This nomagram is based mainly on information from Holtslag and Nieuwstadt (1986) and Olesen et al. (1984). The surface layer and the near neutral upper layer shown in this plot also are found for the unstable boundary layer. The z-less layer, the intermittency region, and the low turbulence region are also shown in this nomagram. Nieuwstadt (1984) subdivides the z-less layer into another region of local scaling. The information in this nomagram is much more arbitrary than that in the same plot for unstable flow, as much of the similarity theory in stable flow lacks experimental evidence for its validity.

### 2.3.3 Velocity and Temperature Scaling in the Atmospheric Boundary Layer

For a flow which is homogeneous in planes parallel to the ground, boundary layer behavior may be characterized by the vertical profiles of velocity and temperature, and the driving forces which influence these profiles, mainly mechanical shear at the surface, and the positive or negative

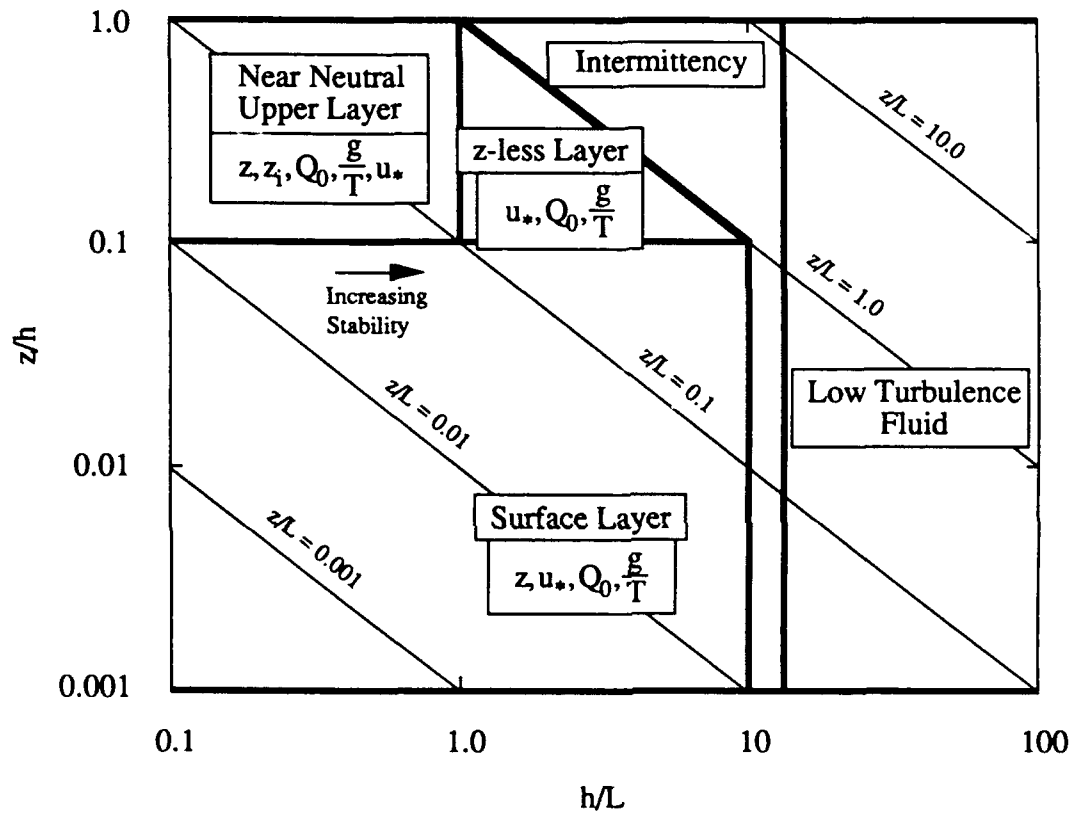


**Figure 2.4** Nomogram for scaling in the idealized stable atmospheric boundary layer. Notation, scaling regimes, and parameters are discussed in the text. Division of the scaling regions in the above graph is very arbitrary due to a lack of confirming experimental data.

heat flux at the surface. For various regions and conditions of the boundary layer, many quantities, such as the mean velocity and temperature, will scale with the quantities indicated in each of the regions of Figures 2.3 and 2.4.

### Surface Layer

A good starting point for the atmospheric boundary layer analysis is the similarity theory of Monin and Obhukhov (1954) which applies in the surface layer of the atmosphere adjacent to the ground. This is the most easily studied and best documented boundary layer region. The surface layer occurs for nearly all conditions, both stable and unstable, in which an atmospheric boundary layer exists. Most of the mean gradient in wind speed and mean potential temperature occur in this part of the boundary layer. Governing equations and assumptions in this theory are discussed by Calder (1966). In this analysis, the Coriolis force due to the rotation of the earth is neglected, as well as radiative heat transfer within the layer itself. Beginning with the mean Reynolds equations, an idealized situation is assumed, such that the statistics of the atmosphere are invariant in time and are homogeneous in surfaces parallel to the ground. The mean velocity is assumed to be in the x direction with zero mean flow in the other coordinate directions. For these assumptions, and using conditions of symmetry, a coupled set of three ordinary differential equations is found. The first is

$$v \frac{d \bar{u}_x}{dz} - \overline{u'_x u'_z} = \frac{\tau_{zx} (z=0)}{\rho} \quad (2.14)$$

where  $\tau_{zx}$  is the total stress, consisting of both Reynolds and viscous stress, and is constant throughout the surface layer. The energy equation yields

$$\alpha \frac{d \bar{T}}{dz} - \overline{\theta u'_z} = - \frac{H (z=0)}{\rho C_p} \quad (2.15)$$

where H is the vertical heat flux, and like  $\tau_{zx}$ , is constant throughout the surface layer and consists of both a conductive term and a Reynolds flux. The momentum equation in the z coordinate direction is given by

$$- \frac{1}{\rho} \frac{d \bar{p}}{dz} + v \frac{d^2 \bar{u}_z}{dz^2} - \frac{d \overline{u'_z u'_z}}{dz} + \frac{T - T_a}{T_a} g = 0 \quad (2.16)$$

with  $T_a$  as an average temperature taken over a horizontal plane.

In these equations, we define groups of dimensional terms, such that

$$u_* = \frac{\tau_{zx}}{\rho} \quad (2.17)$$



where  $u_*$  is the friction velocity, and

$$T_* = \frac{H}{\rho C_p u_*} \quad (2.18)$$

so that  $T_*$  is a temperature parameter. A kinematic heat flux is also sometimes used, given by

$$Q_0 = \frac{H}{\rho C_p} \quad (2.19)$$

This set of equations contains the five independent groups of dimensional parameters  $g/T_a$ ,  $\nu$ ,  $\alpha$ ,  $u_*$ , and  $T_*$ . Neglecting the molecular dissipation gives

$$u_*^2 = \frac{\tau_{zx}}{\rho} = \overline{u'_x u'_z} \quad (2.20)$$

and

$$Q_0 = \overline{\theta' u'_z} \quad (2.21)$$

or

$$T_* = \frac{-H}{\rho C_p u_*} = \frac{-\overline{\theta' u'_z}}{u_*} \quad (2.22)$$

so that one possible method for finding these scaling quantities in the surface layer comes from directly measuring the fluctuating correlations of velocity and temperature. The remaining three dimensional parameters are  $g/T_a$ ,  $u_*$ , and  $T_*$ . A length scale formed from the above scales is

$$L = \frac{u_*^2 T_a}{k g T_*} = \frac{\rho C_p u_*^3 T_a}{k g H} \quad (2.23)$$

where  $L$  is the Monin - Obhukhov length scale, and  $k$  is von Karmans constant ( $k = 0.4$ ). The Monin - Obhukhov length scale is the ratio of the mechanical turbulent energy to that produced by buoyancy. In neutral conditions,  $L \rightarrow \infty$  and shear stresses dominate the entire depth of the boundary layer. For unstable conditions  $L$  takes on negative values, whereas it is positive for stable conditions. The Monin-Obhukhov length is directly related to the Richardson number. Golder (1972) shows  $Ri = z/L$  is valid in unstable conditions. Randerson (1984) summarizes other empirical relations between  $Ri$  and  $z/L$  in a wider range of atmospheric conditions.

Using the three groups  $L$ ,  $u_*$ , and  $T_*$ , which are assumed constant within the surface layer ( $g/T_a$  is not constant), as well as the height  $z$  the similarity relations of Monin and Obhukhov (1954) follow. For the vertical gradient of velocity,

$$\frac{d\bar{u}_x}{dz} = \text{function} [u_*, T_*, L, z] \quad (2.24)$$

This function consists of five groups of terms in three dimensions (length, time, and temperature). Nondimensionalization of these groups will yield two independent terms. One choice of terms is

$$\frac{k}{u_*} \frac{z}{dz} \frac{d\bar{u}_x}{dz} \quad \text{and} \quad \frac{z}{L}$$

which can be arranged as

$$\frac{k}{u_*} \frac{z}{dz} \frac{d\bar{u}_x}{dz} = \phi_m \left[ \frac{z}{L} \right] \quad (2.25)$$

and similarly for the gradient in mean temperature,

$$\frac{k}{T_*} \frac{z}{dz} \frac{d\bar{T}}{dz} = \phi_h \left[ \frac{z}{L} \right] \quad (2.26)$$

where  $\phi_m$  and  $\phi_h$  are both universal functions which, in practice, are found empirically. Integrating these equations yields

$$\bar{u}_z(z) = \frac{u_*}{k} \left[ \ln \left( \frac{z}{z_0} \right) - \psi_m(z/L, z_0/L) \right] \quad (2.27)$$

and

$$\bar{T}(z) = T_0 + 0.74 T_* \left[ \ln \left( \frac{z}{z_0} \right) - \psi_h(z/L, z_0/L) \right] \quad (2.28)$$

where the integrated values  $\psi_m$  and  $\psi_h$  convey the same information as  $\phi_m$  and  $\phi_h$ . This is known as the log-linear profile and is found in thermally stratified flow. A new parameter,  $z_0$ , the roughness height, results from this integration. For neutral conditions, this analysis yields a logarithmic velocity profile.

Empirical forms for the functions  $\psi_m$  and  $\psi_h$  have been given by Paulson (1970), Dyer and Hicks (1970), and Businger et al. (1971) as functions of  $z/L$ . Benoit (1977) and Nickerson and Smiley (1975) improve these functions by including the effect of surface roughness. These functions allow us to estimate values of  $u_*$  and  $T_*$  from mean profile measurements of velocity and temperature. In effect the functions  $\psi_m$  and  $\psi_h$  are the result of closure approximations of  $Q_0 = \overline{\theta u_z}/u_*$  and  $u_* = \overline{u_x' u_z'}$  in flat terrain. These functions are valid in the surface layer within a height for which the original assumptions still hold. In nearly all cases this includes heights up to  $z = |L|$ , below which mechanically generated turbulence dominates.

In addition to the mean profiles of temperature and velocity, the vertical variance should also follow surface layer scaling. An empirical expression from Panofsky et al. (1977) for unstable conditions is

$$\frac{\sigma_w}{u_*} = 1.25 \left( 1 - 3 \frac{z}{L} \right)^{1/3} \quad (2.29)$$

A similar expression is given by Højstrup (1982) as a weak function of the inversion height. According to Panofsky and Prasad (1965), no Monin-Obhukhov scaling is evident for  $\sigma_u$  or  $\sigma_v$ , both of which appear to be constant with height. These variances are affected by upper level velocity fluctuations which extend into the surface layer. Spectral representation of the velocity variance as shown by Højstrup (1982) best illustrates this effect. In the vertical coordinate the velocity fluctuations are constrained to be smaller than the distance to the surface and are amenable to the first-order closure of Monin-Obhukhov scaling.

### **Boundary Layer Height**

Above the surface layer, the only additional parameter found in the nomagrams of Figures 2.3 and 2.4 is the height of the boundary layer. This value will dictate the applicable scaling regions for the upper levels of the boundary layer.

In a boundary layer without a net vertical exchange of heat,  $L \rightarrow \infty$  and the boundary layer is neutral. The height of the frictional boundary layer in this case is taken at an arbitrary limit for which surface friction effects on the mean flow are negligible, usually

$$h = \mathcal{A} \frac{u_*}{f} \quad (2.30)$$

The Coriolis parameter  $f$  governs the free stream flow above the boundary layer, where pressure gradients balance the Coriolis forces. In middle latitudes  $f = 10^{-4}$  Hz. Panofsky and Dutton (1984) give  $\mathcal{A}$  in the range of 0.15 to 0.25. In actuality, neutral flow occurs most often over the sea. It sometimes occurs over land in cloudy conditions with very high wind speeds, but this is a rare occurrence. More often there are weak vertical temperature gradients which produce only near-neutral conditions over land.

Unstable conditions produce a mean vertical potential temperature profile which decreases as a function of height, so the gradient  $d\theta/dz$  is negative. Increasing from the ground, at a height  $h = z_i$ , a temperature inversion occurs (the vertical potential temperature gradient changes sign), which effectively caps the vertical mixing. Turbulent measures, such as the velocity variances or joint correlations of velocity and temperature, decrease markedly through this inversion height.

The boundary layer height is best measured directly, through radiosonde measurements or acoustic soundings. In the morning and early afternoon, the inversion height may be estimated from the intersection of the morning vertical potential temperature profile with the surface potential temperature at the desired time. This method has been used by Benkley and Schulman (1979), and

Holzworth (1967) for estimating inversion heights in air pollution studies. Garrett (1981) uses an initial vertical profile measurement and knowledge of the surface level heat flux history in a model for calculating inversion heights.

In stable conditions, the boundary layer height is marked by a strongly capped mechanically mixed layer. Above this level quantities such as  $\overline{\theta'u_z'}$  or  $\overline{u_x'u_z'}$  become very small. It is most accurate to measure this height directly through atmospheric soundings. Alternatively, Randerson (1984) gives

$$h = 0.4 \left( \frac{u_* L}{f} \right)^{1/2} \quad (2.31)$$

as one estimate. Pasquill and Smith (1983) show the proportionality constant in this equation varies between 0.2 to 0.7, and it decreases with progressive evolution of the boundary layer. Yu (1978) claims this equation to be valid in the range  $5 < u_* L/f < 45$ , which includes conditions of slight to moderate atmospheric stability.

### Near Neutral Upper Layer

For conditions with a small temperature gradient through the boundary layer, where  $|h/L|$  is small (because  $L$  is large) the surface layer scaling will persist through much of the boundary layer. Above this region, we have a near neutral upper layer in which inversion height has an effect on limiting the size of turbulent eddies, and the controlling parameters include all the surface layer parameters in addition to the inversion height  $z_i$  in unstable conditions, or  $h$  in stable conditions. The near neutral upper layer is most likely to exist in cases of high wind speeds over land. At heights near  $z_i$ , or for greater vertical temperature gradients, this layer is not well characterized.

A logarithmic velocity profile may persist throughout the boundary layer in neutral conditions with  $z/L \rightarrow 0$ . Most of the velocity gradient will be within the surface layer. This is given by

$$\bar{u}_z(z) = \frac{u_*}{k} \ln \left( \frac{z}{z_0} \right) \quad (2.32)$$

and typically requires  $-0.01 < Ri < 0.01$ , where  $Ri$  is the Richardson number. Typically, the roughness height  $z_0$  varies from  $10^{-2}$  m for mown grass to .2 ~ .99 m over woodland forests or medium sized suburban buildings, although values as high as 10m are possible in amongst tall buildings. Flat terrain will show a logarithmic profile throughout the boundary layer. In complex terrain, both  $z_0$  and  $u_*$  will depend on the observation height, and possibly on the wind direction, according to Panofsky and Dutton (1984). For example, in gently rolling terrain the velocity

measured closest to the ground (~1 m) will depend mainly on surface vegetation, but at higher levels the value will be affected by shallow hills.

An interesting effect in the boundary layer is the turning of the mean wind direction with height, or Ekman flow, which is due to the increasing effect of the Coriolis acceleration at higher wind velocities and greater heights. In the atmosphere, this is most likely to be evident in neutral conditions. Ekman layer flow is generally not important at the downwind dispersion distances we are studying, but it may be important at distances of a few tens of kilometers.

Variances in the neutral boundary layer, denoted by  $\sigma_u^2$ ,  $\sigma_v^2$ , and  $\sigma_w^2$  are all functions of  $u_*$  only. Using a logarithmic wind law yields

$$\frac{\sigma_u(z)}{\bar{u}_x(z)} = \frac{k \ 2.39}{\ln (z / z_0)} \quad (2.33)$$

$$\sigma_\theta(z) \sim \frac{\sigma_v(z)}{\bar{u}_x(z)} = \frac{k \ 1.92}{\ln (z / z_0)} \quad (2.34)$$

$$\sigma_\phi(z) \sim \frac{\sigma_w(z)}{\bar{u}_x(z)} = \frac{k \ 1.25}{\ln (z / z_0)} \quad (2.35)$$

in a summary of various flat terrain sites, from Panofsky and Dutton (1984), where we have  $k = 0.4$ , and  $k$  is the von Karman constant. The coefficients in these equations agree with wind tunnel measurements in neutral boundary layers. In rolling terrain, the coefficients for  $\sigma_u$  and  $\sigma_v$  are larger by a factor of up to 2, but the value for the vertical coordinate retains the same coefficient. We note that for even slightly unstable stratification, the values of  $\sigma_v$  and  $\sigma_u$  become independent of height, and do not follow these relations.

### **Unstable Boundary Layer Behavior**

The greatest fraction of daytime conditions in the atmospheric boundary layer over land are convective. Upper level regimes in the unstable boundary layer include the mixed layer and the convective matching layer. In a numerical model of the convective boundary layer Deardorff (1970a) scales turbulent velocity and temperature fluctuations in the mixed layer by

$$w_* = \left[ \frac{g}{T_a} z_i \overline{(u_z' \theta)'} \right]^{1/3} = \left[ \frac{g}{T_a} z_i Q_0 \right]^{1/3} \quad (2.36)$$

where  $z = z_i$  is the inversion height and  $w_*$  is the convection velocity. A convective temperature scale is given by

$$\theta_* = \left( \frac{g}{T_a} z_i \right)^{-1/3} \frac{(u_z' \theta)_0^{2/3}}{w_*} = \frac{Q_0}{w_*} \quad (2.37)$$

This scaling also appears to apply in turbulent Rayleigh convection with  $-z_i/L \rightarrow \infty$  and  $u_* = 0$ , according to Deardorff (1972), given that  $z_i$  is the distance between rigid horizontal plates. For laboratory and atmospheric measurements to agree, the product of Raleigh number and Prandtl number in the laboratory must be sufficiently large for the flow to be fully turbulent.

Using the definition of  $w_*$  and  $u_*$  we can get

$$w_* = u_* \left[ -\frac{z_i}{L k} \right]^{1/3} \quad (2.38)$$

as a relation between the two values. From this we see that the only mixed layer parameter not used in the surface layer is  $z_i$ .

Between the mixed layer and the surface layer we have a convective matching layer. In this range  $z_i$  is not a valid scaling parameter and free convection dominates the flow. A velocity scaling parameter in this region is given by

$$u_j = \left[ \frac{g z Q_0}{T_a} \right]^{1/3} = \left[ \frac{g z_i Q_0}{T_a} \right]^{1/3} \left( \frac{z}{z_i} \right)^{1/3} = w_* \left( \frac{z}{z_i} \right)^{1/3} \quad (2.39)$$

which, as shown, can be recast in terms of the convection velocity  $w_*$  and the dimensionless height in the boundary layer.

Mean velocity in these layers shows very little gradient; the greatest change occurs within the surface layer. In the entire mixed layer, the mean temperature is slightly lower than in the surface layer, and the heat flux  $Q_0$  can be assumed constant within the boundary layer. Errors in this assumption come from mixing within the entrainment layer. In very convective conditions,  $\sigma_u = \sigma_v = 0.6w_*$  throughout the boundary layer, even near the ground. The value of  $\sigma_w$  remains a function of height. An examination of atmospheric measurements by Liljegren (1989) shows a maximum  $\sigma_w$  of between  $0.35w_*$  to  $0.42w_*$  at a height of  $\sim 0.35z/z_i$ . The value of  $\sigma_w$  decreases to very small values at the surface.

### **Stable Boundary Layer**

Turbulence in stable conditions is generated at the ground within the surface layer. In the early evening, some upper level turbulence may be present within the region of the unstable boundary layer of the previous day. The fluctuating velocities in these stable conditions may be an

order of magnitude smaller than in daytime unstable conditions. Because of these small values, dimensionless scaling often produces a ratio of two small numbers, with a resultant low degree of accuracy.

Above the surface layer, a  $z$ -less scaling region may be found. In this region, radiational heat transfer between the local air and the surroundings may not be negligible, so that  $Q_0 = -\overline{\theta'u_z'}$  is a function of height. This heat transfer is primarily in the infrared range and is locally affected by the presence of water vapor and carbon dioxide, as well as cloud cover and the surface boundary. Nieuwstadt (1984) proposed a local Monin-Obhukhov length scale in this region of

$$-\Lambda = \frac{-\left(\overline{u_x'u_z'}\right)^{3/2}}{k (g/\theta_a) \overline{u_z'\theta'}} \quad (2.40)$$

which uses the local values of the momentum ( $-\overline{u_x'u_z'}$ ) and heat ( $-\overline{u_z'\theta'}$ ) fluxes, and gives the relation

$$\frac{\Lambda}{L} = \left(1 - \frac{z}{h}\right)^{5/4} \quad (2.41)$$

for scaling within this region.

Flow within the stable atmosphere may become uncoupled at different heights. The mean wind in the stable atmosphere may be at independent speeds and independent directions at different heights. An interesting phenomena which sometimes occurs within the stable boundary layer is the nocturnal jet, which is a layer of air with a velocity greater than the overlying geostrophic wind. The phenomena may be due to an imbalance between lateral pressure gradients and the Coriolis forces. It usually occurs on clear nights over gradually sloping mesoscale terrain.

Variances in the nocturnal boundary layer are best examined through a spectral representation. In this representation, low frequency wanderings, on the order of 10 to 30 minutes occur in wind speed and direction. These wanderings occur even for  $Ri > 0.21$ , so they are not associated with turbulence, but are gravity waves associated with a stably stratified fluid. Flow with mixed turbulence and gravity waves is not well understood.

### **Spectra of Velocity in the Atmospheric Boundary Layer**

Additional information on the velocity variance can come from a spectral representation

$$\sigma_i^2 = \int_0^{\infty} S_{ii}(\kappa) d\kappa \quad (2.42)$$

which is somewhat more insightful for determining the origins of the velocity fluctuations and assessing errors in  $\sigma_i$  while sampling for only a limited time period.

At smaller scales, Kolmogorov's theory postulates an inertial subrange in high Reynolds number flows, such as in the atmospheric boundary layer. This may be represented as

$$S_{uu}(\kappa_x) = \alpha_1 \epsilon^{2/3} \kappa_x^{-5/3} \quad (2.43)$$

With Taylor's hypothesis,  $\kappa_x = 2\pi n/\bar{u}_x$ , a frequency representation can be equivalent to a Eulerian wavenumber formulation. After nondimensionalization using surface layer parameters (Kaimal et al., 1972), this may be written

$$\frac{n S_{uu}(n)}{u_*^2} = \frac{\alpha_1}{(2\pi k)^{2/3}} \phi_\epsilon^{2/3} f^{-2/3} \quad (2.44)$$

where  $\phi_\epsilon = k z \epsilon / u_*^3$  is the dimensionless dissipation rate for turbulent energy. Frequencies in this representation are scaled by  $f = nz/\bar{u}_x$ , where the wavelength of an eddy is given by  $\bar{u}_x/n$ . The value  $n$  is the frequency in Hertz and  $\bar{u}_x$  is the mean wind speed. With this scaling measured spectra in the surface layer collapse to a inertial subrange at higher frequencies, but separate at lower frequencies as a function of  $z/L$ . Velocity spectra of  $v$  and  $w$  also show the same inertial subrange dependence, and the relation of  $S_{vv}(n) = S_{ww}(n) = (4/3)S_{uu}(n)$  which follows from equations valid in homogeneous turbulence (Panofsky and Dutton, 1984, p.97).

This scaling has also been applied in the mixed layer by Kaimal et al. (1976) using

$$\frac{n S_{uu,vv,ww}(n)}{w_*^2 \psi_\epsilon^{2/3}} = C f_i^{-2/3} \quad (2.45)$$

where  $C$  is a constant coefficient,  $\psi_\epsilon = \epsilon T/gQ_0$  is the dimensionless dissipation rate in the mixed layer, and  $f_i$  is the dimensionless frequency  $nz/\bar{u}_x$ . Mixed layer data shown in these units show collapse to a single relation following an inertial subrange with the same 4/3 dependence on the coefficient  $C$ , as in surface layer scaling. There is still a  $z/z_i$  dependence at lower frequencies.

A model for the velocity spectra in unstable through neutral conditions including low wavenumbers is given by Højstrup (1982) for the surface layer in unstable conditions. This model is formulated as the sum of two parts, one which covers the higher frequency mechanically generated shear turbulence and another modeling the lower frequency buoyancy produced turbulence. The form of the model is the sum of two spectra

$$nS_{u,v}(n) = A_{u,v}(f_i) w_*^2 + B_{u,v}(f) u_*^2 \quad (2.46)$$



where the first term is scaled by the convective velocity  $w_*$ , the second term is scaled by the friction velocity  $u_*$ , and  $f_i = nz_i/\bar{u}_x$ , where  $z_i$  is the inversion height.

We can use the definition of  $w_*$  and  $u_*$  to remove  $w_*$  from the above equation,

$$w_*^2 = u_*^2 \left[ -\frac{z_i}{Lk} \right]^{2/3} \quad (2.47)$$

to get

$$\frac{n S_{u,v}(n)}{u_*^2} = A_{u,v}(f_i) \left[ -\frac{z_i}{L} \right]^{-2/3} + B_{u,v}(f) \quad (2.48)$$

after absorbing the Kolmogorov constant  $k$  into the function  $A_{u,v}$ .

For the vertical component, a similar sum is used, except without dependence of the convective A term on  $z_i$ ,

$$\frac{n S_w(n)}{u_*^2} = A_w(f) \left[ -\frac{z}{L} \right]^{-2/3} + B_w(f) \quad (2.49)$$

Højstrup (1982) extends the range of this model up to  $z = 0.5z_i$ , while maintaining agreement in the surface layer, using suitable choices for the functions A and B to agree with meteorological data taken in Minnesota in 1973 (Kaimal, 1978, and Kaimal et al., 1976) and Kansas in 1968 (Kaimal et al., 1972). This fitting gives A and B as functions of  $z/z_i$ ,  $z_i/L$ , and frequency.

At the unstable boundary layer interface given by  $z_i$ , there is entrainment and mixing of fluid between the underlying unstable flow and the stable stratification of the overlying air. Measurements near the top of the surface layer are difficult to accomplish, and there is not a great deal of available data on the entrainment process. Intermittency between turbulent and relatively nonturbulent fluid is important in this layer. Kaimal et al. (1976) presents a discussion on the physics and entrainment effects of buoyant thermals in the unstable layer as they reach the capping inversion. There is evidence that the effects of entrainment may affect temperature and velocity spectra in the entire upper half of the unstable boundary layer.

### 3. THE THEORY OF TURBULENT DISPERSION

In the analysis of turbulent dispersion, we are interested in the transport of gases, vapors, or small particles through the atmosphere. When these items are passively dispersed by the flow, this may be almost entirely a kinematic problem, one in which the characteristics of the dispersion relate to the characteristics of the turbulence. We can consider the material of interest as a fluid marker, so that the primary problem is to determine the transport of marked fluid elements by the velocity field.

With a complete specification for the field of velocity  $u_i(\mathbf{x}, t)$ , determining the evolution of the field of concentration  $c(\mathbf{x}, t)$  would be possible for a specified source of passive material using the Eulerian species equation

$$\frac{\partial c}{\partial t} + u_i \frac{\partial c}{\partial x_i} = \mathcal{D} \frac{\partial^2 c}{\partial x_i^2} \quad (3.1)$$

Because  $u_i(\mathbf{x}, t)$  is a locally correlated but random velocity field, we instead resort to statistical approaches for solving this problem. One method is to solve a simplified form of the Navier-Stokes equation and use the resulting velocity field in the species equation. Another approach is to attempt to simplify the species equation directly, possibly in a first-order gradient-transport closure

$$\frac{\partial \bar{c}}{\partial t} + \bar{u}_i \frac{\partial \bar{c}}{\partial x_i} = \mathcal{K}_i \frac{\partial^2 \bar{c}}{\partial x_i^2} \quad (3.2)$$

and look for suitable forms for  $\mathcal{K}_i$  in an analogy to molecular diffusion. Closure may also be accomplished by approximating higher-order terms and moments.

In a parallel type of solution method, we may use the set of Lagrangian conservation equations for fluid motion (Kao, 1984). In this set of equations, the nonlinear advection term found in the Eulerian conservation equations disappear, but the pressure force, molecular diffusion terms, friction, and heat conduction terms are nonlinear. This results in a much more complicated set of Lagrangian conservation equations than the more familiar Eulerian equations. For species conservation equation, however, we have

$$\left( \frac{\partial c}{\partial t} \right)_{\mathcal{L}} = 0 \quad (3.3)$$

if diffusion is neglected and  $\mathcal{L}$  indicates the Lagrangian form. From Eq. 3.3 we see that elements of fluid marked with a given concentration will retain that value in the evolving flow. For the large turbulent Reynolds number ( $u' \ell / \nu$ ) and mass Peclet number ( $u' \ell / \mathcal{D}$ ) flows in which we are inter-

ested, the assumption of negligible diffusion is reasonable. In estimating dispersion, averages are taken from a large ensemble of independent Lagrangian particle trajectories.

The modeling approaches in this chapter will focus on the results of both simple closure of the Eulerian species equation and the statistical techniques for handling Lagrangian particle or marked fluid trajectories. The chapter begins with a basic analysis of Brownian diffusion in the Eulerian and Lagrangian frames of reference in Section 3.1. The analysis of turbulent dispersion is covered in Section 3.2, followed by a summary of applied mean dispersion models in Section 3.3. Models for concentration fluctuations are covered in two sections. Section 3.4 introduces statistical analysis techniques used in analysis of the spatial characteristics of relative cloud dispersion. In section 3.5 several analysis techniques are used in studying point concentration statistics. The variance in concentration is analyzed using both the statistical techniques and gradient closure methods. Derivations for probability distributions of point concentrations are also presented.

### 3.1 Brownian Diffusion

A distinction is made between molecular diffusion (or Brownian motion) and turbulent dispersion. Diffusion is a mixing of molecular species or aerosol particles by the random thermal motion of the molecules. Turbulent dispersion is a dilution in a fluid of one material into another that is controlled by the fluctuations in velocity of a turbulent flow. A brief discussion of Brownian diffusion will illuminate many of the necessary assumptions made in turbulent dispersion.

#### 3.1.1 The Diffusion Equation and the Langevin Equation

The species conservation equation for constituent A is given by

$$\frac{\partial c}{\partial t} + u_i \frac{\partial c}{\partial x_i} = \mathcal{D} \frac{\partial^2 c}{\partial x_i^2} \quad (3.4)$$

where the mass concentration  $c$  [mass/unit volume] is equal to the partial density  $\rho_A$ . For a one dimensional geometry in a uniform medium at rest we have

$$\frac{\partial c}{\partial t} = \mathcal{D} \frac{\partial^2 c}{\partial x^2} \quad (3.5)$$

With an initial condition of  $c = q \delta(x)$  at  $t = 0$ , the solution to Eq. 3.5 is given by

$$c = \frac{q}{2\sqrt{\pi \mathcal{D} t}} \exp\left(-\frac{x^2}{4 \mathcal{D} t}\right) \quad (3.6)$$

or, with

$$\sigma^2 = 2 \mathcal{D} t \quad (3.7)$$

where  $\sigma$  is a measure of the material spread we find the solution to Eq. 3.5 is the Gaussian distribution given by

$$c = \frac{q}{\sqrt{2\pi} \sigma} \exp\left(-\frac{x^2}{2\sigma^2}\right) \quad (3.8)$$

We may examine the range of validity of the diffusion solution using Langevin's equation,

$$\frac{dv}{dt} = -\beta v + \mathcal{A}(t) \quad (3.9)$$

which represents the acceleration of a single particle undergoing Brownian motion in a Lagrangian coordinate system moving with the particle. The velocity of the particle is  $v$ , the systematic term  $-\beta v$  represents the drag force on the particle, here governed by Stoke's law, where

$$\beta = \frac{6\pi\eta r}{m} \quad (3.10)$$

and  $m$  is the particle mass,  $r$  is the particle radius and  $\eta$  is the viscosity coefficient of the fluid. The term  $\mathcal{A}(t)$  is a random term, due to the fluctuations in collisions with the surrounding molecules. This random term varies rapidly in comparison with variations in  $v$  and it is assumed that  $\mathcal{A}(t)$  is independent of  $v$ .

Integrating Langevin's equation yields

$$v = v_0 \exp(-\beta t) + \exp(-\beta t) \int_0^t \exp(-\beta t') \mathcal{A}(t') dt' \quad (3.11)$$

The Lagrangian velocity correlation of Eq. 3.11 is

$$R_{vv}(\tau) = \frac{\overline{v(0)v(\tau)}}{\overline{v^2}} = \exp(-\beta\tau) \quad (3.12)$$

where the only contribution is from the systematic term, and using Taylor (1921), we have

$$\sigma^2(t) = 2\overline{v^2} \left[ \frac{t}{\beta} - \frac{1}{\beta^2} (1 - \exp(-\beta t)) \right] \quad (3.13)$$

for the mean square displacement. It is possible to use Eq. 3.13 directly in the solution given in Eq. 3.8 for all times  $t$  (the connection will be shown in Section 3.2.1). A constant diffusion coefficient  $\mathcal{D}$  is only found for large  $t$  where

$$\sigma^2 = \frac{2 \overline{v^2}}{\beta} t \quad (3.14)$$

Using  $\sigma^2 = 2\mathcal{D}t$  leaves

$$\mathcal{D} = \frac{\overline{v^2}}{\beta} \quad (3.15)$$

Equation 3.15 implies that all velocity steps are uncorrelated. A random walk model will yield the same result assuming that particle velocities are uncorrelated and move in independent steps (see Chandrasekhar, 1943). This corresponds to the Langevin equation with  $t > 1/\beta$ . Such a solution also follows directly from initial assumptions and the central limit theorem, which states that the sum of a large number of identically distributed random variables has a Gaussian probability density (see van Kampen, 1981).

From the Langevin equation analysis we see that the diffusion equation which uses a constant value of  $\mathcal{D}$  for Brownian motion is valid for time intervals over which the velocities of individual particles are uncorrelated and can be assumed to be random. This time scale is the relaxation time of the particle over which the inertial effects of the initial imposed velocity  $v_0$  becomes negligible, or  $t \gg 1/\beta$ . This requires that concentration changes measured over a distance on the order of the relaxation distance  $\sqrt{\overline{v^2}}/\beta$  are neglected and the mass per unit volume is given as  $c = \Delta M/\mathcal{V}$  with the averaging volume no smaller than

$$\mathcal{V} \approx \left( \frac{\sqrt{\overline{v^2}}}{\beta} \right)^3 \quad (3.16)$$

This 'Stosszahlansatz' or random phase averaging (see van Kampen, 1981, p.58) is a drastic step which removes the irrelevant small scale fluctuations and leads to a differential equation for the slower macroscale diffusion phenomena. For Brownian motion, this restriction does not present a great problem because the rapidly varying quantities found at these small scales are often not of interest. In turbulent dispersion, however, with Lagrangian integral scales of velocity  $t_L$  replacing the Brownian particle time constant, dispersion is important within the correlated region for  $t < t_L$ .

### 3.1.2 Relating the Stochastic Theory and the Diffusion Equation

In the diffusion problem a connection between the random walk solution and the differential equation can be made before completely solving the random walk problem. First, we are interested in the probability density function  $p(\mathbf{x}', t)$  that the point  $\mathbf{x}'$  is within marked fluid at time  $t$ , where

marked fluid simply includes a fraction of the passively dispersing particles of interest. At an earlier time  $t_0$  the distribution of material is given by  $p(\mathbf{x}, t_0)$ , and

$$\int p(\mathbf{x}, t_0) d\mathbf{x} = \int p(\mathbf{x}', t) d\mathbf{x}' = 1 \quad (3.17)$$

from the definition of a probability density function, and the integration is over all space. Concentrations are given by

$$c(\mathbf{x}, t) = q p(\mathbf{x}, t) \quad (3.18)$$

where  $q$  is the total mass of material. We need to relate  $p(\mathbf{x}, t_0)$  to  $p(\mathbf{x}', t)$ . Given the transition probability density function  $\psi(\mathbf{x} - \mathbf{x}', t | t_0)$ , the displacement  $(\mathbf{x} - \mathbf{x}')$  at time  $t$  of a single particle released at  $t_0$  is

$$p(\mathbf{x}, t) = \int p(\mathbf{x}', t_0) \psi(\mathbf{x} - \mathbf{x}', t | t_0) d\mathbf{x}' \quad (3.19)$$

where again the integration is over all space. This Smoluchowski equation describes the evolution of the probability distribution of a cloud of particles in time. A general solution of this equation is given by Wang and Uhlenbeck (1945). We show a somewhat less general approach.

For the diffusion problem, the transition probability density function  $\psi(\mathbf{X}, t | t_0)$  is given by the Gaussian distribution (Csanady, 1973)

$$\psi(\mathbf{x} - \mathbf{x}', t | t_0) = \frac{1}{[4\pi \mathcal{D}(\Delta t)]^{3/2}} \exp\left(-\frac{(\mathbf{x} - \mathbf{x}')^2}{4\mathcal{D}(\Delta t)}\right) \quad (3.20)$$

where  $t - t_0$  is long enough for an individual particle to experience a large number of independent displacements, but with the displacement  $(\mathbf{x} - \mathbf{x}')$  still small. In terms of only the displacement differences and in one dimension only,

$$\psi(\Delta x | \Delta t) = \frac{1}{2\sqrt{\pi \mathcal{D}(\Delta t)}} \exp\left(-\frac{(\Delta x)^2}{4\mathcal{D}(\Delta t)}\right) \quad (3.21)$$

Using

$$p(\mathbf{x}, t + \Delta t) = \int_{-\infty}^{\infty} p(\mathbf{x} - \Delta \mathbf{x}, t) \psi(\Delta \mathbf{x} | \Delta t) d(\Delta \mathbf{x}) \quad (3.22)$$

and a Taylor series expansion of  $p(\mathbf{x} - \Delta \mathbf{x}, t)$ , we obtain

$$p(x, t + \Delta t) = \frac{1}{2\sqrt{\pi \mathcal{D}(\Delta t)}} \int_{-\infty}^{\infty} \exp\left(-\frac{\Delta x^2}{4\mathcal{D}(\Delta t)}\right) \left\{ p(x, t) - \Delta x \frac{\partial p}{\partial x} + \frac{\Delta x^2}{2} \frac{\partial^2 p}{\partial x^2} - \dots \right\} d(\Delta x) \quad (3.23)$$

Integrating gives

$$p(x, t + \Delta t) = p(x, t) + \mathcal{D} \Delta t \frac{\partial^2 p}{\partial x^2} + \mathcal{O}(\Delta t^2) \quad (3.24)$$

Approximating to first order yields

$$\frac{\partial p}{\partial t} = \frac{p(x, t) - p(x, t_0)}{\Delta t} = \mathcal{D} \frac{\partial^2 p}{\partial x^2} \quad (3.25)$$

and with  $p(x, t)$  proportional to concentration  $c(x, t)$ , this is the 1-D diffusion equation. Equation 3.25 is also known as the Fokker-Plank equation. In it we see the relation between the Lagrangian and Eulerian frames of reference. Chandrasekhar (1943) shows the same derivation for the more general 3-D diffusion equation.

### 3.1.3 General Solutions of the Diffusion Equation

A three-dimensional solution of the diffusion equation

$$\frac{\partial c}{\partial t} = \mathcal{D} \left[ \frac{\partial^2 c}{\partial x^2} + \frac{\partial^2 c}{\partial y^2} + \frac{\partial^2 c}{\partial z^2} \right] \quad (3.26)$$

may be found, as

$$c = \frac{q}{[\sqrt{2\pi} \sigma]^3} \exp\left(-\frac{x^2}{2\sigma^2} - \frac{y^2}{2\sigma^2} - \frac{z^2}{2\sigma^2}\right) \quad (3.27)$$

which is a superposition of the three one-dimensional solutions,  $q$  is now an instantaneous point source in units of mass, and  $\sigma^2 = 2\mathcal{D}t$ . A solution for convection of this point source in a uniform wind field  $\bar{u}_x$  in the  $x$  direction is

$$c = \frac{q}{(\sqrt{2\pi} \sigma)^3} \exp\left(-\frac{(x - \bar{u}_x t)^2 + y^2 + z^2}{2\sigma^2}\right) \quad (3.28)$$

Isopleths of concentration for this geometry are spherical surfaces centered at  $(\bar{u}_x t, y, z)$ .

A solution for a continuous point source is found by integrating over a series of instantaneous sources released sequentially in time.

$$c = \int_0^{\infty} \frac{q}{8 [\pi \mathcal{D} (t - t')]^{3/2}} \exp \left( - \frac{\{x - \bar{u}_x (t - t')\}^2 + y^2 + z^2}{4 \mathcal{D} (t - t')} \right) dt' \quad (3.29)$$

and since the behavior of all terms within the integral in time is known, a solution may be found

$$c = \frac{q}{4 \pi \mathcal{D} r} \exp \left( - \frac{\bar{u}_x}{\mathcal{D}} \{r - x\} \right) \quad (3.30)$$

where  $r^2 = x^2 + y^2 + z^2$  and  $q$  is the release rate per unit time. For typical values of the diffusion coefficient, the concentration  $c$  is largest along the  $x$  axis and the simplification of a narrow plume is possible far downwind from the source, for which

$$r \approx x \left[ 1 + \frac{y^2 + z^2}{2x^2} \right] \quad (3.31)$$

so that  $r \approx x$  and  $r - x \approx (y^2 + z^2)/2x$  can be substituted into the solution to get

$$c = \frac{q}{2 \pi \bar{u}_x \sigma^2} \exp \left( - \frac{y^2 + z^2}{2 \sigma^2} \right) \quad (3.32)$$

where

$$\sigma = \sqrt{2 \mathcal{D}} \frac{x}{\bar{u}_x} \quad (3.33)$$

is the standard deviation of the plume centered at  $x$ . This is evidently the solution of

$$\bar{u}_x \frac{\partial c}{\partial x} = \mathcal{D} \left[ \frac{\partial^2 c}{\partial y^2} + \frac{\partial^2 c}{\partial z^2} \right] \quad (3.34)$$

We see that the narrow plume solution neglects diffusion in the direction of the mean velocity. The narrow plume approximation is applied to the problem of turbulent dispersion in Eq. 3.66.

## 3.2 Turbulent Dispersion

Two distinct types of analysis are possible in turbulent dispersion. In an Eulerian analysis we are primarily interested in the probable concentration found at fixed points of the flow field. For the Lagrangian analysis, we inquire into the probable distribution of the diffusing material with respect to points which follow the turbulent fluid motion.

The application of either type of analysis depends on the ratio of the scale of the turbulence to that of the linear size of a cloud of dispersing material. When the ratio is small, the boundary of the marked fluid undergoes small-scale distortion, but the center of mass of the cloud is approxi-



mately stationary (with respect to any mean flow) and an Eulerian analysis is sufficient (this was the case for the previous Brownian diffusion problems for  $t > 1/\beta$ ). For such conditions, the positional characteristics of the cloud with respect to a fixed position may be built up from the motion of a single particle. Conversely, when the scale of the turbulence is much larger than the cloud size, a Lagrangian type of analysis is necessary for quantifying the relative cloud size. This analysis separates the motion of multiple points within the evolving cloud from the translation of the whole cloud.

For a continuously emitting fixed point source, interest is primarily in dispersion relative to the source. In the atmosphere, where the spatial scale of turbulence is often greater than the width of the continuous plume, this is appropriate only for averages taken over a period of time much longer than the time scale of the turbulence. Over shorter time periods, values of concentration at fixed points are likely to vary considerably from the long-term average. The plume will also wander around the path defined by the mean trajectory. For this case, the Eulerian analysis is unable to explain short term values, and a more complex method is needed.

### 3.2.1 Mean Concentrations in Turbulent Dispersion

We are first concerned with the long-term average behavior of a continuous smoke plume. For the mean concentration in a turbulent flow, after Reynold's decomposition of the species conservation in a turbulent flow we have

$$\frac{\partial \bar{c}}{\partial t} + \bar{u}_i \frac{\partial \bar{c}}{\partial x_i} = - \frac{\partial \overline{u'_i c'}}{\partial x_i} + \mathcal{D} \frac{\partial^2 \bar{c}}{\partial x_j^2} \quad (3.35)$$

where primes indicate fluctuating quantities and overbars indicate ensemble averages. Neglecting the molecular diffusion term and replacing the term containing the joint moment of concentration and velocity by a gradient transfer term such as

$$- \overline{u'_i c'} = \kappa_i \frac{\partial \bar{c}}{\partial x_i} \quad (3.36)$$

or

$$- \frac{\partial \overline{u'_i c'}}{\partial x_i} = \kappa_i \frac{\partial^2 \bar{c}}{\partial x_i^2} \quad (3.37)$$

gives a result similar to the equation for molecular diffusion

$$\frac{\partial \bar{c}}{\partial t} + \bar{u}_i \frac{\partial \bar{c}}{\partial x_i} = \frac{\partial}{\partial x_i} \left[ \kappa_i \frac{\partial \bar{c}}{\partial x_i} \right] \quad (3.38)$$

which is a first order closure approximation to the species conservation equation.

Richardson (1926), in this type of analysis has attempted to define values of  $K_i$ , but found that values vary over a range of a billion to one in different atmospheric flow geometries. The value of  $K_i$  is shown to grow with the scale of the dispersing cloud of material. While  $K$ -theory is shown to be adequate for some aspects of the atmospheric dispersion problem, such as vertical dispersion in the surface layer (Nieuwstadt and van Ulden, 1978), the broad range of  $K_i$  values is not suitable for a general solution.

A problem with this method parallels that of Stosszahlansatz or random phase averaging in the diffusion equation. To assume a value of  $K_i$  which is independent of time requires that we restrict the analysis to scales much larger than that of the Lagrangian integral scale of the turbulence, so that particle dispersion is composed of many independent spatial segments. In the atmosphere, however, dispersion is often important at distances smaller than sizes associated with the largest eddies in the flow

For more insight into the problem, we use the statistical theory presented by Batchelor (1949) and use the Lagrangian description for the species equation. We can refer to marked fluid as constant concentration particles if Brownian and molecular diffusion are neglected. In determining the mean concentration from a continuous source, we first look at a puff of marked fluid from which a continuous plume may eventually be found by integrating over a series of sequentially released puffs. The problem is to determine the distribution of mean concentration at fixed points downwind from a source in an Eulerian analysis. Consider an initial blob of marked fluid, where  $p(\mathbf{x}', t_0)$  is the probability density function for finding marked fluid at time  $t_0$ , for any location  $\mathbf{x}'$ . We have

$$\int p(\mathbf{x}', t) d\mathbf{x}' = 1 \quad (3.39)$$

for any time  $t$ , and the integration is over all space. The mean center of the concentration field is given by

$$c_i(t) = \int x_i p(\mathbf{x}, t) d\mathbf{x} \quad (3.40a)$$

$$= c_i(0) + \int (x_i - x'_i) \psi(\mathbf{x} - \mathbf{x}', t | t_0) d\mathbf{x}' \quad (3.40b)$$

$$= c_i(0) + \overline{X_i(t)} \quad (3.40c)$$

and the spread is given by the tensor

$$d_{ij}(t) = \int (x_i - c_i)(x_j - c_j) p(\mathbf{x}, t) d\mathbf{x} \quad (3.41a)$$

$$= d_{ij}(0) + \overline{X_i(t)X_j(t)} \quad (3.41b)$$

We need the probability density function  $p(\mathbf{x}, t)$  that the point  $\mathbf{x}$  is within marked fluid at time,  $t$ . If  $\psi(\mathbf{X}, t | t_0)$  is the transition probability density function of the displacement  $\mathbf{X} = \mathbf{x} - \mathbf{x}'$  in time  $t$ , then

$$p(\mathbf{x}, t) = \int p(\mathbf{x}', t_0) \psi(\mathbf{x} - \mathbf{x}', t | t_0) d\mathbf{x}' \quad (3.42)$$

where the integration is over all volume. In Equation 3.42 we are simply integrating over all of the possible positions of particles at time  $t_0$  multiplied by all of the possible transitions that these particles can experience over time  $t_0$  to  $t$ . For an instantaneous point source we have  $p(\mathbf{x}', t_0) = \delta(\mathbf{x}', t_0)$ , or for a continuous point source  $p(\mathbf{x}', t_0) = \delta(\mathbf{x}')$ . The major problem remains in determining the form of  $\psi(\mathbf{x} - \mathbf{x}', t | t_0)$ .

Using the characteristic functions

$$\phi(\boldsymbol{\kappa}, t | t_0) = \int_{-\infty}^{\infty} \psi(\mathbf{x}, t | t_0) \exp(i \boldsymbol{\kappa} \cdot \mathbf{x}) d\mathbf{x} \quad (3.43)$$

$$\phi(\boldsymbol{\kappa}, t) = \int_{-\infty}^{\infty} p(\mathbf{x}, t) \exp(i \boldsymbol{\kappa} \cdot \mathbf{x}) d\mathbf{x} \quad (3.44)$$

Equation 3.42 may also be expressed as

$$\phi(\boldsymbol{\kappa}, t) = \phi(\boldsymbol{\kappa}, t_0) \phi(\boldsymbol{\kappa}, t | t_0) \quad (3.45)$$

so that the increase in the cumulants of  $p(\mathbf{x}, t)$  from  $t_0$  to  $t$  is equal to the corresponding cumulants of  $\phi(\mathbf{x}, t | t_0)$ <sup>1</sup>. This means that the dispersion of a single fluid particle relative to a fixed point is determined only by the initial location of the particle and the probability density function of the displacement  $X_i(t)$  of a single fluid particle.

In homogeneous, isotropic turbulence, the displacement  $X_i(t)$  has a Gaussian probability density function for a wide range of displacement times, for reasons which vary with the magnitude of the time,  $t$ . For small  $t$  the probability density function of the displacement  $X_i(t)$  is identical to that of the velocity  $u_i(0)$ , from

$$X_i(t) = \int_0^t u_i(t') dt' \approx t u_i(0) \quad (3.46)$$

---

<sup>1</sup> The cumulants,  $\kappa_m$ , of the characteristic function are defined by

$$\log \phi(\boldsymbol{\kappa}, t) = \sum_{m=1}^{\infty} \frac{(i\boldsymbol{\kappa})^m}{m!} \kappa_m$$

and are combinations of the moments of the probability distribution (see Van Kampen, 1981).

Measurements of  $u_i(0)$  in isotropic turbulence have confirmed a Gaussian form within the limits of experimental error<sup>1</sup>. Conversely, at larger times,  $u_i(t)$  loses all correlation with  $u_i(0)$  so  $X_i(t)$  is the integral of a function for which only neighboring values are correlated. A long time series of this function could be considered to be composed of independent segments. For large  $t$  this sum tends to a normal distribution by the central limit theorem (see van Kampen, 1981), so that a Gaussian distribution for  $X_i(t)$  at larger displacement times is also reasonable (but not, as of yet, rigorously proved).

With this normal distribution of displacements, we can use

$$\phi(\kappa, t | t_0) = \exp\left(-\frac{1}{2} \kappa_i \kappa_j \overline{X_i(t) X_j(t)}\right) \quad (3.47)$$

for the characteristic function of the displacement probability density function, and with Eq. 3.45, we get

$$\frac{\partial \phi(\kappa, t)}{\partial t} = \phi(\kappa, t) \left[ -\frac{1}{2} \kappa_i \kappa_j \frac{\partial \overline{X_i(t) X_j(t)}}{\partial t} \right] \quad (3.48)$$

from which can be found a diffusion equation

$$\frac{\partial p(\mathbf{x}, t)}{\partial t} = \mu_{ij} \frac{\partial^2 p(\mathbf{x}, t)}{\partial x_i \partial x_j} \quad (3.49)$$

and the non-constant tensor coefficient is given by

$$\mu_{ij}(t) = \frac{1}{2} \frac{d \overline{X_i(t) X_j(t)}}{dt} \quad (3.50)$$

Using the relation between displacements and velocity given by Taylor (1921), and generalizing to three dimensions, Eq. 3.50 can be manipulated to get

$$\begin{aligned} \mu_{ij}(t) &= \frac{1}{2} \overline{X_i(t) v_j(t)} + \frac{1}{2} \overline{X_j(t) v_i(t)} \\ &= \frac{1}{2} \int_{t_0}^t \overline{v_i(t') v_j(t)} + \overline{v_i(t) v_j(t')} dt' \end{aligned} \quad (3.51)$$

---

<sup>1</sup> In the atmosphere, over flat terrain, probability distributions of  $u(0)$ , in the downwind direction, and  $v(0)$ , in the crosswind direction also show a Gaussian form. The distribution of  $w(0)$ , in the vertical direction however, is definitely not Gaussian, which results in important deviations of the theory from that for homogeneous turbulence in most atmospheric conditions.

where here,  $v_i$  and  $v_j$  are Lagrangian velocities of a fluid particle. In homogeneous turbulence, for which the velocities are stationary random functions of time, the correlation  $\overline{v_i(t)v_j(t')}$  simplifies to be a function only of  $(t - t')$

$$\mu_{ij}(t) = \frac{1}{2} \overline{v_i v_j} \int_0^{t-t_0} [R_{ij}(\xi) + R_{ji}(\xi)] d\xi \quad (3.52)$$

and

$$\frac{d\overline{X_i(t)X_j(t)}}{dt} = \overline{v_i v_j} \int_0^t [R_{ij}(\xi) + R_{ji}(\xi)] d\xi \quad (3.53)$$

$$\overline{X_i(t)X_j(t)} = \int_0^t \int_0^\tau [R_{ij}(\xi) + R_{ji}(\xi)] d\xi d\tau \quad (3.54a)$$

$$\overline{X_i(t)X_j(t)} = \int_0^t (t - \xi) [R_{ij}(\xi) + R_{ji}(\xi)] d\xi \quad (3.54b)$$

Without a specific form for the Lagrangian correlation  $R_{ij}(\xi)$  this equation is can only be simplified at its asymptotic limits. First, for small time intervals,

$$\overline{X_i X_j} = t^2 \overline{v_i v_j} \quad (3.55)$$

where the particle velocity is constant over the time period  $t$ . For larger times, when the time  $(t-t_0)$  is large, the velocity correlation is small, so

$$\overline{X_i X_j} \rightarrow \overline{v_i v_j} \left[ t I_{ij}^{(0)} - I_{ij}^{(1)} \right] \quad (3.56)$$

where

$$\int_0^t [R_{ij}(\xi) + R_{ji}(\xi)] d\xi \rightarrow I_{ij}^{(0)} \quad (3.57)$$

and

$$\int_0^t \xi [R_{ij}(\xi) + R_{ji}(\xi)] d\xi \rightarrow I_{ij}^{(1)} \quad (3.58)$$

are constants for large  $t$ . This form for larger times, leads to a value of  $\mu_{ij}(t)$  which is independent of time and has the same form as for the diffusion solution.

Assuming that  $x$ ,  $y$ , and  $z$  are principle axes, and the probability distributions of  $X_i$  are independent, we have

$$\overline{X_i(t)X_j(t)} = 0 \quad j \neq i \quad (3.59a)$$

$$\overline{X_i(t)X_j(t)} = \sigma_i^2 \quad j = i \quad (3.59b)$$

leaving

$$\frac{\partial p(x,t)}{\partial t} = \left\{ \frac{1}{2} \frac{d \sigma_i^2}{dt} \right\} \frac{\partial^2 p(x,t)}{\partial x_i^2} \quad (3.60)$$

A solution of the differential equation for a point source is

$$p(x, t) = \frac{1}{(2\pi)^{3/2} \sigma_x \sigma_y \sigma_z} \exp \left( -\frac{x^2}{2 \sigma_x^2} - \frac{y^2}{2 \sigma_y^2} - \frac{z^2}{2 \sigma_z^2} \right) \quad (3.61)$$

where the probability density function  $p(x,t)$  is related to concentration through a total mass release  $q$ , for this instantaneous point source by

$$c(x, t) = q p(x, t) \quad (3.62)$$

or, after assuming a mean velocity  $\bar{u}_x$  in the  $x$  direction,

$$c(x, y, z, t) = \frac{q}{(2\pi)^{3/2} \sigma_x \sigma_y \sigma_z} \exp \left( -\frac{(x - \bar{u}_x t)^2}{2 \sigma_x^2} - \frac{y^2}{2 \sigma_y^2} - \frac{z^2}{2 \sigma_z^2} \right) \quad (3.63)$$

a solution for dispersion which was first proposed by Sutton (1932).

For a continuous source, integration over time of an incremental series of instantaneous 'puff' releases is

$$c(x, y, z) = \frac{q}{(2\pi)^{3/2}} \int_0^\infty \frac{1}{\sigma_x \sigma_y \sigma_z} \exp \left( -\frac{(x - \bar{u}_x t)^2}{2 \sigma_x^2} - \frac{y^2}{2 \sigma_y^2} - \frac{z^2}{2 \sigma_z^2} \right) dt \quad (3.64)$$

but the immediate complication is that the factors  $\sigma_x$ ,  $\sigma_y$ , and  $\sigma_z$  are unknown functions of time. This can be circumvented using a slightly different form of the differential equation which assumes a continuous slender plume with negligible diffusion in the  $x$ -direction for

$$\bar{u}_x \frac{\partial p(x,t)}{\partial x} = \left\{ \frac{1}{2} \frac{d \sigma_y^2(t)}{dt} \right\} \frac{\partial^2 p(x,t)}{\partial y^2} + \left\{ \frac{1}{2} \frac{d \sigma_z^2(t)}{dt} \right\} \frac{\partial^2 p(x,t)}{\partial z^2} \quad (3.65)$$

a solution of which is

$$c(x, y, z) = \frac{q}{2\pi \bar{u}_x \sigma_y \sigma_z} \exp \left( -\frac{y^2}{2 \sigma_y^2} - \frac{z^2}{2 \sigma_z^2} \right) \quad (3.66)$$

It is interesting to note that the functions  $\sigma_y$  and  $\sigma_z$  governing the width of the expanding cloud are the same for both the solution from an instantaneous point source and the continuous plume solution. This analysis, which employs ensemble averages of many independent single particle trajectories, could give no other answer. For the case in which the turbulence scale is much smaller than the plume width, it is certainly a reasonable result. For the alternative case, wherein the turbulence scale is larger than the plume width, experimental evidence shows the long term averaged plume widths  $\sigma_y$  and  $\sigma_z$  from a continuous plume to be greater than the equivalent scales from a single instantaneous 'puff' of material, or the instantaneous width of a continuous plume.

A resolution of this problem is that the ensemble averages must be taken over time periods much longer than the Lagrangian integral time scale for the averages to be stable. Describing instantaneous plume widths or puff sizes is not possible with the analysis presented in this section, but requires an analysis beginning with a more elaborate Lagrangian specification of multiple points within the moving cloud. In the present analysis of following the motion of independent single particles, the instantaneous size of the cloud is not relevant.

It still remains to determine the form of  $\sigma_y$  and  $\sigma_z$  as a function of time. Batchelor (1949) has pointed out that we have

$$\sigma_i^2(t) = 2 \overline{u_i^2} \int_0^t (t - \tau) R_{ii}(\tau) d\tau \quad (3.67)$$

from Taylor (1921), so that the changing forms of  $\sigma_y$  and  $\sigma_z$  with time is due to the greater effect of increasingly larger eddies in the dispersion, although even at small times the dispersion is dominated by the larger eddies. We note that  $R_{ii}(t)$  does not correlate multiple particles with each other, but merely the Lagrangian velocity history of a large number of single, individual particles.

Adopting an exponential form for  $R_{ii}$

$$R_{ii}(t) = \exp\left(-\frac{t}{t_L}\right) \quad (3.68)$$

gives

$$\sigma_i^2(t) = 2 \overline{u_i^2} t_L^2 \left[ \frac{t}{t_L} - 1 + \exp\left(-\frac{t}{t_L}\right) \right] \quad (3.69)$$

For  $t \gg t_L$ , this yields the same linear form of  $\sigma_y$  as that for Brownian diffusion. For turbulent dispersion, especially in the atmosphere, we are interested in time scales less than the Lagrangian turbulent integral scale  $t_L$ .

This result for  $\sigma_y$  may also be found for homogeneous turbulence using a Langevin equation of the form

$$dv(t) = \frac{-v(t) dt}{t_L} + \sigma_v \sqrt{\frac{2}{t_L}} dW_t \quad (3.70)$$

for changes in particle acceleration as presented by van Dop et al. (1985). This equation is an obvious analogy to the Langevin equation used for Brownian diffusion. It is a type of Markovian differential equation, where  $dW_t$  is a Gaussian white noise model of fluid acceleration and  $v(t)$  is the Lagrangian velocity of a fluid element. The Lagrangian integral scale is  $t_L$ , whereas  $\sigma_v$  is the standard deviation in velocity. Both are constants in homogeneous turbulence. We have

$$W_t = \int_0^t dW_t \quad (3.71)$$

and  $W_t$  is a Wiener process. Although it is continuous in time  $W_t$  is not strictly differentiable in time (Durbin, 1983). We take  $dW_t$  as a random increment, which ignores the exact nature of the particle acceleration. Using ensemble averages,  $\overline{dW_t} = 0$ ,  $\overline{dW_t^2} = dt$ ,  $\overline{vdW_t} = 0$ , and  $\overline{W_t} = 0$ . Particle position follows from integrating  $dy = dv(t)dt$ , and results in the same solutions for  $\sigma_y^2$  and  $R_{ij}(t)$  as given in the last analysis, with an ensemble average taken over many independent particle trajectories.

A Markovian process, as given here for velocity  $v$  requires a nonanticipating property for the variable of interest. The particle position  $y(t)$  is not Markovian, since it depends on  $y(t-\Delta t)$ . Velocity  $v$  and position  $y$  as given in the above Langevin equation, are jointly Markovian.

To ensure a stable measure of  $\sigma_y^2$ , an ensemble average of many individual particle trajectories is needed. In stationary turbulence, this corresponds to time averages of a continuous plume over periods of time much longer than the Lagrangian integral scale  $t_L$ . The behavior of the concentration field at averaging times which are short compared to  $t_L$  is the focus of Sections 3.4 and 3.5. Some problems which arise in the use of the Langevin equation include specifying the Lagrangian time scale  $t_L$  and the statistics of the process in terms of measured quantities.

### 3.2.2 Mean Dispersion in Anisotropic Flow

Improvements in the dispersion modeling of mean concentrations in the boundary layer can come from a more complete specification of the anisotropic effects, which up to now have been neglected. For dispersion from a continuous source, we can use a gradient transfer model,



$$\bar{u}_x \frac{\partial \bar{c}}{\partial x} = \frac{\partial}{\partial y} \left[ \kappa_y \frac{\partial \bar{c}}{\partial y} \right] + \frac{\partial}{\partial z} \left[ \kappa_z \frac{\partial \bar{c}}{\partial z} \right] \quad (3.72)$$

and adopt suitable forms for  $\kappa_i$  values as a function of position. Earlier solutions of this equation have conformed to profiles of  $\kappa_i$  and  $\bar{u}_x$  which are convenient to solve analytically. A summary of these solutions is given by Pasquill and Smith (1983). Current technology allows numerical solution of the advective diffusion equation using elaborate forms of  $\kappa_i$  and more accurate wind profiles. Some of these  $\kappa$ -theory models produce reasonable predictions in limited regions of the atmospheric boundary layer such as for vertical dispersion very near the surface.

The Lagrangian approach can provide a method for a more insightful investigation of the dispersion. We first use a general form of the Langevin equation, here in one dimension,

$$dX = b(X)dt + a(X)dW_t \quad (3.73)$$

which describes the Lagrangian motion of a fluid particle for which the first term represents the deterministic part of the particle motion and the second term is the random motion. In this example  $dX$  is an increment in particle position over time  $dt$  and the velocity over this time step is uncorrelated. The Fokker-Plank equation for Equation 3.73 is derived by Durbin (1983), and results in

$$\frac{\partial p(x,t)}{\partial t} + \frac{\partial [b(x)p(x,t)]}{\partial x} = \frac{1}{2} \frac{\partial^2 [a(x)p(x,t)]}{\partial x^2} \quad (3.74)$$

Both equations describe the same phenomena, but for different Eulerian and Lagrangian coordinate systems. To compare this equation with the gradient transfer approximation, we let  $a^2(x)/2 = \kappa(x)$  and get

$$\frac{\partial p(x,t)}{\partial t} + \frac{\partial}{\partial x} \left[ \left( b - \frac{\partial \kappa(x)}{\partial x} \right) p(x,t) \right] = \frac{\partial}{\partial x} \left( \kappa(x) \frac{\partial p(x,t)}{\partial x} \right) \quad (3.75)$$

where  $b - \partial \kappa / \partial x$  is an Eulerian mean convection velocity. This shows the relation between dispersion in a Lagrangian system and an Eulerian system for the first-order closure.

A great improvement of this method may be made by beginning with the Langevin equation for velocity, rather than displacement. Such a form models the particle acceleration as random, rather than the velocity. This velocity equation has already been used for homogeneous turbulence, in which the relevant statistics are not a function of position. In inhomogeneous turbulence, the relation between Lagrangian and Eulerian particle motion is a great deal more complicated.

We may investigate the acceleration of a particle at small times, given by

$$\frac{dv_z}{dt} = \frac{du_z}{dt} = \frac{\partial u_z}{\partial t} + u_j \frac{\partial u_z}{\partial x_j} \quad (3.76)$$

where  $v$  is the Lagrangian particle velocity, and  $u$  is the Eulerian fluid velocity at the same position and time. Using Reynold's decomposition, we find for the mean particle acceleration

$$\frac{d\bar{v}_z}{dt} = \frac{d\bar{u}_z}{dt} + \frac{\partial \bar{u}_j \bar{u}_z}{\partial x_j} \quad (3.77)$$

or for turbulence which is inhomogeneous only in the  $z$  direction

$$\frac{d\bar{v}_z}{dt} = \frac{d\bar{u}_z}{dt} + \frac{\partial \bar{u}_z \bar{u}_z}{\partial z} \quad (3.78)$$

This shows that the mean particle acceleration is not equal to the acceleration of the mean flow in inhomogeneous turbulence. Likewise, higher order moments of these two accelerations are also not equal.

Using this principle, van Dop et al. (1985) shows that the Langevin equation must have the form

$$dv_z = \left( -\frac{v(t)}{t_L(z,t)} + a_1(z,t) \right) dt + \sqrt{a_2(z,t)} dW_t \quad (3.79)$$

in inhomogeneous turbulence with  $dW_t$  as a Gaussian random function and  $t_L$  defined as a decorrelation time (Durbin,1983)

$$t_L = \left| \frac{1}{R_{vv}(\tau)} \frac{dR_{vv}(\tau)}{d\tau} \right|_{\tau=0}^{-1} \quad (3.80)$$

to avoid problems of definition with nonstationary Lagrangian velocities.

This may alternately be written as

$$dv_z = -\frac{v_z(t)}{t_L(z,t)} dt + dW_{z,t} \quad (3.81)$$

with

$$dW_{z,t} = a_1(z,t) dt + \sqrt{a_2(z,t)} dW_t \quad (3.82)$$

In determining a useful form for the functions  $a_1$  and  $a_2$ , van Dop et al. (1985) found the Fokker-Plank equation for Eq. 3.82 which results in an equation for the joint probability of  $p(z, v_z, t)$ . Reducing this to an expression for  $p(z, t) = c(z, t)/q$  results in an infinite series of equations contain-

ing joint moments of velocity  $v^n$  and concentration  $c$ . Closure is achieved by matching these moments, after order of magnitude approximations, to the equivalent Eulerian moments found from the diffusion equation after Reynolds decomposition. In this particular form, the coefficients are matched for the first three equations. This results in

$$a_1 = \frac{\partial \overline{u_z^2}}{\partial z} = \frac{d\overline{u_z^2}}{dt} \quad (3.83)$$

and

$$a_2 = 2 \frac{\overline{u_z^2}}{t_L} + \frac{\partial \overline{u_z^2}}{\partial z} + \frac{\partial \overline{u_z^2}}{\partial t} = \frac{d\overline{u_z^2}}{dt} + 2 \frac{\overline{u_z^2}}{t_L} \quad (3.84)$$

Numerical results from using this procedure shows that particles tend to properly diffuse to regions of higher turbulence. In a bounded region, however, this equation does not tend to the correct uniform asymptotic distribution of concentration. This may in part be due to errors in approximating the effect of higher-order moments.

In another approach, Thompson (1984) uses the Langevin equation

$$dv_z = \frac{v_z(t)}{t_L(z,t)} dt + d\omega_t \quad (3.85)$$

but here  $\omega_t$  is not restricted to a Gaussian forcing function. By requiring this equation to result in a uniform concentration distribution for a confined flow, moments of  $d\omega_t$  are found in terms of moments of the Eulerian velocities. Such an approach allows specification of skewed velocity distributions, such as those found in convective conditions for the vertical profile. Closure is achieved in numerical solution by neglecting higher order moments of the velocities. Because  $d\omega_t$  is non-Gaussian, a corresponding Fokker-Plank equation cannot be derived.

For our purposes, an important result found by Durbin (1983) using this modeling technique, is that inhomogeneity of  $t_L$  takes at least one time period to effect the mean displacement of marked particles, in agreement with experimental measurements according to van Dop et al. (1985). This implies that in determining ensemble average concentration distributions, the realizations over which the averages are measured must be taken over times greater than the largest  $t_L(x)$  in the flow.

### 3.3 Models of Mean Dispersion

The concise modeling results previously discussed are for dispersion in homogeneous turbulence. These still have some application in the atmospheric boundary layer after some modifi-

cations. For a narrow continuous plume from a point source, the mean concentration distribution is given by

$$\bar{c}(x,y,z) = \frac{q}{2\pi\sigma_y\sigma_z\bar{u}_x} \exp\left(-\frac{y^2}{2\sigma_y^2} - \frac{(z-z_s)^2}{2\sigma_z^2}\right) \text{ for } z \geq 0 \quad (3.86)$$

with the source located at a height  $z = z_s$ , and the coordinate origin directly below the source at ground level. This form was first used by Sutton (1932) in atmospheric modeling. The measures of the plume spread,  $\sigma_y$  and  $\sigma_z$ , are functions of the downwind distance  $x$ , rather than the travel time  $t$ , through  $x = \bar{u}_x t$ , given that  $\bar{u}_x$  is the velocity at the source height.

For the above equation, material which arrives at  $z = 0$  simply passes through the boundary. A change to the equation may be made through a reflective boundary condition, analytically accomplished by using a mirror source located below the surface at  $(0, 0, -z_s)$  or

$$\bar{c}(x,y,z) = \frac{q}{2\pi\sigma_y\sigma_z\bar{u}_x} \exp\left(-\frac{y^2}{2\sigma_y^2}\right) \left[ \exp\left(-\frac{(z-z_s)^2}{2\sigma_z^2}\right) + \exp\left(-\frac{(z+z_s)^2}{2\sigma_z^2}\right) \right] \quad (3.87)$$

for  $z \geq 0$ . This treatment of the boundary condition at the surface is quite simplistic. In practice, the absorption of a pollutant or tracer at the ground is a complicated function of the chemical and physical characteristics of the surface, the wind field, and the pollutant or tracer. For our own aerosol tracers, there is little deposition and we consider the aerosol as a conservative marker.

One application of this equation is in predicting ground-level concentrations for a reflecting boundary condition using

$$\bar{c}(x,y,0) = \frac{q}{\pi\sigma_y\sigma_z\bar{u}_x} \exp\left(-\frac{y^2}{2\sigma_y^2}\right) \exp\left(-\frac{z_s^2}{2\sigma_z^2}\right) \quad (3.88)$$

We note that this Gaussian plume model neglects several important effects, including the vertical variation in the mean velocity and the fluctuating velocities which control the plume spread. This often leads to errors in the shape of the vertical profile and the magnitude of ground-level concentration, especially in thermally stratified conditions.

A similarity between crosswind profiles of concentration measured in dispersion experiments and the Gaussian form is found in both full scale tests (Pasquill and Smith, 1983 and Randerson, 1984) and in wind tunnel boundary layers (Robins and Fackrell, 1979). This is due in part because of symmetry along the plume axis, and also due to the nearly constant measure of the crosswind velocity fluctuation intensity  $\sigma_v/\bar{u}_x$  with height over flat terrain. We can modify the above model for ground-level concentrations to obtain

$$\bar{c}(x, y, 0) = \bar{c}(x, 0, 0) \exp\left(-\frac{y^2}{2\sigma_y^2}\right) \quad (3.89)$$

which keeps the valid Gaussian crosswind distribution and allows us to find better functional forms of the ground-level concentration, where  $\bar{c}(x, 0, 0) = \bar{c}(x, z_s)$  and  $z_s$  is the source height. In practice, we instead use the crosswind integrated ground-level concentration  $\bar{c}_y(x, z_s)$  which for a Gaussian crosswind profile is related to the centerline concentration by

$$\bar{c}(x, z_s) = \frac{\bar{c}_y(x, z_s)}{\sqrt{2\pi}\sigma_y} \quad (3.90)$$

Gryning et al. (1987) summarizes methods of predicting  $\bar{c}_y(x, z_s)$  using the meteorological scaling parameters and boundary layer regions previously discussed in Section 2.3.

### 3.3.1 Crosswind Integrated Concentration in the Surface Layer

First, for the surface layer Monin-Obukhov similarity applies. Nieuwstadt and van Ulden (1978) have shown that a gradient transfer approximation

$$\bar{u}(z) \frac{\partial \bar{c}(x, z)}{\partial x} = \frac{\partial}{\partial z} \mathcal{K}_z(z) \frac{\partial \bar{c}(x, z)}{\partial z} \quad (3.91)$$

is suitable in this region for determining the concentration distribution, with the  $\mathcal{K}$ -factor approximated using the analogy of  $\mathcal{K}_z = k u_* z / \phi_h(z/L)$ , where  $\phi_h$  is the dimensionless temperature gradient found from empirical measurements. Early solutions for this particular equation were found using power-law approximations for wind speed and  $\mathcal{K}_z$  (see Pasquill and Smith, 1983). These solutions are best expressed by

$$\frac{\bar{c}_y(z)}{q} = \frac{A}{\bar{z} \bar{u}} \exp\left(-\left[\frac{Bz}{\bar{z}}\right]^s\right) \quad (3.92)$$

where  $q$  is the source strength,  $A$  and  $B$  are functions of  $s$  only,  $\bar{z}$  is the mean height of the plume and  $\bar{u}$  is the mean velocity of the plume. Gryning et al. (1983) gives analytical fits to these parameters for numerical simulations using the temperature eddy diffusivity profile for stable, neutral, and unstable conditions. We note that in these fits, the shape parameter  $s$  reaches a stable asymptote of  $s = 3$ , whereas for the unstable case,  $s$  ranges between 0.5 and 0.75 depending on the particular form of  $\phi_h$  used. This solution is valid for  $\bar{z}/z_s > 2$ . Further downwind, when  $\bar{z}$  is larger than the height of the surface layer ( $\bar{z}/h > 0.3$ ), dispersion is dominated by phenomena in the layer

immediately above the surface layer, which may be either the near-neutral upper layer in stable conditions or the mixed layer for unstable atmospheric conditions.

### **Mixed Layer**

This scaling applies for unstable conditions in the boundary layer for  $-z_i/L > 10$  with  $0.1 < z_s/z_i < 0.8$  for the source height. The turbulence in the mixed layer is dominated by thermal updrafts and subsidence. The downdrafts occupy a greater area than the updrafts, which maintain a larger vertical velocity to satisfy continuity. This inhomogeneous turbulence results in the rise of the plume centerline for ground-level sources, and a falling plume centerline for elevated sources.

Parameterization of the behavior uses a downwind distance  $X = (w_s/z_i)(x/\bar{u}_x)$  and cross wind integrated concentration at ground level of  $C_y = \bar{c}_y z_i \bar{u}_x/q$  where  $q$  is the source strength. With this scaling, Briggs (1985) gives an empirical data fit of

$$C_y = \frac{0.9 X^{9/2} Z_s^{-11/2}}{\left[ Z_s^{-3/4} + 0.4 X^{9/2} Z_s^{-9/2} \right]^{4/3}} + \frac{1}{1 + 3X^{-3/2} Z_s^{1/2} + 50X^{-9/2}} \quad (3.93)$$

for  $Z_s = z_s/z_i$ . Briggs states that this is valid in the range  $0.04 \leq Z_s \leq 1$ , which means it also applies in the free-convection region. For  $X > 5$ , the concentration achieves a well mixed profile throughout the boundary layer. Based on their own comparisons of other dispersion data with this fit, Gryning et al. (1987), suggest using  $X = 1.7(w_s/z_i)(x/\bar{u})$  to shift this curve to higher values of  $X$ .

### **Free Convection Layer**

Free convection scaling applies in the region between  $-z_s/L < 1$  and  $z_s/z_i < 0.1$ . This area lies between the surface layer and the mixed layer region for unstable atmospheric conditions. For surface releases, Nieuwstadt (1980b) gives

$$C_y = 0.9 X^{-3/2} \quad (3.94)$$

where the mixed layer scaling is maintained for convenience. This equation is independent of  $z_i$  and  $u_s$ , as is consistent with the concept of the free convection layer. In a comparison with Prairie Grass experiments, Nieuwstadt shows that this equation is valid in the range  $0.03 < X < 0.23$ .

## Other Scaling Regimes

For the near neutral upper layer with  $-10 < h/L < 1$  and  $z_s/h < 0.8$ , the Gaussian-plume model is most applicable. Over dry land these conditions may occur in overcast conditions with high wind speeds. For the ground-level crosswind integrated concentration, we have

$$\frac{\bar{c}_y(x, z_s)}{q} = \frac{1}{\sqrt{2\pi} \bar{u}_x} \exp\left(-\frac{z_s^2}{2\sigma_z^2}\right) \quad (3.95)$$

The vertical plume width is best estimated using a fit similar to that given by Draxler (1976)

$$\sigma_z = \sigma_w t \frac{1}{1 + \sqrt{t/t_{L,z}}} \quad (3.96)$$

but slightly modified by Gryning et al. (1987) so that  $t_{L,z}$  is analogous to the integral time scale for large travel times. This form matches the asymptotic behavior of the relation given by Taylor (1921) for dispersion in homogeneous turbulence. For the unstable case,  $t_{L,z} = 300$  s, and for stable conditions,  $t_{L,z} = 30$  s. The value of  $t$  is the travel time, approximated by  $t = x/\bar{u}_x$ . Direct measurements of  $\sigma_w$  are suggested for use in this equation.

For the stable boundary layer, local and  $z$ -less scaling occurs for the range  $h/L > 1$  and with a source height in the range  $z_s/h > 0.1$  and  $(h-z_s)/\Lambda < 10$ . In this region Nieuwstadt (1984) gives a local Monin Obhukhov length scale to be

$$\Lambda = \frac{[-\overline{uw}]^{3/2}}{k(g/T_v)\overline{w\theta}} \quad (3.97)$$

This form uses the local values of the momentum ( $-\overline{uw}$ ) and heat ( $-\overline{w\theta}$ ) fluxes. Holtslag and Nieuwstadt (1986) suggest  $z$ -less scaling for  $z/\Lambda > 1$  and  $(h-z)/\Lambda < 10$ . These regions are not as well investigated as is the stable surface layer and, for lack of a better method, use of the Gaussian plume model is suggested by Gryning et al. (1987). Calculation of  $\bar{c}_y$  is made in the same manner as for the near neutral upper layer, with  $t_{L,z} = 30$  s.

For the remaining upper-level regions in both the stable and unstable boundary layer, entrainment of overlying fluid becomes important. Entrainment involves the mixing of fluid with higher turbulent intensity fluid into regions of low turbulence fluid, which is seen as an intermittently turbulent signal by a velocity probe. At present, this phenomena is poorly understood. No models are available for predicting dispersion in these intermittent regions of turbulence.

### 3.3.2 Lateral Width Calculations

Dispersion in the lateral plane may be a combined effect of turbulence and lateral wind shear. The second effect is neglected in flat, uniform terrain for times and distances in the microscale (less than 2km from the source, averages up to one hour in duration). Since there is no obvious length scales in the lateral direction for uniform terrain, formulas similar to that given by Taylor (1921) for dispersion in homogeneous turbulence are used. Among these empirical equations is that given by Draxler (1976). We use the modified form of this equation given by Gryning et al. (1987)

$$\sigma_y = \sigma_v \frac{1}{1 + \sqrt{t/t_{L,y}}} \quad (3.98)$$

which is based on a large number of field dispersion experiments in uniform terrain. The value of  $t_{L,y} = 200$  s for horizontal dispersion from a ground level source in all atmospheric conditions except when  $\tilde{z}/h > 0.1$  for which  $t_{L,y} = 600$  s. This particular form of  $\sigma_y$  asymptotically matches the behavior of plume growth near and far from the source predicted by Taylor's theory for homogeneous turbulence, and  $t_{L,y}$  approximates the Lagrangian integral scale of the turbulence. Averages of  $\sigma_y$  and  $\sigma_v$  are taken over periods of 0.5 to 1 hour, and should be measured directly. The value of  $t$  is the travel time, approximated by  $t = x/\bar{u}_z$ , with the velocity taken at the height of the source.

### 3.3.3 Lagrangian Integral Scales in Turbulent Dispersion

Averages of concentration, as modeled by the previously described single-particle dispersion theory, are taken over periods much longer than the largest Lagrangian integral time scale  $t_L$  in the flow. We need to investigate these times, to set a sampling criteria for valid experimental averages. For sampling or averaging periods less than  $t_L$ , relative dispersion, to be discussed in the next section, must be considered.

The value of the Lagrangian integral scale may be estimated from Eulerian velocity measurements. Taylor's frozen field hypothesis uses  $t_E = t_E \bar{u}_x$  to relate the Eulerian time scale to an Eulerian length scale. Gifford (1955) assumes particles travel through this field at a speed  $\sigma_u$ , so the Lagrangian integral time scale  $\sim t_E \sigma_u$ , or

$$\frac{t_L}{t_E} = \beta = G \frac{\bar{u}_x}{\sigma_u} \quad (3.99)$$

The value of  $G$  is an empirical constant which may vary from 0.4 to 0.6, according to Pasquill and Smith, (1983).



Alternatively,  $t_L$  may come from an investigation of the dispersion and a knowledge of the transition from mean plume growth with  $\sigma_y^2$  proportional to  $t$  near the source and proportional to  $t^{1/2}$  farther from the source. This parameter is discussed by Gryning et al. (1987). In lateral measurements,  $t_L$  is given as 200 s for all ground-level sources. In the vertical,  $t_L$  ranges from 30 seconds for near neutral stable conditions to 300 s for near-neutral unstable atmospheric conditions.

Similarity scaling may also be used to estimate a Lagrangian time scale. In the surface layer, Reid (1979) found  $t_{L,z} = 0.26z/u_*$  in the vertical direction. In an examination of experimental data in unstable conditions, Liljegren (1989) finds that  $t_{L,z}$  follows a monotonic distribution in the mixed layer with the maximum  $t_{L,z}$  in a range from  $0.24 z_i/w_*$  to  $0.34 z_i/w_*$ . This decreases considerably near the surface. For the horizontal plane  $t_{L,x}$  and  $t_{L,y}$  are constant throughout the boundary layer and fall in the same range as that for the vertical maximum in the mixed layer.

### 3.4 Fluctuating Concentrations

The dispersion theories for predicting mean concentration distributions discussed in Section 3.2 describe the positional characteristics of an ensemble of single particle trajectories. This is suitable for determining mean concentrations over averaging times much greater than that of the Lagrangian integral time scale of the fluid motion. Information on the relative spatial characteristics of a plume or the variance in concentration at a fixed point can not be recovered with this method, but must be developed using a more elaborate initial statement of the problem.

One of the Lagrangian spatial characteristics of a plume that is of interest is the plume width relative to a moving center of mass. In cases where the scale of the turbulence is larger than some length scale of the plume, the relative width will be less than the time averaged width and will wander over the area defined by the time averaged plume. This wandering plume will cause fluctuations in concentrations at fixed sampling locations. Moments of concentration at these fixed points may also be investigated through this relative motion.

The problem statement could consist of an elaborate joint probability density function of all the particles in the cloud. As a simplification, moments up to second order can be found using the joint probability density function for only two particles, where we have  $p(x', x'', t', t'')$ , the probability density function that separate particles are located at points  $x'$  and  $x''$  at times  $t'$  and  $t''$ , respectively. This can be reduced to the single-particle description used in analysis of mean concentrations through

$$p(x', t') = \int_{-\infty}^{\infty} \int_{-\infty}^{\infty} p(x', x'', t', t'') dx'' dt'' \quad (3.100)$$

and from normalizing the probability density function, we obtain

$$\int_{-\infty}^{\infty} \int_{-\infty}^{\infty} p(\mathbf{x}, t) d\mathbf{x} dt = 1 \quad (3.101)$$

To predict the evolution of the particle distribution, we need the transition probability density function given by  $\Psi(\mathbf{x}', t', \mathbf{x}'', t'' | \mathbf{x}'_0, t'_0, \mathbf{x}''_0, t''_0) d\mathbf{x}'_0 dt'_0 d\mathbf{x}''_0 dt''_0$ , which is defined as the probability that one fluid particle is located within volume element  $d\mathbf{x}'$  at position  $\mathbf{x}'$  at time  $t'$ , while another is located at  $\mathbf{x}''$  within volume  $d\mathbf{x}''$  at time  $t''$ , given that at times  $t'_0$  and  $t''_0$  their positions, were at  $\mathbf{x}'_0$  and  $\mathbf{x}''_0$  respectively. With this transition probability density function, the equation for the joint probability density function of the particle pair is given by

$$p(\mathbf{x}', t', \mathbf{x}'', t'') = \iiint_{-\infty}^{\infty} p(\mathbf{x}'_0, t'_0, \mathbf{x}''_0, t''_0) \cdot \Psi(\mathbf{x}', t', \mathbf{x}'', t'' | \mathbf{x}'_0, t'_0, \mathbf{x}''_0, t''_0) d\mathbf{x}'_0 dt'_0 d\mathbf{x}''_0 dt''_0 \quad (3.102)$$

This shows that a knowledge of the initial position of a particle pair along with the transition probability density function is sufficient for determining the evolution of the joint probability density function. In practice, these functions still need simplification. For steady conditions and a known source strength  $q$  we have

$$\overline{c(\mathbf{x}', t') c(\mathbf{x}'', t'')} = q^2 p(\mathbf{x}', t', \mathbf{x}'', t'') \quad (3.103)$$

which shows that  $p(\mathbf{x}', t', \mathbf{x}'', t'')$  is a very general specification of the second-order moment of the dispersing cloud of particles. We will show the use of this tensor for several purposes, including determining the spatial extent of the evolving cloud, determining the variance in concentration at fixed sampling points, and investigating the small scale spectra of the concentration fluctuations.

### 3.4.1 Theory of Relative Cloud Dispersion

To describe an evolving cloud of particles from one instant in time to a later instant, we take  $t' = t''$ , and have

$$p(\mathbf{x}', \mathbf{x}'', t) = \iiint_{-\infty}^{\infty} p(\mathbf{x}'_0, \mathbf{x}''_0, t_0) \cdot \Psi(\mathbf{x}', \mathbf{x}'', t | \mathbf{x}'_0, \mathbf{x}''_0, t_0) d\mathbf{x}'_0 d\mathbf{x}''_0 dt_0 \quad (3.104)$$

This simplification can be used to describe a single evolving puff of particles, or for a continuous source, a single short time increment of the total release. For homogeneous turbulence, a substit-

tion of  $\mathbf{X} = \mathbf{x}' - \mathbf{x}_0'$  and  $\mathbf{Y} = \mathbf{x}'' - \mathbf{x}'$  in the above expression is useful in that there is no dependence on the specific initial values  $\mathbf{x}_0'$  or  $\mathbf{x}_0''$  in the transition probability density function  $\Psi(\mathbf{X}, \mathbf{Y}, t | \mathbf{Y}_0, t_0)$  for homogeneous turbulence. The value  $\mathbf{X}$  describes the translation of one particle with respect to a fixed coordinate, and the parameter  $\mathbf{Y}$  is the relative separation between the particle pairs. Normalization of this transition probability density function is

$$\int_{-\infty}^{\infty} \int_{-\infty}^{\infty} \Psi(\mathbf{X}, \mathbf{Y}, t | \mathbf{Y}_0, t_0) d\mathbf{X} d\mathbf{Y} = 1 \quad (3.105)$$

The displacement transition probability density function alone is

$$\Psi(\mathbf{X}, t | t_0) = \int_{-\infty}^{\infty} \Psi(\mathbf{X}, \mathbf{Y}, t | \mathbf{Y}_0, t_0) d\mathbf{Y} \quad (3.106)$$

whereas the relative separation probability density function is given by

$$\Psi(\mathbf{Y}, t | \mathbf{Y}_0, t_0) = \int_{-\infty}^{\infty} \Psi(\mathbf{X}, \mathbf{Y}, t | \mathbf{Y}_0, t_0) d\mathbf{X} \quad (3.107)$$

For high Reynolds number flows and a restriction on the particle pair separation, the displacement probability density function  $\mathbf{Y}$  is dominated by large eddies while smaller eddies dominate the separation probability density function (Batchelor, 1952). Assuming that these two processes are independent because of the large separation in wavenumbers dominant for displacement and separation, then

$$\Psi(\mathbf{X}, \mathbf{Y}, t | \mathbf{Y}_0, t_0) \approx \Psi(\mathbf{X}, t | t_0) \Psi(\mathbf{Y}, t | \mathbf{Y}_0, t_0) \quad (3.108)$$

For  $p(\mathbf{x}', \mathbf{x}'', t)$  we can use the substitution of  $\mathbf{X}$  and  $\mathbf{Y}$  to get an equivalent joint probability density function of  $p(\mathbf{X}, \mathbf{Y}, t)$ . This particular distribution can be reduced to describe the positional characteristics

$$p(\mathbf{X}, t) = \int_{-\infty}^{\infty} p(\mathbf{X}, \mathbf{Y}, t) d\mathbf{Y} \quad (3.109)$$

or the relative extent of the cloud through

$$p(\mathbf{Y}, t) = \int_{-\infty}^{\infty} p(\mathbf{X}, \mathbf{Y}, t) d\mathbf{X} \quad (3.110)$$

where

$$\int_{-\infty}^{\infty} \int_{-\infty}^{\infty} p(X, Y, t) dX dY = 1 \quad (3.111)$$

We have already investigated the nature of the positional characteristics of dispersion in the discussion on mean concentrations. The evolution of the relative dispersion of the cloud is given by

$$p(Y, t) = \int_{-\infty}^{\infty} \int_{-\infty}^{\infty} p(Y_0, t_0) \Psi(Y, t | Y_0, t_0) dY_0 dt_0 \quad (3.112)$$

This is more complicated than the equivalent expression for single particle trajectories (Eq. 3.42), because the transition that these two processes are independent depends not only on time  $t$ , but on the initial relative separation of the particle pair  $Y_0$ .

The relative spread of the two particles is given by

$$\zeta_{ij}(t | Y_0, t_0) = \overline{Y_i(t) Y_j(t)} = \int_{-\infty}^{\infty} Y_i Y_j \Psi(Y, t | Y_0, t_0) dY \quad (3.113)$$

Using Eq. 3.113, we can describe a relative cloud dispersion tensor

$$\Sigma_{ij} = \int_{-\infty}^{\infty} \int_{-\infty}^{\infty} (x_i'' - x_i')(x_j'' - x_j') p(x', x'', t) dx' dx'' \quad (3.114a)$$

$$= \int_{-\infty}^{\infty} Y_i Y_j p(Y, t) dY \quad (3.114b)$$

$$= \int_{-\infty}^{\infty} \int_{-\infty}^{\infty} Y_i Y_j p(Y', t_0) \Psi(Y, t | Y', t_0) dY dY' \quad (3.114c)$$

$$= \int_{-\infty}^{\infty} p(Y', t_0) \left[ \int_{-\infty}^{\infty} Y_i Y_j \Psi(Y, t | Y_0, t_0) dY \right] dY' \quad (3.114d)$$

$$= \int_{-\infty}^{\infty} p(Y', t_0) \zeta_{ij}(t | Y', t_0) dY' \quad (3.114e)$$

so that a knowledge of  $\zeta_{ij}(t | Y', t_0)$  and  $p(Y', t_0)$  is sufficient for determining relative cloud dispersion.

The cloud dispersion tensor  $\Sigma_{ij}(t)$  for particle pairs can be related to the motion of a cloud of particles about its center of mass. This requires the use of single trials  $N(x, t)$  consisting of a cloud of particles with the normalization

$$\int_{-\infty}^{\infty} N(\mathbf{x}, t) d\mathbf{x} = q \quad (3.115)$$

where  $q$  is the total mass or number of particles in the expanding cloud. For single trials denoted by  $N(\mathbf{x}', t)$  and  $N(\mathbf{x}'', t)$  we have averages given by

$$\overline{N(\mathbf{x}', t)} = q p(\mathbf{x}', t) \quad (3.116)$$

and

$$\overline{N(\mathbf{x}', t) N(\mathbf{x}'', t)} = q^2 p(\mathbf{x}', \mathbf{x}'', t) \quad (3.117)$$

The first moment of the instantaneous field yields

$$\mathbf{g}(t) = \frac{1}{q} \overline{\int_{-\infty}^{\infty} \mathbf{x} N(\mathbf{x}, t) d\mathbf{x}} \quad (3.118)$$

where  $\mathbf{g}(t)$  is the center of mass of the cloud. For the second moment we have

$$\Sigma_{ij}(t) = \frac{1}{q^2} \overline{\int_{-\infty}^{\infty} \int_{-\infty}^{\infty} (x_i'' - x_i')(x_j'' - x_j') N(\mathbf{x}', t) N(\mathbf{x}'', t) d\mathbf{x}' d\mathbf{x}''} \quad (3.119a)$$

$$= \frac{1}{q^2} \overline{\int_{-\infty}^{\infty} \int_{-\infty}^{\infty} [x_i'' x_j'' + x_i' x_j' - x_i' x_j'' - x_i'' x_j'] N(\mathbf{x}', t) N(\mathbf{x}'', t) d\mathbf{x}' d\mathbf{x}''} \quad (3.119a)$$

$$= 2 \frac{1}{q^2} \left[ \overline{\int_{-\infty}^{\infty} x_i x_j N(\mathbf{x}, t) d\mathbf{x}} - \overline{\int_{-\infty}^{\infty} x_i N(\mathbf{x}, t) d\mathbf{x}} \overline{\int_{-\infty}^{\infty} x_j N(\mathbf{x}, t) d\mathbf{x}} \right] \quad (3.119c)$$

$$= \frac{2}{q^2} \left[ \overline{\int_{-\infty}^{\infty} x_i x_j N(\mathbf{x}, t) d\mathbf{x}} - \overline{g_i(t)} \overline{g_j(t)} \right] \quad (3.119d)$$

and

$$\Sigma_{ij}(t) = \frac{2}{q^2} \overline{\int_{-\infty}^{\infty} (x_i - g_i)(x_j - g_j) N(\mathbf{x}, t) d\mathbf{x}} \quad (3.119e)$$

so that the cloud dispersion tensor for particle pairs  $\Sigma_{ij}(t)$  is twice the dispersion about the center of mass  $\mathbf{g}_i(t)$  of the moving cloud.

For simplification, if we assume independence in the three coordinate directions, such that  $x_i x_j = 0$  and  $\Sigma_{ij} = 0$  for  $i \neq j$ , the representation of  $\Sigma_{ij}$  can be manipulated to get

$$\frac{\Sigma_{ii}(t)}{2} q^2 = \overline{\int_{-\infty}^{\infty} x_i^2 N(x,t) dx} + g^2(t) \overline{\int_{-\infty}^{\infty} N(x,t) dx} - 2g(t) \overline{\int_{-\infty}^{\infty} x_i N(x,t) dx} \quad (3.120a)$$

$$= \overline{\int_{-\infty}^{\infty} x_i^2 N(x,t) dx} - [g_i(t)]^2 \quad (3.120b)$$

The first term on the right-hand side in this expression is the mean-square cloud spread in the fixed frame of reference

$$\sigma_i^2(t) = \frac{1}{q^2} \overline{\int_{-\infty}^{\infty} x_i^2 N(x,t) dx} \quad (3.121)$$

The last term is the mean-square spread of the center of mass calculated for each trial (times the source strength), so

$$\frac{\Sigma_{ii}(t)}{2} = \sigma_i^2(t) - \frac{g_i^2(t)}{q^2} \quad (3.122)$$

Defining the relative dispersion about the moving center of mass  $\sigma_{r,i}^2(t) = \Sigma_{ij}^2/2$  and the center of mass term as  $\sigma_{g,i}^2(t) = g_i^2/q^2$ , we have

$$\sigma_i^2(t) = \sigma_{r,i}^2(t) + \sigma_{g,i}^2(t) \quad (3.123)$$

which says that the total mean square spread of a ensemble of particles  $\sigma_i(t)$  is equal to the mean square of their spread about the moving center of mass  $\sigma_{r,i}^2(t)$  plus the mean square spread of the ensemble of their center of mass trajectories  $\sigma_{g,i}^2(t)$ . This is a very useful expression.

We have seen that the average plume profile follows a Gaussian distribution. The distribution of many independent center of mass trajectories, through the central limit theorem, will also converge to a Gaussian distribution. The ensemble average distribution about the moving center of mass therefore must also conform to a Gaussian profile. Instantaneous profiles can vary considerably from this average profile.

For investigating the kinematics of relative particle dispersion, we have the relative spread of a particle pair given by

$$\zeta_{ij}(t | Y_0, t_0) = \overline{Y_i(t) Y_j(t)} = \int_{-\infty}^{\infty} Y_i Y_j \Psi(Y, t | Y_0, t_0) dY \quad (3.124)$$

which can be related to the relative particle velocities given by

$$\overline{Y_i(t) Y_j(t)} = \overline{Y_i(t_0) Y_j(t_0)} + \int_{t_0}^t \int_{t_0}^t v_i(t') v_j(t'') dt' dt'' \quad (3.125)$$

The relative velocity  $v_i(t)$  is not stationary since the range of eddies affecting the dispersion is increasing with time and particle separation. In general, the correlation  $v_i(t')v_j(t'')$  depends on  $t'$  and  $t''$  separately and requires specification of  $Y_0$  and  $t_0$ . This expression can be simplified for asymptotic limits of  $(t - t_0)$ . For small  $(t - t_0)$  we may write

$$\overline{Y_i(t) Y_j(t)} = Y_i(t_0) Y_j(t_0) + (t - t_0)^2 \overline{v_i(t_0) v_j(t_0)} \quad (3.126a)$$

$$= Y_i(t_0) Y_j(t_0) + (t - t_0)^2 \left[ \overline{u_i'(t_0) - u_i''(t_0)} \right] \left[ \overline{u_j'(t_0) - u_j''(t_0)} \right] \quad (3.126b)$$

$$= Y_i(t_0) Y_j(t_0) + (t - t_0)^2 \left[ 2 R_{ij}(0, t_0) - 2 R_{ij}(Y_0, t_0) \right] \overline{u_i u_j} \quad (3.126c)$$

where  $R_{ij}$  is a symmetrical Eulerian velocity correlation and it is assumed that the turbulence is homogeneous. For a large  $(t - t_0)$ , the particles wander independently, so the correlation of relative velocities is

$$\overline{v_i(t') v_j(t'')} = 2 \overline{u_i(t') u_j(t'')} \quad (3.127)$$

where  $u_i(t)$  is the total Eulerian velocity of the particle at time  $t$ . The relative spread of the particles is then

$$\overline{Y_i(t) Y_j(t)} \rightarrow 2 \overline{X_i(t) X_j(t)} \quad (3.128)$$

which means that the center of mass does not wander and the total mean-square plume width is equal to the average instantaneous mean-square plume width. In a practical situation, this occurs at times which are very large compared to the Lagrangian integral scale of the flow. For the general case, the relative velocity correlation can be written in terms of total velocities

$$\begin{aligned} \overline{v_i(t') v_j(t'')} &= \left[ \overline{u_i'(t') - u_i''(t')} \right] \left[ \overline{u_j'(t'') - u_j''(t'')} \right] \\ &= \overline{u_i'(t') u_j'(t'')} + \overline{u_i''(t') u_j''(t'')} \\ &\quad - \overline{u_i'(t') u_j''(t'')} - \overline{u_i''(t') u_j'(t'')} \end{aligned} \quad (3.129)$$

In most cases,  $|v|$  is small compared with  $|u|$  so expressing the relative velocity correlation in terms of total velocity may lead to errors of subtraction. The Eulerian correlations, however, are much easier to measure experimentally than are the joint Lagrangian correlation.

### 3.4.2 Relative Dispersion Modeling Results

Smith and Hay (1961) offer some enlightenment into the nature of relative particle dispersion by assuming that Lagrangian and Eulerian velocity correlations have a similar shape. With this assumption they are able to develop a partition of the turbulent kinetic energy spectra for homogeneous turbulence into dispersive and translating components for an evolving cloud of particles. These contributions to puff growth and mean plume wandering are complementary.

For a small source in homogeneous turbulence, they find

$$\frac{\partial \sigma_r}{\partial x} = \frac{2}{3} C \frac{\sigma_u^2 + \sigma_v^2 + \sigma_w^2}{\bar{u}_x^2} \quad (3.130)$$

which is valid for a wide range of the dispersion, except very near the source. This implies that puff size varies linearly with distance from the source,  $x$ , or travel time,  $x/\bar{u}_x$ . With the proportionality constant  $C \sim 1$ , Michelson (1983) finds good agreement with data taken in neutral atmospheric conditions for continuous plume widths using

$$\sigma_{y,r} = \frac{2}{9} \frac{\sigma_v x}{\bar{u}_x} \quad (3.131)$$

which neglects the initial source dimensions.

More detailed examinations of relative cloud dispersion focus on numerical Monte-Carlo simulations of two-particle trajectories. Two basic techniques are used. The first simulates the full inter-particle velocity correlations, whereas the second method is a conditional one-particle model, for which inter-particle correlations are accounted for in the initial velocities, but are subsequently neglected.

In a typical application of the first method, Lee and Stone (1986), model the two particle velocities as a Markov process in homogeneous turbulence. The particle positions are advanced in time using

$$y_{n+1}' = y_n' + u_n' \delta t \quad (3.132)$$

and

$$y_{n+1}'' = y_n'' + u_n'' \delta t \quad (3.133)$$

where single and double primes indicate different particles, the subscript indicates a step increment,  $n = 0, 1, 2, \dots$ , and  $\delta t$  is a small jump in time. Velocities are given by

$$u_{n+1}' = \mathcal{A} u_n' + \mathcal{B} u_n'' + \mathcal{J} dW_t'' + dW_t' \quad (3.134)$$



$$u_{n+1}'' = C u_n'' + \mathcal{D} u_n' + \mathcal{J} dW_t' + dW_t'' \quad (3.135)$$

with  $dW_t'$  and  $dW_t''$  as random numbers selected from a Gaussian distribution. The influence between the two particles is assumed to be symmetrical. In this model, the coefficients  $\mathcal{A}, \mathcal{B}, \mathcal{C}$ , and  $\mathcal{D}$  are found using the above two equations and the two-particle correlation given by

$$u_n' u_n'' = \exp \left( - \frac{|y' - y''|}{L} \right) \exp \left( - \frac{|t' - t''|}{t_E (1 - t_E \bar{u}_x / \ell)^{-1}} \right) \quad (3.136)$$

where  $\ell$  is the Eulerian integral length scale and  $t_E (1 - t_E \bar{u}_x / \ell)^{-1}$  is the Eulerian integral time scale in the convective frame of reference. This exponential correlation is a direct result of the assumed Markov properties of velocity, but does neglect the proper dissipative and inertial range scaling of turbulence.

Results from simulations of the model for large numbers of particle pairs are presented in terms of  $\sigma_y(t)$ ,  $\sigma_{r,y}(t)$ , and  $\sigma_{g,y}(t)$  versus various initial particle separations. Asymptotic limits show relative growth,  $\sigma_{r,y}(t)$ , is proportional to travel time,  $t$ , for times less than the Lagrangian integral scale time, whereas for large travel times the growth is proportional to  $t^{1/2}$ .

Models given by Durbin (1980) and Sawford (1982a,b) are very similar to the outline presented for that of Lee and Stone (1986), except in both of these cases mixed Eulerian and Lagrangian velocity correlations are used which somewhat complicates the analysis.

An application of the conditional one-particle method is used in a model described by Lee and Stone (1983). The notation is presented in the same manner as for the two-particle trajectory model. At the finite sized source, particles are correlated through

$$u_0' u_0'' = \exp \left( - \frac{|y' - y''|}{L} \right) \exp \left( - \frac{|t' - t''|}{t_E (1 - t_E \bar{u}_x / \ell)^{-1}} \right) \quad (3.137)$$

where the arguments have the same definition as in Eq. 3.154. For steps  $n > 0$ , the inter-particle correlations are neglected. The position of each particle is found independently, through

$$y_{n+1} = y_n + u_n \delta t \quad (3.138)$$

and

$$u_{n+1} = \mathcal{A} u_n + \mathcal{J} dW_t \quad (3.139)$$

where  $\mathcal{A}$  and  $\mathcal{J}$  are found through the characteristics of the turbulence, consistent with the theoretical discussion already presented for single particle dispersion. In numerical simulations, asymptotic limits show that relative growth  $\sigma_{r,y}(t)$  is proportional to travel time  $t$  for small times, and is

proportional to  $t^{1/2}$  at larger times. This is the same result found for the two-particle dispersion model.

The conditioned one-particle method is much less computationally intensive than the two-particle trajectory model. Data comparisons at this point are unable to distinguish between the relative suitability of either method in modeling dispersion. It is possible, however, that the conditioned one-particle method is useful near the source, whereas the two-particle method, which maintains the effect of the interparticle velocity correlations, is suitable for longer travel times.

### 3.4.3 Relative Dispersion Measurements

We recall

$$\sigma_i^2(t) = \sigma_{r,i}^2(t) + \sigma_{g,i}^2(t) \quad (3.140)$$

where  $\sigma_i(t)$  is the total mean square spread of an ensemble of particles  $\sigma_{r,i}^2(t)$  is the mean square of their spread about the moving center of mass, and  $\sigma_{g,i}^2(t)$  is the mean square spread of the ensemble of their center of mass trajectories. For our purposes this expression is useful in analysis of instantaneous measures of crosswind plume profiles, or of aerial photographs of a surface level plume in the atmospheric boundary layer.

We are primarily interested in short travel times, for which  $t < t_L$ . For relative dispersion, we have in the crosswind plane

$$\sigma_{y,r} = \frac{2}{9} C^{1/3} \frac{\sigma_v x}{\bar{u}_x} \quad (3.141)$$

from Smith and Hay (1961), with  $C \sim 1$ . This shows relative plume width is proportional to travel time,  $t = x/\bar{u}_x$ , similar to the more elaborate Monte Carlo models. It also assumes the initial source size is small. For small dispersion times, we find the total mean square spread from Taylor (1921) is given by

$$\sigma_y = \frac{\sigma_v x}{\bar{u}_x} \quad (3.142)$$

so the ratio of relative width  $\sigma_{r,y}(x)$  to total width  $\sigma_y(x)$  should be  $\sim 0.22$ .

Plots of data for  $\sigma_v x/\bar{u}_x$  versus  $\sigma_y(x)$ ,  $\sigma_{r,y}(x)$ , and  $\sigma_{g,y}(x)$  will yield experimental information on the ratio between relative plume width and the total plume width. This ratio should be relatively constant for short travel times ( $< t_L$ ) and for small sources.

Carras and Williams (1986) present extensive relative dispersion measurements for convective conditions, using dispersion data from a number of power plants and smelter plants in Australia. Plume widths were measured using both aerial photography and flights through the

plume with plume-sensitive instruments. Near field data are given for relative and total plume widths for dimensionless distances of  $X = (xw_*)/(z_i \bar{u}_x) < 1$ , whereas relative data alone are given out to  $X \sim 15$ . All of these small, isolated sources were located in the bottom 15% of the boundary layer.

For the data taken at  $X < 1$ , both  $\sigma_y$  and  $\sigma_{r,y}$  show a power-law dependence on travel time  $t$ . The average ratio between  $\sigma_{r,y}$  and  $\sigma_y$  for these data ranges between approximately 0.25 and 0.40 for different sources, a result which is fairly consistent with the conclusions of Smith and Hay (1961), given the scatter in the experimental measurements and the neglected initial source size. For larger travel times (to  $X \sim 15$ ), relative plume width still show a power-law dependence on  $t$ . The spread in the relative diffusion data for all downwind distances is nearly a factor of 10, which adds to the difficulty in determining an average ratio between  $\sigma_{r,y}$  and  $\sigma_y$ .

Mikkelsen (1983) presents relative dispersion data for a small ground-level source for two dispersion experiments in moderately convective conditions. These measurements were made from aerial photographs and were limited to small travel times. In this data set, dimensionless scaling is not used, but data are presented for  $\sigma_y(x)$ ,  $\sigma_{r,y}(x)$ , and  $\sigma_{g,y}(x)$  as a function of downwind distance. The ratio between  $\sigma_{r,y}$  and  $\sigma_y$  is about 0.28 for these data, and a power-law growth with travel time is seen in all three measures of the plume width.

We can draw several conclusions from these data. Given that the ratio of relative to total plume width is approximately 0.22, we find that

$$\sigma_{y,r}^2 = 0.05 \sigma_y^2 \quad (3.143)$$

and

$$\sigma_{g,y}^2 = \sigma_y^2 - \sigma_{r,y}^2 = 0.95 \sigma_y^2 \quad (3.144)$$

so that the greatest fraction of the total plume dispersion is due to the wandering of the mean-square center-of-mass trajectories.

#### 3.4.4 Peak to Mean Ratios Found from the Relative Dispersion Analysis

We know that an average plume crosswind profile follows a Gaussian distribution, and the distribution of the center of mass trajectories, through the central limit theorem, will also converge to a Gaussian distribution. From the equation

$$\sigma_y^2(t) = \sigma_{r,y}^2(t) + \sigma_{g,y}^2(t) \quad (3.145)$$

we require that the ensemble average distribution about the moving center of mass also conform to a Gaussian profile.

Gifford (1959) has used this expression in a wandering plume model which assumes that the instantaneous profile is Gaussian, and is described by the relative plume parameters. Because the relative plume width is much narrower than the average plume width, it is possible to define a ratio of the centerline concentration of the relative plume to that of the time-averaged plume by

$$\frac{\text{Peak}}{\text{Average}} = \frac{\sigma_y}{\sigma_{y,r}} \exp \left( \frac{y^2}{2 \sigma_y^2} \right) \quad (3.146)$$

Gifford (1960) refers to this as the peak to average concentration ratio. It shows a minimum at the plume centerline and increases toward the plume edge. Another derivation from this analysis is that the probability distribution of concentration is continuous and follows a power law.

This technique of estimating peak concentrations is based on the assumption that the instantaneous profile is Gaussian. For an initially spherical puff of marked fluid, there is certainly no guarantee of a spherical Gaussian growth as noted by Richardson (1926). Distortion will be mainly dependent on the scales of eddies nearly the same size as the expanding cloud. The relative profile is Gaussian only after an ensemble average of many realizations. Examples of irregularly shaped instantaneous profiles and the Gaussian shaped ensemble average relative profile are shown by Murthy and Csanady (1971) using a florescent tracer release in a lake current and a boat fitted with fast-response underwater instrumentation.

Relating the properties of relative dispersion to point values of concentration is probably best accomplished using the stochastic model outlined by Durbin (1980). This is discussed in the following sections. Although it is perhaps advantageous to directly relate results from relative dispersion measurements to point concentration probability distributions, the stochastic averaging technique outlined by Durbin indicates this is not an easy task.

### 3.5 Concentration Fluctuations at a Point

#### 3.5.1 Variance in Concentration at a Point

##### Statistical Analysis

In a two-particle analysis, we have shown that

$$p(\mathbf{x}', t', \mathbf{x}'', t'') = \iiint \int_{-\infty}^{\infty} p(\mathbf{x}_0', t_0', \mathbf{x}_0'', t_0'') \cdot \Psi(\mathbf{x}', t', \mathbf{x}'', t'' | \mathbf{x}_0', t_0', \mathbf{x}_0'', t_0'') d\mathbf{x}_0' dt_0' d\mathbf{x}_0'' dt_0'' \quad (3.147)$$

which also is

$$\overline{c(x', t') c(x'', t'')} = q^2 p(x', t', x'', t'') \quad (3.148)$$

This equation can be manipulated, according to Durbin (1980), by integrating over a suitably small volume  $\mathcal{V}_\eta$  and dropping the time dependence for convenience to get

$$\overline{c^2(x)} = \frac{1}{\mathcal{V}_\eta^2} \int_{\mathcal{V}_\eta} \int_{\mathcal{V}_\eta} \overline{c(x') c(x'')} dx' dx'' \quad (3.149)$$

which is equivalent to

$$\overline{c^2(x)} = q^2 \frac{1}{\mathcal{V}_\eta^2} \int_{\mathcal{V}_\eta} \int_{\mathcal{V}_\eta} p(x', x'') dx' dx'' \quad (3.150a)$$

$$= q^2 \frac{1}{\mathcal{V}_\eta^2} \int_{\mathcal{V}_\eta} \int_{\mathcal{V}_\eta} \left[ \int_{-\infty}^{\infty} \int_{-\infty}^{\infty} p(x_0', x_0'') \cdot \right. \\ \left. \Psi(x', x'' | x_0', x_0'') dx_0' dx_0'' \right] dx' dx'' \quad (3.150b)$$

or

$$\overline{c^2(x)} = q^2 \frac{1}{\mathcal{V}_\eta^2} \int_{\mathcal{V}_\eta} \int_{\mathcal{V}_\eta} \left[ \int_{-\infty}^{\infty} \int_{-\infty}^{\infty} p(x_0') p(x_0'') \cdot \right. \\ \left. \Psi(x', x'' | x_0', x_0'') dx_0' dx_0'' \right] dx' dx'' \quad (3.150c)$$

where the initial source configuration is specified. A conventional definition of the variance at a point is found by letting  $x' - x'' \rightarrow 0$ , and implicitly  $x' - x'' < \eta$ , where  $\eta = (v^3/\epsilon)^{1/4}$  is the Kolmogorov microscale. This may be written as

$$\overline{c^2(x)} = q^2 \int_{-\infty}^{\infty} \int_{-\infty}^{\infty} \lim_{\frac{x' - x''}{\eta} \rightarrow 0} p(x_0') p(x_0'') \cdot \\ \Psi(x', x'' | x_0', x_0'') dx_0' dx_0'' \quad (3.151)$$

and is satisfied in the limit only when the particle pairs follow identical trajectories, which is equivalent to the single particle model

$$\overline{c_u^2(\mathbf{x})} = q^2 \int_{-\infty}^{\infty} p^2(\mathbf{x}_0) \cdot \Psi(\mathbf{x} | \mathbf{x}_0) d\mathbf{x}_0 \quad (3.152)$$

and  $\overline{c_u^2(\mathbf{x})}$  refers to concentration fluctuations over an unmixed measurement volume, since in this definition all diffusive and turbulent mixing processes are neglected. We may assume that  $p(\mathbf{x})$  has a uniform value of one over a very small region  $\mathcal{V}$  at location  $\mathbf{x}$ . The variance in concentration is found through

$$\sigma_u^2(\mathbf{x}) = \overline{c_u^2(\mathbf{x})} - [\bar{c}(\mathbf{x})]^2 \quad (3.153a)$$

$$\sigma_u^2(\mathbf{x}) = q^2 \int_{-\infty}^{\infty} \delta^2(\mathcal{V}) \Psi(\mathbf{x} | \mathbf{x}_0) d\mathbf{x}_0 - q^2 \left[ \int_{-\infty}^{\infty} \delta(\mathcal{V}) \Psi(\mathbf{x} | \mathbf{x}_0) d\mathbf{x}_0 \right]^2 \quad (3.153b)$$

$$\sigma_u^2(\mathbf{x}) = q^2 \left[ \int_{\mathcal{V}} \Psi(\mathbf{x} | \mathbf{x}_0) d\mathbf{x}_0 - \left\{ \int_{\mathcal{V}} \Psi(\mathbf{x} | \mathbf{x}_0) d\mathbf{x}_0 \right\}^2 \right] \quad (3.153c)$$

or from Csanady (1973),

$$\sigma_u^2(\mathbf{x}) = q \bar{c}(\mathbf{x}) - \bar{c}^2(\mathbf{x}) \quad (3.153d)$$

so that the standard deviation  $\sigma_u$  is a function only of the mean concentration distribution. This is a result of the taking the measurement volume limit  $\mathbf{x}' - \mathbf{x}'' \rightarrow 0$ .

Durbin (1980) offers a modified definition of  $\overline{c^2(\mathbf{x})}$ , for flows with a large turbulent mass Peclet number,  $u'l/\mathcal{D}$ , by taking  $(\mathbf{x}' - \mathbf{x}'')/l \rightarrow 0$ , so that we still have  $\mathbf{x}' - \mathbf{x}'' > \eta$ . This averaging is applicable to many experimental measurements, including our own, where the sampling volume is somewhat larger than  $\eta$ . In this definition, contributions to fluctuations in concentration can come from both single particle contributions and the mixing of particles of given marked concentration within the measurement volume.

With this definition and taking the limit of a small sampling or measurement volume

$$\begin{aligned} \overline{c^2(\mathbf{x})} = q^2 \iint_{-\infty}^{\infty} \lim_{\frac{\mathbf{x}' - \mathbf{x}''}{l} \rightarrow 0} p(\mathbf{x}_0') p(\mathbf{x}_0'') \cdot \\ \Psi(\mathbf{x}', \mathbf{x}'' | \mathbf{x}_0', \mathbf{x}_0'') d\mathbf{x}_0' d\mathbf{x}_0'' \end{aligned} \quad (3.154a)$$

or

$$\overline{c^2(\mathbf{x})} = q^2 \int_{-\infty}^{\infty} \int_{-\infty}^{\infty} p(\mathbf{x}_0') p(\mathbf{x}_0'') \cdot \Psi(\mathbf{x}, \mathbf{x} | \mathbf{x}_0', \mathbf{x}_0'') d\mathbf{x}_0' d\mathbf{x}_0'' \quad (3.154b)$$

for the second moment of concentration at a point. We see that this definition still depends on the two-particle transition probability density function.

### Solutions of the Statistical Formulations for Concentration Variance

We can find analytical solutions of the second moments of concentration  $\overline{c_u^2(\mathbf{x})}$  and  $\overline{c^2(\mathbf{x})}$  for a simple geometry. Given a continuous finite-sized source much smaller than the integral scale of the turbulence, we can write

$$p(\mathbf{x}_0) = \begin{cases} 1/2\delta & \mathbf{x}_0 \leq \delta \\ 0 & \mathbf{x}_0 > \delta \end{cases} \quad (3.155)$$

for a one dimensional problem. The mean concentration distribution can be found from the one-particle model and is given by

$$\bar{c}(\mathbf{x}) = \frac{1}{\sqrt{2\pi}\sigma_x} \int_{-\delta}^{\delta} q/2\delta \exp\left(-\frac{(\mathbf{x}-\mathbf{x}')^2}{2\sigma_x^2}\right) d\mathbf{x}' \quad (3.156)$$

where  $\sigma_x$  is a function of time. Since  $q$  is uniform over the range  $-\delta$  to  $\delta$  we have, from Csanady (1973),

$$\bar{c}(\mathbf{x}) = \frac{q}{4\delta} \left[ \operatorname{erf}\left(\frac{\delta - \mathbf{x}}{\sigma_x \sqrt{2}}\right) + \operatorname{erf}\left(\frac{\delta + \mathbf{x}}{\sigma_x \sqrt{2}}\right) \right] \quad (3.157)$$

where

$$\operatorname{erf} \zeta = \frac{2}{\sqrt{\pi}} \int_0^{\zeta} \exp(-g^2) dg \quad (3.158)$$

is the error function. With the approximation of  $\delta \ll \sigma_x$ , this simplifies to the familiar result

$$\bar{c}(\mathbf{x}) = \frac{q}{\sqrt{2\pi}\sigma_x} \exp\left(-\frac{\mathbf{x}^2}{2\sigma_x^2}\right) \quad (3.159)$$

where  $\sigma_x$  is a function of time and  $q$  is the total source strength. To find the relative fluctuation intensity, we use

$$\frac{\sigma_u^2(x)}{\bar{c}^2(x)} = \frac{q}{\bar{c}(x)} - 1 \quad (3.160)$$

With substitution of the mean field of concentration Eq. 3.160 yields

$$\frac{\sigma_u^2(x)}{\bar{c}^2(x)} = \sqrt{2\pi} \sigma_x \exp\left(2 \frac{\sigma_x^2}{x^2}\right) - 1 \quad (3.161)$$

At the centerline, for  $x = 0$ , this ratio grows with increasing  $\sigma_x$  and thus increases with time.

The definition given by Durbin (1980) requires a two-particle analysis with

$$\overline{c^2(x)} = q^2 \int_{-\infty}^{\infty} \int_{-\infty}^{\infty} p(x_0') p(x_0'') \Psi(x, x | x_0', x_0'') dx_0' dx_0'' \quad (3.162)$$

We use  $x = x'$  and  $\Delta = x' - x''$  to get

$$\overline{c^2(x)} = q^2 \int_{-\infty}^{\infty} \int_{-\infty}^{\infty} p(x_0, \Delta_0) \Psi(x | x_0, \Delta_0) dx_0 d\Delta_0 \quad (3.163)$$

Recasting the limits of the source configuration we have

$$p(x_0, \Delta_0) = \begin{cases} (1/2\delta)^2 & |\Delta_0| \leq 2\delta \text{ and } |x_0| \leq \delta \\ 0 & |\Delta_0| > 2\delta \text{ and } |x_0| > \delta \end{cases} \quad (3.164)$$

which gives

$$\overline{c^2(x)} = \left(\frac{q}{2\delta}\right)^2 \int_{-2\delta}^{2\delta} \int_{-\delta}^{\delta} \Psi(x_0, \Delta_0) dx_0 d\Delta_0 \quad (3.165)$$

Durbin (1980) gives an analytical solution of this equation, using an appropriate form of  $\Psi$ , as

$$\overline{c^2(x)} = \frac{q^2}{2\pi\sigma_x^2} 0.9 \sqrt{2} \left(\frac{l}{\sqrt{2}\delta}\right)^{1/3} \exp\left(-\frac{x^2}{2\sigma_x^2}\right) \quad (3.166)$$

The fluctuation intensity is given by

$$\frac{\sigma_c^2}{\bar{c}^2} = 0.9 \sqrt{2} \left[\frac{l}{\sqrt{2}\delta}\right]^{1/3} \exp\left(-\frac{x^2}{2\sigma_x^2}\right) - 1 \quad (3.167)$$

This solution assumes limits of  $\delta/l \rightarrow 0$ ,  $\delta/\sigma_x \rightarrow 0$ , and  $\Delta^2/l^2 \ll 1$ . Notice that centerline values for  $x = 0$  maintain a constant value with increasing time, unlike the previous definition. In this analy-



sis, we see that the centerline value depends on the ratio of  $l/\delta$ , whereas the crosswind distribution scales with the similarity variable  $x/\sigma_x$ .

### **Eulerian Conservation Equation Analysis**

The Eulerian species conservation equation may also be used to investigate the field of concentration variance. We limit the analysis to geometries of a point source of tracer dispersing into an extended homogeneous region of turbulence (in one or more dimensions). An analytical conservation equation for mean square fluctuations of concentration is found by multiplying the conservation equation for fluctuating concentration

$$\frac{\partial c'}{\partial t} + \frac{\partial \bar{c} u'_i}{\partial x_i} + \frac{\partial \bar{u}_i c'}{\partial x_i} = - \frac{\partial}{\partial x_i} \left[ u'_i c' - \overline{u'_i c'} \right] + \mathcal{D} \frac{\partial^2 c'}{\partial x_i^2} \quad (3.168)$$

by  $2c'$ , taking an ensemble mean average and using the continuity equation to get

$$\frac{\partial \overline{c'^2}}{\partial t} + u_i \frac{\partial \overline{c'^2}}{\partial x_i} = -2 \overline{u'_i c'} \frac{\partial \bar{c}}{\partial x_i} + \frac{\partial}{\partial x_i} \left[ \mathcal{D} \frac{\partial \overline{c'^2}}{\partial x_i} - \overline{u'_i c'^2} \right] - 2 \mathcal{D} \left( \frac{\partial c'}{\partial x_i} \right)^2 \quad (3.169)$$

The terms in this equation relate respectively to: the time rate of change of the mean square fluctuations; an advection term; a flux term; a spatial transfer term of the mean square fluctuations; and a dissipation rate of the mean square fluctuations.

Csanady (1973, 1967) has simplified this equation for a steady solution, uniform constant mean flow, and used a gradient transfer approximation and an assumed axisymmetric Gaussian mean concentration profile to get a self-preserving form of a nonhomogeneous ordinary differential equation governing the distribution of mean-square fluctuations. A simpler solution can be found directly from the concentration variance equation. Assuming low diffusion and a large spatial transfer term, this equation reduces to

$$\frac{\partial \overline{c'^2}}{\partial t} + u_i \frac{\partial \overline{c'^2}}{\partial x_i} = \frac{\partial}{\partial x_i} \left[ - \overline{u'_i c'^2} \right] \quad (3.170)$$

Using a gradient transfer approximation this becomes

$$\frac{\partial \overline{c'^2}}{\partial t} + u_i \frac{\partial \overline{c'^2}}{\partial x_i} = \frac{\partial}{\partial x_i} \left[ \kappa_i \frac{\partial \overline{c'^2}}{\partial x_i} \right] \quad (3.171)$$

which is the same operator found for the equation for conservation of mean concentration

$$\frac{\partial \bar{c}}{\partial t} + \bar{u}_i \frac{\partial \bar{c}}{\partial x_i} = \frac{\partial}{\partial x_i} \left[ \kappa_i \frac{\partial \bar{c}}{\partial x_i} \right] \quad (3.172)$$

We see that the transport of concentration variance is very similar to the transport of concentration itself.

### Solutions for the Field of Concentration Variance

Practical solutions for the field of concentration variance can be formulated along the same lines as those used in the Gaussian plume model for mean concentrations. One partial solution for dispersion from a point source is

$$\sigma_c^2(x,y) = \sigma_c^2(x,0) \exp \left( - \frac{y^2}{\sigma_y^2} \right) \quad (3.173)$$

for the ground-level distribution of concentration variance downwind from a surface-level source (of concentration variance) with  $y$  in the crosswind direction and  $x$  in the downwind direction. This solution retains the Gaussian plume solution for the crosswind direction in the same manner as it was retained for the mean dispersion in Eq. 3.89. The length scale  $\sigma_y$  is the same as used in mean dispersion models, by virtue of the similarity in operators found in the last section.

Using a different scaling, this may be written as

$$\frac{\sigma_c(x,y)}{\bar{c}(x,0)} = \alpha \left[ \exp \left( - \frac{y^2}{2\sigma_y^2} \right) \right]^{1/2} \quad (3.174)$$

where  $\alpha = \sigma_c(x,0)/\bar{c}(x,0)$  is a function greater than one. Since the variance and the mean concentration show a Gaussian distribution (in the crosswind coordinate, at least, for atmospheric sources), the ratio of standard deviation versus mean concentration given by  $\sigma_c(x,y)/\bar{c}(x,y)$  versus  $y/\sigma_y$ , leads to

$$\frac{\sigma_c(x,y)}{\bar{c}(x,y)} = \alpha \exp \left( - \frac{y^2}{4\sigma_y^2} \right) \quad (3.175)$$

This equation shows a rapid increase in concentration fluctuation intensity with increasing distance from the mean plume centerline. The plume centerline concentration fluctuation intensity,  $\sigma_c(x,0)/\bar{c}(x,0) = \alpha$  is uniquely related to the concentration fluctuation intensity at the plume centerline. Variation in  $\alpha$  is attributed to the finite and varying source sizes in dispersion experiments, a

factor which is insignificant in describing mean plume profiles. The ratio of the source size to the characteristic eddy size in a turbulent flow (measured by the integral scale) will control the center-line concentration fluctuation intensity. In a given flow, a smaller finite-sized source will have greater fluctuations of concentration downstream and will fit a larger  $\alpha$ . For cases in which the source size is smaller than the turbulent integral scale, Csanady (1973) finds  $\alpha > 1$ . This solution is very similar to that found by Durbin (1980) using statistical analysis techniques. Both solutions are dependent on the ratio of  $\delta/l$  and the crosswind scaling of  $x/\sigma_x$ .

### 3.5.2 Probability Density Function of Concentration of a Point

Two particle correlations are necessary for prediction of second-order spatial correlations or for prediction of variance in concentration at a point. To predict higher-order moments we need to follow the path of a greater number of correlated particles and describe the evolution of a probability density function given by  $p(x^{(1)}, x^{(2)}, \dots, x^{(n)})$ , where  $n$  is the number of correlated particles and also the maximum order of any calculated moment. For the calculation of variance at a point, we have

$$\langle c^2(x) \rangle = \iint_{-\infty}^{\infty} p(x_0', x_0'') \Psi(x | x_0', x_0'') dx_0' dx_0'' \quad (3.176)$$

Higher order moments would come from

$$\langle c^n(x) \rangle = \int \dots \int p(x_0^{(1)}, x_0^{(2)}, \dots, x_0^{(n)}) \Psi(x | x_0^{(1)}, x_0^{(2)}, \dots, x_0^{(n)}) dx_0^{(1)} dx_0^{(2)} \dots dx_0^{(n)} \quad (3.177)$$

where  $n$  is the number of correlated particles and also the value of the calculated moment.

These calculations have been accomplished by Kaplan and Dinar (1988) in a one dimensional solution, with predictions of higher-order moments of the concentration field. Such a formulation requires the simulation of a new realization of the velocity field at each time step for each particle location. The modeling results are qualitatively similar to experimental measurements from Hanna (1984b).

It may be possible to offer a quite simple form of the probability density function for a single point  $x$ , in the concentration field without using this complicated expression for the motion of correlated particles if several assumptions are applied. In this analysis, we first begin with a discrete set of particles.

In a spatial region, we have a joint p.d.f.  $p(x^{(1)}, x^{(2)}, \dots, x^{(n)}, t)$ . Considering a discrete representation of  $N$  particles, and nonoverlapping volumes  $\mathcal{V}^{(1)}, \mathcal{V}^{(2)}, \dots, \mathcal{V}^{(n)}$  coinciding with the posi-

tions  $x^{(1)}, x^{(2)}, \dots, x^{(n)}$ , an equivalent specification of the p.d.f. at an instant is given by  $p(\mathcal{V}^{(1)}, \mathcal{V}^{(2)}, \dots, \mathcal{V}^{(n)}, t)$  where

$$p(\mathcal{V}^{(1)}, \mathcal{V}^{(2)}, \dots, \mathcal{V}^{(k)}, t) = \text{PROB} \left[ c(\mathcal{V}^{(1)}) = \frac{n_1}{N}, c(\mathcal{V}^{(2)}) = \frac{n_2}{N}, \dots, c(\mathcal{V}^{(k)}) = \frac{n_k}{N}, t \right] \quad (3.178)$$

and  $n_i$  is the number of particles within  $\mathcal{V}_i$ . For independent, identical particles, and assuming the distribution is not a function of the actual value of  $t$ , this is the polynomial distribution

$$P(\mathcal{V}^{(1)}, \mathcal{V}^{(2)}, \dots, \mathcal{V}^{(n)}) = C_N^{n_1 \dots n_k} \left[ Q(\mathcal{V}^{(1)}) \right]^{n_1} \left[ Q(\mathcal{V}^{(2)}) \right]^{n_2} \dots \left[ Q(\mathcal{V}^{(k)}) \right]^{n_k} \cdot \left[ 1 - Q(\mathcal{V}^{(1)}) - Q(\mathcal{V}^{(2)}) - \dots - Q(\mathcal{V}^{(k)}) \right]^{n_0} \quad (3.179)$$

with

$$C_N^{n_1 \dots n_k} = \frac{N!}{n_1! \dots n_k! n_0!}$$

$$n_0 = N - n_1 - \dots - n_k$$

and

$$Q(\mathcal{V}_{(1)}) = p(x^{(1)}) \approx \left\langle \frac{n_1}{N} \right\rangle, \quad N \rightarrow \infty$$

In turbulent dispersion these particles are correlated. This correlation decreases with increasing separation in both space and time. In general, for this correlated system of particles, we require  $Q_{(1) \dots (k)}(\mathcal{V}^{(1)}, \dots, \mathcal{V}^{(k)})$ . This distribution specifies the probability of finding  $n_i$  particles in volume  $\mathcal{V}^{(i)}$  for positions 1 to  $k-1$ . When we consider only a single location, this joint distribution reduces to  $Q_{(1)}(\mathcal{V}^{(1)})$ .

Considering this volume  $\mathcal{V}$  at a single location  $x$ , the polynomial distribution (Eq. 3.179) simplifies to the binomial distribution

$$p(x, N, n) = p(\mathcal{V}) = \frac{N!}{n! (N-n)!} \left[ Q(\mathcal{V}) \right]^n \left[ 1 - Q(\mathcal{V}) \right]^{(N-n)} \quad (3.180)$$

Looking at realizations over a short time increment  $\Delta t$  within a much longer time period  $T$ , and assuming that particles move independently of each other and thus arrive at  $x$  at random times, the condition that a given particle is within volume  $\mathcal{V}$  is given by  $\Delta t/T$ . Similarly, the probability that the particle is not within  $\mathcal{V}$  is  $(T-\Delta t)/T$ . The binomial distribution is then

$$p(x, N, n) = \frac{N!}{n! (N-n)!} \left[ \frac{\Delta t}{T} \right]^n \left[ 1 - \frac{\Delta t}{T} \right]^{N-n} \quad (3.181)$$

With the average number of particles found in  $\mathcal{V}$  given by

$$\langle n \rangle_{Av} = N \left[ \frac{\Delta t}{T} \right] = \lambda \quad (3.182)$$

the distribution can be written in terms of  $\lambda$

$$p(x, N, n) = \frac{N!}{n! (N-n)!} \left[ \frac{\lambda}{N} \right]^n \left[ 1 - \frac{\lambda}{N} \right]^{N-n} \quad (3.183)$$

and the dependence on  $x$  remains because  $\lambda$  is a function of position.

We now take  $N$  and  $T$  to infinity while holding  $\lambda$  constant, first by expanding the factorial

$$p(x, n) = \frac{1}{n!} N(N-1)(N-2)\dots(N-n+1) \left[ \frac{\lambda}{N} \right]^n \left[ 1 - \frac{\lambda}{N} \right]^{N-n} \quad (3.184a)$$

$$= \frac{\lambda^n}{n!} \left[ 1 - \frac{1}{N} \right] \left[ 1 - \frac{2}{N} \right] \dots \left[ 1 - \frac{n-1}{N} \right] \left[ 1 - \frac{\lambda}{N} \right]^{N-n} \quad (3.184b)$$

taking the limit of large  $N$

$$p(n) = \lim_{N \rightarrow \infty} P(N, n) \\ = \frac{\lambda^n}{n!} \lim_{N \rightarrow \infty} \left[ \left( 1 - \frac{1}{N} \right) \left( 1 - \frac{2}{N} \right) \dots \left( 1 - \frac{n-1}{N} \right) \left( 1 - \frac{\lambda}{N} \right)^{N-n} \right] \quad (3.184c)$$

$$= \frac{\lambda^n}{n!} \lim_{N \rightarrow \infty} \left( 1 - \frac{\lambda}{N} \right)^N \quad (3.184d)$$

which yields a probability density function.

$$p(x, n) = \frac{\lambda^n}{n!} \exp(-\lambda) \quad (3.184e)$$

Such a distribution has been shown to apply for discrete particles dispersing in a fluid (Adrian, 1983b), where both the measuring volume and particle concentration are very small and the field is continuous.

In some cases  $\lambda$  is a very large number, so that interest is associated with only values of  $n$  which are close to the mean  $\lambda$ . We have

$$\log [ p(x, n) ] = n \log \lambda - \lambda - \log n! \quad (3.185)$$

Using Sterling's formula, we have

$$\log p(n) = n \log \lambda - \lambda - \left[ n + \frac{1}{2} \right] \log n - \frac{1}{2} \log 2\pi + O(n^{-1}) \quad (3.186)$$

Letting  $n = \lambda + \delta$ , yields

$$\log p(x, n) = - \left[ \lambda + \delta + \frac{1}{2} \right] \log \left( 1 + \frac{\delta}{\lambda} \right) + \delta - \frac{1}{2} \log (2\pi\lambda) + O(n^{-1}) \quad (3.187)$$

Now using  $\frac{\delta}{\lambda} \ll 1$  and a series expansion for the logarithm, we have

$$\log p(x, n) = - \frac{\delta^2}{2\lambda} - \frac{1}{2} \log (2\pi\lambda) \quad (3.188)$$

or

$$p(x, n) = \frac{1}{(2\pi\lambda)^{1/2}} \exp \left( - \frac{\delta^2}{2\lambda} \right) \quad (3.189)$$

which is a Gaussian distribution.

In other cases,  $\lambda$  is a very small number and the domain of interest is for small  $n$ . For the Poisson probability density function

$$p(x, n) = \frac{\lambda^n}{n!} \exp(-\lambda) \quad (3.190)$$

the probability distribution is given by

$$P(x, n = k) = \sum_{n=0}^k \frac{\lambda^n}{n!} \exp(-\lambda) \quad (3.191)$$

and normalization for  $n \rightarrow \infty$  is

$$\begin{aligned} P(x, n \rightarrow \infty) &= \left[ 1 + \lambda + \frac{\lambda^2}{2!} + \frac{\lambda^3}{3!} + \dots \right] \exp(-\lambda) \\ &= \exp(\lambda) \exp(-\lambda) = 1 \end{aligned} \quad (3.192)$$

For  $n = 0$

$$P(x, 0) = \exp(-\lambda) \quad (3.193)$$

and for  $n > 0$

$$\text{Prob}[n > 0] = 1 - \exp(-\lambda) \quad (3.194)$$

It is of use to apply this distribution to a continuous field of concentration, rather than discrete particles. For the period when material is present at location  $x$ , we have

$$\text{Prob} [ n > 0 ] = 1 - \exp(-\lambda) = 1 - \exp \left[ - \frac{N}{T} \Delta t \right] \quad (3.195)$$

where  $\frac{T}{N} = \bar{c}_s(\mathbf{x})$  represents the average sample size and  $\Delta t = c(\mathbf{x})$  represents the particular sample size of interest, so for a representation in continuous variables

$$\text{Prob} [ c(\mathbf{x}) | c(\mathbf{x}) > 0 ] = 1 - \exp \left( - \frac{c(\mathbf{x})}{\bar{c}_s(\mathbf{x})} \right) \quad (3.196)$$

which is valid only for the period for which material is present at  $\mathbf{x}$ , or  $c(\mathbf{x}) > 0$ . The value  $\bar{c}_s$  represents the conditional mean concentration, averaged only over periods of positive concentrations. This distribution can be made valid for the condition  $c(\mathbf{x}) = 0$  by explicitly including the intermittency  $I$ , which is defined as the fraction of time that marked fluid is present at the sampling location.

$$P(\mathbf{x}, c) = 1 - I \exp \left( - \frac{I(\mathbf{x}) c}{\bar{c}(\mathbf{x})} \right) \quad (3.197)$$

and the total mean  $\bar{c}$  is related to the conditional mean  $\bar{c}_s$  through

$$\bar{c}_s = \frac{\bar{c}}{I} \quad (3.198)$$

The probability density function for this distribution is given by

$$p(\mathbf{x}, c) = \frac{[I(\mathbf{x})]^2}{\bar{c}(\mathbf{x})} \exp \left( - \frac{I(\mathbf{x}) c}{\bar{c}(\mathbf{x})} \right) + [1 - I] \delta(c) \quad (3.199)$$

There are two independent parameters in this distribution, and we can relate the standard deviation in concentration, the mean concentration, and the intermittency, through

$$\frac{\sigma_c}{\bar{c}} = \left[ \left( \frac{2}{I} \right) - 1 \right]^{1/2} \quad (3.200)$$

Note that the derivation of this distribution assumes the values of  $I(\mathbf{x})$  or  $\bar{c}(\mathbf{x})$ , are only functions of position (and not time) the motion of a particle is independent of other particles, and the value of  $\lambda$  is small.

With  $\lambda = N (\Delta t / T)$ , an estimate of  $N$  is necessary to determine the validity of using the exponential distribution. One estimate is given by  $N_{\text{eff}} = (T/2t_L)$  where  $t_L$  is the Lagrangian integral scale of the turbulence. We now have  $\lambda = \Delta t / 2t_L$ , and values of  $t_L$  in the atmosphere for

microscale measurements are several minutes in duration. Sampling rates of one to ten seconds will clearly give a small value of  $\lambda$  and an exponential - like probability distribution.

In some atmospheric measurements of concentration, instruments with response times of several minutes are often considered to be fast enough to capture transient data. This analysis shows that these slower responding instruments will bias histograms of the data through instrument smoothing. This biasing is also likely to occur in smaller scale turbulent flows, for which a correspondingly faster instrument is needed. In some cases, the smoothing will not be a artifact of the instrument, but will be due to molecular dissipation. To avoid this smoothing, a large turbulent mass Peclet number  $u'l/D$  is needed, and the application of Eq. 3.197 is limited to early stages of the dispersion.

### 3.5.3 Concentration Exceedance

Useful information on statistics and concentration probability can be found from the single point probability distribution of concentration. From the probability density function, we can determine information such as the probability that a given concentration level occurs, or from the probability distribution, we can find the probability,  $P_0 = P(c_{\text{limit}})$ , that a given concentration  $c_{\text{limit}}$  is not exceeded, or the probability  $(1 - P_0)$  that it is exceeded. For the probability distribution given by

$$P(c) = 1 - I \exp\left(-I \frac{c}{\bar{c}}\right) \quad (3.201)$$

which is valid for dispersion from a point source, the probability that  $c_{\text{limit}}$  is exceeded is given by

$$\text{Prob} [c > c_{\text{limit}}] = 1 - P(c_{\text{limit}}) = I \exp\left(-I \frac{c_{\text{limit}}}{\bar{c}}\right) \quad (3.202)$$

Using probability theory we also may determine the mean continuous length of time that a given concentration will be exceeded. This is a more specific function than provided by the integral scale of the concentration signal which is really only a measure of the average lower frequency concentration fluctuations. More generally we can determine the probability that the concentration level  $c_{\text{limit}}$  will be exceeded for any arbitrary time interval  $t_{\text{limit}}$ .

This type of information, where the probability of occurrence is specified for both an exposure level and a time increment can be useful in cases for which the biological effect of exposure is a nonlinear function of dose and time. This specification may also be used to estimate the expected mean concentration and variance in that mean concentration over any given time interval.



## The Probability Distribution of Concentration Exceedance

For any given concentration  $c_{\text{limit}}$  we can achieve a probability distribution of the time durations that the value of  $c_{\text{limit}}$  is exceeded. We may first use the particular  $c_{\text{limit}}$  to generate a step function from a record of concentration which is unity for  $c > c_{\text{limit}}$  and is equal to zero for  $c \leq c_{\text{limit}}$ . Working with this step function, we are interested in the distribution of time intervals that our step function is equal to 1. If this set of time intervals is random, their distribution is governed by a Poisson process. It is useful to note here that the total fraction of time that the step function is equal to 1 is given by

$$\text{Prob} [c > c_{\text{limit}}] = 1 - P(c_{\text{limit}}) = I \exp \left( -I \frac{c_{\text{limit}}}{\bar{c}} \right) \quad (3.203)$$

We may analyze this distribution of time intervals by defining another function comprised of delta functions which occur as  $c = c_{\text{limit}}$  and  $dc/dt|_{c_{\text{limit}}} > 0$ . These delta functions define the start of an episode of  $c > c_{\text{limit}}$ . An example of these step and delta functions for a particular concentration signal is shown in Figure 3.1. The distribution of these discrete delta functions will be random in time and is given by

$$p(j, \lambda t) = \frac{(\lambda t)^j}{j!} \exp(-\lambda t) \quad (3.204)$$

where  $\lambda$  is the average number of events per unit time and  $j$  is the number of events found in the time interval  $t$ . For a given time interval  $t$  we are looking for zero delta function events in that interval, so that the occurrence of  $c > c_{\text{limit}}$  can be at least as long as the interval  $T$ . For this situation,  $j = 0$ , so that

$$\text{Prob} [j = 0] = p(0, \lambda t) = \exp(-\lambda t) \quad (3.205)$$

Now if any delta function events are found in the time interval  $T$  we know that  $c > c_{\text{limit}}$  is not satisfied for the entire interval. Because the assumption of randomness implies that past knowledge has no bearing on the occurrence of any future event<sup>1</sup>, the probability distribution of finding at least a single delta function event in a time interval  $t$  is the complement of the above equation, or

$$P(t) = 1 - \exp(-\lambda t) \quad (3.206)$$

so the distribution of these single events is exponential in time.

---

<sup>1</sup> Knowledge of the starting time of an episode of  $c > c_{\text{limit}}$  gives no help in determining when it will end, and, once it has ended, contributes nothing to determining the next occurrence of  $c > c_{\text{limit}}$ .

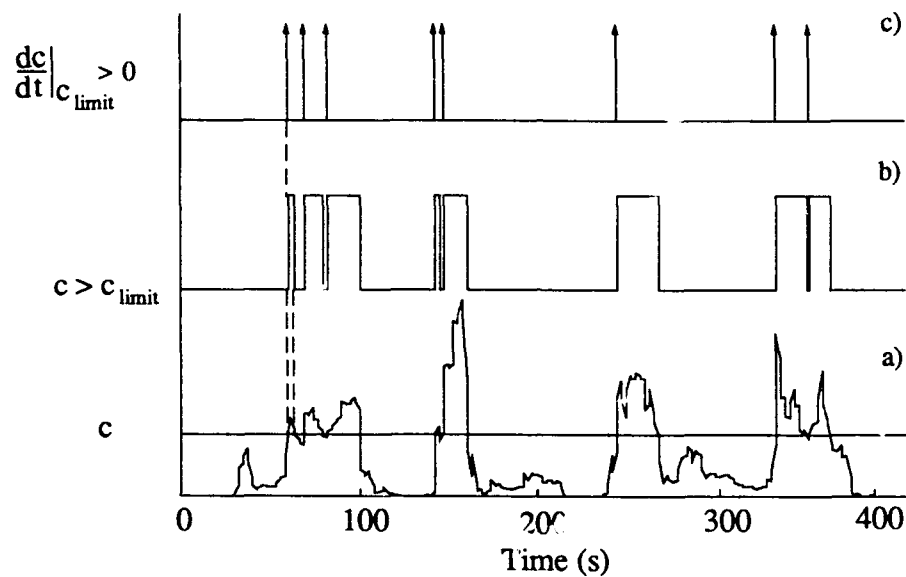


Figure 3.1 An example of the step and delta functions for a record of concentration at a point. The limiting value of concentration is set at an arbitrary level for the concentration signal in (a), the step function found using this level is shown in (b), and the delta function defined at the start of each positive transition in the step is given in (c).

To relate this back to the expected duration of a single episode of  $c > c_{\text{limit}}$ , we know that the average number of delta function events in an arbitrary time interval  $T$  is  $N = T\lambda$ , with  $T \gg t$ . This is also the number of continuous individual occurrences of  $c > c_{\text{limit}}$  in the same time interval. Knowing the number of events of  $c > c_{\text{limit}}$  and the total time for which  $c > c_{\text{limit}}$  in the time  $T$ , as

$$T [1 - P(c_{\text{limit}})] = T I \exp \left( -I \frac{c_{\text{limit}}}{\bar{c}} \right) \quad (3.207)$$

yields the average duration of single events  $c > c_{\text{limit}}$  as

$$\frac{1}{\lambda_u} = \frac{T I \exp \left( -I \frac{c_{\text{limit}}}{\bar{c}} \right)}{N} = \frac{1}{\lambda} I \exp \left( -I \frac{c_{\text{limit}}}{\bar{c}} \right) \quad (3.208)$$

so the rate  $\lambda_u$  is

$$\lambda_u = \frac{\lambda}{I \exp \left( -I \frac{c_{\text{limit}}}{\bar{c}} \right)} \quad (3.209)$$

The probability distribution in time of these events  $c > c_{\text{limit}}$  given by

$$P(t | c > c_{\text{limit}}) = 1 - \exp(-\lambda_u t)$$

Note that the distribution is valid for any  $c_{\text{limit}}$ , including  $c_{\text{limit}} = 0$ , which demarcates the presence or absence of material at the sampler. It is also important to note that the function  $\lambda = \lambda(c_{\text{limit}})$ , is unknown at this point. The distribution of temporal exceedance levels, given some arbitrary  $t_{\text{limit}}$ , may be written as  $\text{Prob}[t > t_{\text{limit}} | c > c_{\text{limit}}] = 1 - P(t | c > c_{\text{limit}}) = \exp(-\lambda_u t)$ .

Noting that the period of time that  $c \leq c_{\text{limit}}$  over a time  $T$  is

$$T P(c_{\text{limit}}) = T \left[ 1 - I \exp \left( -I \frac{c_{\text{limit}}}{\bar{c}} \right) \right] \quad (3.210)$$

and that the rate of events  $\lambda$  for  $c = c_{\text{limit}}$  and  $dc/dt |_{c_{\text{limit}}} > 0$  is the same as that for  $c = c_{\text{limit}}$  and  $dc/dt |_{c_{\text{limit}}} < 0$ , then we can find the average rate  $\lambda_d$  and the probability distribution of contiguous periods of time for which  $c \leq c_{\text{limit}}$  using

$$\lambda_d = \frac{1}{1 - I \exp \left( -I \frac{c_{\text{limit}}}{\bar{c}} \right)} \quad (3.211)$$

and

$$P(t | c \leq c_{\text{limit}}) = 1 - \exp(-\lambda_d t) \quad (3.212)$$

Although the values of  $\lambda_d$  and  $\lambda_u$  can be found in terms of  $\lambda$ , the form and value of  $\lambda$  is still unknown.

### **Average Duration or Rates of a Concentration Exceedance**

One obvious method of determining the function,  $\lambda(c_{\text{limit}}) = N/T$ , is directly from the time record of data. To find the number of times  $N$  that  $c_{\text{limit}}$  is exceeded in a duration  $T$ , we can count the events over the record where both the concentration is equal to  $c_{\text{limit}}$  and  $dc/dt | c_{\text{limit}} > 0$ , which is simply the condition for a delta function. Counting these conditional events gives the same result as counting the number of continuous bursts greater than  $c_{\text{limit}}$  in determining  $N$ .

It is evident that the actual determined value of  $N$  and  $\lambda$  depends on the total record length  $T$ , and the sampling interval of the data  $\Delta t$ . The probability distribution of time increments  $t$ , as well will be affected by the finite bandwidth of the sampled data. For a sampling record of duration  $T$ , the longer duration intervals will be undersampled, or if  $t > T$ , they will not be found at all. At smaller values of  $t$ , we will not detect occurrences of  $c > c_{\text{limit}}$  less than  $\Delta t$  in duration, but will instead find higher a number of occurrences just above  $\Delta t$  than would be present in data unbiased by the sampling speed. In our own experiments, the data have been sampled at a rate which will hopefully make these effects on the average value  $1/\lambda$  negligible. The sampling speed necessary to entirely avoid this high frequency bias is near the dissipation range of the concentration fluctuations which is entirely beyond the capability of our instruments.

## **4. METEOROLOGICAL INSTRUMENTATION AND MEASUREMENTS**

In the field dispersion experiments we have undertaken, it was necessary to measure and adequately characterize three basic items: the wind field, the source and passive tracer characteristics, and the concentration field downwind from the source. Descriptions of the dispersion site and background information are given in this chapter. This includes discussions of the wind measurements and instruments, meteorological data reduction, and sampler placement for each of both the Camp Atterbury, Indiana site and the Meadowbrook site.

For the remaining instrumentation a general discussion is presented in Chapter 5. This includes information on the aerosol characteristics and mean dosage sampling. Descriptions of the fog-oil smoke source and chemical analysis method are given, followed by similar information for the HC smoke. Chapter 5 concludes with a discussion on the design and development of the real-time sampling system.

### **4.1 The Camp Atterbury Site**

The Camp Atterbury site consists of an open field approximately 1 km<sup>2</sup> in size. Over this area the terrain is moderately flat with a maximum elevation difference of less than 6 m and with the ground cover consisting of dense weeds 0.5 to 1.5 m tall and small isolated stands of deciduous trees 5 to 20 m tall. The terrain surrounding this field consists of hills and ridges rising up to 45 m above the open flat area. The terrain upwind of the selected release point is relatively flat for a distance of 800 m before rising into the surrounding hills, and is about 25% forested with deciduous trees 10 to 20 m tall. During the November testing period, the trees were bare of leaves. A map of the test site with instrumentation employed for the experiments is shown in Figure 4.1.

#### **4.1.1 The Sampling Grid at Camp Atterbury**

To aid in the orientation the sampling grid, meteorological records for the previous two years were acquired from the National Weather Service in Indianapolis, which is 60 miles north of the site. In analysis of these data, Liljegren (1989) found the predominant wind direction is from the southwest. Two weeks before experimentation began, we erected two portable wind vanes at the locations shown in Figure 4.1 and logged wind and temperature data. These data confirmed the wind directions determined from the long term records. Figure 4.2 shows a time trace of wind and temperature records for these two stations. The wind direction during the daytime is from the northwest and is fairly regular except for frontal passage on October 17. Stable nighttime tests at this site are not possible because of stagnant nighttime conditions.

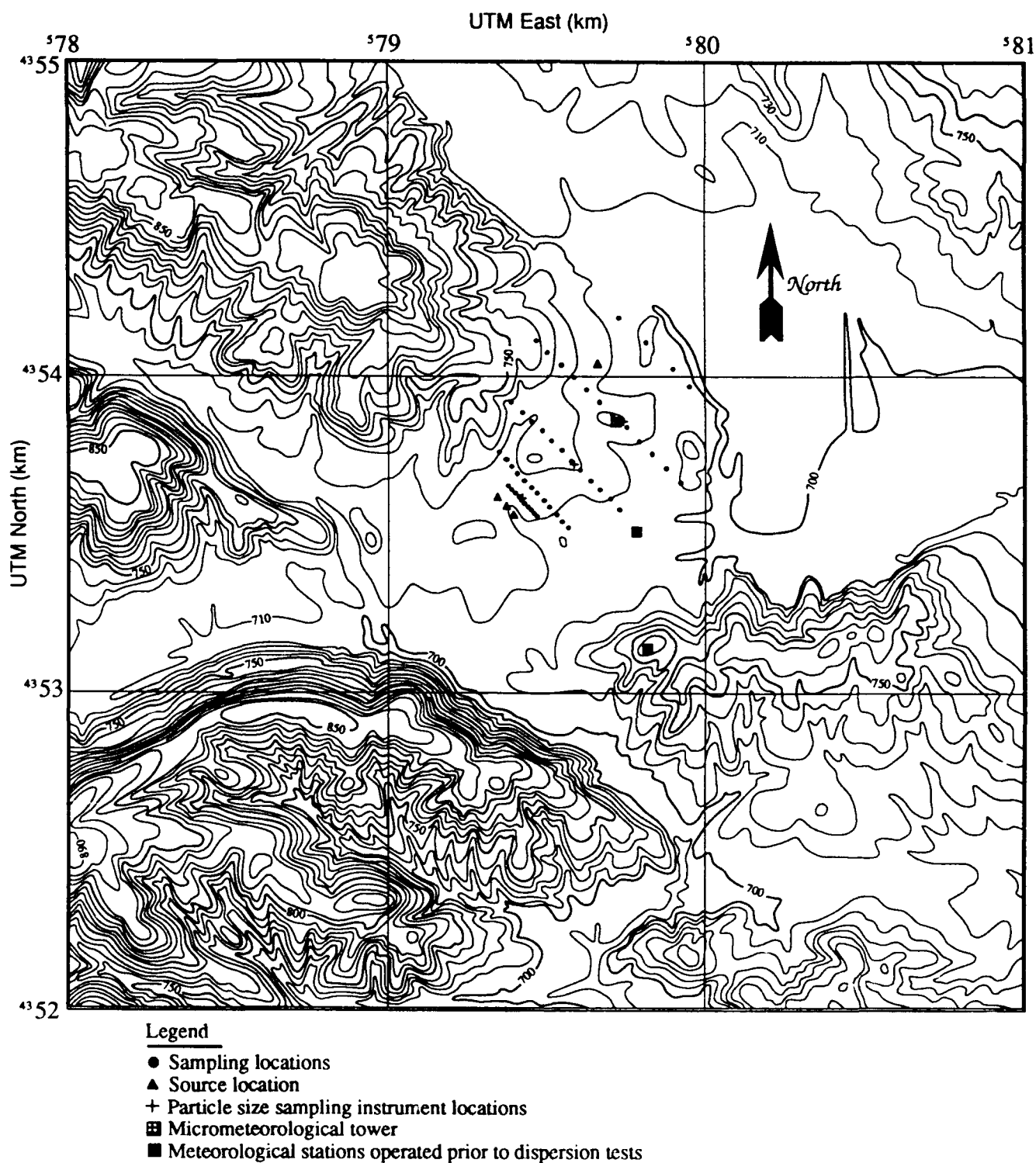


Figure 4.1 Topographical map of the dispersion test site at Camp Atterbury. Elevations are in feet above sea level with isopleths in increments of 10 ft. The horizontal grid is in Universal Transverse Mercator coordinates with marked increments of 1 km. Topographical data are from a USGS map of Ninevah, Indiana.

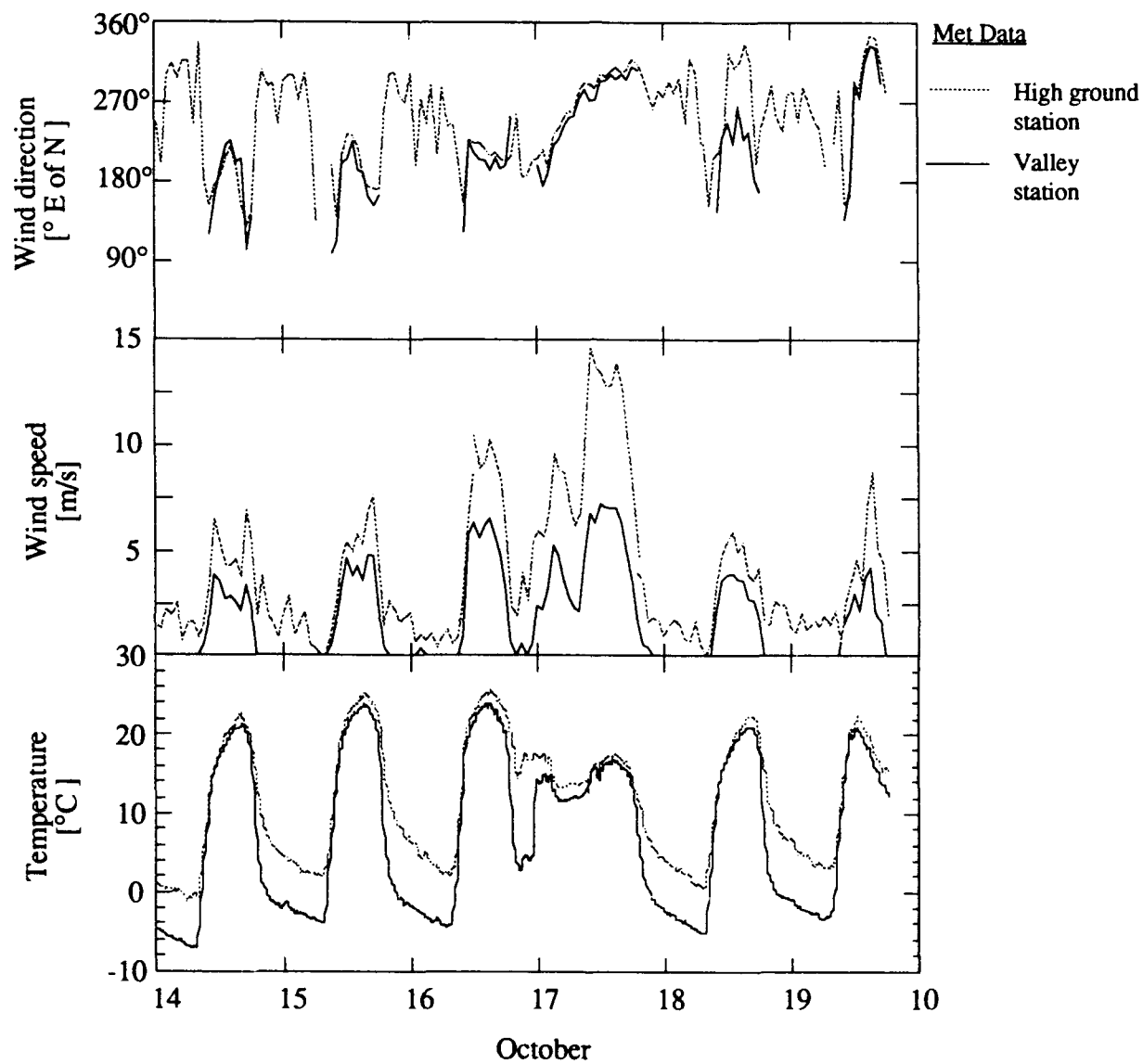


Figure 4.2 Long term meteorological data from Camp Atterbury beginning on October 14, 1987 at midnight and continuing for six days.

The samplers were located in lines at geometrically increasing distances from the source of 100 m, 200 m, 300 m, 500 m and 800 m. Each line of samplers subtended at least a 90° degree arc from the source, except for the farthest transect which consisted of just 4 sampling locations. These sampling transects are shown in the map of Figure 4.1.

#### **4.1.2 Meteorological Instrumentation at Camp Atterbury**

In the most simple conditions of uniform terrain and stationary atmospheric conditions, measurement of a single vertical profile of velocity and temperature would be sufficient to adequately characterize the state of the atmosphere. Although the Camp Atterbury site was not perfectly uniform, we believed a single vertical profile measurement near the center of the dispersion site was adequate for our purposes.

This vertical profile was measured with a single meteorological tower. Wind and temperature sensors were located at geometrically increasing heights of 2 m, 4 m, 6 m, and 10 m. At all of these levels, the wind speed was measured with a Gill three-cup anemometer. This anemometer consists of a vertical bearing-mounted spindle with three axially mounted hemispherical cups. The rotation of the spindle, and thus the wind speed, is monitored through a photochopper output. The horizontal wind direction was monitored at the 2-m height with a Gill microvane. At the higher levels both the horizontal and vertical angles of the wind direction were measured with Gill bivanes. The microvane consists of a counterbalanced vane with a vertically oriented flat-plate tail fin and is free to rotate in a plane parallel to the ground, with the position sensed through a potentiometer. Each bivane consists of a gimbal-mounted vane free to rotate through both vertical and horizontal deflection angles. The tail of the vane has both vertical and horizontal flat-plate fins. Both axes of the vane position are sensed through gear-driven potentiometers. All wind instruments were manufactured by R.M. Young.

Since each of these instruments measure only a part of the needed wind vector at a given height, careful matching of the instrument response between the vanes and anemometers is necessary. The manufacturer accomplishes this by matching the phase lag of both the wind speed and direction sensors to minimize the total errors in the calculated wind vector. The response of these instruments is such that frequency spectra of the wind data will be unbiased by the instruments up to at least 0.1 Hz or better for all tests. Wind variances will always be underestimated due to the low pass filtering effects inherent in these instruments and the finite averaging period; the degree of error depends on the particular atmospheric conditions of each test as quantified in Section 4.1.2.

Temperature was monitored at all the instrumented heights using Campbell Scientific thermistor temperature sensors mounted in aspirated radiation shields. These shields minimize solar heating of the sensors thus reducing radiation errors. Although these sensors have a relatively slow



response time, they are sufficient for determining mean temperatures and the vertical temperature gradient.

All sensor outputs were sampled using a Campbell Scientific 21X Micrologger coupled with a Zenith Z-181 portable computer for archiving the data onto floppy disks. All inputs were sampled at a frequency of 1 Hz.

The above data are augmented by wind and temperature measurements taken near the source location at a height of 2 m. The near source measurements are made using a Gill wind monitor from R.M. Young. This device is a polystyrene wind direction vane with a vertical airfoil tail and a helical four-blade propeller at the head of the vane for measuring the wind speed. The frequency spectra of the wind measurements are unbiased up to at least 0.1 Hz or better for all tests. The degree that variances of the wind speed and direction are underestimated through the response of this instrument is quantified in Section 4.1.2.

Cup and propeller anemometers usually give slightly different wind speeds in the field, even though they typically yield identical values in steady wind tunnel calibrations. This is because the cup anemometer over-responds to wind velocities in the vertical plane whereas the helical propeller follows a more ideal cosine response function for off-axis winds. MacCready (1966) has found the cup anemometer to overestimate true wind speed by up to 6% whereas errors for the propeller anemometer were found to be less than 1%.

#### **4.1.3 Meteorological Parameters and Scaling Variables**

Upon averaging the meteorological measurements, we find that the velocity increases as a function of height at the meteorological tower. In all cases the 2-m velocity measured at the source is smaller than the 2-m value measured on the meteorological tower. This difference is larger than can be attributed to the different wind instruments at the two locations and may be caused by the changes in terrain. The vertical temperature profile in most cases is not smooth but instead shows an apparent change in temperature gradient within the height of the meteorological tower. This may be due to the limited accuracy of the sensors or an effect of the changing terrain surrounding the tower. All of these tests were conducted in the daytime during which we expect conditions to range from near neutral to very convective.

#### **Surface-Layer Scaling**

Surface-layer scaling parameters in the atmosphere can be determined using several different methods. Our analysis is based on the bulk Richardson number defined by

$$Ri_B = \frac{g z \Delta T}{T \bar{u}^2} \quad (4.1)$$

where  $T$  and  $\bar{u}$  are typically taken at the 10-m height and  $\Delta T = T - T_0$ . The value of  $Ri_B$  can establish the relative stability of the atmosphere over the test site. Larger positive values indicate more stable conditions and larger negative values indicate greater instability.

The bulk Richardson number  $Ri_B$  is used to find surface-layer scaling parameters in a method given by Irwin and Binkowski (1981). We first need an estimate of the roughness height  $z_0$  for the test site. A crude estimate from Randerson (1984) gives  $z_0$  as 10% of the vegetation height. This yields a value of  $z_0 = 0.10$  m. The elevation variation over the 1 km<sup>2</sup> test site (4.2 m root mean square) will also contribute to the roughness height so the value of 0.10 m is probably an underestimate. However, the underestimation of roughness height is recommended by Irwin and Binkowski when employing their method.

Benoit (1977) provides a velocity function  $F = \bar{u}/u_*$  for unstable conditions which is given by

$$F = \frac{\bar{u}(z)}{u_*} = \frac{1}{k} \left[ \ln \left( \frac{z}{z_0} \right) + \ln \left( \frac{(\zeta_0^2 + 1)(\zeta_0 + 1)^2}{(\zeta^2 + 1)(\zeta + 1)^2} \right) + 2 \left[ \tan^{-1}(\zeta) - \tan^{-1}(\zeta_0) \right] \right] \quad (4.2)$$

where

$$\zeta \equiv \left[ 1 - \frac{\gamma z}{L} \right]^{1/4} \quad (4.3)$$

and

$$\zeta_0 \equiv \left[ 1 - \frac{\gamma z_0}{L} \right]^{1/4} \quad (4.4)$$

The corresponding temperature function is

$$G = \frac{T(z) - T_0}{T_*} = \frac{R}{k} \left[ \ln \left( \frac{z}{z_0} \right) + 2 \ln \left( \frac{\lambda_0 + 1}{\lambda + 1} \right) \right] \quad (4.5)$$

where

$$\lambda \equiv \left[ 1 - \frac{\gamma' z}{L} \right]^{1/2} \quad (4.6)$$

and

$$\lambda_0 \equiv \left[ 1 - \frac{\gamma' z_0}{L} \right]^{1/2} \quad (4.7)$$

Finally,  $Ri_B$  is related to  $F$  and  $G$  through the expression

$$Ri_B = \frac{G}{k F^2} \left( \frac{z}{L} \right) \quad (4.8)$$

In these equations we use coefficients of  $k = 0.4$ ,  $R = 1.0$ , and  $\gamma = \gamma' = 16$  from Dyer (1974). The temperature and velocity functions  $F$  and  $G$  are similar in form to those given by Paulson (1970) and Businger et al. (1971) except they include a dependence on the roughness height  $z_0$ .

To determine surface-layer scaling parameters, we first determine  $Ri_B$  from the data, then estimate  $z_0$ , and lastly find  $L$  through an iterative solution of the functions  $F$  and  $G$ . The 6-m wind velocity is used in these calculations. For  $\Delta T$  the 2-m and 6-m values are used because of apparent errors in the 10-m temperature measurement. Other characteristic parameters may also be found. These include the friction velocity

$$u_* = \frac{\bar{u}}{F} \quad (4.9)$$

the temperature parameter

$$T_* = \frac{T u_*^2}{L k g} \quad (4.10)$$

$$Q_0 = -\overline{\theta u'_z} = -T_* u_*$$

and the heat flux

$$H = -T_* u_* [\rho C_p] = -T_* u_* \left[ 1229 \frac{J}{m^3 \text{ } ^\circ K} \right] \quad (4.11)$$

where  $H$  is expressed in units of  $W/m^2$ . These parameters are shown in Table 4.1 for the tests at Camp Atterbury.

The vertical profiles of temperature and velocity we have measured should follow surface-layer scaling with

$$\bar{u}(z) = \frac{u_*}{k} \left[ \ln \left( \frac{z}{z_0} \right) - \psi_m(z/L, z_0/L) \right] \quad (4.12)$$

and

$$T(z) = T_0 + \frac{R T_*}{k} \left[ \ln \left( \frac{z}{z_0} \right) - \psi_h(z/L, z_0/L) \right] \quad (4.13)$$

These relations, with some algebraic manipulation, are plotted in Figures 4.3 and 4.4. The empirical relations for  $\psi_m$  and  $\psi_h$  are found from the functions  $F$  and  $G$  given in Eqs. 4.2 and 4.5. Other

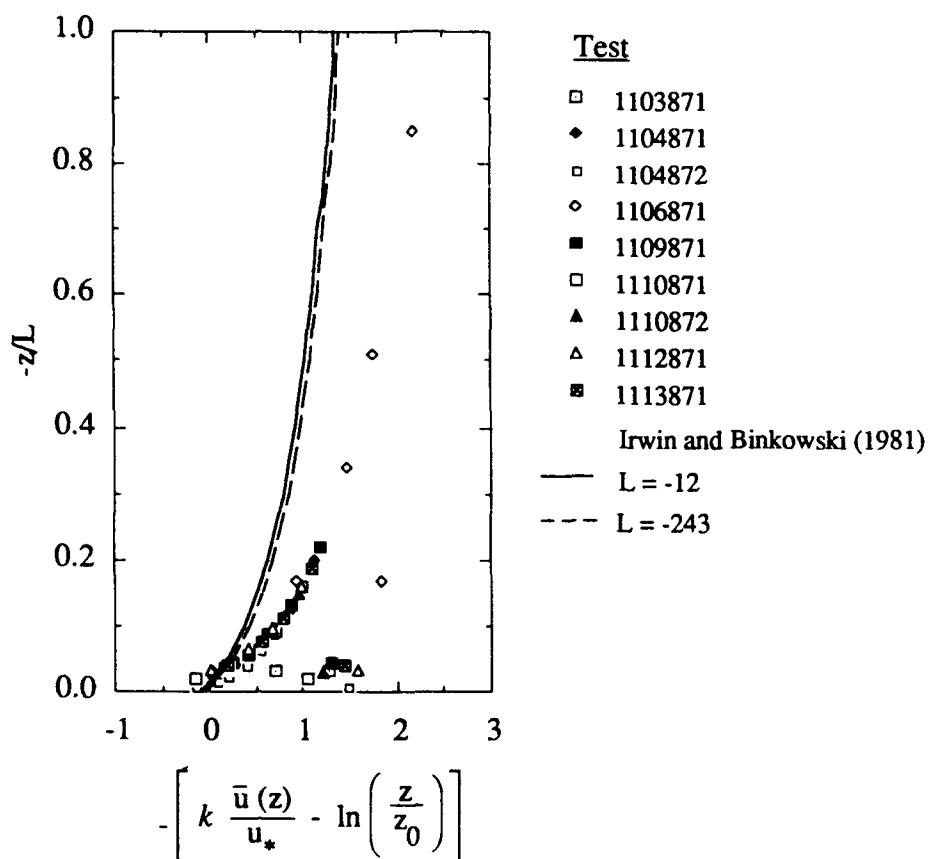


Figure 4.3 Mean velocity profiles from Camp Atterbury meteorological data. Values of  $L$ ,  $u_*$ , and  $T^*$  in these graphs are from a bulk Richardson number parameterization discussed by Irwin and Binkowski (1981) that uses empirical parameters from Dyer (1974). A roughness height of 0.10 m is used and data from both the meteorological tower and the source are shown.

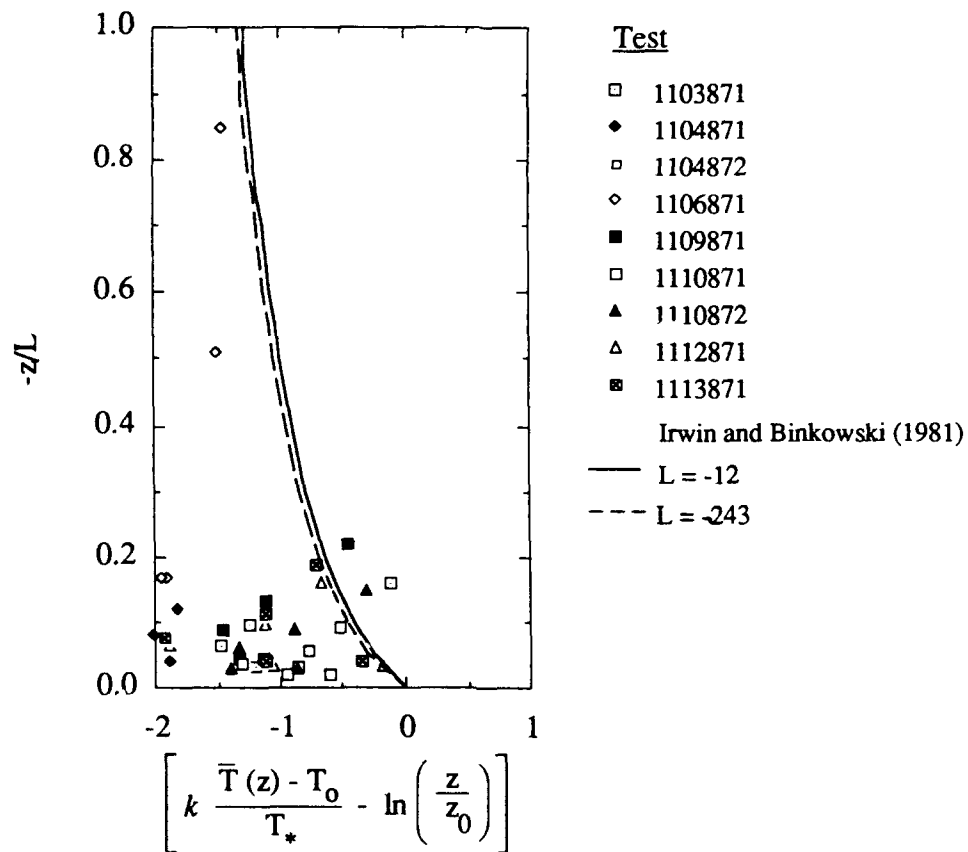


Figure 4.4 Mean temperature profiles from Camp Atterbury meteorological data. Values of  $L$ ,  $u_*$ , and  $T_*$  in these graphs are from a bulk Richardson number parameterization discussed by Irwin and Binkowski (1981) that uses empirical parameters from Dyer (1974). A roughness height of 0.10 m is used and data from both the meteorological tower and the source are shown.

Table 4.1 Meteorological scaling values for the Camp Atterbury dispersion tests.

Test	$\bar{u}_{10\text{ m}}$ (m/s)	L (m)	$u_*$ (m/s)	$T_*$ (°K)	H (W/m <sup>2</sup> )	$z_i$ (m)	$w_*$ (m/s)
1103871	5.54	-63	0.61	-0.45	341	668	1.83
1104871	5.11	-51	0.59	-0.51	372	305	1.46
1104872	4.66	-243	0.44	-0.06	33	1135	1.00
1106871	1.60	-12	0.26	-0.42	138	557	1.30
1109871	4.36	-46	0.51	-0.41	256	649	1.68
1110871	7.07	-110	0.72	-0.34	300	448	1.57
1110872	5.17	-68	0.57	-0.33	229	434	1.42
1112871	4.91	-63	0.54	-0.34	228	816	1.73
1113871	4.30	-53	0.49	-0.33	199	500	1.41

comparable forms of  $\psi_m$  and  $\psi_h$  come from Paulson (1970), Businger et al. (1971), or Dyer and Hicks (1970) for flat terrain.

For the velocity, values at higher levels on the meteorological tower and at the source location are all overpredicted by up to 50%. The sensitivity of the profile fit can be found by varying the value of  $z_0$ . A 100% change in  $z_0$  gives a change in L of  $\pm 44\%$  and a change in  $u_*$  of  $\pm 15\%$ . In contrast, the same change in  $z_0$  gives only a 2% change in the convection velocity  $w_*$ . The convection velocity is an upper-layer scaling parameter which should be insensitive to  $z_0$ .

The scatter of the temperature data about the predicted profile in Figure 4.4 is considerably greater than that shown in the velocity profile in Figure 4.3. This scatter may be due, in part, to the limited accuracy of the temperature sensors, but it may also be due to the varied terrain surrounding the test site. Recalling the data for long-term measurements shown in Figure 4.2, the daytime temperature found at the hill station near the test site is consistently higher than that measured at the valley station. This spatial variation in surface temperatures along with elevation changes and advection could cause the temperature profile to deviate from the empirical form developed using flat terrain data.

In addition to the mean temperature and velocity profiles, the vertical variance in velocity should also follow surface-layer scaling. The ratio  $\sigma_w/u_*$  is plotted versus  $-z/L$  in Figure 4.5. This generally good agreement supports the validity of the scaling analysis described above. A fit given by Panofsky et al. (1977)

$$\frac{\sigma_w}{u_*} = 1.25 \left( 1 - 3 \frac{z}{L} \right)^{1/3} \quad (4.14)$$

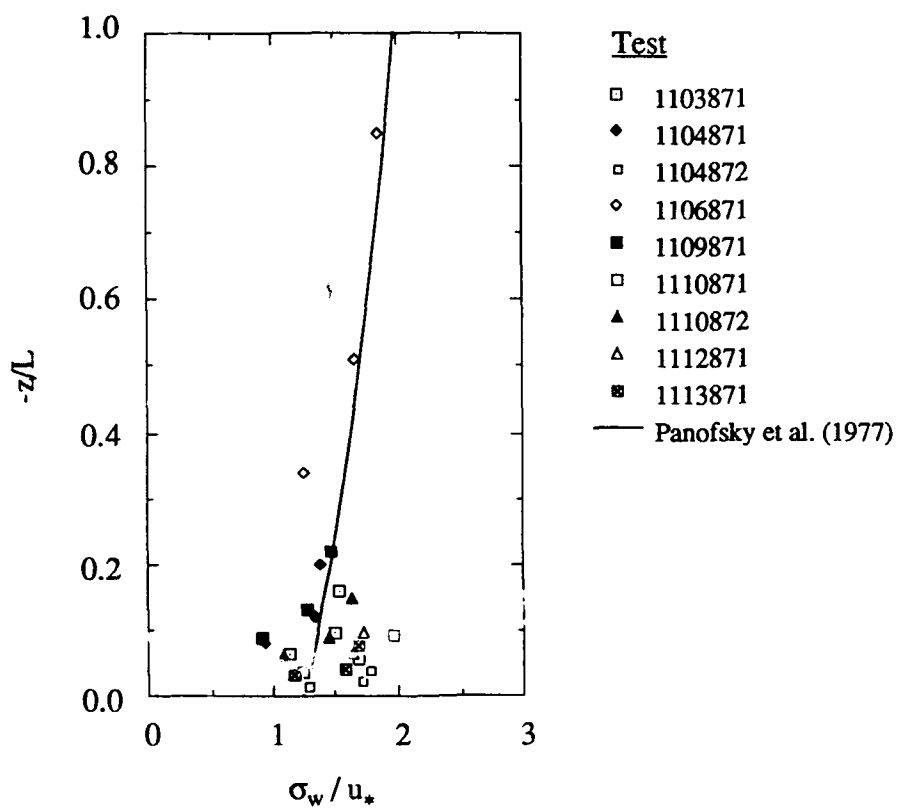


Figure 4.5 Vertical standard deviation of velocity measured on the 10-m meteorological tower. The data in this plot are scaled by parameters found from the bulk Richardson number. A roughness height of .1 m is used.

also shows reasonable agreement with the data.

### **Upper-Layer Scaling**

Upper-layer scaling is needed to find the inversion height  $z_i$  and the convection velocity  $w_*$ . These are related by the expression

$$-\frac{z_i}{L} = k \left( \frac{w_*}{u_*} \right)^3 \quad (4.15)$$

so that only one independent parameter is needed.

We can estimate the inversion height  $z_i$  by finding the level at which the morning vertical potential temperature profile intersects the surface potential temperature at Camp Atterbury during the dispersion test.

To implement this procedure, rawinsonde measurements at Peoria, Illinois and Dayton, Ohio taken daily at 00:00 GMT (18:00 CST) and 12:00 GMT (06:00 CST) were obtained from the National Climatic Data Center, Ashville, North Carolina (NCDC). The 12:00 GMT sounding corresponds to a morning sounding over the central United States. These soundings include temperature, pressure, and the height above sea level from which we can calculate the vertical potential temperature profile in the atmosphere. We also have NCDC surface station measurements at Dayton, Evansville, Indianapolis, Louisville, and Peoria which are used in the calculations. The potential temperature is found using

$$\theta = T \left[ \frac{P_{00}}{P} \right]^{\mathcal{R}/C_p} \quad (4.16)$$

with  $P_{00} = 1000$  mb and  $\mathcal{R}/C_p = (\gamma-1)/\gamma = 1/3.5$ . This would be the temperature achieved in bringing a parcel of air to  $P_{00}$  in an isentropic process. Height is found through a hydrostatic approximation.

Because the test site and the location of both daily soundings are separated by 120 km, corrections to the vertical profile are necessary. These corrections are intended to compensate for different morning surface temperatures between the sounding and test site locations. For each sounding, we adjusted the surface potential temperature to the minimum value recorded at Indianapolis for the same morning. The potential temperature and height at the 700 mb pressure level are held fixed and data values between the surface and this point are linearly interpolated to new values using



$$z_2 = z_1 - \left[ z_{1, \text{ surface}} - z_{2, \text{ surface}} \right] \frac{[z_1 - z_{700 \text{ mb}}]}{[z_{1, \text{ surface}} - z_{700 \text{ mb}}]} \quad (4.17)$$

for height above sea level and

$$T_2 = T_{2, \text{ surface}} - \left[ T_{2, \text{ surface}} - T_{700 \text{ mb}} \right] \frac{[T_1 - T_{1, \text{ surface}}]}{[T_{700 \text{ mb}} - T_{1, \text{ surface}}]} \quad (4.18)$$

for potential temperatures. A subscript of 2 indicated a corrected value whereas a subscript of 1 corresponds to an the original value.

The 700-mb pressure value is used for an interpolation end point in the soundings because both the height and the potential temperature at this level are well correlated at Dayton and Indianapolis. Over our two-week testing period the correlation coefficient for the 700-mb height is 0.81 and for the potential temperature the correlation coefficient is 0.79. Average values at this pressure were 3085 m and 300.4 K.

The minimum temperature recorded at Indianapolis from NCDC data is used in this calculation because this value was not recorded at Camp Atterbury. Indianapolis is the NCDC station closest to the Camp Atterbury site. The minimum morning potential temperature occurred between 6:00 to 8:00 on every day during the test period except for November 9, for which the temperature was seen to continuously decline throughout the day.

In calculating the surface potential temperature at Camp Atterbury during the test period we use the average air temperature measured at the source. For the atmospheric pressure we use a value derived from NCDC surface station measurements at Dayton, Evansville, Indianapolis, Louisville, and Peoria at the test time. These pressures are adjusted from the surface station altitude to sea level and averaged. This value is then corrected for the altitude at Camp Atterbury and the result used in the calculation of surface potential temperature.

In determining the inversion height, a least squares fit was made to the corrected data from both Peoria and Dayton for the potential temperature profile. This was then solved for the surface potential temperature at the test time. Results from this calculation are shown in Table 4.2. Also shown is the slope of the data fit in the region of the inversion height. This indicates the sensitivity of the inversion height to changes in surface temperature.

No value of the inversion height is found for November 9, 1987 using this method because of synoptic cooling throughout the morning and afternoon. For this test we instead used the inversion height measured directly in the 00:00 GMT soundings at Peoria and Dayton.

A method similar to the one we have used for calculating the inversion height is discussed by Benkley and Schulman (1979). Their method includes corrections due to advection of the air mass

Table 4.2 Inversion heights for the Camp Atterbury tests.

Test:	$z_i$	$dz/d\theta _{z_i}$
1103871	668	122
1104871	305	90
1104872	1135	232
1106871	557	105
1109871	649	—
1110871	448	63
1110872	434	62
1112871	816	86
1113871	500	67

between the sounding and the time of the inversion height which were not necessary for our data. Differences in morning surface temperature at the sounding location and the test site are corrected by assuming a linear temperature gradient between the morning surface potential temperature and the nocturnal mixing height.

We may estimate the accuracy in our scaling parameters using the standard deviation of the  $u$ ,  $v$ , and  $w$  wind components measured at the test site. The horizontal fluctuations should be a function of both mixed-layer and surface-layer parameters. For highly convective conditions, values of  $\sigma_u$  and  $\sigma_v$  approach a limiting value of  $\sigma_u = \sigma_v \sim 0.58w_*$ . In the neutral limit over flat terrain, we have  $\sigma_u = 1.9u_*$  and  $\sigma_v = 2.4u_*$  from Panofsky and Dutton (1984). Both  $\sigma_u$  and  $\sigma_v$  are relatively independent of height. In neutrally to moderately unstable conditions and using flat terrain data, Højstrup (1982) gives

$$\frac{\sigma_u^2}{u_*^2} = 0.6 \left[ -\frac{z_i}{L} \right]^{2/3} + 4.8 \frac{(1 - z/z_i)^2}{(1 + 15 z/z_i)^{2/3}} \quad (4.19)$$

and

$$\frac{\sigma_v^2}{u_*^2} = 0.7 \left[ -\frac{z_i}{L} \right]^{2/3} + 2.7 \frac{(1 - z/z_i)^2}{(1 + 2.8 z/z_i)^{2/3}} \quad (4.20)$$

from integration of a spectral model. In convective-layer scaling with the above equations, the value of  $u_*$  may be replaced by  $w_* = u_* (-z_i/Lk)^{1/3}$ , since  $z_i$  and  $L$  may be treated as independent parameters. In doing so, both sides of each equation are multiplied by  $(-z_i/Lk)^{-2/3}$ . Plots of the

horizontal standard deviations in wind velocity are shown in Figure 4.6 and 4.7, with values from the above equations shown for the largest and smallest values of  $z_i/L$  found in our data set.

Vertical standard deviations in wind direction are shown in Figure 4.8. Numerical integration of a spectral model given by Højstrup (1982) for our largest and smallest values of  $z_i/L$  are also plotted. A model for the free-convection limit from Kaimal et al. (1976) is also shown. Overall agreement between the model and the data is reasonable.

### **Spectra of the Velocity Data**

In spectral analysis of the meteorological data, components are nondimensionalized using the variances for each sensor and a  $(z_i/w_*)$  convective time scale for each test. Results are shown in Figure 4.9. Examination of the spectra reveals a  $-5/3$  power law behavior for  $S_{uu}(n)$  versus  $n$  for the  $u$ -component in all tests, but the other components do not show this behavior. Ratios of  $S_{vv}(n)/S_{uu}(n)$  and  $S_{ww}(n)/S_{uu}(n)$  also do not reach an asymptotic ratio of  $4/3$  which is expected at higher frequencies. Data from Kaimal et al. (1972) suggests that our sampling frequency and height are both too low for observing this inertial subrange behavior in the  $v$  and  $w$  crosswind components.

Using the spectra we may estimate integral scales of the turbulence using

$$t_{E,i} = \frac{2 \pi S_{ii}(n \rightarrow 0)}{\sigma_i^2} \quad (4.21)$$

for each of  $u$ ,  $v$ , and  $w$ . These values are compared with model values given by Højstrup (1982) for our limiting test conditions in Figure 4.10. For the horizontal components the data fall within the range provided by the model. Integral scales in the vertical direction are biased by a factor of 2 toward longer times relative to those obtained using the model of Højstrup.

We may quantify the underestimates in the standard deviations in velocity due to our finite test duration and high frequency resolution using the spectra. At the low frequency end we extrapolate the  $S_{ii}(n)$  versus  $n$  spectra using a zero slope. Integration shows that standard deviations in the  $u$ ,  $v$ , and  $w$  directions are underestimated by less than 3% by neglecting spectral contributions with a period longer than 10 minutes. This error bound includes only spectra within the microscale range.

At the high frequency limit, we may extrapolate the spectra with a  $-5/3$  slope. In the mean flow direction the average underestimate in the standard deviation of  $u$  is 3%; the corresponding maximum error is 7%. For the crosswind direction the average underestimate is 15% with a corresponding maximum of 50%. In the vertical, this method produces an average underestimate of 40% with a corresponding maximum of 90%. In all cases the error is greatest for the most nearly

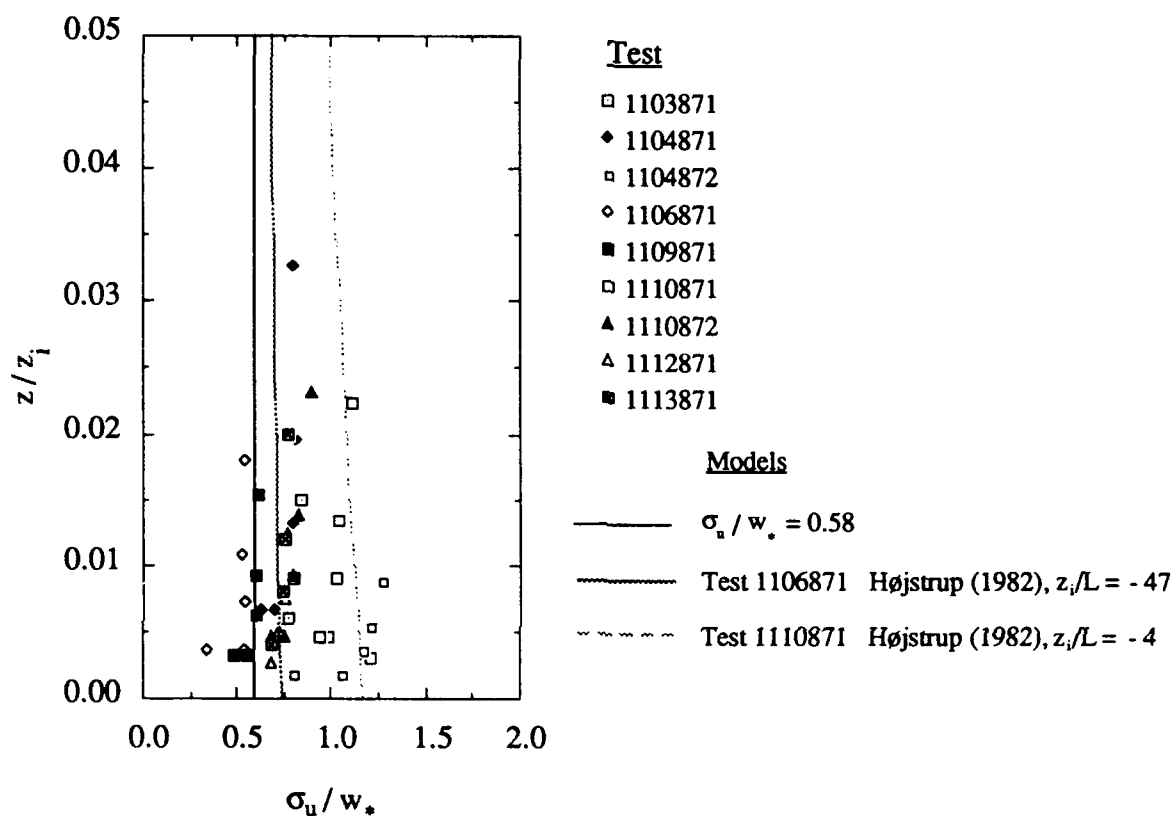


Figure 4.6 Standard deviations in u-component velocity for the Camp Atterbury meteorological data. These values are scaled by parameters found through the NCDC upper air data from Peoria and Dayton, Camp Atterbury surface temperature measurements, and bulk Richardson number scaling. The free convection limit is shown, along with profiles given by Højstrup (1982) for the most unstable and most nearly neutral tests in the data set.

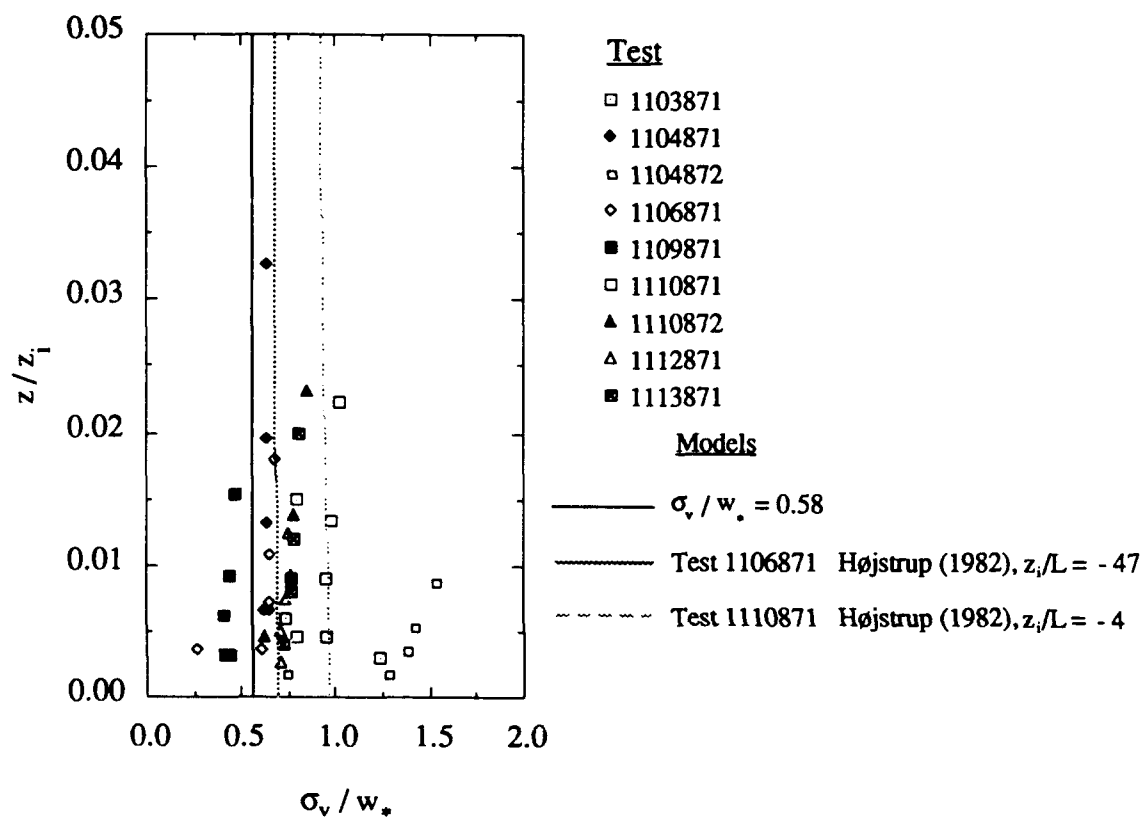


Figure 4.7 Standard deviations in v-component velocity for the Camp Atterbury meteorological data. These values are scaled by parameters found through the NCDC upper air data from Peoria and Dayton, Camp Atterbury surface temperature measurements, and bulk Richardson number scaling. The free convection limit is shown, along with profiles given by Højstrup (1982) for the most unstable and most nearly neutral tests in the data set.

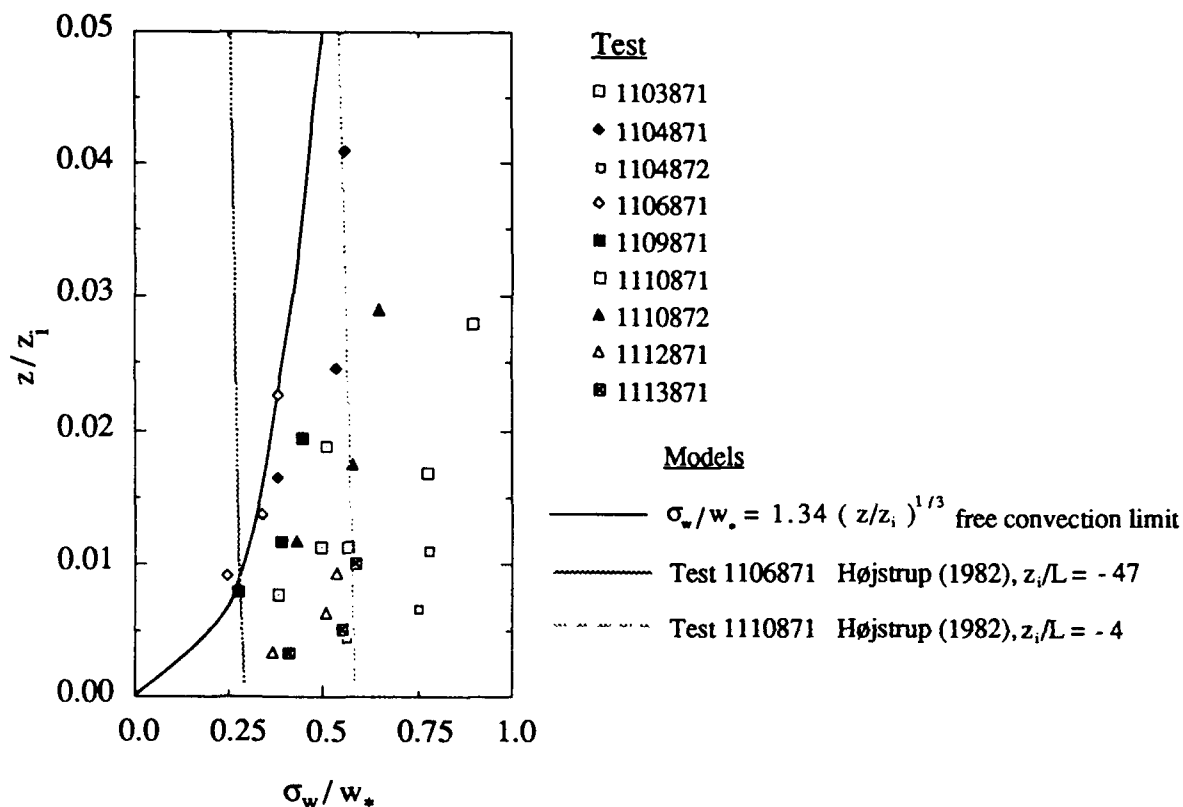
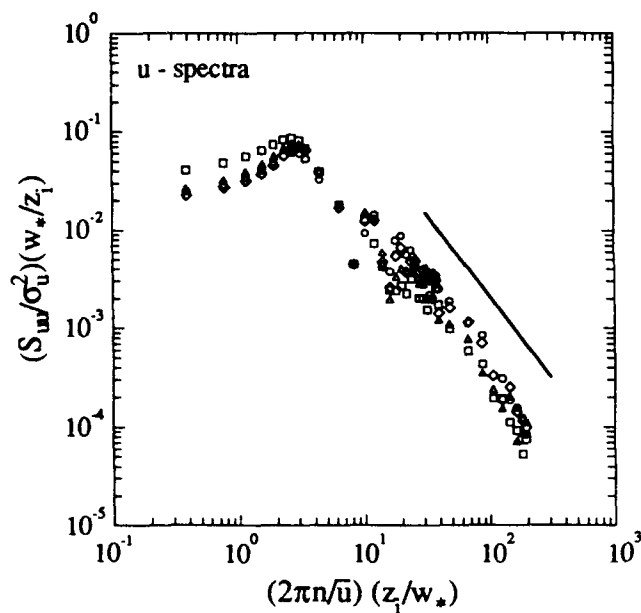


Figure 4.8 Standard deviations in w-component velocity for the Camp Atterbury meteorological data. These values are scaled by parameters found through the NCDC upper air data from Peoria and Dayton, Camp Atterbury surface temperature measurements, and bulk Richardson number scaling. The free convection limit given by Kaimal et al. (1976) is shown, along with profiles given by Højstrup (1982) for the most unstable and most nearly neutral tests in the data set.



Test 1103871

- 10 m
- △ 6 m
- ◇ 4 m
- 2 m
- - 5/3 slope

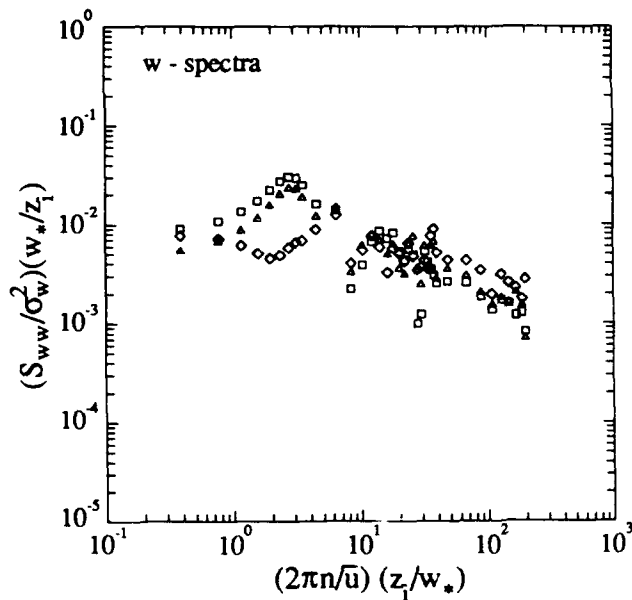
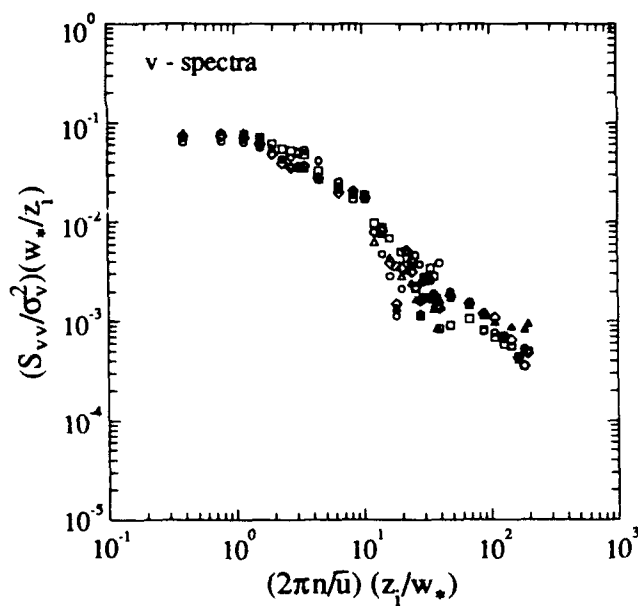
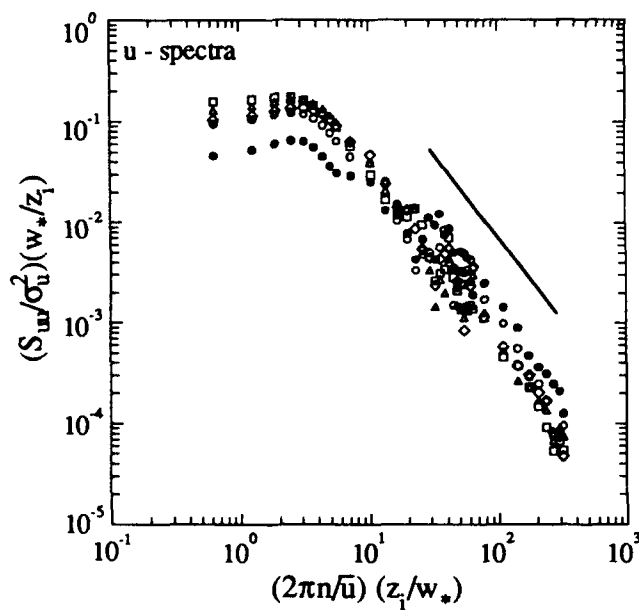


Figure 4.9 Spectra of the wind data from Camp Atterbury for Test 1103871. The spectra were normalized by the the calculated variance for each data record and the convective time scale for this test.



Test 1104871

- 10 m
- △ 6 m
- ◇ 4 m
- 2 m
- - 5/3 slope

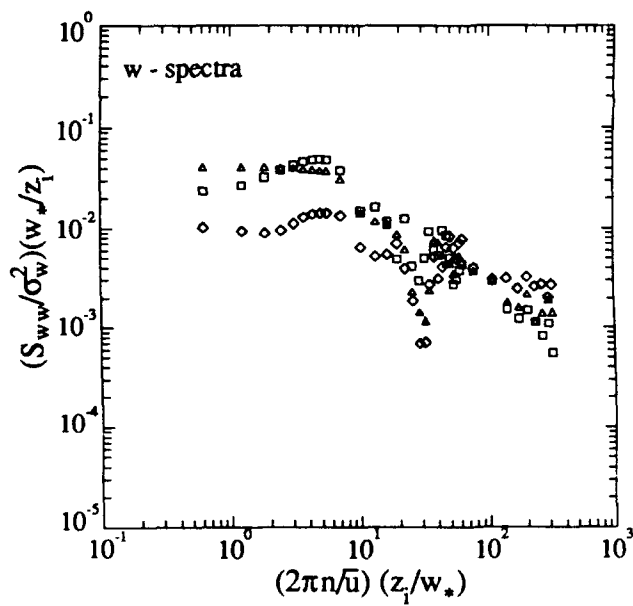
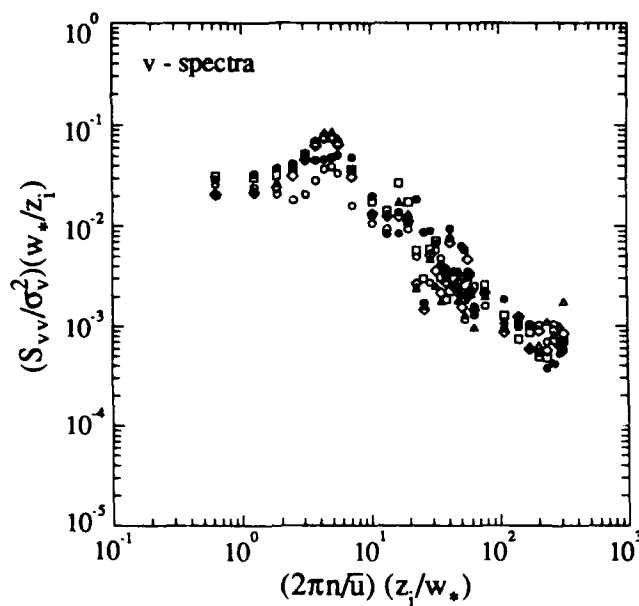


Figure 4.9 (continued) Spectra of the wind data from Camp Atterbury for Test 1104871. The spectra were normalized by the the calculated variance for each data record and the convective time scale for this test.



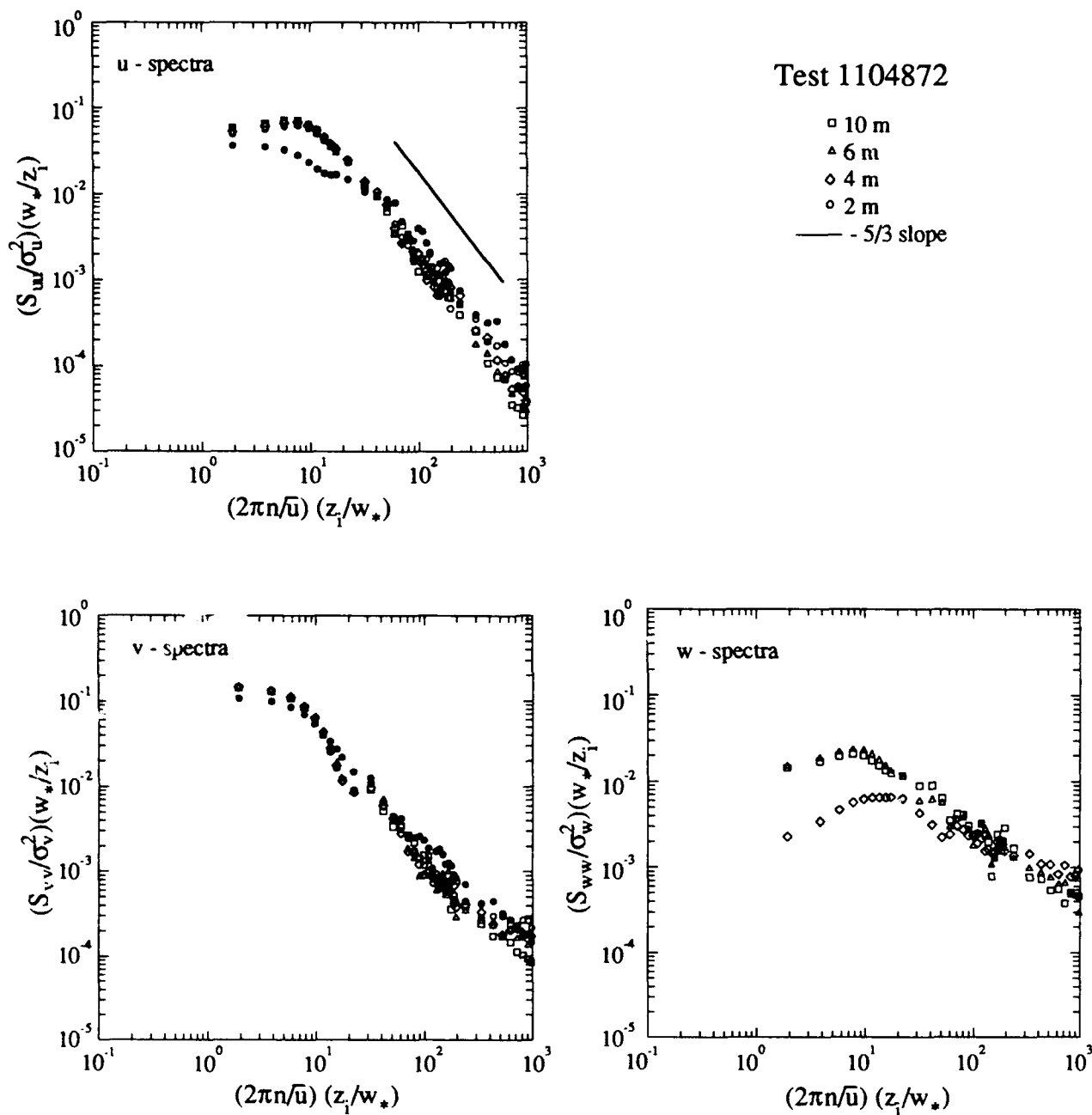
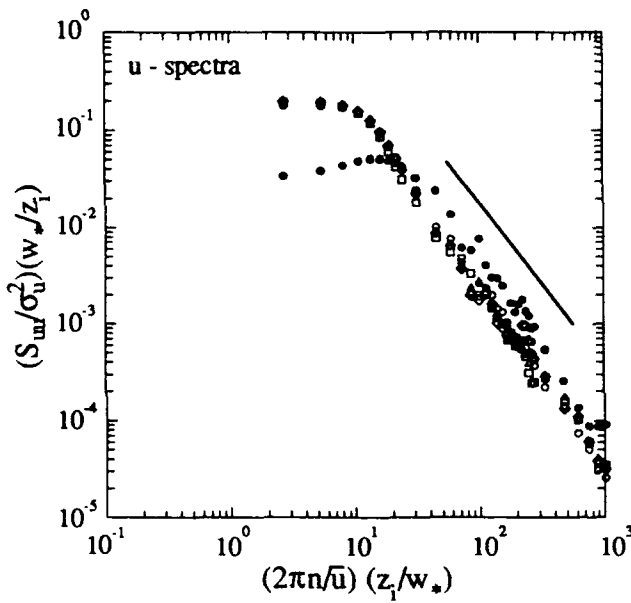


Figure 4.9 (continued) Spectra of the wind data from Camp Atterbury for Test 1104872. The spectra were normalized by the the calculated variance for each data record and the convective time scale for this test.



Test 1106871

- 10 m
- △ 6 m
- ◇ 4 m
- 2 m
- - 5/3 slope

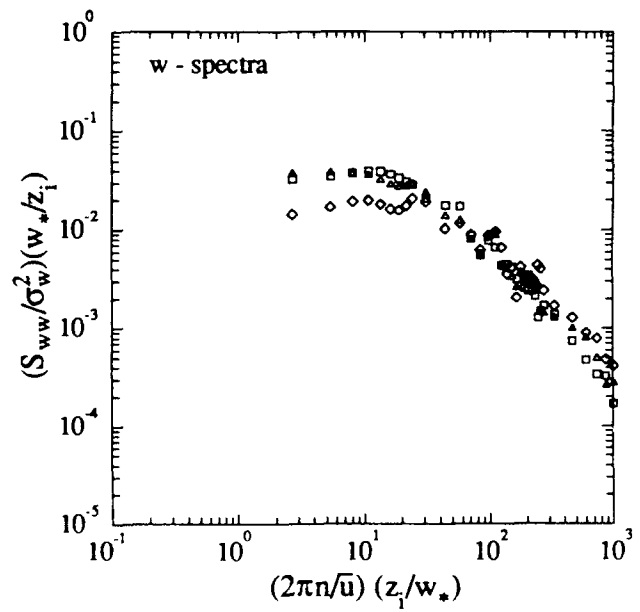
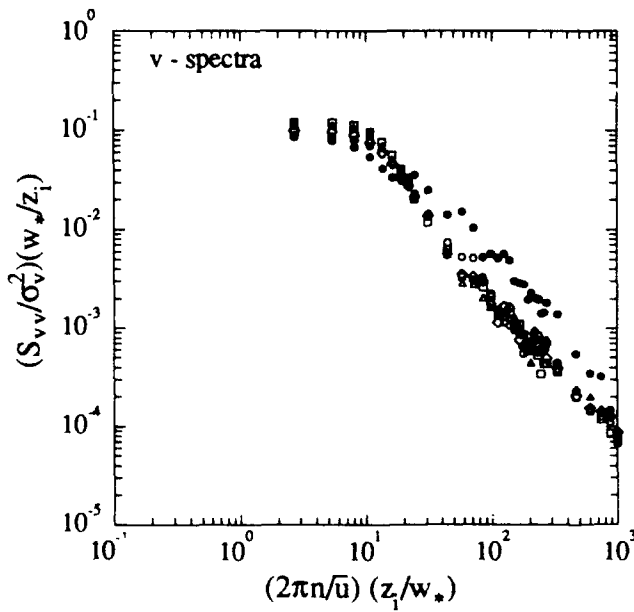
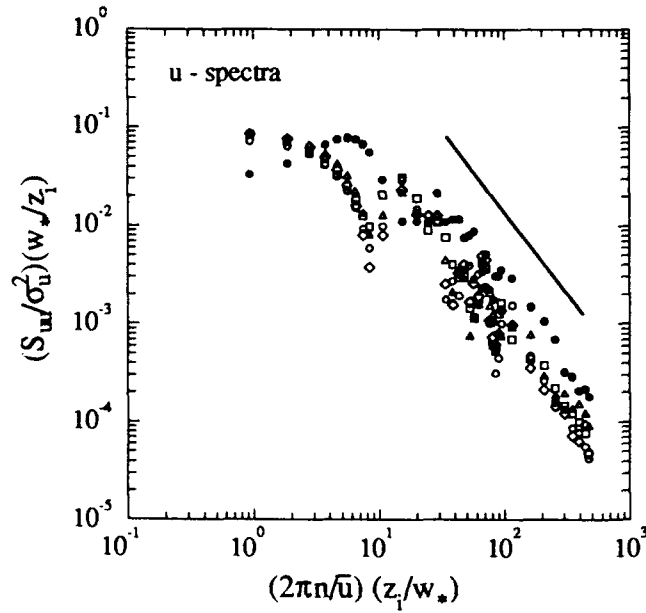


Figure 4.9 (continued) Spectra of the wind data from Camp Atterbury for Test 1106871. The spectra were normalized by the the calculated variance for each data record and the convective time scale for this test.



Test 1109871

- 10 meter
- △ 6 meter
- ◇ 4 meter
- 2 meter
- 2 meter source
- - 5/3 slope

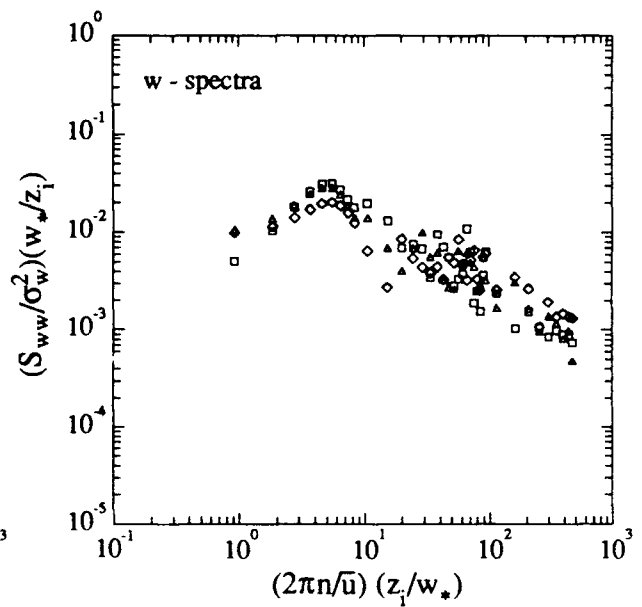
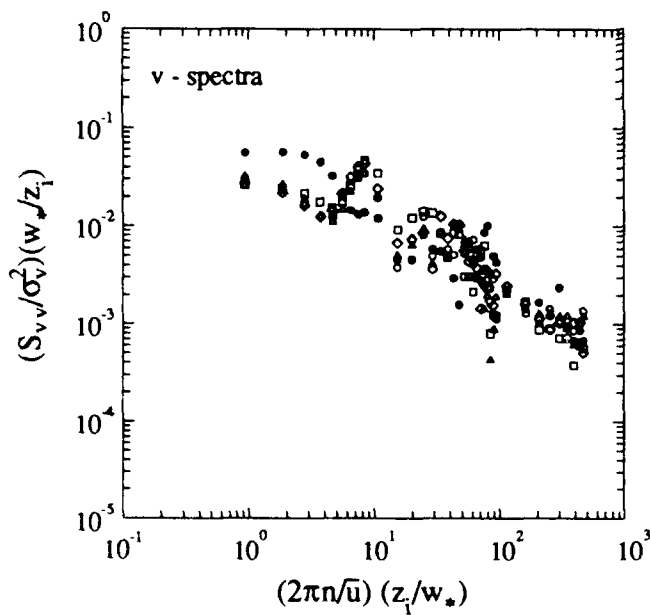


Figure 4.9 (continued) Spectra of the wind data from Camp Atterbury for Test 1109871. The spectra were normalized by the the calculated variance for each data record and the convective time scale for this test.

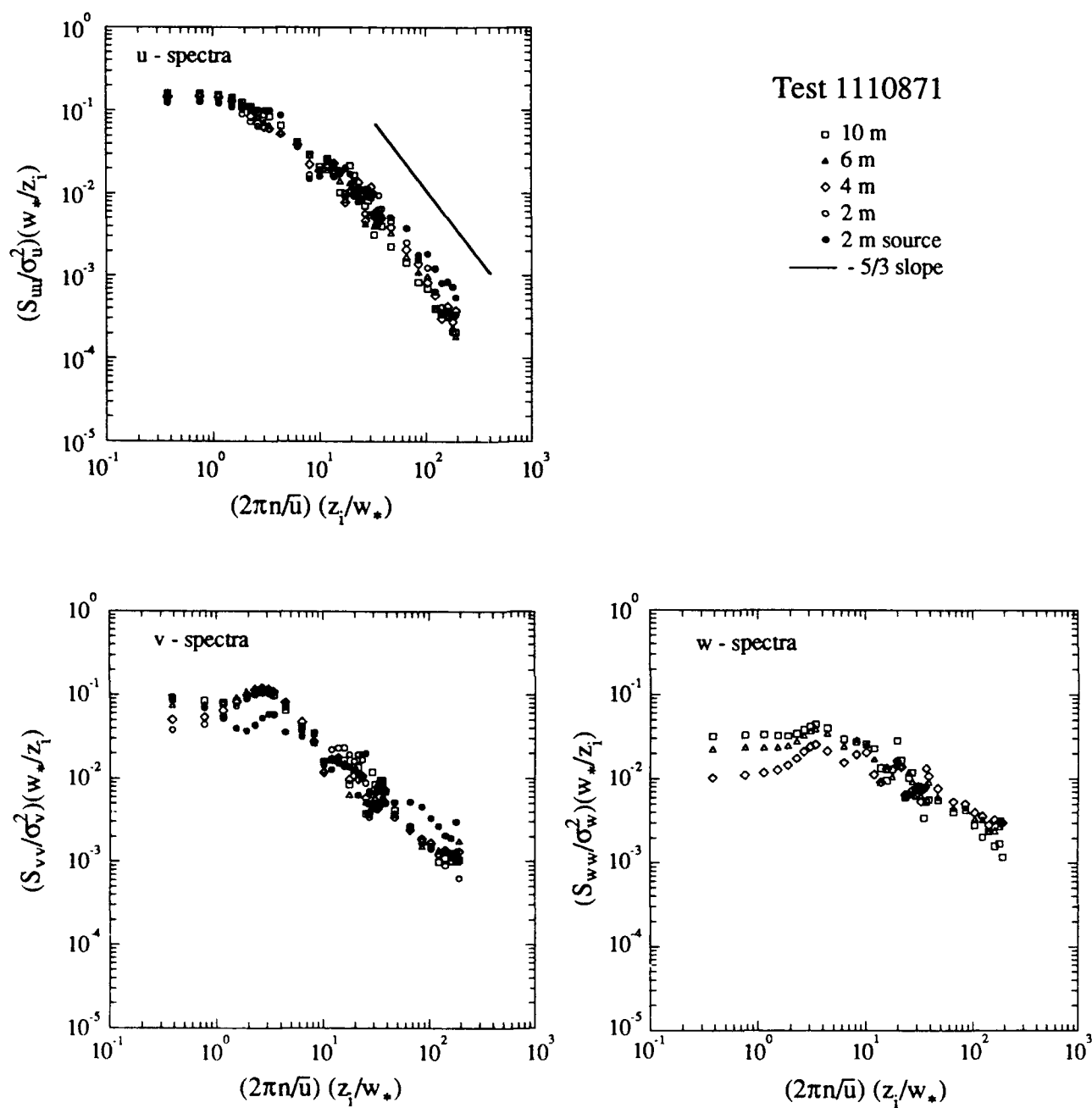


Figure 4.9 (continued) Spectra of the wind data from Camp Atterbury for Test 1110871. The spectra were normalized by the the calculated variance for each data record and the convective time scale for this test.

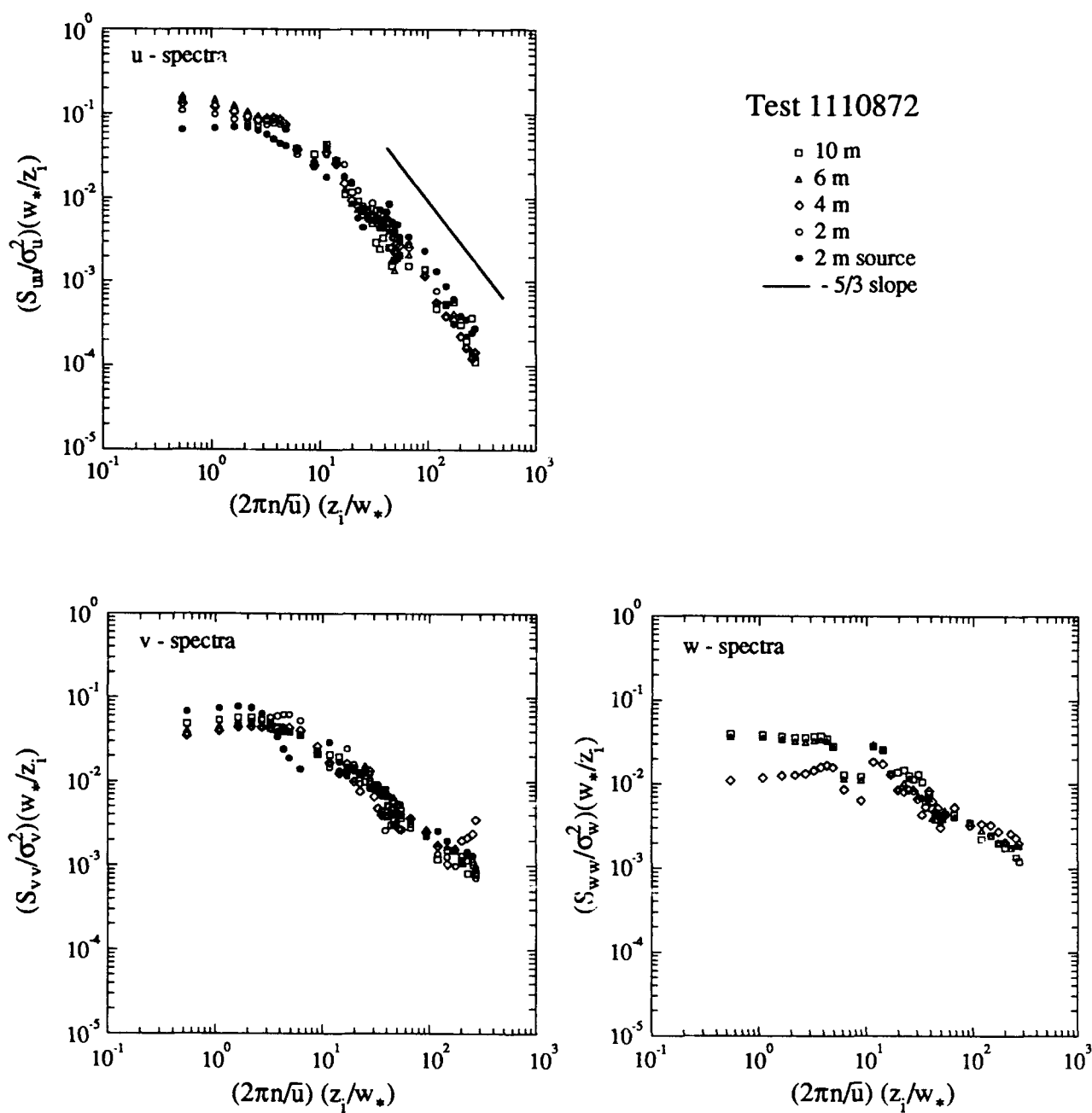


Figure 4.9 (continued) Spectra of the wind data from Camp Atterbury for Test 1110872. The spectra were normalized by the the calculated variance for each data record and the convective time scale for this test.

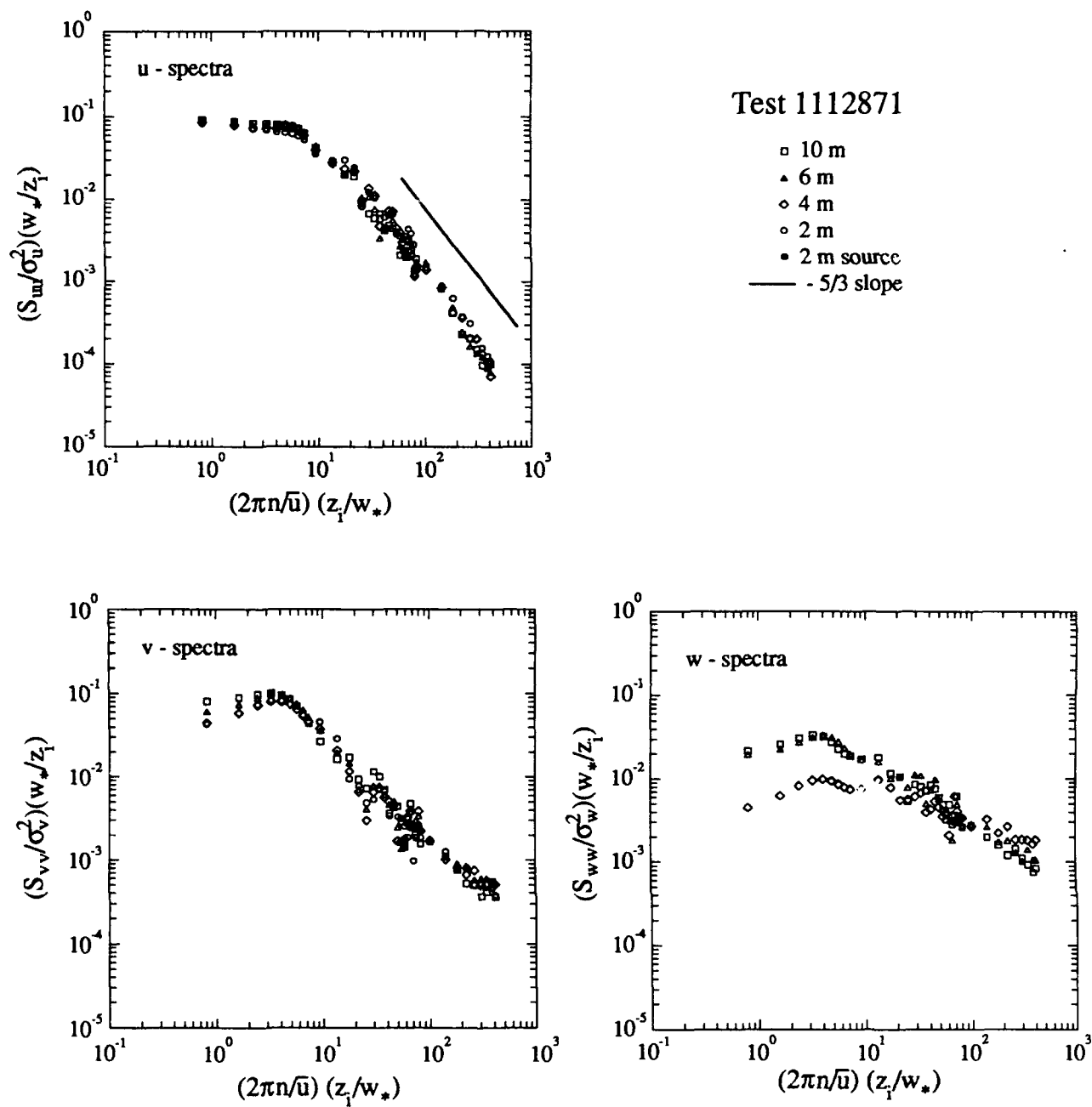
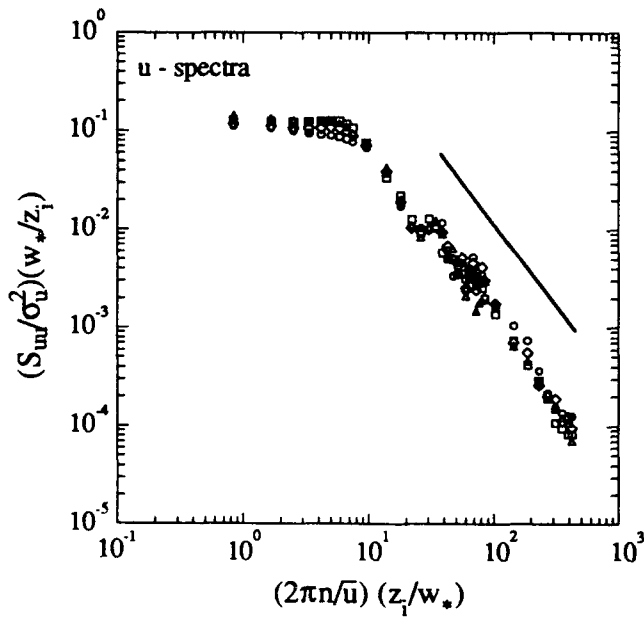


Figure 4.9 (continued) Spectra of the wind data from Camp Atterbury for Test 1112871. The spectra were normalized by the the calculated variance for each data record and the convective time scale for this test.



Test 1113871

- 10 m
- ▲ 6 m
- ◇ 4 m
- 2 m
- 2 m source
- - 5/3 slope

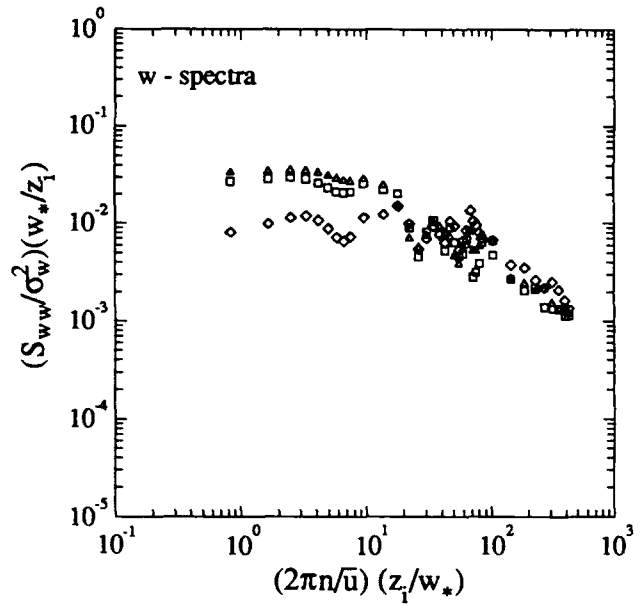
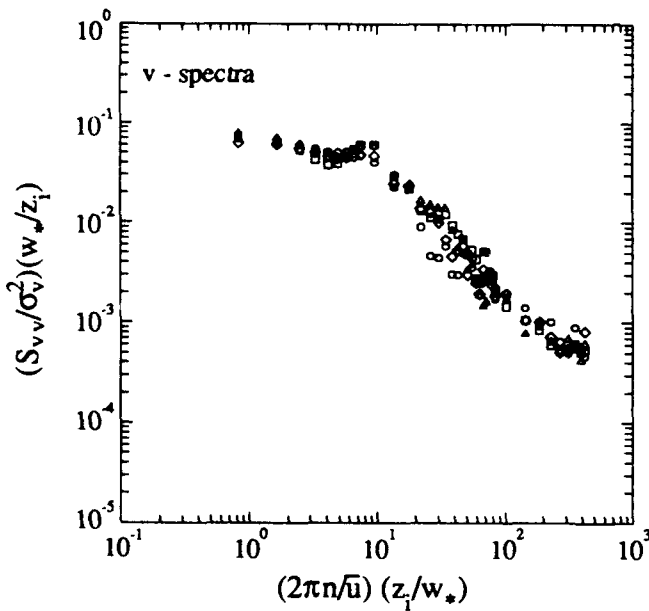


Figure 4.9 (continued) Spectra of the wind data from Camp Atterbury for Test 1113871. The spectra were normalized by the the calculated variance for each data record and the convective time scale for this test.

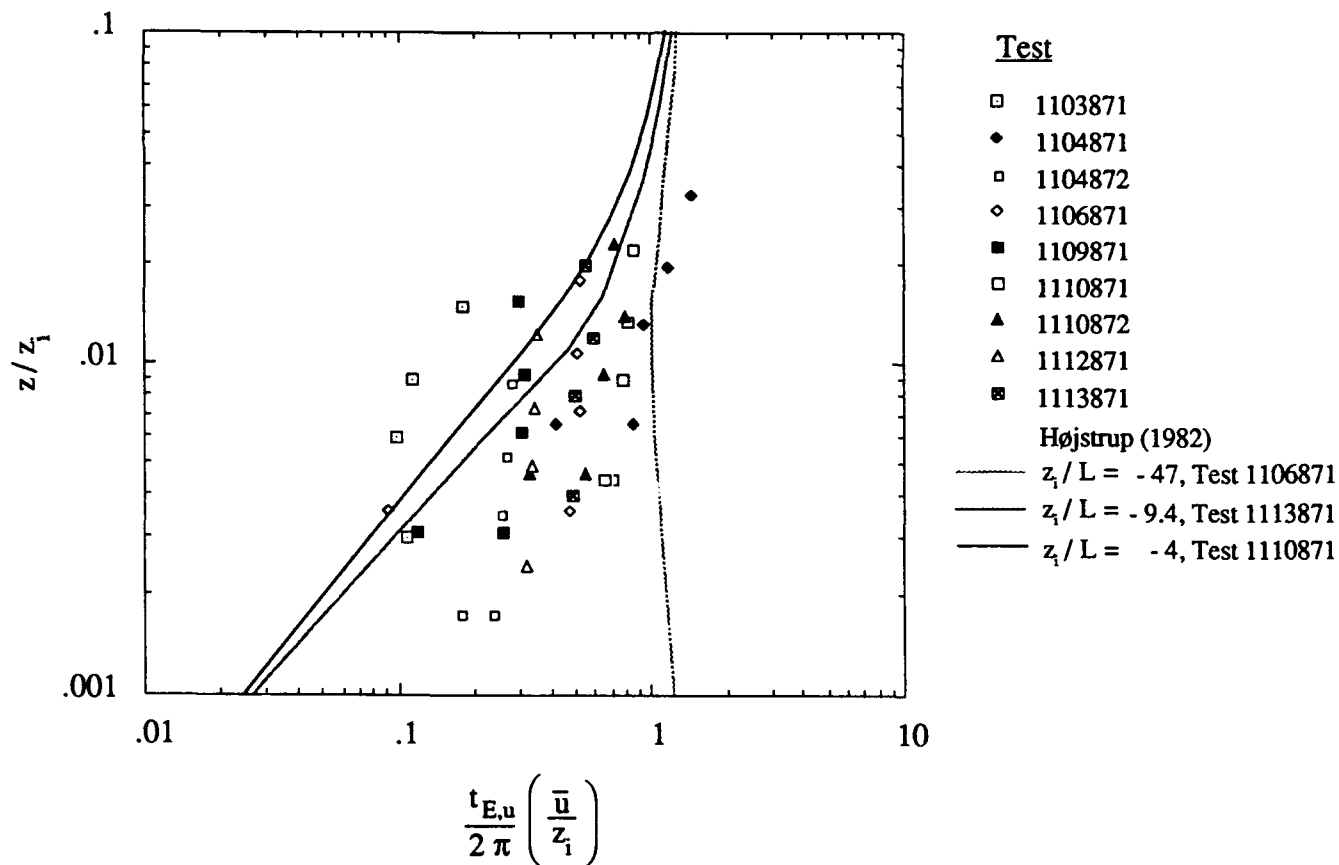


Figure 4.10 Integral scales for the u-velocity component from the Camp Atterbury meteorological data. The model values are from Højstrup (1982), and are plotted using scaling parameters for the most nearly neutral and most unstable tests in our data set along with an intermediate value.



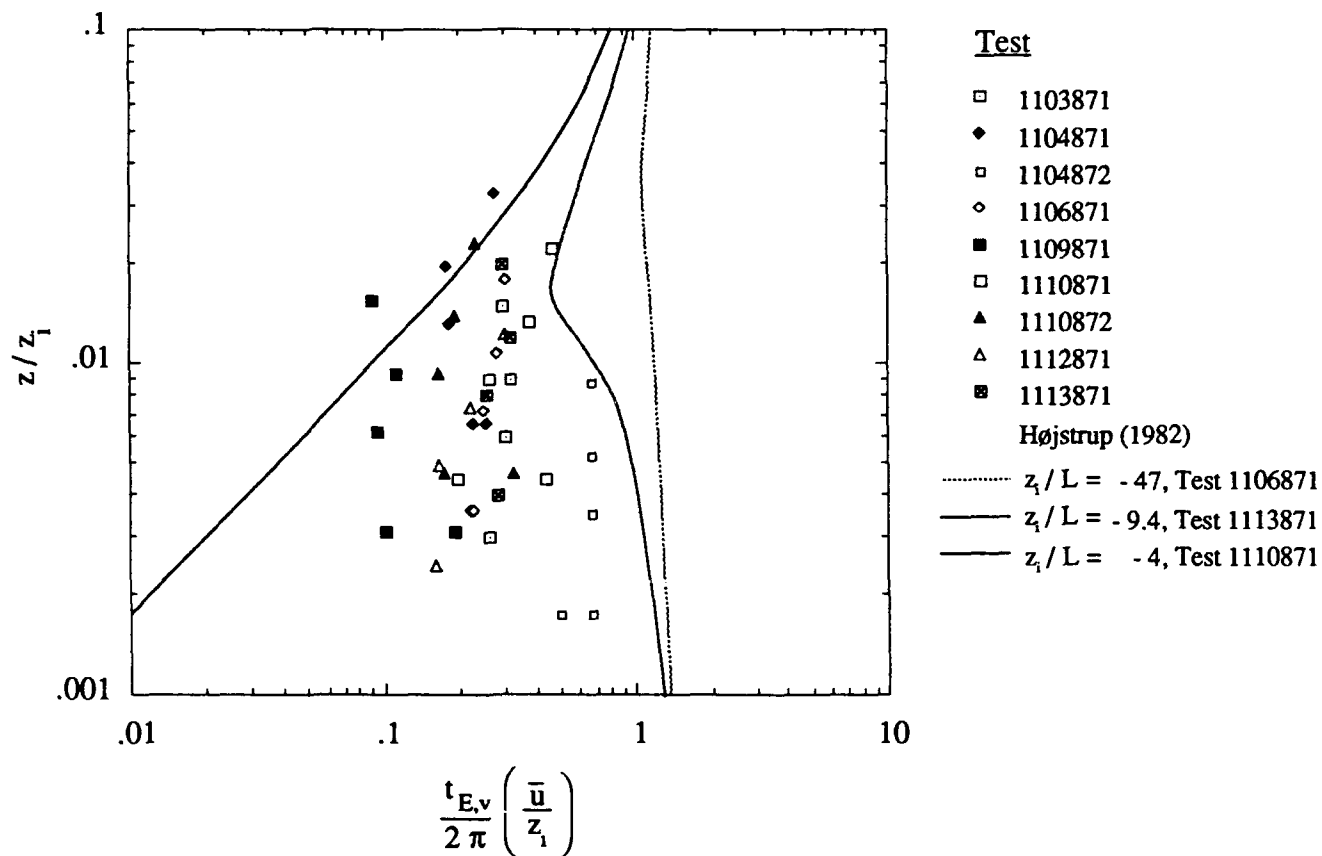


Figure 4.10 (continued) Integral scales for the v-velocity component from the Camp Atterbury meteorological data. The model values are from Højstrup (1982), and are plotted using scaling parameters for the most nearly neutral and most unstable tests in our data set along with an intermediate value.

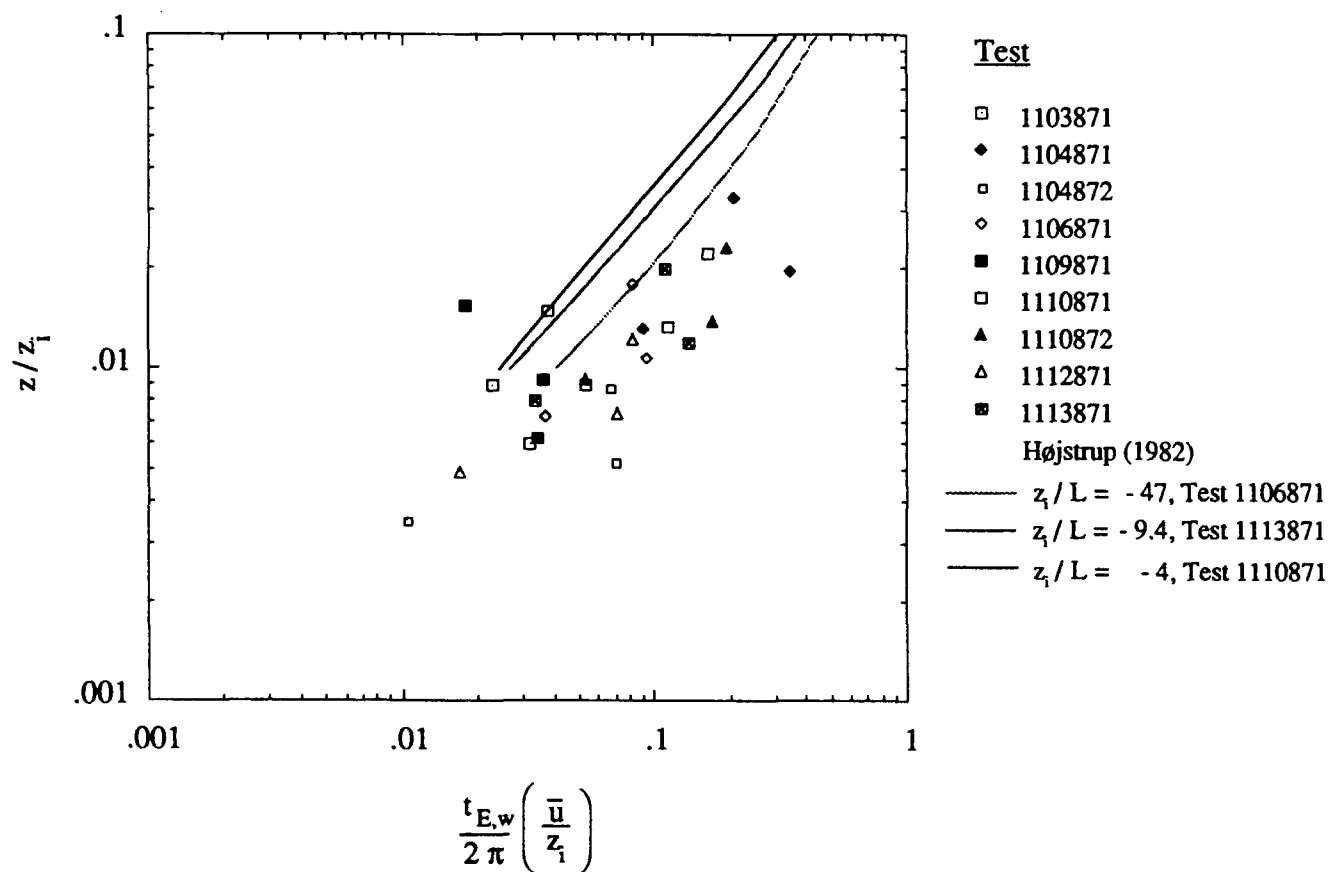


Figure 4.10 (continued) Integral scales for the w-velocity component from the Camp Atterbury Meteorological data. The model values are from Højstrup (1982), and are plotted using scaling parameters for the most nearly neutral and most unstable tests in our data set along with an intermediate value.

neutral tests. Faster response instruments or a taller meteorological tower is needed to more completely resolve the high frequency spectra in the vertical and horizontal directions.

### **Errors in the Scaling Parameters**

In comparing values of  $\sigma_u/u_*$ ,  $\sigma_v/u_*$ ,  $\sigma_u/w_*$ , and  $\sigma_v/w_*$  with model predictions from Højstrup (1982) we find that the error in  $w_*$  and  $u_*$  is  $\pm 25\%$  for a one standard deviation confidence interval. This means our estimates of scaling velocities will be within 25% of the true value 68% of the time. For several inversion height prediction methods similar to the one which we have used, Garrett (1981) has found errors between measured and predicted values of 25%. Based on the sensitivity of  $L$  to changes in  $u_*$ , the error in the Monin-Obukhov length is  $\pm 75\%$ .

## **4.2 The Meadowbrook Site**

The dispersion studies we conducted at the Meadowbrook Site were part of a larger meteorological measurement study conducted by the US Army Atmospheric Sciences Laboratory (ASL) in complex terrain in the foothills of the Sierra Nevada mountains. This detailed study was centered in a forked canyon valley formed from the joining of Payne Creek and Plum Creek about 20 miles east of Red Bluff, California. In addition to our own fog-oil dispersion measurements at the site, dispersion tests were conducted using gaseous tracer by the Air Resources Laboratory of the National Oceanic and Atmospheric Administration (NOAA).

Researchers from Risø National Laboratory in Denmark (RISØ) aerially photographed the smoke plumes, light permitting, over the period of each test at approximately one-minute intervals. Additional photo-documentation was provided by the US Forest Service who video taped the smoke releases from elevated locations during the daytime tests.

The meteorology in this area is dominated by the density driven diurnal upslope-downslope flow characteristic of a mountain-valley system. The site has about a 350-m drop in elevation from east to west over a distance of 10 km. Regionally there is an approximate average east to west drop in elevation of 2000 m in 100 km, from the Sierra Nevada mountain range in the east to the valley of the Sacramento River to the west.

### **4.2.1 Meadowbrook Meteorology**

In a mountain-valley weather system, the surface mesoscale wind flow is dominated by a breeze of cooler, denser air which flows down the mountain slopes into the valleys at night and a flow of warmer, lighter air in the daytime which flows back up the slopes. Upper-level geostrophic flow also influences the surface-level winds. The Boise-Cascade mountain range to

the east of the Sacramento River blocks most of the moist air from the Pacific Ocean causing the local area to be extremely dry. This absence of moisture reinforces wide diurnal temperature swings and the strong gravity driven surface flow.

The meteorology of the Meadowbrook Site is well established, both through the nature of the terrain and through three previous large-scale wind field studies carried out by ASL. Ten surface stations at this site were operated by the Physical Sciences Laboratory at New Mexico State University under contract to ASL. These were designated by A101 through A110 as shown in the map of Figure 4.11. The surface stations operated continuously over the two-week testing period, and data were recorded as 1-min average measurements. Four additional surface stations, designated A111 through A114 were operated by NOAA during the dispersion test periods. Data at these surface stations were recorded at a 1-Hz sampling rate. Measurements at all of the surface stations included the wind speed, direction and standard deviation at a 10-m height with a sampling rate of once per minute using a wind vane. The temperature at heights of 10 m and 2 m was also measured on the ASL surface stations with the exception of A103 and A104, which only recorded the 10-m temperature. A micrometeorological tower with instrumentation at heights of 2, 4, 8, 16 and 30 m was located near the center of the test site for the characterization of the behavior of the boundary layer with height. The instruments on this tower included u,v,w propeller anemometers, cup anemometers, and temperature sensors.

Two sonic anemometers at a 7-m height were operated by RISØ. One of these was operated over the duration of the daytime dispersion tests, while the other was continuously operated over the entire two week testing period. Data from these instruments were sampled at a 20-Hz rate. These fast response data are used in determining the covariant fluxes: friction velocity  $u_* = \tau_{zx}/\rho =$

$\overline{u_x' u_z'}$  and heat flux  $Q_0 = H/C_p \rho = \overline{(\theta' u_z')} u_*$ . With  $Q_0$  and  $u_*$ , a direct estimate of the Monin - Obhukhov length  $L = u_*^3 T / (k g Q_0)$  can be made.

A topographical map of the test site with the specified location of the meteorological towers and our source and sampler locations is shown in Figure 4.11. In our sampling of the fog-oil smoke, the large area of the site and the two opposing wind directions necessitated our dividing the sampling equipment between two grids and two source locations, one for stable, downslope night-time tests, and another for the unstable, daytime upslope dispersion tests. These grids are shown in the topographical map. Vegetation types and heights varied over the test site. A map showing the distribution of vegetation is given in Figure 4.12, and a map of the vegetation heights is shown in Figure 4.13. These maps were created from data supplied by ASL.

The smoke source for the daytime test was located near 4462500N (m), 585500E (m) in UTM coordinates as shown on the topographical map. The predominant wind is from west to east. Samplers were operated at up to 250 m from the source for the daytime unstable tests in three

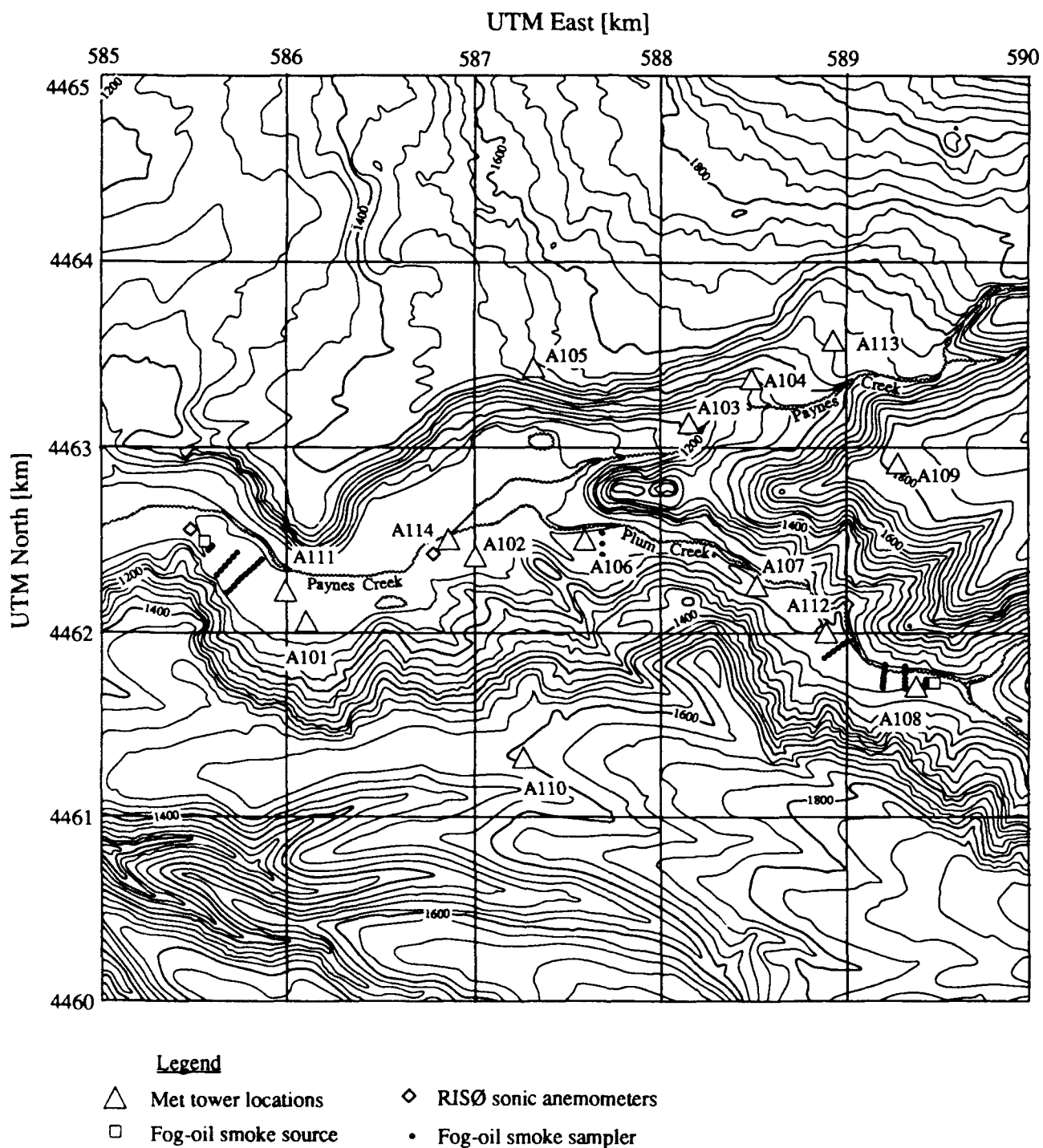


Figure 4.11 Topographical map of the Meadowbrook dispersion site. Elevations are in ft above sea level with contour lines at increments of 40 ft. The horizontal scale is in Universal Transverse Mercator coordinates, with the grid marked in km. The topographical information is from a USGS map of Inskip Hill, California.

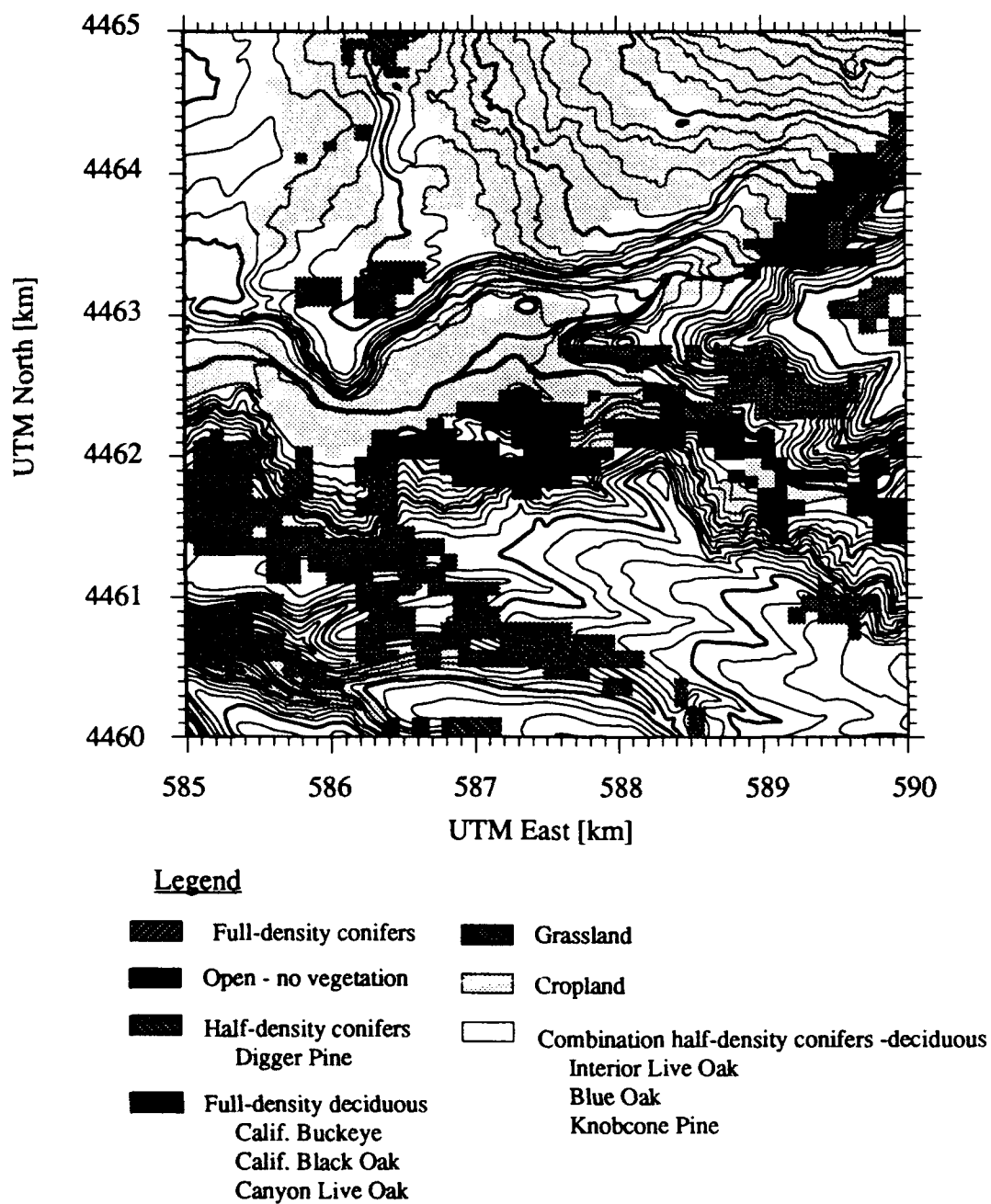


Figure 4.12 Vegetation types for the Meadowbrook test site. The information is from an ASL survey of the vegetation at the site averaged over 100-m square increments.

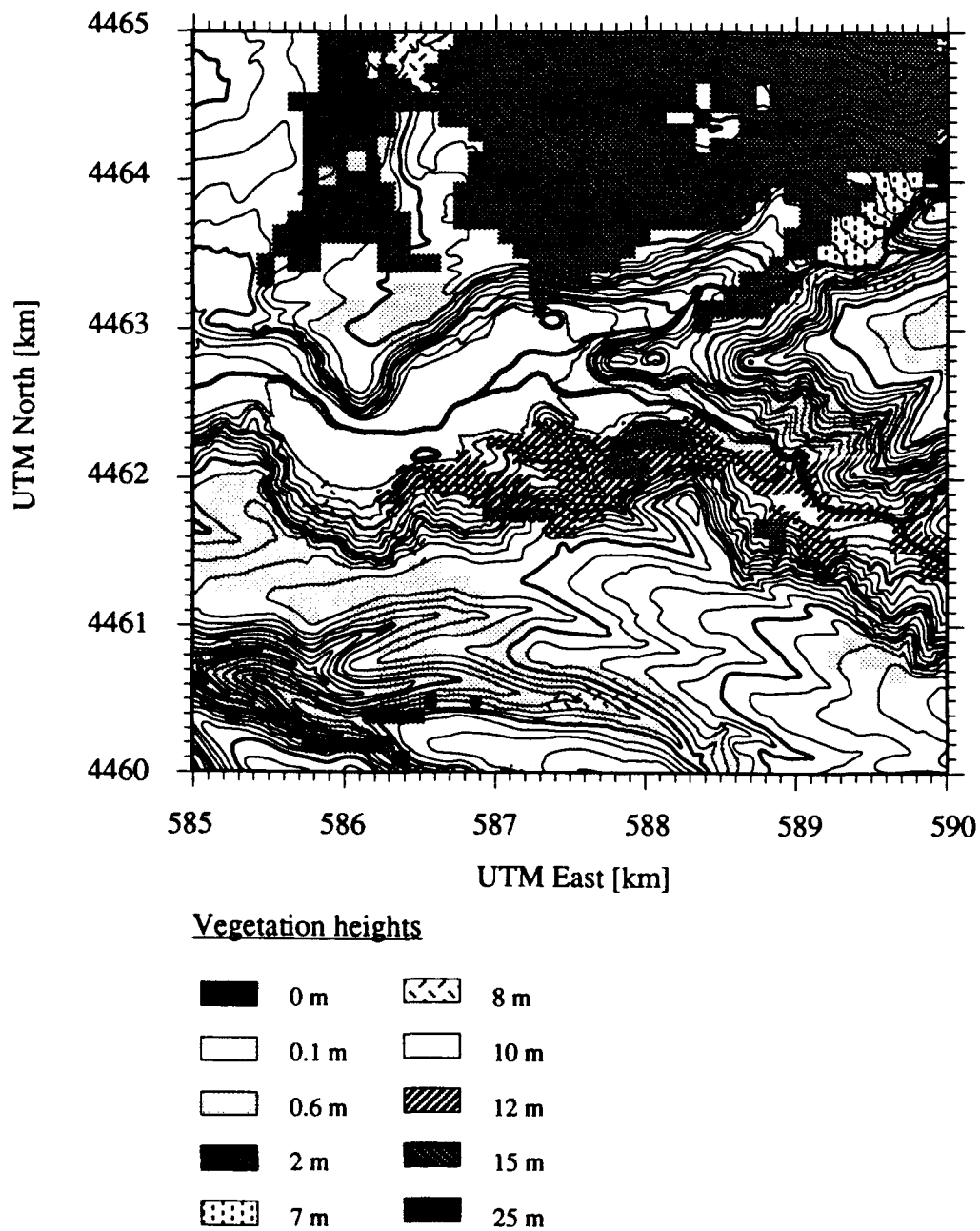


Figure 4.13 Vegetation heights for the Meadowbrook test site. The information is from an ASL survey of the average vegetation over the test site in 100-m square increments.

transects. The high dilution rate of the smoke prevented its measurement at greater distances. A straightforward analysis of the daytime data is possible because of the limited dispersion distance, the highly convective conditions, and the locally homogeneous terrain.

For the nighttime tests in stable atmospheric conditions, the smoke source was located near 4461750N, 589500E in the Plum Creek valley. The nighttime wind followed the downward gradient of this valley. Five rows of samplers were used out to a distance of 2 km at geometrically increasing distances from the source. In a fraction of the tests, a row of samplers used in the daytime dispersion grid were operated. Results from these samplers showed detection of the smoke at a distance of 3 km from the source. A stable source for the upwind Payne Creek valley was not used because of the presence of a trout hatchery in this area.

For the 10 surface stations which were operated over the entire duration of the testing period, we have records of wind direction and velocity as shown in Figure 4.14 and 4.15. A rapid wind direction change at dawn and again at dusk is seen for the plots of Figure 4.14. Nighttime wind directions measured at each surface station are very similar throughout both the long-term test period and during each individual night for those surface stations located within a valley. Slightly more variation in direction is seen in the daytime periods. In Figure 4.15 the magnitude of wind velocity, for the majority of cases, shows two peaks in a diurnal cycle, one corresponding to the daytime winds and another to the nighttime winds. Like the wind direction, this is more consistent for the surface stations located within the bounds of the creek valleys. A record of the temperature is shown in Figure 4.16. This shows both a wide diurnal variation in temperature and a longer term mesoscale trend. The magnitude of temperature change is greater for those sensors in the valleys near the creeks, which become cooler at night than the sensors located on the ridges. This spatial temperature gradient and the associated density stratification drives the mountain-valley winds seen at the test site.

#### **4.2.2 Meadowbrook Tests under Unstable Meteorological Conditions**

##### **Surface Layer Scaling**

It is most convenient to divide the discussion of tests at Meadowbrook into daytime unstable cases and nighttime stable cases. For investigating the behavior of the average wind field in the daytime, vector maps of the wind measured at a 10-m height on the meteorological towers are shown in Figure 4.17. Maps of the spatial variation of the bulk Richardson number  $Ri_B$  at these meteorological towers follow these wind maps in Figure 4.18. This bulk Richardson number is defined as  $Ri_B = gz\Delta T/(\bar{u}^2)$  where  $T$  and  $\bar{u}$  are taken at the 10-m height and  $\Delta T = T_{10m} - T_{2m}$ .

In these maps, we see that the wind speed, direction, and horizontal standard deviation is fairly consistent over the entire test area in most cases, except for the test of 0928871 which was



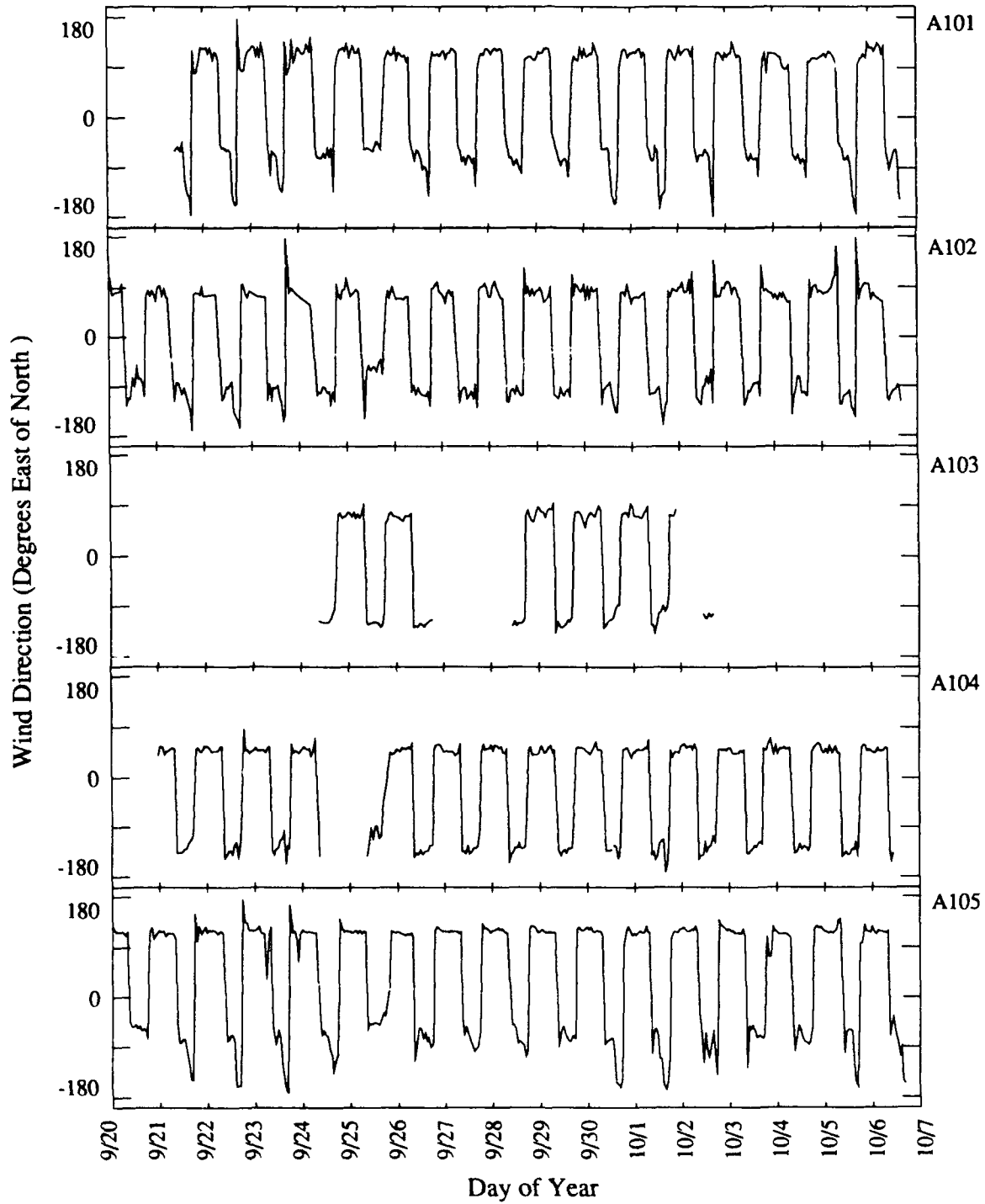


Figure 4.14 Long term records of wind direction for the Meadowbrook meteorological towers. The day axis is marked at midnight.

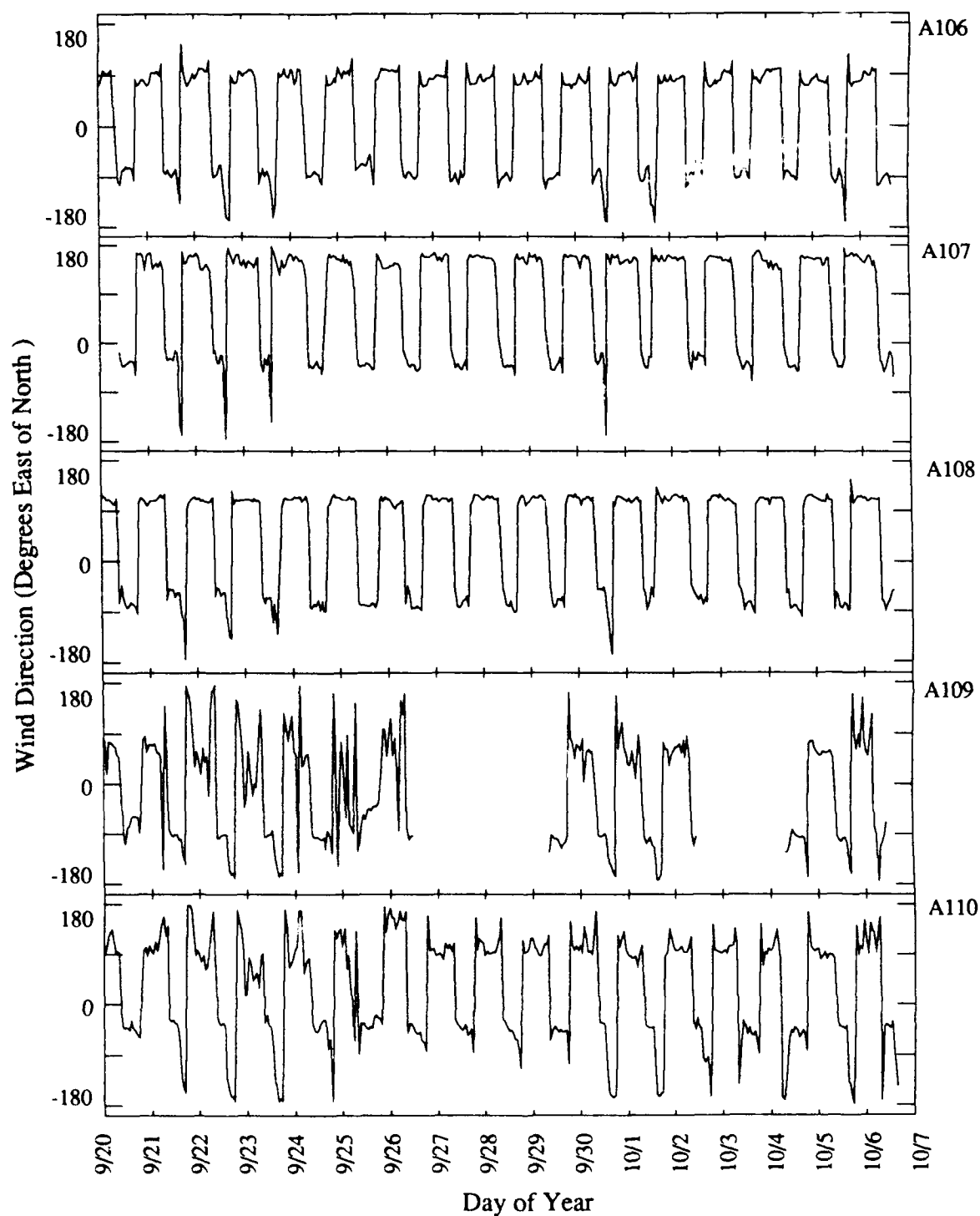


Figure 4.14 (continued) Long term records of wind direction for the Meadowbrook meteorological towers. The day axis is marked at midnight.

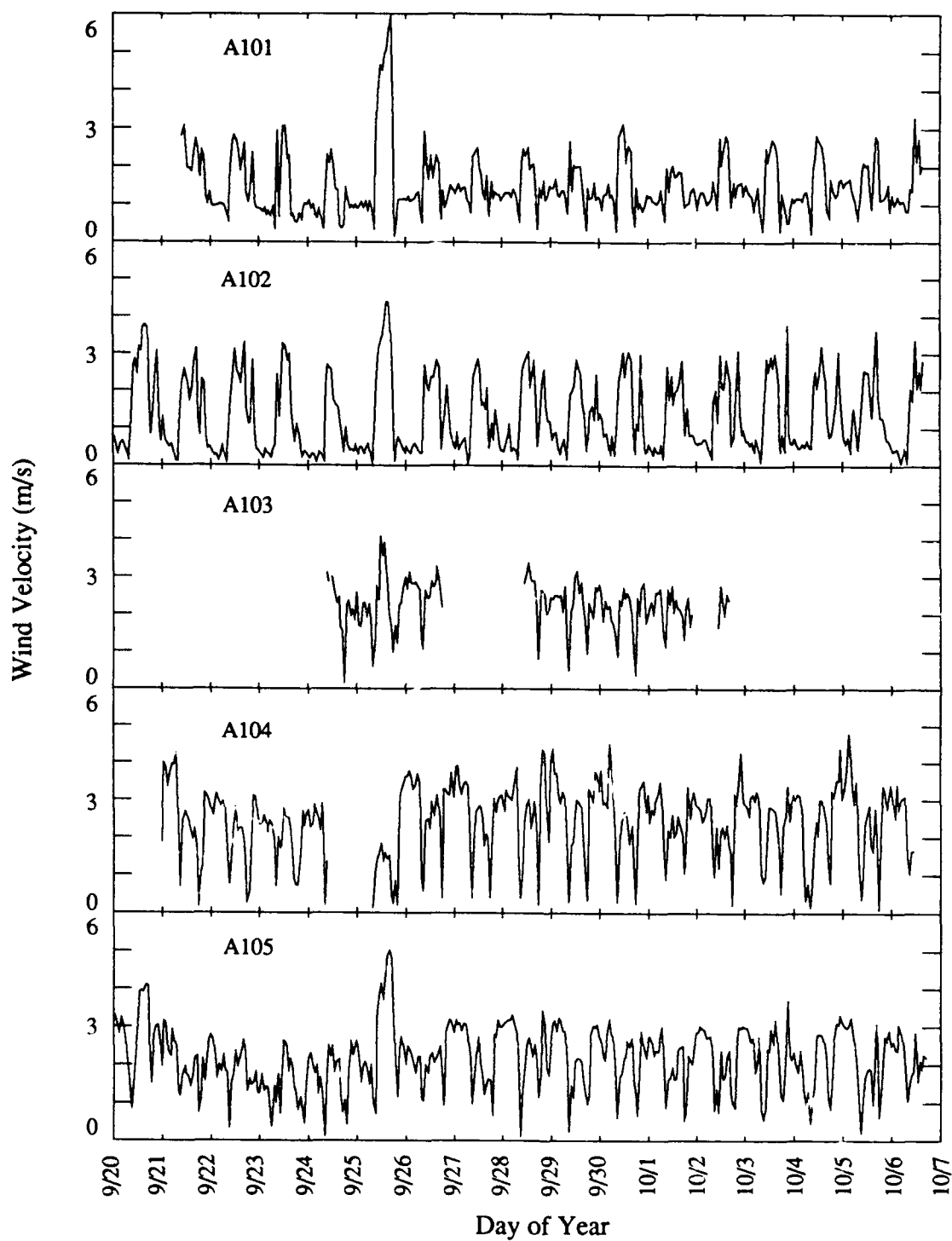


Figure 4.15 Long term wind velocity records for the Meadowbrook meteorological towers. The day axis is marked at midnight.

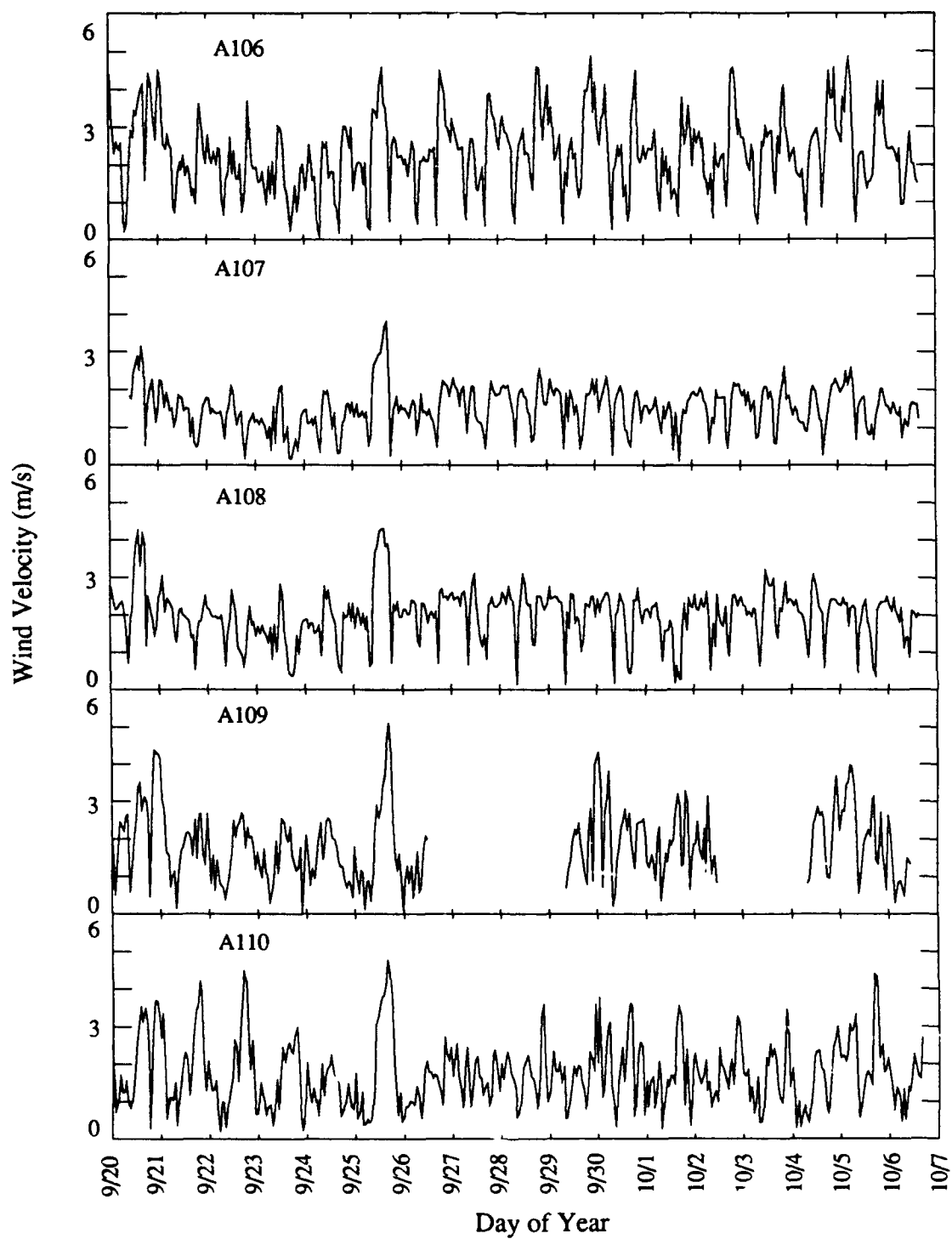


Figure 4.15 (continued) Long term wind velocity records for the Meadowbrook meteorological towers. The day axis is marked at midnight.

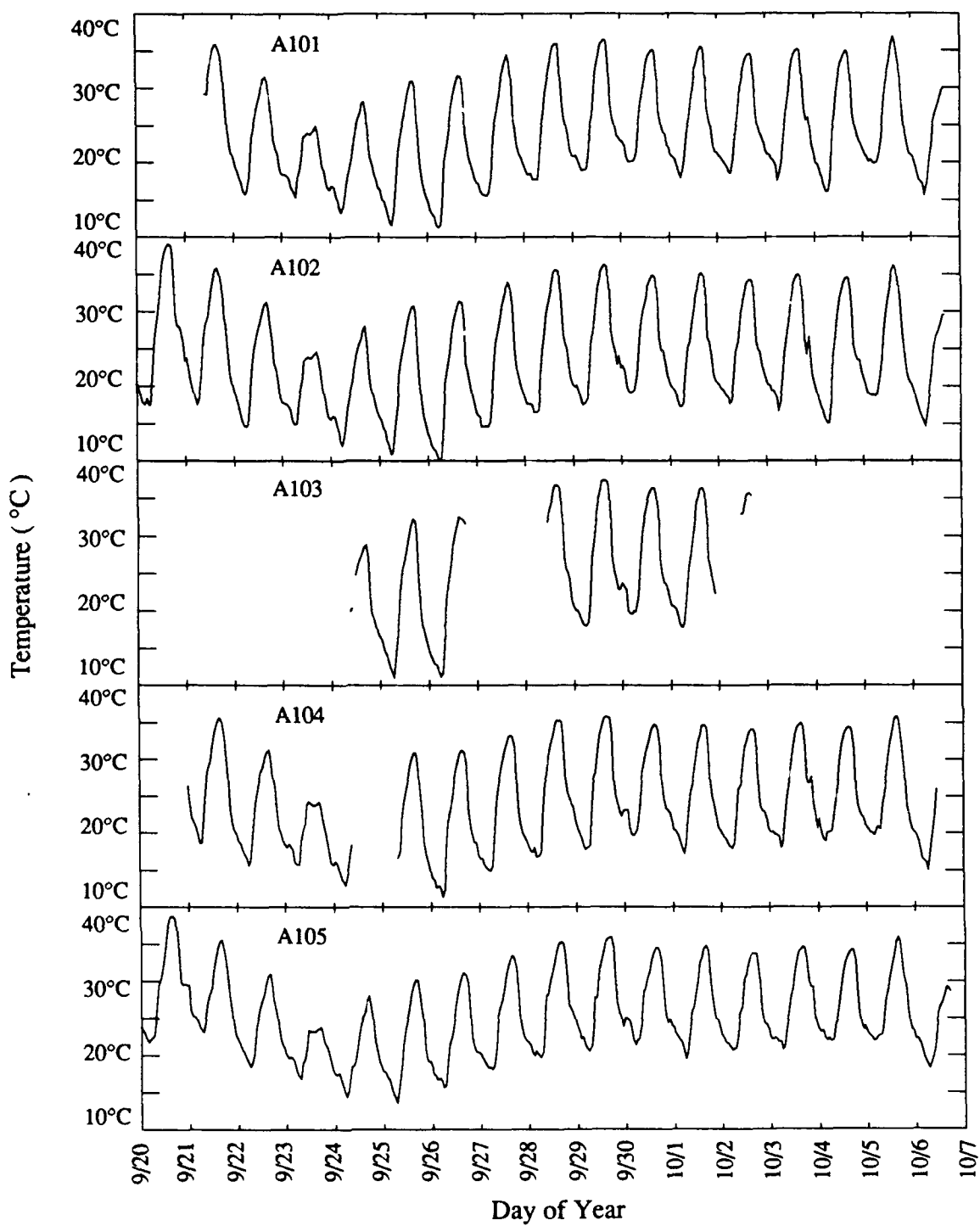


Figure 4.16 Long term temperature records for the Meadowbrook meteorological towers. The day axis is marked at midnight.

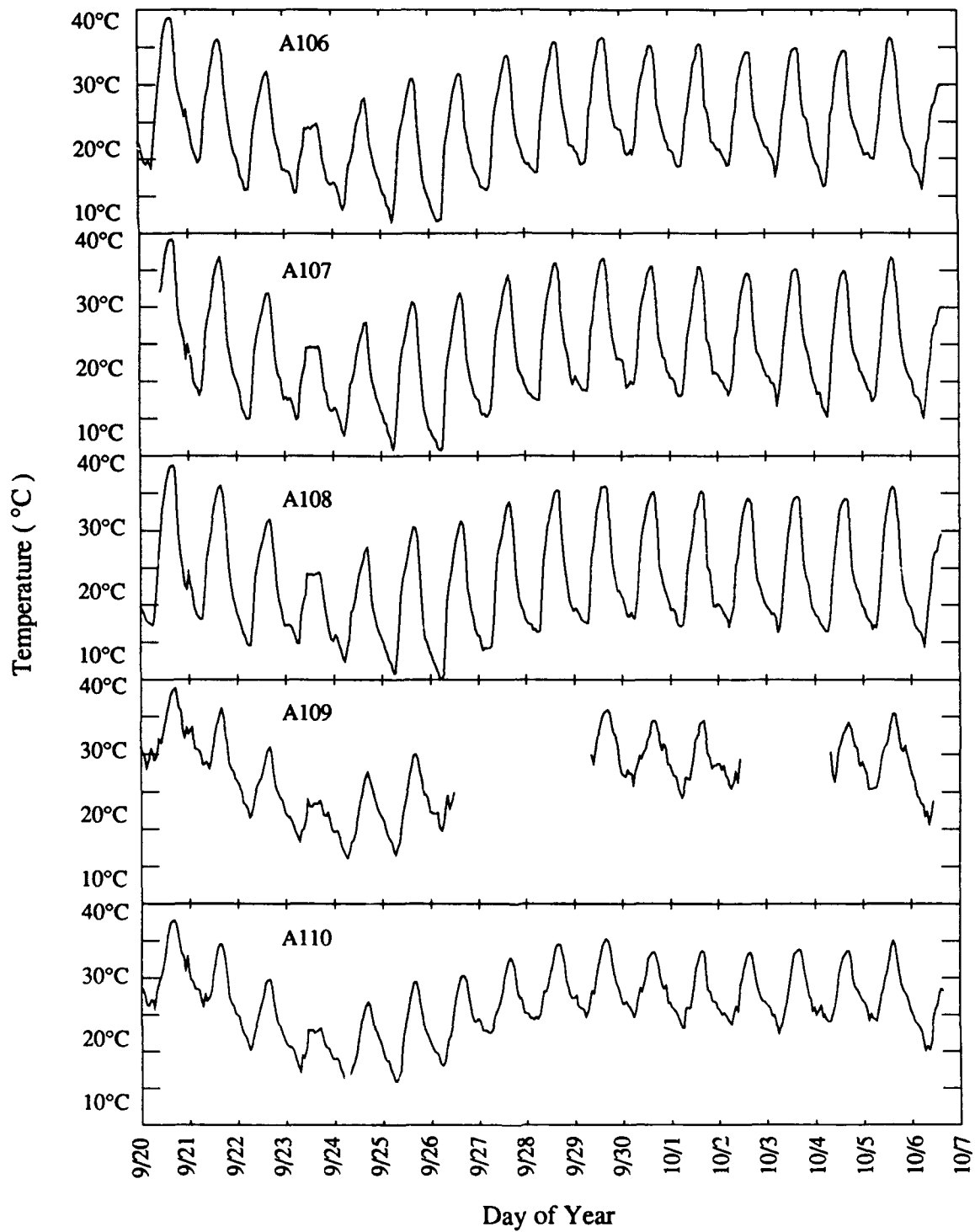


Figure 4.16 (continued) Long term temperature records for the Meadowbrook meteorological towers. The day axis is marked at midnight.

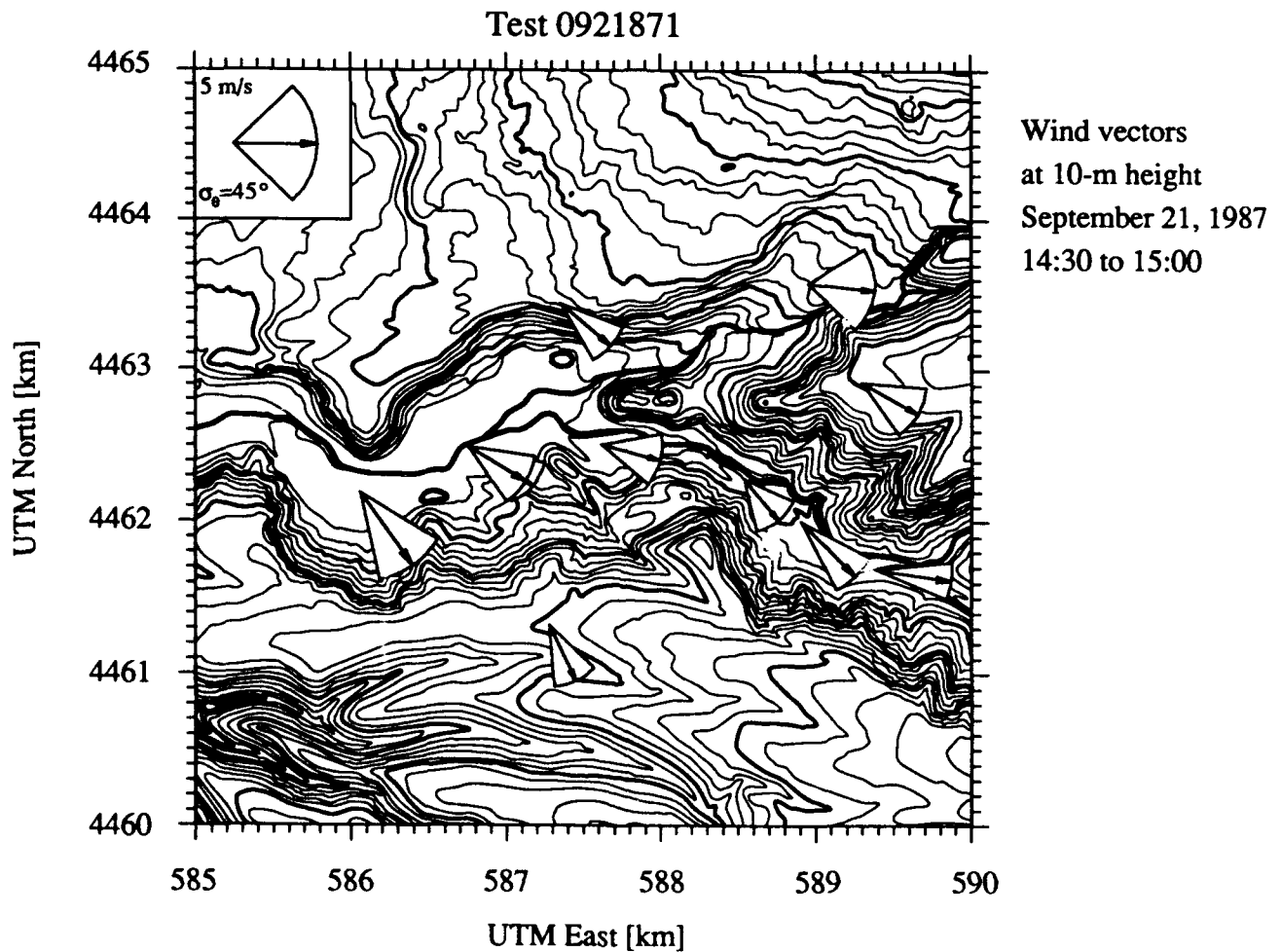


Figure 4.17 Wind vector map for Test 0921871. These data are from the 10-m surface stations. The amplitude of the vector is scaled by its length and the standard deviation in wind direction is given by the half width of the indicated arc.

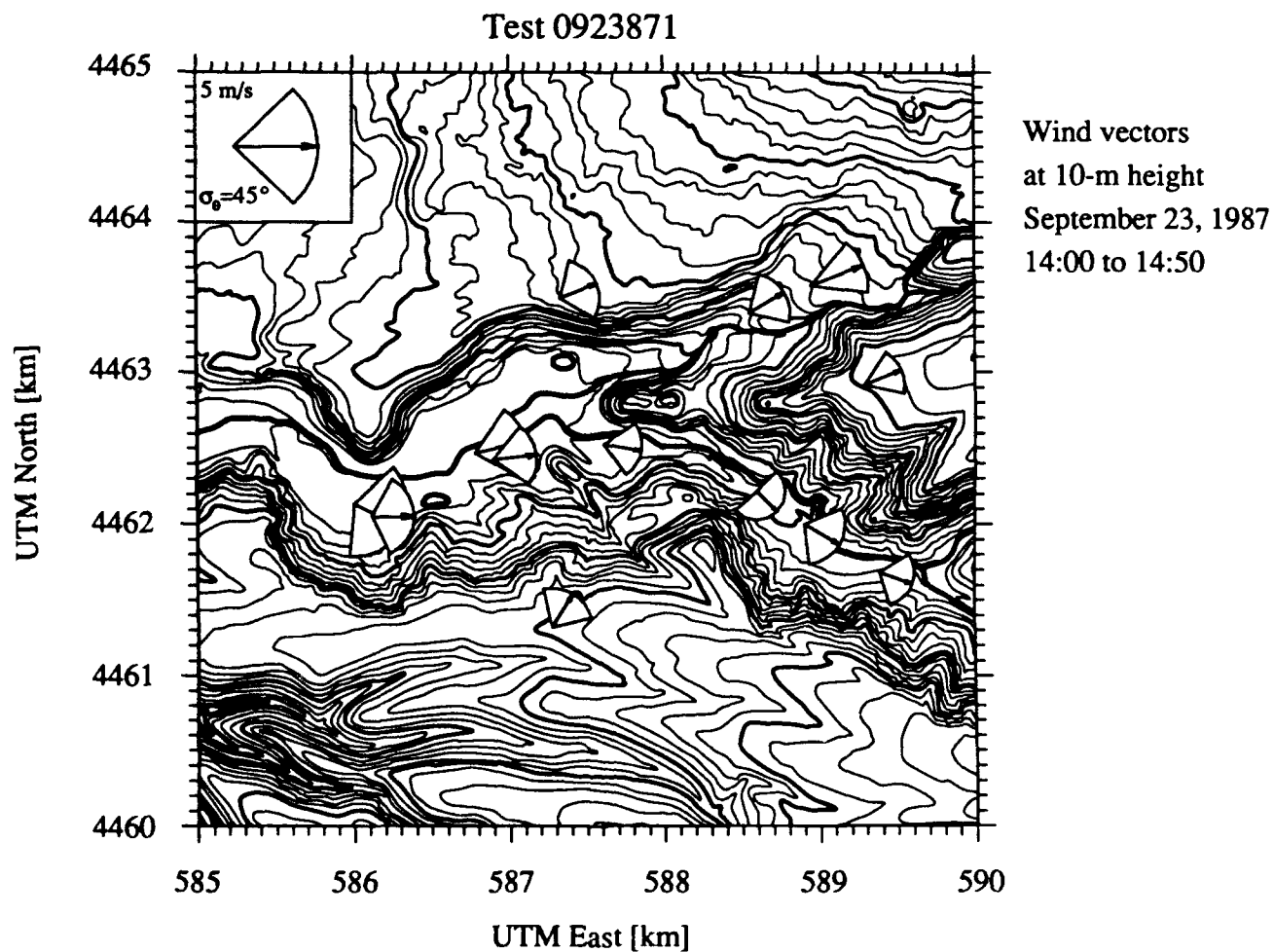


Figure 4.17 (continued) Wind vector map for Test 0923871. These data are from the 10-m surface stations. The amplitude of the vector is scaled by its length and the standard deviation in wind direction is given by the half width of the indicated arc.



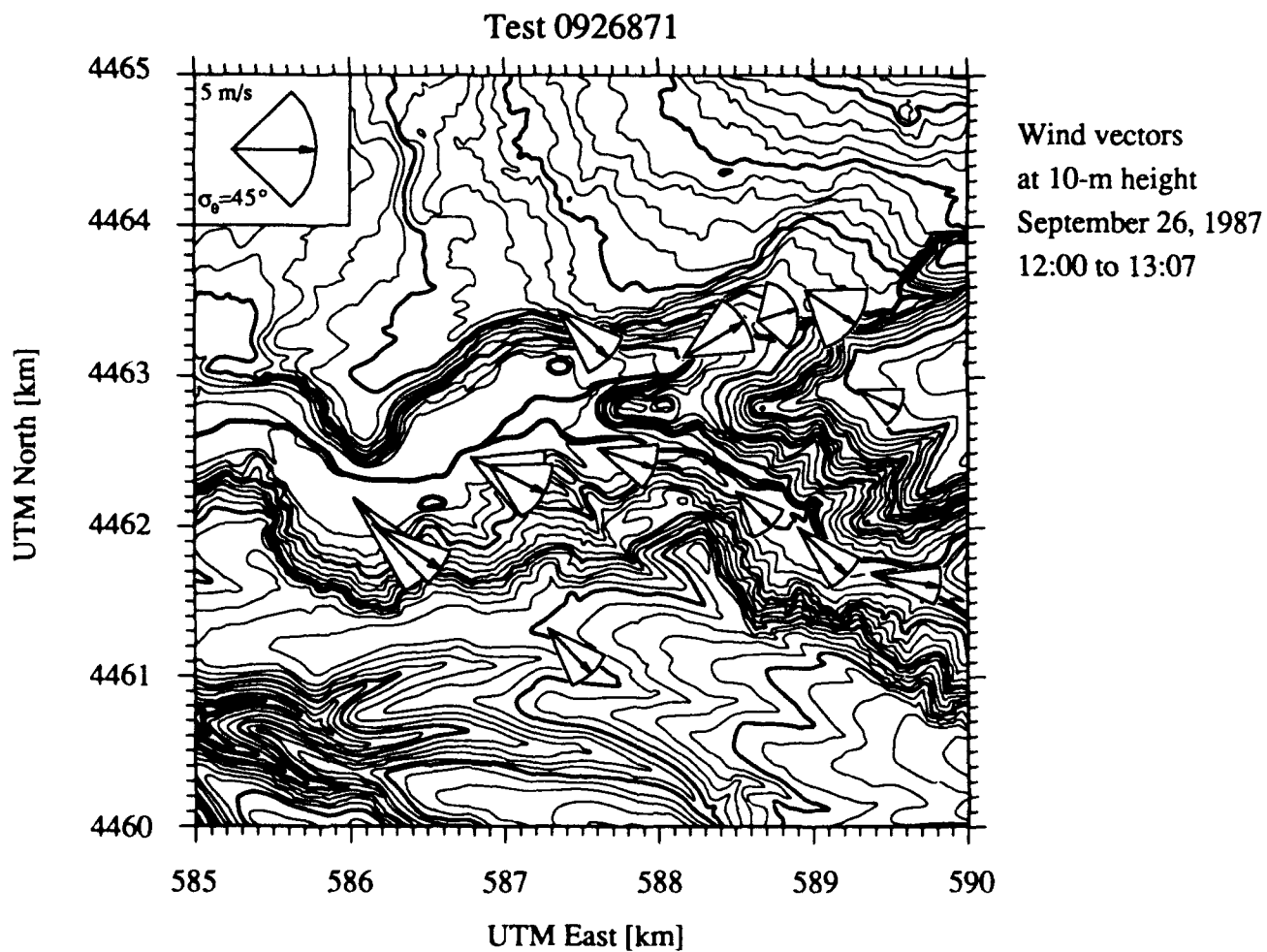


Figure 4.17 (continued) Wind vector map for Test 0926871. These data are from the 10-m surface stations. The amplitude of the vector is scaled by its length and the standard deviation in wind direction is given by the half width of the indicated arc.

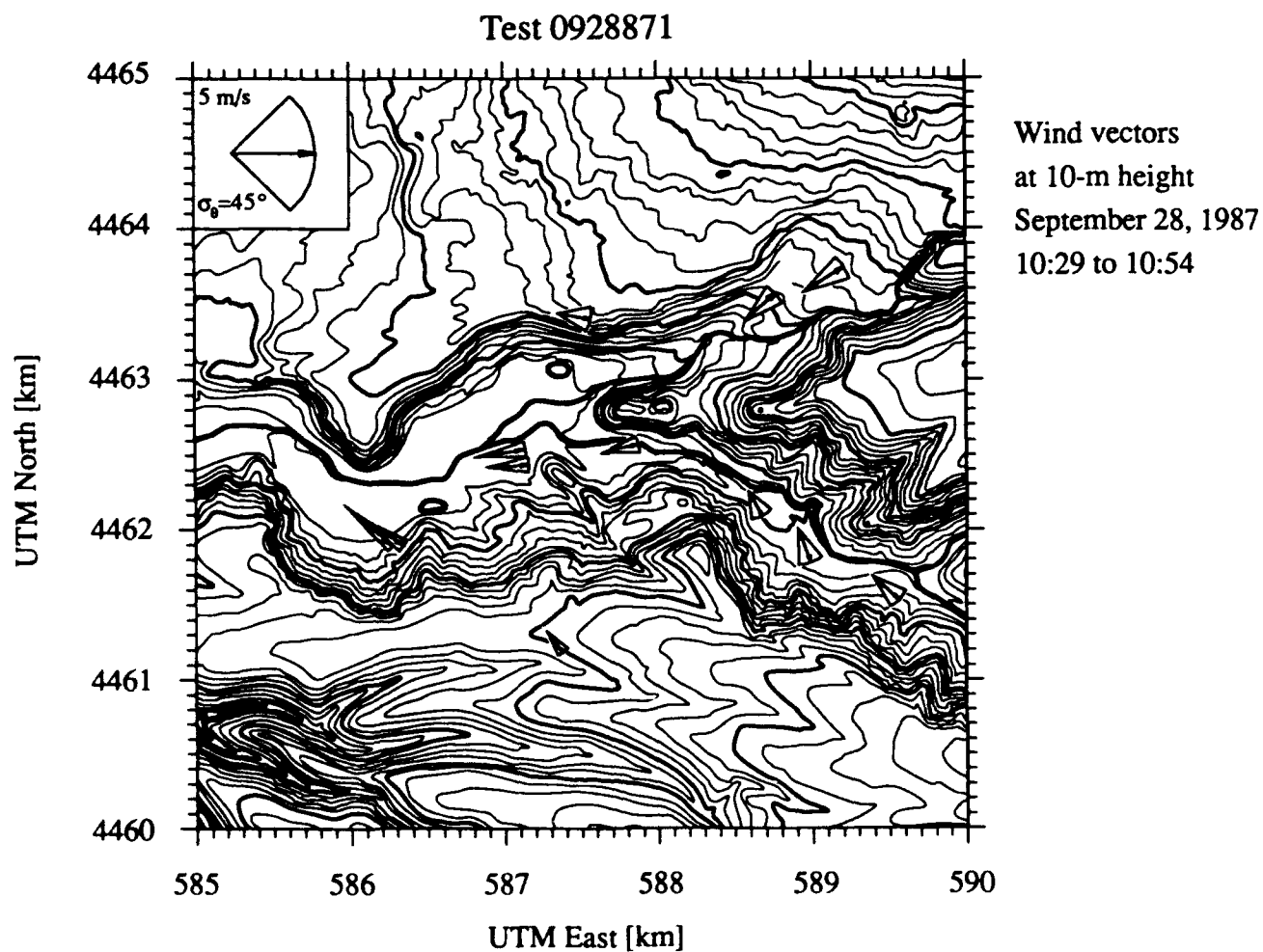


Figure 4.17 (continued) Wind vector map for Test 0928871. These data are from the 10-m surface stations. The amplitude of the vector is scaled by its length and the standard deviation in wind direction is given by the half width of the indicated arc.

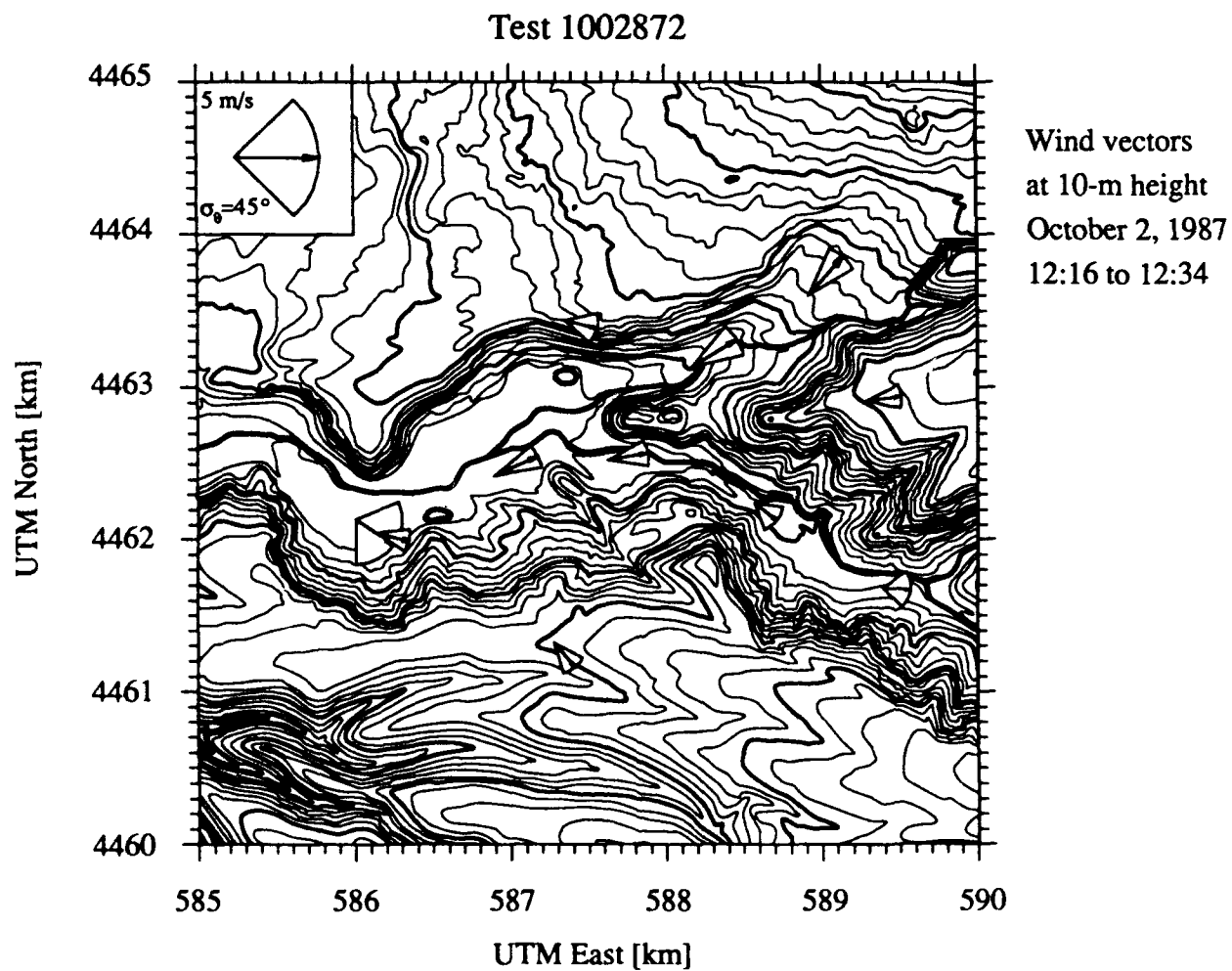


Figure 4.17 (continued) Wind vector map for Test 1002872. These data are from the 10-m surface stations. The amplitude of the vector is scaled by its length and the standard deviation in wind direction is given by the half width of the indicated arc.

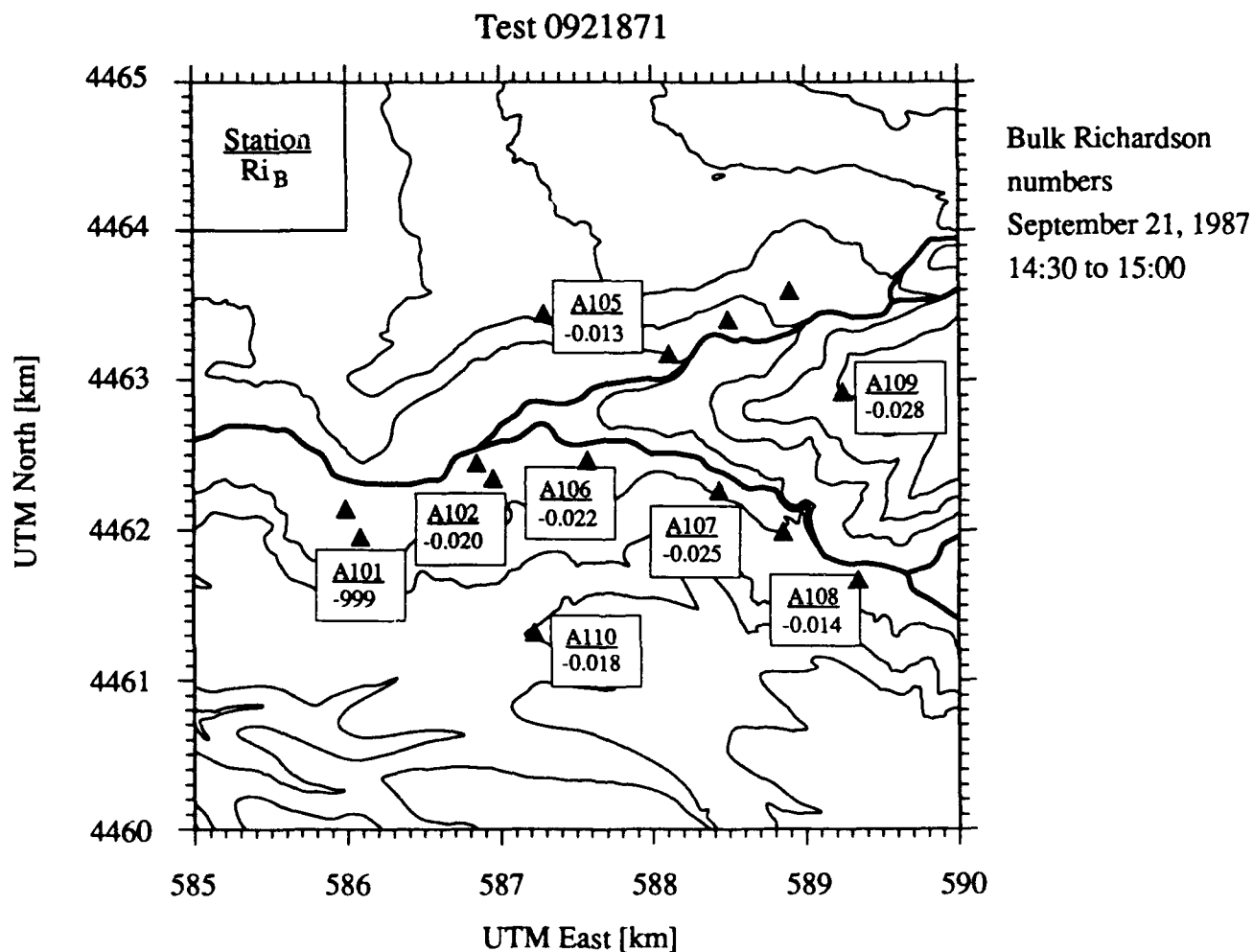


Figure 4.18 Distribution of the bulk Richardson number over the testing site for Test 0921871. These data are available for the 10-m surface stations which recorded temperature at both the 2-m and 8-m heights. A value of -999 indicates a surface station was not operational during this test.

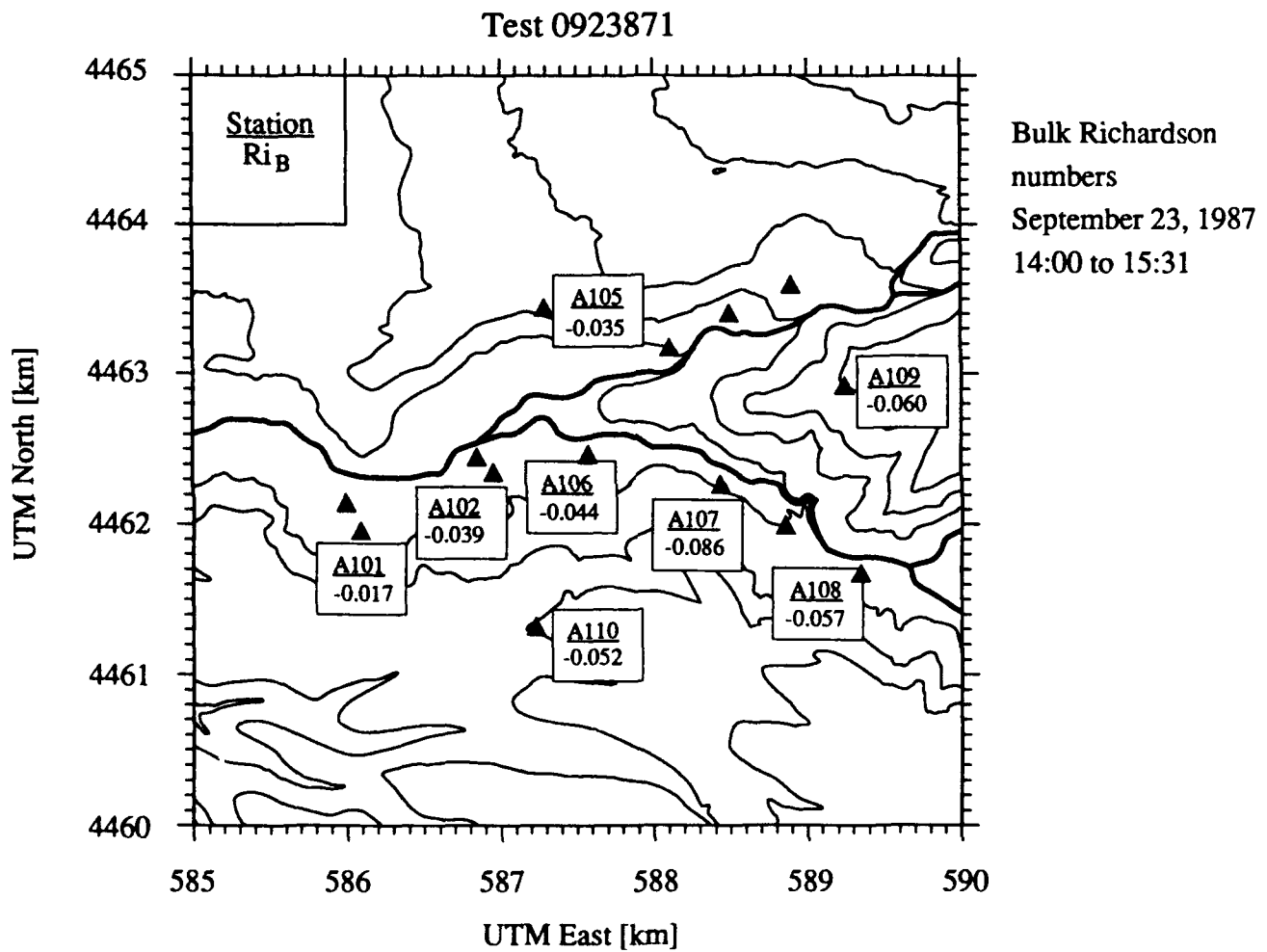


Figure 4.18 (continued) Distribution of the bulk Richardson number over the testing site for Test 0923871. These data are available for the 10-m surface stations which recorded temperature at both the 2-m and 8-m heights. A value of -999 indicates a surface station was not operational during this test.

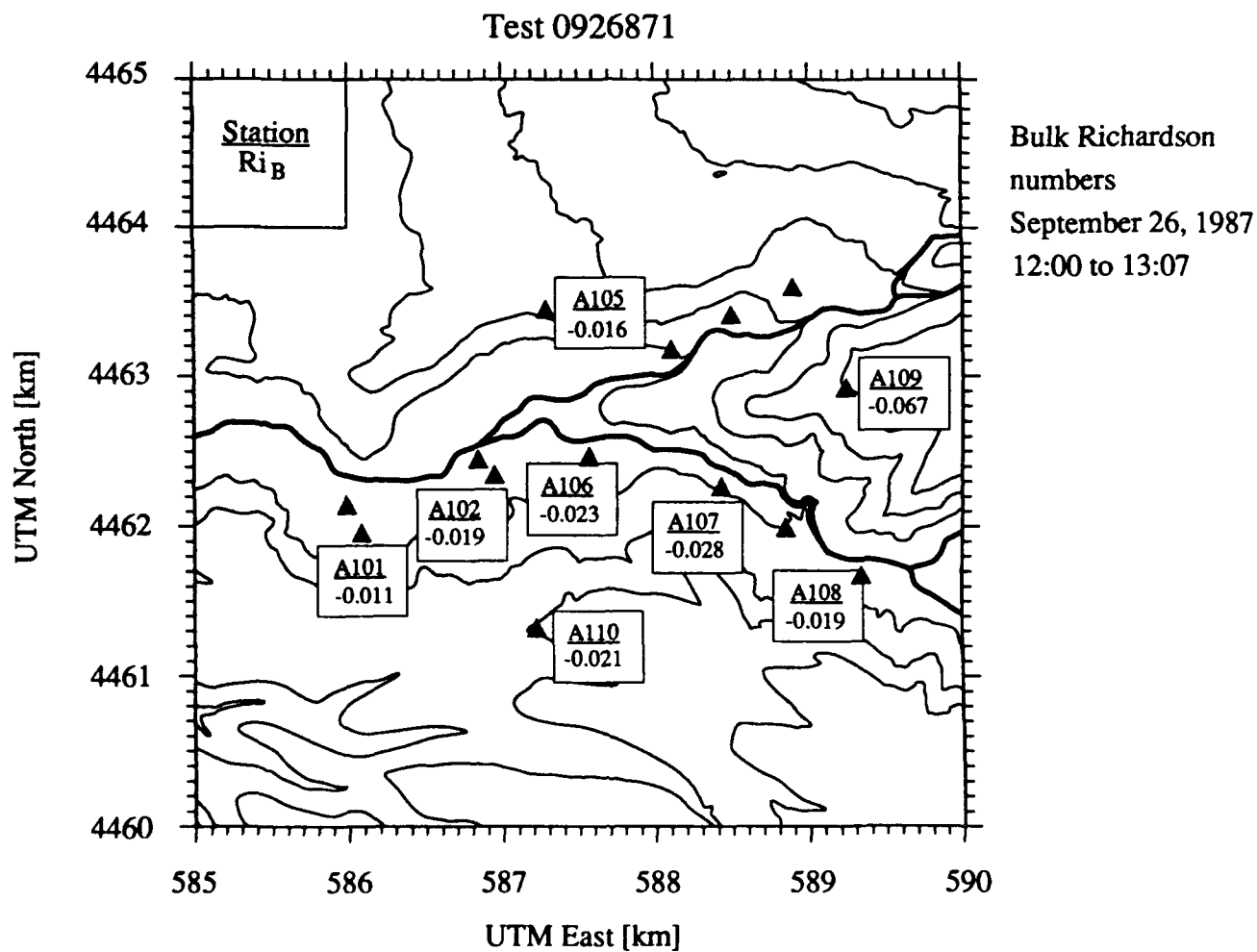


Figure 4.18 (continued) Distribution of the bulk Richardson number over the testing site for Test 0926871. These data are available for the 10-m surface stations which recorded temperature at both the 2-m and 8-m heights. A value of -999 indicates a surface station was not operational during this test.

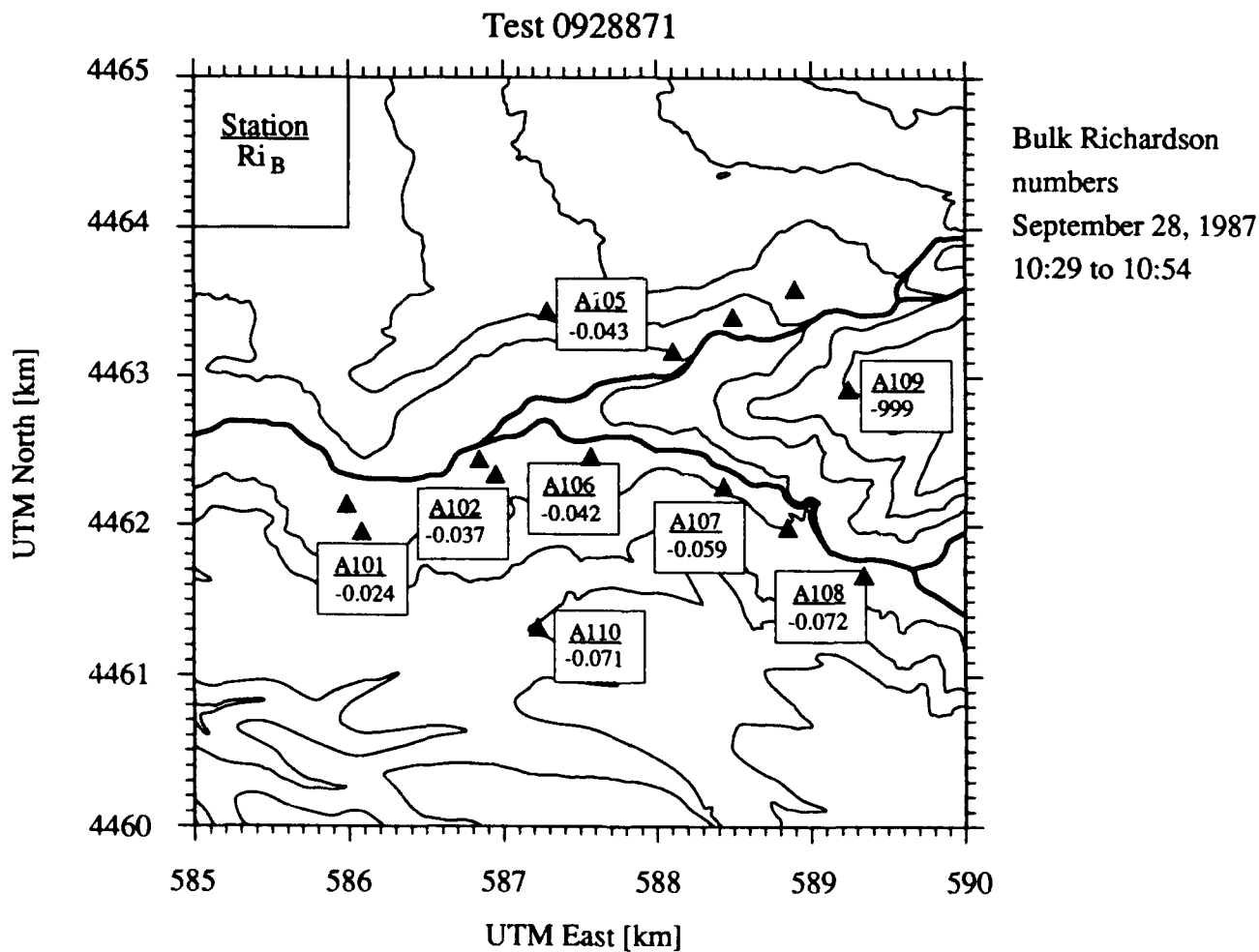


Figure 4.18 (continued) Distribution of the bulk Richardson number over the testing site for Test 0928871. These data are available for the 10-m surface stations which recorded temperature at both the 2-m and 8-m heights. A value of -999 indicates a surface station was not operational during this test.

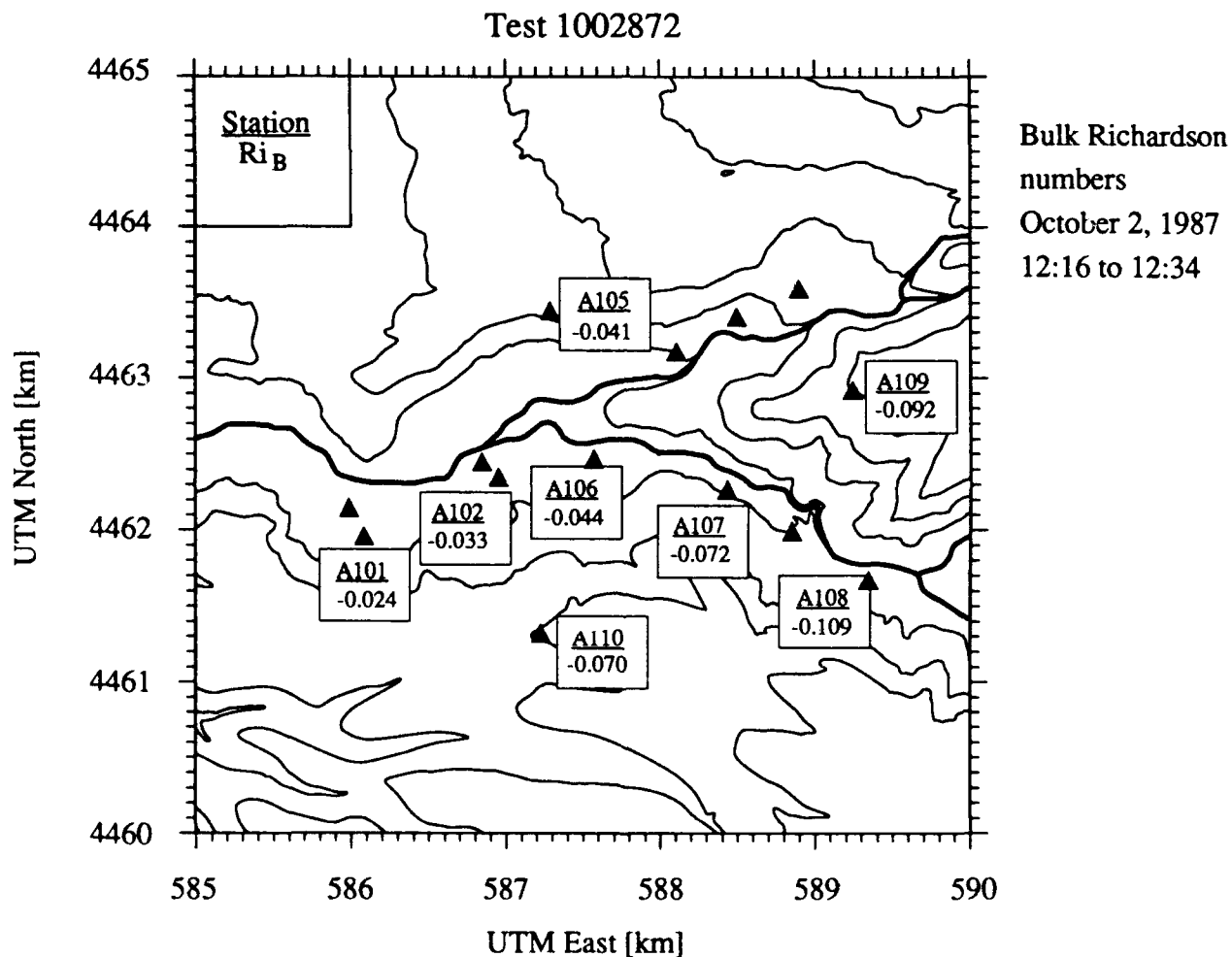


Figure 4.18 (continued) Distribution of the bulk Richardson number over the testing site for Test 1002872. These data are available for the 10-m surface stations which recorded temperature at both the 2-m and 8-m heights. A value of -999 indicates a surface station was not operational during this test.



earlier in the day than the other unstable tests. All the values of  $R_{iB}$  are negative numbers in a range which indicates moderate to very unstable atmospheric conditions.

Turbulent stress measurements made with the RISØ sonic anemometers can be used to directly calculate surface layer scaling parameters from the  $\overline{u_x' u_z'}$  and  $\overline{\theta' u_z'}$  correlations. Derived values of  $u_*$  and  $L$  are given in Table 4.3. The location of the sonic anemometers is shown in the map of Figure 4.11.

Table 4.3 Meteorological surface-layer scaling parameters for the unstable Meadowbrook dispersion tests. These values are from the RISØ sonic anemometers.

Location:	4462474N, 585523E		4462417N, 586756E	
Test	1/L	$u_*$	1/L	$u_*$
0921871	-0.013	0.76	-0.016	0.67
0923871	-0.059	0.76	-0.015	0.58
0926871	-0.011	0.80	-0.006	0.74
0928871	-0.456	0.20	-0.352	0.15
1002872	-0.080	0.43	-0.355	0.30

### Upper-Level Scaling Parameters

Soundings of the atmosphere were taken with a theodolite by ASL prior to each dispersion test. This instrument consists of a small package which measures pressure, temperature, and humidity as it is carried aloft by a balloon. The data is telemetered to the ground along with the balloon position and velocity. We use this data to determine the inversion height for our tests. A mini-sodar (an acoustic sounder with a range to 300 m) was used by researchers from Argonne National Laboratory to measure the velocity and temperature distribution through the lower boundary layer during each test. Unfortunately data from this instrument has not yet been made available for our use.

For the test of September 21, 1987, no theodolite sounding was taken. On September 23, the sounding was taken just prior to the test. The other sounding for the convective tests were taken in the morning period before the unstable boundary layer developed. With the collected information we can calculate the vertical potential temperature profile and the height through a hydrostatic approximation. Plots of height versus potential temperature for the theodolite data records are shown in Figure 4.19.

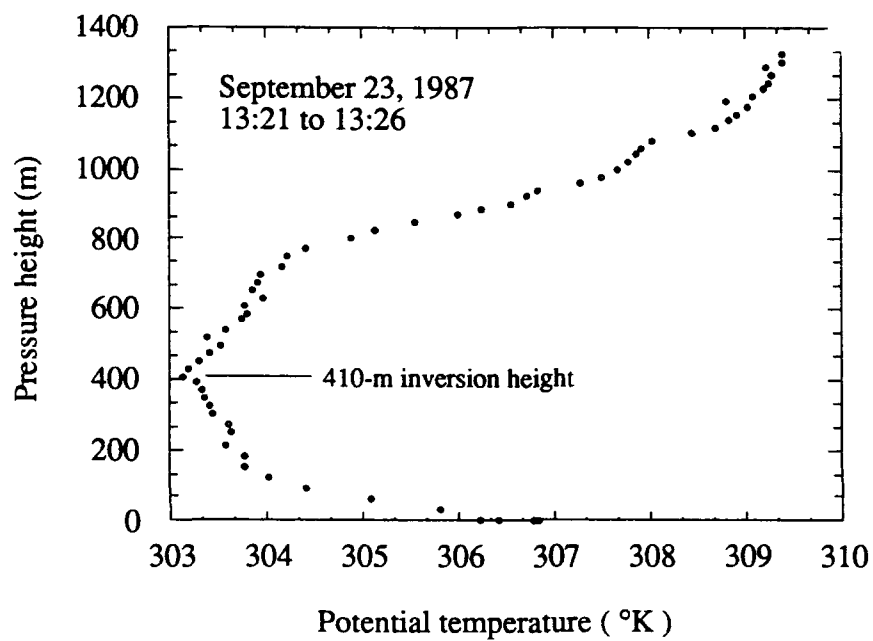


Figure 4.19 Potential temperature profile for Test 0923871. The inversion height is taken at 410 m from this plot. The sounding was taken just prior to the dispersion test.

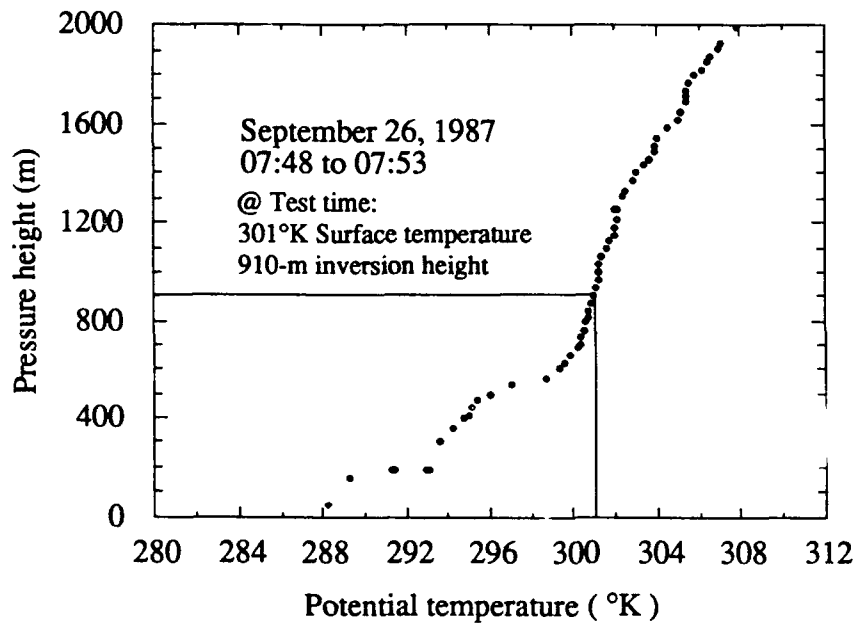


Figure 4.19 (continued) Potential temperature profile for Test 0926871. The sounding for this test was taken early in the morning. The intersection of the surface level potential temperature at the test time with this sounding profile taken earlier in the morning yields an inversion height of 910 m.

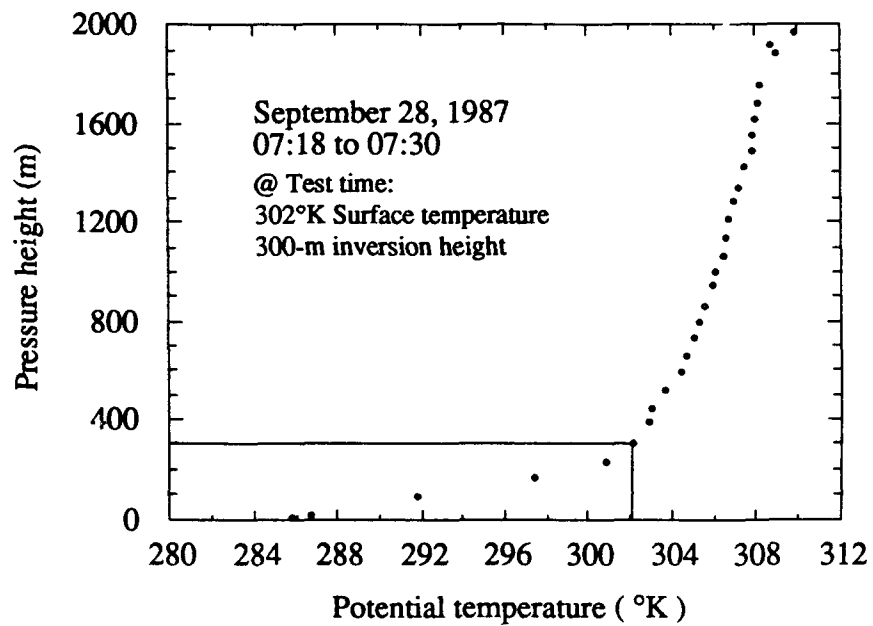


Figure 4.19 (continued) Potential temperature profile for Test 0928871. The sounding for this test was taken early in the morning. The intersection of the surface level potential temperature at the test time with this sounding profile taken earlier in the morning yields an inversion height of 300 m.

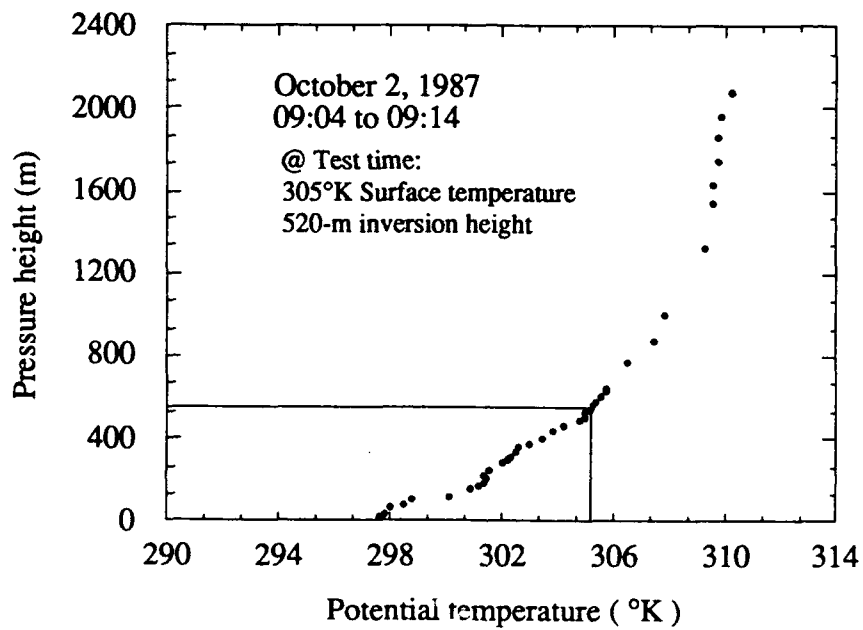


Figure 4.19 (continued) Potential temperature profile for Test 1002872. The sounding for this test was taken early in the morning. The intersection of the surface level potential temperature at the test time with this sounding profile taken earlier in the morning yields an inversion height of 520 m.

For Test 0921871 we can directly estimate the inversion height at the position where  $d\theta/dz = 0$  to get  $z_i = 410$  meters. Because the sounding was taken less than an hour before the test in the early afternoon, it is used directly in our scaling. For the other tests, soundings were taken in the morning. We estimate the inversion height at our test time through the intersection of the morning potential temperature profile with the ground level potential temperature at the time of the test. This method yields the information as shown in Table 4.4.

Table 4.4 Inversion heights estimated for the unstable Meadowbrook dispersion tests.

Test	Test time	$\theta_s$ ( $^{\circ}\text{K}$ )	$z_i$ (m)
0921871	14:30 - 15:00	-	-
0923871	14:05 - 14:50	304	410
0926871	12:00 - 13:06	301	910
0928871	10:29 - 10:53	302	300
1002871	12:16 - 12:36	305	520

We may use the friction velocity, inversion height, and Monin - Obhukhov length to find a convective velocity scale using  $(w_*/u_*)^3 = (-z_i/Lk)$ . This is shown in Table 4.5 using the sonic anemometer data near the fog-oil source location. These values are appropriate for scaling the data near the dispersion grid.

We may use scaling values derived from the other sonic anemometer for analyzing data from the 30-m meteorological tower. A plot of the normalized horizontal standard deviation in wind direction for the 30-m meteorological tower is given in Figures 4.20 and 4.21, along with a line for  $\sigma_v \sim \sigma_u = 0.58w_*$ , which indicates the free convection limit. These data are reasonably consistent with this limit. The vertical standard deviation on the 30-m meteorological tower is shown in Figure 4.22. These data also follow the free convection limit.

#### 4.2.3 Meadowbrook Tests under Stable Meteorological Conditions

For the nighttime stable tests, maps of the average wind field from the surface stations are presented in Figure 4.23. Associated maps of the spatial variation of the bulk Richardson number  $Ri_B$  at these surface stations are shown in Figure 4.24.

On these maps, the standard deviation in wind direction is much smaller than in the daytime tests, while the direction and amplitude is evidently strongly affected by the local terrain. For the stable tests which are several hours after dusk (0925871), or very early in the morning (0927871),

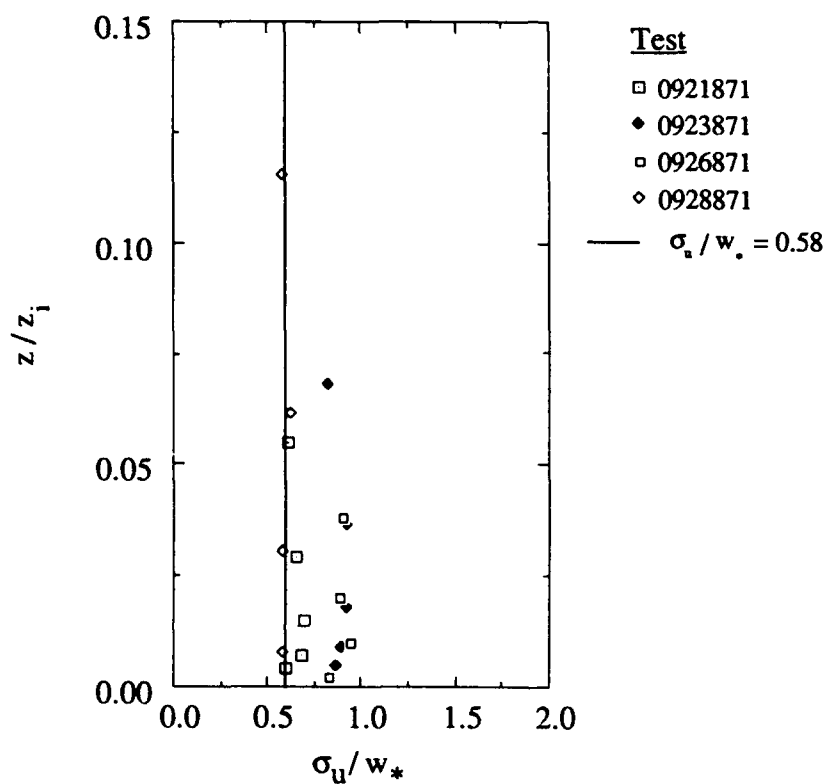


Figure 4.20 Standard deviations in u-component velocity for the Meadowbrook 30-m meteorological tower data. These values are scaled by parameters found from the sonic anemometer and the morning upper air data. The free convection limit is shown.

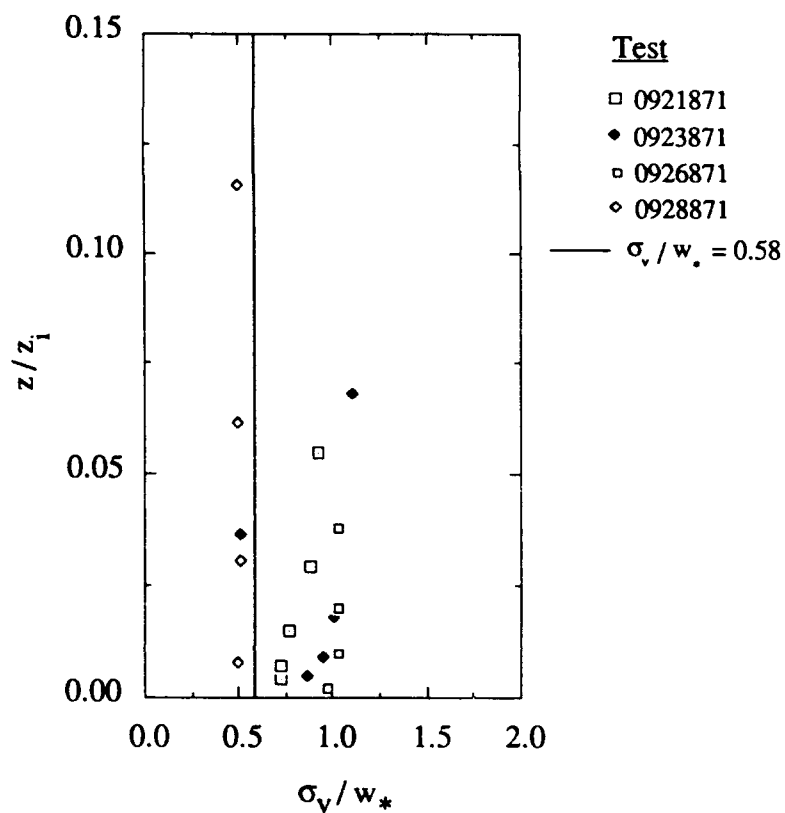


Figure 4.21 Standard deviations in v-component velocity for the Meadowbrook 30-m meteorological tower data. These values are scaled by parameters found from the sonic anemometer and the morning upper air data. The free convection limit is shown.



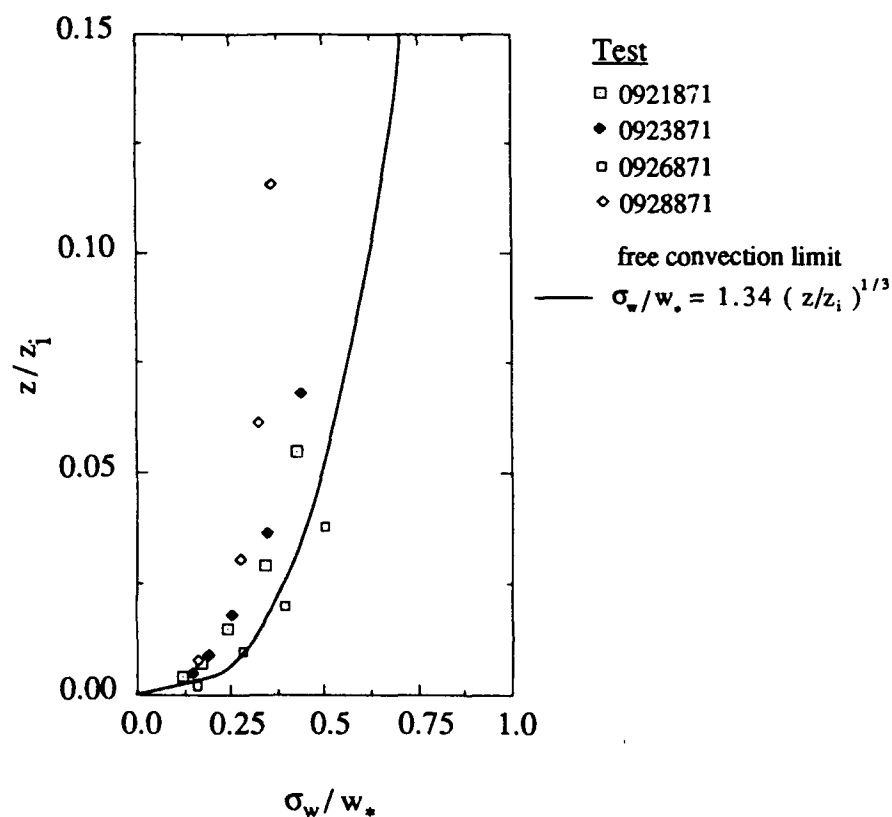


Figure 4.22 Standard deviations in w-component velocity for the Meadowbrook 30-m meteorological tower data. These values are scaled by parameters found from the sonic anemometer and the morning upper air data. The free convection limit given by Kaimal et al. (1976) is shown.

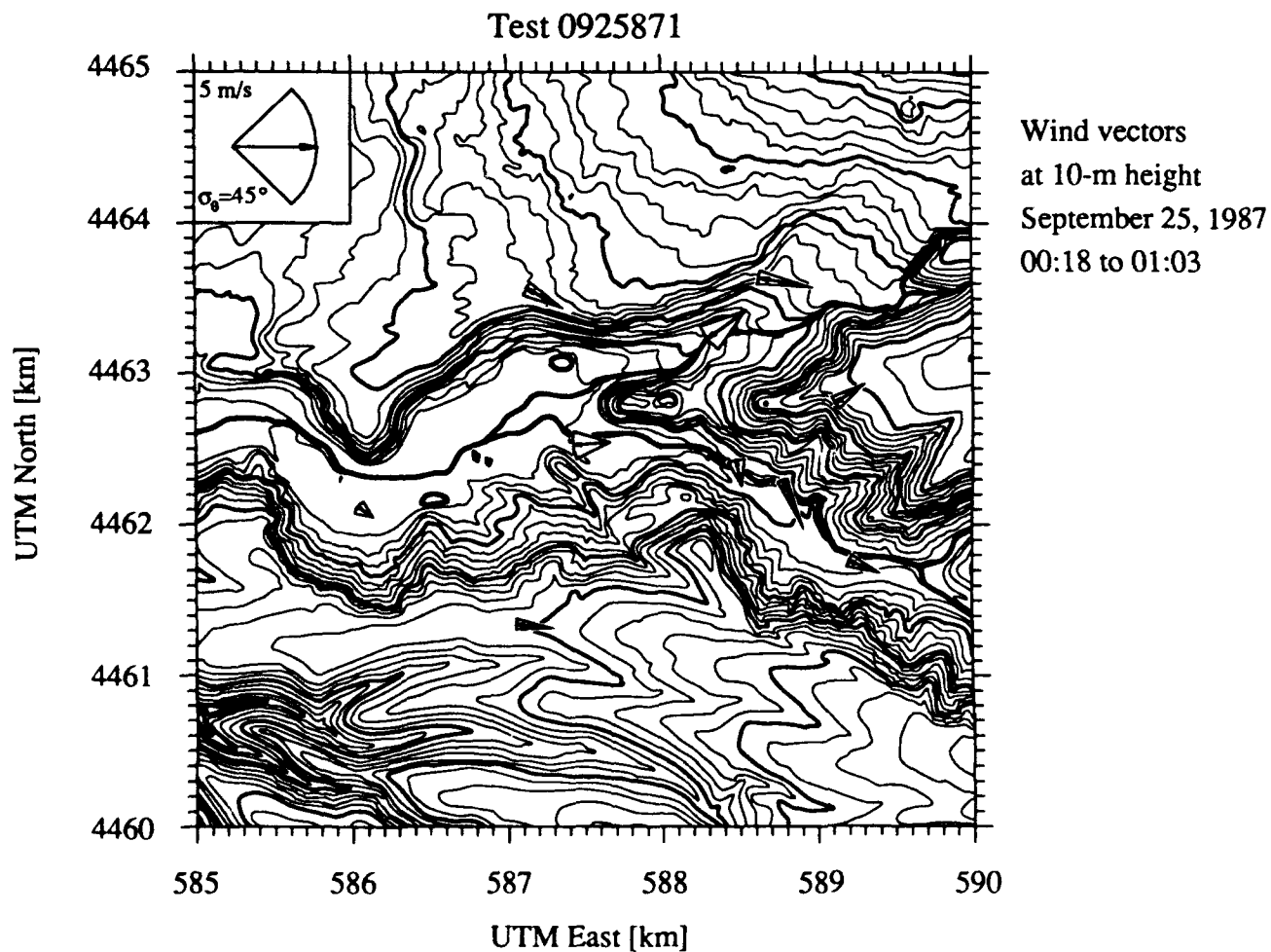


Figure 4.23 Wind vector map for Test 0925871. These data are from the 10-m surface stations. The amplitude of the vector is scaled by its length and the standard deviation in wind direction is given by the half width of the indicated arc.

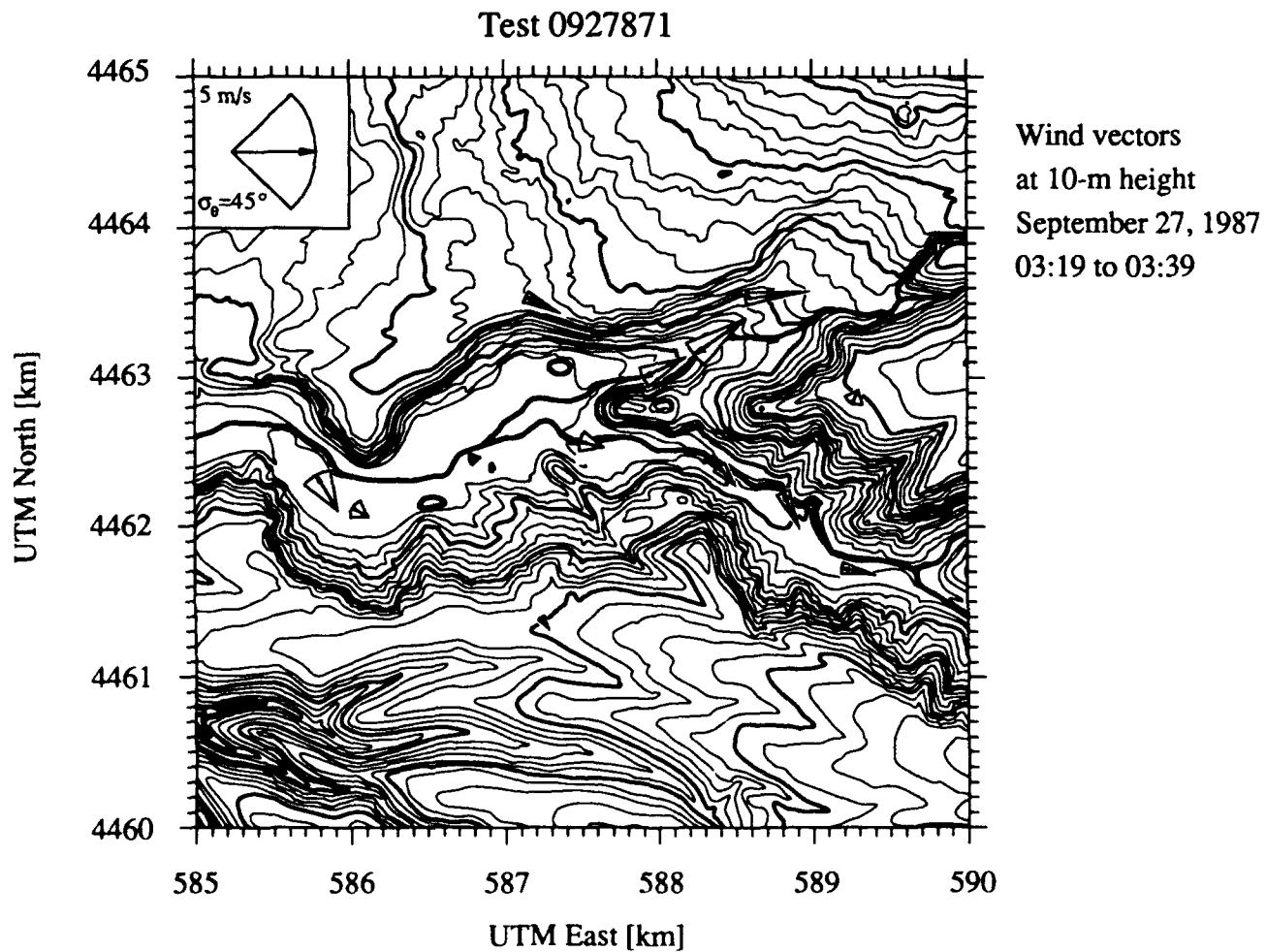


Figure 4.23 (continued) Wind vector map for Test 0927871. These data are from the 10-m surface stations. The amplitude of the vector is scaled by its length and the standard deviation in wind direction is given by the half width of the indicated arc.

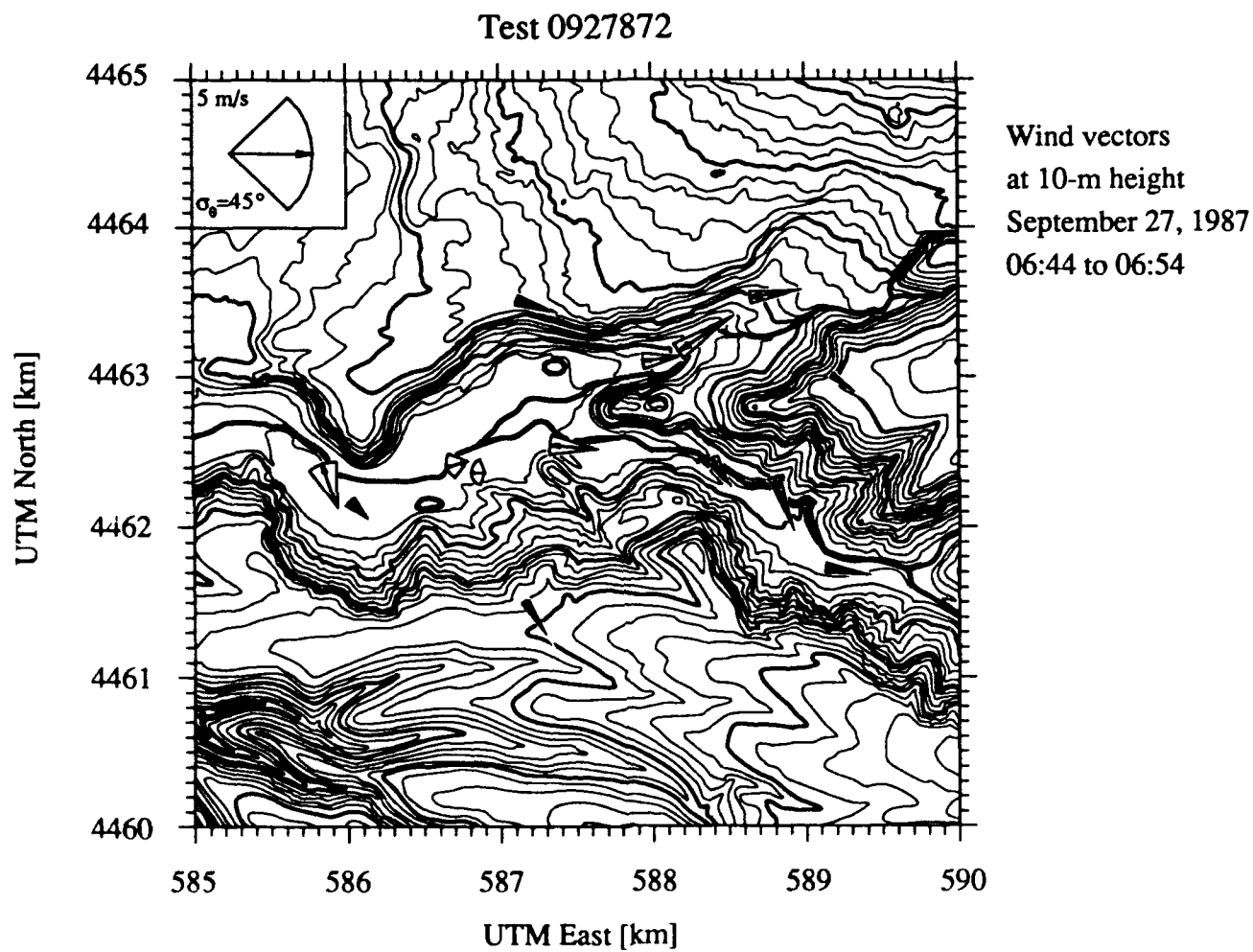


Figure 4.23 (continued) Wind vector map for Test 0927872. These data are from the 10-m surface stations. The amplitude of the vector is scaled by its length and the standard deviation in wind direction is given by the half width of the indicated arc.

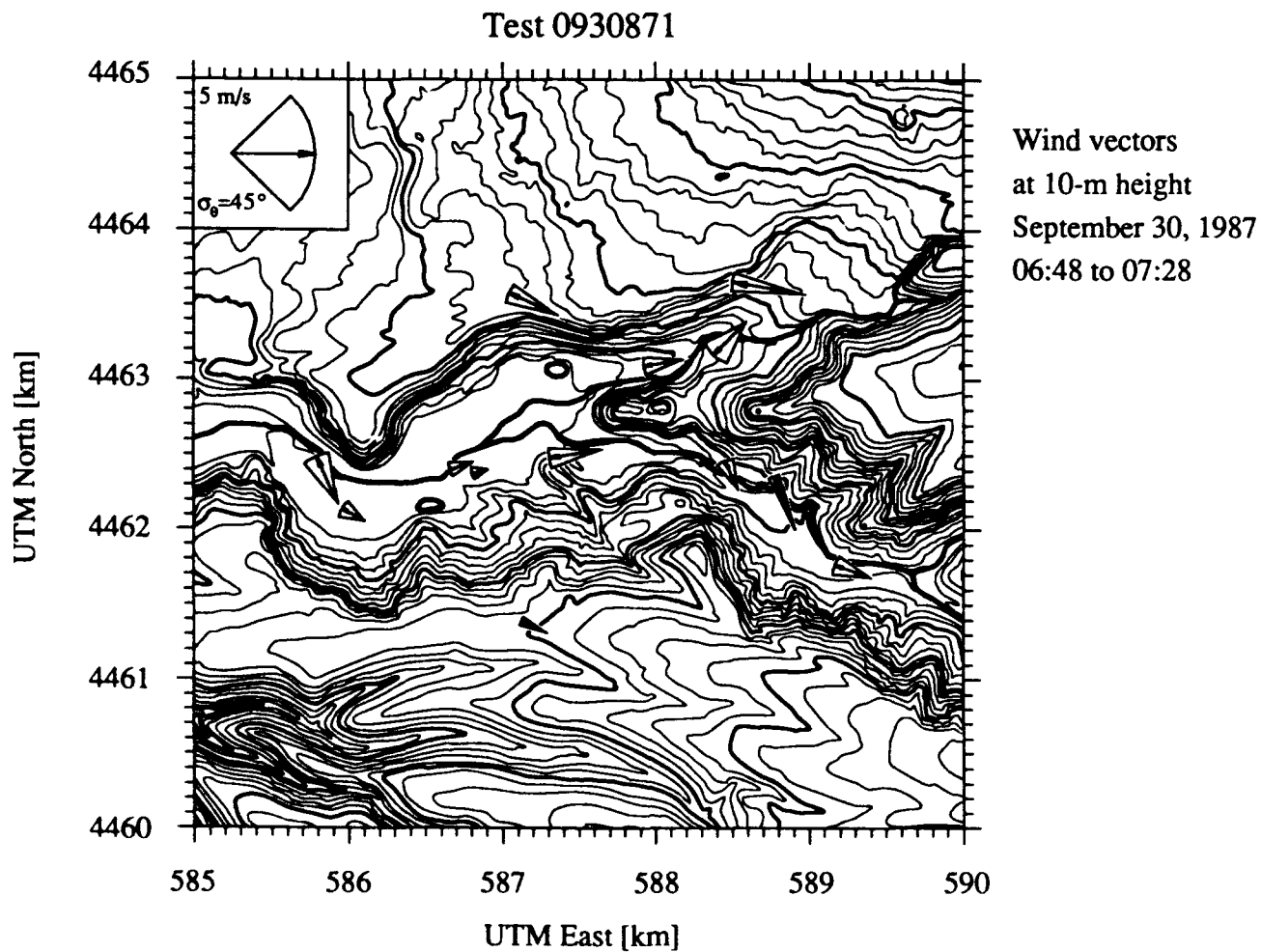


Figure 4.23 (continued) Wind vector map for Test 0930871. These data are from the 10-m surface stations. The amplitude of the vector is scaled by its length and the standard deviation in wind direction is given by the half width of the indicated arc.

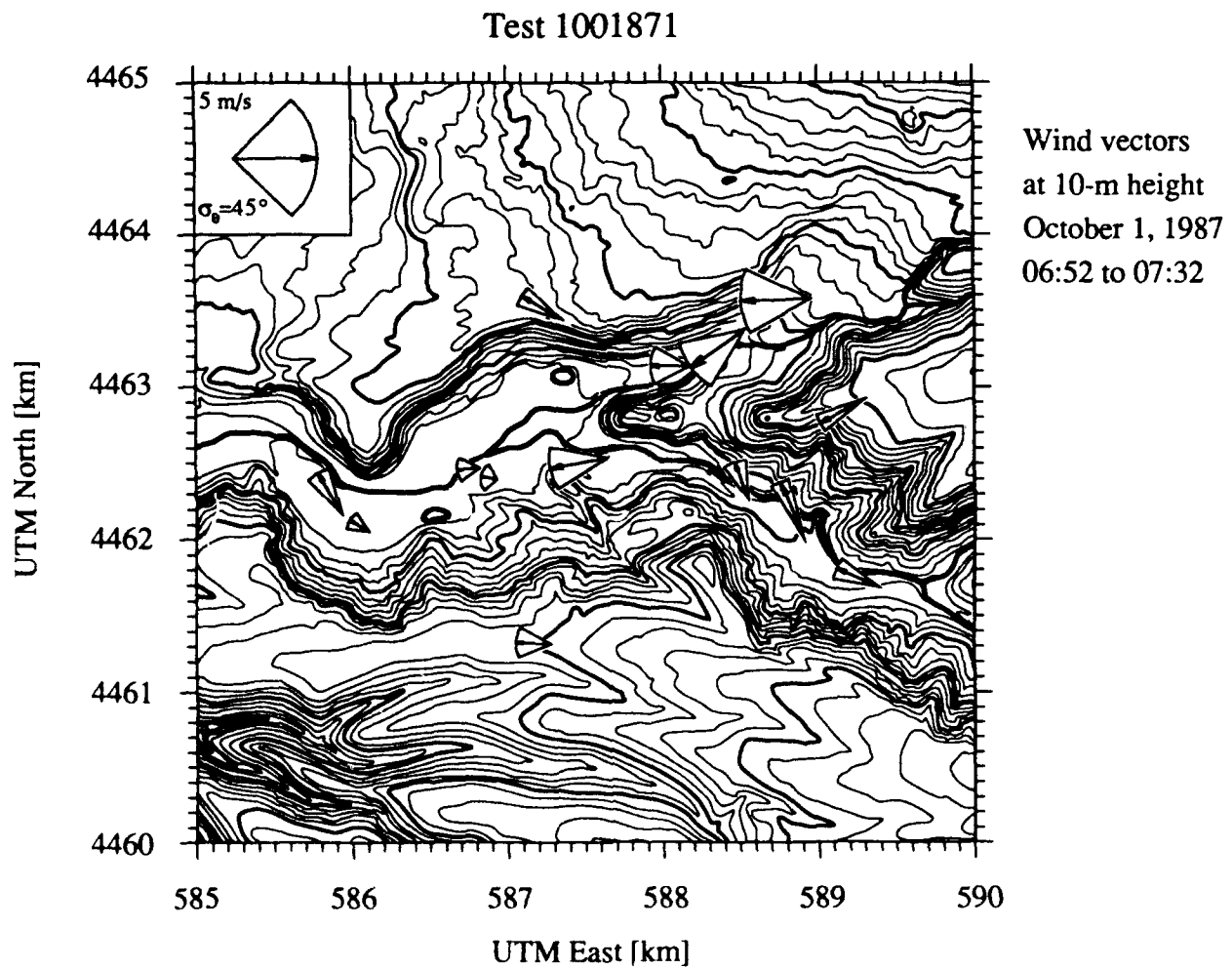


Figure 4.23 (continued) Wind vector map for Test 1001871. These data are from the 10-m surface stations. The amplitude of the vector is scaled by its length and the standard deviation in wind direction is given by the half width of the indicated arc.

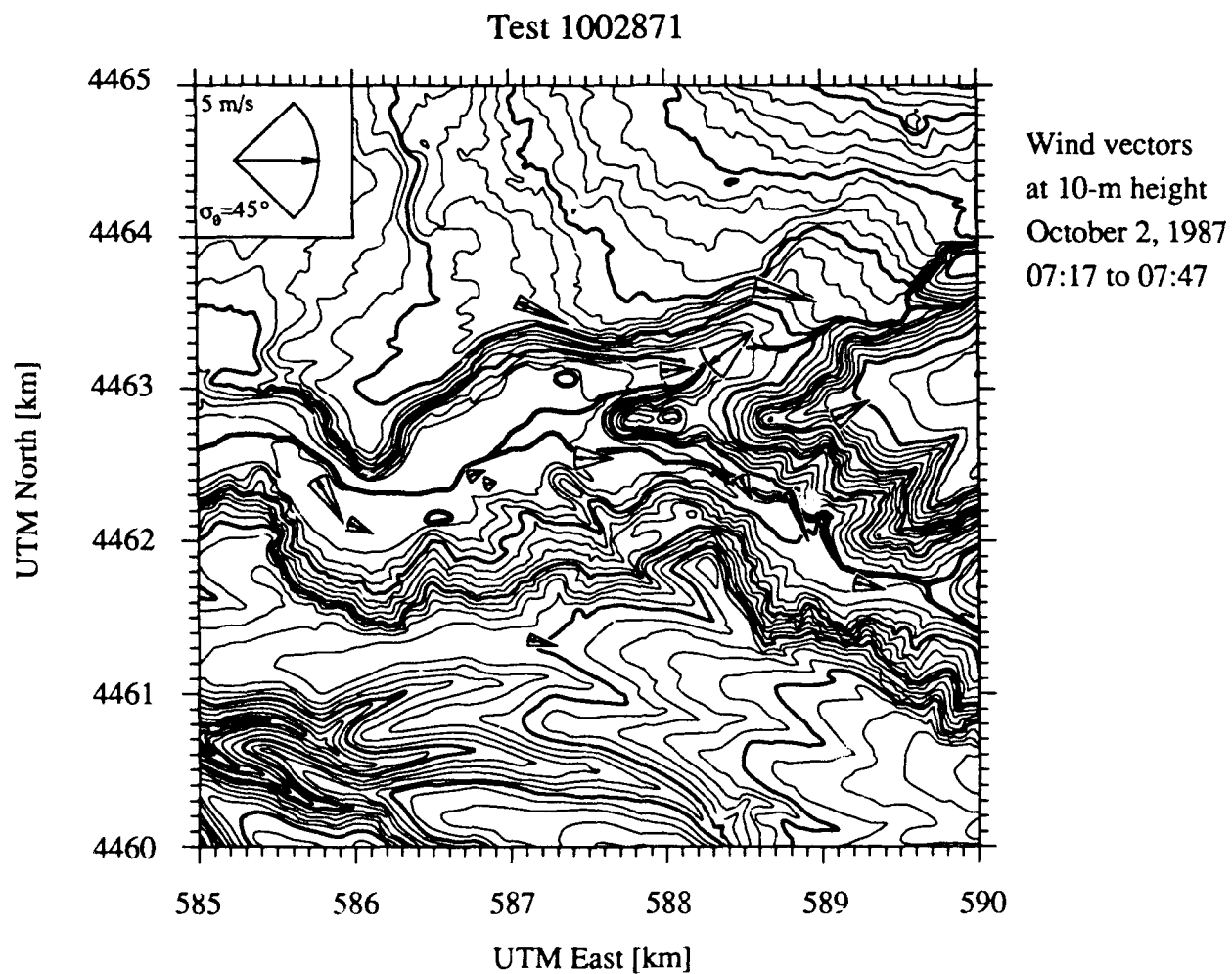


Figure 4.23 (continued) Wind vector map for Test 1002871. These data are from the 10-m surface stations. The amplitude of the vector is scaled by its length and the standard deviation in wind direction is given by the half width of the indicated arc.

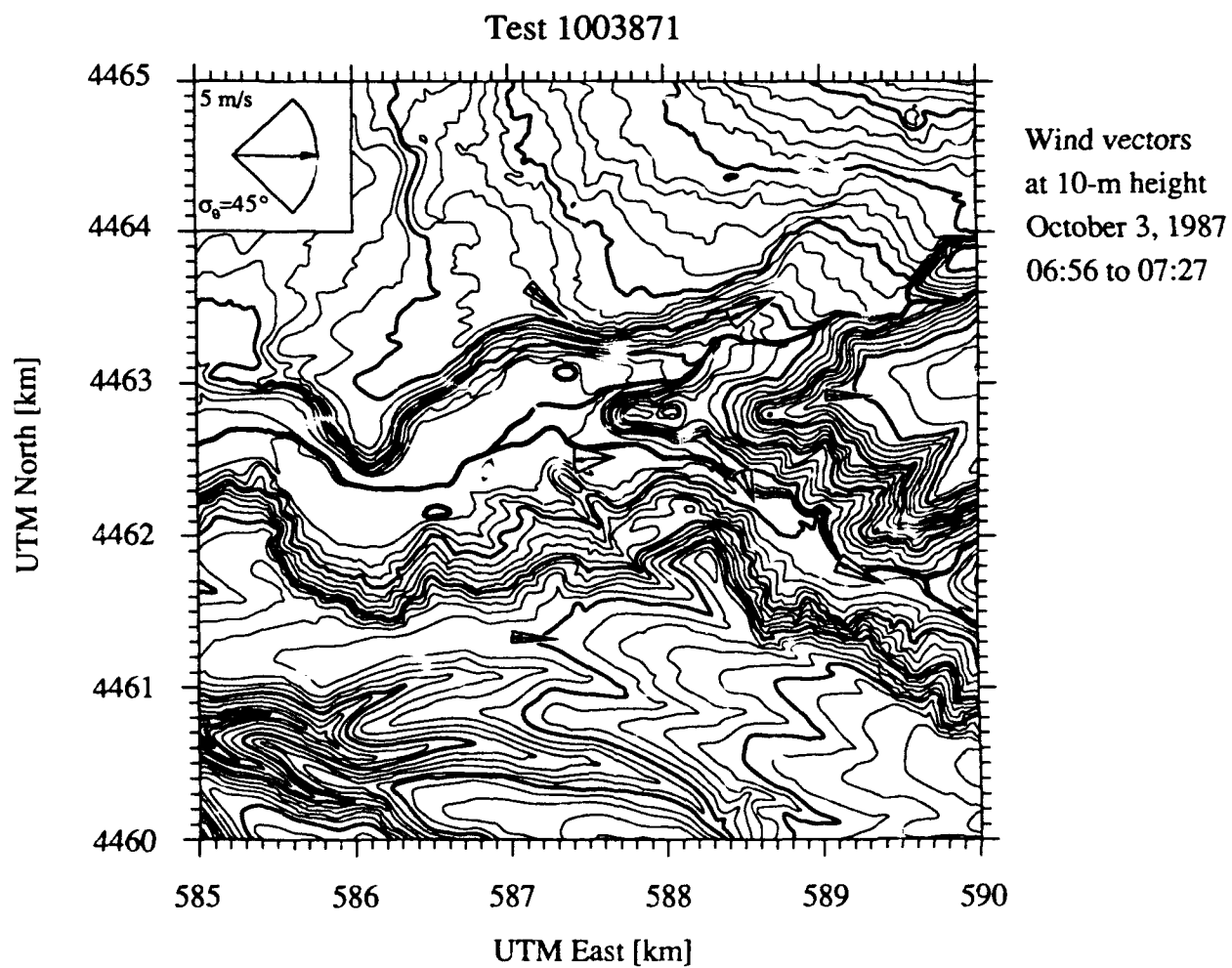


Figure 4.23 (continued) Wind vector map for Test 1003871. These data are from the 10-m surface stations. The amplitude of the vector is scaled by its length and the standard deviation in wind direction is given by the half width of the indicated arc.



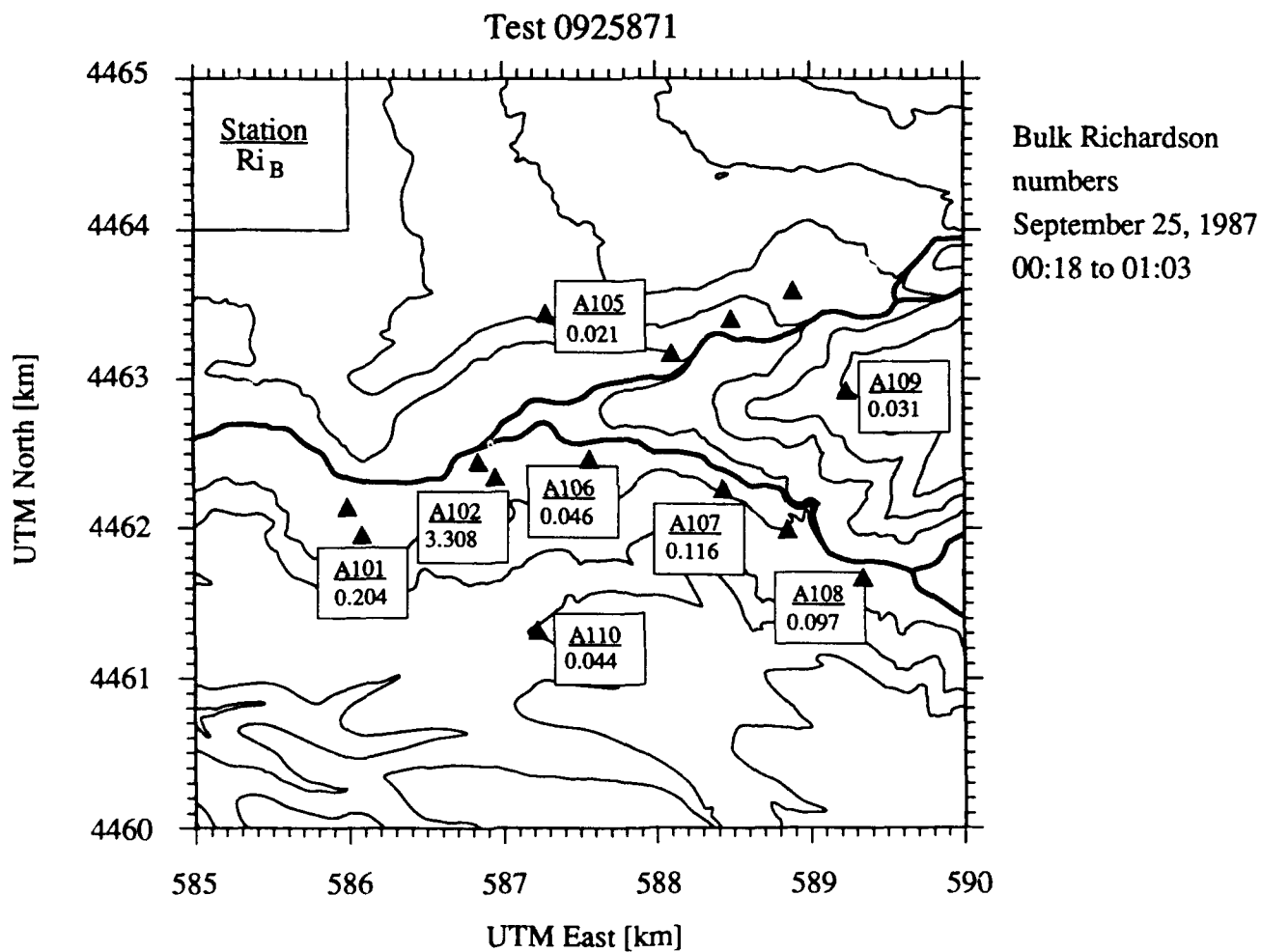


Figure 4.24 Distribution of the bulk Richardson number over the testing site for Test 0925871. These data are available for the 10-m surface stations which recorded temperature at both the 2-m and 8-m heights. A value of -999 indicates a surface station was not operational during this test.

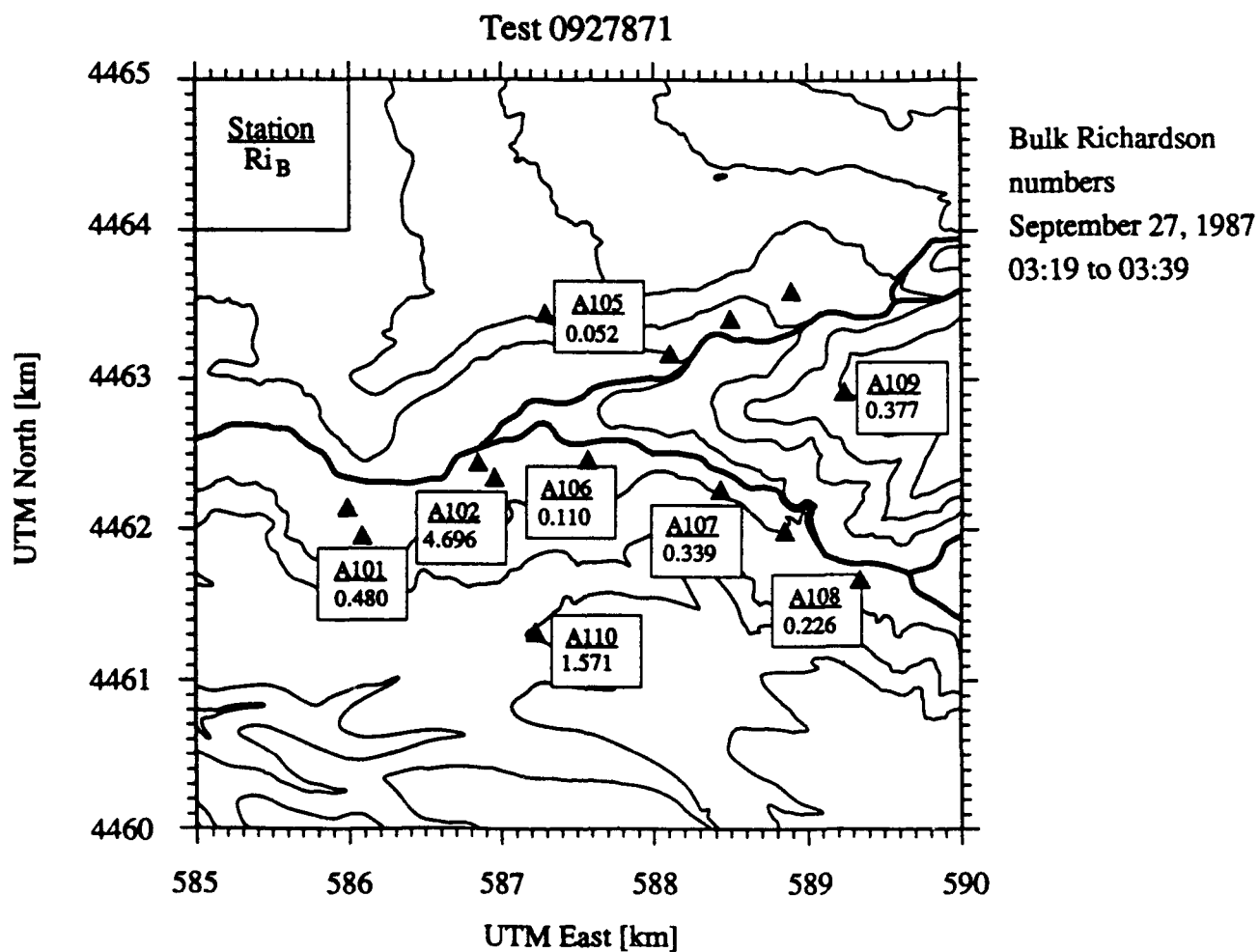


Figure 4.24 (continued) Distribution of the bulk Richardson number over the testing site for Test 0927871. These data are available for the 10-m surface stations which recorded temperature at both the 2-m and 8-m heights. A value of -999 indicates a surface station was not operational during this test.

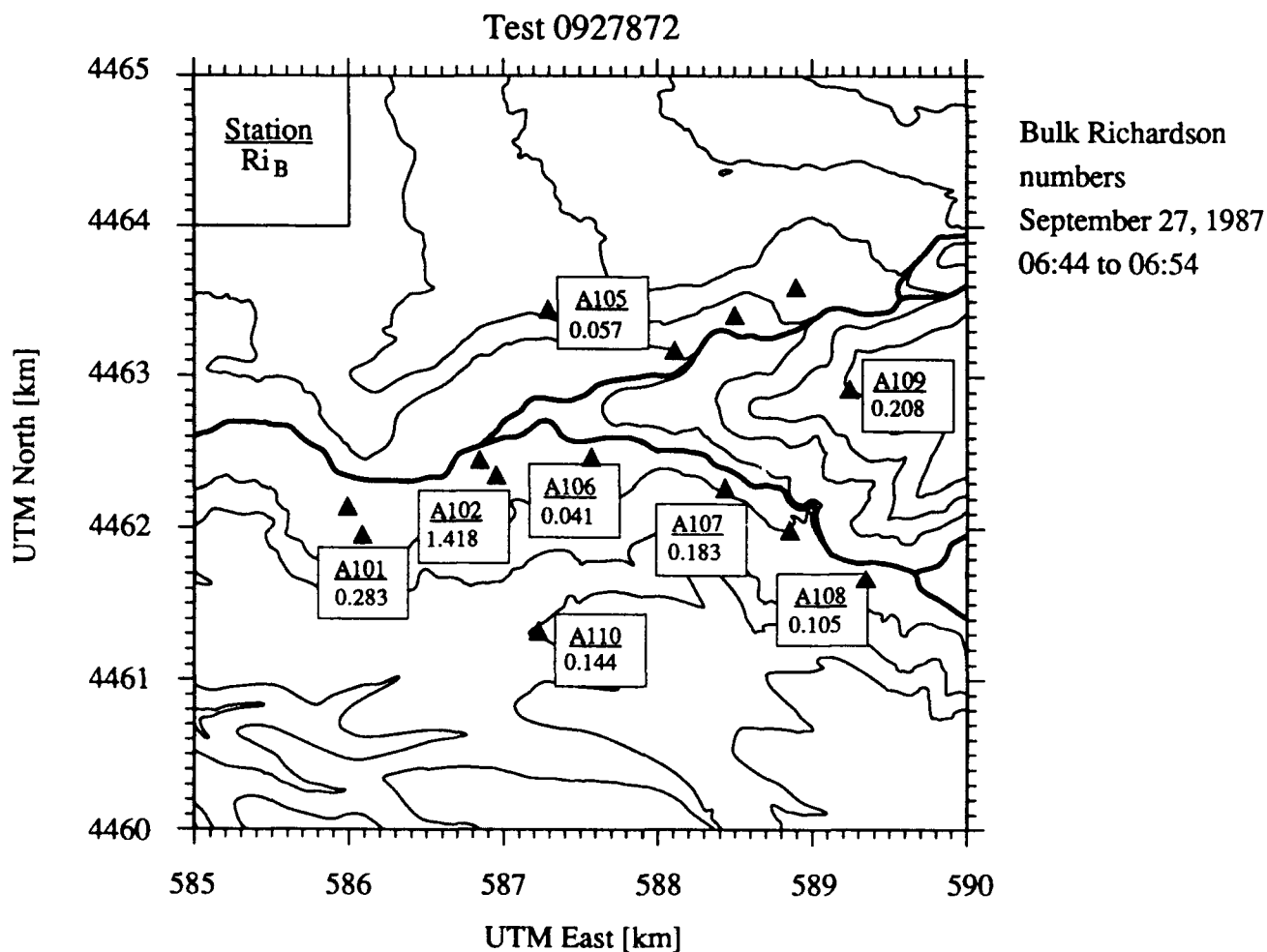


Figure 4.24 (continued) Distribution of the bulk Richardson number over the testing site for Test 0927872. These data are available for the 10-m surface stations which recorded temperature at both the 2-m and 8-m heights. A value of -999 indicates a surface station was not operational during this test.

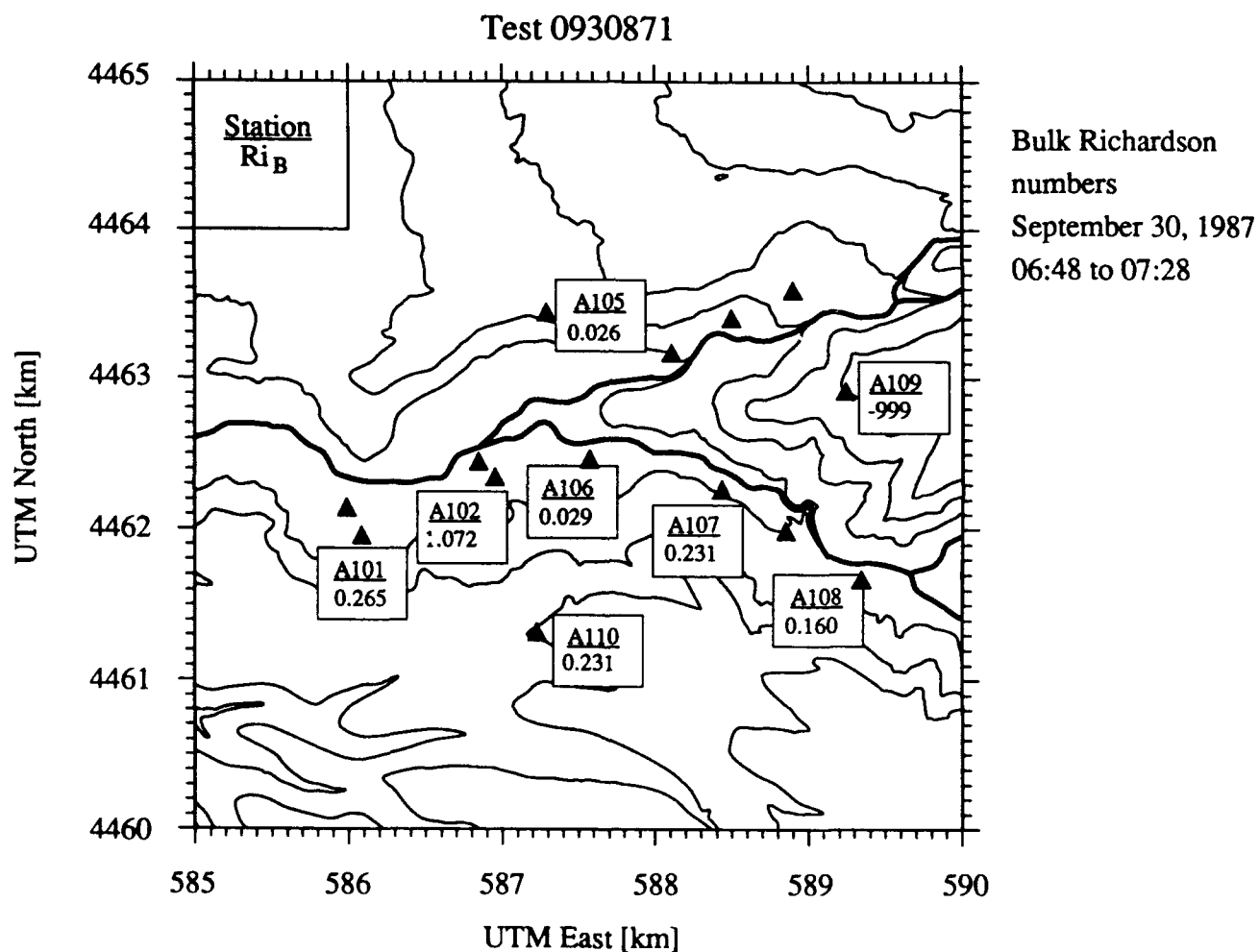


Figure 4.24 (continued) Distribution of the bulk Richardson number over the testing site for Test 0930871. These data are available for the 10-m surface stations which recorded temperature at both the 2-m and 8-m heights. A value of -999 indicates a surface station was not operational during this test.

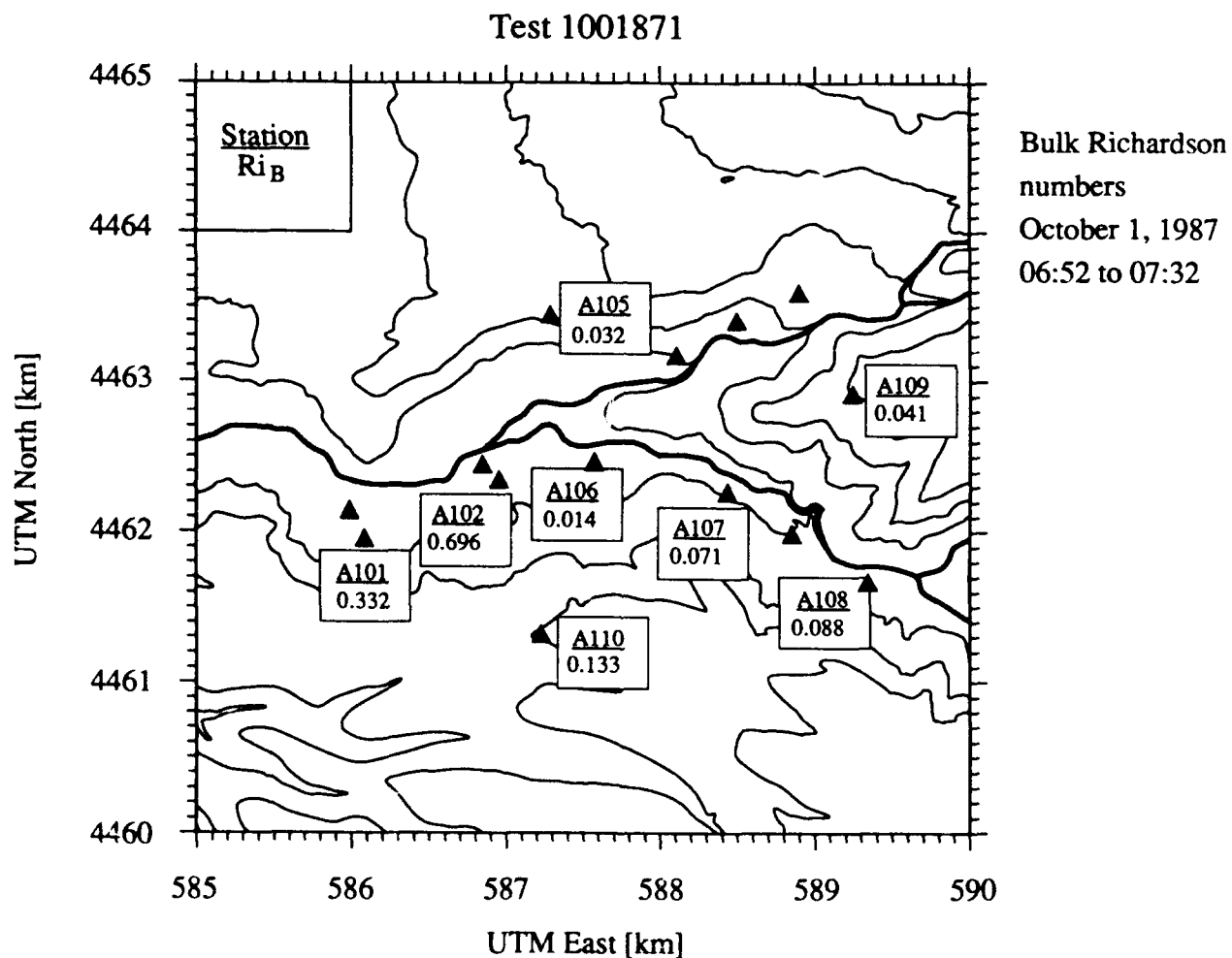


Figure 4.24 (continued) Distribution of the bulk Richardson number over the testing site for Test 1001871. These data are available for the 10-m surface stations which recorded temperature at both the 2-m and 8-m heights. A value of -999 indicates a surface station was not operational during this test.

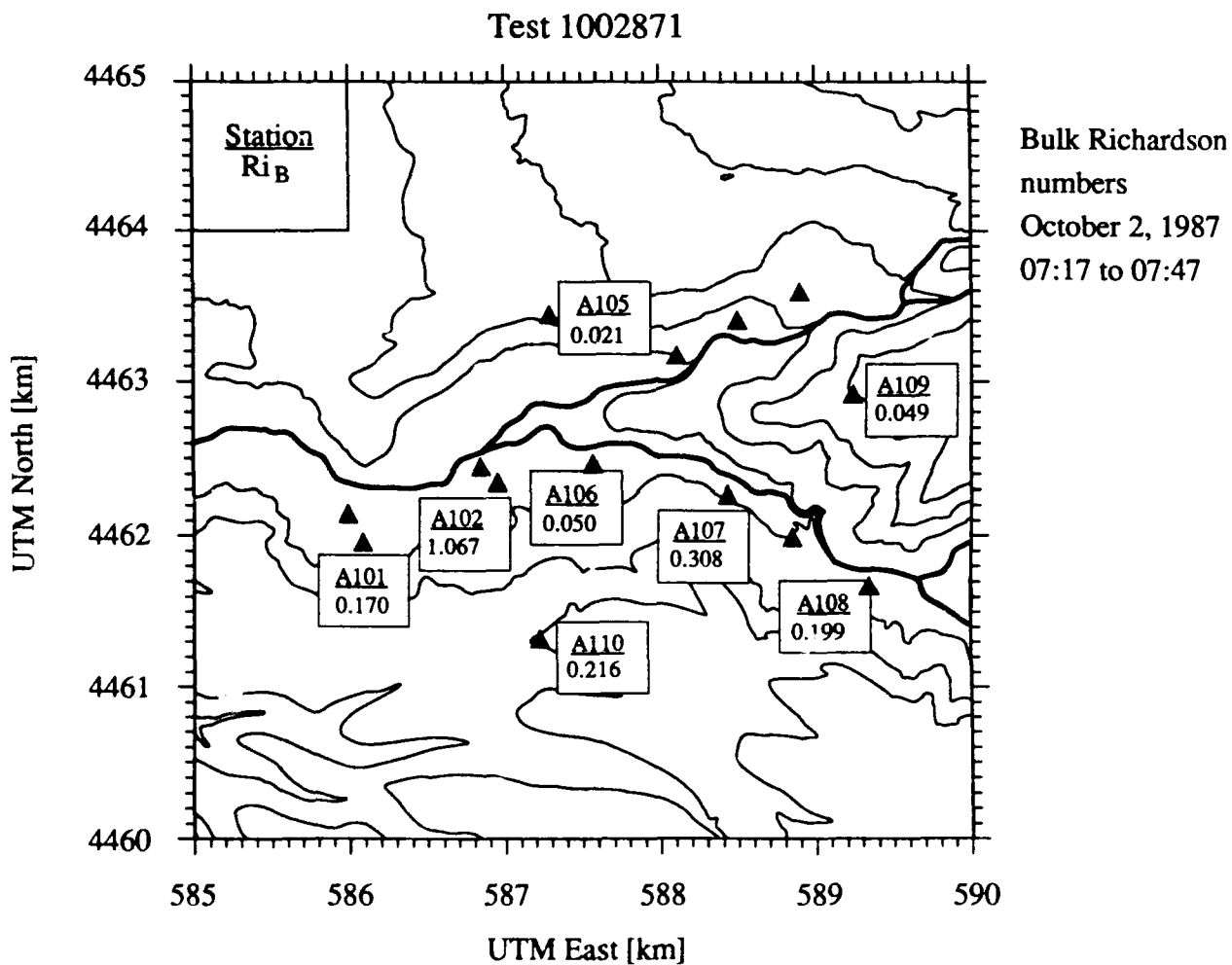


Figure 4.24 (continued) Distribution of the bulk Richardson number over the testing site for Test 1002871. These data are available for the 10-m surface stations which recorded temperature at both the 2-m and 8-m heights. A value of -999 indicates a surface station was not operational during this test.

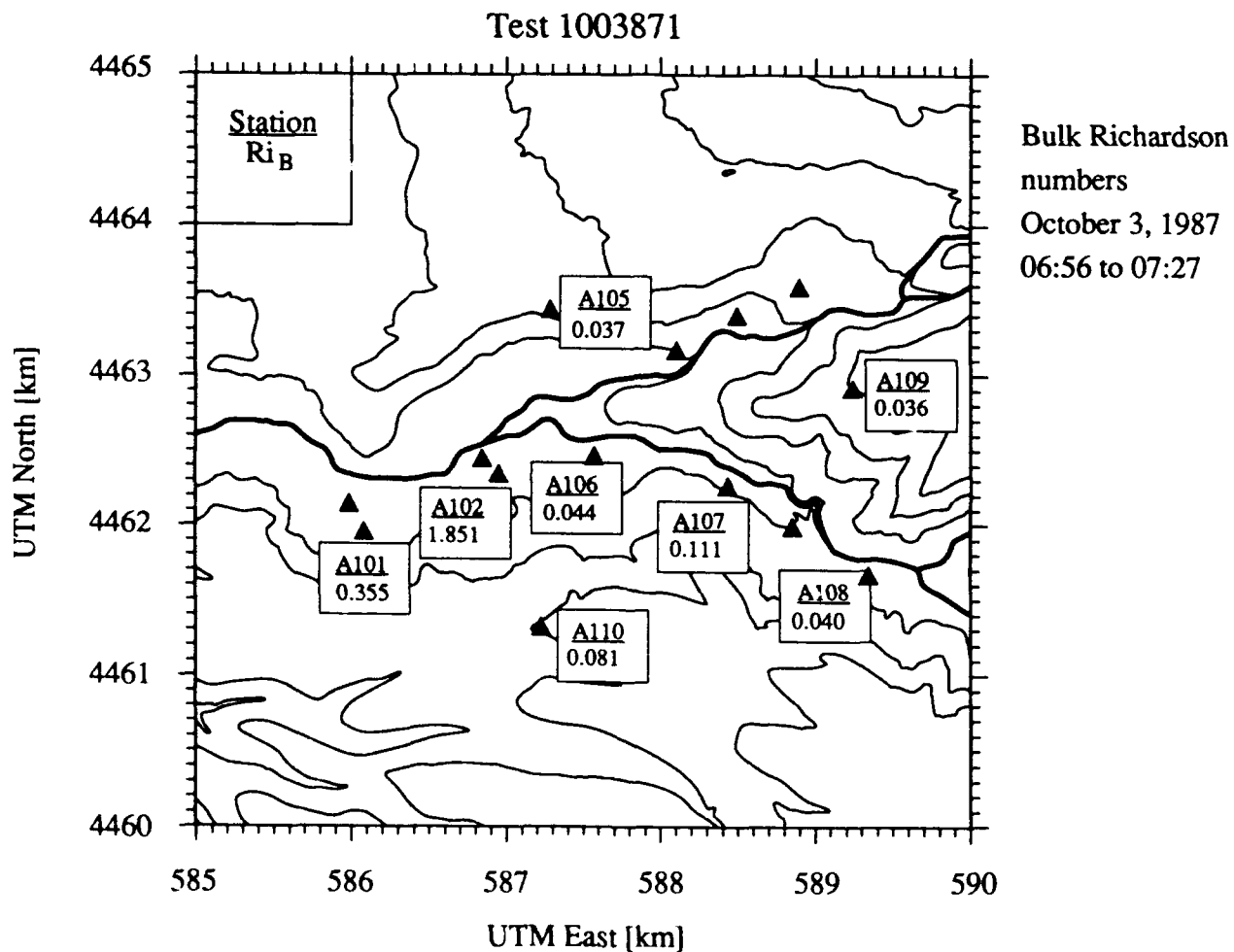


Figure 4.24 (continued) Distribution of the bulk Richardson number over the testing site for Test 1003871. These data are available for the 10-m surface stations which recorded temperature at both the 2-m and 8-m heights. A value of -999 indicates a surface station was not operational during this test.

Table 4.5 Meteorological scaling parameters for the unstable Meadowbrook dispersion tests. A rough estimate of the inversion height for Test 0921871 is given in the table.

Test	L	$u_*$	$z_i$ (m)	$w_*$
0921871	-76.9	0.76	550 (est.)	1.98
0923871	-17.0	0.76	410	2.98
0926871	-90.9	0.80	910	2.34
0928871	-2.19	0.20	300	1.39
1002872	-12.5	0.41	520	2.02

the distribution of  $Ri_B$  values shows small positive values on the sloped ground while large positive values are found in the flat central region of the dispersion site at stations A102 and A101. Along with the wind vector maps, this result for  $Ri_B$  indicates a pooling of stagnant air in the middle of the valley with a strong stable thermal stratification. Morning or dawn tests, which show smaller  $Ri_B$  values in the sloped areas of the site, do not have this stagnant region.

Since the wind field for these stable tests is dominated by the inhomogeneous terrain, a simple boundary layer parameterization is not possible. Modeling dispersion in these conditions is beyond the scope of this report. It may be of value to consider a potential flow solution for analysis, since it is likely that the terrain will dominate the dispersion to a greater degree than the turbulence.



## 5. SAMPLING, ANALYSIS, AND CHARACTERIZATION OF SMOKE

This chapter begins with information on the mean dosage sampling equipment in Section 5.1. This is followed by a discussion of the aerosol particle size distributions for both fog-oil smoke and HC smoke in Section 5.2. Descriptions of the fog-oil smoke source and chemical analysis method are given in Section 5.3, followed by similar information for the HC smoke in Section 5.4. Section 5.5 concludes with a discussion of our design and development of the real-time smoke sampling system.

### 5.1 Mean Dosage Sampling Equipment

The need to determine the concentration fields in our dispersion experiments required an extensive analysis of the characteristics of the smokes we were to use and research into methods of sampling available to us. As a practical matter we were limited to surface-level measurements which only extended into the lowest fraction of the boundary layer. Sampling locations were arrayed in transects which were normal to the prevailing wind direction and were at geometrically increasing distances from the source. From these sampling transects we acquired surface-level information on the crosswind plume dimensions and the decrease in concentration with increasing distance from the source.

The system for collecting dosage samples of aerosol consisted of aspirated filter samplers located along several transects. The separation between samplers was small enough to capture sufficient detail in the lateral profile of concentration, with positive measurements on 5 or 6 sampling masts on each transect. Mean concentrations are calculated from the time-averaged mass of material collected on a filter divided by the total flow through each filter over the test duration.

Each sampler consists of a hollow vertical 8-m mast with nipples at 1-m increments along the mast. Filter cassettes are mounted on, and aspirated through, some of the mast nipples, while the other nipples are plugged. At Camp Atterbury, concentration measurements were taken at heights of 1, 2, 4, and 8 m. At Meadowbrook the samples were taken at heights of 2 m and 8 m. The aspiration for each mast is provided by a 500-W vacuum pump, several of which are located along each sampling transect. The power for the pumps is provided by a 4.5-kW generator. The total flow through each hollow mast was monitored through a rotameter flow meter. Since flow losses in the masts are very small compared to those in the filters, flow through each filter on the mast is the total flow through the mast divided by the number of filters on the mast.

The particular filter used depended on the type of smoke type released. Binderless glass-fiber filters are used for the fog-oil smoke and 0.45- $\mu\text{m}$  pore size cellulose ester membrane filters are used for sampling the HC-smoke aerosol. Both of these filter types are manufactured by

Nucleopore (Pleasanton, California) and are mounted in 37-mm diameter cassette filter holders. The type of filter is dictated by the analysis method for each type of smoke and is covered in more detail in the respective discussions of fog-oil and HC smoke in Sections 5.3 and 5.4.

At Camp Atterbury we used 50 sampling masts in 5 transects. The 4 nearest transects extended along at least a 90° arc from the source, with the remaining transect covered a 20° arc from the source. For the Meadowbrook tests, we used 20 masts for the unstable dispersion tests in 3 transects and up to 38 masts in 6 transects for the stable tests. These transects covered the width of the valley floor for both the stable and unstable dispersion tests.

## 5.2 Aerosol Measurements and Collection

To estimate deposition and impaction losses we measured the aerosol size distribution during each test at Camp Atterbury for both the fog-oil smoke and the HC smoke. For dilute aerosols it is sufficient to treat the motion of each particle independently. Motion is usually within the Stoke's flow regime with  $Re_p = v_i d_p \rho_f / \mu < 3$  and  $C_D = 24/Re_p$  for a spherical particle of diameter  $d_p$  and fluid density  $\rho_f$ . A detailed treatment of aerosol mechanics is given by Hinds (1982).

### 5.2.1 Aerosol Particle Size Measurement Instrumentation

Aerosol size measurements for fog-oil smoke and HC smoke were included in the Camp Atterbury dispersion tests. These measurements were made using a California Measurements model PC-2 Aerosol Particle Analyzer Quartz Crystal Microbalance Cascade Impactor System. This instrument uses a sequential series of ten inertial impactors. A single impactor stage is shown in Figure 5.1. Particles are separated in this instrument by accelerating a stream of air through a nozzle to impinge on a collection plate. Particles of sufficient inertia cannot follow the streamlines and are collected on the substrate. Successive stages have smaller nozzle sizes and higher flow velocities to collect progressively smaller particles on succeeding stages. In this instrument, each collection plate is an oscillating quartz crystal. Changes in the resonant frequency, determine the mass collected on each stage.

The operation of an impactor and the particle collection efficiency depend on several parameters. Among these are the nozzle-collection plate geometry, the nozzle Reynolds number  $Re_j = UW\rho_f/\mu$ , and the Stoke's number

$$St = \frac{\beta U}{W/2} = \frac{d_p^2 \rho_p U}{9 \mu W} \quad (5.1)$$

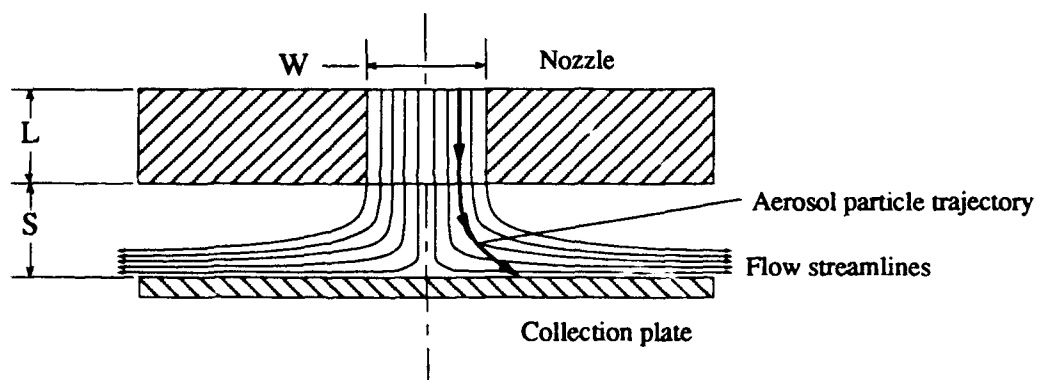


Figure 5.1 Schematic of a impaction stage for an aerosol particle separator. The dimensions are used in the text.

where  $U$  is the average velocity through the nozzle throat,  $W$  is the nozzle diameter, and  $\mu$  is the kinematic fluid viscosity. The value of  $St$  is the ratio of the particle stopping distance to half the nozzle throat diameter. The particle stopping distance is given by  $\beta U$  with  $\beta$  from Eq. 3.10.

Impactors may be designed so that collection efficiency is a function of Stokes number only. Constraints on the geometry are discussed by Mercer (1963), McFarland and Zeller (1963) and Cohen and Montan (1967). Values and the range in Stokes number for a 50% collection efficiency are given by Marple and Liu (1974).

A typical impactor efficiency curve is shown in Figure 5.2. Deviation from a step function for this curve will occur even for an ideal impactor as a consequence of the physical size of the impactor nozzle and the multiple streamlines within the impactor jet. Collection for a particular particle will depend both on the Stoke's number and the distance from the nozzle axis at which a particular particle enters the nozzle. Such deviations limit the resolution possible in a particle size histogram measured with a cascade impactor. Particles cut sizes for an impactor are usually taken at the 50% collection efficiency level. For the ten stages of the California Measurements PC-2 the cut sizes are given in Table 5.1. The cut sizes are adjusted for different particle densities using the assumption that the Stokes number for 50% collection efficiency will remain constant.

Table 5.1 Cut sizes for the California Measurements PC-2 cascade impactor. Values are shown for both the fog-oil smoke with the particle density  $\rho_p = 0.91 \text{ g/m}^3$  and for the HC-aerosol smoke using a value of  $\rho_p = 2.0 \text{ g/m}^3$ .

Stage	$d_p$ [ 50% cut ]	
	$\rho_p = 2.0 \text{ g/cm}^3$	$\rho_p = 0.91 \text{ g/cm}^3$
1	25.0 $\mu\text{m}$	37.0 $\mu\text{m}$
2	12.5 $\mu\text{m}$	18.5 $\mu\text{m}$
3	6.4 $\mu\text{m}$	9.49 $\mu\text{m}$
4	3.2 $\mu\text{m}$	4.74 $\mu\text{m}$
5	1.6 $\mu\text{m}$	2.37 $\mu\text{m}$
6	0.80 $\mu\text{m}$	1.19 $\mu\text{m}$
7	0.40 $\mu\text{m}$	0.59 $\mu\text{m}$
8	0.20 $\mu\text{m}$	0.30 $\mu\text{m}$
9	0.10 $\mu\text{m}$	0.15 $\mu\text{m}$
10	0.05 $\mu\text{m}$	0.07 $\mu\text{m}$

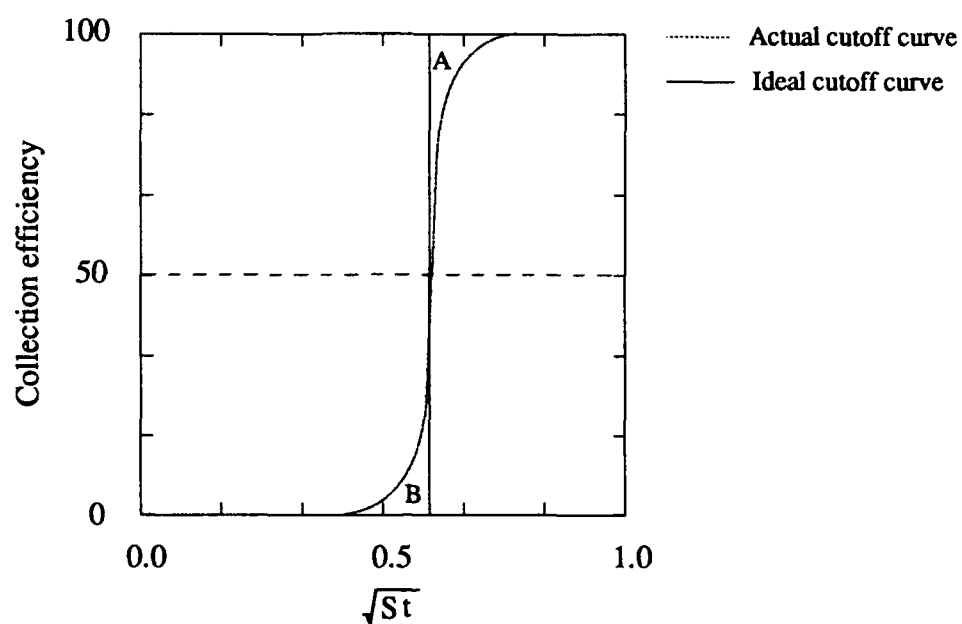


Figure 5.2 Comparison of actual and ideal cutoff curves for the cascade impactor. Areas A and B denote regions of discrepancy between ideal and actual values.

We used the bulk fog-oil density in the cut-size calculations. Since the oil is not chemically transformed in the smoke generator, this is a reasonable assumption. The HC density is taken from Katz et al. (1980b). Since the HC smoke is a combustion product that is composed of many chemical constituents, the assumed density may be subject to some error. The major combustion product of the HC smoke mixture is zinc chloride, which is a hygroscopic material. Hygroscopic effects on the HC smoke particle size distribution and particle density are currently unresolved.

In the operation of an impactor, it is assumed that particle trajectories which intersect the collection plate are removed from the sampling stream. For liquid particles, such as fog-oil, this is a reasonable assumption, and we used the instrument with uncoated collection plates. Dry particles, on the other hand, may bounce off the plates and pass through to lower stages. This problem is averted for the HC aerosol by coating the collection plates with a solution of Apezion-L grease in hexane and allowing the hexane to evaporate, leaving a very thin layer of sticky grease to collect the dry particles. The effect of various collection substrates and coatings on the collection efficiency is discussed by Rao and Whitby (1978). They conclude that sticky impermeable collection surfaces provide the best agreement with theoretical collection efficiency curves for dry aerosol particles.

### 5.2.2 Aerosol Particle Size Distributions

Most single source particle size distributions follow a lognormal distribution (the logarithm of the particle diameter follows a normal distribution). A particle size distribution can be considered as a count distribution, or a mass weighted distribution, as measured in the cascade impactor. These distributions are quite different for a polydisperse aerosol. If the count distribution is given by  $p(d_p)dd_p$ , then the mass distribution is given by

$$p_m(d_p) dd_p = \frac{d_p^3 p(d_p) dd_p}{\int_0^{\infty} d_p^3 p(d_p) dd_p} \quad (5.2)$$

For the purpose of our measurements, we may characterize the aerosol size by a mean and a variance. The most appropriate mean for the expected log-normal distribution is the geometric mean  $d_g$  defined by

$$\ln d_g = \frac{\sum n_i \ln d_i}{N} \quad (5.3)$$

Other mean values include the mode  $\hat{d}$  (most frequently occurring diameter), the count mean diameter  $\bar{d}$ , the count median  $\bar{d}_{50}$  (equal to  $d_g$  for a lognormal distribution), the diameter of average mass

$d_m$  (that diameter, when multiplied by the total number of particles, gives the total mass), the mass median diameter  $\bar{d}_{m50}$  (50% point of the mass weighted distribution), or the mass mean diameter given by  $\bar{d}_{mm}$ . The variance is characterized by the geometric standard deviation

$$\ln \sigma_g = \left[ \frac{\sum n_i (\ln d_i - \ln d_g)^2}{N - 1} \right]^{1/2} \quad (5.4)$$

which is the standard deviation of the logarithm of the particle diameters. The saving grace of the lognormal distribution is that all weighted distributions will also be lognormal and all will have the same geometric standard deviation. For the lognormal distribution, given  $\sigma_g$  and one mean quantity, all other positional values may be found using conversion equations derived by Hatch and Choate in 1929 as discussed in Hinds (1982).

As shown in Figures 5.3 and 5.4 our measured data follow the profile of the lognormal distribution for both for fog-oil smoke and HC smoke. Both figures are shown on lognormal axes, for which a lognormal distribution yields a straight line. Representative average values are presented in terms of the mass median diameter  $\bar{d}_{m50}$  and the geometric standard deviation  $\sigma_g$  in Table 5.2. The standard deviation in the data is indicated by a multiplicative value  $\sigma(\text{mult})$ , also given in this table. Other average values are found using the analytical conversions given by Hinds (1982) for a lognormal distribution. These are presented in Table 5.3 using averages of the data taken in our tests. It is evident from this table that a larger value of  $\sigma_g$  produces a wider separation in the weighted particle diameters. Mean values, such as the count mode, which occur at the limits of the measurement range for our instrument as given in Table 5.1, are likely to be in the greatest error.

Our measured values of the particle distribution can be compared with previous measurements. For a study of fog-oil smoke in 1985 at Dugway Proving Grounds in Utah, we measured a  $\bar{d}_{m50}$  of  $0.7 \mu\text{m}$  with  $\sigma_g = 3.4$  using a 7 stage cascade impactor (In-Tox Products, Albuquerque, New Mexico). This median particle diameter is similar to that found in the Atterbury 1987 study, but there is a much broader distribution of particle sizes (larger  $\sigma_g$ ). Katz et al. (1980a) measured the fog-oil aerosol size distribution in the laboratory using a California Instruments PC-2 Impactor, and found  $\bar{d}_{m50} = 0.9 \mu\text{m}$  and  $\sigma_g = 1.5$ , which is reasonably consistent with our most recent field measurements.

For the HC smoke, Katz et al. (1980b) found a  $\bar{d}_{m50}$  of  $1 \mu\text{m}$  with  $\sigma_g = 2.5$  using an Anderson cascade impactor in a field test using smoke from a single 30 lb. M5-HC smoke pot. This is reasonably consistent with our field measurements. In laboratory measurements discussed in the same report, Katz found mass median diameters in the range of  $0.3 \mu\text{m}$  to  $0.4 \mu\text{m}$  when 12 g

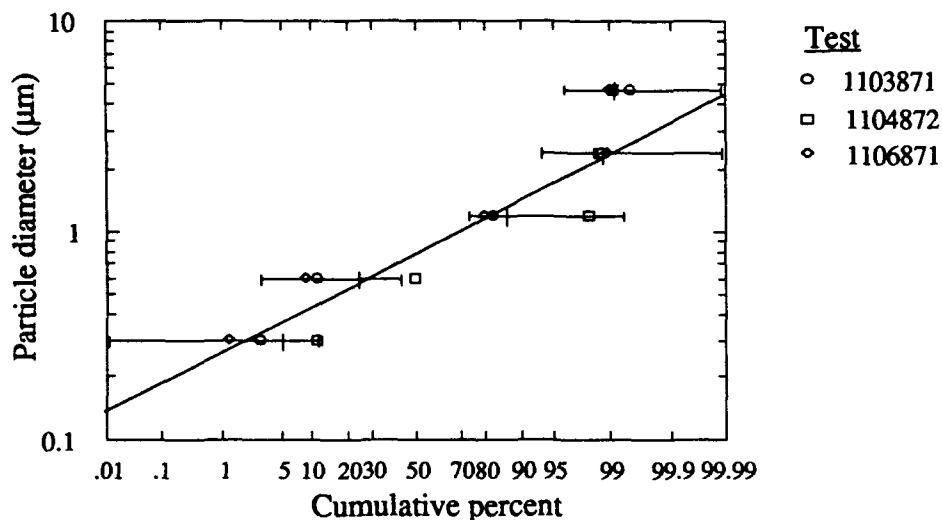


Figure 5.3 Particle size distributions for fog-oil smoke measured in the Camp Atterbury field tests. The normalized mean and standard deviation of the mass percent collected on each stage is shown by the error bars. The solid lines indicate the best fit of this data to a lognormal distribution.

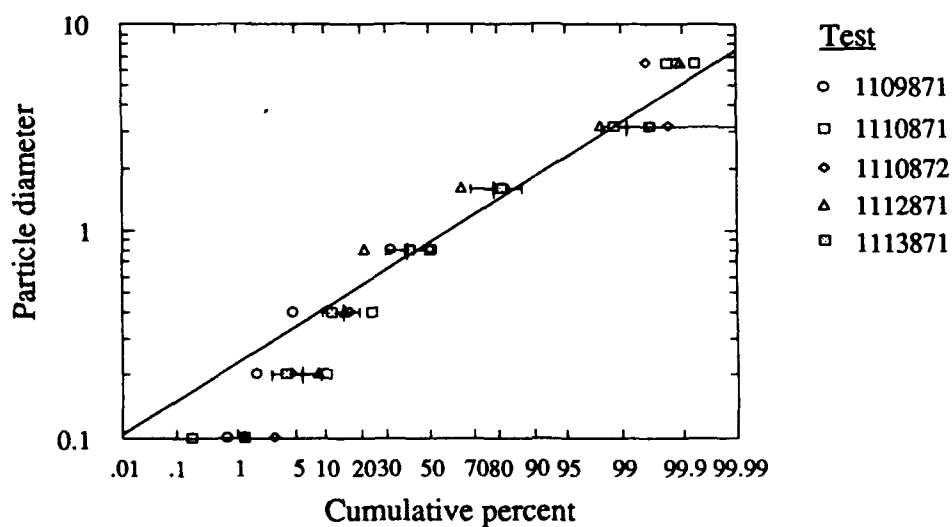


Figure 5.4 Particle size distributions for HC smoke measured in the Camp Atterbury field tests. The normalized mean and standard deviation of the mass percent collected on each stage is shown by the error bars. The solid lines indicate the best fit of this data to a lognormal distribution.



of reagent was burned in an enclosed chamber. Differences between the laboratory and field results in their work can be attributed to the different combustion temperatures for the widely different masses of reagent in the two experiments.

Table 5.2 Measured particle size parameters for the lognormal distribution. The value of  $\bar{d}_{m50}$  is multiplied by  $\sigma(\text{mult})$  to find +1 standard deviation and is divided by  $\sigma(\text{mult})$  to find -1 standard deviation from the mean value.

Test	Smoke	$\bar{d}_{m50}$	$\sigma(\text{mult})$	$\sigma_g$	$\sigma(\text{mult})$
1103871	fog-oil	0.86	1.16	1.55	1.09
1104872	fog-oil	0.56	1.07	1.71	1.08
1106871	fog-oil	0.90	1.05	1.53	1.10
average	fog-oil	0.71	1.23	1.50	1.16
1109871	HC	0.99	1.31	1.78	1.25
1110871	HC	0.73	1.09	2.36	1.12
1110872	HC	0.78	1.10	2.07	1.13
1112871	HC	1.05	1.21	2.41	1.10
1113871	HC	0.88	1.13	2.05	1.08
average	HC	0.71	1.24	2.10	1.27

Table 5.3 Calculated particle diameters for fog-oil smoke and HC smoke using the Hatch-Choate equations for the lognormal distribution.

Value	Symbol	Fog-oil data	HC smoke data
Geometric standard deviation	$\sigma_g$	1.50	2.10
Count mode	$\hat{d}$	0.37 $\mu\text{m}$	0.10 $\mu\text{m}$
Count median diameter	$\bar{d}_{50}$	0.43 $\mu\text{m}$	0.17 $\mu\text{m}$
Count mean diameter	$\bar{d}$	0.47 $\mu\text{m}$	0.22 $\mu\text{m}$
Diameter of average mass	$\bar{d}_m$	0.55 $\mu\text{m}$	0.39 $\mu\text{m}$
Mass median diameter	$\bar{d}_{m50}$	0.71 $\mu\text{m}$	0.88 $\mu\text{m}$
Mass mean diameter	$\bar{d}_{mm}$	0.77 $\mu\text{m}$	1.16 $\mu\text{m}$

## 5.3 Fog-oil Smoke

Two types of smoke were used in our dispersion tests. The greatest number of tests were carried out using fog-oil smoke. This smoke is produced using a US Army M3A4 Smoke Generator which vaporizes the oil in an engine exhaust manifold. The exhaust cools and condenses to form an aerosol with a mean particle size of roughly  $1\text{ }\mu\text{m}$ . The chemical nature of the smoke droplets is similar to the bulk oil. Details of the source configuration, the dosage sampling and analysis methods, and an error analysis of these measurements are included in this section.

### 5.3.1 Source Characteristics and Measurements

For purposes of assessing the dispersion of pollutants or tracer material into the atmosphere, several specifications of the source are necessary. These include the location of the source, the exit temperature and velocity of the material leaving the source, the release rate of material, and a characteristic size of the exit plume. Most of these parameters can be used to assess the deviation from an ideal point source in terms of the momentum, buoyancy and initial size of the source.

The smoke generator we have used in the fog-oil dispersion experiments at Camp Atterbury and Meadowbrook was a US Army M3A4 Smoke Generator. The major components of the generator are an oil pump and a small gasoline powered pulse-jet engine. Oil is injected into the jet engine exhaust manifold, beyond the combustion area, at a rate of 95 to 227 liters per hour. It vaporizes in the hot engine and rapidly condenses into a heavy, white fog when blown from the exhaust ports into the atmosphere. Figure 5.5 shows a diagram of the exit region of this smoke generator.

The hydrocarbon oil used in the generators is similar in properties to 10W motor oil. The distillation temperature of the fog-oil ranges from  $200^{\circ}\text{C}$  at 10% distillation to  $320^{\circ}\text{C}$  at 90% distillation by volume. It consists of several thousand individual chemical constituents. Our laboratory and field tests indicate that the properties and chemical composition of the smoke are the same as the bulk oil, although the low resolution of our chemical separation technique may obscure subtle changes. The release rate of oil was typically between 25 to 50 g/s for the M3A4 with most of the variance due to the variable performance of the oil pump and the widely changing viscosity of the oil with ambient temperature.

The smoke leaves the generator through three, 1.9-cm diameter ports which point upward at an angle of  $45^{\circ}$  with respect to the ground. The center port points straight ahead and the side ports are angled away from the centerline at an angle of  $20^{\circ}$ . The exit velocity varies between 65 and 80 m/s as measured with a pitot-static probe and corrected for density variations. The three individual jets merge to form a single jet within a distance of roughly 1 m. The exhaust just leaving the ports

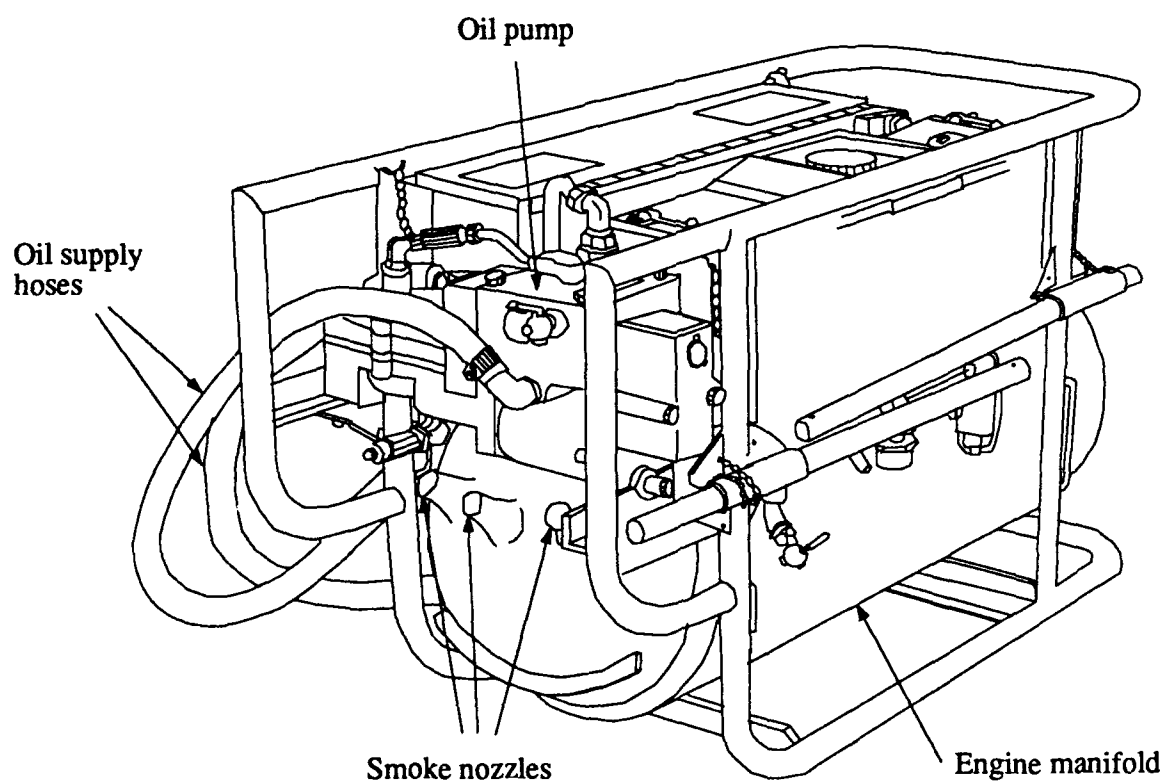


Figure 5.5 Diagram of the US Army M3A4 fog-oil smoke generator.

is clear in color, but within 5 cm from each exhaust port the oil vapor condenses into a dense white cloud. The larger single plume beyond the joining of the three single jet plumes is about a meter across and is nearly cooled to the ambient temperature. Smoke from the generator, outside of a half meter from the exhaust is dry to the touch and includes very few large oil droplets. Within several meters of the jet exhaust exits, the momentum and buoyancy is dissipated by the dilution and mixing in the atmosphere. In the field these generators, along with the associated measuring and recording instrumentation, were operated from the bed of a pickup truck .

Instrumentation of the fog-oil smoke source included continuous exit temperature and release rate measurements. Type K (chromel/alumel) thermocouples were used to measure the temperature at each of the three exhaust ports. All three ports exhibited the same trends in temperature but actual values were sensitive to the position of the thermocouple relative to the jet. The oil release rate was calculated by digitally logging the weight of the 55-gallon oil supply drum. In software we finite difference this signal and low pass filter with a 60-s time constant to get a continuous release rate. These measurements were made at 1-s increments over the duration of the test and logged using a Campbell Scientific 21X micrologger. The micrologger was connected to a Zenith Z-181 portable computer which recorded the digital data to floppy disk. In addition, the wind velocity, wind direction, and ambient temperature were recorded at a 2-m height for all fog-oil tests. Records of the fog-oil release rate and generator exit temperature are given in Figure 5.6 and Table 5.4. These are presented in groups for the Atterbury Tests, the unstable Meadowbrook Tests, and the stable Meadowbrook Tests. Overall, the release rate is fairly steady for many of these tests, except for some isolated periods during which problems in the mechanical operation of the generator occurred. Plots of release rate are not given for Tests 1103871, 0921871 and 1002871, because the recording equipment failed in these experiments.

### **5.3.2 Analysis Methods for the Mean Dosage Samples of Fog-oil Smoke**

The fog-oil smoke consists mainly of liquid aerosol droplets less than 1  $\mu\text{m}$  in diameter. Only a small fraction of the relatively nonvolatile oil exists as a vapor. A method for quantifying the total dosage of the fog-oil smoke at sampling points within the plume is presented in this section. This method is an improvement on an earlier method (DeVaul, 1985).

#### **Background of Oil Aerosol Analysis Methods**

The concentration of oil aerosol in air has routinely been determined using fluorescent emission from the oil as described in papers by Ray (1970), Houghton and Lee (1960), and in NIOSH (National Institute for Occupational Safety and Health) Method P&ACM 159 (1977). A variation

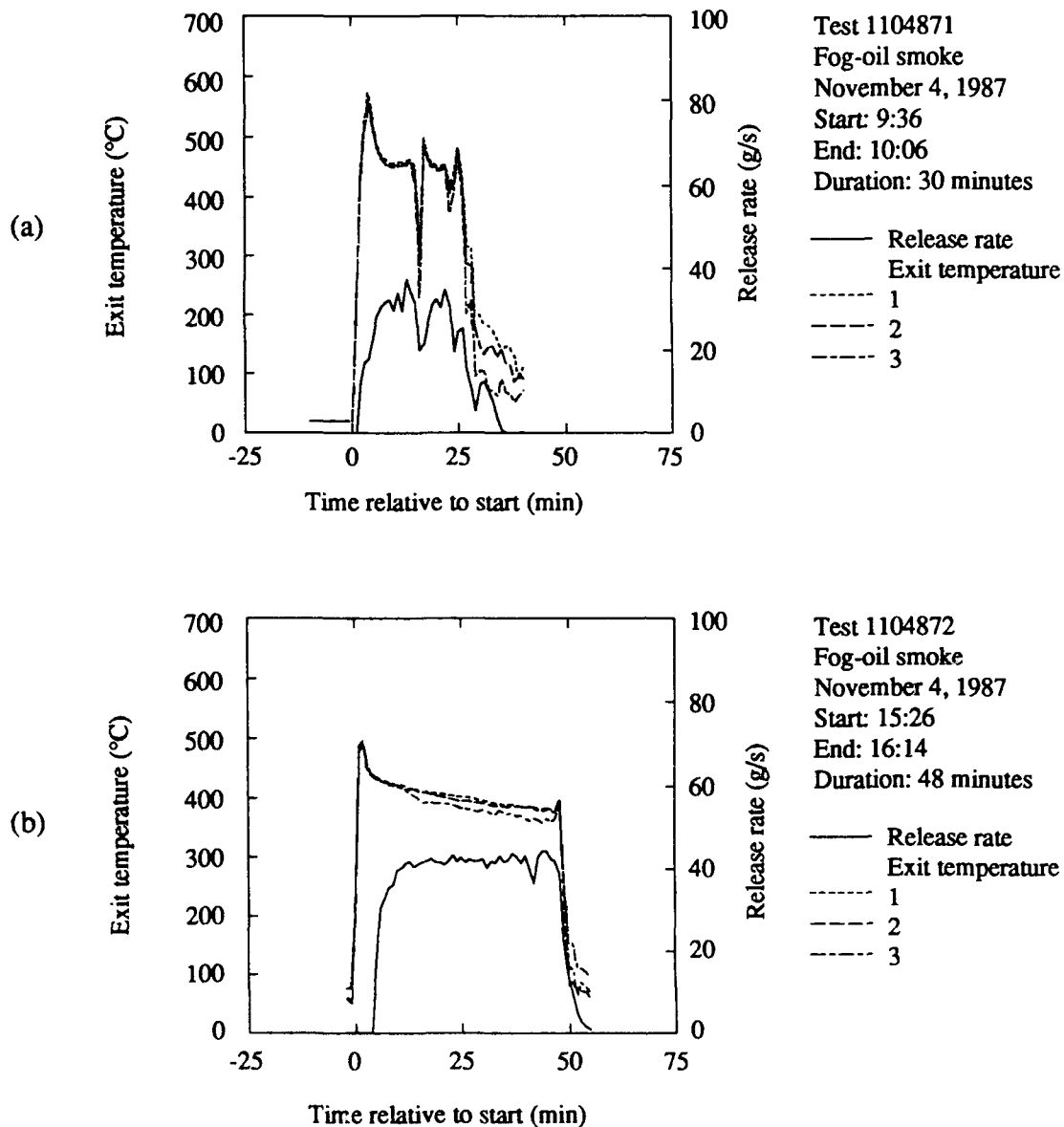


Figure 5.6 Release rate and exit temperature histories for the fog-oil smoke generator at Camp Atterbury for (a) Test 1104871 and (b) Test 1104872.

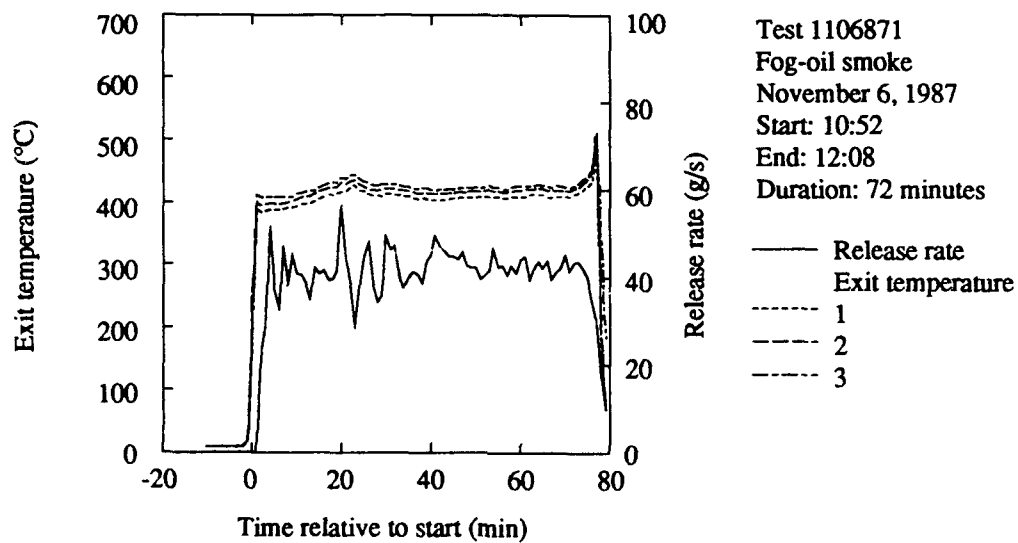


Figure 5.6 (continued) Release rate and exit temperature histories for the fog-oil smoke generator at Camp Atterbury for Test 1106871.

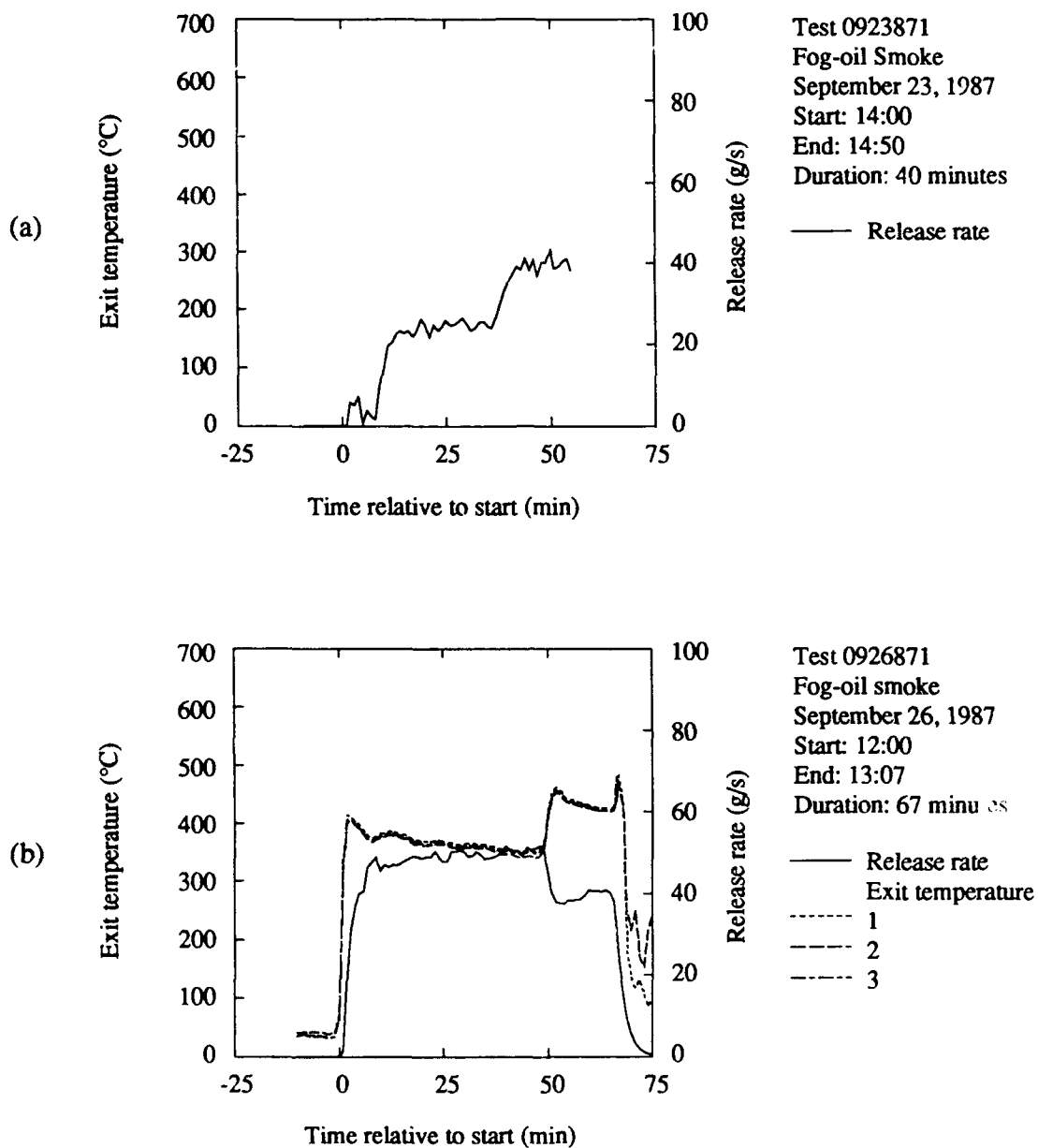


Figure 5.6 (continued) Release rate and exit temperature histories for the fog-oil smoke generator at Meadowbrook during the daytime unstable dispersion tests for (a) Test 0923871 and (b) Test 0926871.

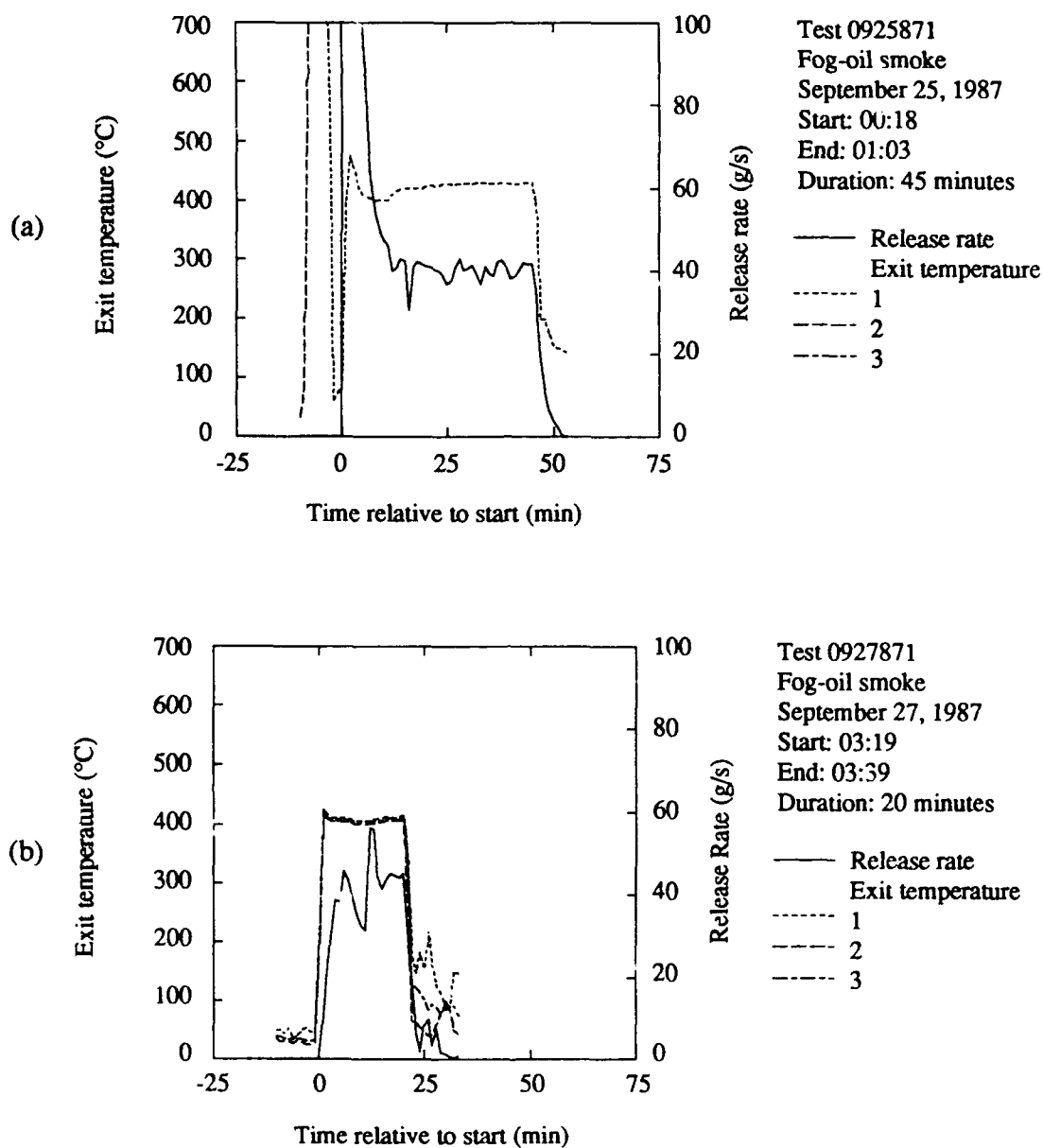


Figure 5.6 (continued) Release rate and exit temperature histories for the fog-oil smoke generator at Meadowbrook during the nighttime stable dispersion tests for (a) Test 0925871 and (b) Test 0927871.



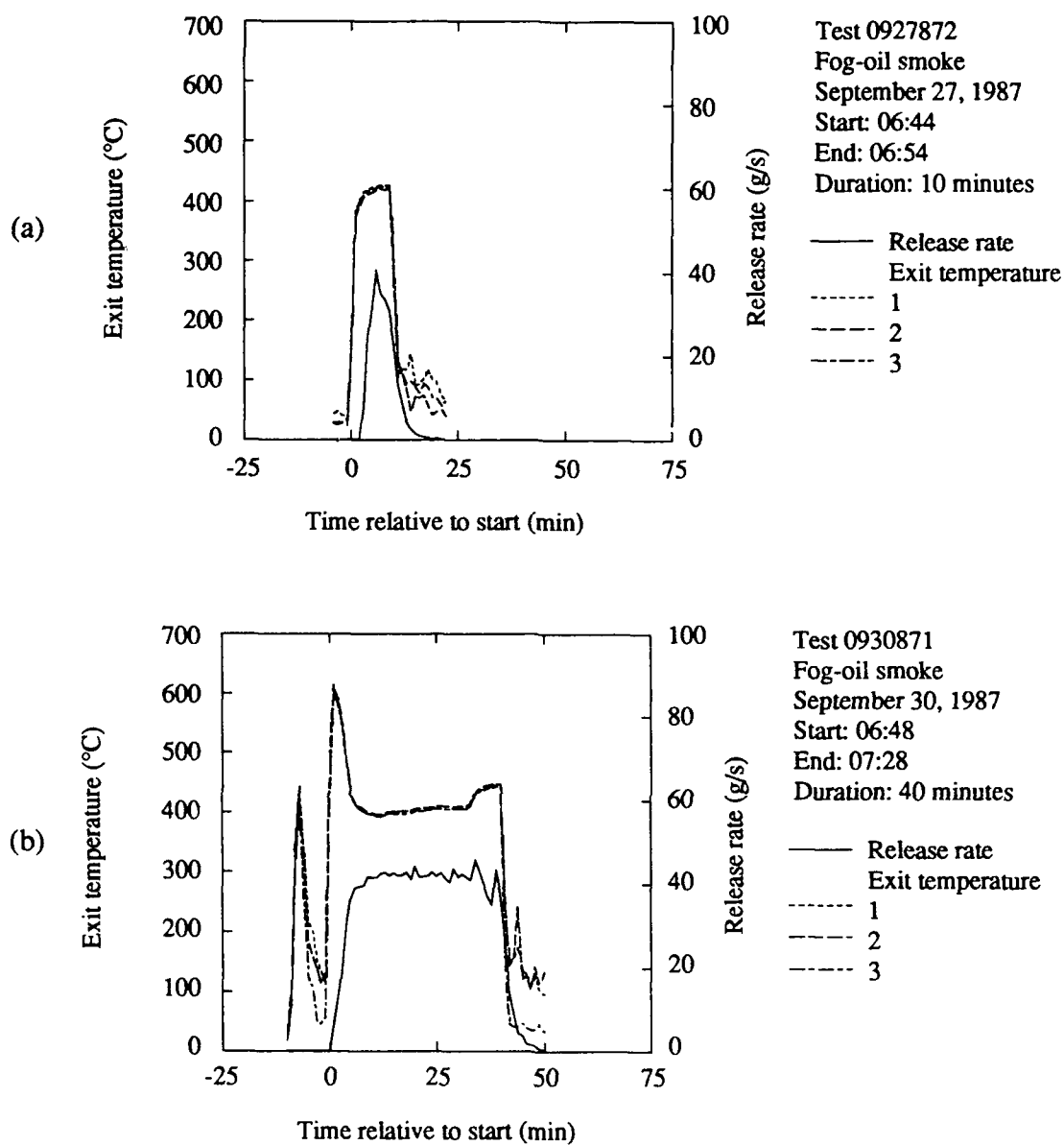


Figure 5.6 (continued) Release rate and exit temperature histories for the fog-oil smoke generator at Meadowbrook during the nighttime stable dispersion tests for (a) Test 0927872 and (b) Test 0930871.

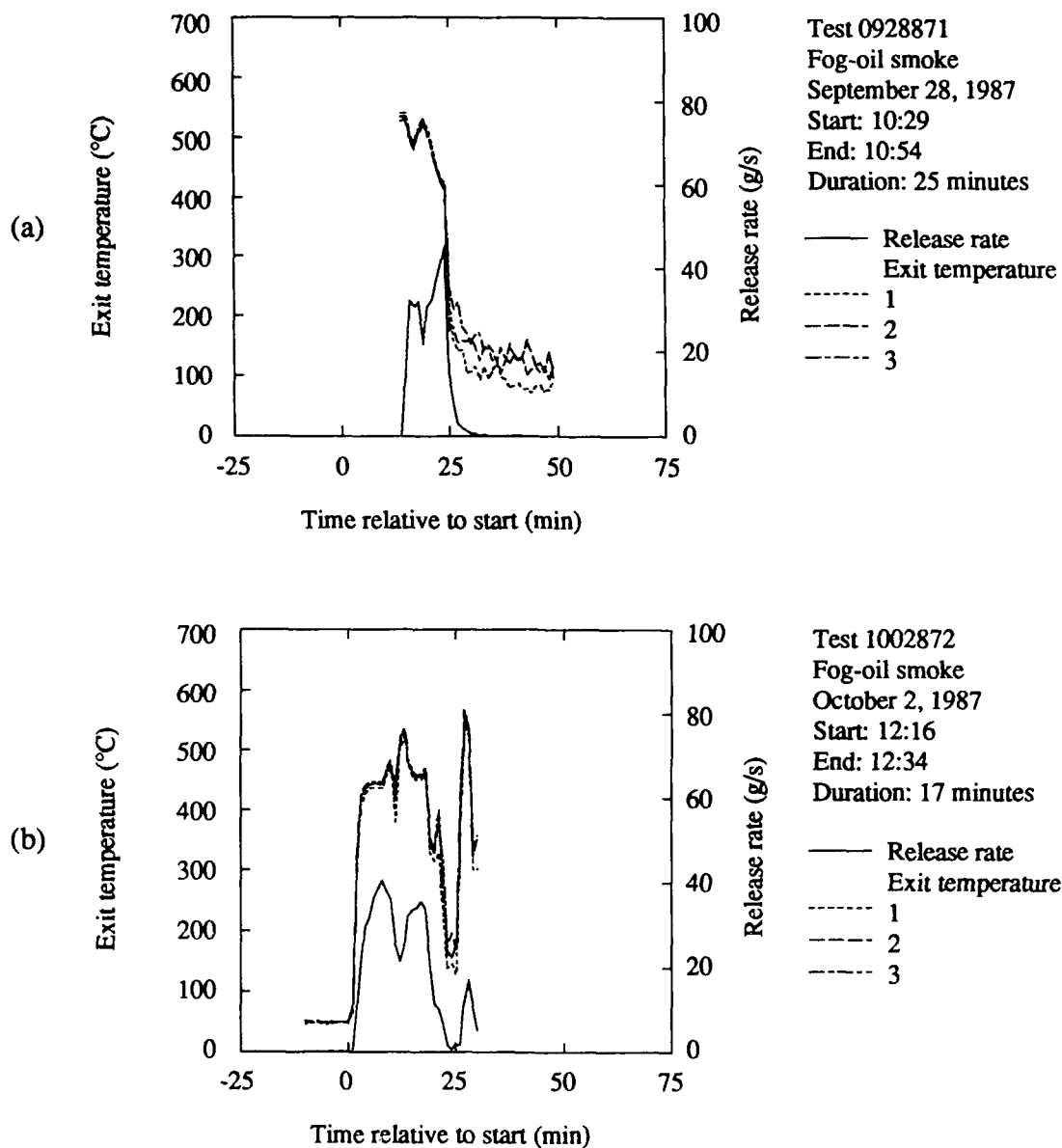


Figure 5.6 (continued) Release rate and exit temperature histories for the fog-oil smoke generator at Meadowbrook during the daytime unstable dispersion tests for (a) Test 0928871 and (b) Test 1002872.

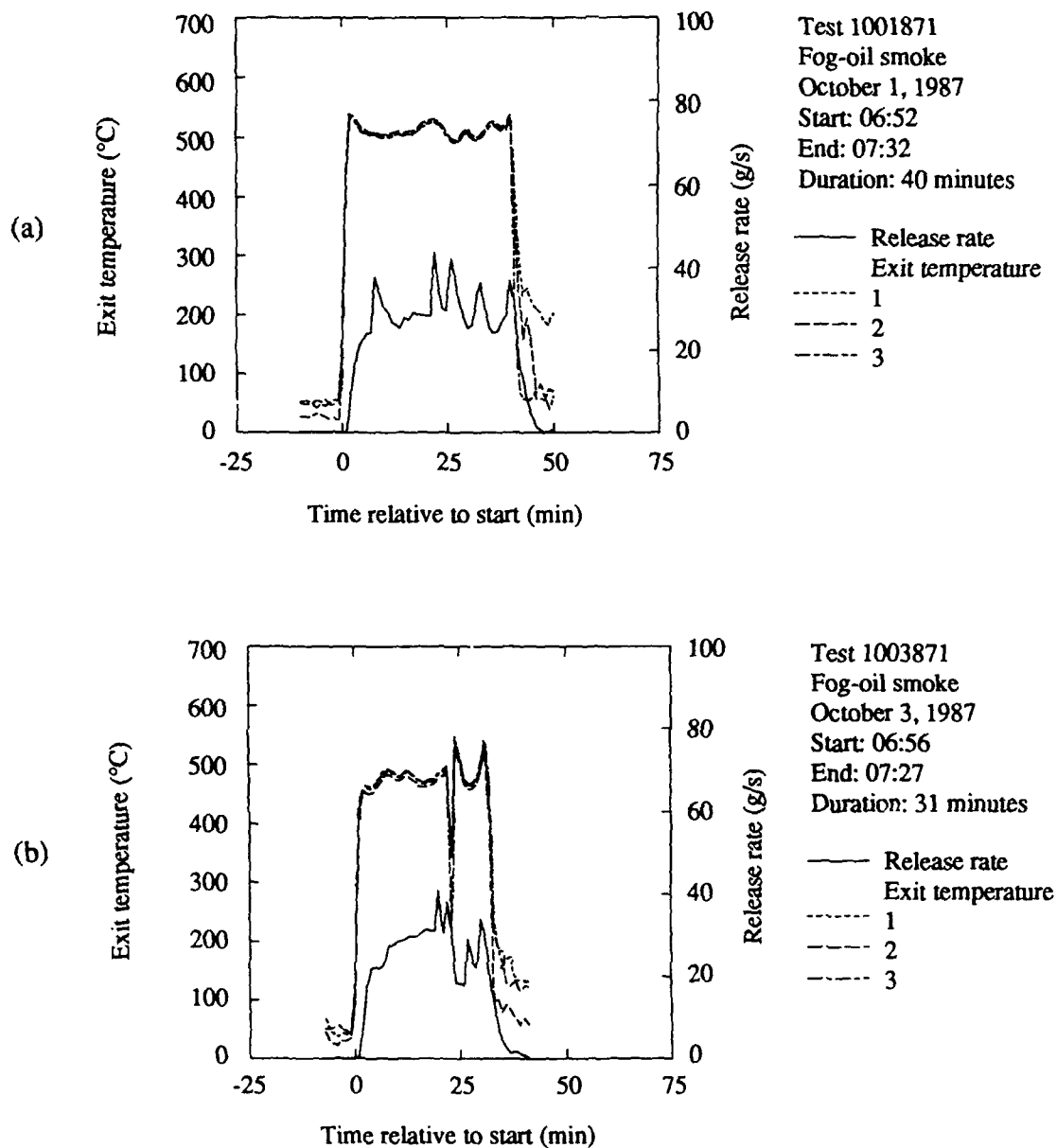


Figure 5.6 (continued) Release rate and exit temperature histories for the fog-oil smoke generator at Meadowbrook during the nighttime stable dispersion tests for (a) Test 1001871 and (b) Test 1003871.

Table 5.4 Mass release rates for the fog-oil smoke generator. The rate given for Test 0921871 is an estimate because the mass of oil was not recorded.

Test	Duration (min)	Mass released (kg)	Release rate (g/s)
Atterbury			
1103871	55.0	115.9	34.6
1104871	29.0	44.0	26.7
1104872	48.0	117.8	40.7
1106871	76.0	193.0	42.2
Meadowbrook - Unstable			
0921871	30.0	-	26.3 (est.)
0923871	40.0	63.0	26.3
0926871	67.0	181.2	45.1
0928871	25.0	49.1	32.7
1002872	17.0	35.0	34.3
Meadowbrook - Stable			
0925871	45.0	109.0	40.4
0927871	20.0	53.4	44.5
0927872	10.0	20.8	34.7
0930871	40.0	97.0	40.4
1001871	40.0	71.8	29.9
1002871	30.0	73.4	40.8
1003871	31.0	52.4	28.2

of this method was used by Barad and Shorr (1958) in a series of fog-oil smoke dispersion experiments. In a typical application, an air sample is collected on an aspirated cellulose membrane filter, extracted in chloroform, and the fluorescence of the chloroform solution is measured in a spectrophotometer. Oil samples in the range 0.005 to 0.5 mg can be measured with this method. A bulk sample of the oil is needed for calibration purposes to determine the fluorescence spectra of the oil. Chemical changes in the oil, which may occur during the generation process, cannot be determined with this method, and interferences are possible from other fluorescent material in the atmosphere.

A more chemically selective method for collecting organic vapor samples uses tubes filled with activated charcoal. After exposure, the organic material is extracted from the charcoal with carbon disulfide and analyzed by gas chromatography. This method was used by Fraust and Hermann (1966), Reid and Halpin (1968), and White et al. (1970) for sampling organic vapors

and is described in NIOSH method P&CAM 127 (1977). It has a sensitivity of 0.01 mg to 0.1 mg of sample for many types of organic compounds. Jenkins et al. (1982, 1983) have successfully used a variation of the carbon-disulfide extraction procedure for analyzing diesel-fuel smoke collected on both filters for the aerosol and using adsorbent tubes for the vapor collection. This method employs a capillary column sufficient for separating the oil sample into its chemical constituents. This analysis method will aid in determining the chemical composition of the oil, but is unsuitable for analyzing a large number of samplers because of the analysis time required.

An alternative method for analysis of fog-oil samples is described in this section. The intent of this method is to maintain the accuracy and sensitivity of the previously mentioned procedures while reducing the analysis time. In this method, fog-oil is thermally vaporized from a collected sample, swept onto an analysis column, and analyzed by gas chromatography. This allows the gross chemical composition of the sample to be determined. Both glass-fiber filters for collecting the aerosol, and absorbent filled tubes for collection of vapor may be used with this method. A sensitivity of 0.01 mg total mass of fog-oil has been achieved, and samples up to 20 mg can be analyzed easily. Larger samples are measured by analyzing a fraction of the filter.

The hardware needed for this system is very similar to that used in the thermal desorption of gases and vapors from adsorbent tubes for analysis by gas chromatography, except that the relatively non-volatile fog-oil requires much higher operating temperatures. Several representative methods for thermal desorption of vapors with gas chromatography are described by Russell and Shadoff (1977), Russell (1975), Gelbicova-Ruzickova et al. (1972), Novak et al. (1965), and Cropper and Kaminsky (1963), all of which use an apparatus separate from the gas chromatograph for heating the collected sample. In systems used by Zlatkis et al. (1973) and Bertsch et al. (1974), the injector heater within the gas chromatograph was employed for desorbing the samples. The method described in this paper also employs the injector heater of the gas chromatograph. This helps avoid problems of condensing vapor within the chromatographic system, since the vapor proceeds from the injector directly into the chromatograph oven. Any cool spots in the sample path, which can easily occur for systems which employ a heated transfer line, could allow the relatively nonvolatile fog-oil to condense and foul the system.

### **Analysis System**

The gas chromatograph used is a Perkin-Elmer Sigma 300. A Perkin-Elmer LCI-100 Laboratory Computing Integrator and a Perkin-Elmer 7500 computer is used for data acquisition as well as for automated valve switching. A schematic of the valve and regulator arrangement of the system is shown in Figure 5.7.

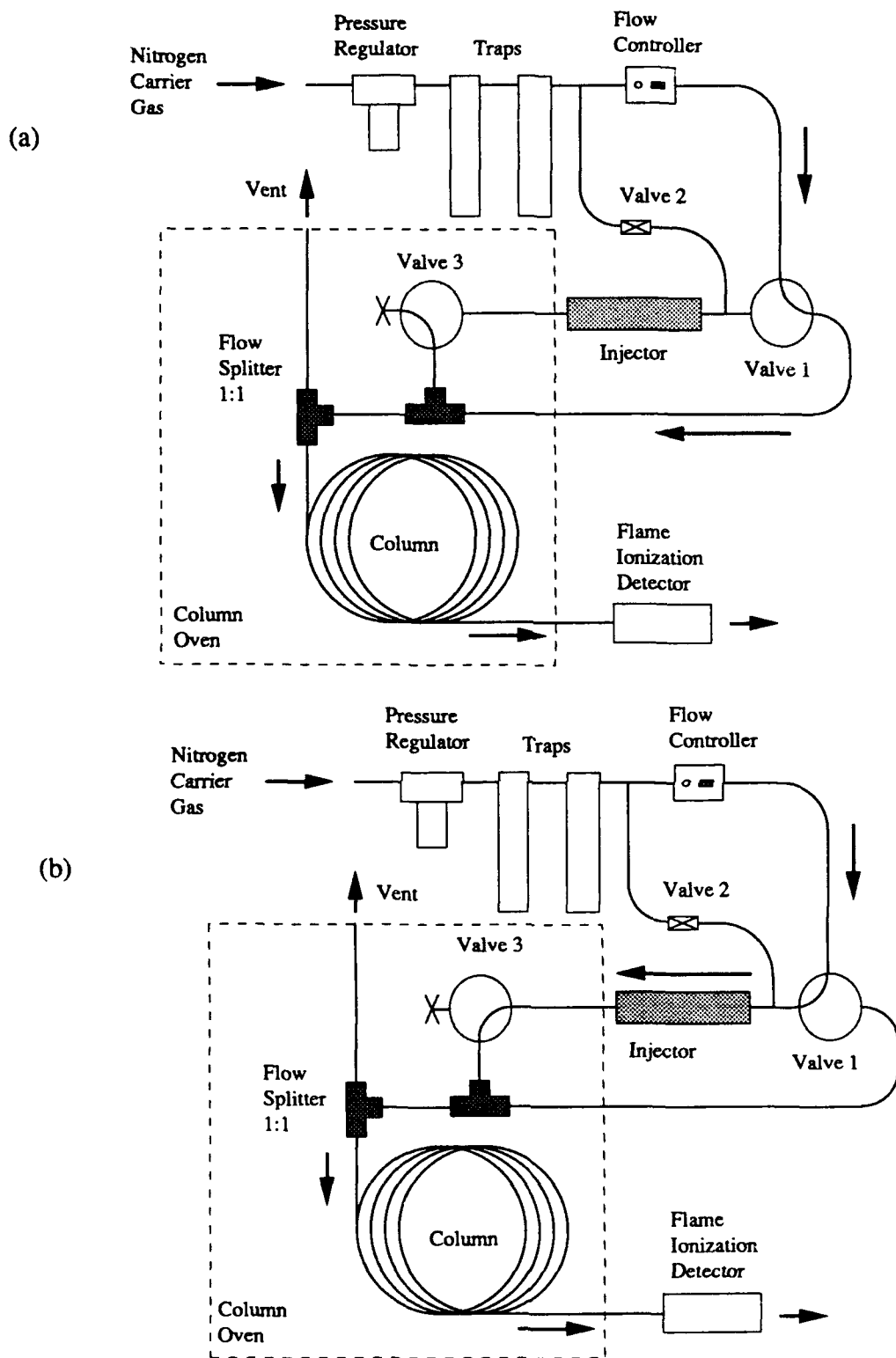


Figure 5.7 Gas chromatograph schematic. The proper valving and carrier gas path is shown (a) between analyses and (b) during an analysis.

Nitrogen carrier gas passes through a two-stage regulator, several purification traps, then through a laminar element flow controller. From the flow controller, the carrier gas is routed to Valve 1 which switches the flow either through the injector or directly onto the column. Modification of the injector on the gas chromatograph to accommodate filter or adsorption tube samples was accomplished by removing the glass liner and spring from the injector body. A stainless steel sample tube 0.63 cm in diameter and 8.9 cm long could then fit within the injector body. The standard carrier gas inlet to the injector was capped. A 1/4-in Swagelock fitting, through which carrier gas is supplied, replaces the septum and septum cap on the injector.

Valve 3, located within the chromatograph oven, is a Valco Instruments three port rotary valve for high temperature use. This valve is pneumatically actuated by two solenoid-controlled valves located outside the chromatograph oven. Valves are in the position shown in Figure 5.7(a) at the start of an analysis. The injector port may be opened for insertion or removal of a sample without interruption of carrier gas flow. After passing through Valve 3, the carrier gas flow runs through a 1:1 splitter and onto a stainless steel column 4 ft. in length and 1/8 inch in diameter which is packed with 3% Dexsil 300 on 100/120 mesh Chromasorb W-HP. The elutant from the column is analyzed in a flame ionization detector.

### **Sample Analysis**

For analysis of a sample, the injector port is opened, a sample is inserted into the injector, and the Swagelock fitting is replaced and tightened. Valve 2 is manually opened for a short interval to pressurize the injector port to the same level as the column head pressure and then closed. The analysis is then immediately started. The oven temperature program is given in Table 5.5.

At the start, valve 3 is switched and pressure in the injector body and column head equalizes. Valve 1 is then switched to direct carrier gas through the sample tube, and sample is carried onto the column. During an analysis the valves remain in this position, as shown in Figure 5.7(b). Valves 1 and 3 are switched back to their original position (Figure 5.7(a)) after all sample components have eluted from the column. A flow splitter is used in order to maintain a high flow rate through the injector, and an optimum flow rate through the column.

### **Fog-oil Sampling Methods**

Two basic sampling methods are used in the collection of fog-oil smoke. Glass fiber filters are used to collect the droplet fraction of smoke, and stainless steel tubes, filled with Tenax-GC adsorbent and mounted in series behind a filter, are used to collect the vapor fraction of the fog-oil.

Table 5.5 Key parameters of gas chromatography method used to analyze fog-oil smoke vapor samples

Chromatograph:	Perkin -Elmer Sigma 300 with LCI- 100 Integrator and Model 7500 Computer
Detector:	Flame Ionization
Column:	4 ft., .25 in OD, 3% Dexsil 300 GC on Chromasorb WHP
Temperatures:	
Modified Injector	300 °C
Detector	350 °C
Column	
Initial	150 °C *
Ramp	25 °C/min.
Final	330 °C for 5 min.
Carrier gas:	Ultra-pure Nitrogen
Flow rates:	
Column	35 ml/min
Inlet	70 ml/min
Split ratio	1 : 1
Desorption time:	
Start.....	0.0 min
End .....	15 min
Analysis time:	12 min.
Cycle time:	16 min.

\* The initial oven temperature is decreased to 100 °C for analysis of the more volatile fog-oil vapor samples.

The body of the absorbent-filled stainless steel tubes we are using are 0.63 cm outside diameter, 0.46-cm inside diameter, and 8.9 cm long. A circumferential groove is pressed into the tube 1.5 cm from one end, leaving a ridge on the inside of the tube. A 0.47 cm diameter 100 mesh stainless steel screen is seated on this groove and the tube is filled with 0.20 g of 60/80 mesh Tenax GC adsorbent. A second screen is pressed into the tube to a depth of 0.7 cm. This give a 6.7 cm long bed of absorbent in each tube. These adsorbent samplers are inserted into the chromatograph injector for analysis by thermal desorption.

The adsorbent samplers must be conditioned before use by heating and purging the tenax with carrier gas. This is done in the gas chromatograph injector by allowing carrier gas to flow



through a tenax-filled tube until all the extraneous volatiles are desorbed from the adsorbent. About thirty minutes of conditioning is usually adequate for each tube.

For sampling the aerosol, 37-mm diameter cassettes packed with glass-fiber filters are used. The filters are removed from the cassettes after exposure, folded, and inserted into the injector for analysis. Glass fiber filters (binderless) are the only filter types which will not decompose in the high heat of the thermal desorption. The greatest fraction of samplers in our dispersion tests were filter samples.

If the glass-fiber filters are not analyzed within several days after exposure to the oil smoke, significant losses of oil from the filter can occur. Although evaporation occurs, the majority of the oil loss may be attributed to wicking of the oil from the filter onto parts of the cassette housing. For our samples, an empirical factor is used to correct for such losses. Alternatively, transferring the folded glass-fiber filters into empty stainless steel tubes of the same dimensions as the tenax sampling tubes and storing the stainless steel tubes within glass screw top test tubes was found to reduce these losses to a negligible fraction of the total mass. Our analysis presented later in this section demonstrates that filters stored in this manner have shown no significant changes in the mass of oil on the sample after a year of storage. However, we were not able to employ this conservative storage method because of the labor required to pack the stainless steel tubes and the large number of samplers collected in each of the dispersion tests.

### **Data Analysis**

Chromatograms produced using this method give a qualitative molecular weight distribution of the oil. Similar chromatograms are generated with ASTM Method 2887 (1982) for petroleum fractions and ASTM Method 3710 (1982) for gasoline fractions. The basic principles are described by Adlard in Heftman (1983). A fog-oil chromatogram produced with this method is shown in Figure 5.8.

It is necessary to analyze a series of n-paraffins under the same operating conditions as the fog-oil samples to get qualitative results of the fog-oil composition. Using the elution times for these known n-paraffins as shown in Figure 5.8 (the elution times increase for increasing molecular weight, boiling point, etc. for n-paraffins), the time axis of the chromatogram may be rescaled in terms of carbon numbers in the n-paraffins, or the boiling point of the n-paraffins. From this rescaling of the time axis, molecular weight distribution and a distillation curve for the fog-oil sample may be determined, if desired. This is shown in Table 5.6. For total mass measurement such as required for our sample analysis, the chromatograph is calibrated with known quantities of oil, and the total integrated area under the entire chromatogram is scaled.

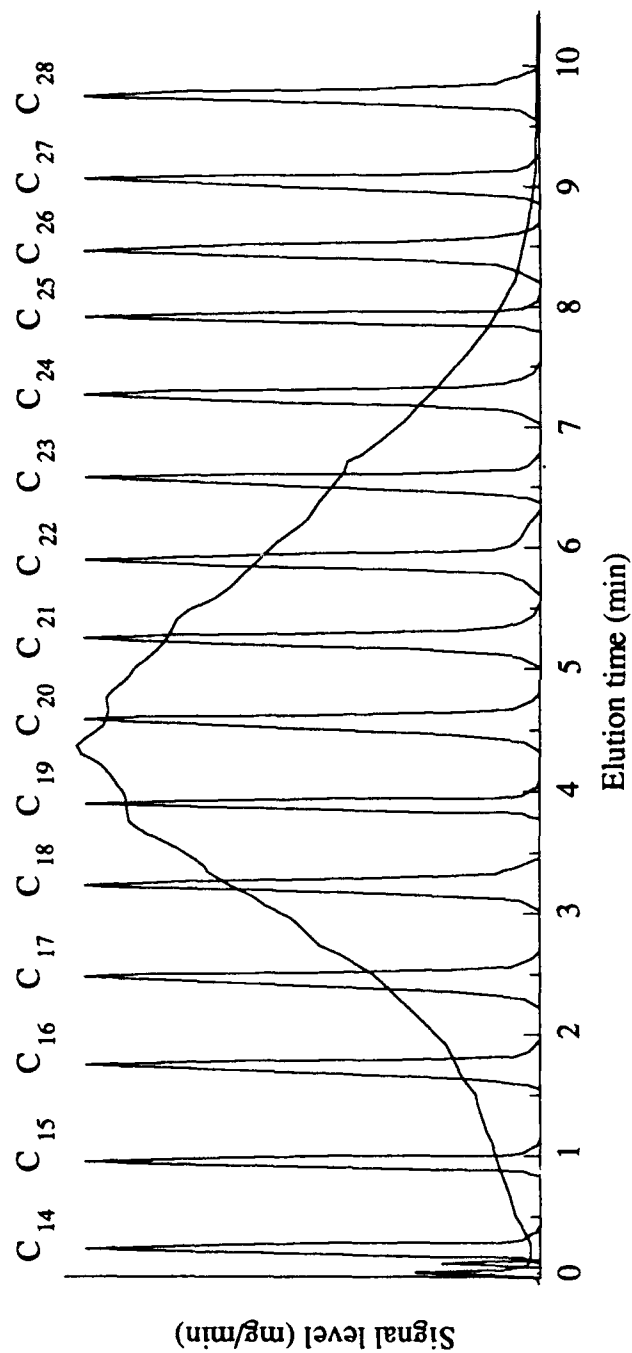


Figure 5.8 A chromatogram of fog oil overlaid with a chromatogram of a series of n-Paraffin oils. The n-Paraffins are discrete peaks, and the fog oil is a continuous band. These runs were made at an initial temperature of 150° C and an oven ramp rate of 25°C/min.

Table 5.6 Approximate fog-oil molecular weight distribution. The retention times are for an initial oven temperature of 150°C and a ramp rate of 25°C/minute.

Chemical name		Boiling point (°C)	Retention time (min)	Equivalent fraction of paraffin oil	Distillation fraction
n- Tetradecane	C <sub>14</sub> H <sub>30</sub>	253.6	0.2	0.019	0.019
n-Pentadecane	C <sub>15</sub> H <sub>32</sub>	270.5	1.0	0.034	0.053
n-Hexadecane	C <sub>16</sub> H <sub>34</sub>	286.5	1.8	0.053	0.106
n-Heptadecane	C <sub>17</sub> H <sub>36</sub>	301.7	2.6	0.079	0.186
n-Octadecane	C <sub>18</sub> H <sub>38</sub>	316.0	3.3	0.091	0.278
n-Nonadecane	C <sub>19</sub> H <sub>40</sub>	329.8	4.0	0.129	0.407
n-Eicosane	C <sub>20</sub> H <sub>42</sub>	343.0	4.6	0.121	0.529
n-Heneicosane	C <sub>21</sub> H <sub>44</sub>	355.7	5.3	0.110	0.639
n-Docosane	C <sub>22</sub> H <sub>46</sub>	368.1	5.9	0.095	0.734
n-Tricosane	C <sub>23</sub> H <sub>48</sub>	380.2	6.5	0.076	0.809
n-Tetracosane	C <sub>24</sub> H <sub>50</sub>	392.3	7.1	0.062	0.870
n-Pentacosane	C <sub>25</sub> H <sub>52</sub>	404.3	7.7	0.049	0.920
n-Hexacosane	C <sub>26</sub> H <sub>54</sub>	416.4	8.3	0.038	0.958
n-Heptacosane	C <sub>27</sub> H <sub>56</sub>	428.6	8.9	0.023	0.980
n-Octacosane	C <sub>28</sub> H <sub>58</sub>	441.2	9.6	0.011	0.992
n-Nonacosane	C <sub>29</sub> H <sub>60</sub>	454.2	10.2	0.008	1.000

### 5.3.3 Fog-oil Mean Concentration Error Analysis

#### Chromatograph Sensitivity and Calibration

Calibration and n-paraffin runs with this system are made by doping a clean, empty stainless steel tube with the liquid sample from a microsyringe, and analyzing the doped tube in the same manner as the field samples. For a large number of 1-mg calibration runs with this system, the standard deviation was found to be  $\sigma=0.109$ , and this accuracy is uniform over the usable range of the method. Background levels are found to be equivalent to 0.008 mg of oil. Using a level of  $2\sigma$  above the background level (a 6dB signal to noise ratio) establishes a minimum detectable mass of 0.015 mg for the analyzed sample. Because only half the filter is used in most of the Camp Atterbury and Meadowbrook sample analyses, the effective minimum detectable dose on a filter is 0.03 mg. Analyzing half-sections of the filter samples allowed reanalysis of questionable data.

## Field Sampling Errors

Several errors in concentration measurements can occur with our sampling procedure. These include simple errors such as those involved in measuring the total flow through the filter. Other sampling errors may arise in aerosol collection for which the inertial and settling forces on the particles must be investigated.

## Flow Rate

The aspiration flow rate was monitored in our field tests with a rotameter mounted between the vacuum pump and the filter support mast. In this flow geometry the inlet of the rotameter is not at atmospheric pressure, for which the flow meter is calibrated, but at some lower pressure primarily dictated by the flow resistance of the filter cassettes.

This bias error in the measured volumetric flow rate may be adjusted by compensating for the density of the fluid in the rotameter, according to Miller (1983) by:

$$Q_{\text{actual}} = Q_{\text{design}} \sqrt{\frac{P_{\text{design}}}{P_{\text{actual}}}} \quad (5.5)$$

or, using the ideal gas equation of state, we have

$$Q_{\text{actual}} = Q_{\text{design}} \sqrt{\left[ \frac{T_{\text{actual}}}{T_{\text{design}}} \right] \left[ \frac{P_{\text{design}}}{P_{\text{actual}}} \right]} \quad (5.6)$$

where T and P are both in absolute units. Design conditions for this rotameter are standard atmospheric conditions, or 25°C and 1atm. Based on laboratory measurements of the pressure, for 37-mm diameter filters mounted on a single mast we have the corrections shown in Table 5.7.

Table 5.7 Flow meter corrections for the sampling filters

Total number of filters	Measured flowrate [lpm]	$\frac{P_{\text{design}}}{P_{\text{actual}}}$	$\frac{Q_{\text{design}}}{Q_{\text{actual}}}$	Actual flowrate [lpm]
4	11.8	1.038	0.98	11.6
4	17.6	1.059	0.97	17.1
4	23.6	1.091	0.96	22.7
2	23.6	1.073	0.96	22.7
2	35.4	1.125	0.94	33.3
2	47.2	1.177	0.92	43.4

Errors in flow rate due to this pressure correction are at most 8%, but are usually much smaller. Temperature corrections to the flow rates are applied using the average ambient temperature for the period of the test. In the more severe conditions encountered in our field tests [45°C at Meadowbrook] this amounts to a correction of only 4%.

The flow rate through each sampling mast was set at the beginning of each test and remained constant over the duration of the test. There was no evidence of reduced flow rate over the duration of the test, probably because the flow restriction of the fiber filters used in these tests does not appreciably change at the mass loading levels we have experienced.

### **Aerosol Sampling Losses**

In sampling of aerosols, losses of particles before they are collected on a filter may occur due to gravitational settling, inertial forces (anisokinesis), diffusion, or electrostatic forces. For atmospheric aerosols in the 0.34  $\mu\text{m}$  to 1.73  $\mu\text{m}$  size range, which encompass 95% of the particle size range for fog-oil droplets (on a mass basis) in our experiments, electrostatic and diffusion losses are negligible. It is necessary, however, to further quantify any inertial or gravitational settling losses which may occur for this aerosol.

### **Inertial Particle Losses**

Inertial losses of particles may occur in aerosol sampling due to the inability of the particles to identically follow the flow field near the sampler inlet for conditions when the flow is accelerated or decelerated. This may cause the measured concentration to be either larger or smaller than the ambient aerosol concentration. For inlets aligned into the flow direction, inertial losses will be eliminated if the face velocity  $V$  at the inlet is equal to the external flow velocity  $W$ . This is called isokinetic sampling. For conditions where this does not occur, the collection efficiency will be a function of both the velocity ratio  $W/V$ , and the particle Stokes number, given by

$$\text{St} = \frac{d_p^2 \rho_p V}{9\nu D_s} \quad (5.7)$$

where  $d_p$  is the particle diameter,  $\rho_p$  is the particle density,  $\nu$  is the kinematic viscosity, and  $D_s$  is the inlet diameter of the sampler. The Stokes number physically represents the ratio of the particle stopping distance to the characteristic probe dimension. The particle stopping distance calculated in this manner is valid only when the drag on the particle is in the Stokes flow regime, which includes only very small Reynolds numbers (based on the particle diameter). The collection efficiency for probes with this orientation have been experimentally investigated by Belyaev and Levin (1974)

and Davies (1968). In general their results show the collection efficiency has greater deviation from unity for increasing Stokes number.

For inlet geometries where the probe is oriented at an angle relative to the external flow velocity, the collection efficiency is a function of the probe angle as well as the velocity ratio  $W/V$ , and the particle Stokes number  $St$ . This effect has been investigated by Fuchs (1975), Durham and Lundgren (1980), and Tufto and Willike (1982). For this sampling geometry the collection efficiency generally decreases with increasing angle between the probe inlet and the approaching flow.

In field experiments, the sampler orientation with respect to the wind direction is constantly changing and the velocity ratio  $W/V$  also is not steady. Corrections to the data from wind tunnel tests could not be made without a great deal of inherent error. The only hope in avoiding collection efficiency problems due to this effect is in selecting a sampling geometry which minimizes inertial losses of particles by operating in a range with a small Stokes number.

For the fog-oil aerosol ( $\rho_p = 0.91 \text{ g/cm}^3$ ) typical values of the particle stopping distance (in cm) are as shown in Figure 5.9. The Stokes number in this graph uses the filter inlet velocity. All values in this plot have a particle Reynolds number which is less than 3, so the particle-flow interaction is always within the Stokes flow regime.

In consideration of isokinetic sampling losses, Hinds (1982) shows no significant losses for flow mismatch ( $V/W \neq 1$ ) or probe misalignment for  $St < 0.1$ , and the fog-oil smoke easily meets this criteria. For sampling in still air, Davies (1968) cites a conservative upper limit of  $St < 4 \times 10^{-3}$  based on the filter face velocity. This criteria is also easily met with this aerosol.

### Gravitational Settling Losses

In gravitational settling, collection efficiency may be affected by the finite downward velocity  $v_s$  of the particles if the filter inlet is not normal to the gravity vector. This is a more significant problem with larger aerosol particles. In stagnant air, the settling velocity of a particle is the terminal velocity of a particle for which the aerodynamic drag on the particle is equal to the gravitational force. Typical calculated values for the fog-oil smoke at the mass mean diameter  $\bar{d}_{mm}$  and at  $+1\sigma_g$  and  $+2\sigma_g$  of the particle distribution are given in Table 5.8. Evident from these values is the fact that the settling velocity is very small for fog-oil smoke particles. To estimate sampling losses, this velocity is typically nondimensionalized by the sampler flow velocity  $V$  as

$$V'_s = \frac{v_s}{V} \quad (5.8)$$

Settling losses are more significant for larger  $V'_s$ , so that these effects are greater in stagnant conditions. Davies (1968), cites a conservative upper limit on the nondimensionalized settling velocity of  $V'_s < 4 \times 10^{-2}$  which, if met, ensures that gravitational settling is an insignificant effect

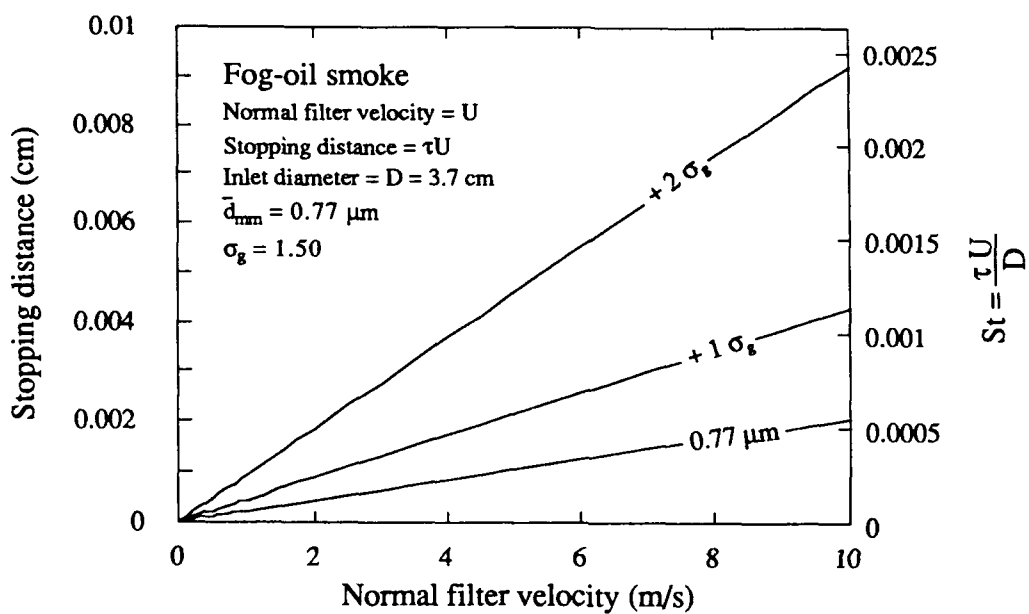


Figure 5.9 Velocity versus particle stopping distance and Stokes number for fog-oil smoke aerosol. Lines are calculated for the mass mean diameter, and at +1 and +2 geometric standard deviations from the mean.

relating to collection efficiency. The largest particle size in the table corresponds to a minimum acceptable mean sampling velocity of about 0.23 cm/s, which is easily met for our testing conditions.

Table 5.8 Settling velocities for fog-oil smoke aerosol.

	Particle diameter ( $\mu\text{m}$ )	Settling velocity (cm/sec)
$\bar{d}_{mm}$	0.77	0.0021
+1 $\sigma_g$	1.15	0.0043
+2 $\sigma_g$	1.73	0.0091

Agarwal and Lin (1980) specify a criteria for at least 90% collection efficiency for conditions when the product  $(St)(V'_s) < 0.1$ . This criteria is also met for all of our sampling conditions. In summary, then, there is a good theoretical basis for assuming that the collection efficiency of our samplers is not affected by inertial effects or gravitation setting of the aerosol particles for our fog-oil smoke.

Another criteria of settling velocity is the effect of deposition on the conservative nature of the aerosol. For the particles in the aerosol smoke, the settling velocity is small enough to be neglected in dispersion at the downwind distances at which we are making measurements. Most deposition in the atmosphere may be neglected for particles smaller than 1  $\mu\text{m}$  and dispersion distances less than several kilometers.

### Aerosol-Vapor Partitioning of the Fog-oil Smoke

Although fog-oil is a relatively nonvolatile liquid, the aerosol smoke from this liquid will evaporate if it is sufficiently dilute. The dynamics of an evaporating droplet are controlled by the diffusion of vapor surrounding the droplet, which is represented by

$$\frac{dd_p}{dt} = \frac{4 \mathcal{D}_v M}{\mathcal{R} \rho_p d_p T_\infty} [P_\infty - P_s] \quad (5.9)$$

from Hinds (1982) for a single component droplet. This equation neglects the Fuchs effect, where for small droplets ( $< 0.1 \mu\text{m}$ ) evaporation is controlled by the kinetic theory of gases. It also neglects cooling of the droplet by evaporation, which is important for highly volatile droplets, and the Kelvin effect, for which the saturation vapor pressure surrounding a very small droplet is increased. In this equation,  $\mathcal{R}$  is the ideal gas constant,  $\rho_p$  is the droplet density,  $d_p$  is the droplet diameter,  $T_\infty$  is the ambient temperature,  $\mathcal{D}_v$  is the diffusivity of the vapor in air,  $M$  is the molecular



weight of the droplet, and  $[P_{\infty} - P_s]$  is the difference in the partial pressure of the vapor across the diffusion layer.

As a simplification of the multi-component fog-oil, we may investigate the behavior of single component droplets of *n*-paraffin in a molecular weight range similar to the constituents of the fog-oil. The heaviest of these constituents show time constants for changes in micron sized droplets which are only several tenths of a second in magnitude, and several millisecond for the lighter weight components. Because the droplet sizes quickly adjust to changes in  $P_{\infty}$ , we are mainly interested in the case of  $dd_p/dt = 0$ , or  $P_{\infty} = P_s$ . In this method for determining the equilibrium liquid-vapor partition, we can neglect the Fuchs effect and the Kelvin effect for  $d_p > 0.1 \mu\text{m}$ .

Given that there is saturated vapor for constituent A in air at atmospheric conditions, we have

$$\eta_A = \frac{P_{s,A}}{P_{\text{atm}} + P_{s,A}} \quad (5.10)$$

where  $\eta_A$  is the mole fraction and  $P_{s,A}$  is the saturation vapor pressure. The mass fraction is given by

$$\phi_A = \frac{\eta_A M_A}{M_{\text{air}} + \eta_A M_A} \quad (5.11)$$

and the mass concentration of the vapor is

$$c_{A,v} = \phi_A \rho_{\text{atm}} = \phi_A (1.225 \times 10^6 \text{ mg/m}^3) \quad (5.12)$$

where  $\phi_A$  is assumed small. For *n*-paraffins in the range  $C_8$  to  $C_{20}$ , calculations of the mass concentration of saturated vapor are given in Figure 5.10. For a given constituent in this graph, total concentrations at a lower value than given by the plotted curve would exist entirely as vapor, whereas higher concentrations would exist as a saturated vapor with some fraction of condensed liquid aerosol. For typical measured mean concentrations in our experiments, only components of the oil which have a higher molecular weight than approximately  $C_{13}$  or  $C_{14}$  are seen mainly as condensed liquid aerosol. This is shown in Figure 5.11 for a laboratory sample of fog-oil smoke in which most of the total mass is aerosol, but the lightest weight fraction exists primarily as a vapor. At much lower concentrations than those seen in our dispersion experiments, we would expect that a greater fraction of the heavier weight constituents would exist primarily as vapor.

### **Experimental Considerations of Particle Losses**

To further quantify any losses in sampling efficiency for the fog-oil smoke, or evaporation of oil from the filters, a diagnostic field test was conducted at Camp Atterbury on July 9, 1986. In this test, sets of sampling masts were located in groups of four downwind from a fog-oil

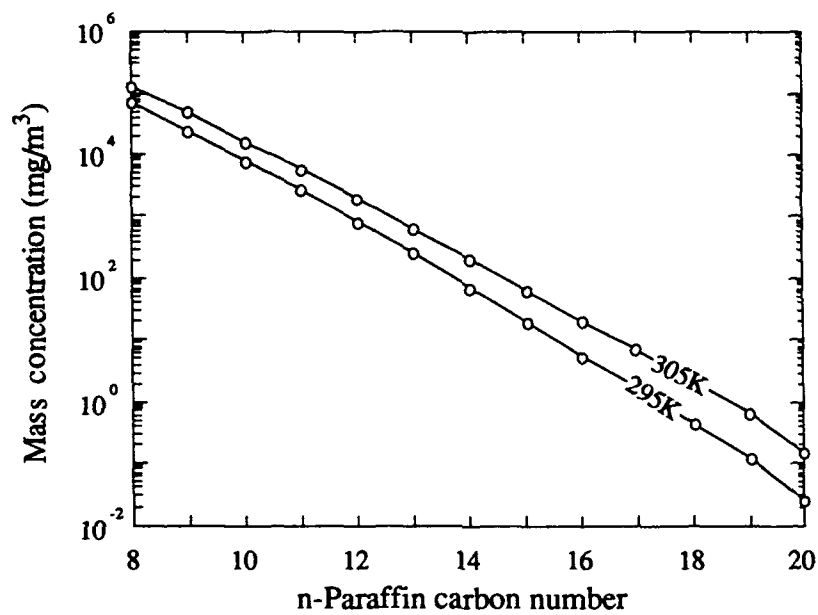
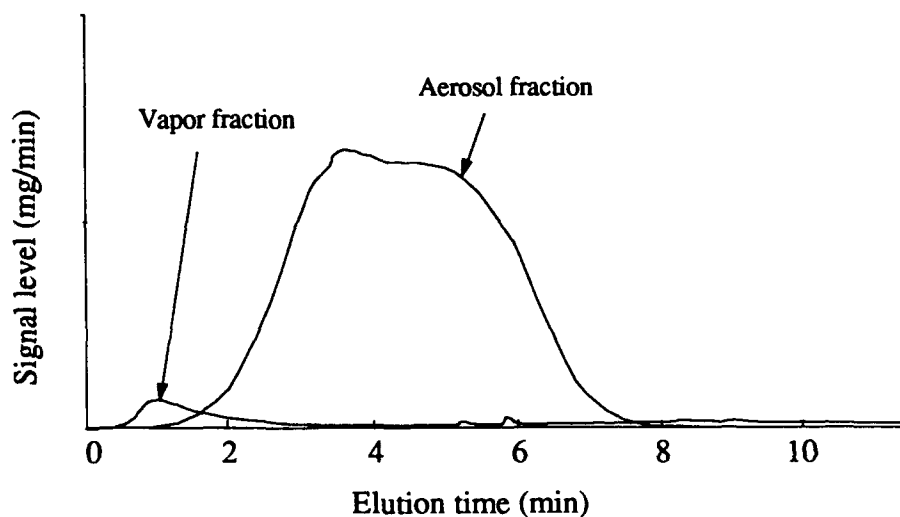


Figure 5.10 Minimum mass concentrations of n-Paraffins required for saturated vapor to exist at atmospheric pressure and temperatures.



**Figure 5.11** Partitioning of vapor and aerosol in a fog-oil smoke sample. This laboratory sample was collected with an aspirated glass fiber filter backed by a Tenax sample tube. The aerosol was collected on the filter with the vapor collected by the Tenax polymer adsorbant. The greatest fraction of oil in this sample exists as a liquid aerosol. These chromatograms were produced with an initial oven temperature of 150°C and an oven ramp rate of 25°C/min.

generator. The masts in each group were arranged as follows: one faced into the wind and was aspirated at 22.7 liters/min; another faced 180° opposite to the wind direction and was aspirated at the same flow rate; another was aspirated for an extended period of 30 minutes after the smoke termination; and another was aspirated at a half flow rate of 11.6 liters/min. Corrections to the flow meter readings based on the absolute pressure just upstream from the flow meter were applied to the data, and the samples were analyzed within two days of the test. Agreement between concurrently located filters were good and no trend was evident in the data. The ratio of standard deviation to mean in this sample set was  $\sigma/\bar{c} = 0.17$ , which is within the standard error of the fog-oil analysis method. This test demonstrated that losses due both to anisokinetic sampling and evaporation of oil from the filters during a test were within reasonable limits compared with the overall accuracy of the sampling method.

### **Storage Losses**

Evaporation of fog-oil aerosol or collected samples on a filter can be significant over a several week period. In 1986, several dispersion experiments were undertaken and many months were required for the dosage sample analysis to be completed. This meant that some filters were stored for a considerable period of time before being analyzed. Loss of oil was found to have occurred on these samples during the storage period. The loss between one split set of samples analyzed the day after a test and six months later averaged 69%. The difference between a calibrated aerosol photometer and fog-oil samples analyzed a similar amount of time after exposure was 82%. This problem pointed out the need for further investigation.

### **Laboratory Tests**

In an attempt to duplicate the losses due to extended storage of samples before analysis, laboratory tests were made. In these tests, sets of 28 filter cassettes were simultaneously dosed with fog-oil smoke in a laboratory setup consisting of a small smoke generator and a well mixed aerosol chamber in a continuous flow setup. These filters were all aspirated at the same flow rate and should all have the same dose of oil within a group. Any differences in dose upon analysis can be attributed to losses in storage. Several sets of filters were dosed with oil and stored in various ways, some to duplicate previous methods of storing the samples, and some to find better ways of storing the samples in future field tests. These methods were as follows:

Storage Method A. The dosed filters were kept in filter cassettes without separating them from the backup support, in the same manner as most of the 1986 and 1987 Camp Atterbury samples were stored.

Storage Method B. The filters were separated from the backup support, but kept loosely in the original filter cassette for storage. Most of the Meadowbrook samples taken in 1987 were stored in this manner.

Storage Method C. The filters were removed from the cassette holders after exposure, cut, and folded into a stainless steel tube which was capped with plastic end caps.

Storage Method D. The filters were prepared as in C but instead of plastic end caps, the stainless steel tubes were stored in clean glass screw top culture tubes. Since only sections of the filter could fit into the stainless steel tubes, the filters used here were from the same set as C.

The data for the mass of oil measured on the filter versus the time between exposure and analysis are presented in the following graphs. The data in these graphs, as shown in Figure 5.12, indicate progressively less scatter in the data for Storage Methods A through D.

For Storage Method A, a few of the filters analyzed after long storage times had losses similar in magnitude to those found for the field samples taken in 1986. There is also considerable scatter in the data which creates a problem in finding a correction factor as a function of storage time. For extended storage of samples, as occurred for samples taken at Camp Atterbury in 1986, a correction factor of 5, corresponding to a 80% loss of oil is appropriate. All of the samples taken at Camp Atterbury in 1987 were also stored in this manner and a similar correction factor of 5 is appropriate.

The filters from the Meadowbrook dispersion tests were stored using Storage Method B. Although the storage losses are less than with Storage Method A, they are still considerable and need correction. For a single test, on September 23, 1987, in the Meadowbrook field studies, the filters were cut in half and one set was stored loosely in the cassettes (Storage Method B) while the other half was stored using Method D. The average of the mass ratios measured for each sample fragment under the two different storage methods gives a good correction factor since the losses using Method D are negligible. The ratio of values in this case is 3.1, which amounts to a loss of 68% of the oil. This is consistent with the laboratory tests in that the measured value shows less oil loss than filters stored using Method A.

It is notable that the error for Methods C and D is very close to the standard error in determining the mass of oil with the gas chromatograph alone. Since the gas chromatograph error is included in the above figures, almost no additional error can be attributed to storage losses in these cases. The problem in storing filters in this manner is only in the time and labor required to pack

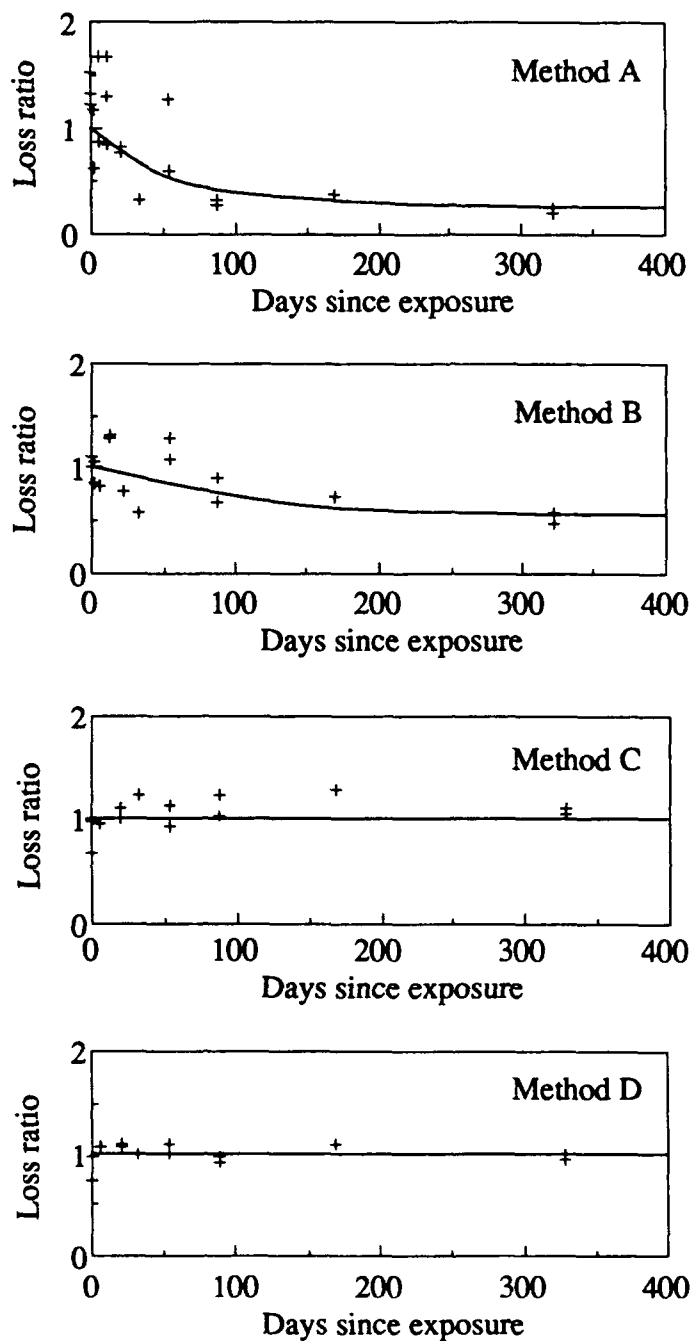


Figure 5.12 Oil losses for several methods of filter storage. The plot shows losses of oil with time of a series of identically dosed samples. A) The filter cassettes were simply capped. B) The filters were peeled from the cellulose backing disc and stored loosely within the cassette housing. C) Filters were removed from the cassettes and sealed in clean stainless steel tubes capped with plastic endcaps. D) Filters were removed from the cassettes, packed in clean stainless steel tubes, then sealed within glass screw top test tubes.

the filters in the storage tubes. In field situations, where a quick cycle time is required for the next day of testing and hundreds of dosage samples are taken in each test, we simply lacked the personnel to use either of these methods.

To minimize the relative bias error between dosage samples for a single test, the group of samples taken in a particular test were analyzed together. Analysis of a single set of samples could be completed in about six days. In this way, a single correction factor is applied to all the data for a given test, and although the absolute mass in each case is subject to a degree of error, the relationship between relative dosages in a test is still maintained.

The standard error for samples analyzed with this method can be estimated from the large group of laboratory samples which were each dosed with a identical mass of fog-oil smoke. For this purpose, the samples analyzed at times greater than three months were neglected, giving an estimated error of  $\sigma/\bar{c} = 0.24$  for the Meadowbrook dispersion studies and  $\sigma/\bar{c} = 0.38$  for the Camp Atterbury data. This magnitude of standard error is consistent with other similar one-hour mean concentration measurements made in the atmosphere using different tracer methods.

Another source which may be useful in estimating the standard error in mean concentrations are the experimental data themselves. For unstable atmospheric conditions, there should be little gradient in concentration over the 8-m height of the sampling masts and the scatter in measured values over a single mast is attributable to the sampling and analysis method. This is shown in Figure 5.13 for the Camp Atterbury fog-oil data where the scatter in values is plotted as a function of concentration. The greatly increased scatter at lower concentrations can be attributed to the increased noise in these smaller samples.

## 5.4 HC Smoke Analysis

### 5.4.1 Source Characteristics and Chemical Constituents of the HC Smoke

Five dispersion tests were conducted at Camp Atterbury using a total quantity of 100 M5-HC 30-lb smoke pots from the US Army. The M5-HC smoke pot was a cylindrical sheet metal container, 21.5 cm in diameter by 24 cm high, filled with approximately 16.6 kg of HC smoke mixture and 0.5 kg of a fast burning HC smoke mixture. The pots were tapered at the bottom to facilitate stacking. They were covered by a circular tear strip which is removed before use. A plastic cup containing a starter mixture was embedded in the top of the smoke mixture. An electric squib provided with the pot was used to ignite the material in our tests.

Composition of the HC smoke mixture is specified (Katz et al., 1980b) in Table 5.9. The ratio of hexachloroethane to zinc oxide is maintained at a ratio of 1:1 to 1:1.04. The amount of aluminum is varied to alter the burn time. The bulk of the mixture is maintained at 5-7% aluminum whereas the fast burning mixture contains 7-11% aluminum, according to design specifications.

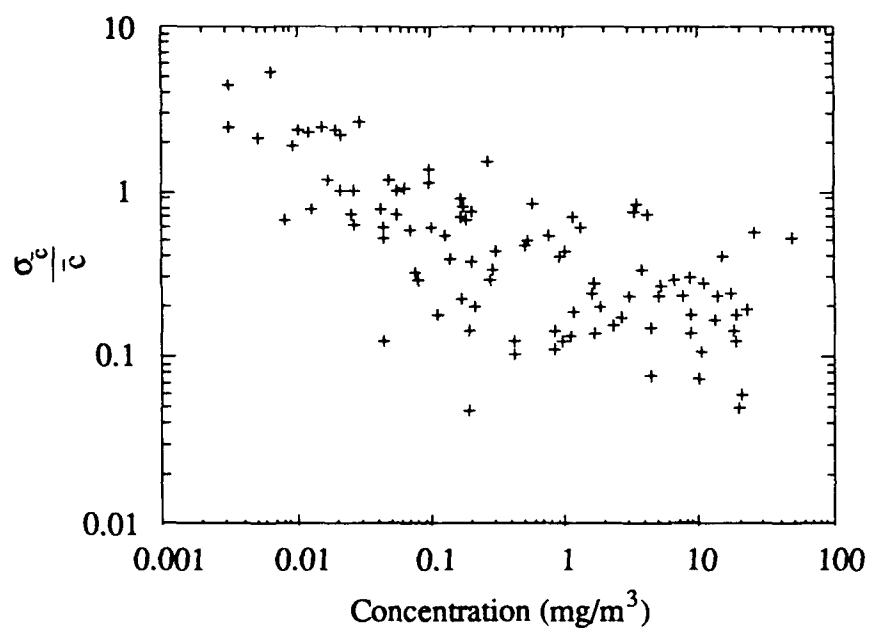


Figure 5.13 Ratio of standard deviation to variance for average mean concentrations measured by multiple filters on the same sampling mast for the fog-oil dispersion tests



Table 5.9 Composition of unburned HC smoke mixture.

Description		Weight % (approx.)
Grained Aluminum	Al	6.7 %
Zinc Oxide	ZnO	46.6 %
Hexachloroethane	C <sub>2</sub> Cl <sub>6</sub>	46.7 %

The ignited pots burn as hot as 1500°C. According to Katz et al., (1980b) the bulk of the combustion products condense to aerosol particles consisting of zinc chloride (ZnCl<sub>2</sub>) and aluminum oxide (Al<sub>2</sub>O<sub>3</sub>) with a fraction of condensed organic compounds including hexachloroethane. Gases found in the burned mixture, as analyzed by the same authors, are given in Table 5.10, where the mass fraction is relative to the HC reagent. A wide range of variability is noted in the table, probably due to the difference between laboratory and field conditions under which the range of samples were obtained. Approximately 30% of the reagent, once burned, remains in and near the pot as residue.

Table 5.10 Gaseous combustion products of HC smoke.

Description		Weight %
tetrachloroethylene	C <sub>2</sub> Cl <sub>4</sub>	3.0 - 17.0%
tetrachloromethane	CCl <sub>4</sub>	1.0 - 3.0%
hexachloroethane	C <sub>2</sub> Cl <sub>6</sub>	0.3 - 5.0%
carbonyl chloride	COCl <sub>2</sub>	0.1 - 1.0%
hexachlorobenzene	C <sub>6</sub> Cl <sub>6</sub>	0.4 - 0.9%
carbon monoxide	CO	0.9 - 3.7%
hydrogen chloride	HCl	0.03 - 3.4%
chlorine	Cl <sub>2</sub>	0.3 - 1.9%

The Army uses single pots or stacks of 3 to 5 pots, with the upper levels igniting lower levels as they burn. We used several different arrangements of pots in our dispersion tests. In order to determine the effects of different configurations on combustion characteristics, we burned two single pots, one upright and one on its side, to determine approximate burn times, exit temperature, and release rate. The weight of the pot was monitored on a scale and the exit temperatures were monitored with thermocouples. Both of these were digitally recorded using a Campbell Scientific 21X datalogger. Finite differences of the weight record in time produced a mass release rate. These results are shown in Figure 5.14. The temperature shown in this figure was measured with

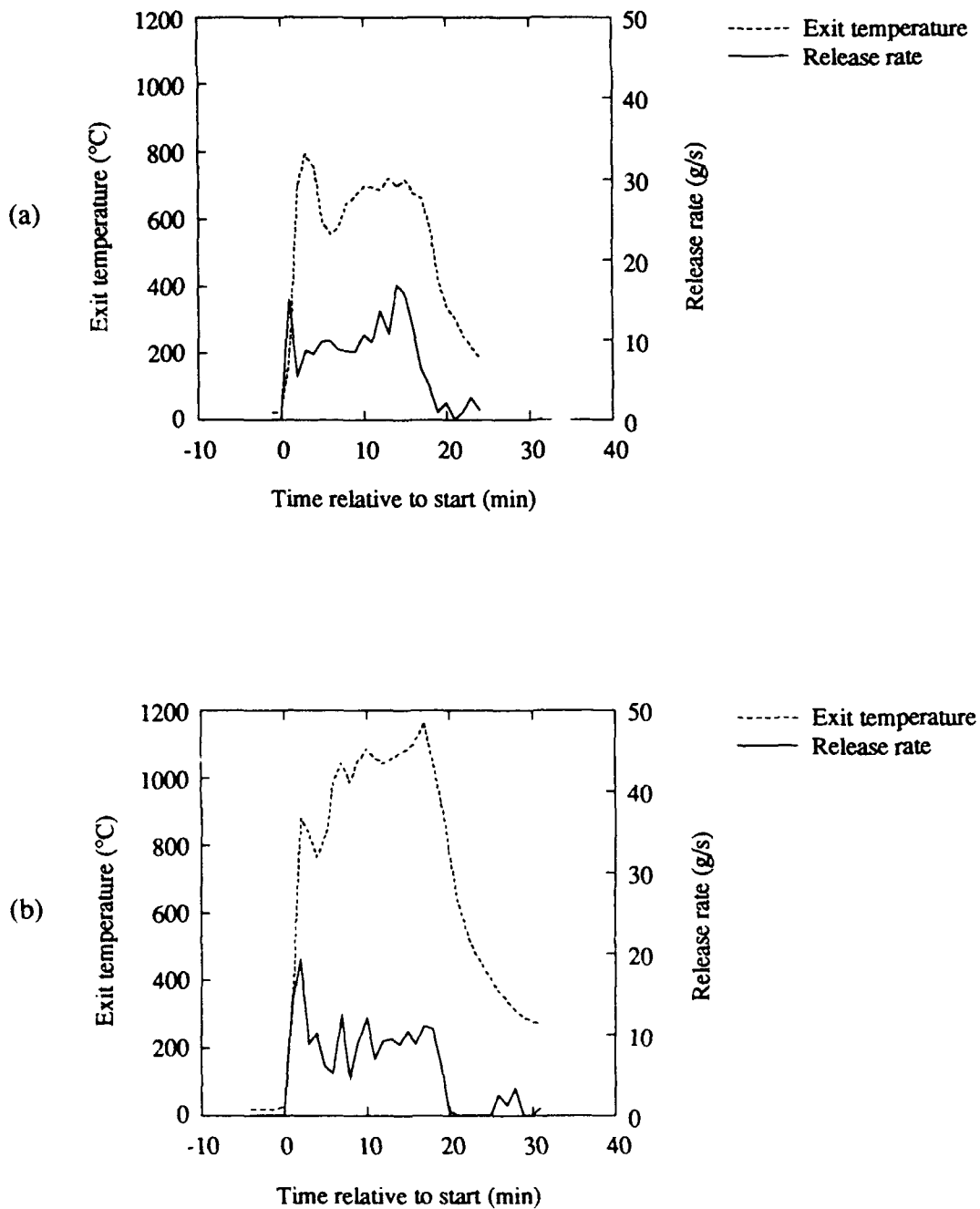


Figure 5.14 Release rate and exit temperature histories for single HC smoke pots (a) positioned upright and (b) positioned on side.

a thermocouple located 3 to 5 cm from the top of the pot. Variations in temperature between the two releases are due to variations in the precise location of the thermocouple.

In five full-scale dispersion tests which were conducted, approximately 20 pots were burned per test. These were grouped on the scale to provide release rate information and to keep the fire hazard to a minimum. Plots of the release rate versus time for all the tests are given in Figure 5.15. For Test 1109871 the pots were arrayed in a single layer 5 by 4 grid on the scale and electrically wired with the intention of firing a set of five pots every 20 minutes for a total 80 minute release. In operation, the first set of pots soon ignited all of the others, so that this test was only twenty-five minutes in duration, resulting in a very high release rate. For Test 1110871, 4 stacks of 5 pots each were arrayed on the scale with the first layer ignited to start the test. This arrangement produced a better result, with the only modification in the remaining tests being a wire fence surrounding the stacks to keep the pots from falling into a pile. The later Tests 1110872 and 1112872 had a much more stable release as a function of time. For Test 1113871 no data are available, since the recording equipment failed. The smoke release in Test 1113871 was very similar to that of Test 1112871. The temperature monitored several centimeters from the top of one stack of pots with a thermocouple is given in Figure 5.15 for Test 1112871.

The HC smoke pots release a dirty mixture of many chemical species. In our calculations, the zinc is used as a conservative marker in the dispersion, with other concentrations indirectly related to the zinc concentration. Analysis of 912 smoke samples from all our tests showed the the average ratio of zinc to aluminum in the smoke aerosol to be 1:0.045, as shown in Table 5.11.

Table 5.11 Ratio of zinc to aluminum in HC smoke.

For mass of Zn	(mass Zn /Al)	$\sigma$
$\chi_{Zn} > 50 \mu g$	0.045	0.026
$0.5 \mu g < \chi_{Zn} < 50 \mu g$	1.50	1.85

Increasing scatter in this ratio, for zinc sample smaller than 50  $\mu g$ , gives an indication of the increased error with a lower measured dose. Given this ratio and the specification for the composition of the unburned HC smoke mixture, we have the mass of Zn given by  $\chi_{Zn}$ , and from the molecular weight ratio of ZnO we have the mass of oxygen in the reagent relative to zinc given by

$$\chi_O = \chi_{Zn} ( 16.0 / 65.39 ) \quad (5.13)$$

From the Zn to Al ratio given in Table 5.11 we have

$$\chi_{Al} = \chi_{Zn} ( 0.043 ) \quad (5.14)$$

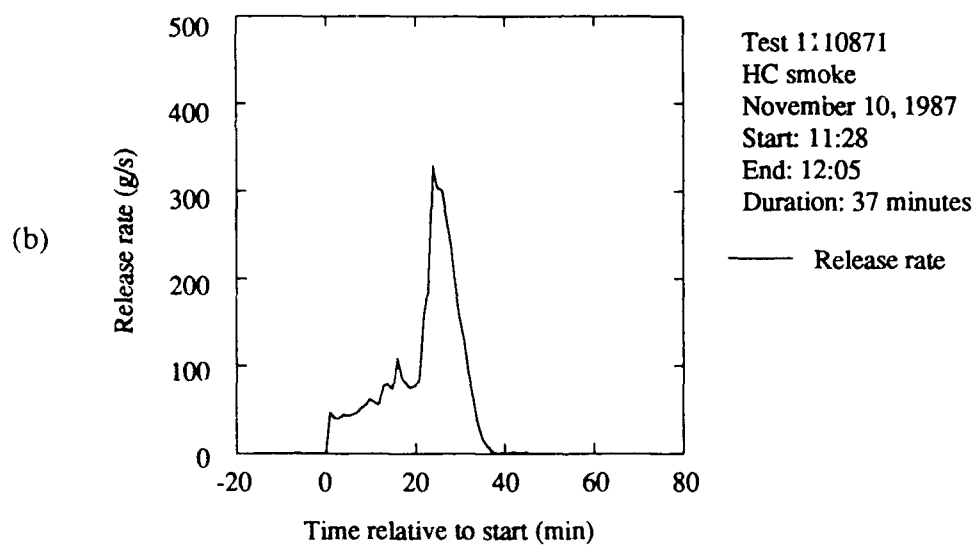
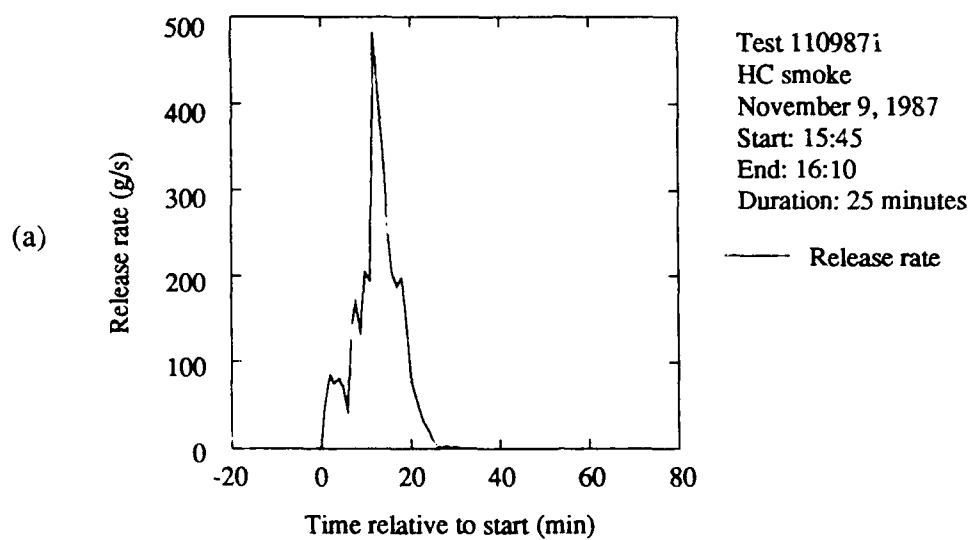


Figure 5.15 Release rate histories for the HC smoke dispersion tests at Camp Atterbury for (a) Test 1109871 and (b) Test 1110871.

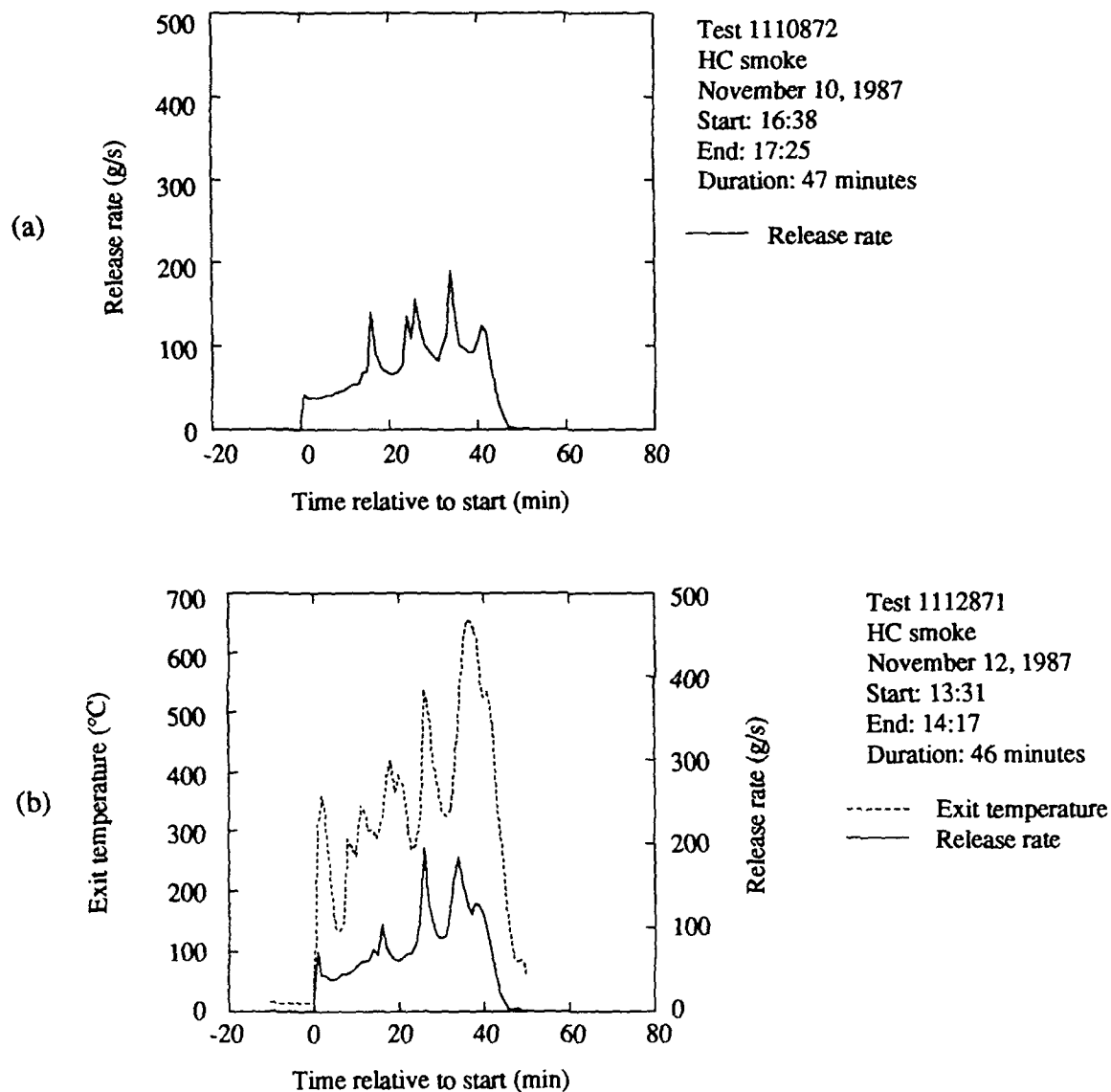


Figure 5.15 (continued) Release rate and exit temperature histories for HC smoke at Camp Atterbury for (a) Test 1110872 and (b) Test 1112871.

For the 1:1 ratio of Zn to  $C_2Cl_6$  given in Table 5.9

$$\chi_{C_2Cl_6} = \chi_{Zn} (1.00) \quad (5.15)$$

Substitution gives

$$\chi_{Total} = \chi_{Zn} + \chi_O + \chi_{Al} + \chi_{C_2Cl_6} = 2.29 \chi_{Zn} \quad (5.16)$$

This relates the mass of reagent to zinc concentrations in the smoke. A list of release information for our HC smoke dispersion tests is given in Table 5.12 in terms of total mass, the mass of aluminum, and the mass of zinc.

Table 5.12 Mass released and mean release rates for HC smoke tests.

Test	Total duration (min)	Mass released (kg)			Mean release rate (g/s)			Number of pots
		Total	Zn	Al	Total	Zn	Al	
1109871	25	222.1	97.0	4.17	148.1	64.7	2.8	19
1110871	36	229.3	100.1	4.31	106.2	46.4	2.0	20
1110872	47	219.5	95.9	4.12	77.8	34.0	1.5	20
1112871	45	218.5	95.4	4.10	80.9	35.3	1.5	20
1113871	43	202.0	88.2	3.79	78.3	34.2	1.5	18
upright pot	18	10.7	4.6	0.20	9.9	4.3	0.18	1
pot on side	17	10.2	4.4	0.20	10.0	4.4	0.19	1

#### 5.4.2 Analysis Method for HC Smoke

Dosage samples of the HC-smoke aerosol were collected on 37-mm cellulose ester filters with a 0.45- $\mu$ m pore size using the same aspiration equipment as for the fog-oil smoke. All of these filter samples were analyzed by Coors Analytical Laboratory of Boulder, Colorado during the period from December 7, 1988 through January 13, 1989. All filters were analyzed for the mass of zinc and aluminum. Thirty-two filters were subjected to anion analysis for bromide, chloride, iodide, nitrate, and sulfate. Of these 32 samples, 22 were analyzed for arsenic, cadmium, mercury, and lead. The remaining 10 samples were analyzed for the presence of 40 elements.

Vapor samples were also taken in the five dispersion tests. Each sampler consisted of a cellulose ester membrane filter to remove particulates followed by a Tenax polymer adsorbent tube. Each of these were aspirated at 100 ml/min over the test duration. A total of 12 samples were taken. These samples were analyzed for tetrachloromethane, tetrachloroethylene, hexachloro-

ethane, and hexachlorobenzene using a thermal desorption-gas chromatography system in our own laboratory over a period from March 16 - 18, 1988.

### **Analysis of HC Smoke Aerosol Samples**

The Coors Laboratory analysis of filter samples for the mass of Al and Zn was accomplished by first digesting them in nitric acid, then using an inductively coupled argon plasma atomic emission spectrometer (ICAP-AES) technique on the Model 1100 Thermo Jarrell Ash system with normal aqueous aerosol sample introduction.

For digestion, the samples were placed in clean, dry 150-ml beakers. A 100- $\mu$ l aliquot of 1000-mg/liter Co was added as an internal standard. A 2.5-ml aliquot of very high purity nitric acid was added, a refluxing watch glass placed over the beaker, and the sample was heated for fifteen minutes over medium heat to dissolve the filter. The sample was not allowed to evaporate to dryness. The samples were quantitatively transferred to 10 ml test tubes and rinsed with 5% very high purity nitric acid. The test tubes were capped and the contents manually mixed by shaking the tubes.

In the ICAP-AES instrument, a sample of the liquid solution of the dissolved filter is sprayed into an argon plasma. Atomic emission spectra is used for quantifying the concentration in the argon plasma of the element of interest. The plasma excitation source is responsible for the exceptional sensitivity of this instrument. Reduced results are given in terms of the total mass of each of Zn or Al on the filter. Mean concentrations, which are presented in terms of Zn and Al, are calculated from the average flow rate over the test duration.

In the detailed analysis of the 32 filter samples, arsenic and selenium were analyzed using the ICP-hydride technique. Bromide, chloride, iodide, nitrate, and sulfate were analyzed using ion chromatography. The remaining elements were analyzed in the same manner as the aluminum and zinc samples. Results of this analysis are used to find an average composition of the HC smoke aerosol and are given in Table 5.13. The elements present in this analysis are consistent with the composition of the source, including the canisters, possible composition of the starter mixture, and trace elements present in the refining of zinc. As expected, the greatest fraction of the aerosol is zinc chloride.

The sum of the mass fractions relative to the HC reagent add to 1.107, so that this composition differs from the results of Katz et al., (1980b), which were found from burning the HC smoke material in a laboratory setting. Almost all of this difference can be attributed to the iron, which comes from the vaporized sheet metal canisters, not present in the laboratory tests.

Table 5.13 Average composition of the HC-smoke aerosol. No amount of iodide, mercury (Hg), gold (Au), cerium (Ce), potassium (K), lanthanum (La), lithium (Li), neodymium (Nd), palladium (Pd), praseodymium (Pr), platinum (Pt), thorium (Th), or yttrium (Y) was detected in these samples.

		Mass ratio to zinc			Mass fraction relative to reagent
Description		Average	$\sigma$	$\sigma$ /avg	
Zinc	Zn	1.000	-	-	0.437
Chloride		0.881	0.2016	0.23	0.385
Iron	Fe	0.221	0.0721	0.33	0.096
Sodium	Na	0.155	0.0578	0.37	0.068
Aluminum	Al	0.080	0.0187	0.23	0.035
Sulfate		0.040	0.0234	0.59	0.018
Calcium	Ca	0.033	0.0273	0.83	0.014
Lead	Pb	0.026	0.0085	0.33	0.011
Phosphorous	P	0.020	-	-	0.009
Silicon	Si	0.015	0.0071	0.47	0.00638
Nitrate		0.012	0.0051	0.43	0.00521
Bromide		0.012	0.0072	0.60	0.00509
Tin	Sn	0.0084	0.0047	0.56	0.00366
Boron	B	0.0059	0.0020	0.34	0.00259
Magnesium	Mg	0.0046	0.0016	0.35	0.00203
Chromium	Cr	0.0039	0.0036	0.92	0.00169
Barium	Ba	0.0030	0.0013	0.43	0.00129
Zirconium	Zr	0.0024	0.0009	0.38	0.00104
Vanadium	V	0.0023	0.0004	0.17	0.00101
Cobalt	Co	0.0020	-	-	0.00085
Silver	Ag	0.0019	0.0017	0.89	0.00084
Nickel	Ni	0.0019	0.0001	0.053	0.00083
Copper	Cu	0.0016	0.0010	0.63	0.00071
Titanium	Ti	0.0015	0.0029	1.93	0.00067
Cadmium	Cd	0.0013	0.0006	0.46	0.00057
Molybdenum	Mo	0.0012	0.0012	1.00	0.00051
Antimony	Sb	0.00054	0.0004	0.74	0.00024
Beryllium	Be	0.00036	0.0001	0.28	0.00016
Manganese	Mn	0.00033	0.0002	0.61	0.00015
Strontium	Sr	0.00017	0.0001	0.59	7.2869E-05
Arsenic	As	0.00015	0.0001	0.67	6.7271E-05
Selenium	Se	0.00015	0.0001	0.67	6.4323E-05



## Analysis of HC Smoke for Gaseous Combustion Products

The analysis of the gaseous constituents of the HC smoke collected on the Tenax polymer adsorbent tubes was accomplished using a thermal desorption gas chromatography system as previously described in Section 5.3.2. Operating conditions for the instrument are presented in Table 5.14. The primary differences between the HC vapor analysis and the previous fog-oil analysis is the substitution of a different separative column and the lower initial oven temperature. Cooling of the oven to the 20°C initial temperature is aided by injecting liquid N<sub>2</sub> into the column oven.

Table 5.14 Key parameters of gas chromatography method used to analyze HC smoke vapor samples

Chromatograph:	Perkin -Elmer Sigma 300 with LCI- 100 Integrator and Model 7500 Computer
Detector:	Flame Ionization
Column:	12 ft., .25 in OD, AP-L 15% Chrom W 80/100 mesh
Temperatures:	
Modified Injector	300 °C
Detector	350 °C
Column	
Initial	20 °C
Ramp	8 °C/min.
Final	300 °C for 20 min.
Carrier gas:	Ultra-pure Nitrogen
Flow rates:	
Column	35 ml/min
Inlet	70 ml/min
Split ratio	1 : 1
Analysis time:	60 min.

Calibration of the flame ionization detector (FID) is provided by analysis of pure samples of tetrachloromethane, tetrachloroethylene, hexachloroethane, and hexachlorobenzene. The solid hexachloroethane and hexachlorobenzene were dissolved in solutions of 1 mg/liter of hexane and doped on clean Tenax sample tubes to find the elution time and the FID detector sensitivity. For the volatile tetrachloromethane and tetrachloroethylene liquids, vapor samples were aspirated onto clean Tenax sample tubes and analyzed to determine the elution times. Calibration for these vapor

samples was provided by determining the effective sensitivity of the FID detector, which has a response proportional to carbon concentration, for n-dodecane and hexane, then calculating the effective sensitivity for tetrachloromethane and tetrachloroethylene.

Results of this sample analysis are given in Table 5.15. The data are presented in terms of the average ratio of the particular vapor to that of the zinc, along with the standard deviation of this ratio for the sample set. All of the field samples were dosed with very small quantities of vapor, and the scatter between the samples is high. The chromatogram for sample 1110872.4.7.1, which was the most heavily dosed in the set, is repeated in Figure 5.16, with the elution peaks of the identified compounds marked.

Table 5.15 Ratio of zinc concentration and reagent to that of the identified organic vapor compound. Means and standard deviations for this ratio are shown.

Description	Mass ratio vapor to Zn		Vapor/reagent mass fraction	
	Mean	$\sigma$	Mean	$\sigma$
tetrachloromethane	0.1043	0.160	0.0716	0.11
tetrachloroethylene	0.0458	0.074	0.0324	0.05
hexachloroethane	0.0496	0.073	0.0319	0.05
hexachlorobenzene	0.2581	0.464	0.2026	0.36

Up to 35 unidentified peaks are seen in the chromatogram of Figure 5.16. We are unable to identify most of these compounds using our technique. For the other eleven chromatograms in the data set, the shape and ratio of the set of resolved peaks varies considerably between the different samples as illustrated by the wide error bars for the data of Table 5.15.

#### 5.4.3 HC Smoke Analysis Errors

##### Field Sampling Errors

Several errors in concentration measurements can occur with our sampling procedure for HC aerosol smoke. These includes errors such as those involved in measuring the total flow through a filter and clogging of the filters with increasing mass loading. Other sampling errors may arise in aerosol collection for which the inertial and settling forces on the particles must be investigated.

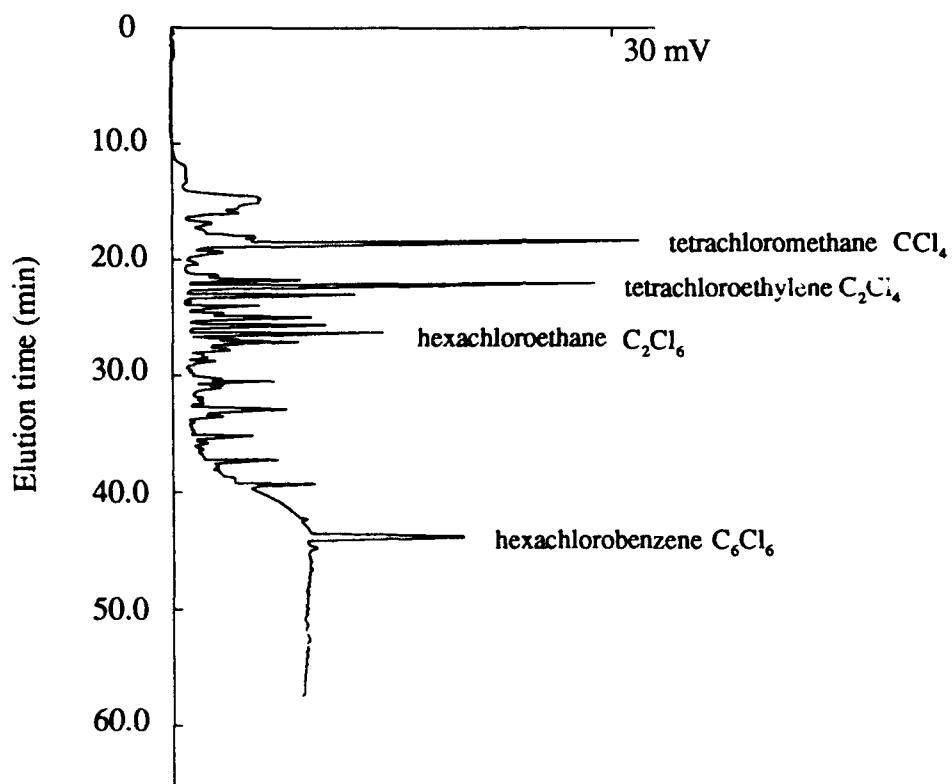


Figure 5.16 A chromatogram of HC smoke vapor. This sample is from Test 1110872 and was located near Mast 7 on Transect 4 at a sampling height of 1 m.

## Flow Rate

The same equipment was used to measure the flow rate in the HC tests as in the fog-oil tests. The filters in the HC tests are 37-mm diameter, 0.45- $\mu\text{m}$  pore size cellulose-ester membrane filters. Corrections to rotometer readings due to flow resistance may be made using Eq. 5.8 and are shown in Table 5.16. These values are for clean filters and the flow correction is substantial because of the large pressure drop across the filter.

Table 5.16 Flow meter corrections for the sampling filters.

Total Number of filters	Measured flowrate [lpm]	$\frac{P_{\text{design}}}{P_{\text{actual}}}$	$\frac{Q_{\text{design}}}{Q_{\text{actual}}}$	Actual flowrate [lpm]
4	23.6	1.565	0.76	18.0
8	11.8	1.206	0.92	10.8

The flow rate through each sampling mast was set at the beginning of each test, and appeared to remain constant over the duration of the test. After the tests were completed however, there was evidence that the more highly dosed filters were clogged and the flow was severely restricted for these samples.

The membrane filters trap particles in 0.45- $\mu\text{m}$  diameter capillaries etched through the filter. Each collected particle clogs a capillary so that the pressure drop and flow rate depends on the filter loading. We can calculate the maximum loading for these Nucleopore membrane filters using data from the manufacturer. Each 37-mm filter is etched with close tolerance 0.45  $\mu\text{m}$  diameter capillaries to a porosity of 79%, for a total of  $6.8 \times 10^9$  holes. For the HC aerosol, and using a diameter of average mass in the range of 0.4 to 0.6  $\mu\text{m}$ , this translates into a maximum aerosol mass to completely clog the filter in the range of 0.45 to 1.5 mg.

Examination of the data for the analyzed filters shows a maximum filter load for each of the tests in the range of 0.96 to 1.34 mg, so that it is probable that filter clogging is significant for our data. This effect was not evident during our tests because the flow meter reading  $Q_{\text{design}}$  remained approximately constant while the actual flow  $Q_{\text{actual}}$  decreased with decreasing absolute pressure  $P_{\text{actual}}$  seen by the flow meter.

This effect of the filter clogging became clear when the concentration results were analyzed. The concentrations on the highly dosed masts near the source varied little over distances exceeding 100 m in some cases. In order to correct this problem, a correction factor was developed for these data which took into account the lower aspiration rates created by high filter loading. This correction factor assumes a collection efficiency of 100% for filter loadings less than 120 $\mu\text{g}$  and

lowers the efficiency exponentially for loadings above this threshold. The development and application of this correction scheme is discussed thoroughly in DeVaul et al. (1989).

### **Aerosol Sampling Losses**

In sampling of the HC aerosol, losses of particles before they are collected on a filter may occur due to gravitational settling and inertial forces and must be quantified.

### **Inertial Particle Losses**

We calculate the Stokes number for the aerosol and filter inlet geometry to determine if inertial effects are significant. The Stokes number is the ratio of the particle stopping distance to the characteristic probe dimension. For the HC aerosol, ( $\rho_p = 2.0 \text{ g/cm}^3$ ), typical values of the particle stopping distance (in cm) are as shown in Figure 5.17. All values in this plot are for particle motion in the Stokes regime. Although the same 37-mm diameter filter cassettes were used for both the fog-oil smoke and the HC aerosol, the samplers for the HC smoke were operated with a protective cover in place which had a reduced inlet size of 0.42 cm. The Stokes number is calculated using this diameter, and is also shown in this graph. In terms of anisokinetic sampling, for conditions shown in this graph more than 96% of the aerosol mass distribution will show no losses using the  $St < 0.1$  criteria given by Hinds (1982). Davies (1968) cites a conservative upper limit for neglecting inertial effects in aerosol collection in stagnant air of  $St < 4 (10^{-3})$ . This is also shown on the figure and is exceeded only by the larger sized aerosol particles.

### **Gravitational Settling Losses**

In gravitational settling, collection efficiency may be affected by the finite downward velocity  $v_s$  of the particles. Typical calculated values for the HC smoke are given in Table 5.17. The settling velocity is nondimensionalized using  $V'_s = v_s/V$  and  $V$  is the sampler flow velocity. Davies (1968), cites a conservative upper limit on the nondimensionalized settling velocity of  $V'_s < 4(10^{-2})$  which, if met, insures that gravitational settling is an insignificant effect relating to collection efficiency. This limit is easily met for our sampling conditions.

Particle settling velocities also effect the conservative nature of the aerosol, with deposition becoming significant for the larger particles at greater downwind distances. For the largest particles in the HC aerosol size distribution, the settling velocity is significant. This settling can be neglected for over 96% by mass of the aerosol size distribution.

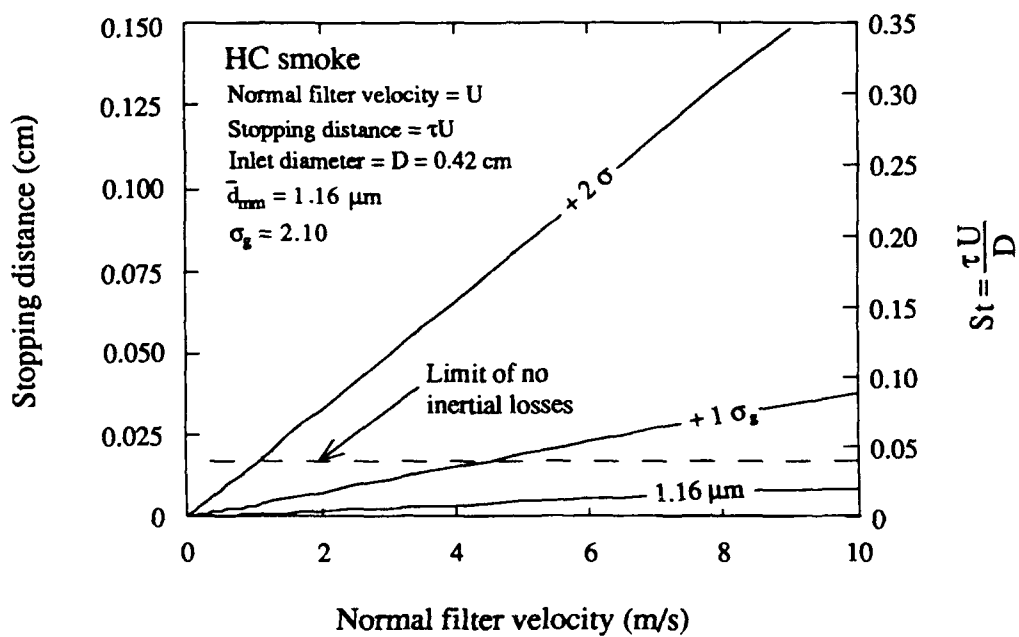


Figure 5.17 Velocity versus particle stopping distance and Stokes number for HC aerosol smoke. Lines are calculated for the mass mean diameter, and at +1 and +2 geometric standard deviations from the mean.

Table 5.17 Settling velocities for HC-smoke aerosol.

	Particle diameter ( $\mu\text{m}$ )	Settling velocity (cm/sec)
Mass mean diameter	1.16 $\mu\text{m}$	0.0088
+1 $\sigma_g$	2.43 $\mu\text{m}$	0.0368
+2 $\sigma_g$	5.11 $\mu\text{m}$	0.1600

#### 5.4.4 HC Smoke Field Sample Analysis Errors

While the chemical sampling analysis was performed by a commercial laboratory without a detailed error analysis, we can estimate the scatter in mean concentration measurements from sets of filters taken from a single sampling mast. This scatter in mean values is shown in Figure 5.18 as a function of the measured concentration. There is a slight decrease in the noise for smaller sample sizes. The data cluster between 0.1 and 1  $\text{mg}/\text{m}^3$  is due to the filter clogging at higher mass loading which biases the higher actual concentrations to smaller values. Overall scatter in these values is very similar to the scatter in the fog-oil concentration measurements.

### 5.5 Real-Time Concentration Measurement Instruments

Several types of instruments are available for measuring various properties of pollutants or tracers at a speed sufficient to be considered real-time detection instruments. Since we are limited to aerosol tracers, it is most direct to measure an aerosol property rather than some molecular property of the particular constituents of the aerosol. Although this method is not as selective as measuring a chemical property, it can be sensitive enough to easily detect concentrations above the background levels of aerosol in the atmosphere.

For our mass release rates, mean concentration measurements are typically of the order of 50  $\text{mg}/\text{m}^3$  at the samplers located nearest the smoke generator (about 50 m downwind) and decay with increasing downwind distances and off the plume axis to about 0.01  $\text{mg}/\text{m}^3$ . Fluctuating concentrations may vary by a factor of 10 from these mean values. It can be difficult to make an *a priori* guess of concentration at a given instrument location before a test because of the fluctuating wind direction.

Instrument response times needed in measurements of turbulent fluctuations depend on the smallest scale of contaminant dispersed in the flow. A lower limit on the smallest scales which may be resolved in a flow can be estimated using Kolmogorov microscales for the dispersing contaminants, but this sampling speed is beyond our capability. A less restrictive criteria is to sample at a speed sufficient to resolve the inertial-convective subrange in the flow. Since turbulent

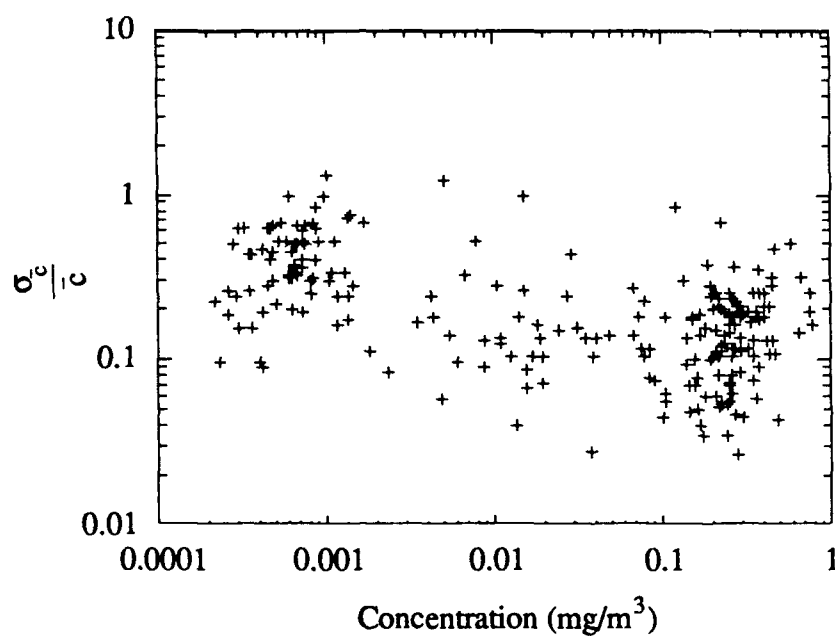


Figure 5.18 Ratio of standard deviation to variance for mean HC smoke concentrations measured by multiple filters on the same sampling mast.



Reynolds numbers in the atmosphere can be huge, with a correspondingly large inertial subrange, this is a much less restrictive criteria than sampling at rates determined by the Kolmogorov time scale. To meet this restriction, we sample at a rate much faster than the Lagrangian integral time scale of the flow.

#### **5.5.1 Types of Real-Time Measurement Instruments**

Two basic types of instruments are available for measuring real-time aerosol concentrations. These are collection based instruments and instruments which directly measure the aerosol in place. With the first type of instrument, the aerosol is collected, then some determination of the collected mass is made. The second type of instrument usually relies on optical properties to detect the aerosol particles, and some correlation to relate the detected quantity to mass.

##### **Collection Based Instruments**

In the first class of instruments we have the  $\beta$ -gauge, the piezoelectric microbalance, and the tapered element oscillating microbalance. Other types of real-time collection measurements, such as an incrementing filter, do not have the temporal response necessary to capture the turbulent fluctuations in concentration and can be immediately dismissed.

The  $\beta$ -gauge instrument collects an aerosol sample on an impaction film or filter. Changes in the attenuation of  $\beta$ -radiation through the collector with time indicate the aerosol mass collected on the filter or film. This instrument can measure concentrations in the range 0.01 to 150 mg/m<sup>3</sup>. The precision and accuracy of this instrument in aerosol mass measurements is investigated by Courtney et al. (1982).

The piezoelectric microbalance collects aerosol using an electrostatic precipitator or an impaction jet on a quartz crystal disc oscillating near 10 MHz. The change in resonant frequency of the disc is directly related to the mass collected on the center of the disc. This instrument has a relatively narrow linear operating range (in frequency) and the quartz crystal surface must be frequently cleaned to remove collected aerosol. This instrument is expensive, which makes it unsuitable for multiple point measurements. Concentrations of aerosol in the range 0.01 to 10 mg/m<sup>3</sup> may be measured with the piezoelectric microbalance. Our particle size measurements were made with an instrument of this type which employed 10 sequential collection stages, each with a piezoelectric crystal sensor and associated support circuitry.

The tapered-element oscillating microbalance (TEOM) is similar in operating principle to the quartz-crystal microbalance in that it measures the change in resonant frequency of a mechanical element as the mass of that element changes with an increasing load of collected aerosol. The design of this patented instrument is discussed by Patashnick and Rupprecht (1986). Operation in

several experiments is described by Wang et al. (1980) and Ariesson and Wang (1985). With this instrument a filter element is mounted at the end of a high strength tapered tube (usually glass) oscillating at a frequency of several hundred Hertz between two field plates. The frequency of oscillation is measured by an optoelectric device and used in a feedback loop to keep the tube vibrating at the resonant frequency. Changes in the mass of the filter element are detected as changes in the resonant frequency of oscillation of the tube. The linear operating range of this instrument is claimed to be six orders of magnitude, from micrograms to grams. Improvements in operation of this instrument over the piezoelectric microbalance are many, and are accompanied by a commensurate increases in price.

For all of these collection-type instruments, overloading the instrument negates future measurements during a test. They also require cleaning prior to future use. There is a trade-off between the accuracy in the mass measurement and the sampling rate. At present, the collection type instruments do not have the sensitivity to allow reasonably fast measurements of concentration while maintaining a wide linear operating range. Practical sampling times range from 10 s to several minutes. The TEOM instrument may be amenable to faster measurements, but not at multiple locations because of its very high cost.

### **Direct Reading Aerosol Measurements**

Direct reading instruments measure properties of the aerosol in situ. This class of instruments includes the aerosol photometer, which we used in our measurements, the aerosol nephelometer, transmissometers, and many types of aerosol particle counters. All of these instruments rely on the scattering or extinction properties of the aerosol to infer aerosol properties. In addition, the response of this type of instrument is not dependent on the history of the measurement period and overloading, if it occurs, is only temporary.

Single aerosol particle detection requires very low particle concentrations, usually using laser illumination and a photomultiplier tube or photodiode detection for measurement of pulses of scattered light. Response functions for this type of instrument are discussed by Cooke and Kerker (1975). The aerosol used in our experiments is much too concentrated for use in this type of instrument without dilution. For the aerosol photometer, many particles are within the illuminated viewing volume at the same time, and the total intensity of scattered light is measured. The aerosol nephelometer is similar to the aerosol photometer, but the name is usually reserved for instruments which measure more detailed properties of the scattered light. A transmissometer measures the extinction of a beam of light over a long path. This type of instrument is not suitable for point measurements, unless the illuminating beam is folded, but this usually requires delicate and precisely aligned optical components which are not suitable for our testing conditions.

The instrument most suitable for our measurements is the aerosol photometer, which measures the light scattered from particles within a detection volume. This measurement can be related to the mass concentration of aerosol by a scattering coefficient which is a function of the size distribution and shape of the particles, the index of refraction of the particles, the incident light, and the optical geometry. For a given aerosol composition, the scattering coefficient is fairly constant. In our tests a filter sampler was located at each photometer location for determining the average mass concentration. A linear calibration for our photometer instruments is found by equating the average mass concentration to the average signal voltage measured at each sampling location for each test.

The operating range of the aerosol photometer can be very wide. Heintzenburg and Bäcklin (1983) describe an extremely sensitive instrument capable of measuring scattering coefficients as small as  $\alpha_{\text{sca}} = 10^{-8} \text{ m}^{-1}$ . Gucker et al. (1947) describes an instrument with a sensitivity of  $10^{-9} \text{ mg/m}^3$  in aerosol measurement. At the other extreme range Holmburg et al. (1982) have designed an instrument for measurement of dense aerosols with mass concentrations up to  $4 \times 10^3 \text{ mg/m}^3$ .

Commercial aerosol photometers are available which fit many of our criteria but to better meet cost goals we designed and built 35 of our own instruments. The electronic components for detection in this device are readily available and do not present a problem in terms of frequency response or sensitivity. With attention to flow through the detector volume we achieved an unbiased frequency response to 1 Hz. This instrument operates with aerosol mass concentrations in the range of 0.1 to 200  $\text{mg/m}^3$ .

#### 5.5.2 Design, Construction, and Refinement of an Aerosol Photometer

The instruments we have used in measuring the concentration fluctuations in a smoke plume are intended to complement the mean dosage measurements. The light scattering method of detection used in these instruments is only a relative measurement and requires calibration against a dosage measurement of mean concentration for each use.

Several criteria were used in our design and construction of the aerosol photometers. Cost constraints are important, since detectors were required at multiple locations. Our custom design and construction of these instruments, rather than purchasing a set of commercial aerosol photometers, saved about 80% in initial costs. The design is also necessarily simple, since there was only a five month lead time in a decision to schedule the 1987 field dispersion tests. The set of instruments had to be fully designed, built, and their response characteristics tested within this five month time frame.

The data recording systems available for our use in logging the information from these detectors consists of a  $\mu\text{MAC-4000}$  Measurement and Control System (Analog Devices) with 12 multi-

plexed analog inputs sampled at 30 Hz, an input range fixed at  $\pm 10$  V, and a 13 bit dual-slope analog to digital converter. The  $\mu$ MAC-4000 is controlled through a 9600 baud RS-232 serial port by a Zenith Z-181 Laptop Computer running our data recording and display software. The data were sampled at 1-s intervals and stored in memory, with on-screen graphics of the real-time signals. Up to 110 minutes of continuous data can be recorded with this arrangement. For archival purposes, the data are transferred to a floppy disk after a test.

## **Hardware**

A schematic of the aerosol photometer is shown in Figure 5.19. In the photometer, a 110-V, 25-W tungsten lamp is directed through a collimator made from steel electrical conduit and mounted partially within a 2-in (nominal) diameter PVC pipe. The silicon photodetector is located at a right angle to the illuminating radiation, out of direct view of the lamp. The intersection of the light beam and the detector field of view provides a 1.5-cm diameter by 3-cm long viewing volume.

Air is aspirated through the pipe by a 20 cfm squirrel cage blower through the PVC pipe and the viewing volume. The air inlet and exit contain serpentine light traps to protect the viewing volume from ambient illumination. The interior of the instrument is painted flat black to minimize interior light reflections. The exhaust from the blower is directed at the collimator to aid in dissipating heat from the tungsten bulb.

No lenses were used in this detector in order to minimize maintenance during field test use and to avoid breakage and alignment problems. The geometry of the illumination and detector, although not optimized to collect the maximum amount of scattered light, is quite sufficient for the detection of smoke in concentrations found in our field experiments. The design does not require a precise optical orientation of the components to be maintained, and is fairly rugged, which is important for field use.

## **Photometer Light Scattering Characteristics**

As shown in Figure 5.20 the spectra of light from an incandescent tungsten filament bulb at 2780K has the emission spectra of a black body. The response curve for a silicon photodetector, which indicates the efficiency of the detector in converting the incident power to a signal current at a given wavelength, is also shown in this figure. This efficiency is a characteristic of the material, and all unfiltered silicon detectors behave similarly. With this combination, a total fraction of 17.5% of the spectrum of energy emitted by the tungsten bulb is detectable with the silicon detector. Most modern detectors, including photodiodes, phototransistors, and photodarlington transistors, maintain a linear signal current to incident radiation intensity over a suitably wide range.

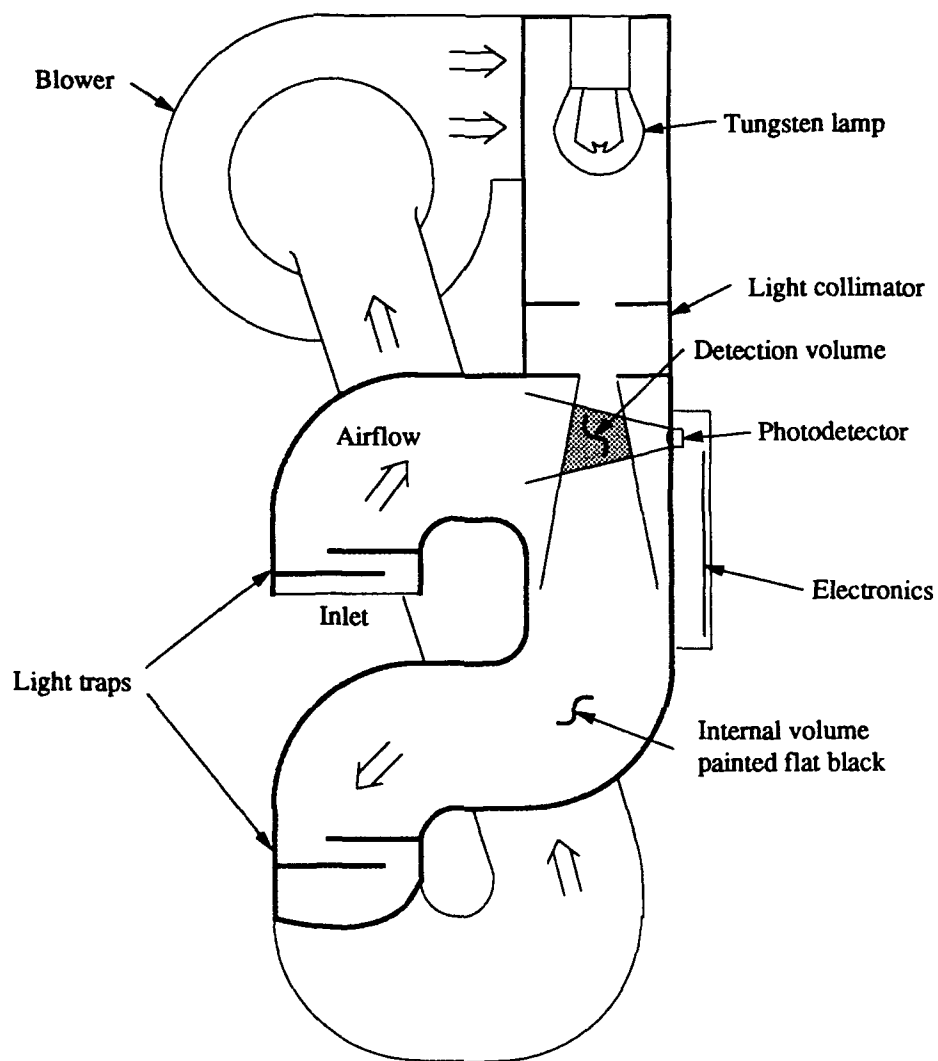


Figure 5.19 Mechanical diagram of the aerosol photometer. A cutaway view of the illuminator and the scattering volume is shown. The instrument is approximately 30 cm in height.

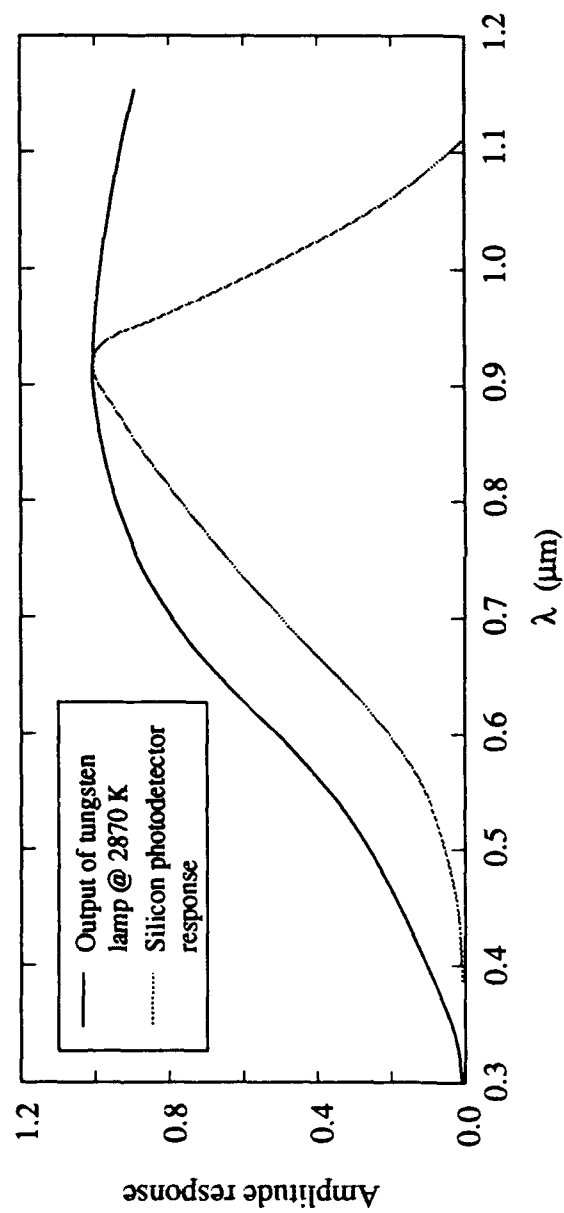


Figure 5.20 Normalized unfiltered spectral response of a silicon photodetector and light output of a tungsten bulb. Data are taken from the Texas Instruments Optoelectronics Data Book, 1978.

The broad spectrum of the light and the distribution of aerosol particle sizes causes smearing of the peaks and valleys in single particle and single wavelength Mie scattering diagrams. We may estimate the total light scattered by integrating the intensity  $I(\theta, \lambda, a)$  over the particle size distribution and the light spectra by using Eq 5.17

$$\frac{I(\theta) R^2}{I_0 N} = \int_{\lambda=0}^{\infty} \int_{a=0}^{\infty} \frac{I_0(\lambda)}{I_0} \frac{N(a)}{N} \frac{\lambda^2}{8 \pi^2} \left[ i_t(\theta, \lambda, a) + i_r(\theta, \lambda, a) \right] da d\lambda \quad (5.17)$$

where  $N(a)$  is the number of particles in the scattering volume,  $N$  is the total number of particles,  $I_0$  is the total irradiance, and  $R$  is the distance from the scattering volume.

In this equation, we use the tungsten bulb spectra visible to the silicon photodetector, and a lognormal particle count size distribution given by

$$\frac{N(d_p)}{N} = \frac{1}{\sqrt{2\pi} d_p \ln(\sigma_g)} \exp \left( - \frac{(\ln d_p - \ln \bar{d}_{50})^2}{2 (\ln \sigma_g)^2} \right) \quad (5.18)$$

where  $d_p$  is the particle diameter,  $\bar{d}_{50}$  is the count median diameter, and  $\sigma_g$  is the geometric standard deviation. Data from the measured particle distribution discussed in Section 5.2 are used in these calculations.

We may relate the information provided by this relation to the mass concentration of aerosol  $c$ , rather than the number concentration  $N$ , using

$$c = N \frac{\rho \pi}{6} \bar{d}_m^3 \quad (5.19)$$

where  $\bar{d}_m$  is the diameter of average mass. For a lognormal distribution, we have

$$\bar{d}_m = \bar{d}_{50} \exp \left( 1.5 (\ln \sigma_g)^2 \right) \quad (5.20)$$

and the count median diameter is related to the mass median diameter through

$$\bar{d}_{m50} = \bar{d}_{50} \exp \left( 3 (\ln \sigma_g)^2 \right) \quad (5.21)$$

For fog-oil smoke with  $m = 1.55$  and  $\rho = 0.90 \text{ g/cm}^3$ , calculations for the scattering as a function of angle are shown in Figure 5.21. Here we have taken an average  $\bar{d}_{m50}$  and  $\sigma_g$  from our field measurements. A range of values which were taken from the scatter in our field measurements of  $\bar{d}_{m50}$  is also shown. This range gives an indication of the sensitivity of the detector to a changing particle-size distribution. A similar figure is shown using parameters of the HC smoke particle size. For this we use  $m = 1.7$ , as found for zinc chloride. The geometric standard deviation

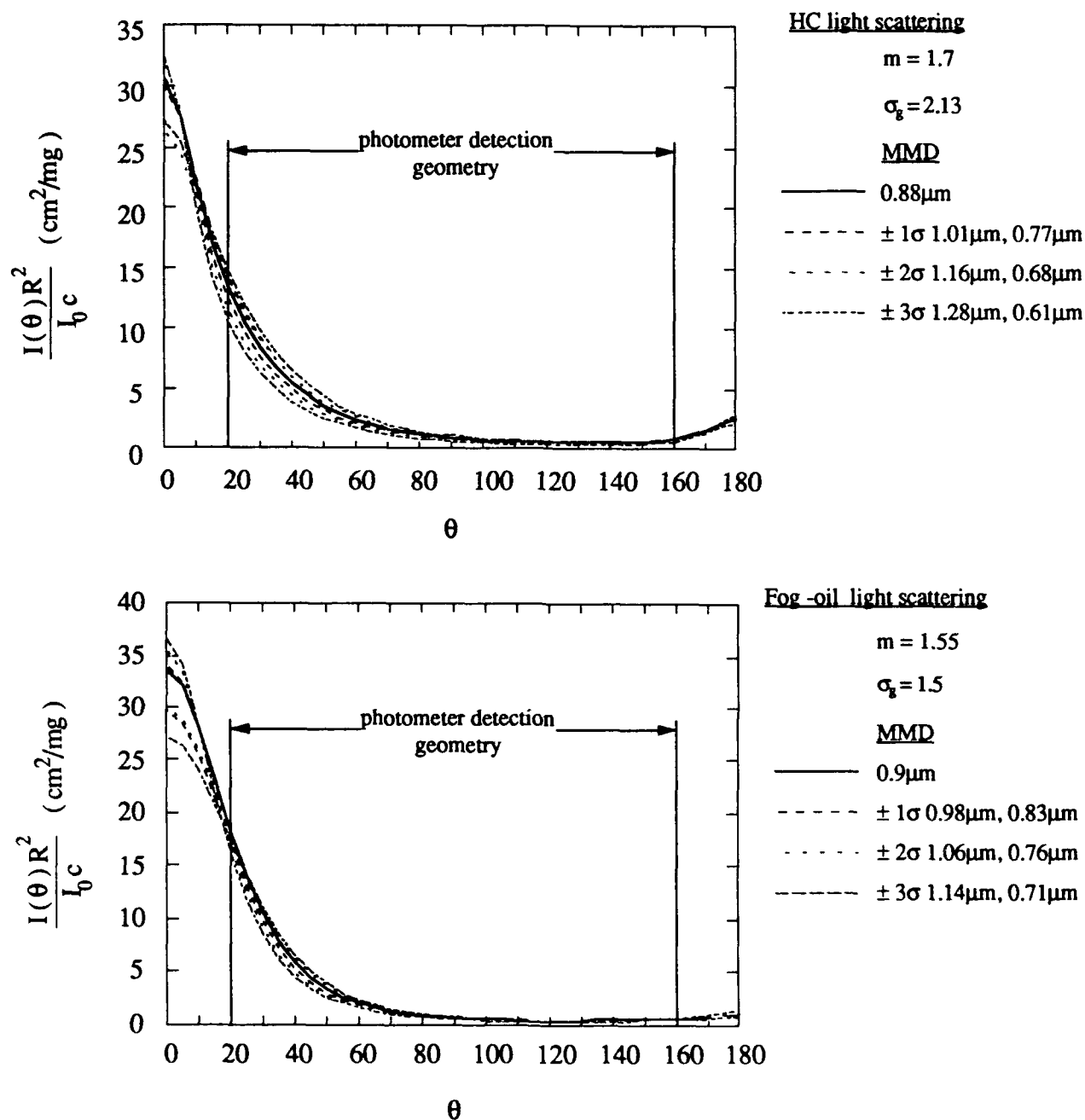


Figure 5.21 Light scattering for fog-oil smoke and HC smoke using a tungsten filament bulb with a silicon detector. The vertical axis is given in units of  $\text{cm}^2/\text{mg}$ , where the mass is that quantity within the viewing volume. Typical values of the refractive index are used along with measured values of the particle size distribution and variances about that distribution.



tion for the HC aerosol size distribution is considerably larger than that for the fog-oil smoke. The silicon detector and optical geometry we have used integrates the light scattered between 20° and 160°. In this range, the intensity of scattered light is not a strong function of the mean particle diameter.

An approximate view factor for the illumination of the detector volume can be simply calculated because of the lack of mirrors or lenses in the detector body. With a uniform spherical irradiation from the tungsten filament, and the diameter of the collimator used, we find the fraction of radiation reaching the detector is 0.0012, which translates into a value of  $I_0 = 0.038 \text{ W/cm}^2$  in the viewing volume for a 25-W bulb. This value may be used in the plots of the last figure, along with a view volume of  $12 \text{ cm}^3$ , to estimate the intensity of light scattered by a given mass of aerosol. For a  $1\text{-mg/m}^3$  aerosol concentration (of either HC or fog-oil smoke), the scattered light incident on the detector is approximately  $5 \times 10^{-3} \text{ mW/cm}^2$ . Variation in sensitivity between different photodetectors, however, prevents an accurate estimate of signal current for a given detector illumination.

### **Electronics**

In our circuit design a silicon photodarlington transistor is used as the light detector. Selection of the photodarlington transistor is a tradeoff of linearity and sensitivity. The photodarlington transistor has a linear range over 3 orders of magnitude, which is greater than can be sensed with our fixed range 13 bit A/D converter. The use of the photodarlington transistor also eliminates the need for a low-noise, high-gain amplifier in the supporting circuitry as compared with PIN photodiodes or photomultiplier detectors.

In operation, the small amount of stray light in the detector field of view is sufficient to bias the sensor into conduction. Increasing the illumination of the detector causes an increase in the signal current. The output of the photodarlington is amplified and buffered through an op-amp and then filtered through a 4-pole Bessel filter with a cutoff frequency of 1 Hz. A reference voltage is provided through a voltage divider and an op-amp buffer. The differential output is taken between the filter output and the reference voltage. The power and signal for the detector electronics are sent through a shielded four wire cable for each detector to a central analog to digital converter. Cabling distances up to 300 m away from the A/D converter were used in the field experiments, with no electrical noise problems. A schematic for the electronics is given in Figure 5.22.

### **Detector Response**

The frequency response of the electronics was measured using the modulated output of a sinewave driven light emitting diode with a small direct current bias. The amplitude of the output



was measured on an oscilloscope as a function of the driven frequency. A plot of the result is shown in Figure 5.23. In this plot, the frequency rolloff begins at 1 Hz. The step response was measured using a two-level switched output from a light emitting diode and sensing the electronics output on an oscilloscope. This response is shown in Figure 5.24. Because of the minimized phase shift with the Bessel filter, there is a distinct lack of ringing in the response. This is important for the asymmetric signals sensed with a photometer.

The mechanical response of the photodetector is modeled as a simple first order lowpass system, with the internal volume of the detector and the flow rate through the detector controlling the response time. The time constant for this system is given by  $\mathcal{V}/Q$ , where  $\mathcal{V}$  is an 'effective' internal volume and  $Q$  is the volumetric flow rate. The response to a step increase in concentration sensed through this detector is

$$\frac{c(t)}{c_0} = 1 - \exp\left(-\frac{t}{(\mathcal{V}Q)}\right) \quad (5.22)$$

We desire a value of the mechanical time constant close to that found for the detector electronics. A flow rate of 120 liters/min is used. In Figure 5.24, the approximate response of the detector to a switched supply of aerosol smoke is shown. This is slower than that found with the electronics response alone, but it is still reasonable given our 1-Hz sampling rate.

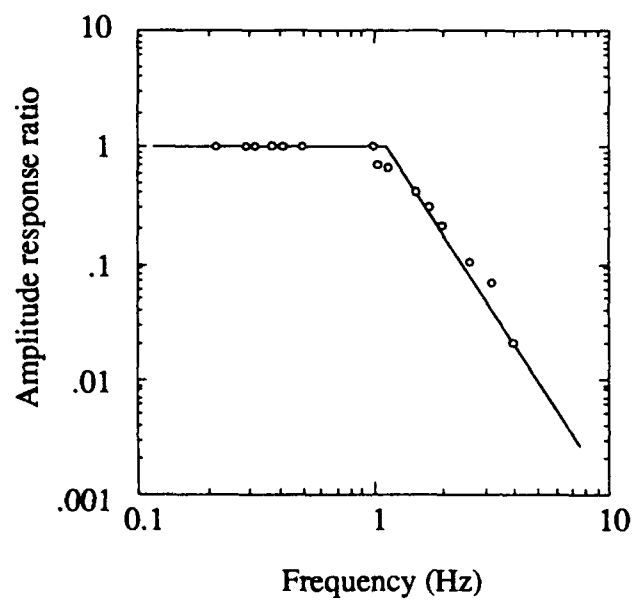


Figure 5.23 Frequency response for the aerosol photometer detection electronics.

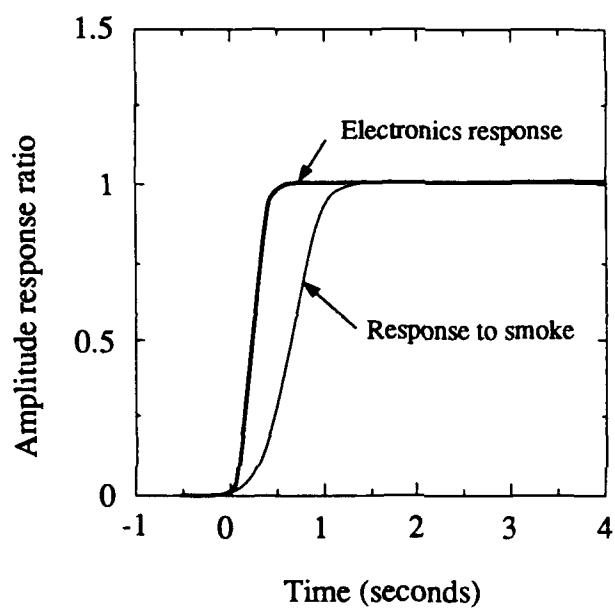


Figure 5.24 Temporal response for the aerosol photometer. Both the response of the detector electronics alone and the response to a step increase in smoke concentration is shown.

## 6. EXPERIMENTAL RESULTS AND ANALYSIS

This chapter is concerned with the reduction of concentration data from the dispersion experiments. This includes both the mean concentration data and the fluctuating concentrations from four primary sets of experiments at two dispersion sites. The first site consists of moderately uniform terrain at Camp Atterbury, Indiana, for which dispersion tests were undertaken for two different source types, a fog-oil smoke and an HC chemical smoke. The second site is near Red Bluff, California in rough terrain for which the experiments are divided into convective daytime tests and stable nighttime tests, both of which used the fog-oil smoke. Errors in the model-data comparison are examined in Chapter 7.

### 6.1 Camp Atterbury Fog-oil Smoke Data Analysis

The fog-oil data from Camp Atterbury consist of four experiments. For three of the four trials the dosage measurement set is sufficiently complete for a detailed examination of the data. A diagram of the grid on which the samples were taken is given in Figure 6.1. Vectors for the mean wind direction are also shown in this figure. Values of the concentrations from dosage measurements and standard deviations in concentrations from the calibrated photometer measurements, both of which are given in units of  $\text{mg}/\text{m}^3$ , are shown in Figure 6.2. The profiles of concentration in these plots are shown looking from the source downwind, with peaks in concentration corresponding to a line through the source which is parallel to the average wind direction. Tests 1103871, 1104872, and 1106871 are the best of this set, and capture most of the crosswind profile at each transect. The wind on Test 1104871 carried most of the plume off the grid. Convective meteorological conditions existed for all of these tests.

Several important points can be made from the graphs in Figure 6.2. First, the decay with distance of the mean concentrations is very rapid. The measured concentrations at different heights at the same location agrees well at the closer distances, but the scatter is greater at further distances. No trend is evident in this scatter, but it is likely due to the decreased accuracy of the analysis method at lower concentrations. Finally, the standard deviation in concentration which is plotted in these graphs is always greater than the magnitude of measured concentration at the same 2-m height.

#### 6.1.1 Mean Concentration Data

It is useful to separate behavior in the concentration field into downwind  $x$  and crosswind  $y$  directions. In our tests, the wind is not normal to the plume trajectory. A method is described in the next section which assumes a Gaussian profile in the crosswind direction and allows correc-

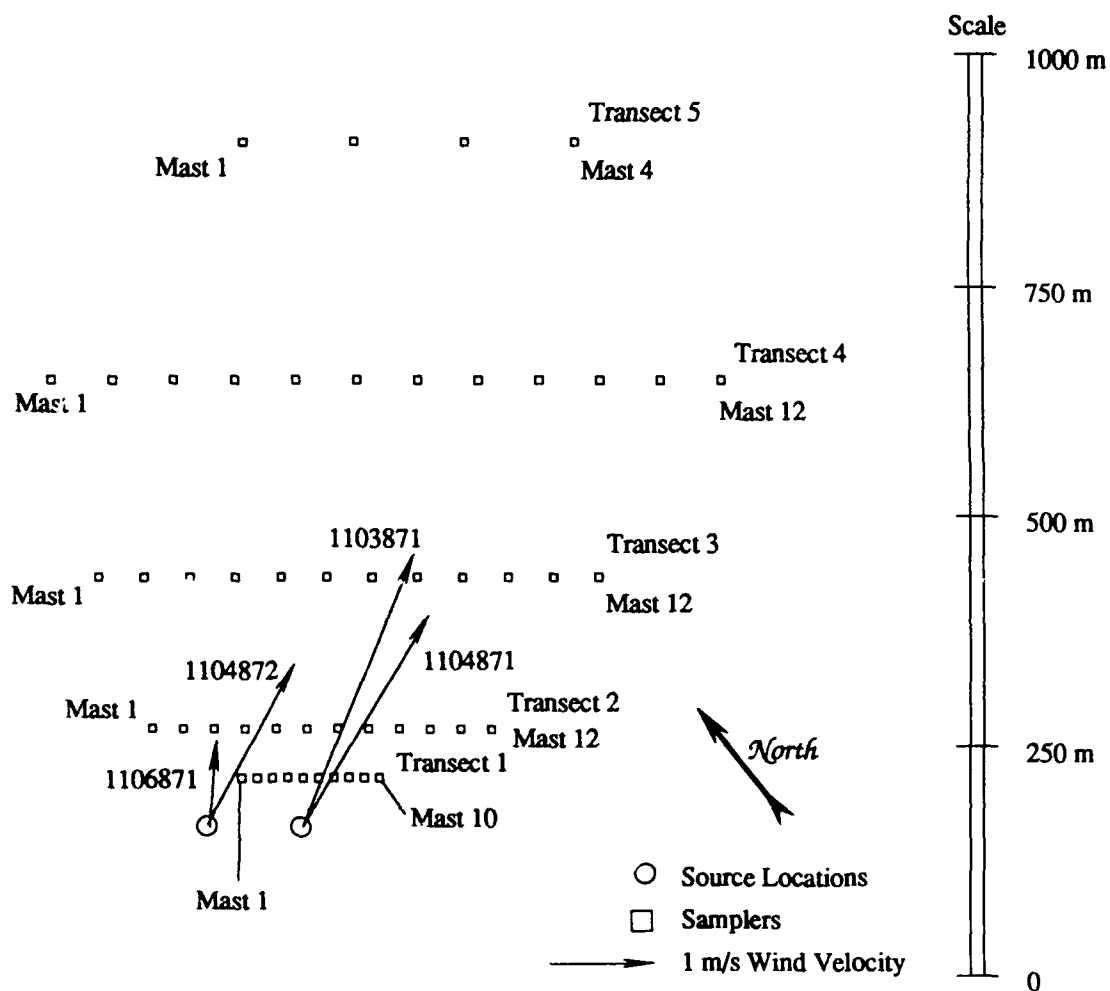


Figure 6.1 Sampler and source locations for the fog-oil smoke dispersion tests at Camp Atterbury. The wind vectors indicated in the figure are averages over the test duration at the source location. The transects in the figure are labeled 1 to 5. The masts in each of these lines are numbered, from northwest to southeast, beginning with one in each transect.

Concentration data  
fog-oil smoke  
Test 1103871  
November 3, 1987  
10:31:06 to 11:27:00

—○— 8 m mean  
—●— 4 m mean  
—○— 2 m mean  
—○— 1 m mean  
—■— 2 m std. dev.

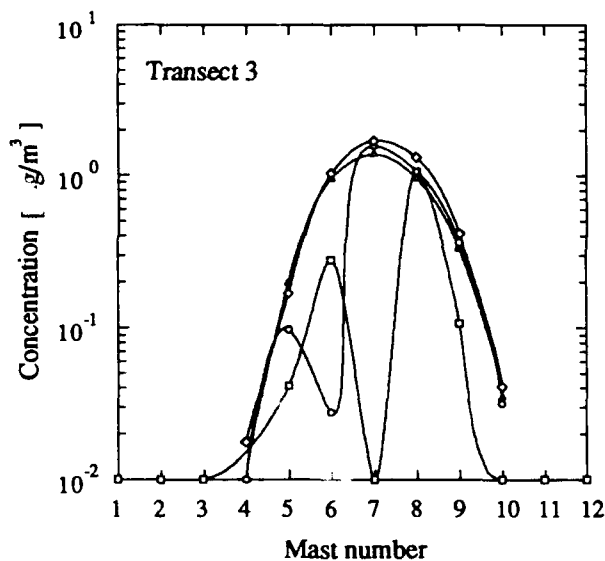
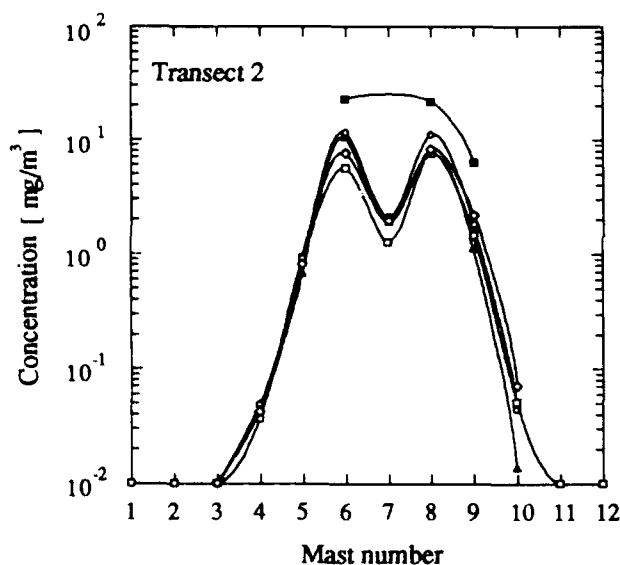
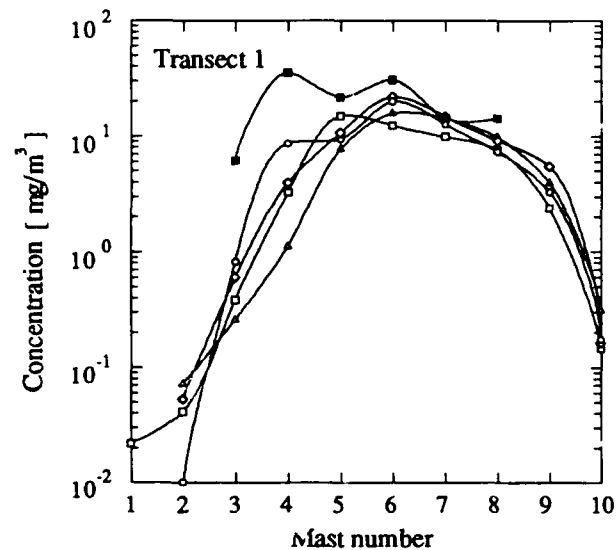


Figure 6.2 Profiles of fog-oil concentration measured along the sampling transects in the Atterbury dispersion tests. These plots are for Test 1103871, and the crosswind view in these graphs is looking downwind from the source. In addition to the mean concentrations, the standard deviation in concentration from the aerosol photometers is also shown in these plots.



Concentration data  
fog-oil smoke  
Test 1103871  
November 3, 1987  
10:31:06 to 11:27:00

—○— 8 m mean  
—▲— 4 m mean  
—○— 2 m mean  
—○— 1 m mean  
—■— 2 m std. dev.

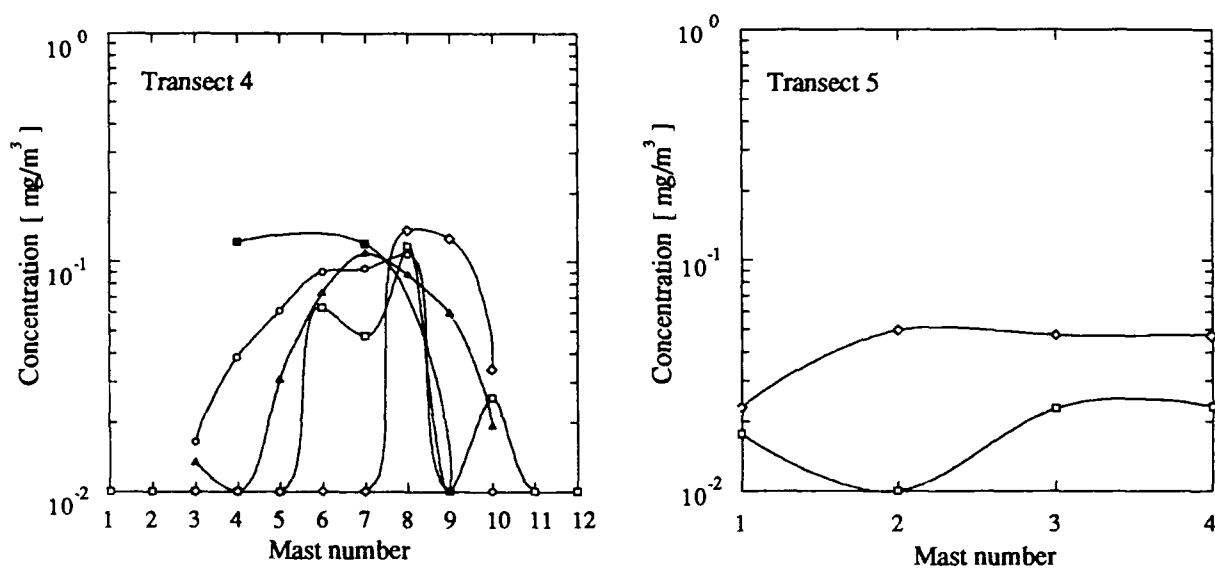


Figure 6.2 (continued) Profiles of fog-oil concentration measured along the sampling transects in the Atterbury dispersion tests. These plots are for Test 1103871, and the crosswind view in these graphs is looking downwind from the source. In addition to the mean concentrations, the standard deviation in concentration from the aerosol photometers is also shown in these plots.

Concentration data  
fog-oil smoke  
Test 1104871  
November 4, 1987  
09:36:33 to 10:06:00

—○— 8 m mean  
—▲— 4 m mean  
—○— 2 m mean  
—○— 1 m mean  
—■— 2 m std. dev.

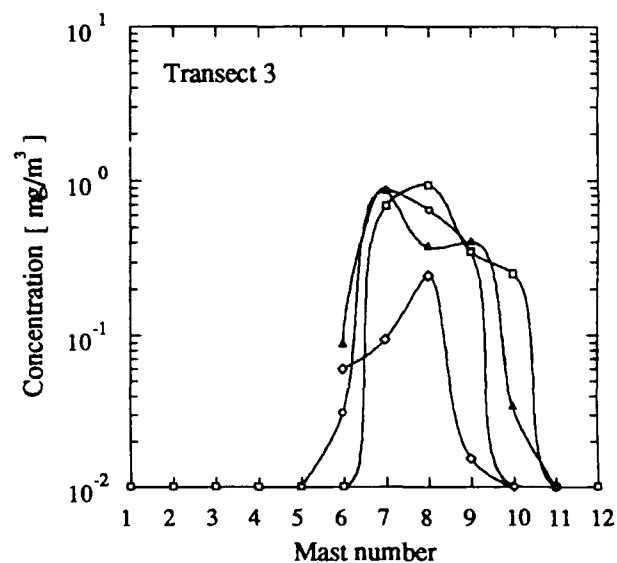
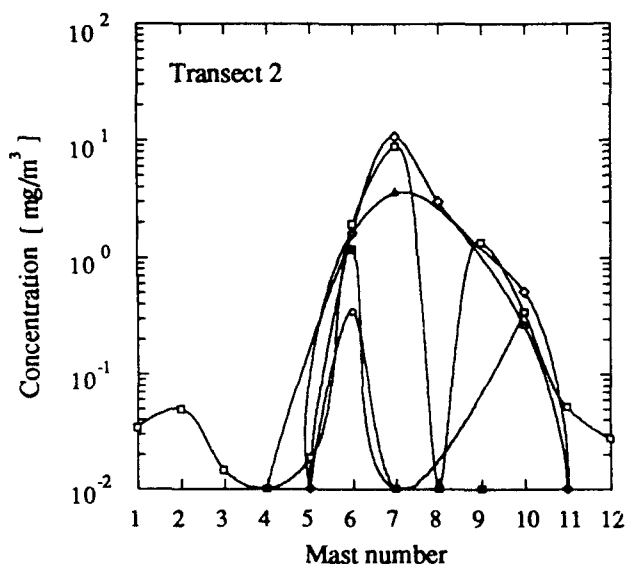
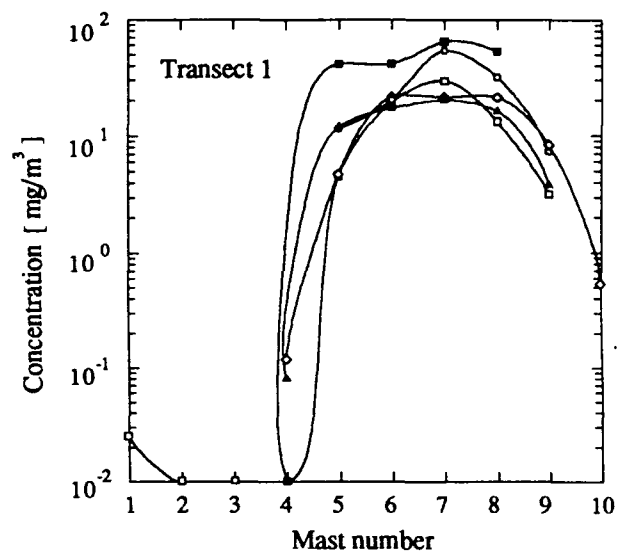


Figure 6.2 (continued) Profiles of fog-oil concentration measured along the sampling transects in the Atterbury Dispersion tests. These plots are for Test 1104871, and the crosswind view in these graphs is looking downwind from the source. In addition to the mean concentrations, the standard deviation in concentration from the aerosol photometers is also shown in these plots.

Concentration data  
fog-oil smoke  
Test 1104871  
November 4, 1987  
09:36:33 to 10:06:00

—○— 8 m mean  
—▲— 4 m mean  
—○— 2 m mean  
—○— 1 m mean  
—■— 2 m std. dev.

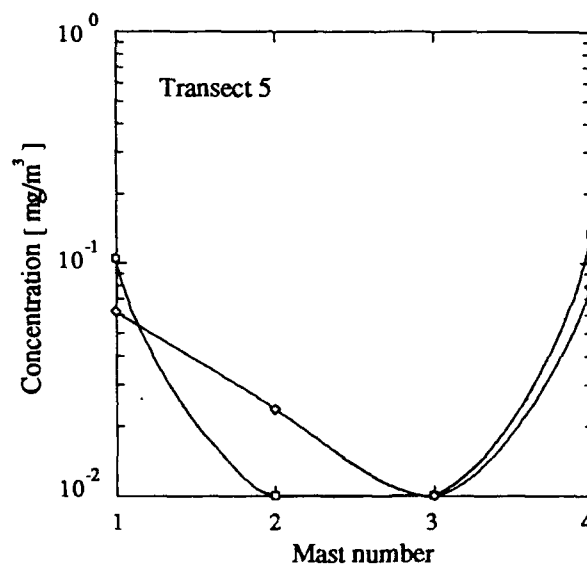
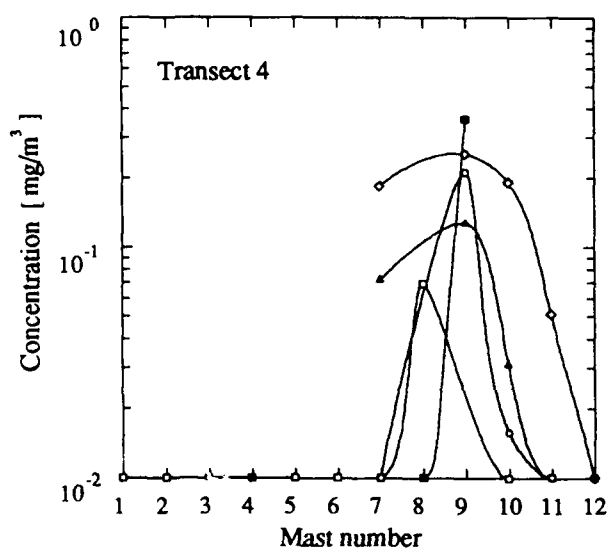


Figure 6.2 (continued) Profiles of fog-oil concentration measured along the sampling transects in the Atterbury dispersion tests. These plots are for Test 1104871, and the crosswind view in these graphs is looking downwind from the source. In addition to the mean concentrations, the standard deviation in concentration from the aerosol photometers is also shown in these plots.

Concentration data  
fog-oil smoke  
Test 1104872  
November 4, 1987  
15:25:50 to 16:14:00

—○— 8 m mean  
—▲— 4 m mean  
—○— 2 m mean  
—○— 1 m mean  
—■— 2 m std. dev.

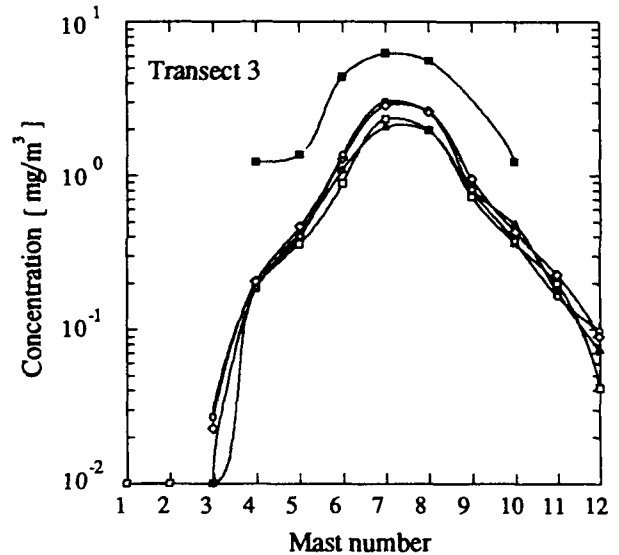
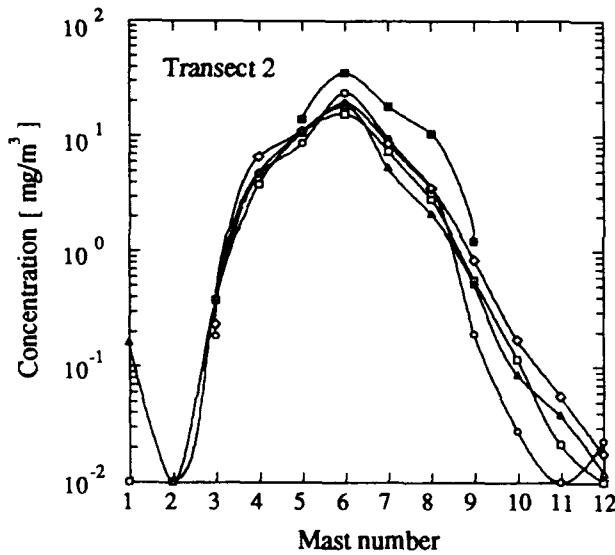
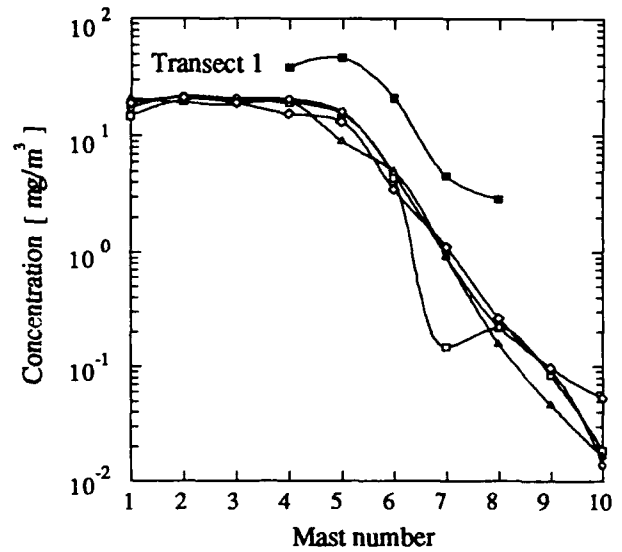


Figure 6.2 (continued) Profiles of fog-oil concentration measured along the sampling transects in the Atterbury dispersion tests. These plots are for Test 1104872, and the crosswind view in these graphs is looking downwind from the source. In addition to the mean concentrations, the standard deviation in concentration from the aerosol photometers is also shown in these plots.

Concentration data  
fog-oil smoke  
Test 1104872  
November 4, 1987  
15:25:50 to 16:14:00

—○— 8 m mean  
—△— 4 m mean  
—○— 2 m mean  
—○— 1 m mean  
—●— 2 m std. dev.

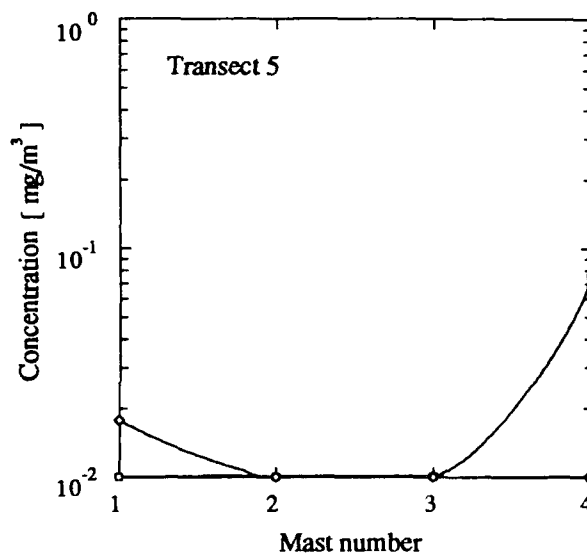
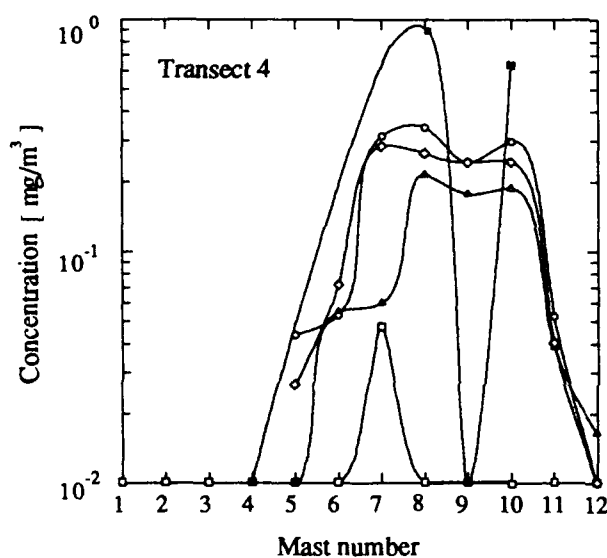


Figure 6.2 (continued) Profiles of fog-oil concentration measured along the sampling transects in the Atterbury dispersion tests. These plots are for Test 1104872, and the crosswind view in these graphs is looking downwind from the source. In addition to the mean concentrations, the standard deviation in concentration from the aerosol photometers is also shown in these plots.

Concentration data  
fog-oil smoke  
Test 1106871  
November 6, 1987  
10:51:50 to 12:08:00

—○— 8 m mean  
—△— 4 m mean  
—□— 2 m mean  
—◇— 1 m mean  
—■— 2 m std. dev.

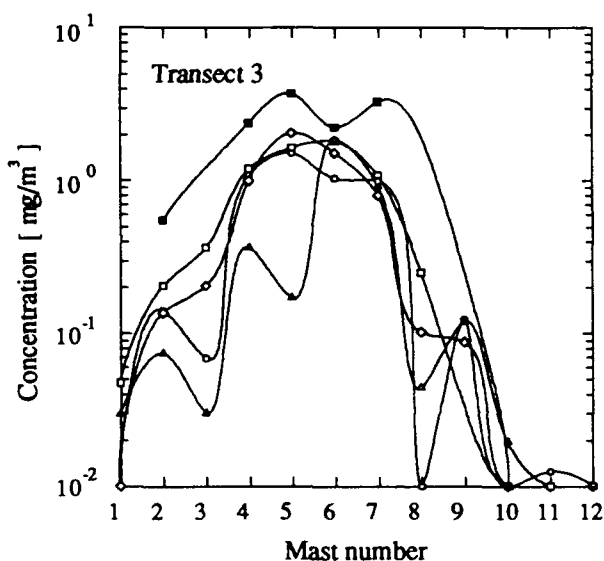
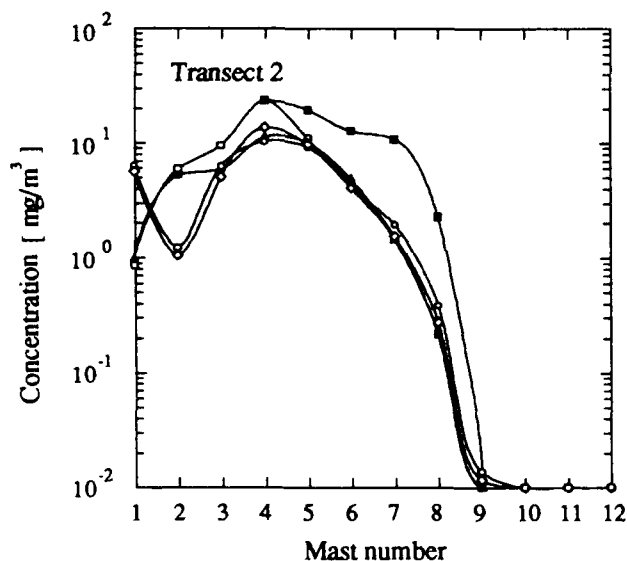
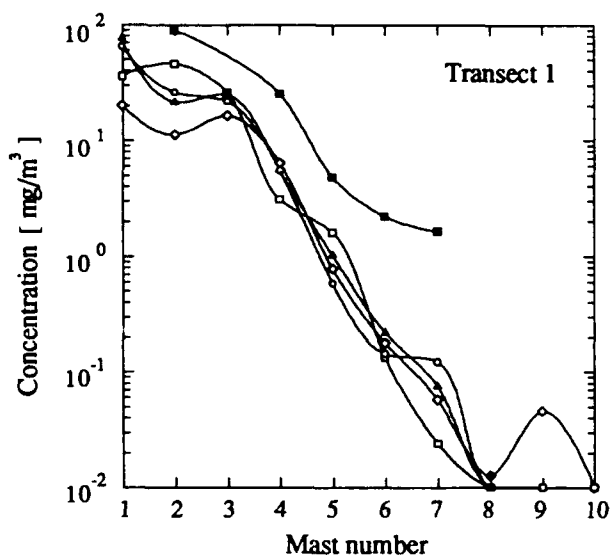


Figure 6.2 (continued) Profiles of fog-oil concentration measured along the sampling transects in the Atterbury dispersion tests. These plots are for Test 1106871, and the crosswind view in these graphs is looking downwind from the source. In addition to the mean concentrations, the standard deviation in concentration from the aerosol photometers is also shown in these plots.

Concentration data  
fog-oil smoke  
Test 1106871  
November 6, 1987  
10:51:50 to 12:08:00

—○— 8 m mean  
—▲— 4 m mean  
—●— 2 m mean  
—○— 1 m mean  
—■— 2 m std. dev.

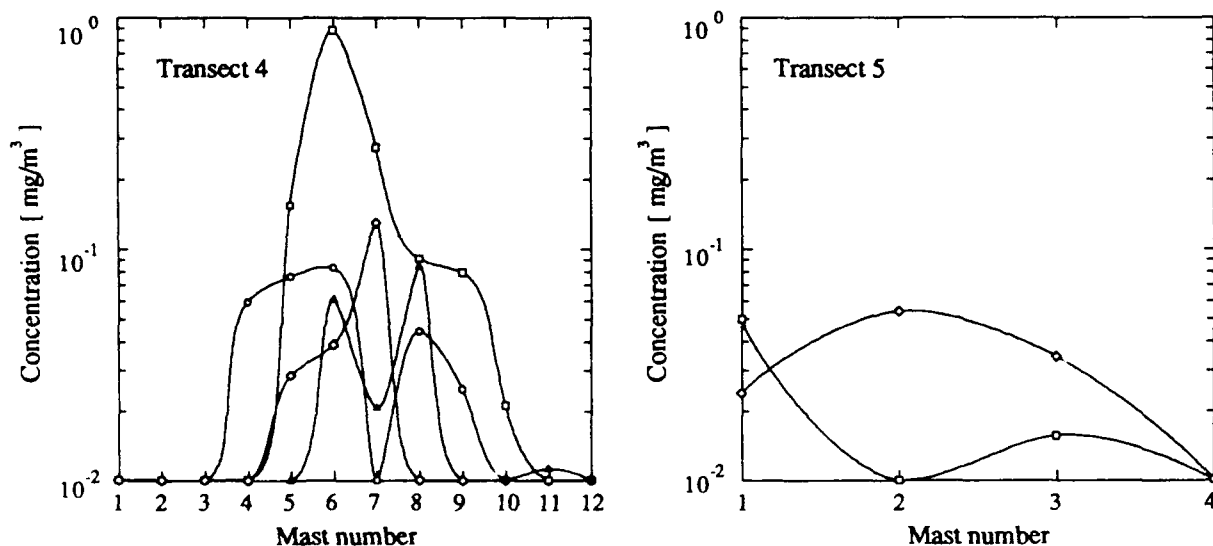


Figure 6.2 (continued) Profiles of fog-oil concentration measured along the sampling transects in the Atterbury dispersion tests. These plots are for Test 1106871, and the crosswind view in these graphs is looking downwind from the source. In addition to the mean concentrations, the standard deviation in concentration from the aerosol photometers is also shown in these plots.

tions to the data for the trajectory error. Model comparisons are made for several aspects of the data as a function of downwind distance from the source including the plume width and the crosswind integrated ground-level concentration. The Gaussian profile assumption is also compared with the corrected data.

### **Separation of Mean Plume Behavior**

We need to examine the dispersion of the smoke plume in the downwind and crosswind direction. An ideal test would be one in which the mean wind direction is perfectly normal to the transect lines. For small errors in this angle, the difference is usually ignored in determining the plume spread and the crosswind-integrated concentration. Because we are interested in examining the behavior in greater detail, corrections to the data are applied. A suitable starting point is provided by a Gaussian plume model for a ground-level source and ground-level samplers.

For a fixed downwind distance  $x$ , the crosswind profile of the concentration should follow a Gaussian distribution because of the homogeneous nature of the turbulence in the horizontal plane. Data presented as  $[\bar{c}(x,y,0)/\bar{c}(x,0,0)]$  versus  $[y/\sigma_y]$  should conform to a Gaussian profile given by

$$\frac{\bar{c}(x, y, 0)}{\bar{c}(x, 0, 0)} = \exp\left(-\frac{y^2}{2\sigma_y^2}\right) \quad (6.1)$$

if the model is valid in the crosswind plane. The parameters  $\sigma_y$  and  $\bar{c}(x,0,0)$  in the model can be fitted by a number of empirical functions.

In the field experiments we have conducted, data were taken on a rectangular grid of crosswind transects. In all of these tests, the wind blew normal to the transects within about  $15^\circ \sim 20^\circ$ . Sampler points were all at different downwind distances  $x$  and crosswind distances  $y$ . This problem was overcome by fitting sets of measurements from each transect to a Gaussian model of the form

$$\bar{c}(x,y,0) = \frac{q}{\pi \bar{u}_x \sigma_y \sigma_z} \exp\left(-\frac{y^2}{2\sigma_y^2}\right) \quad (6.2)$$

and using  $\sigma_y = A x$  to relate lateral plume spread to a constant value  $A$  and  $\sigma_z = B x$  to relate vertical plume spread to another constant value  $B$ . More generally, each of these parameters is a changing function of  $x$  which is proportional to  $x$  at closer distances (at which our measurements are made) and  $x^{1/2}$  at farther distances. No advantage was found in using more complicated relations for  $\sigma_y$  and  $\sigma_z$ , however, mainly because of the relatively small range of downwind distances  $x$  needed for each transect fit. The constants  $A$  and  $B$  were found in a linear least squares fit of the data set of  $(x,y)$  and  $c(x,y)$  for a given transect using



$$\bar{c}(x,y,0) = \frac{A}{x^2} \exp\left(-\frac{y^2}{Bx^2}\right) \quad (6.3)$$

Four complete transects were used per test. With this curve fit, a lateral length scale  $\sigma_y$  and a centerline concentration  $\bar{c}(x,0,0)$  can be found for each data point  $\bar{c}(x,y,0)$ , but only one independent data pair is found per transect. The crosswind integrated concentration for a Gaussian profile is related to centerline concentrations through

$$\bar{c}_y(x) = \int_{-\infty}^{\infty} \bar{c}(x,y) dy = \sqrt{2\pi} \sigma_y \bar{c}(x,0) \quad (6.4)$$

where  $x$  is the downwind direction,  $y$  is the crosswind axis, and  $\sigma_y$  is the standard deviation of the plume spread.

We can use the values of  $\sigma_y(x)$  and  $\bar{c}_y(x)$  to investigate the behavior of the plume growth using several types of models and suitable scaling of the data. For investigating the surface-level plume width we use

$$\sigma_y = \sigma_v t \left[ \frac{1}{1 + \sqrt{t/t_{L,y}}} \right] \quad (6.5)$$

from Gryning et al. (1987), which is a slight modification of a very similar form given by Draxler (1976). This equation has the proper asymptotic limits needed by Taylor's theory for dispersion in homogeneous turbulence, where  $\sigma_y \sim t$  near the source and  $\sigma_y \sim t^{1/2}$  at travel times much greater than the Lagrangian integral scale  $t_{L,y}$ . In this equation  $t = x/\bar{u}_x$  is the travel time, and we have elected to use  $t_{L,y} = 300$  s from Gryning. The variance of velocity in the horizontal plane  $\sigma_v$  is taken as the average of the values measured at all heights on the 10-m meteorological tower. This equation and the calculated data are shown in Figure 6.3. Agreement between the model and the data is good. Moreover, we see that plume growth is proportional to travel time. The asymptotic growth proportional to  $t^{1/2}$  is not evident from these data.

Both axes of Figure 6.3 are in units of seconds. To make this graph dimensionless, we need a suitable time scale. The most logical choice is perhaps  $t_{L,y}$ . However, this scaling is not very sensitive to the actual value of the Lagrangian integral scale, because we have  $t \ll t_{L,y}$ .

In looking at concentrations, the effect of ground-level deposition and evaporation for the fog-oil smoke aerosol are predicted to be negligible for the distances of interest, so we may use conservative models to predict the concentration. For the crosswind integrated concentration, we plot the data in terms of  $\bar{c}_y \bar{u}_x / q$  versus the travel time  $t = x/\bar{u}_x$ .

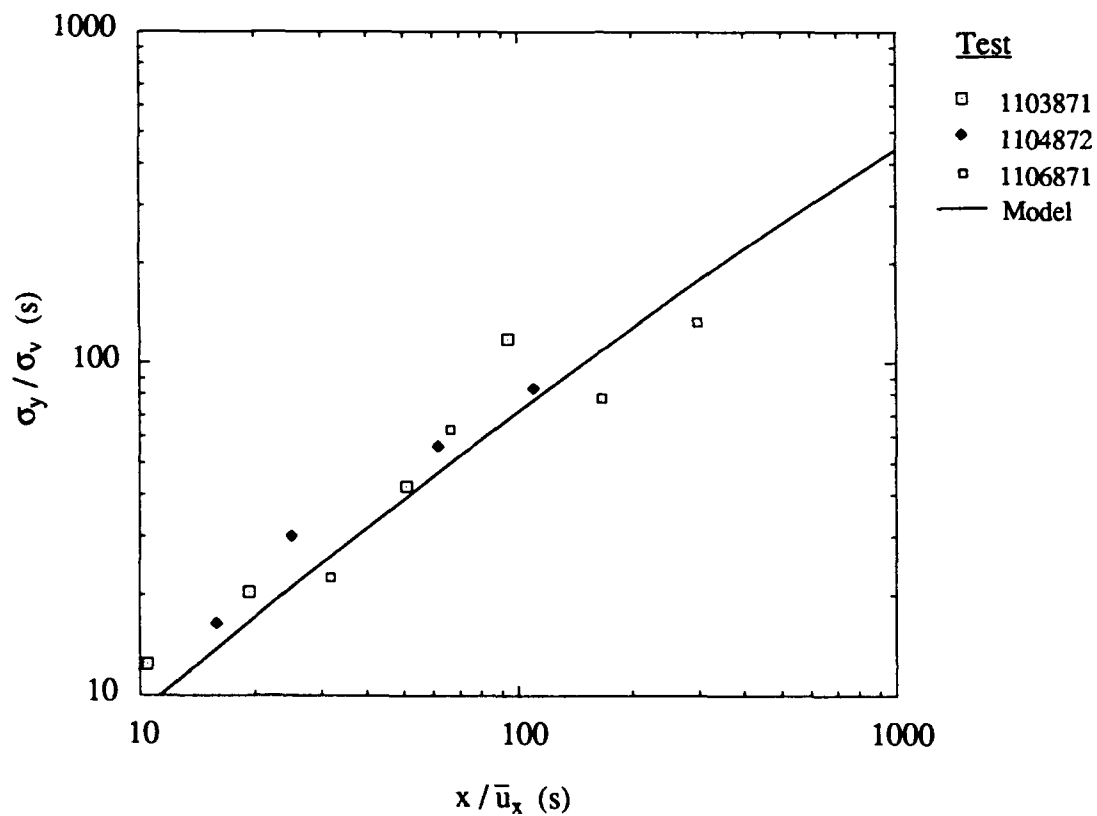


Figure 6.3 Estimated plume widths for the fog-oil dispersion tests at Camp Atterbury as compared with an adaptation from Gryning et al (1987) of a model given by Draxler (1976).

Two different approaches are appropriate for modeling the decay of ground-level concentration with distance. The first comes from the Gaussian plume model

$$\frac{\bar{c}_y \bar{u}_x}{q} = \sqrt{\frac{2}{\pi}} \frac{1 + \sqrt{t/t_{L,z}}}{\sigma_w t} \quad (6.6)$$

The value of the standard deviation in vertical wind direction  $\sigma_w$ , is taken as an average over the 10-m meteorological tower and is similar for all three tests. The Lagrangian integral scale  $t_{L,z}$  is estimated as 300 s from Gryning (1987). This Gaussian plume model is most applicable to dispersion in near neutral conditions. The second approach uses mixed-layer scaling from Nieuwstadt (1980b), where the dimensionless scaling is

$$\frac{\bar{c}_y \bar{u}_x}{q} = 0.9 \sqrt{z_i} \left[ \frac{1}{w_* t} \right]^{3/2} \quad (6.7)$$

This scaling is applicable in convective conditions. The values of  $w_*$  and  $z_i$  can be estimated from meteorological data analysis. These two model predictions, which have differing trends with travel time, along with our data are shown in Figure 6.4. Closer to the source, the Gaussian plume model predictions show better agreement with the data, whereas the mixed-layer scaling more accurately predicts the data at longer travel times. This changing nature of the dispersion occurs because the plume moves from the surface-layer to the mixed-layer as it expands with distance from the source. Overall agreement is better for the mixed-layer model. We used the dimensional scaling in Figure 6.4 in order to illustrate both types of models on the same axes.

### Dimensionless Scaling

In examining the effects differing meteorological conditions, nondimensionalization of the crosswind integrated concentration is a useful practice for collapsing the measured data. Surface-layer scaling is appropriate, as shown by Pasquill and Smith (1983) for dispersion data taken in neutral atmospheric conditions. The fog-oil tests at Camp Atterbury were taken in thermally unstable conditions and mixed-layer scaling, rather than surface-layer scaling, may be more appropriate. A suitable nondimensionalization of the concentration data is provided by Deardorff and Willis (1975), using  $\bar{c}_y(x) \bar{u}_x z_i / q$  where  $z_i$  is the inversion height,  $\bar{u}_x$  is the mean velocity,  $q$  is the source strength, and  $\bar{c}_y(x)$  is the cross wind integrated ground-level concentration. The downwind distance  $x$  is scaled as  $(w_* x) / (\bar{u}_x z_i)$ .

A plot of our data using mixed-layer scaling is given in Figure 6.5. Data from twenty convective cases of the Prairie Grass dispersion studies conducted in 1958 are shown in this plot along with a empirical fit to the Prairie Grass data given by Nieuwstadt (1980b)

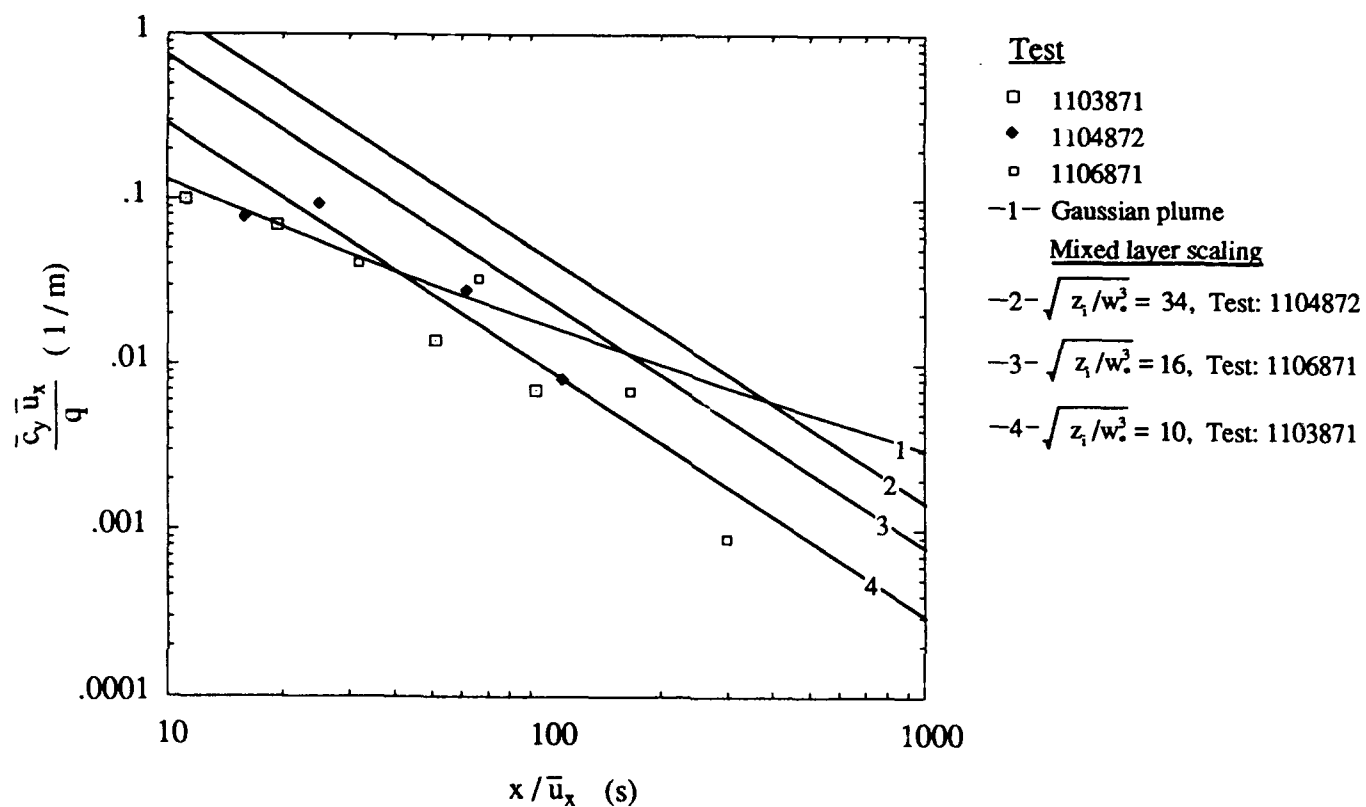


Figure 6.4 Cross wind integrated concentrations versus travel time for the fog-oil tests at Camp Atterbury. The data are compared with a Gaussian curve from Gryning et al. (1987) and a mixed-layer model from Niewstadt (1980).

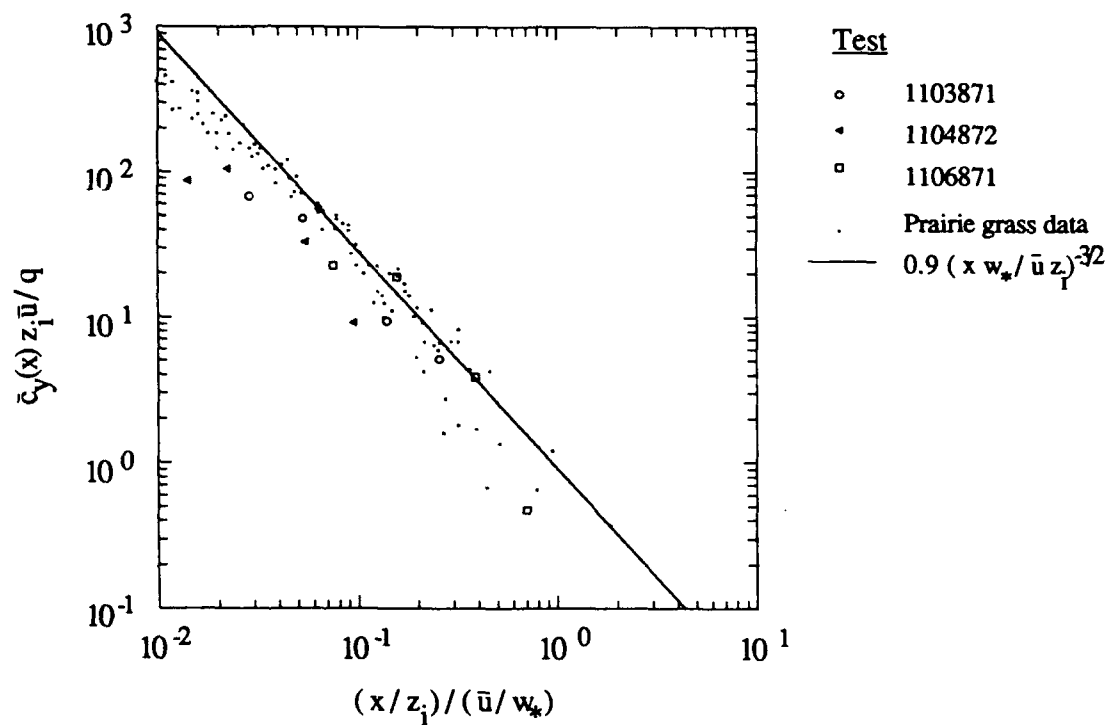


Figure 6.5 Mixed-layer scaling for the cross wind integrated ground level concentrations measured in the Camp Atterbury fog-oil dispersion tests. The Prairie Grass data and empirical relation are given by Nieuwstadt (1980b).

$$\frac{\bar{c}_y z_i \bar{u}_x}{q} = 0.9 \left( \frac{w_* x}{\bar{u}_x z_i} \right)^{-3/2} \quad (6.8)$$

The velocity  $\bar{u}_x$  for the Prairie Grass data is at an 8-m elevation in this plot for the Prairie Grass data and as the mean value for the 10-m meteorological tower in our own data. The agreement between our data and the fit is comparable with that obtained by Nieuwstadt using the original Prairie Grass data set. A plot of the dimensionless plume width  $\sigma_y/z_i$  is shown in Figure 6.6. This figure again shows good agreement with the analysis of Nieuwstadt.

### **Crosswind Profile of the Mean Concentration**

Nondimensional profiles of the crosswind concentrations may be useful. Such a plot is shown in Figure 6.7 with an overlaid Gaussian profile given by

$$\frac{\bar{c}(x,y)}{\bar{c}(x,0)} = \exp \left( - \frac{y^2}{2\sigma_y^2} \right) \quad (6.9)$$

On average, this profile is seen to be a reasonable approximation to the experimental data, although considerable scatter in individual data points is evident. The skewness or kurtosis of the spatial crosswind profile reveal little because only five or six data points are available for each sampling transect.

#### **6.1.2 Standard Deviation in Concentration**

A nondimensionalization of the standard deviation in concentration data is possible (see Csanady, 1973) beginning with

$$\frac{\sigma_c(x,y)}{\bar{c}(x,0)} = \alpha \left[ \exp \left( - \frac{y^2}{2\sigma_y^2} \right) \right]^{1/2} \quad (6.10)$$

where  $\alpha$  is a function of the ratio of the source size to the Lagrangian integral scale  $\delta/L$ , which is expected to be small. The plume width  $\sigma_y$  is the same value as found in the mean dispersion results. Our data are shown in Figure 6.8 using scaling parameters from the above equation. Here, we see that  $\sigma_c(x,0)/\bar{c}(x,0)$  is not a function of  $x$ , so a constant value of  $\alpha$  is suitable. The above equation, with  $\alpha = 2$  is also shown in Figure 6.8. This form compares well with the data. More extensive experimental data for a wider range of  $\delta/L$  values may reveal a variable form for  $\alpha$  depending on downwind distance, source size, and atmospheric conditions.

A scaling of the data using a combination of Equations 6.9 and 6.10 is given by

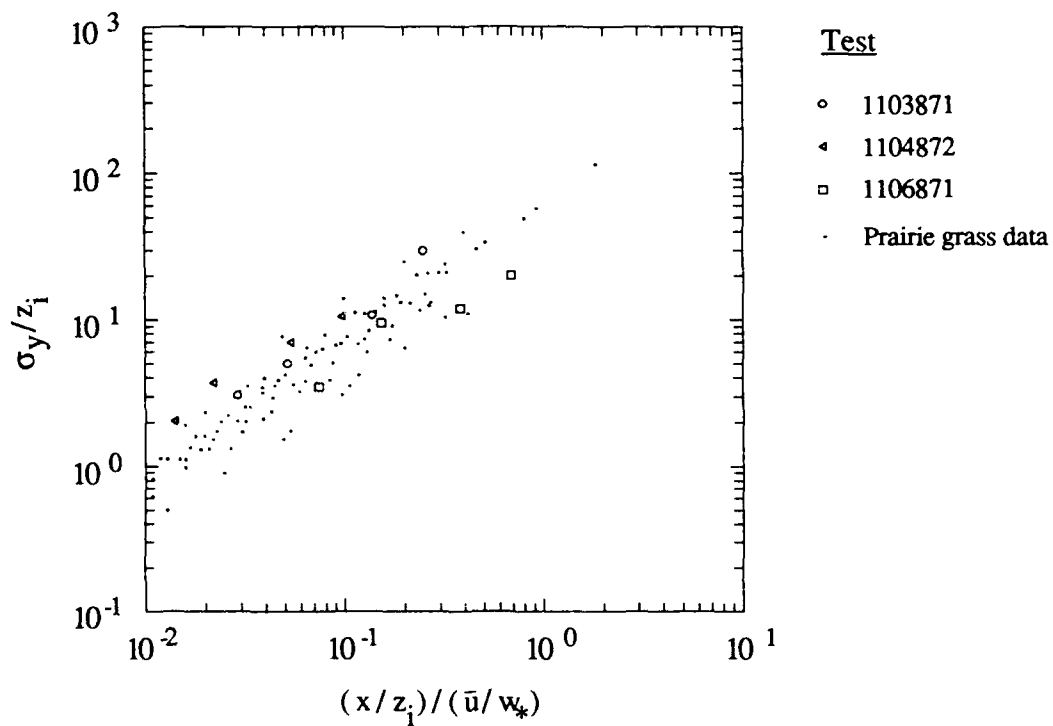


Figure 6.6 Mixed-layer scaling for the time averaged plume widths measured in the Camp Atterbury fog-oil dispersion tests as a function of downwind distance. The Prairie Grass data and empirical relation are given by Nieuwstadt (1980b).

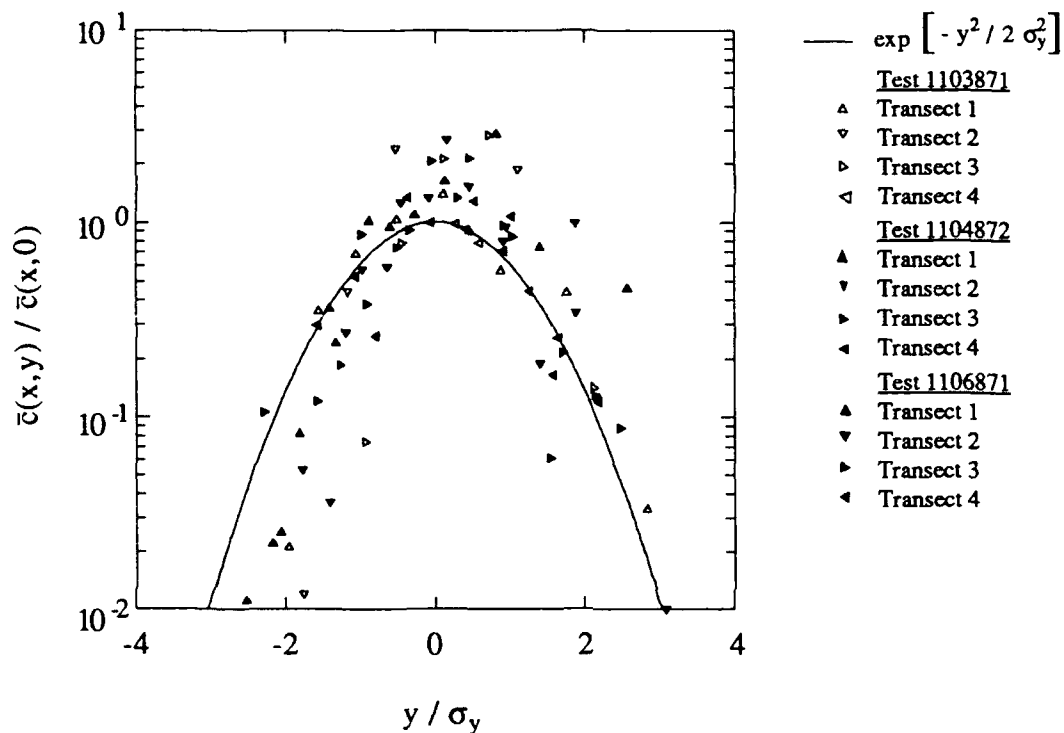


Figure 6.7 Normalized crosswind profile of mean concentrations for the Camp Atterbury fog-oil dispersion tests. These data are compared with the Gaussian profile. Transects correspond, respectively, to downwind distances of 50, 100, 250, and 450 m.



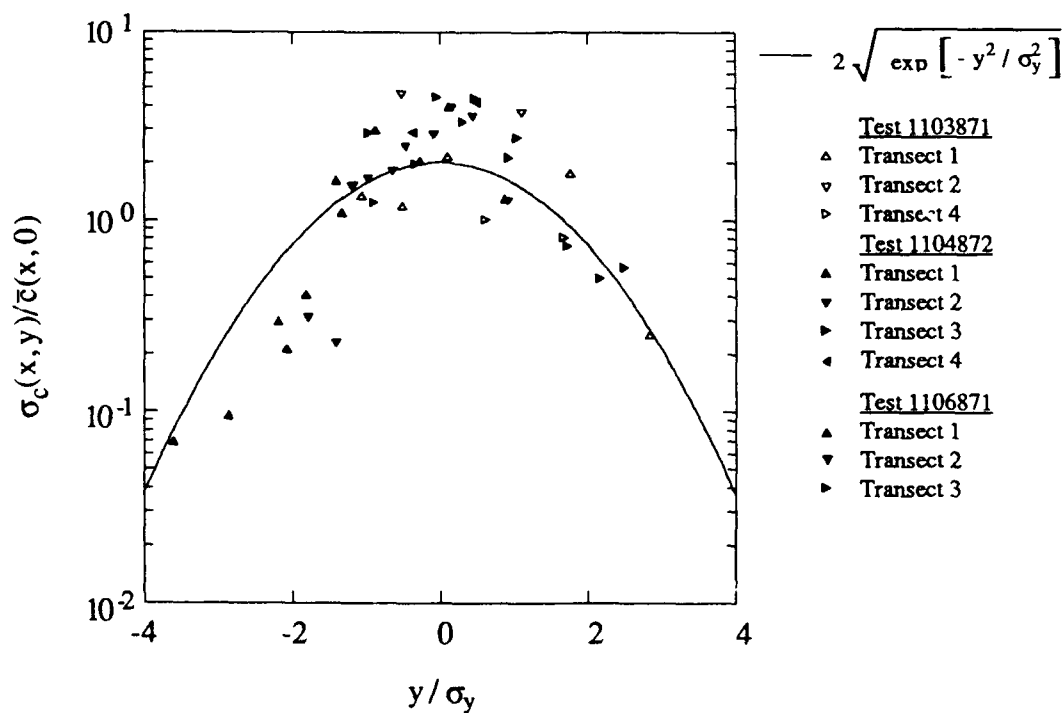


Figure 6.8 Crosswind profile of the standard deviation of concentration for the Camp Atterbury fog-oil dispersion tests. The standard deviations are normalized by the centerline mean concentration, and these data are compared with the square root of the Gaussian profile. Transects 1, 2, 3, and 4 correspond, respectively, to downwind distances of 50, 100, 250, and 450 m.

$$\frac{\sigma_c(x,y)}{\bar{c}(x,y)} = \alpha \exp \left( \frac{y^2}{4 \sigma_y^2} \right) \quad (6.11)$$

so that the fluctuation intensity, or ratio of standard deviation to mean concentration, is now a local value. The data are given in Figure 6.9 using this scaling and show very high concentration fluctuation intensity  $\sigma_c/\bar{c}$  throughout the plume, but especially near the plume edge, where the ratio is greater than 10.

Between different flow geometries in dispersion from a single source, the value of  $\alpha$  may vary considerably. This may be related to the ratio of the source size to the characteristic eddy size in a turbulent flow (measured by the integral scale). In a given flow a smaller finite-sized source will have greater fluctuations of concentration downstream and will fit a larger value of  $\alpha$ . For  $\alpha < 1$  the source size would be larger than the turbulent integral scale, and the Gaussian solution to the concentration variance equation may not be valid. Instead the peak fluctuations will be seen in the region of the highest concentration gradient and not at the centerline. This flow regime is examined by Csanady (1973). It is common in jets and wakes where the extent of the turbulence is limited to the width of the jet or wake itself.

### 6.1.3 The Concentration Probability Distribution

The record of concentration at a point may be described by the mean and the variance. A more complete description is given by the cumulative probability distribution where  $P(c_\xi)$  is the probability that  $c \leq c_\xi$ . A suitable form of this distribution for atmospheric dispersion from a point source is given by

$$P(c) = 1 - I \exp \left( - \frac{I c}{\bar{c}} \right) \quad (6.12)$$

where  $I$  is the intermittency, or the fraction of time that smoke is present at a given sampler, and  $\bar{c}$  is the mean concentration. This distribution is analytically developed in Section 3.5.2. Both  $\bar{c}$  and  $I$  are functions of position. This relation is shown in Figure 6.10 for the histograms calculated from each test using an equivalent form of the distribution given by

$$\ln \left( \frac{1 - P(c)}{I} \right) = - I \frac{c}{\bar{c}} \quad (6.13)$$

This distribution shows very good agreement with the exponential form of the concentration probability density function. The greatest deviation from this predicted distribution occurs at the extreme limits of the measured data. The scatter at  $c/\bar{c} = 0$  is due to the baseline noise of the

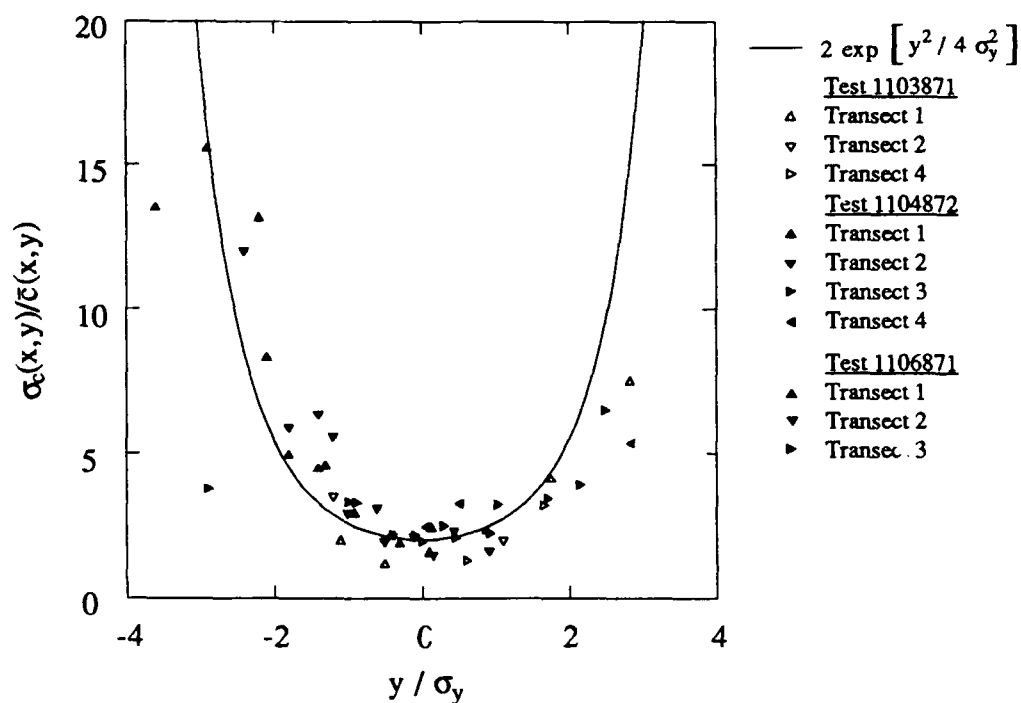


Figure 6.9 Crosswind profile of concentration fluctuation intensity for the fog-oil tests at Camp Atterbury. These data are compared with the Gaussian profile. Transects 1, 2, 3, and 4 correspond, respectively, to downwind distances of 50, 100, 250, and 450 m.

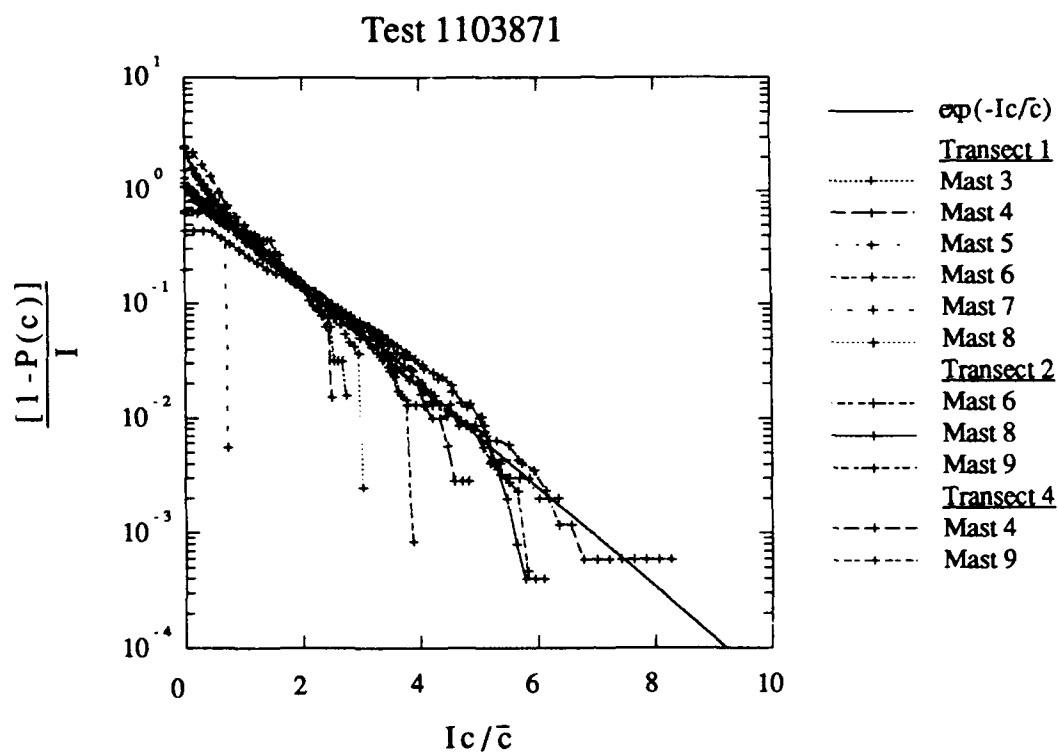


Figure 6.10 A comparison of the histograms in concentration with the exponential distribution for Test 1103871. The mast numbers refer to the location along a given transect.

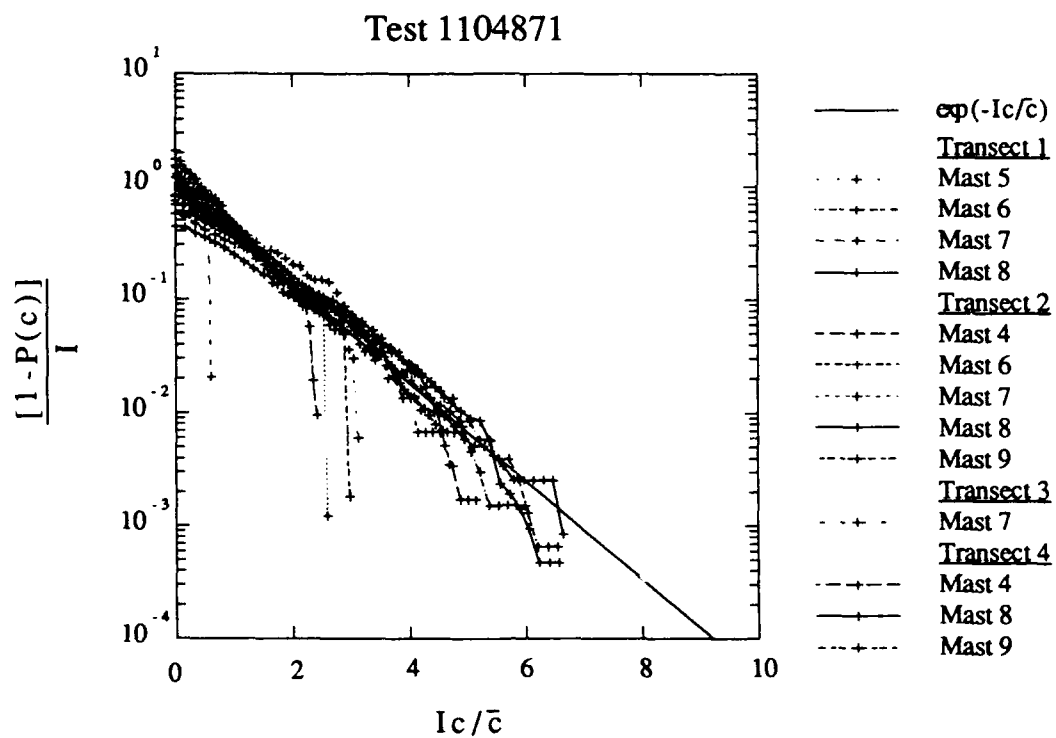


Figure 6.10 (continued) A comparison of the histograms in concentration with the exponential distribution for Test 1104871. The mast numbers refer to the location along a given transect.

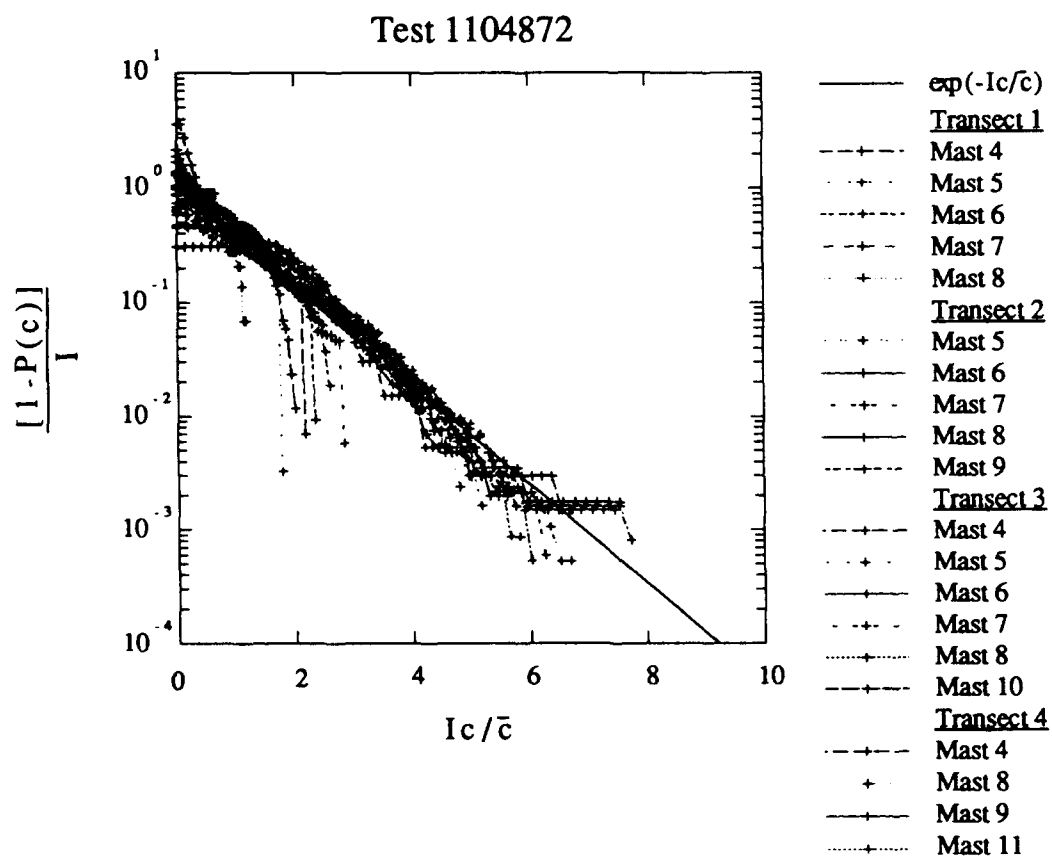


Figure 6.10 (continued) A comparison of the histograms in concentration with the exponential distribution for Test 1104872. The mast numbers refer to the location along a given transect.

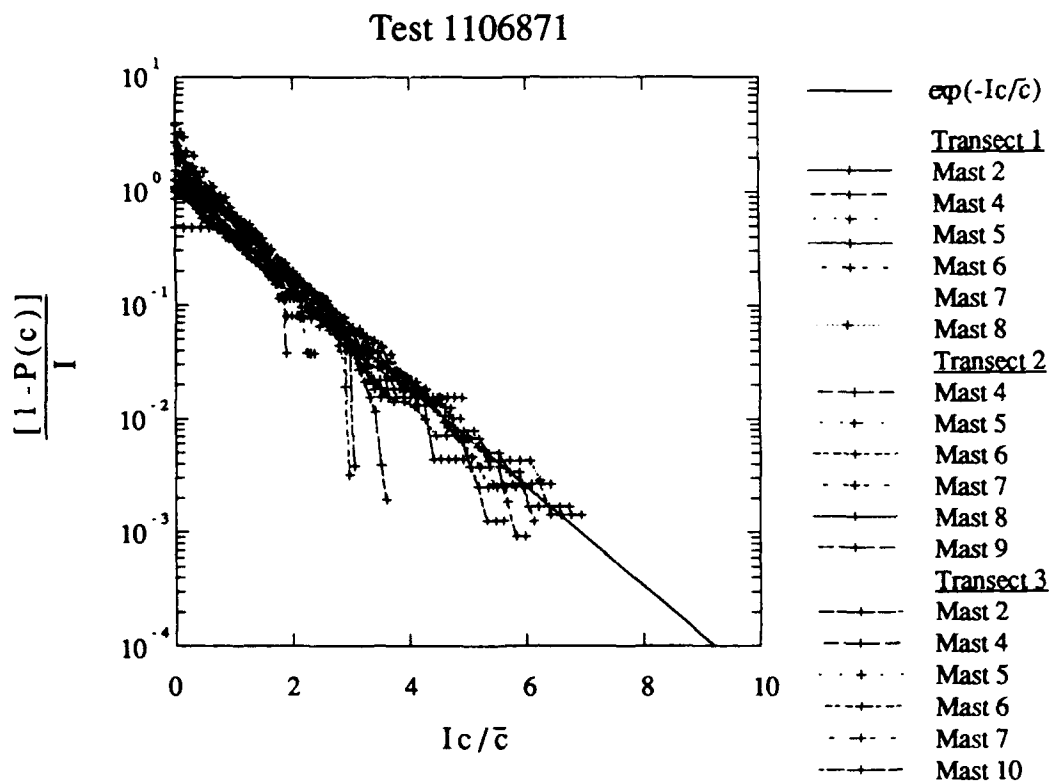


Figure 6.10 (continued) A comparison of the histograms in concentration with the exponential distribution for Test 1106871. The mast numbers refer to the location along a given transect.

instrument and reflects the inaccuracy in determining the intermittency of the signal. Clipping of the signal produces the hard upper limit (vertical line segments) seen on some of the data plots. This artifact of the sampling occurs at different points for each sampler because of the wide range in average  $\bar{c}$  values for the entire data set.

Because this probability distribution is characterized by only two parameters,  $I$  and  $\bar{c}$ , knowledge of any two parameters, such as the mean and the standard deviation of concentration at a point, is sufficient for calculating other single-point statistical quantities of interest. The ratio of standard deviation to mean concentration for this distribution is given by

$$\frac{\sigma_c}{\bar{c}} = \left[ \left( \frac{2}{I} \right) - 1 \right]^{1/2} \quad (6.14)$$

Combined with the crosswind profile of  $\sigma_y/\bar{c}$ , this yields an expression for the intermittency of

$$I = 2 \left[ \alpha^2 \exp^2 \left( \frac{y^2}{2 \sigma_y^2} \right) + 1 \right]^{-1} \quad (6.15)$$

This expression, along with the measured experimental data is shown in Figure 6.11. The average trend of the data is followed by the analytical expression with  $\alpha = 2$  as used in the earlier plots. There is considerable scatter of the data about this predicted line which increases for larger values of  $|y/\sigma_y|$ .

In comparison with the exponential distribution, which has been shown to agree with our data, a lognormal distribution is often used to plot histograms of concentration occurrence, especially in urban environments. This lognormal distribution disallows zero levels of concentration. It does not fit probability distributions of measured concentration in dispersion from a single isolated source.

#### 6.1.4 Spatial Correlations of the Instantaneous Concentration Measurements

The behavior of the instantaneous smoke plume may be investigated using two point spatial correlations at a single instant in time. For this we may use the correlation coefficient between the points 1 and 2, given by

$$\rho_{12} = \frac{[c(x_1, y_1) - \bar{c}(x_1, y_1)] [c(x_2, y_2) - \bar{c}(x_2, y_2)]}{\sigma_c(x_1, y_1) \sigma_c(x_2, y_2)} \quad (6.16)$$



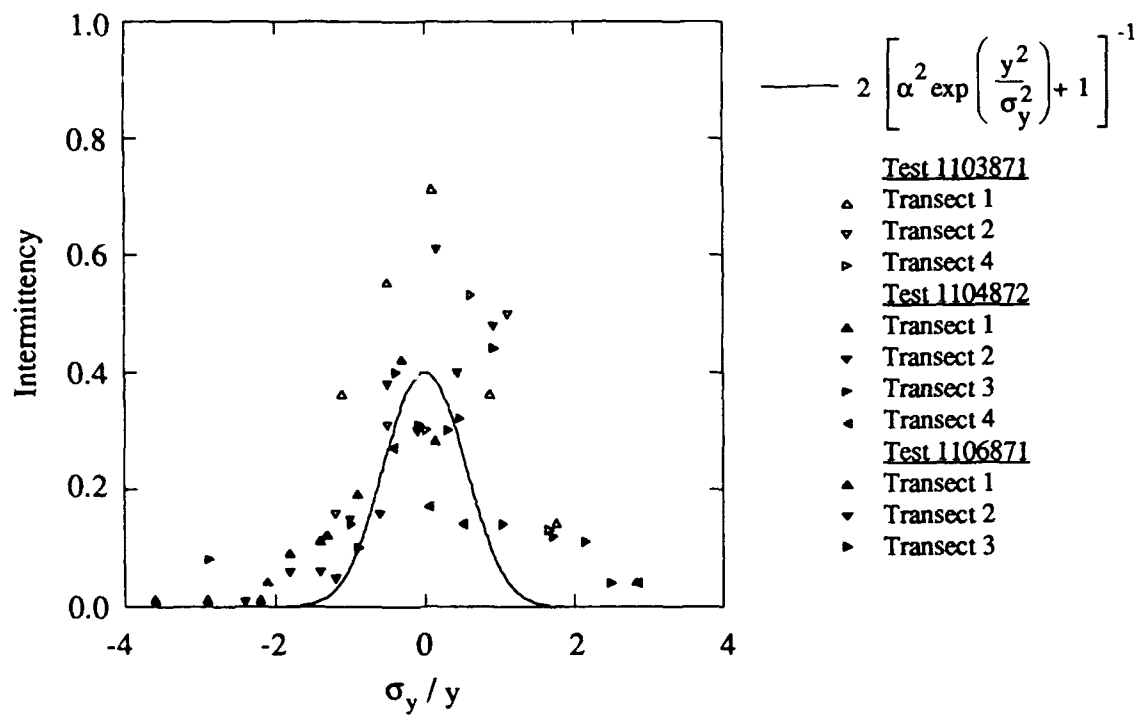


Figure 6.11 Crosswind plume intermittency for the Camp Atterbury fog-oil dispersion tests. The analytical solution uses a value of  $\alpha = 2$  in the expression shown.

which varies from -1 to 1. Ordinarily, we would have insufficient data to specify this relation. Since the crosswind scaling exists for time-average mean concentrations, it appears possible to replace the sampler positions  $(x_1, y_1)$  and  $(x_2, y_2)$  with the time-averaged scaling of  $(\sigma_y/y)_1$  and  $(\sigma_y/y)_2$  to find the crosswind behavior of the instantaneous plume. This reduction in the number of independent variables permits the data to be represented in the form shown in Figure 6.12. In this plot, symmetry along the mean plume axis is used to reflect positive and negative values of  $y/\sigma_y$ , thus increasing the accuracy of the isopleths.

We may define other parameters in addition to  $\rho_{12}$  for investigating the spatial plume structure. One of these is the joint intermittency, or fraction of time that smoke is simultaneously present at both samplers during the test duration. A plot of this function is shown in Figure 6.13. The contribution of zero values is seen to be significant. Along the line  $(\sigma_y/y)_1 = (\sigma_y/y)_2$ , the values of the joint intermittency are equal to the intermittency values found in the single-point analysis.

By working with  $\overline{c_1 c_2} / (\sigma_{c1} \sigma_{c2})$  which is a structure function, rather than the correlation coefficient given in Eq. 6.16, we may further investigate the plume behavior. This function is shown in Figure 6.14. Since we have already determined that our measured values of  $\sigma_c/\bar{c}$  are greater than 1, the structure function  $\overline{c_1 c_2} / (\sigma_{c1} \sigma_{c2})$  will only vary from 0 to less than 2.

We may use Figure 6.14 in a linear mean-square estimate of the root-mean-square plume width about a moving center of mass. For a scalar, this may be written as

$$c(x) \langle c(x+r) | c(x) \rangle = \langle c(x) c(x+r) \rangle \quad (6.17)$$

from Adrian (1983a), where the brackets indicate an ensemble average and the vertical bar indicates a conditional average. We use  $x = x_1 = (y/\sigma_y)_1$  as an absolute position and  $r = x_1 - x_2$  as a relative cloud width. In addition to Eq. 6.17 we constrain  $c(x)$  to be a spatial peak concentration along the transect. This yields the relative profile shown in Figure 6.15 for several values of  $x$ .

The relative width of the plume using this method is  $\sigma_{r,y} = 0.22\sigma_y$  which is the same value analytically by Smith and Hay (1961) and experimentally by Michelson (1983). For values of  $x$  larger than those represented in Figure 6.15, there is an increased error in determining the relative plume width due to the smaller quantity of sampled data farther from the axis of the mean plume.

### 6.1.5 Autocorrelations and Spectra of the Concentration Records

The small-scale fluctuations of scalar concentration spectra in atmospheric dispersion typically show a  $-5/3$  Kolmogorov power-law dependence in the inertial-convective subrange (see Tennekes and Lumley, 1972 for example). The similarity behavior of scalar variance is discussed by several authors, including Corrsin (1951), Batchelor (1959), and Gibson and Schwarz (1963).

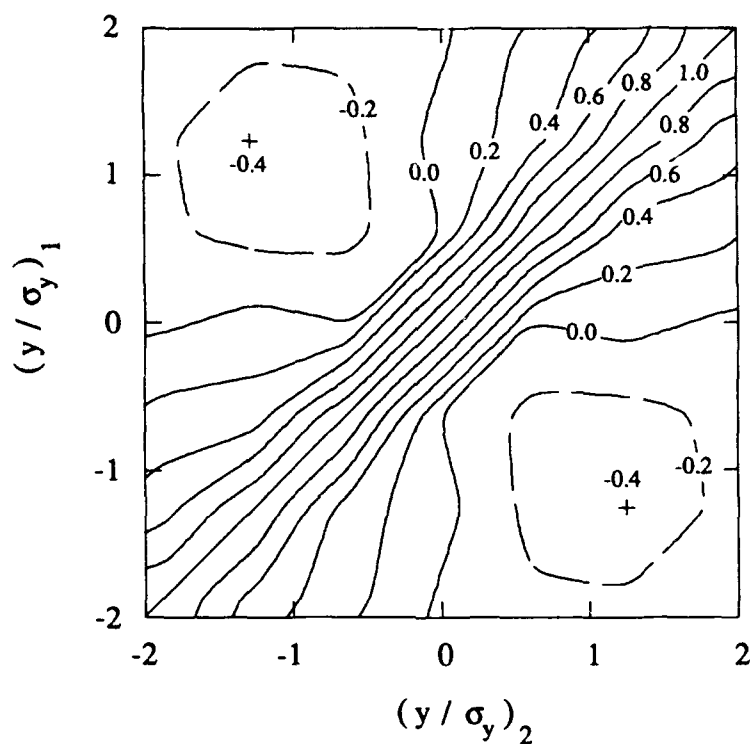


Figure 6.12 Cross correlation coefficients for the data taken in the Camp Atterbury field dispersion experiments. The data for all the transects were used in the above contour plot and were reflected about the centerline axis in order to provide a better fit.

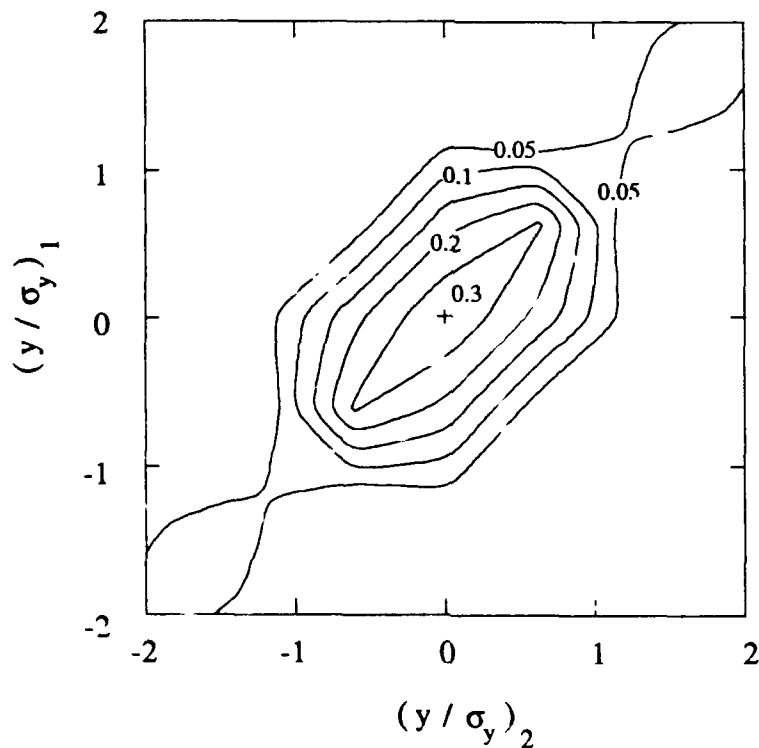


Figure 6.13 Joint intermittency for the data taken in the Camp Atterbury field dispersion experiments. The data for all the transects were used in the above contour plot and were reflected about the centerline axis in order to provide a better fit. Note that the line through (0,0) with a slope of 1 yields the single point intermittency curve.

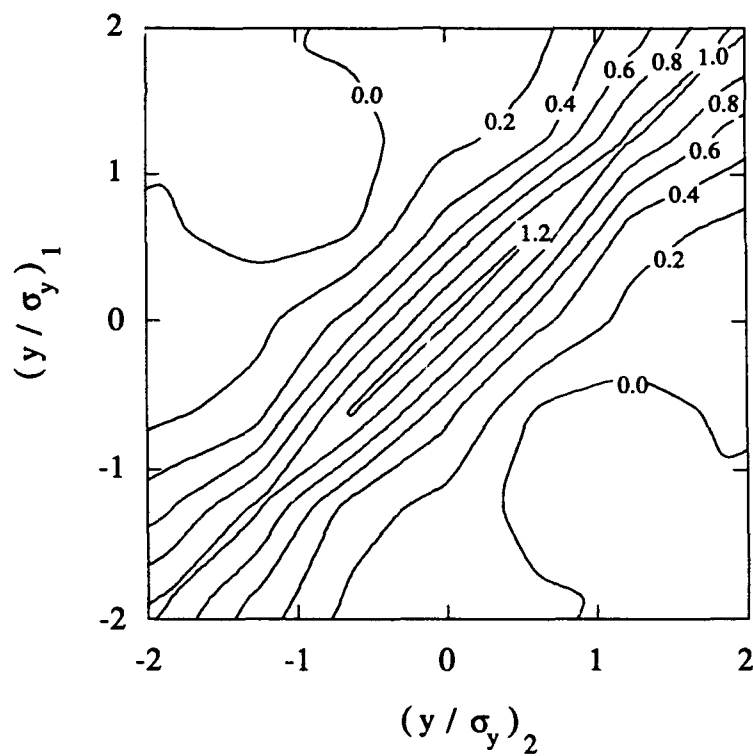


Figure 6.14 Structure function for the concentration data taken in the Camp Atterbury field dispersion experiments. The data for all the transects were used in the above contour plot and were reflected about the centerline axis in order to provide a better fit.

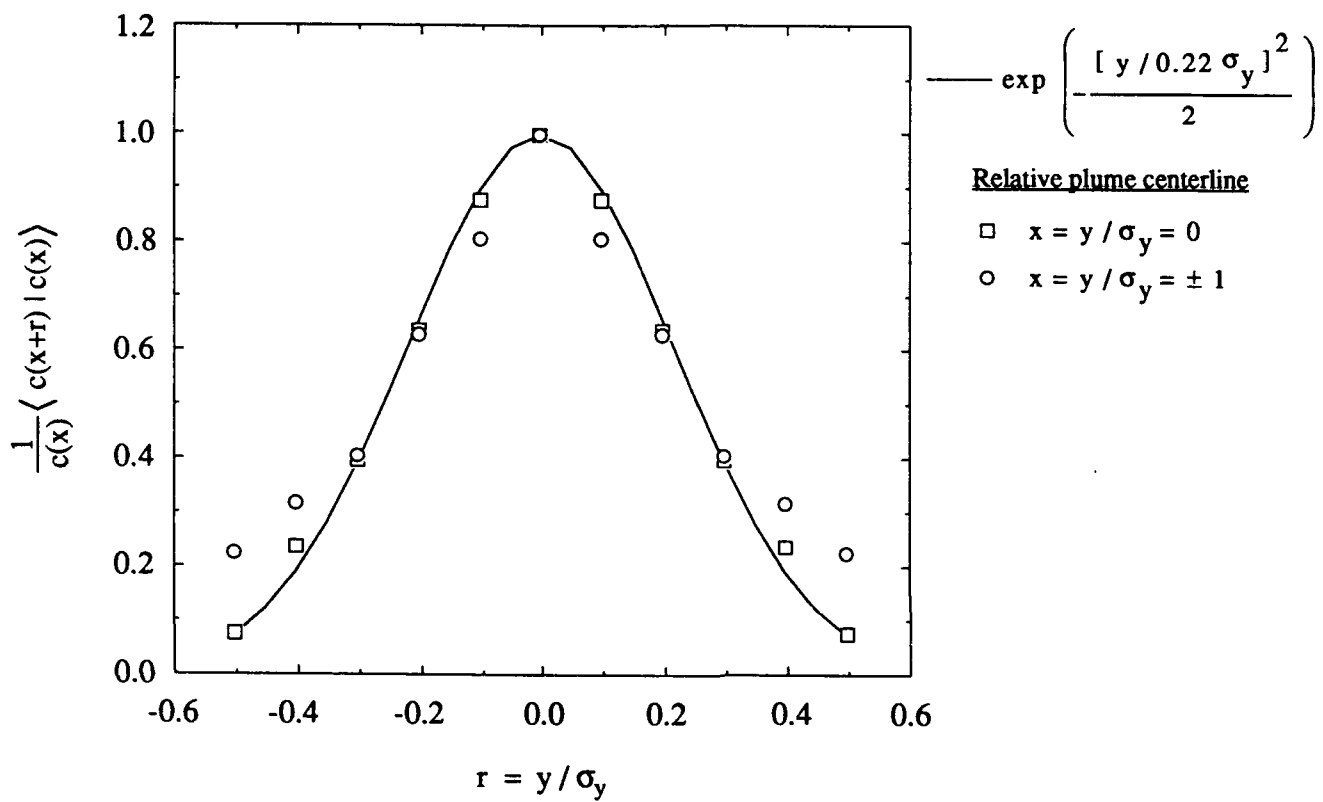


Figure 6.15 The root mean square plume width about its relative centerline. Comparison is made with the prediction of Smith and Hay (1961) at the mean plume centerline and at  $\pm 1 y/\sigma_y$  from the mean plume centerline.

Spectra of the data from the individual aerosol photometers are shown in Figure 6.16. The data for this figure are computed by first performing a fast Fourier transform on the individual data records using a 1024 point transform with a 512 point  $7\sigma$  Gaussian window. As is standard with spectra calculations, the data are overlapped by half the transform width to reduce the random error, and then the results are bandpass averaged to reduce the bias error. The spectra data are then normalized by the calculated variance for each data record. This figure demonstrates the power-law scaling in the inertial-convective subrange for all the Atterbury fog-oil tests. For this figure, the range is given by a  $-2/3$  slope for  $nS_{cc}(n)$ , rather than a  $-5/3$  slope for  $S_{cc}(n)$ .

Because the spectra from all of the samplers within a given test are reasonably similar in shape, we may ensemble-average the spectra for the set of concentration records. This result is shown in Figure 6.17 for frequency versus  $S_{cc}/\sigma_c^2$ , where the inertial-convective subrange behavior follows a  $-5/3$  slope. Much of the noise in the spectra from individual samplers is removed by the ensemble averaging process. The  $-5/3$  region of this spectra is matched by the velocity spectra in the mean-wind direction. Fully isotropic inertial subrange behavior, as found by examining all components of the velocity spectra, occurs at higher frequencies than our meteorological instrumentation was capable of resolving.

Lower frequency fluctuations in the concentration spectra may be quantified using an integral time scale. We have several different methods of estimating this quantity, all of which are subject to random error because of the limited durations for our dispersion tests. Among these methods, we have estimates from the correlation function using the integration over the lag time

$$\tau_c = \int_{-\infty}^{\infty} R_{cc}(\tau) d\tau \quad (6.18)$$

or, assuming an exponential form of  $R_{cc}(\tau_c)$ , the time where  $R_{cc}(\tau_c) = \exp(-1)$ . This correlation function may come from direct calculations or Fourier inversion of the spectra for each sampler as previously shown in Figure 6.16. For an exponential correlation, we may also find an approximate value of the integral scale using

$$\tau_c = \frac{1}{2 \pi n_{\max}} \quad (6.19)$$

where  $n_{\max}$  is the peak of the frequency-weighted power spectrum  $nS_{cc}(n)$ . Among these various methods, the standard deviation in estimates of  $\tau_c$  can be of the same magnitude as  $\tau_c$  for a given data record. The difficulty in determining  $\tau_c$  is revealed by visually estimating the peak values in the individual spectra of Figure 6.16.

Calculated values of the integral scale are in the range of 10 s to 60 s. These values are not a strong function of downwind distance within a given test, and are 10% greater on the mean plume

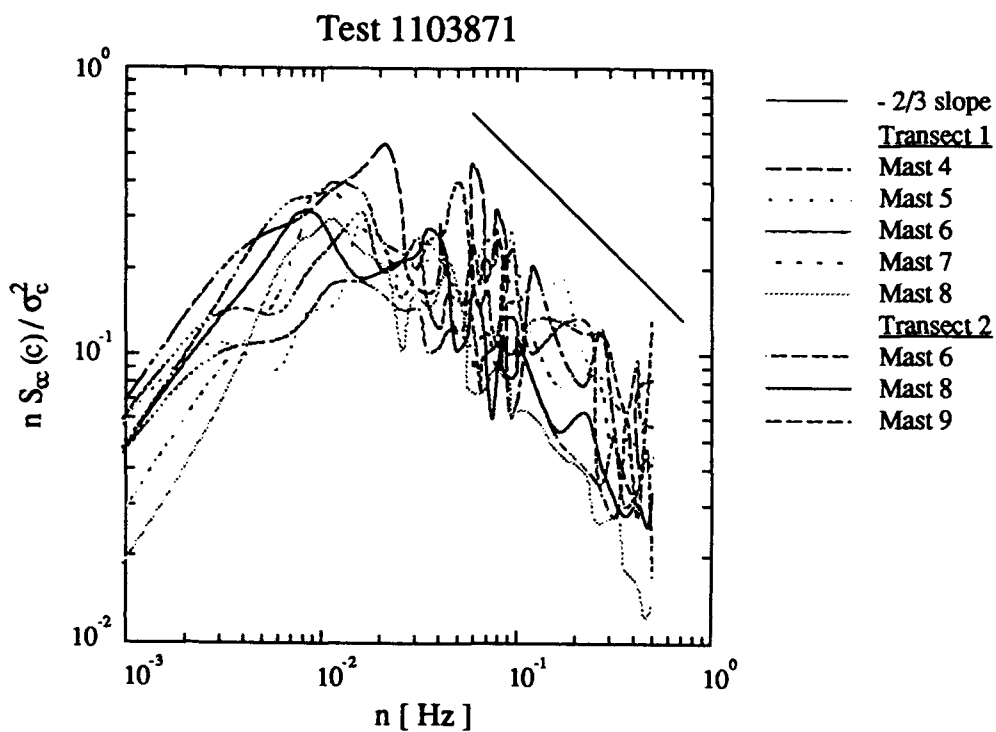


Figure 6.16 Spectra of the concentration variance for all samplers in Test 1103871 in which the mean signal was greater than 5 times the background noise of the instrument. The spectra are normalized by the calculated variance for each data record.



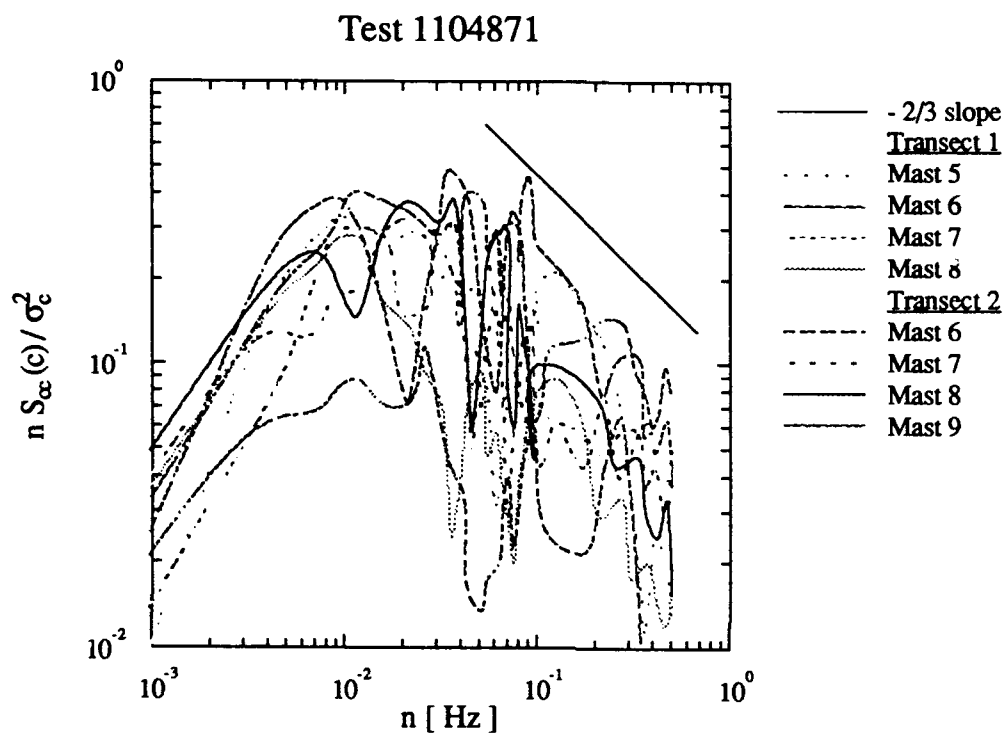


Figure 6.16 (continued) Spectra of the concentration variance for all samplers in Test 1104871 in which the mean signal was greater than 5 times the background noise of the instrument. The spectra are normalized by the calculated variance for each data record.

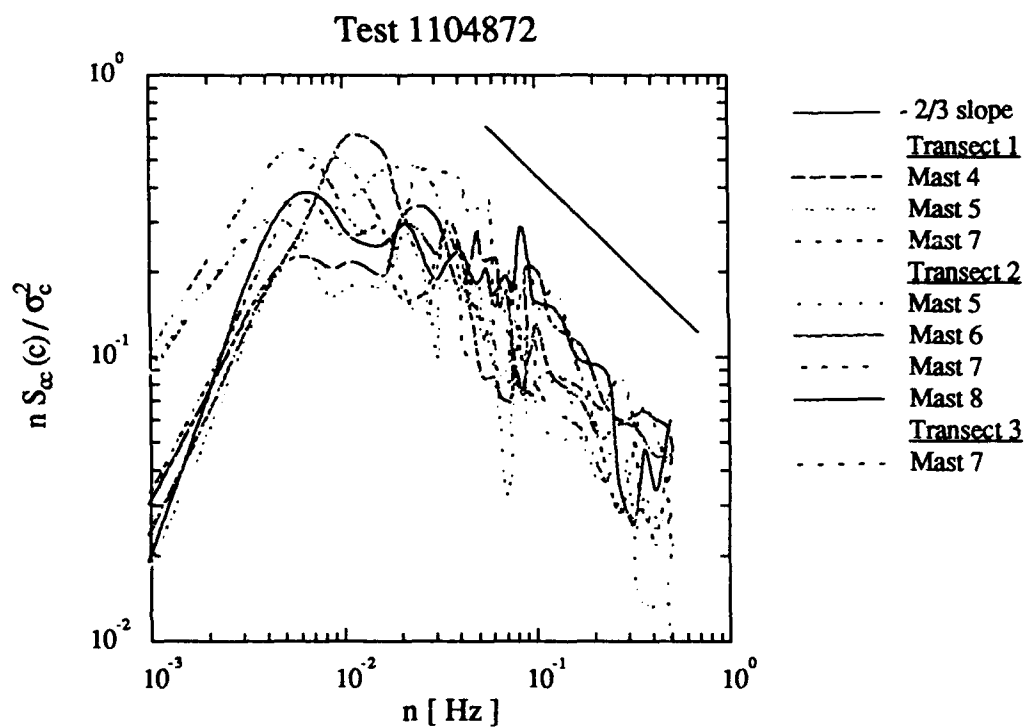


Figure 6.16 (continued) Spectra of the concentration variance for all samplers in Test 1104872 in which the mean signal was greater than 5 times the background noise of the instrument. The spectra are normalized by the calculated variance for each data record.

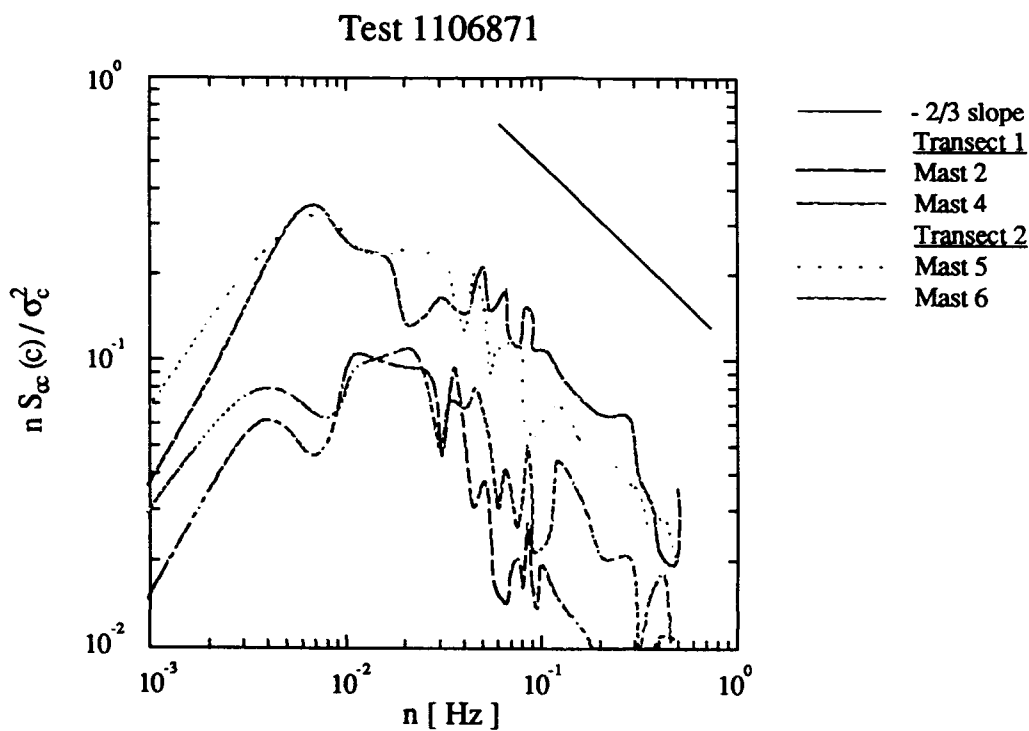


Figure 6.16 (continued) Spectra of the concentration variance for all samplers in Test 1106871 in which the mean signal was greater than 5 times the background noise of the instrument. The spectra are normalized by the calculated variance for each data record.

centerline than near the plume edge. Noise in these values prevents an accurate estimate of spatial trends. For the fog-oil tests we have average values as given in Table 6.1. Trends in the low frequency behavior can be seen in the ensemble averaged spectra of Figure 6.17. For all cases, the integral scale of the concentration fluctuations was smaller than the convective velocity time scale.

Table 6.1 Average integral scales of the concentration fluctuations for the Camp Atterbury fog-oil dispersion tests.

Test	$\tau_c$	$\tau_c/(z_i/w_*)$
1103871	15.4	0.042
1104872	24.2	0.021
1106871	22.5	0.052

With measurements of the integral scale and the variance in concentration, it is possible to estimate the accuracy in our measured average concentrations, using

$$\frac{\sigma_{\bar{c}}}{\bar{c}} = \frac{\sigma_c}{\bar{c}} \left( \frac{T}{2\tau_c} \right)^{-1/2} \quad (6.20)$$

from Bendat and Piersol (1971), where the contribution at times small compared to  $\tau_c$  is neglected,  $T$  is the averaging, or total sample time, and  $T > \tau_c$ . Values of  $\sigma_{\bar{c}}/\bar{c}$  calculated for a one hour test along the plume centerline vary from 0.09 to 0.22. We note that the magnitude of  $\sigma_{\bar{c}}/\bar{c}$  estimated from this method is close to the values found in analysis of the scatter in mean concentration measurements from multiple samplers on a single sampling mast, as shown in Figure 5.13.

#### 6.1.6 Concentration Exceedance

A technique which may be of use in the analysis of the concentration records is examining the behavior of time durations for which the concentration exceeds some limit at a given sampler. Here, we are primarily interested in continuous periods during which  $c > 0$ . We denote the mean value by  $1/\lambda_u(c_{\text{limit}})$  and take  $c_{\text{limit}} = 0$ . From analysis of the data records, we find the behavior shown in Figure 6.18. The values of  $1/\lambda_u(0)$  appear to be directly related to the integral scale in concentration at a given sampler. The spatial variation in  $1/\lambda_u(0)$  is similar to that seen for  $\tau_c$  for the different tests, with no clear trend with distance from the source and no significant crosswind variation is seen. This lack of variation may be due to the noise in the signal near  $c = 0$ .

We may examine the distribution of the time durations of individual bursts, which if random, should follow the exponential distribution given by

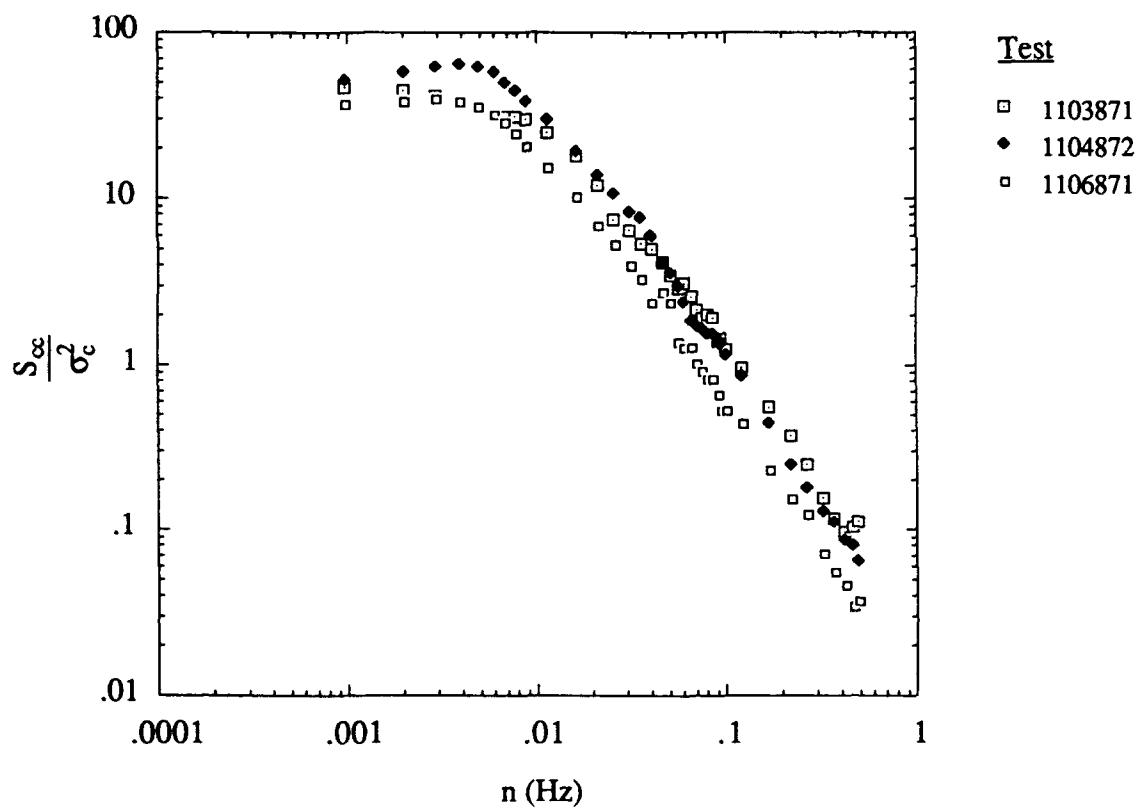


Figure 6.17 Ensemble averaged spectra of the concentration fluctuations measured in the Atterbury dispersion tests. These data are the ensemble average of all the spectra from a given test from which the mean signal level exceeded the background noise by a factor of 2.

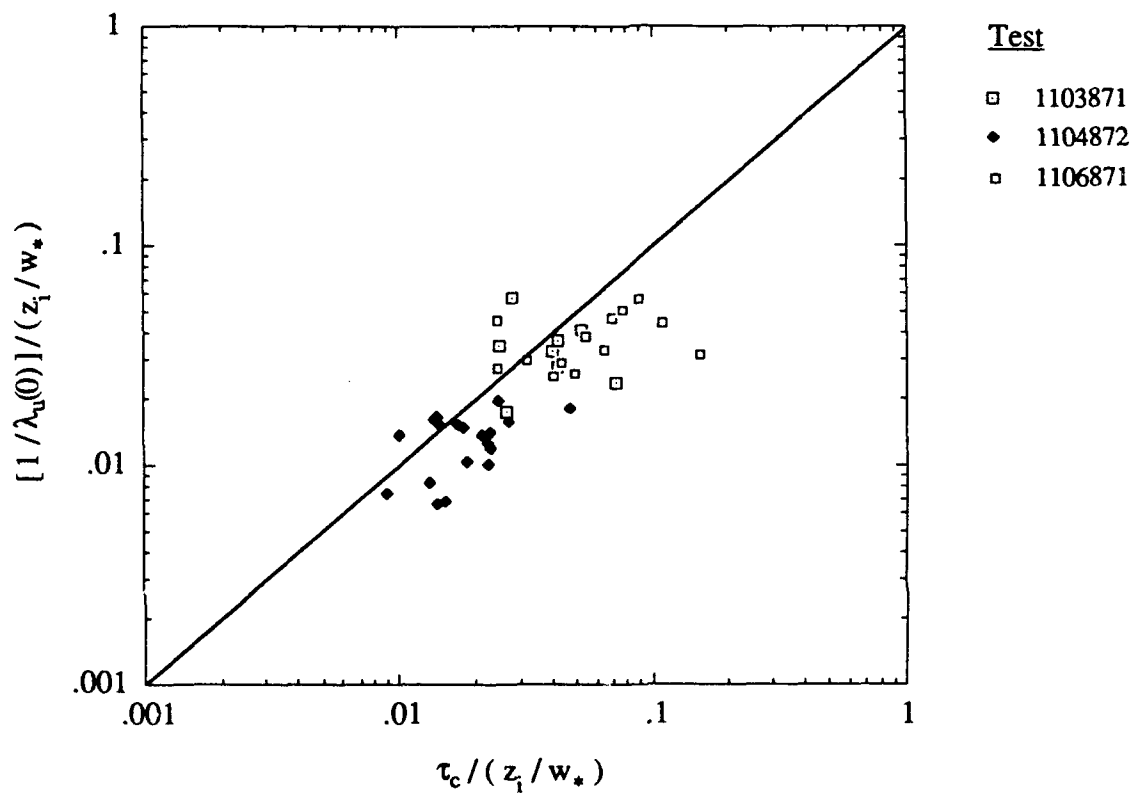


Figure 6.18 Duration of bursts in concentration with  $c > 0$ , versus the integral scale in concentration for the Camp Atterbury fog-oil dispersion tests.

$$P(t | c_{\text{limit}}) = 1 - \exp(-\lambda_u t) \quad (6.21)$$

in counting single exceedance events and the average duration is  $1/\lambda_u$  for a given  $c_{\text{limit}}$ . The histogram of data for our samplers is shown in Figure 6.19 for  $P(t | c_{\text{limit}}=0)$  along with the predicted exponential distribution. The data distribution is actually hyperexponential. Deviation from the exponential may be due to the sampling duration of the test at longer frequencies and the limited 1-Hz sampling frequency at the short time increments.

Another aspect of concentration exceedance which is useful is  $\lambda(0)$ , the rate of occurrence of events with  $c > 0$  in a single continuous burst. We can find  $\lambda(0) = I\lambda_u(0)$  where  $I$  is the intermittency. Scaling by the convective time scale, the crosswind distribution of this quantity is shown in Figure 6.20. This shows the rate of bursts is greater near the center of the mean plume, and is less near the mean plume edges. A model of this distribution is given by

$$\lambda(z_i/w_*) = \frac{1}{\tau_c(w_*/z_i)} \frac{2}{\alpha^2 \exp^2(y^2/2\sigma_y^2) + 1} \quad (6.22)$$

where we use the derived distribution of intermittency along with the near-constant value of  $\tau_c(w_*/z_i)$  found from the ensemble averaged concentration spectra.

Some conclusions can be made from analysis of the temporal records of concentration fluctuation. One interesting result is that  $1/\lambda_u(0) \sim \tau_c$ , and that in a given test this value is nearly constant. This means that the mean duration of a smoke burst at any sampler position is nearly constant for a given test. A result of this approximation is that for frequencies higher than  $1/2\pi\tau_c$ , the concentration spectra follows a -5/3 power law behavior. Quite apart from the nearly constant values of  $1/\lambda_u(0)$  found in a given test, we have an exponential-like probability distribution of the duration of individual events with  $c > 0$ . We also find the average rate of occurrence of bursts  $\lambda(0)$  at a sampler is higher near the mean plume centerline than at the edges, whereas the mean duration of a burst  $1/\lambda_u(0)$  is approximately constant over the plume width. We may relate the two rate parameters through  $\lambda(0) = I\lambda_u(0)$ .

## 6.2 Camp Atterbury HC Smoke Data Analysis

A total of five dispersion experiments were conducted using HC smoke. Wind vectors measured at the source for each of these tests are shown in Figure 6.21 along with a map of the sampling grid. The measured average values of concentration from the filter samples and standard deviation in concentration from the aerosol photometers are shown in Figure 6.22. These are presented in terms of the measured mass of zinc per cubic meter, where zinc is used as the conservative species in the HC smoke. Tests 1112871 and 1113871 are most suitable for our detailed

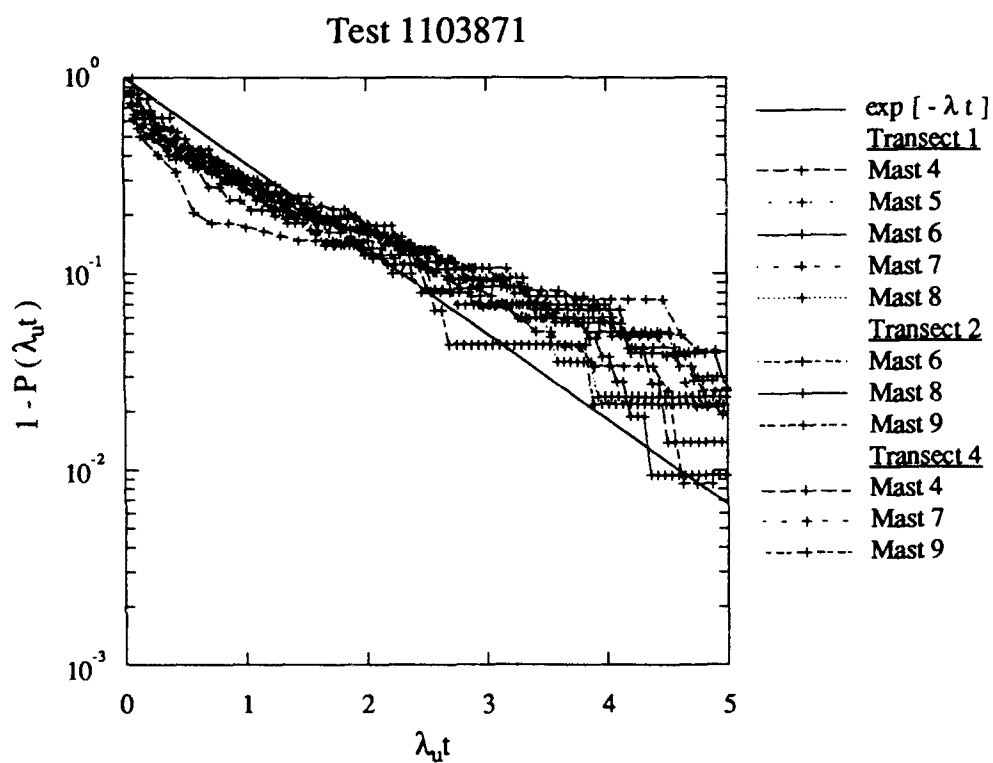


Figure 6.19 Histogram of time intervals for which the concentration exceeds zero for Test 1103871. The data from all records for which  $I > 0.1$  are included in the above plot.



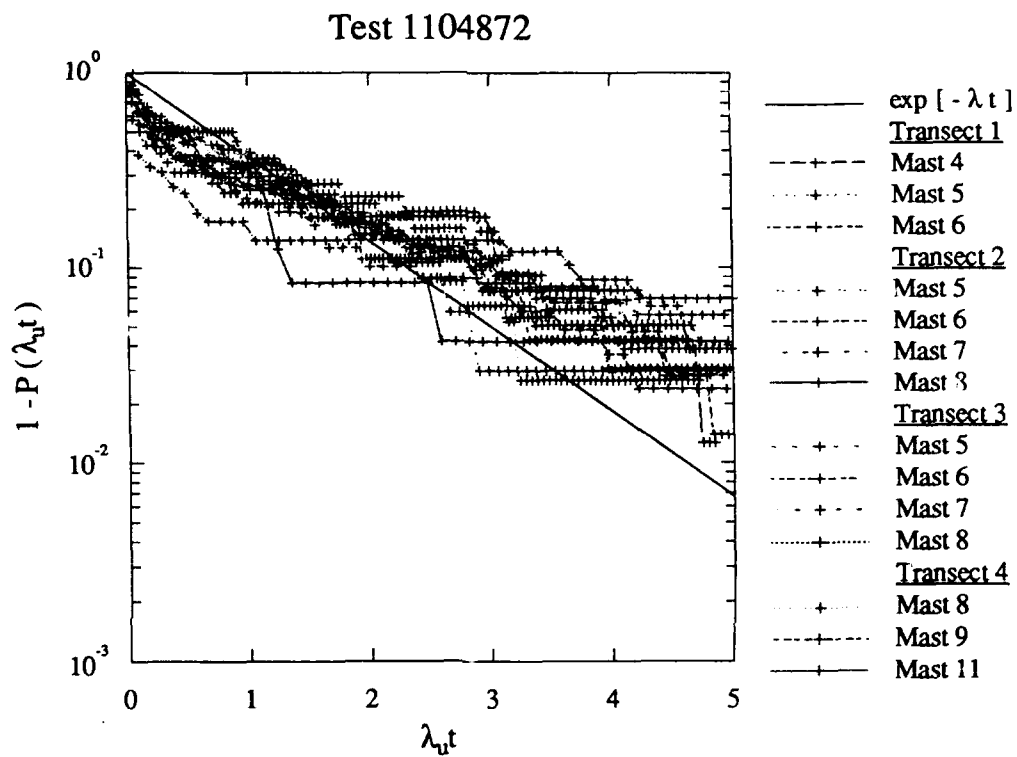


Figure 6.19 (continued) Histogram of time intervals for which the concentration exceeds zero for Test 1104872. The data from all records for which  $I > 0.1$  are included in the above plot.

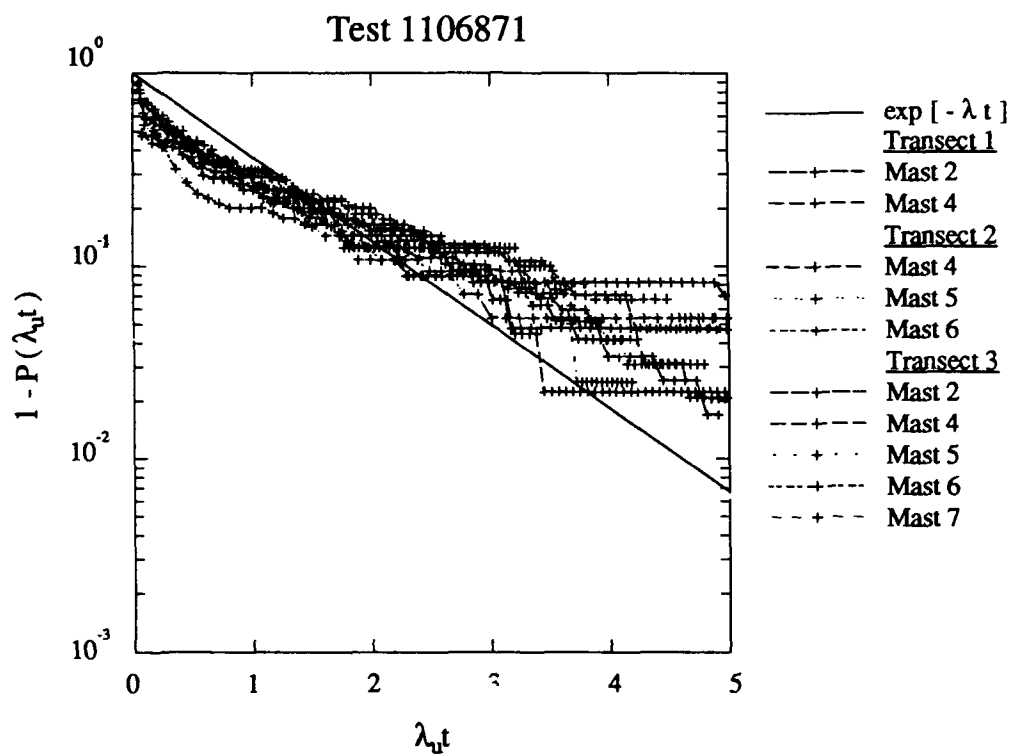


Figure 6.19 (continued) Histogram of time intervals for which the concentration exceeds zero for Test 1106871. The data from all records for which  $I > 0.1$  are included in the above plot.

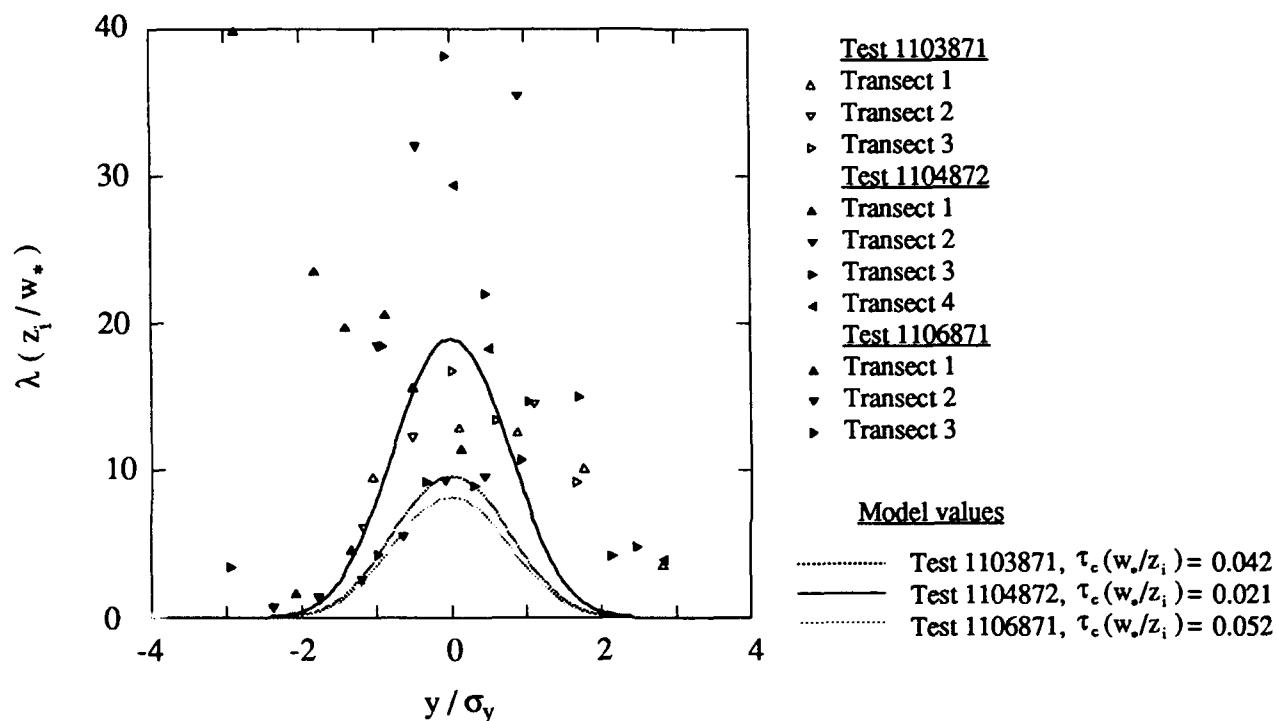


Figure 6.20 The crosswind distribution of intervals between smoke event starts for the tests at Camp Atterbury using fog-oil smoke. These data are nondimensionalized by the mean plume width and the convective time scale and are compared with model given by Equation 6.22.

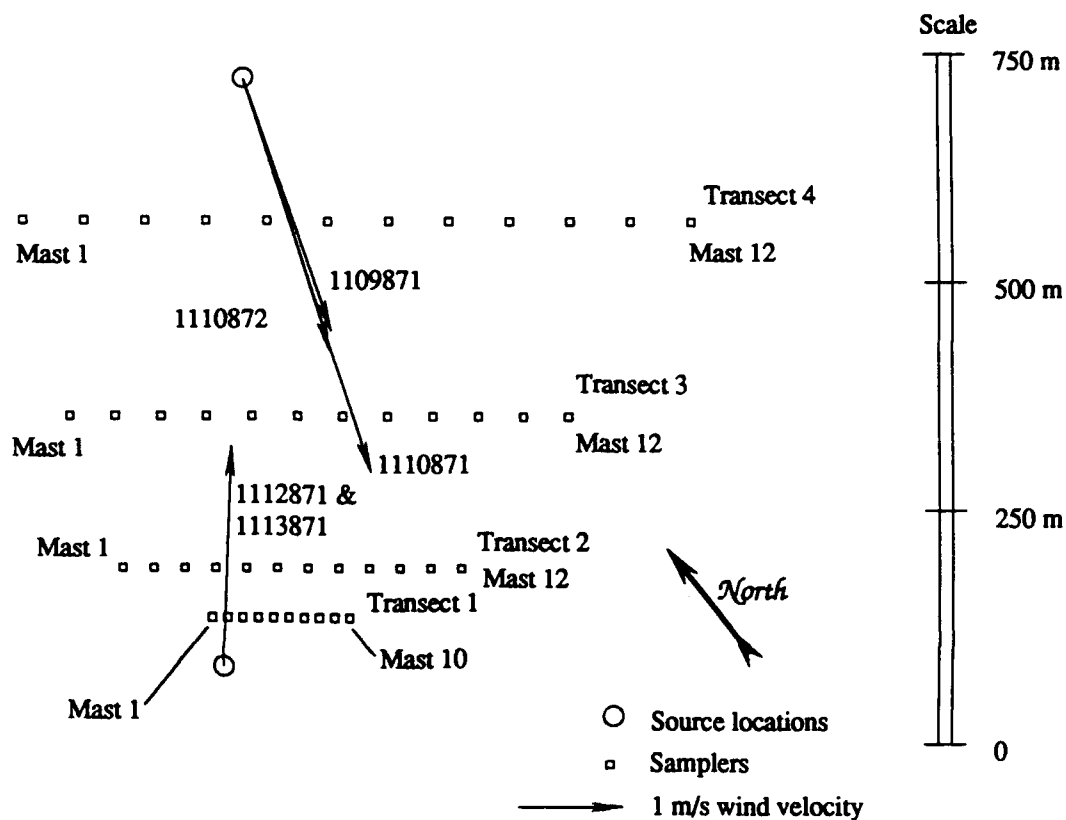


Figure 6.21 Sampler and source locations for the HC smoke dispersion tests at Camp Atterbury. The wind vectors indicated in the figure are averages over the test duration at the source location. The masts in each of these lines are numbered, from northwest to southeast, beginning with one in each transect. An alternate release point for Tests 1109871, 1110871, and 1110872 was chosen due to mean wind direction.

Concentration data  
 HC smoke  
 Test 1109871  
 November 9, 1987  
 15:45:00 to 16:10:00

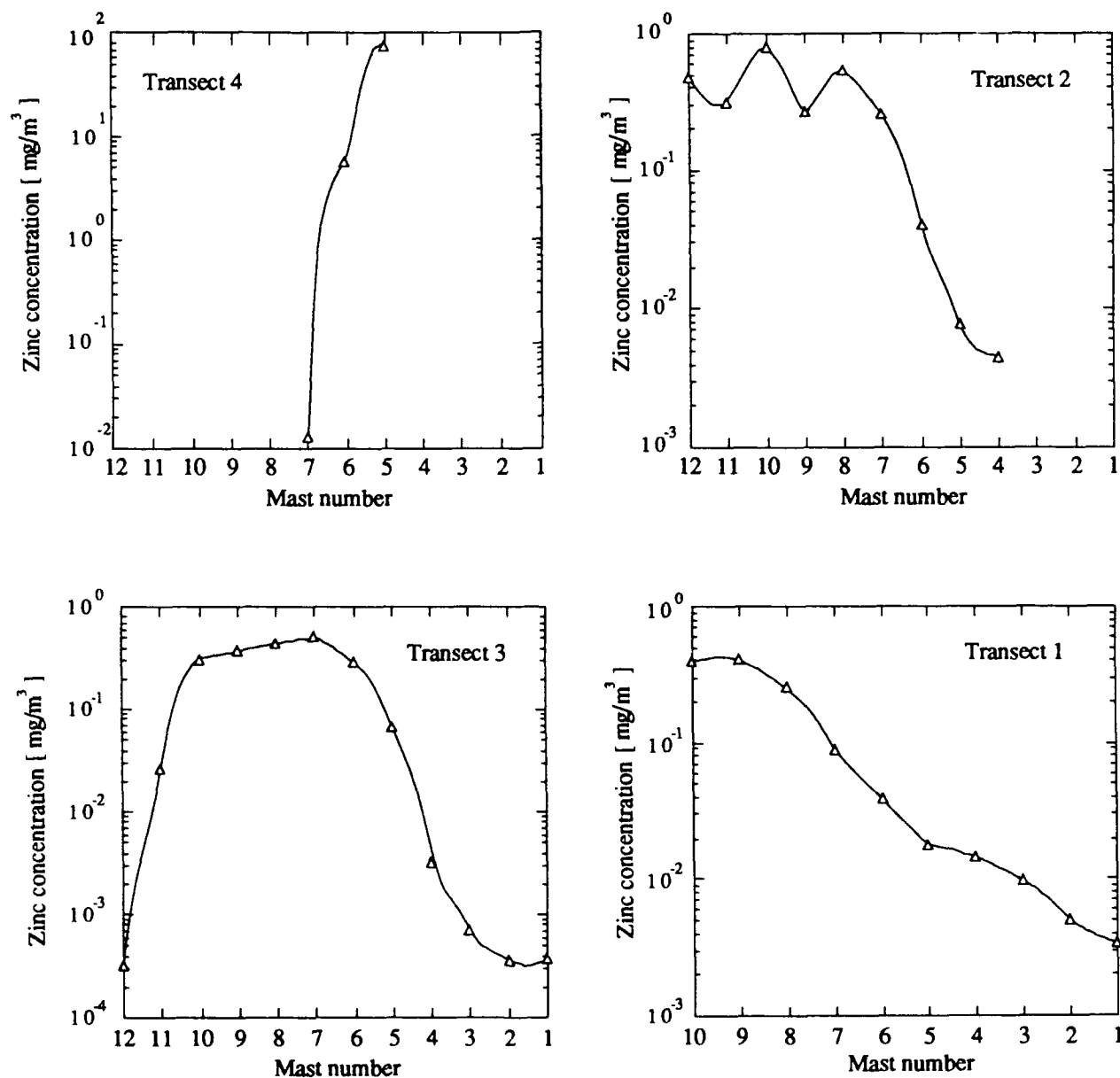


Figure 6.22 Profiles of zinc concentration in the HC smoke dispersion experiments at Camp Atterbury. These plots show mean concentration data averaged from the 1-m, 2-m, 4-m, and 8-m levels of each sampling mast for Test 1112871. The crosswind view in these graphs is looking downwind from the source. This requires the reversed mast number axis because of the alternate source location for this test.

Concentration data  
 HC smoke  
 Test 1110871  
 November 10, 1987  
 11:27:30 to 12:04:00

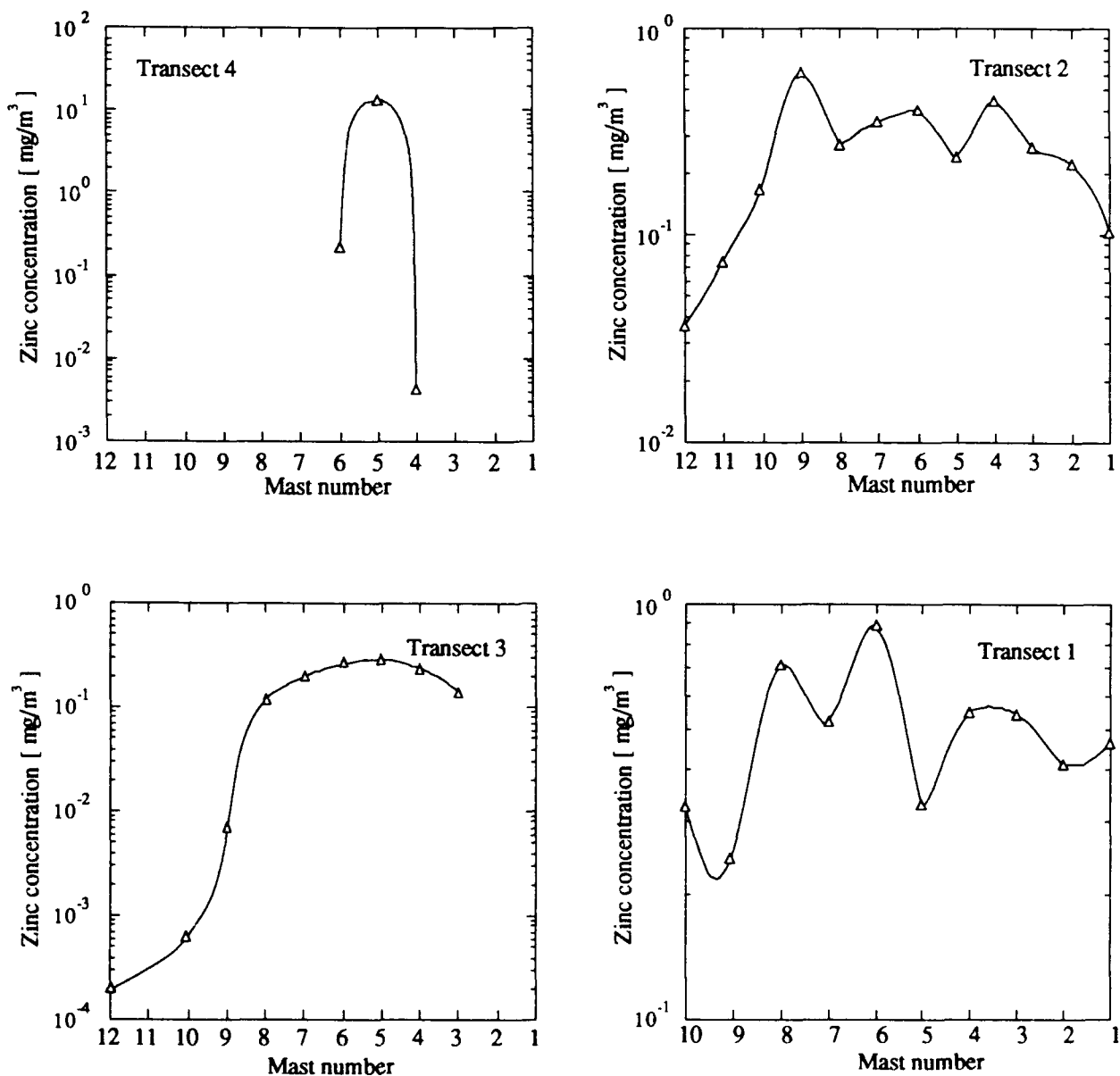


Figure 6.22 (continued) Profiles of zinc concentration in the HC smoke dispersion experiments at Camp Atterbury. These plots show mean concentration data averaged from the 1-m, 2-m, 4-m, and 8-m levels of each sampling mast for Test 1110871. The crosswind view in these graphs is looking downwind from the source. This requires the reversed mast number axis because of the alternate source location for this test.

Concentration data  
 HC smoke  
 Test 1110872  
 November 10, 1987  
 16:37:41 to 17:25:00

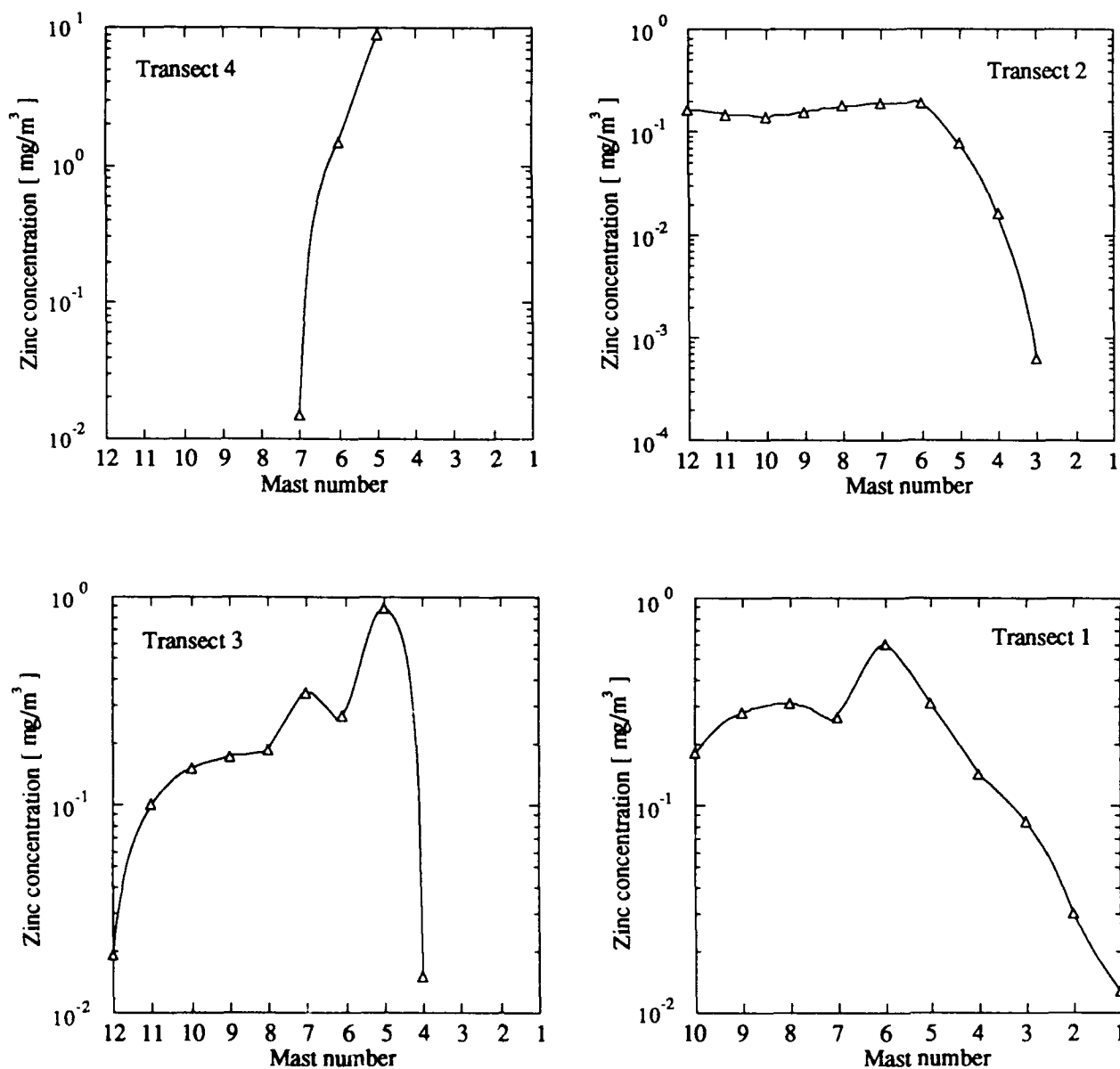


Figure 6.22 (continued) Profiles of zinc concentration in the HC smoke dispersion experiments at Camp Atterbury. These plots show mean concentration data averaged from the 1-m, 2-m, 4-m, and 8-m levels of each sampling mast for Test 1110872. The crosswind view in these graphs is looking downwind from the source. This requires the reversed mast number axis because of the alternate source location for this test.

Concentration data  
 HC smoke  
 Test 1112871  
 November 12, 1987  
 13:31:20 to 14:17:00

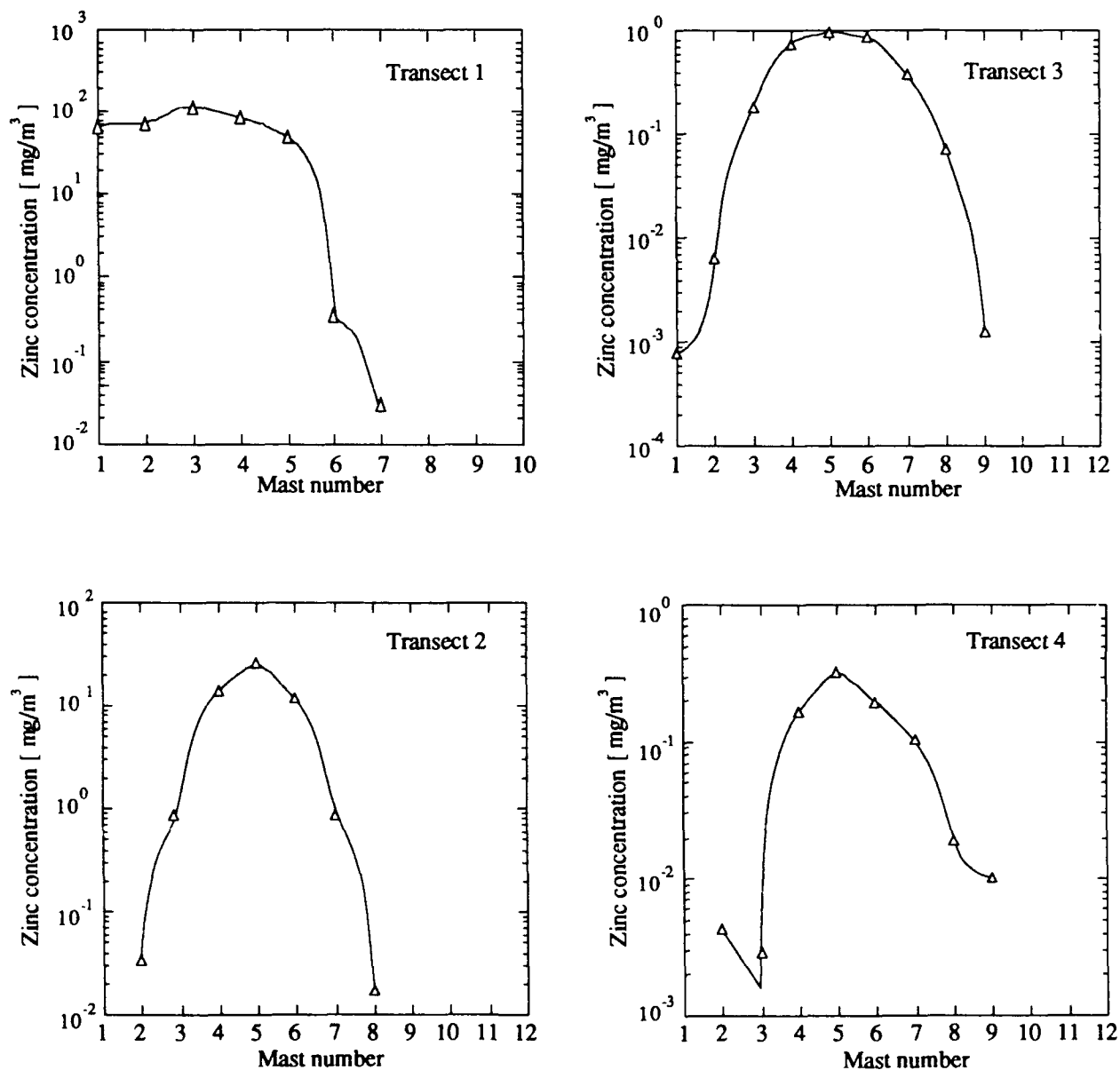


Figure 6.22 (continued) Profiles of zinc concentration in the HC smoke dispersion experiments at Camp Atterbury. These plots show mean concentration data averaged from the 1-m, 2-m, 4-m, and 8-m levels of each sampling mast for Test 1112871. The crosswind view in these graphs is looking downwind from the source.



Concentration data  
 HC smoke  
 Test 1113871  
 November 13, 1987  
 10:21:00 to 11:04:00

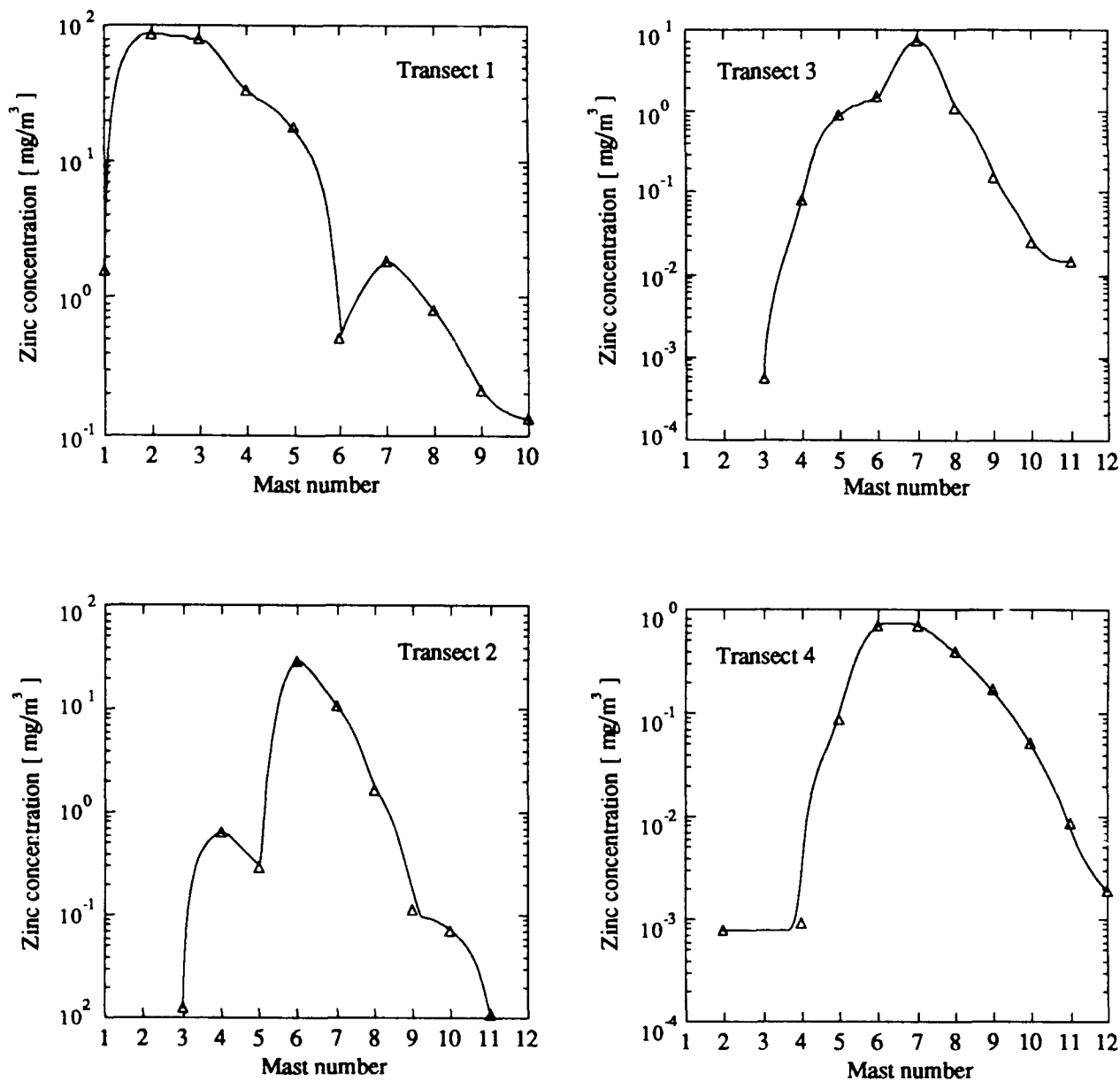


Figure 6.22 (continued) Profiles of zinc concentration in the HC smoke dispersion experiments at Camp Atterbury. These plots show mean concentration data averaged from the 1-m, 2-m, 4-m, and 8-m levels of each sampling mast for Test 1113871. The crosswind view in these graphs is looking downwind from the source.

analysis, whereas the other tests, due to the alternate source location as shown in Figure 6.21 and the limited resolution of the plume, are not analyzed in detail.

### 6.2.1 Mean Concentrations

We do have a problem with the mean concentrations measured in these tests. In the samples with high filter loading, the flow was restricted which resulted in a lower total flow through the filter than expected and a lower calculated mean concentration than the actual value. This problem is most likely related to the nature of the membrane filter used to collect the HC smoke and is probably further exacerbated by the fact that liquid water surrounds the much smaller zinc chloride particle. A correction factor was developed for these data which took into account the lower aspiration rates created by high filter loading. This correction factor assumes a collection efficiency of 100% for filter loadings less than 120 $\mu$ g and lowers the efficiency exponentially for loadings above this threshold.

These corrected data may be compared with the predicted results from a Gaussian-plume model and a mixed-layer scaling model. The Gaussian model is given by

$$\bar{c}(x,y) = \frac{q}{\pi \sigma_y \sigma_z \bar{u}_x} \exp\left(-\frac{y^2}{2 \sigma_y^2}\right) \quad (6.23)$$

and the mixed-layer scaling model is given by

$$\bar{c}(x,y) = \frac{0.9 q \sqrt{z_i}}{\sqrt{2\pi} \sigma_y \bar{u}_x} \left(\frac{\bar{u}_x}{w_* x}\right)^{3/2} \exp\left(-\frac{y^2}{2 \sigma_y^2}\right) \quad (6.24)$$

Both models are fully described in Section 3.3. These models, along with the data are shown for Tests 1112871 and 1113871 in Figure 6.23.

With these data plume width can be estimated for these two data sets. A plot of the result for each transect, along with the model prediction given in Eq. 6.5 from Gryning et al. (1987) is shown in Figure 6.24. The growth in plume width is proportional to travel time, which is the same near field range as seen in the Camp Atterbury fog-oil tests.

An estimate of the crosswind integrated concentration for the HC tests is found by fitting a Gaussian profile to the data and is shown in Figure 6.25. The data and the model appear to agree fairly well. Nondimensionalized crosswind profiles of the mean concentration data along each transect are compared with a Gaussian distribution (Eq. 6.9) in Figure 6.26. Considering the filter clogging problem, the comparison in this plot is reasonable.

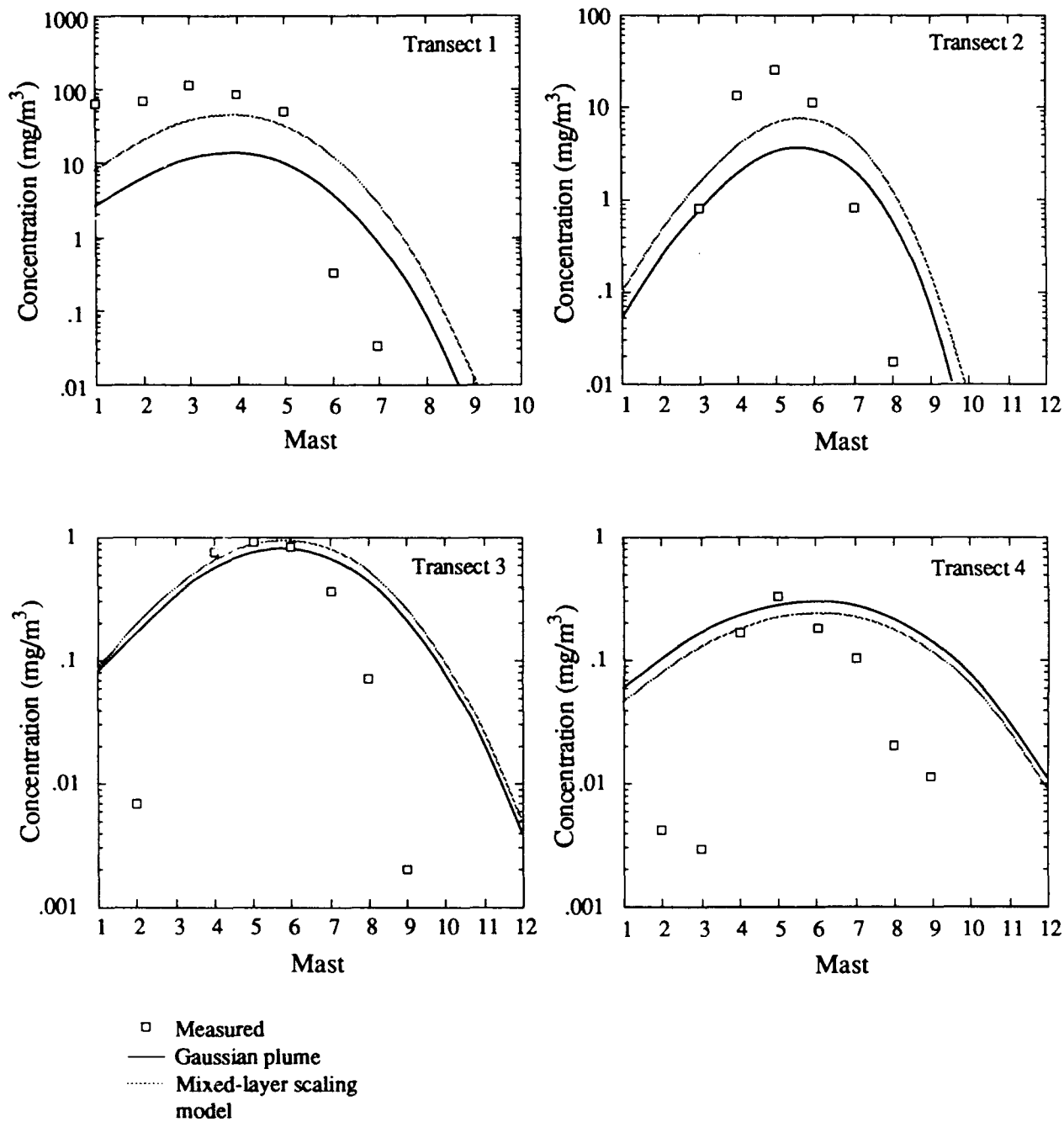


Figure 6.23 A model-data comparison for the HC smoke concentration data taken in Test 1112871. The models are described in the text.

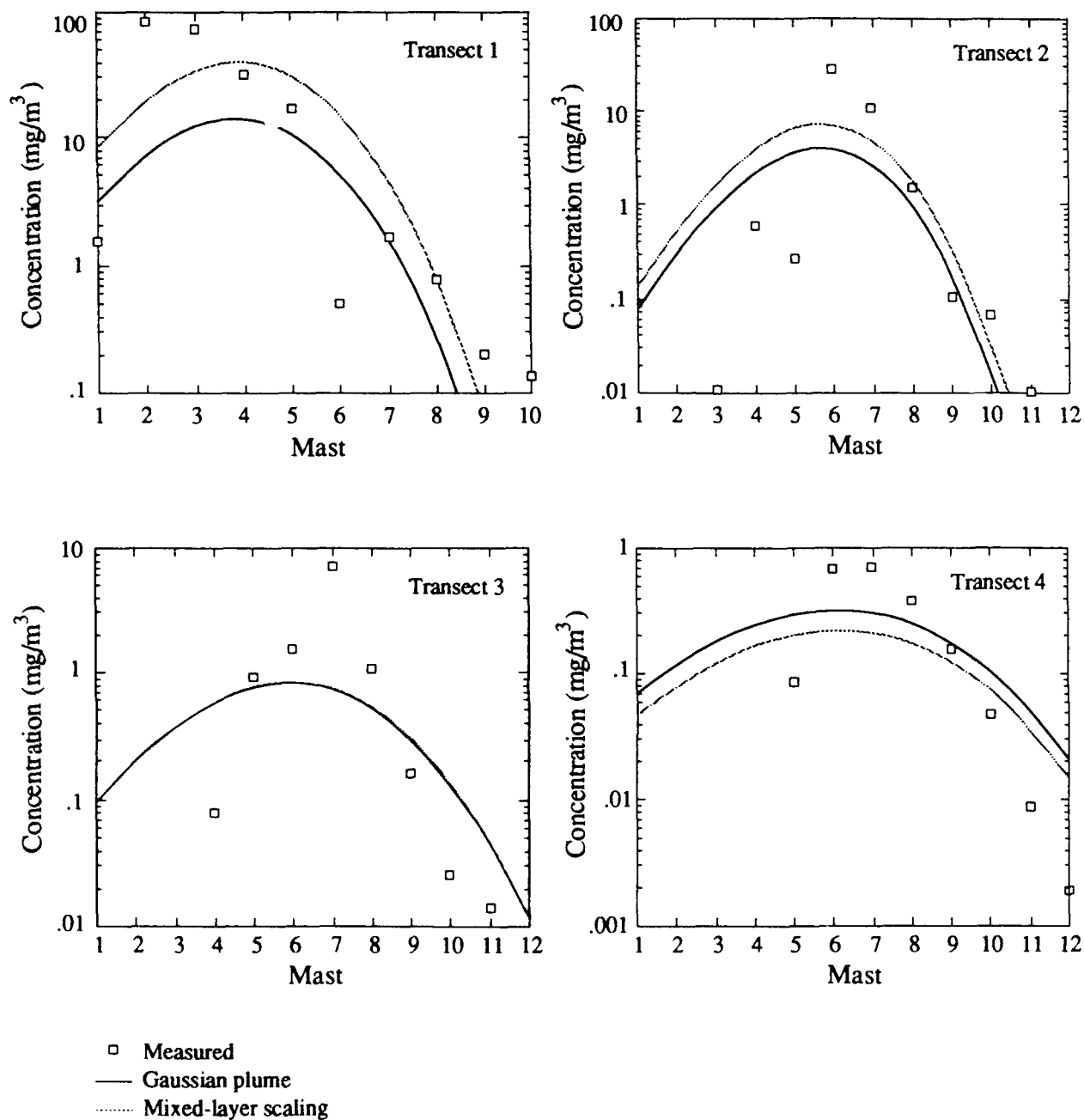


Figure 6.23 (continued) A model-data comparison for the HC smoke concentration data taken in Test 1113871. The models are described in the text.

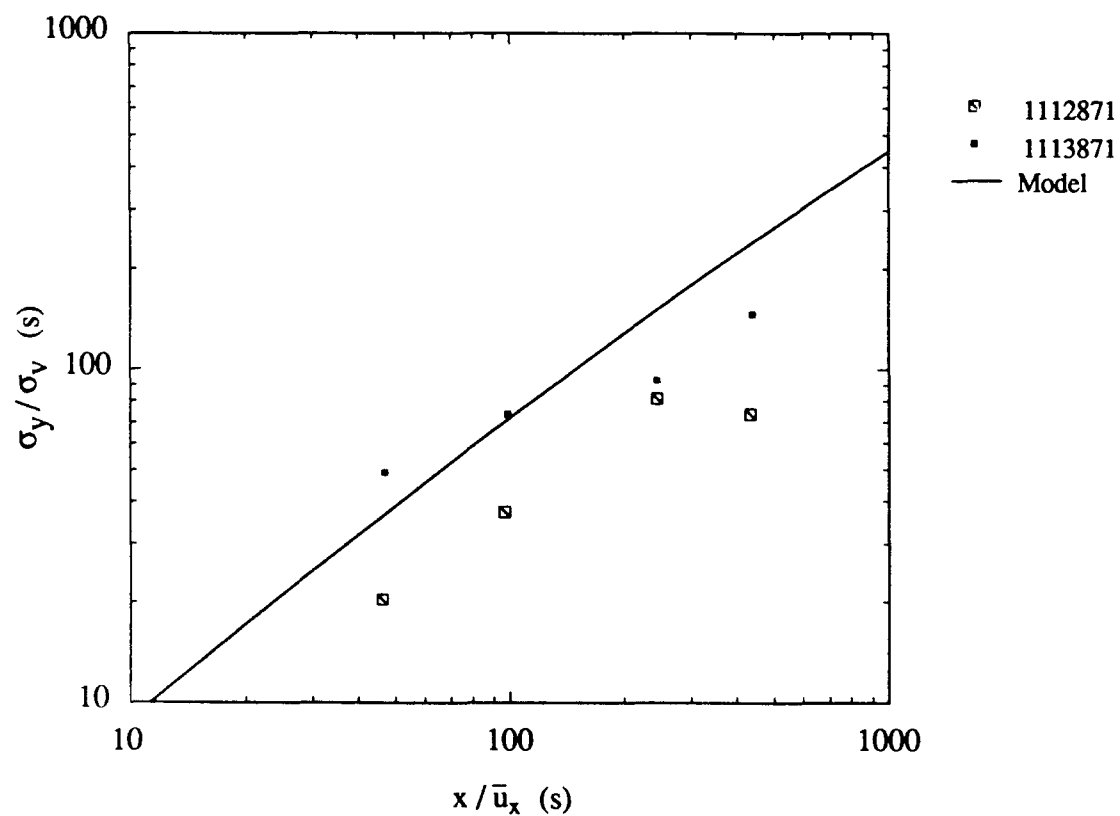


Figure 6.24 Estimated plume widths for the HC dispersion tests at Camp Atterbury as compared with an adaptation from Gryning et al (1987) of a model given by Draxler (1976).

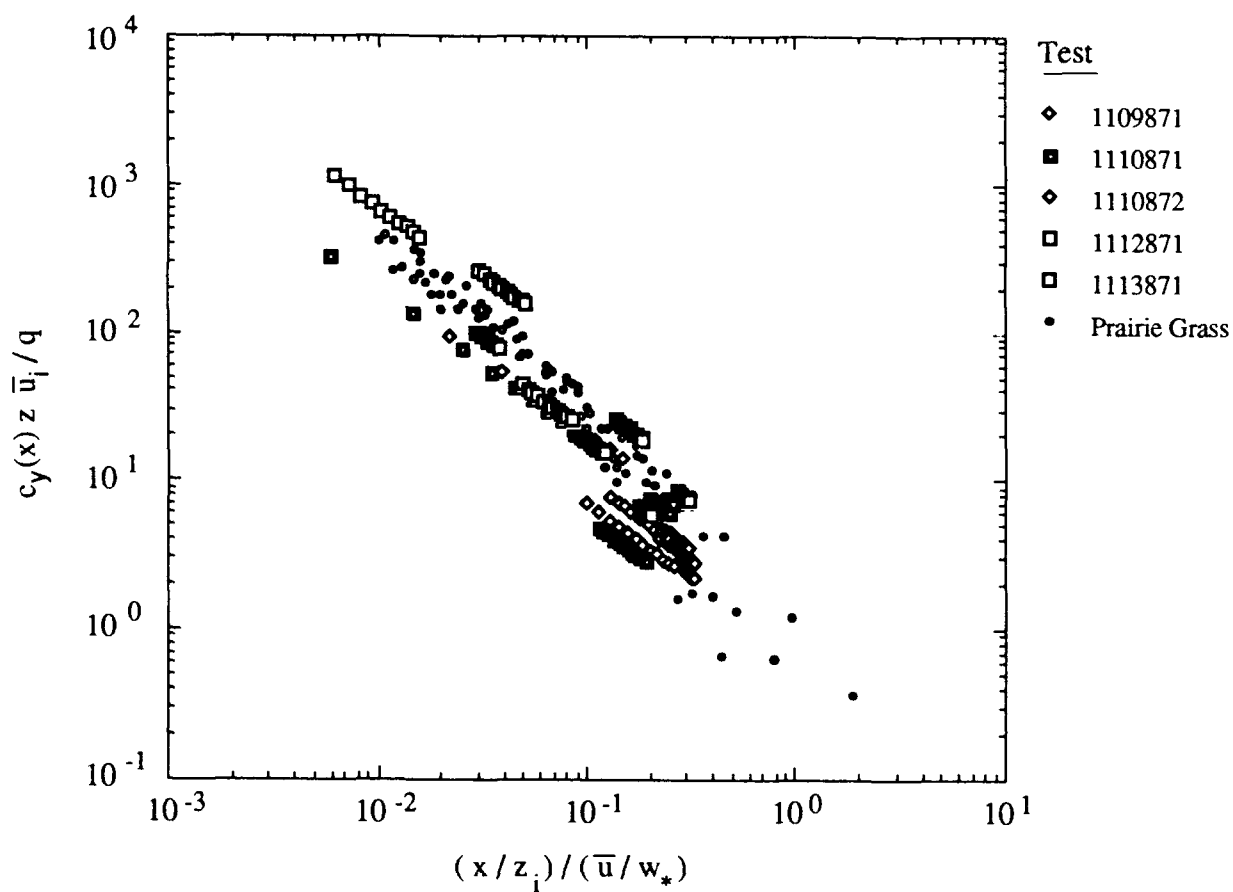


Figure 6.25 Mixed-layer scaling for the crosswind integrated ground level concentrations measured in the Camp Atterbury dispersion tests. Crosswind integrated concentration is determined from pointwise measurements by fitting the transect data to a Gaussian lateral profile. Comparisons with Prairie Grass data (Nieustadt 1980b) are provided.

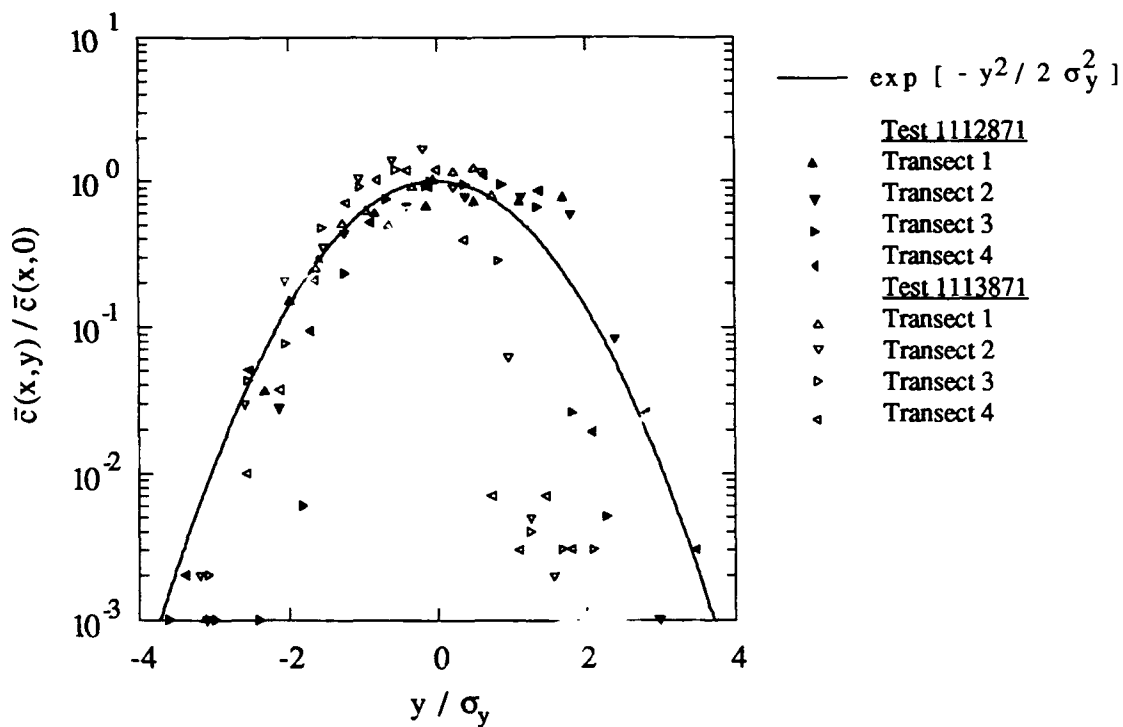


Figure 6.26 Normalized crosswind profile of the mean concentration for the Camp Atterbury HC smoke dispersion tests. Lateral plume spread versus a ratio of measured concentration to the fitted centerline concentration is shown in this plot. The data are compared with a Gaussian profile. The transects correspond, respectively, to downwind distances of 50, 100, 250, and 450 m.

### 6.2.2 Fluctuations in Concentration

For the concentration fluctuation intensity, ratios of  $\sigma_c(x,y)/\bar{c}(x,y)$  can be found for each aerosol photometer without using values of concentration from the dosage samplers. This result is shown in Figure 6.27 using the plume widths previously measured. No dependence of this ratio on downwind distance is seen in this plot. The modeled crosswind distribution is given by Eq. 6.11 with  $\alpha = \sigma_c(x,0)/\bar{c}(x,0) = 2$ . This is the same centerline ratio as found for the fog-oil data at Camp Atterbury. The value of  $\alpha$  should be a function of the ratio of the source size to the Lagrangian integral scale. Because we have found  $\alpha = 2$  for both the fog-oil tests and the HC smoke tests,  $\alpha$  does not appear to be very sensitive to the source-integral scale ratio for our two sets of dispersion experiments undertaken at Camp Atterbury.

The crosswind distribution of intermittency is shown in Figure 6.28. These data are consistent with the crosswind profile predicted for intermittency, previously given in Eq. 6.15. for the Camp Atterbury fog-oil data comparisons. Plots of the concentration probability distribution are shown in Figure 6.29. These results follow the distribution given in Eq. 6.12 with the same degree of agreement as seen for the previously discussed fog-oil tests. Deviations from the analytical distribution occur because of instrument noise at low concentrations and signal clipping by the photometer electronics on a few masts at higher concentrations..

### 6.2.3 Correlations and Spectra

Spatial correlations are not presented for the HC smoke tests. Spectra of the concentration data given in Figure 6.30 show a  $-2/3$  power law behavior for  $nS_{cc}(n)$  at higher frequencies. An ensemble average of this spectra for each experiment is shown in Figure 6.31. Much of the random noise in the individual sampler spectra is removed by this averaging. A  $-5/3$  power law inertial-convective range scaling for  $S_{cc}(n)$  is seen in this plot at the higher frequencies.

The integral scale is found using the average value of  $R_{cc}(\tau) = \exp(-1)$  from all of the samplers. For both tests, we find values as shown in Table 6.2. These values are similar in magnitude to the Camp Atterbury fog-oil measurements.

Table 6.2 Integral scales of concentration for the HC dispersion tests at Camp Atterbury.

Test	$\tau_c$	$\tau_c/(z_i/w^*)$
1112871	20.4	0.043
111387	19.6	0.055



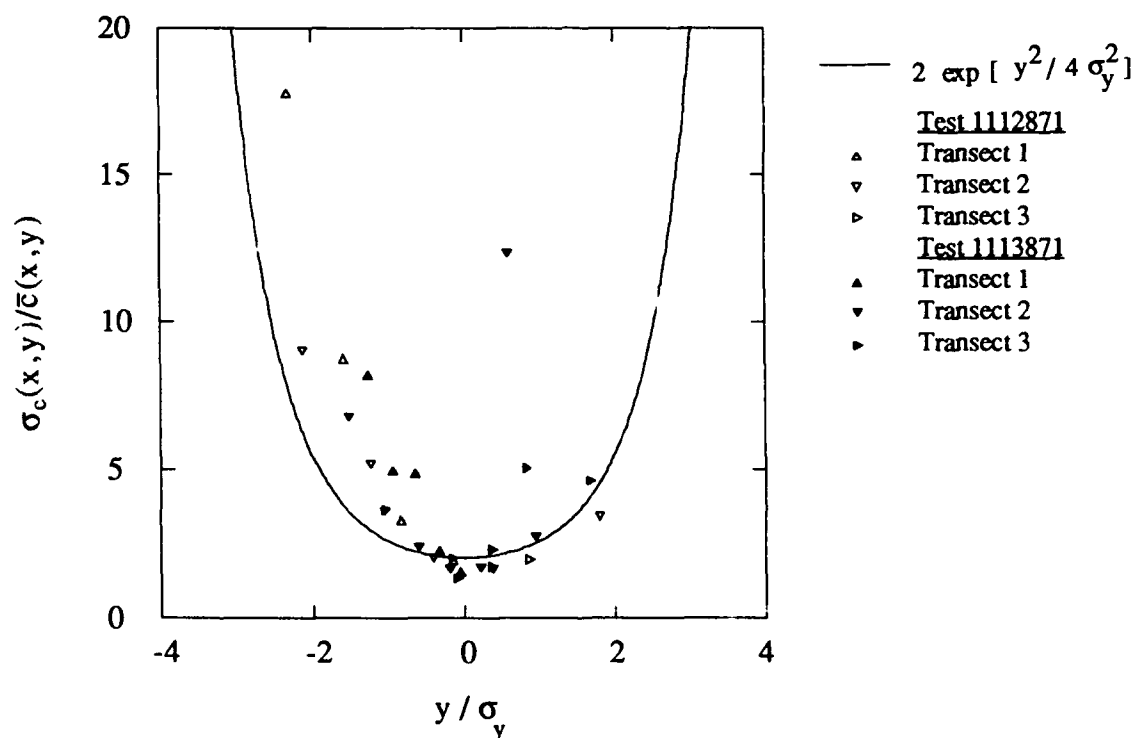


Figure 6.27 Crosswind profile of the relative fluctuation intensity of concentration for the HC smoke tests at Camp Atterbury. The data from our tests are plotted as a dimensionless profile of the local values of the standard deviation in concentration and the mean concentration. The model profile is also plotted, with a coefficient of 2.

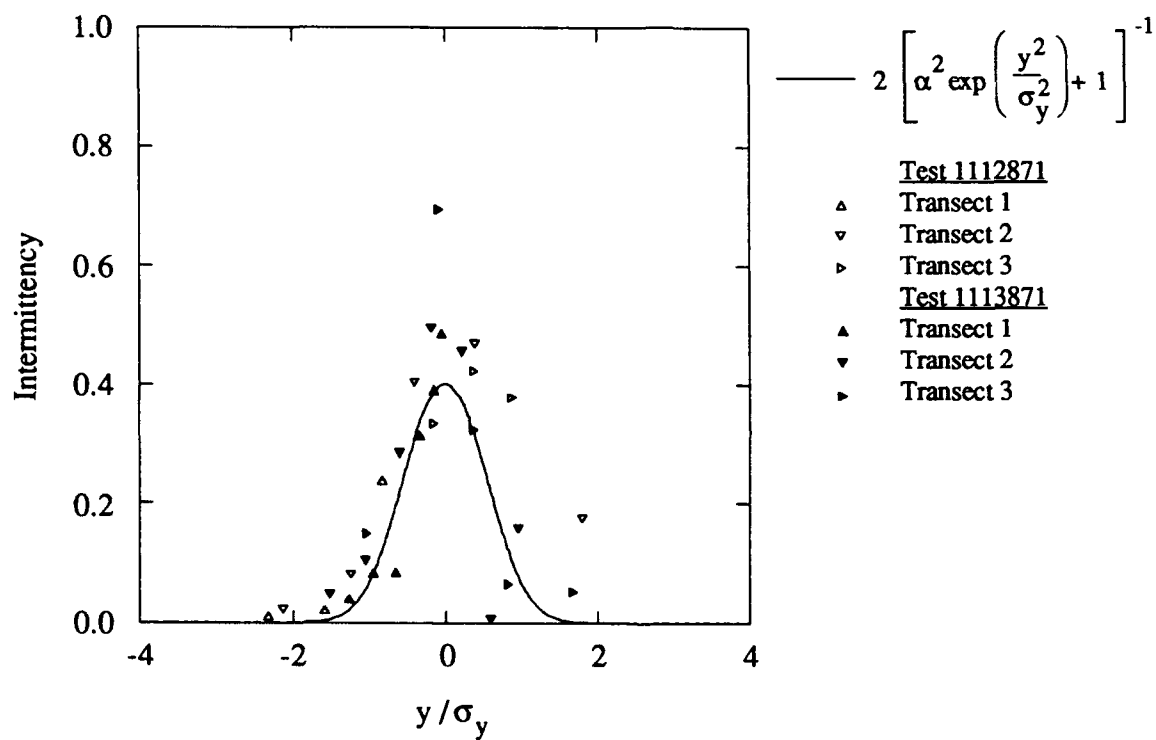


Figure 6.28 Crosswind plume intermittency for the Camp Atterbury HC dispersion tests. The analytical solution uses a value of  $\alpha = 2$  in the expression shown.

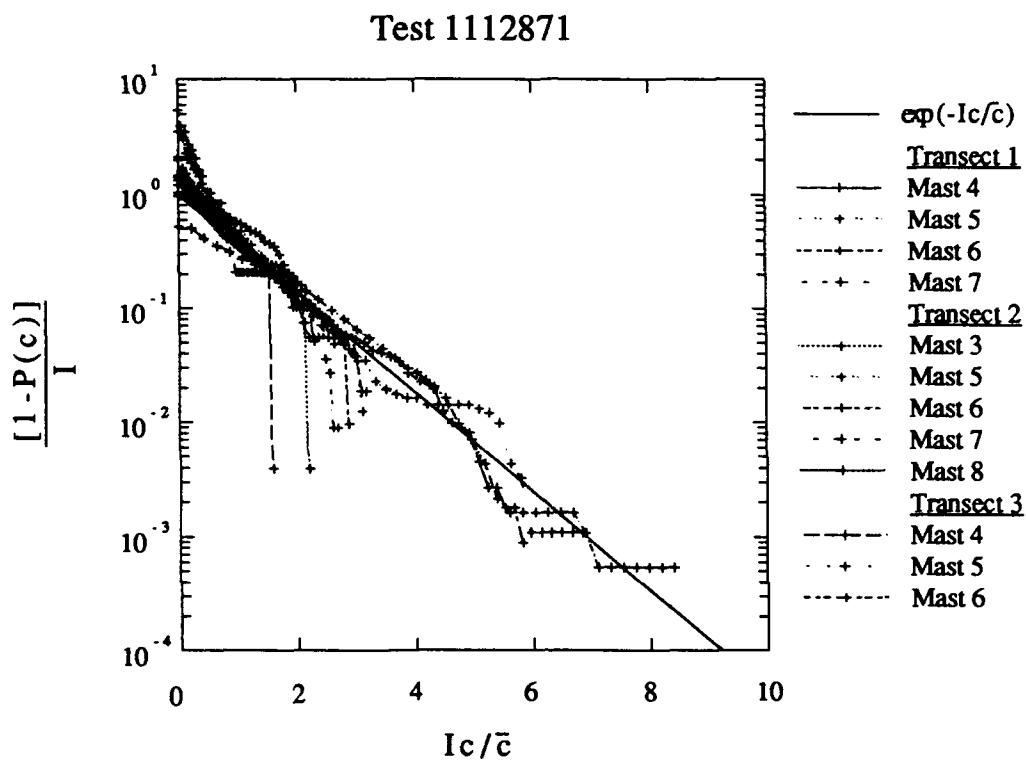


Figure 6.29 A comparison of the histograms in concentration with the exponential distribution for Test 1112871. The mast numbers refer to the location along a given transect.

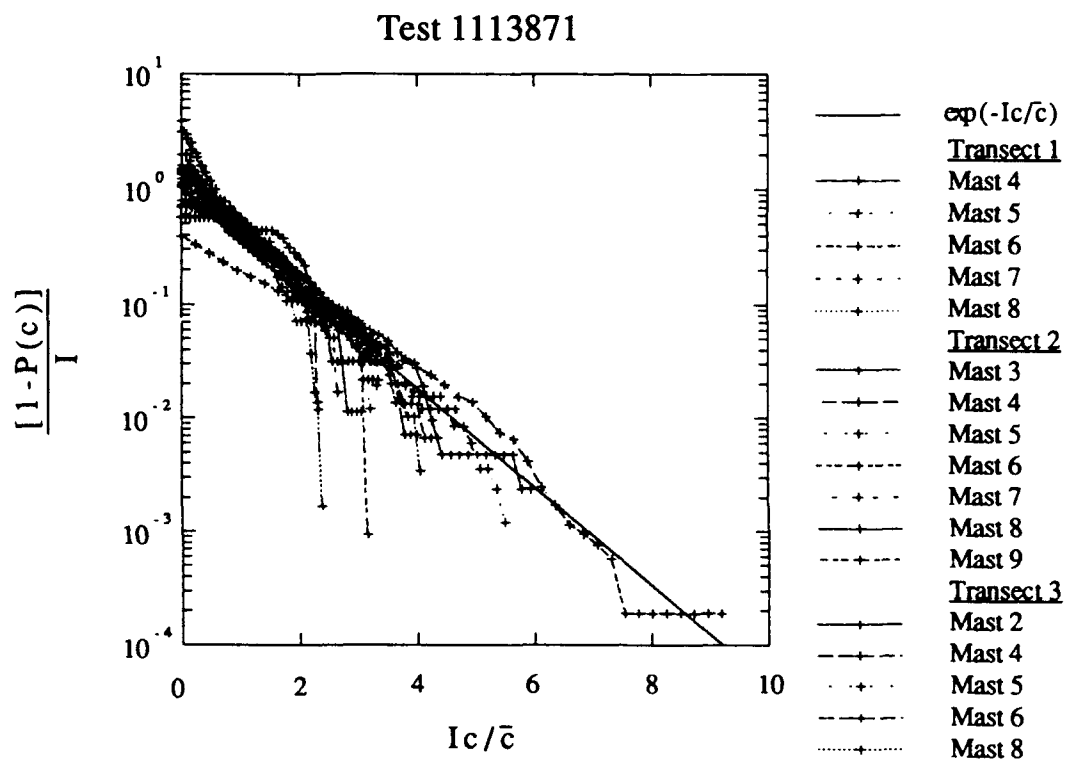


Figure 6.29 (continued) A comparison of the histograms in concentration with the exponential distribution for Test 1113871. The mast numbers refer to the location along a given transect.

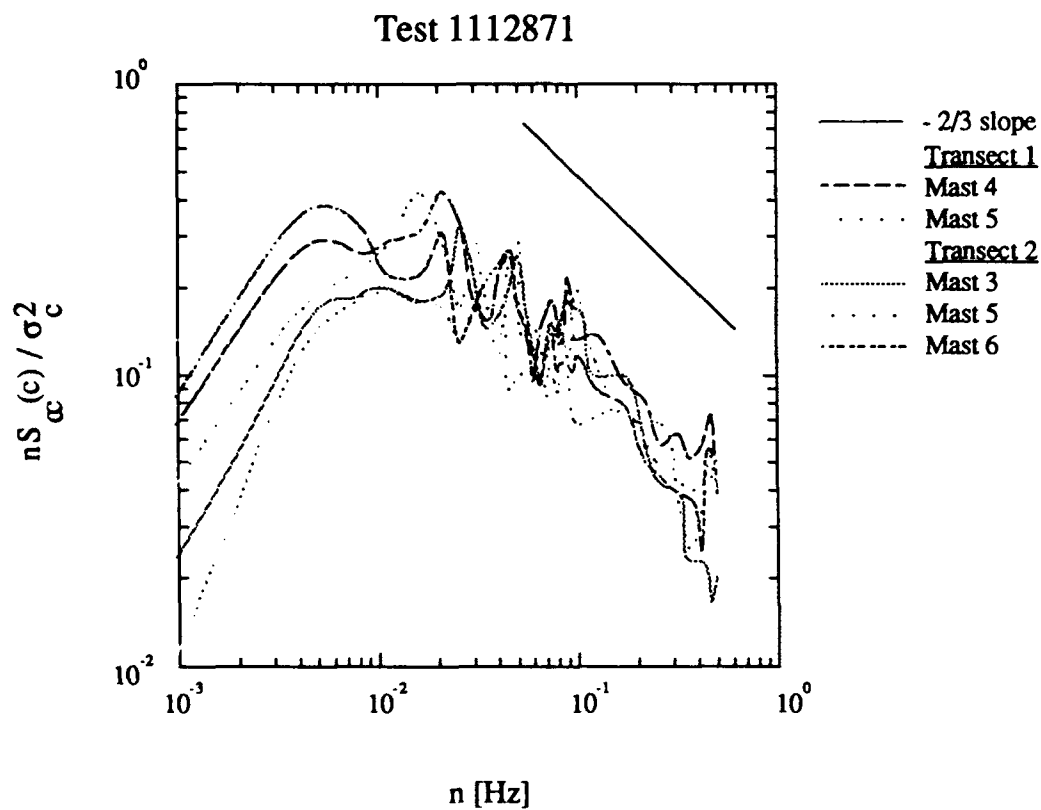


Figure 6.30 Spectra of the concentration variance for all samplers in Test 1112871 in which the mean signal was greater than 5 times the background noise of the instrument. The spectra are normalized by the calculated variance for each data record.

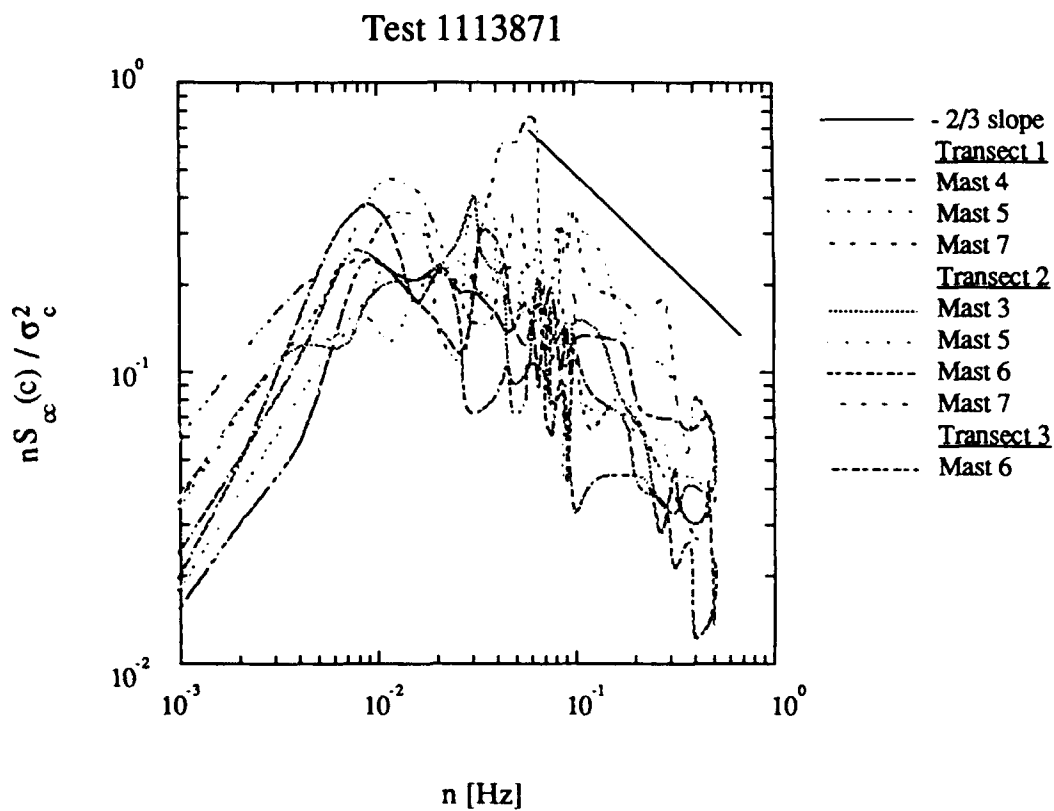


Figure 6.30 (continued) Spectra of the concentration variance for all samplers in Test 1113871 in which the mean signal was greater than 5 times the background noise of the instrument. The spectra are normalized by the calculated variance for each data record.

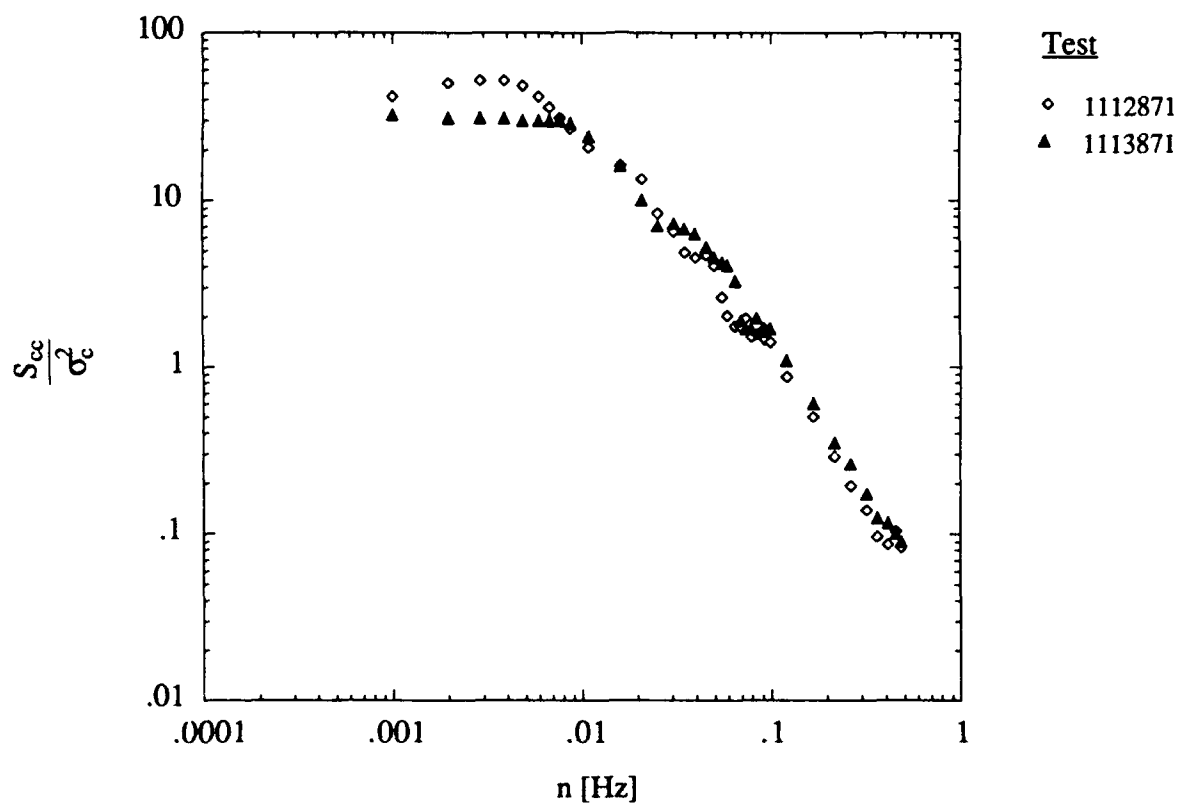


Figure 6.31 Ensemble averaged spectra of the concentration fluctuations measured in the HC smoke dispersion tests at Camp Atterbury. These data are the ensemble average of all the spectra from a given test for which the mean signal level exceeded the background noise by a factor of 2.

Other methods of determining the integral scale produce values which are consistent with the above results. In examining integral scales calculated from individual concentration records, no dependence on position is found. This is probably due to random noise, which masks the details of the spatial distribution.

#### 6.2.4 Concentration Exceedance

In examining the behavior of time intervals for which the concentration at a given sampler is greater than zero, we find that the mean burst duration  $1/\lambda_u(0)$  is approximately equal to the integral scale of the turbulence. This is shown for our HC smoke tests in Figure 6.32. Like the integral scale of concentration, this mean burst duration shows little definite dependence on position.

The probability distribution of the burst durations for individual samplers is shown in Figure 6.33. Also shown is the curve for an exponential distribution given in Eq. 6.21. Deviation of the data in these plots from this expected distribution may be due to the sampling duration of the test at longer frequencies and the limited 1-Hz sampling frequency at the short time increments.

Although the mean burst duration  $1/\lambda_u(0)$  or rate  $\lambda_u(0)$  does not depend on position, we find a crosswind spatial dependence of the rate of occurrence of these bursts  $\lambda(0)$ . These parameters are related through  $\lambda(0) = I \lambda_u(0)$ , where  $I$  is the intermittency. The crosswind dependence of  $\lambda(0)$  is shown in Figure 6.34. In this figure we use the convective time scale  $(z_i/w_*)$  to form dimensionless ratios. This plot shows the rate of bursts is greater near the center of the mean plume, and is less near the mean plume edges. A model of this distribution is also shown. Although there is considerable scatter of data the curve does represent the average behavior of the distribution.

### 6.3 Meadowbrook Fog-oil Dispersion Tests in Unstable Atmospheric Conditions

The dispersion tests in California were conducted on a site with complex terrain features. Releases were made within a bifurcating canyon valley running the length of the  $5 \times 5$  km test site. The ground cover at the site consisted of varying types, densities and heights of vegetation. With these varying terrain features, a general analysis must be approached with caution. It is not as applicable to other sites as the previously discussed flat terrain measurements at Camp Atterbury.

In the Meadowbrook study, tests were conducted in both unstable daytime conditions and nighttime or early dawn stable atmospheric conditions. Separate sampling grids were used for each type of test, and the following discussion is similarly divided into two separate sections for each group of tests.

A total of five dispersion tests were conducted during the daytime. Because of the extreme dilution of smoke under convective conditions and our limited number of samplers, concentrations



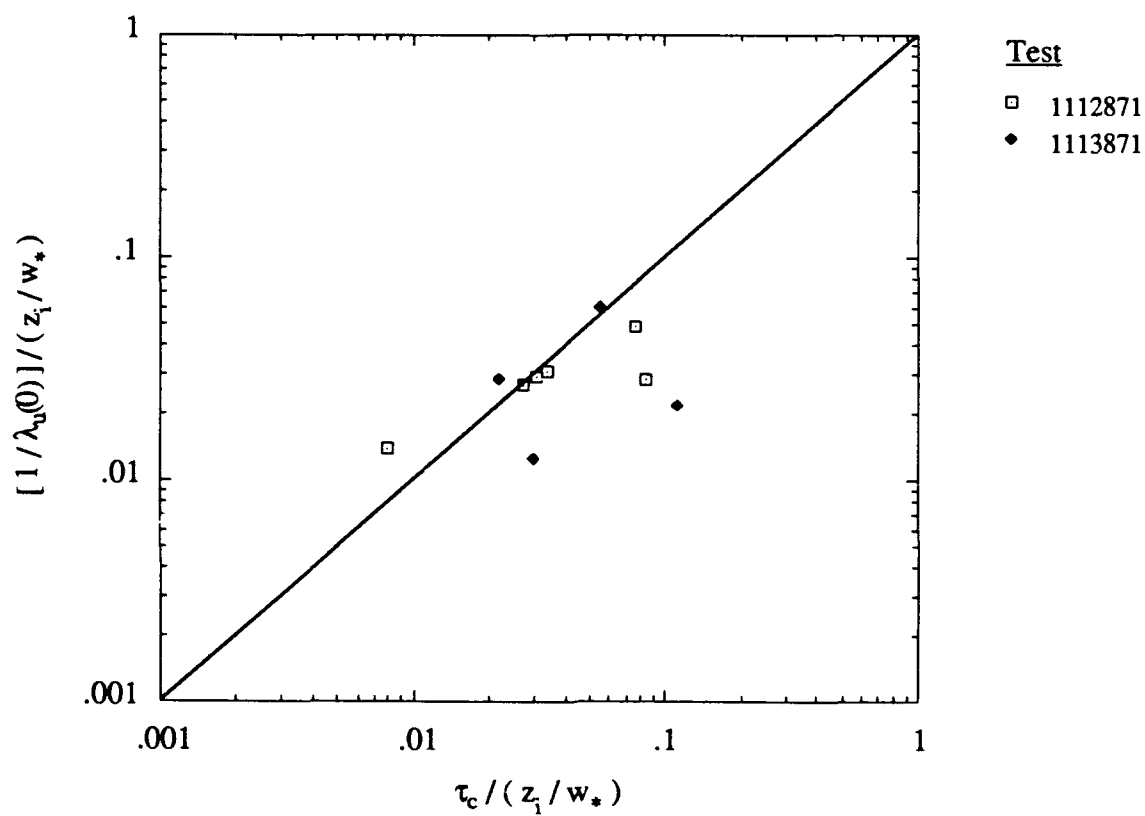


Figure 6.32 Duration of bursts in concentration with  $c > 0$ , versus the integral scale in concentration for the Camp Atterbury HC smoke dispersion tests.

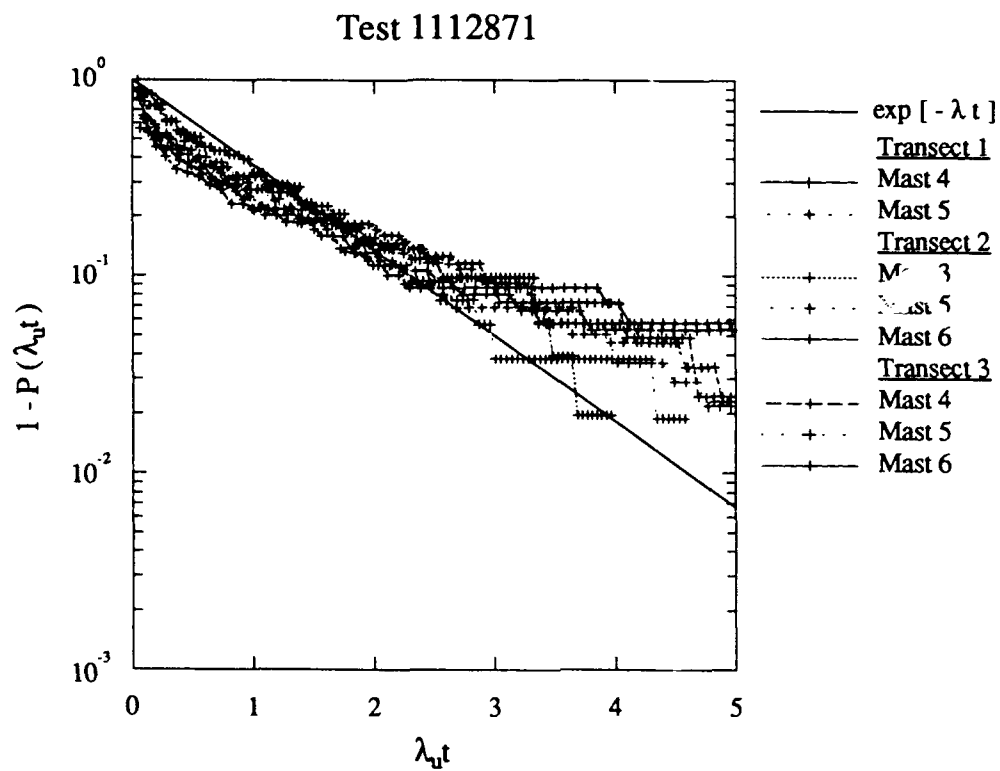


Figure 6.33 Histogram of time intervals for which the concentration exceeds zero for Test 1112871. The data from all records for which  $I > 0.1$  are included in the above plot.

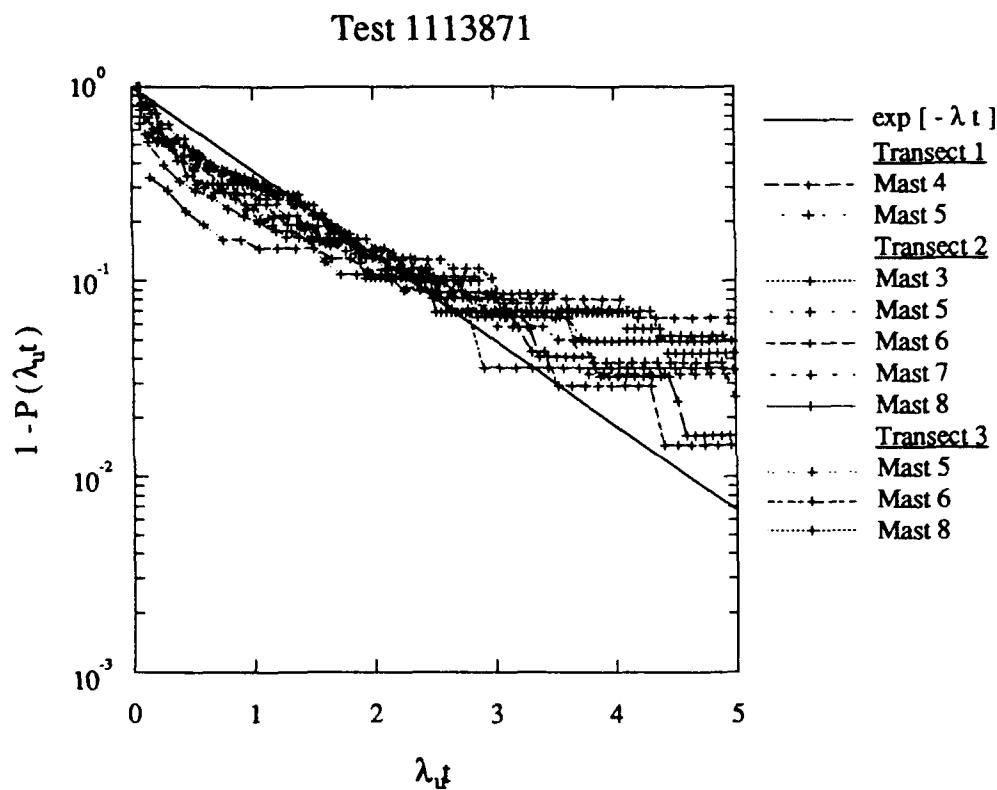


Figure 6.33 (continued) Histogram of time intervals for which the concentration exceeds zero for Test 1113871. The data from all records for which  $I > 0.1$  are included in the above plot.

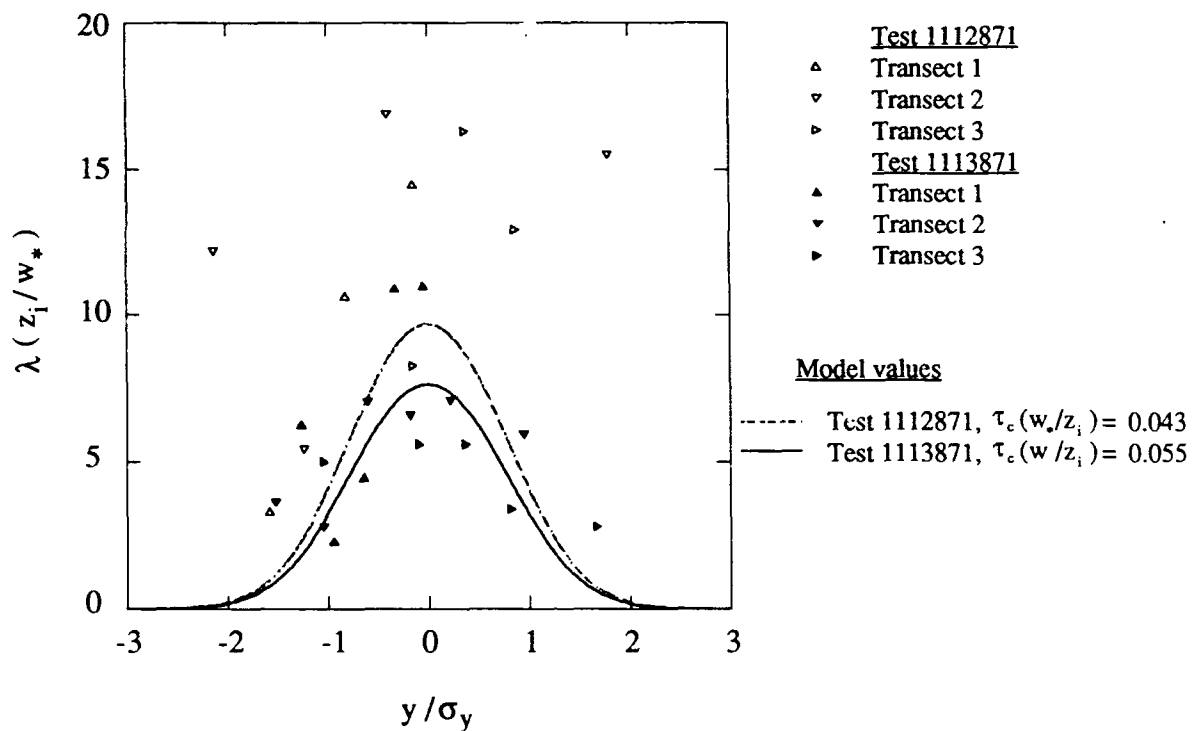


Figure 6.34 The crosswind distribution of intervals between smoke event starts for the HC tests at Camp Atterbury using fog-oil smoke. These data are nondimensionalized by the mean plume width and the convective time scale and are compared with model given by Equation 6.22.

were measured only to 250 m from the source. A detailed map of the sampling grid, ground cover, and terrain is shown in Figure 6.35. The site over which the samplers is located is very flat compared to the surrounding terrain, with a maximum elevation difference of less than 4 m. Ground cover in the range of the sampling grid consists of a harvested wheat field of 0.1-m tall straw.

Three wind sensors were located adjacent to the sampling grid. Their location and mean wind vectors for our dispersion tests are shown in Figure 6.36. There is a small deviation in the mean wind field between these sensors for several of the tests. This can affect the distribution of the mean smoke plume. With the limited distance covered and the uniform site characteristics, a fairly simple analysis of the concentration field is possible using the averaged locally measured wind characteristics.

### 6.3.1 Mean Concentrations

Values of concentration and the standard deviation in concentration for the tests are shown in Figure 6.37. From examination of these plots and consideration of the source operating characteristics, Tests 0921871, 0923871, and 0926871 are most suitable for detailed analysis, although concentrations along the transects are still at the low end of the detectable range. Test 0928871 did not sufficiently contact the sampling grid. Excessive trouble with the smoke generator for the Test 1002872 rendered this set of concentration data questionable for a steady state analysis.

We may use the transect profiles of the data in a manner similar to that for the Camp Atterbury tests, where data for each transect is fitted to a Gaussian profile to yield a plume width and a crosswind integrated concentration. We can compare plume widths from several of the tests with analytical expressions. From Gryning et al. (1987) we have the relation given in Eq. 6.5. Using average values of the meteorological data at the 10-m height, the data and model is shown in Figure 6.38. The agreement in this comparison is reasonable, but the data are very sparse. For Test 0921871, a width is not shown for Transect 2 because of the limited number of measured dosage samples. For Test 0923871, no value is shown for Transect 3 because of low measured concentration levels.

For these data taken in unstable meteorological conditions, we may use mixed-layer scaling to examine the crosswind integrated ground-level concentrations. This result is shown in Figure 6.39. The inversion height in this scaling is taken from the atmospheric soundings, whereas the convection velocity is found using surface-layer scaling values from the nearest sonic anemometer. In this comparison, the data values are very close to the fit given by Nieuwstadt (1980b). For the plume width, mixed-layer scaling is shown in Figure 6.40. The good agreement with flat-terrain dispersion measurements is surprising because of the complex terrain features in the area.

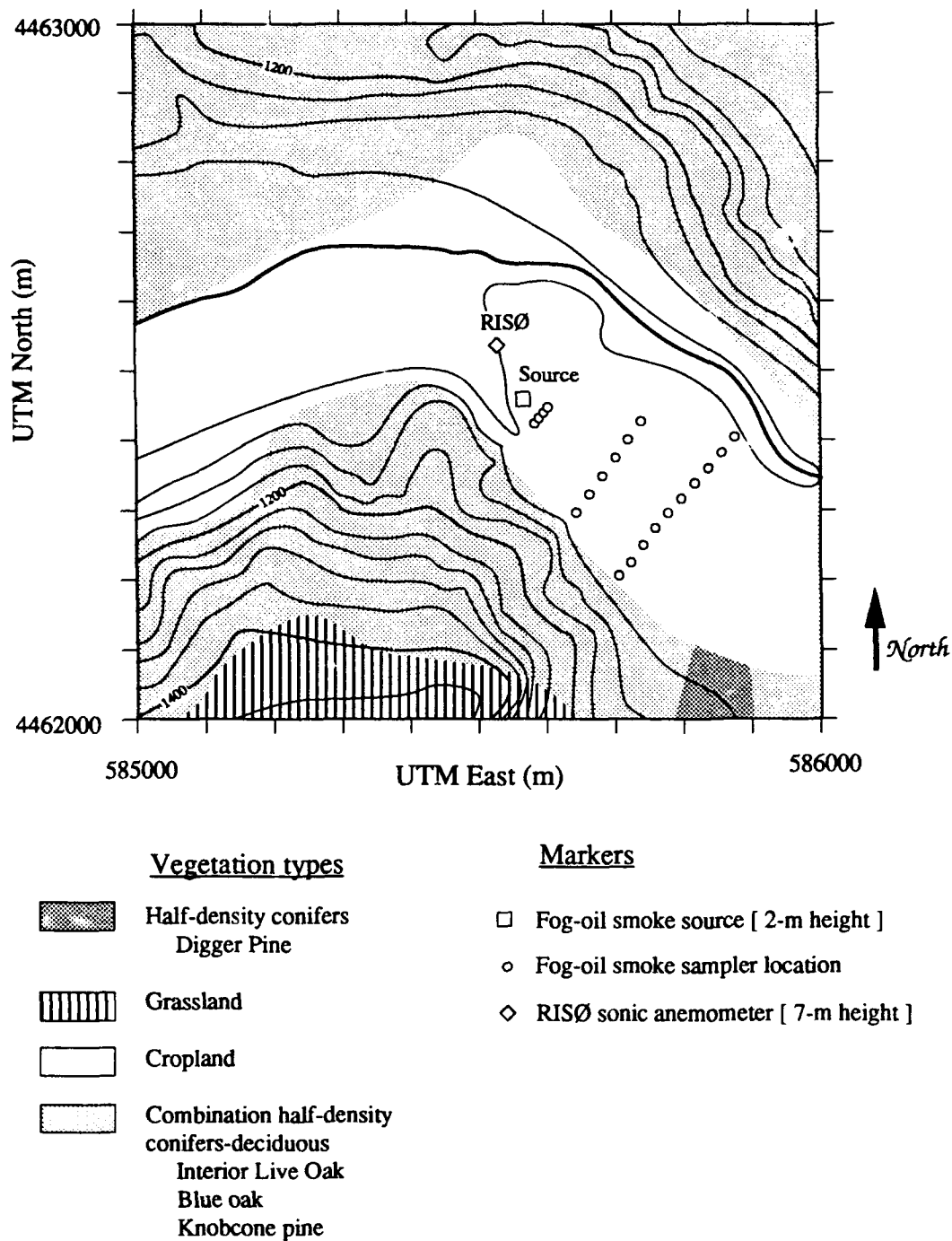


Figure 6.35 Terrain, instrument locations, and vegetation for the daytime unstable Meadowbrook dispersion site. The elevations are in ft above sea level with contour lines at 40-ft increments. Elevations and the UTM coordinates were taken from the USGS map of Inskip Hill, California. The vegetation information is from a survey by ASL.

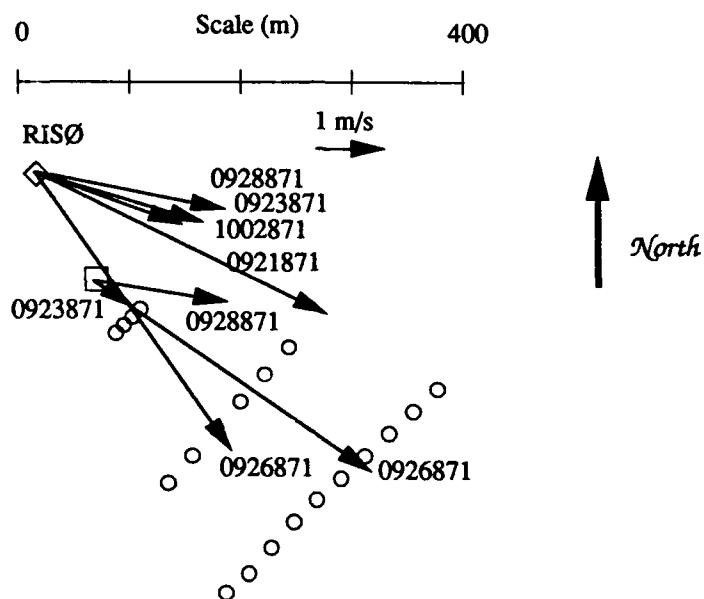


Figure 6.36 Measured wind vectors over the test duration for the daytime unstable dispersion tests at Meadowbrook. The source measurements were made at a height of 2 m, while the RISØ sonic anemometer measurements were made at a height of 7m. All wind vectors are with respect to true north.

Concentration data  
Meadowbrook site  
unstable meteorology  
Test 0921871  
September 21, 1987  
14:30:00 to 15:00:00

—○— 1 m mean  
—○— 2 m mean  
—○— 8 m mean  
—■— 2 m std. dev.

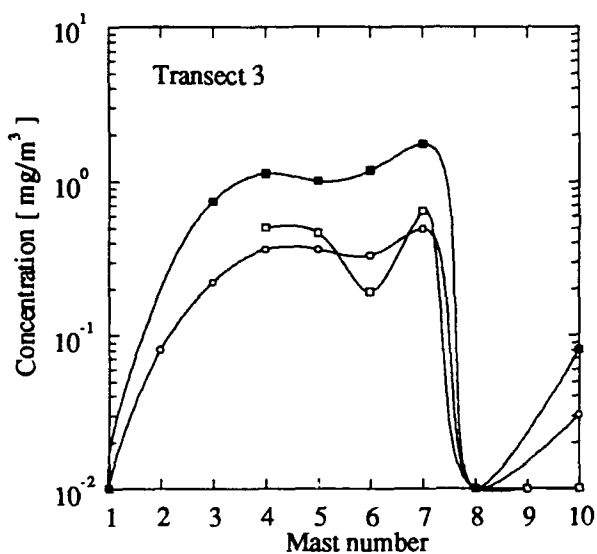
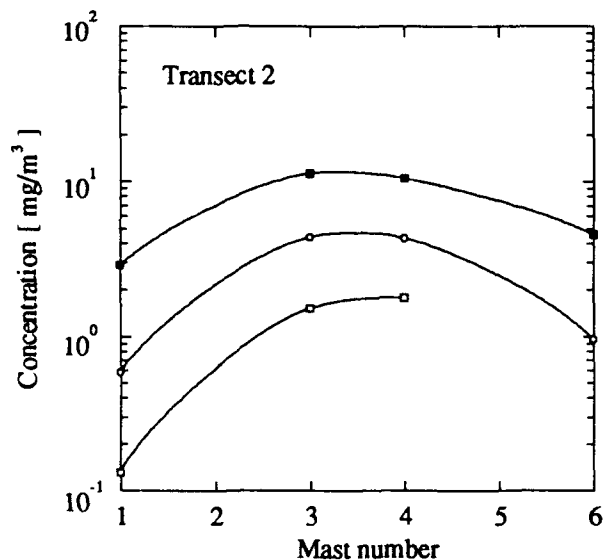
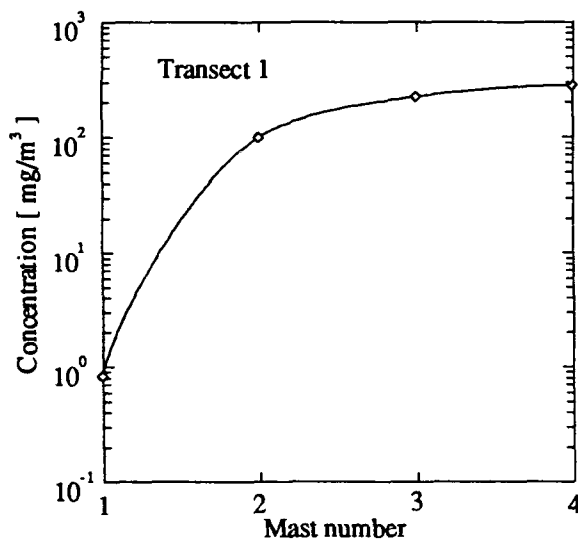


Figure 6.37 Profiles of fog-oil concentration measured along the sampling transects in the daytime unstable Meadowbrook dispersion tests. These plots are for Test 0921871, and the crosswind view in these graphs is looking downwind from the source. In addition to the mean concentrations, the standard deviation in concentration from the aerosol photometers is also shown in these plots.



Concentration data  
Meadowbrook site  
unstable meteorology  
Test 0923871  
September 23, 1987  
14:00:00 to 14:50:00

—○— 1 m mean  
—○— 2 m mean  
—○— 8 m mean  
—■— 2 m std. dev.

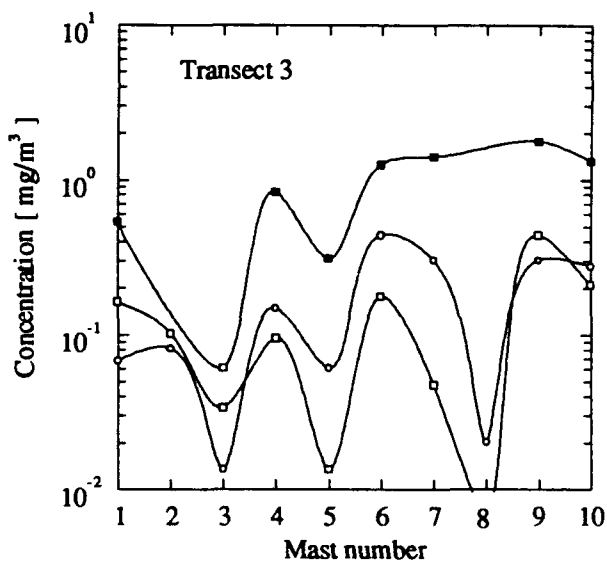
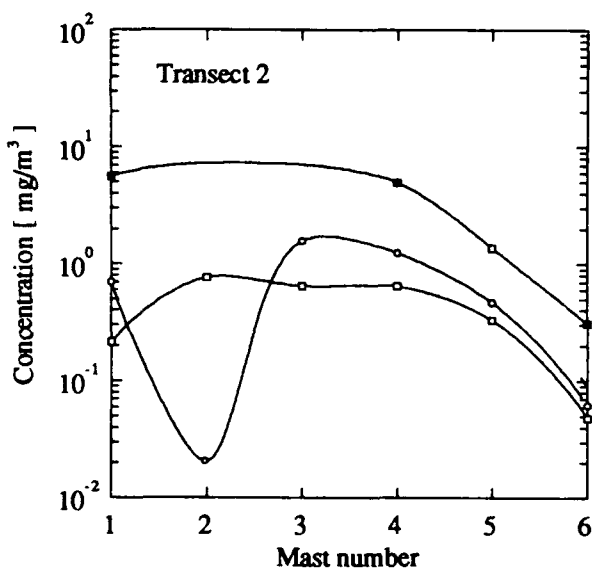
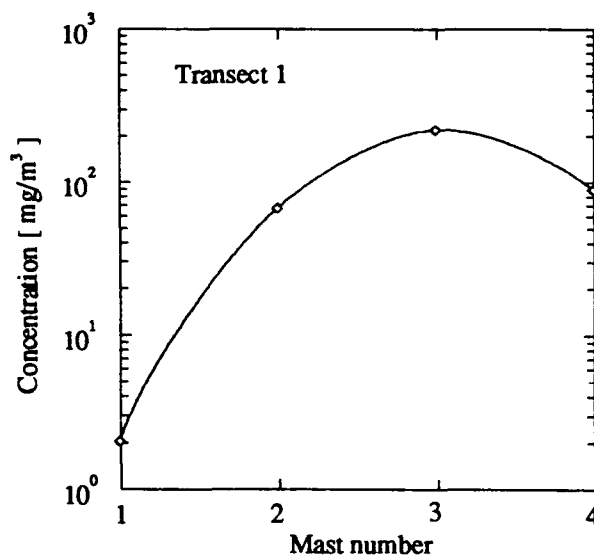


Figure 6.37 (continued) Profiles of fog-oil concentration measured along the sampling transects in the daytime unstable Meadowbrook dispersion tests. These plots are for Test 0923871, and the crosswind view in these graphs is looking downwind from the source. In addition to the mean concentrations, the standard deviation in concentration from the aerosol photometers is also shown in these plots.

Concentration data  
Meadowbrook site  
unstable meteorology  
Test 0926871  
September 26, 1987  
12:00:00 to 13:06:40

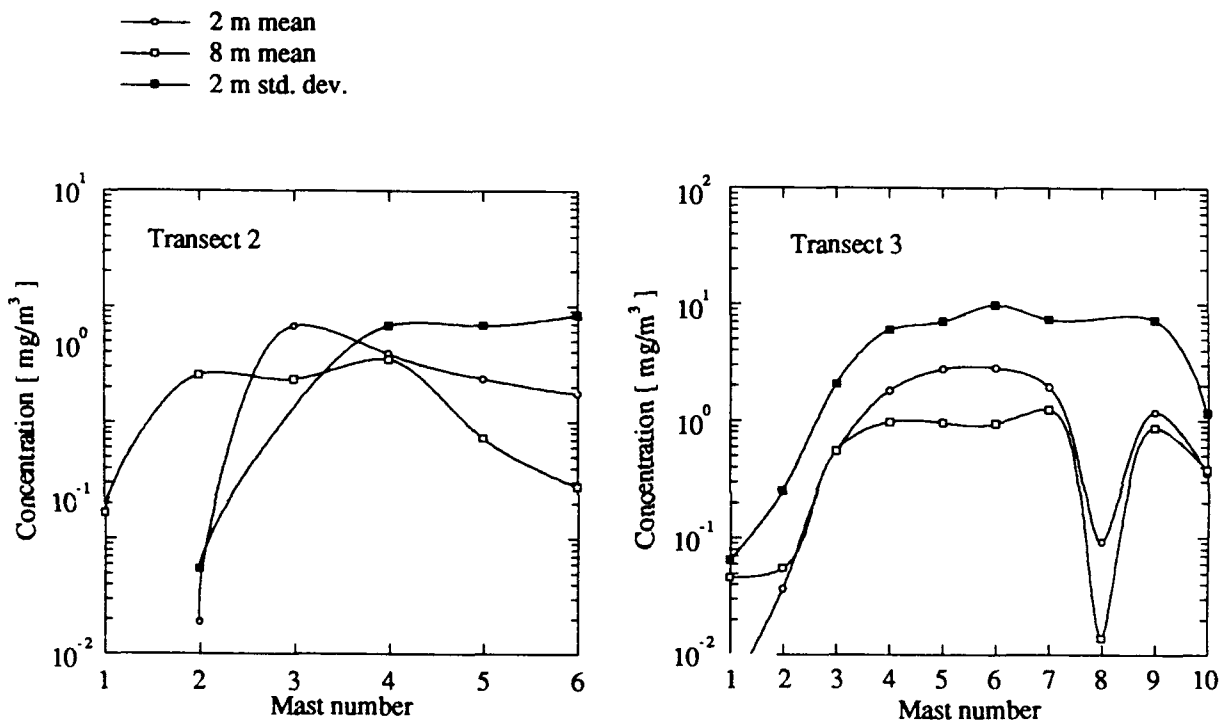


Figure 6.37 (continued) Profiles of fog-oil concentration measured along the sampling transects in the daytime unstable Meadowbrook dispersion tests. These plots are for Test 0926871, and the crosswind view in these graphs is looking downwind from the source. In addition to the mean concentrations, the standard deviation in concentration from the aerosol photometers is also shown in these plots.

Concentration data  
Meadowbrook site  
unstable meteorology  
Test 0928871  
September 28, 1987  
10:29:00 to 10:54:00

—○— 1 m mean  
—○— 2 m mean  
—○— 8 m mean  
—■— 2 m std. dev.

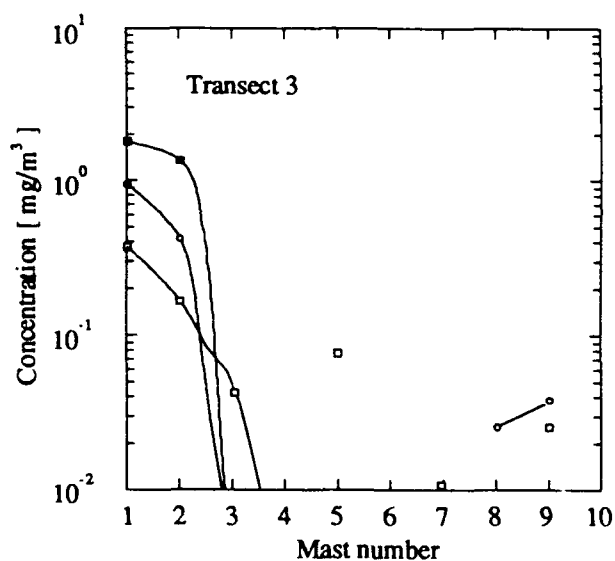
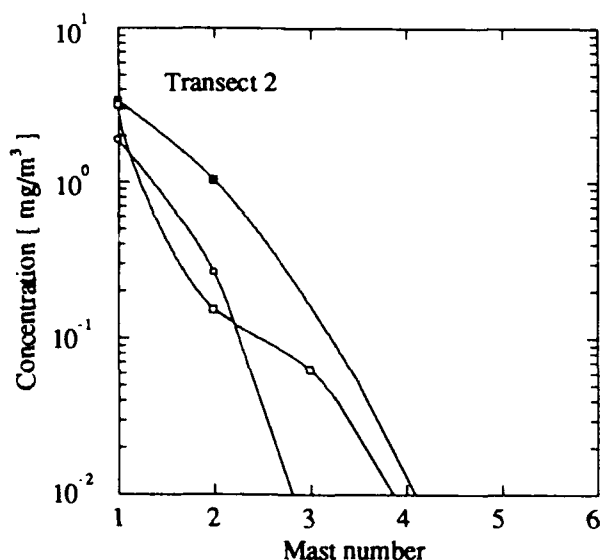
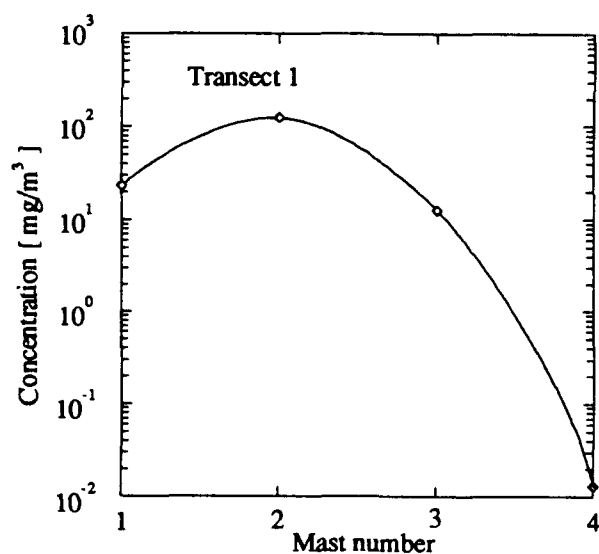


Figure 6.37 (continued) Profiles of fog-oil concentration measured along the sampling transects in the daytime unstable Meadowbrook dispersion tests. These plots are for Test 0928871, and the crosswind view in these graphs is looking downwind from the source. In addition to the mean concentrations, the standard deviation in concentration from the aerosol photometers is also shown in these plots.

Concentration data  
Meadowbrook site  
unstable meteorology  
Test 1002872  
October 2, 1987  
12:16:00 to 12:34:00

—○— 1 m mean  
—○— 2 m mean  
—○— 8 m mean  
—●— 2 m std. dev.

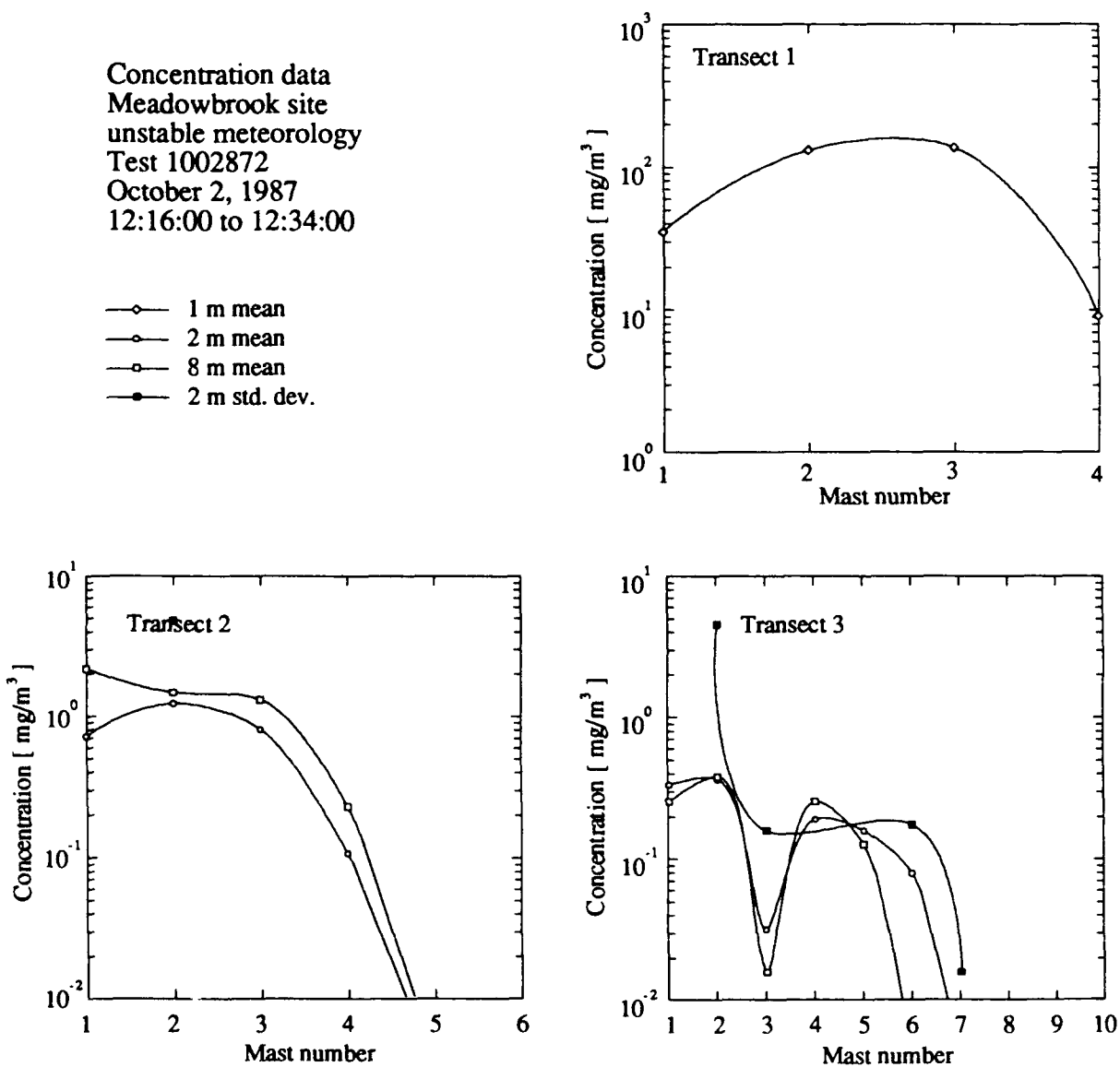


Figure 6.37 (continued) Profiles of fog-oil concentration measured along the sampling transects in the daytime unstable Meadowbrook dispersion tests. These plots are for Test 1002872, and the crosswind view in these graphs is looking downwind from the source. In addition to the mean concentrations, the standard deviation in concentration from the aerosol photometers is also shown in these plots.

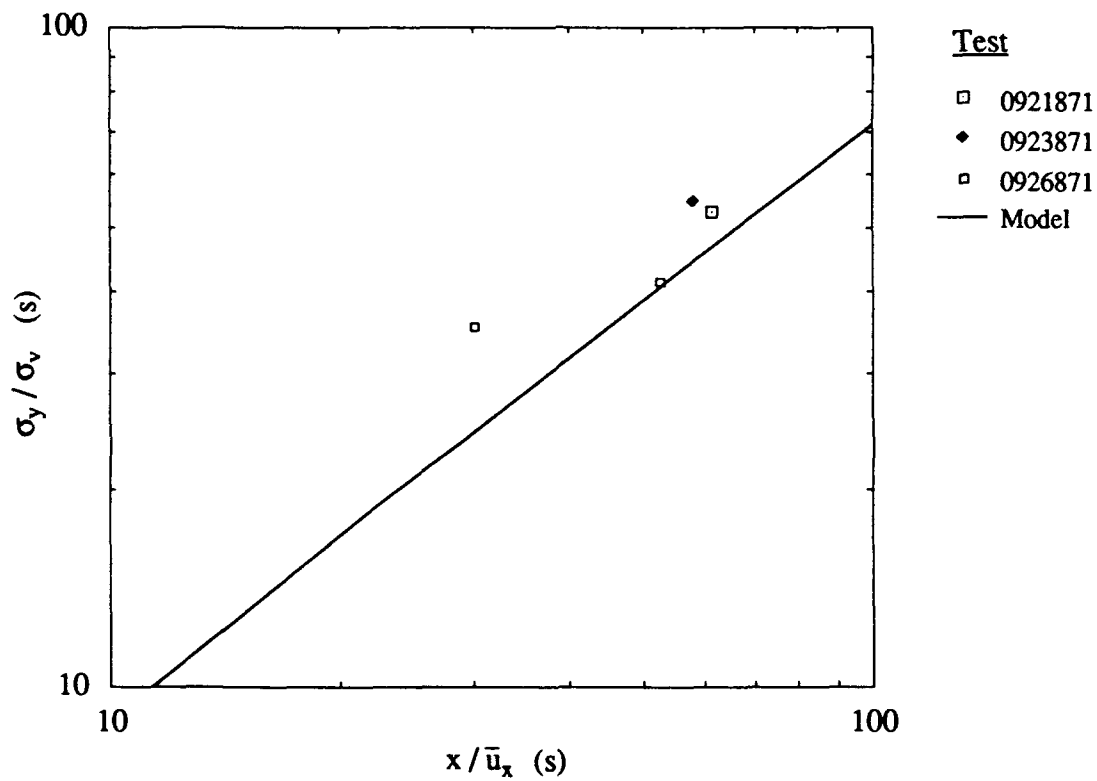


Figure 6.38 Estimated plume widths for the fog-oil dispersion tests at Meadowbrook in daytime unstable conditions as compared with Gryning's adaptation of Draxler's model.

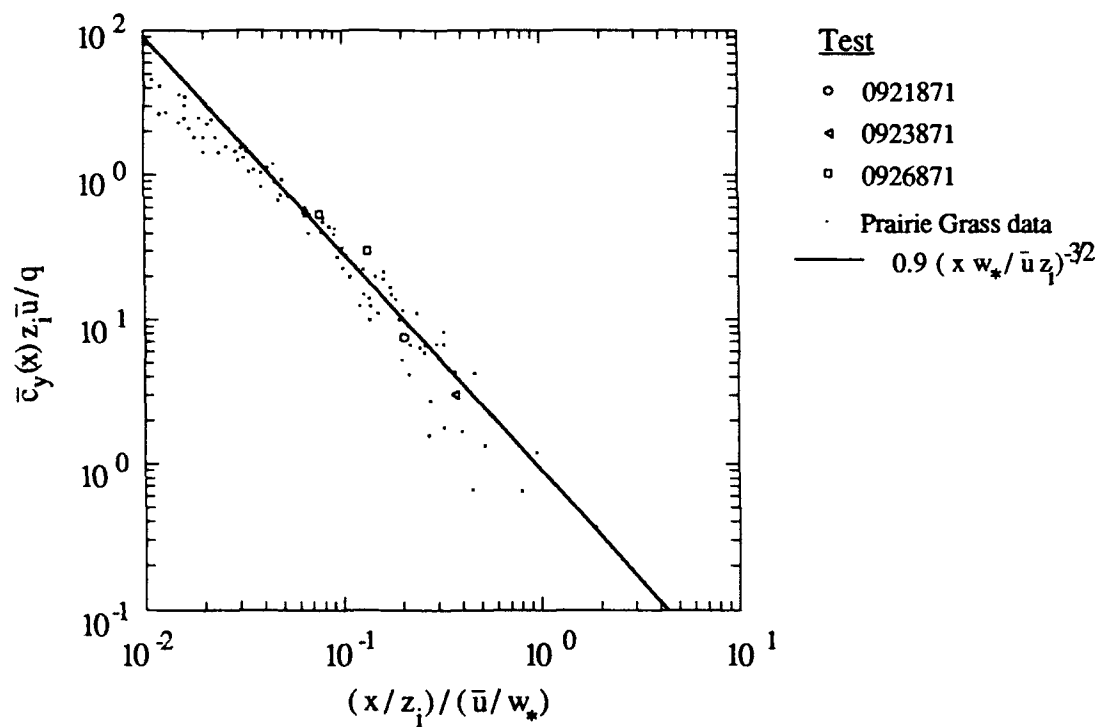


Figure 6.39 Mixed-layer scaling using the free convection limit for the cross wind integrated ground level concentrations measured in the daytime unstable fog-oil dispersion tests at Meadowbrook. The Prairie Grass data and curve fit are from Nieuwstadt (1980b).

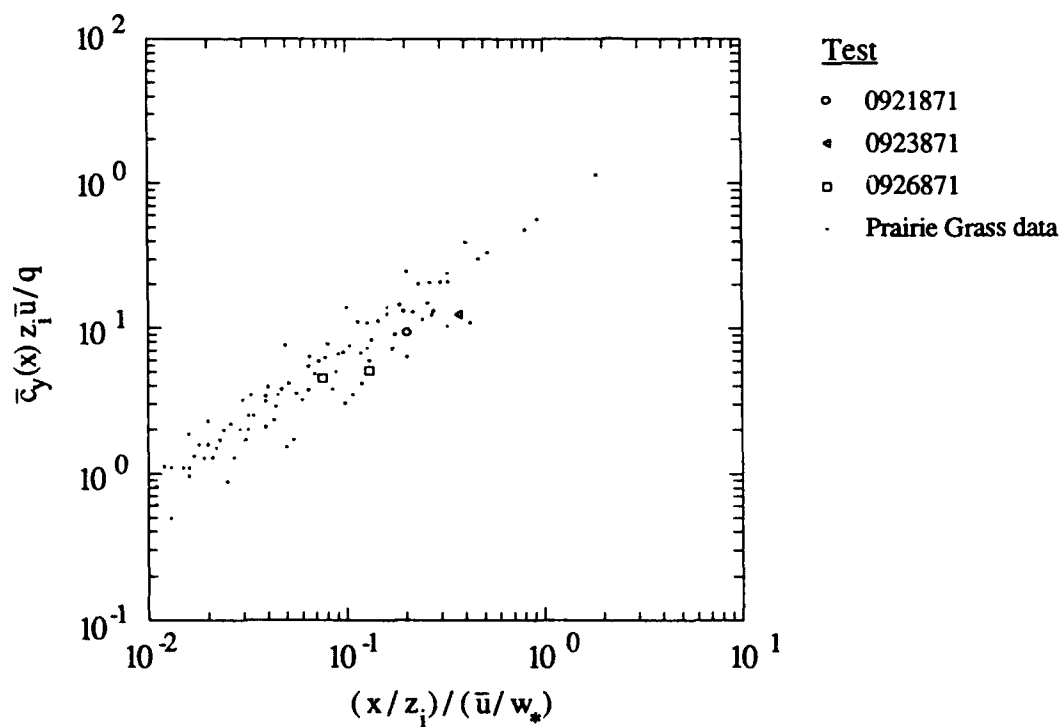


Figure 6.40 Mixed-layer scaling using the for the time averaged normalized plume widths measured in the daytime unstable fog-oil dispersion tests at Meadowbrook as a function of downwind distance. The Prairie Grass data are from Nieuwstadt (1980b).

We can compare the crosswind mean concentration data with a Gaussian crosswind profile given in Eq. 6.9 because of the relatively uniform terrain surrounding the dispersion site. Results are shown in Figure 6.41. The average of the data is seen to adequately follow the Gaussian profile, although there is considerable scatter in the data.

### 6.3.2 Fluctuations in Concentration

Crosswind profiles of the standard deviation in concentration are shown in Figure 6.42 for  $\sigma_c(x,y)/\bar{c}(x,0)$  versus  $\sigma_y/y$  and Figure 6.43 for  $\sigma_c(x,y)/\bar{c}(x,y)$  versus  $\sigma_y/y$ . The behavior in these plots follows the models given in Eqs. 6.10 and 6.11 which were previously used for the Camp Atterbury tests, although the centerline fluctuation intensity  $\alpha$  is higher for this set of tests. The value of  $\alpha = \sigma_c(x,0)/\bar{c}(x,0)$  should be a function of only the source size and the Lagrangian turbulent integral scale. Here we use  $\alpha = 3$ , which is higher than the  $\alpha = 2$  value found in the Atterbury tests. Since the same source is used in both the Atterbury and Meadowbrook studies, the varying  $\alpha$  must be due to differences in the terrain or meteorology between the two sites.

As demonstrated in Figure 6.44, the probability distribution of concentration at points in the flow field is seen to follow the probability distribution given in Eq. 6.12 for all of the daytime convective tests. Scatter of the data at  $c/\bar{c} = 0$  is seen in this plot. Vertical line at higher concentrations are caused by clipping of the photometer signal at higher concentrations.

For data amenable to crosswind scaling, the distribution of intermittency versus the crosswind distance is given in Figure 6.45. This figure also includes a plot of Eq. 6.15. Figure 6.45 shows a much lower average centerline intermittency found in these tests as compared with the Camp Atterbury tests.

### 6.3.3 Correlations and Spectra

There are insufficient data in this set to investigate spatial correlations. Spectra of the individual concentration records taken in these tests are shown in Figure 6.46. These show a  $-2/3$  power law behavior for  $nS_{cc}(n)$  at the higher frequencies. Within a test the spectra from individual samplers is similar in magnitude and shape. Ensemble averaging of these data sets produces the result shown in Figure 6.47, where a  $-5/3$  power law behavior for  $S_{cc}(n)$  in the inertial-convective subrange is seen.

An integral scale of the concentration fluctuations is found using  $R_{cc}(\tau_c) = \exp(-1)$ . Average values are given in Table 6.3. No definite spatial variation in the integral scale calculated from individual concentration records is seen.



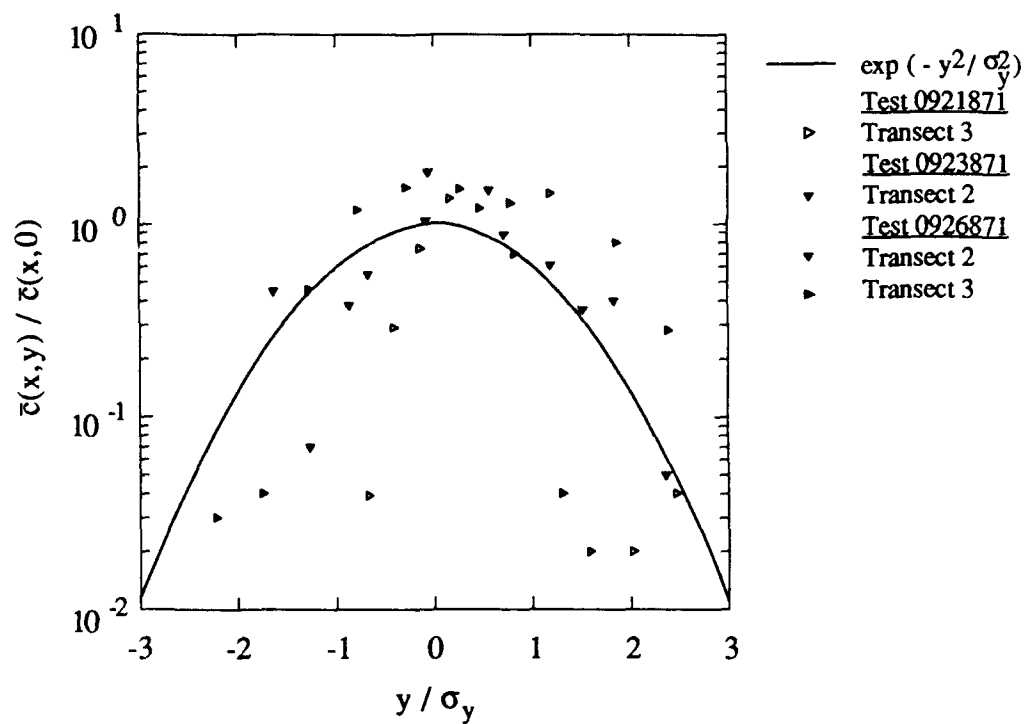


Figure 6.41 Normalized crosswind profile of mean concentration for the daytime unstable Meadowbrook dispersion tests. Lateral plume spread versus a ratio of actual concentration to the fitted centerline concentration is given in this plot. Comparison of the data with a Gaussian profile is also shown.

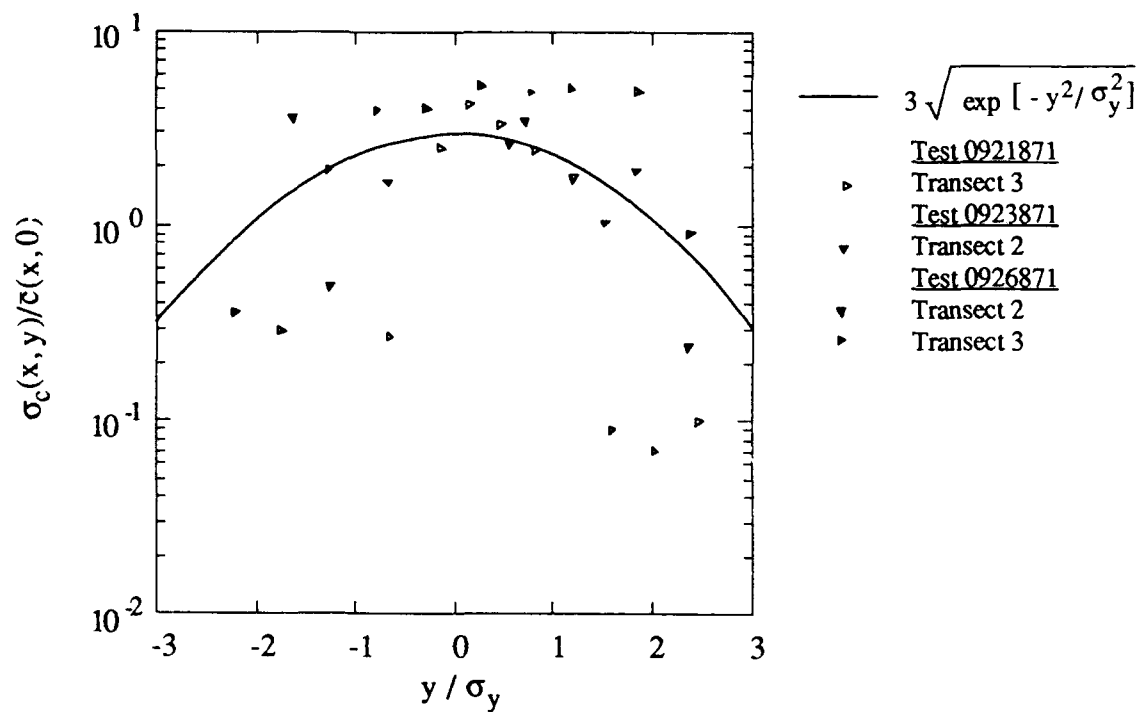


Figure 6.42 Crosswind profile of the standard deviation in concentration normalized by the centerline mean concentration for the daytime unstable Meadowbrook dispersion tests. The square root of a Gaussian profile with a constant scaling coefficient of 3 is also shown.

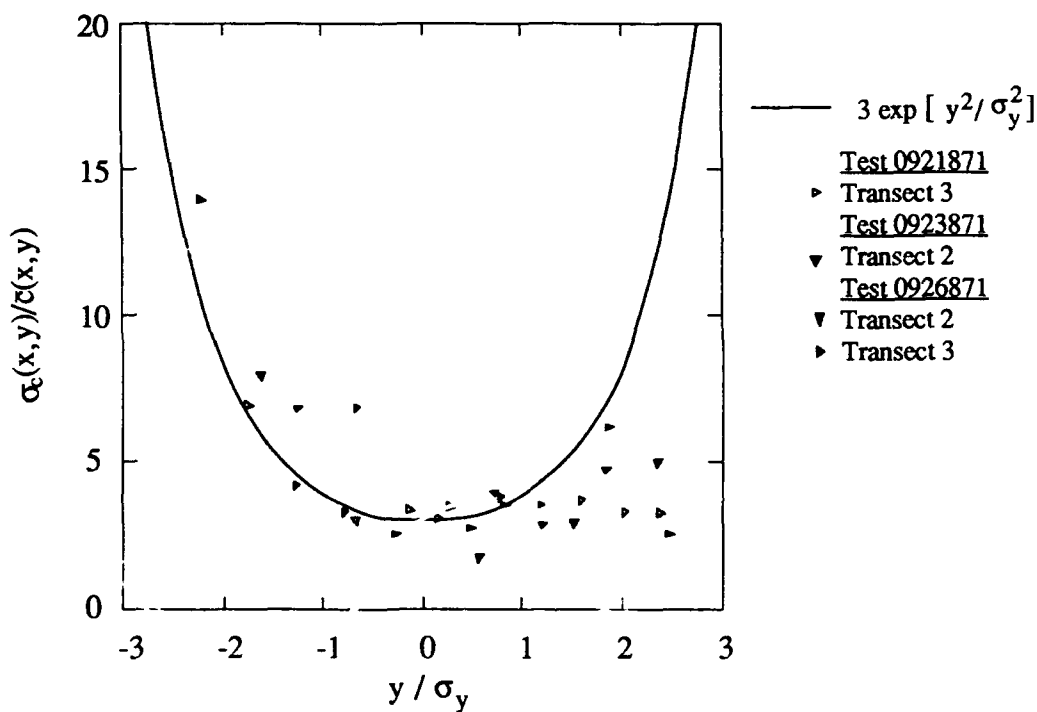


Figure 6.43 Crosswind profile of relative fluctuation intensity of concentration for the daytime unstable dispersion tests at Meadowbrook. The data from our tests are plotted as a dimensionless profile of the local values of the standard deviation in concentration and mean concentration. The model profile with a coefficient of 3 is also shown.

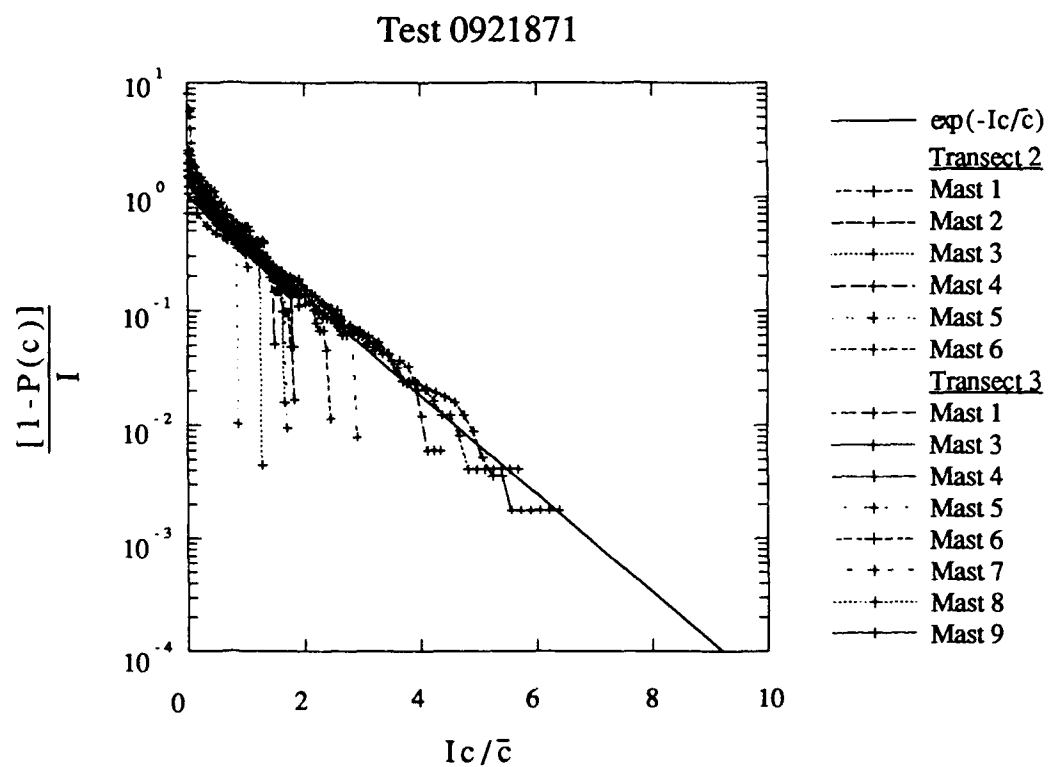


Figure 6.44 A comparison of the histograms in concentration with the exponential distribution. This plot is for Test 0921871. The mast numbers refer to the location along a given transect.

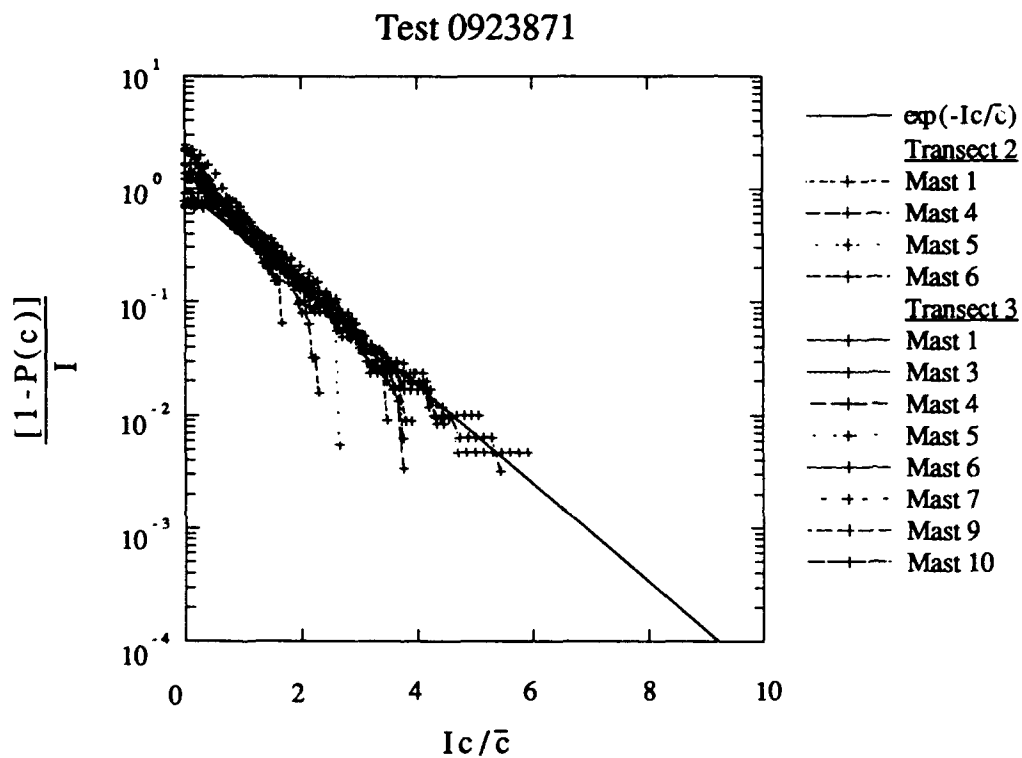


Figure 6.44 (continued) A comparison of the histograms in concentration with the exponential distribution. This plot is for Test 0923871. The mast numbers refer to the location along a given transect.

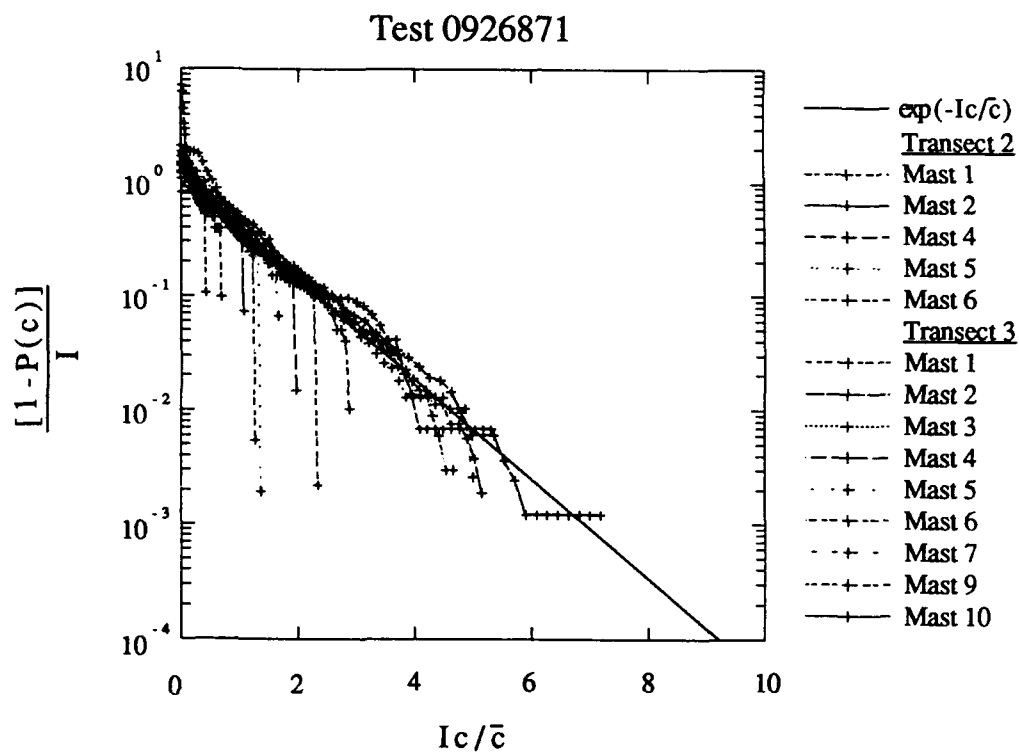


Figure 6.44 (continued) A comparison of the histograms in concentration with the exponential distribution. This plot is for Test 0926871. The mast numbers refer to the location along a given transect.

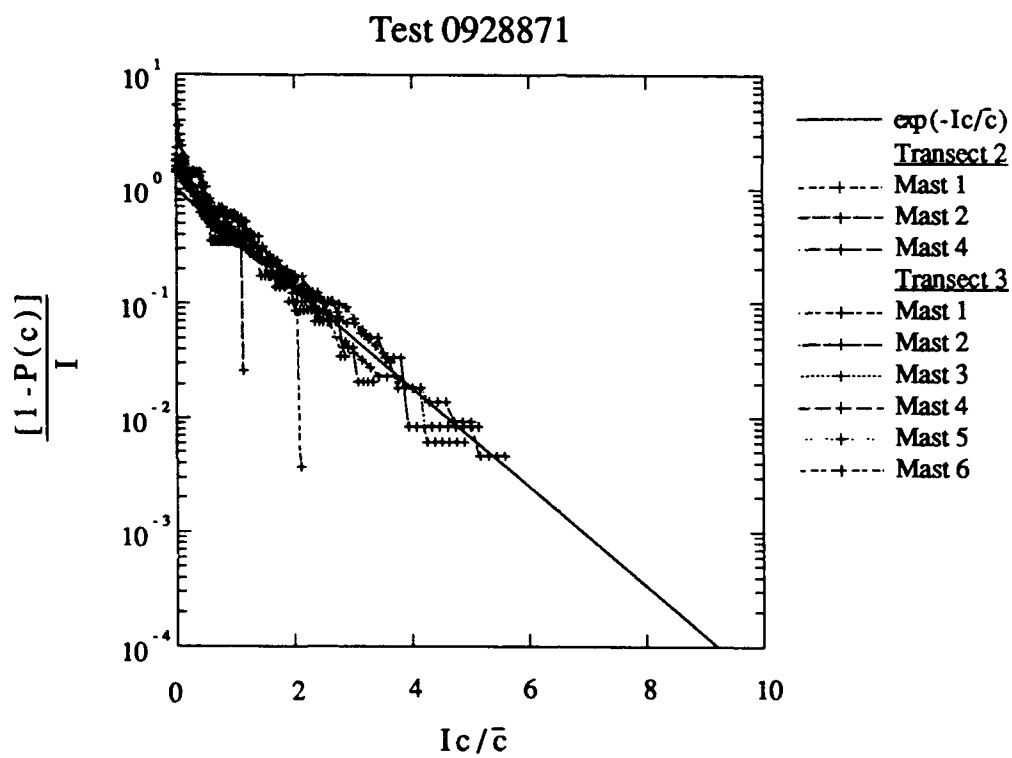


Figure 6.44 (continued) A comparison of the histograms in concentration with the exponential distribution. This plot is for Test 0928871. The mast numbers refer to the location along a given transect.

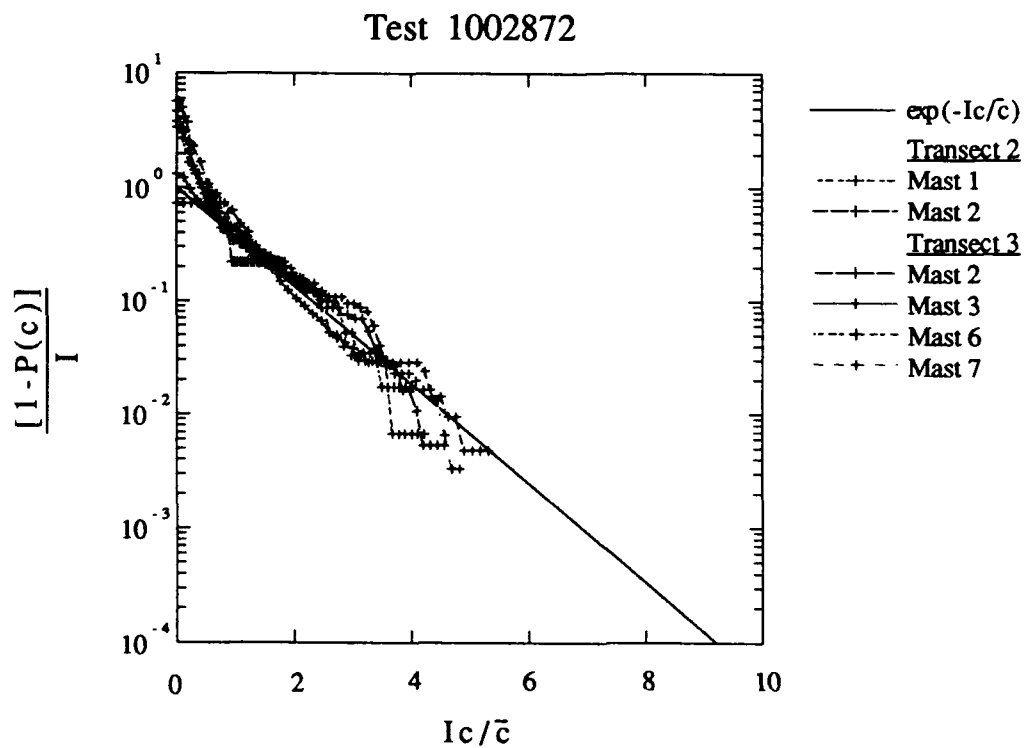


Figure 6.44 (continued) A comparison of the histograms in concentration with the exponential distribution. This plot is for Test 1002871. The mast numbers refer to the location along a given transect.



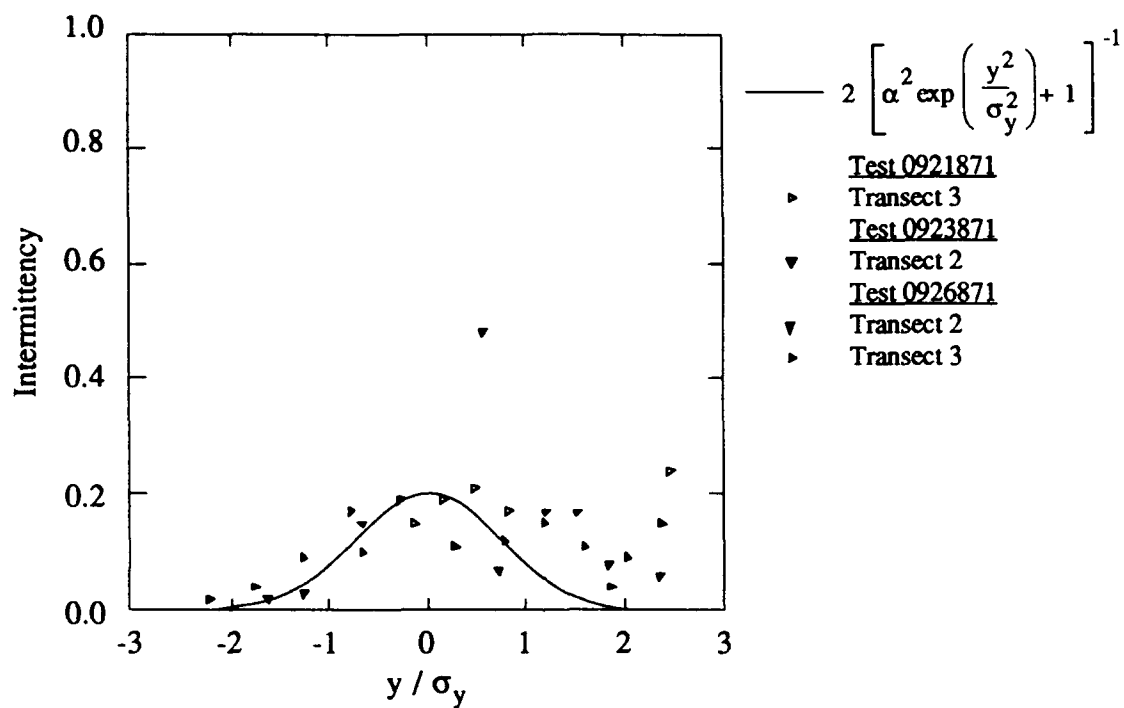


Figure 6.45 Crosswind plume intermittency for the Meadowbrook fog-oil dispersion tests. The analytical solution uses a value of  $\alpha = 3$  in the expression shown.

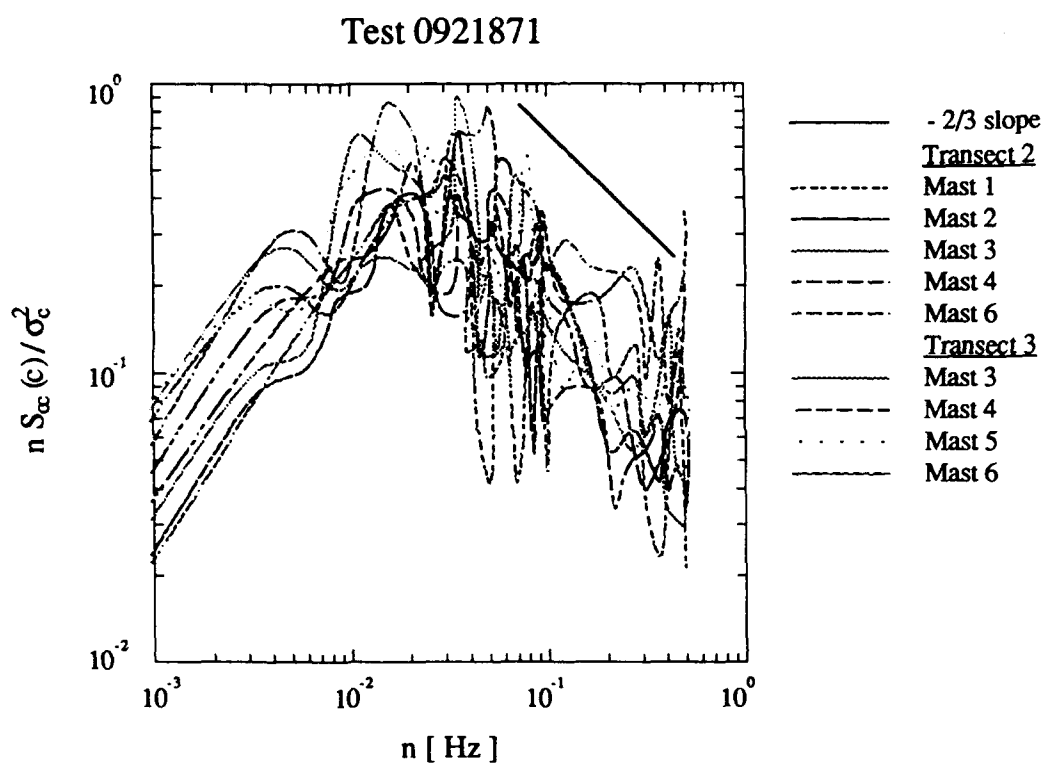


Figure 6.46 Spectra of the concentration variance. This plot includes data from all samplers in Test 0921871 for which the mean signal exceeded 5 times the background noise of the instrument. The spectra were normalized by the calculated variance for each data record.

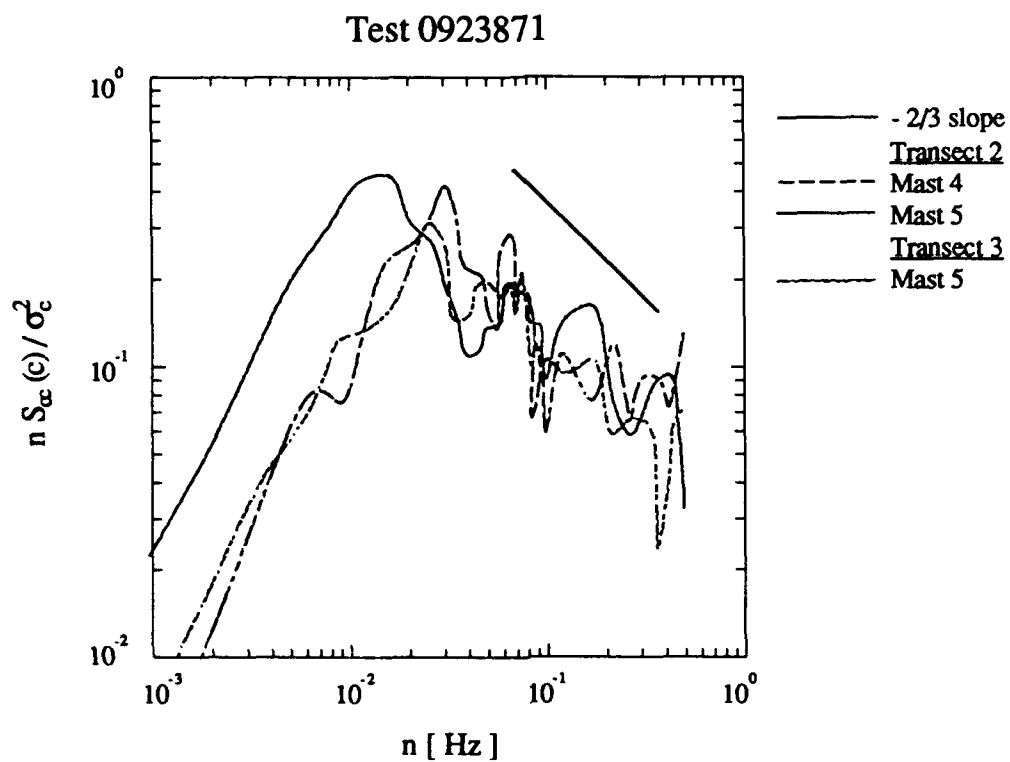


Figure 6.46 (continued) Spectra of the concentration variance. This plot includes data from all samplers in Test 0923871 for which the mean signal exceeded five times the background noise of the instrument. The spectra were normalized by the calculated variance for each data record.

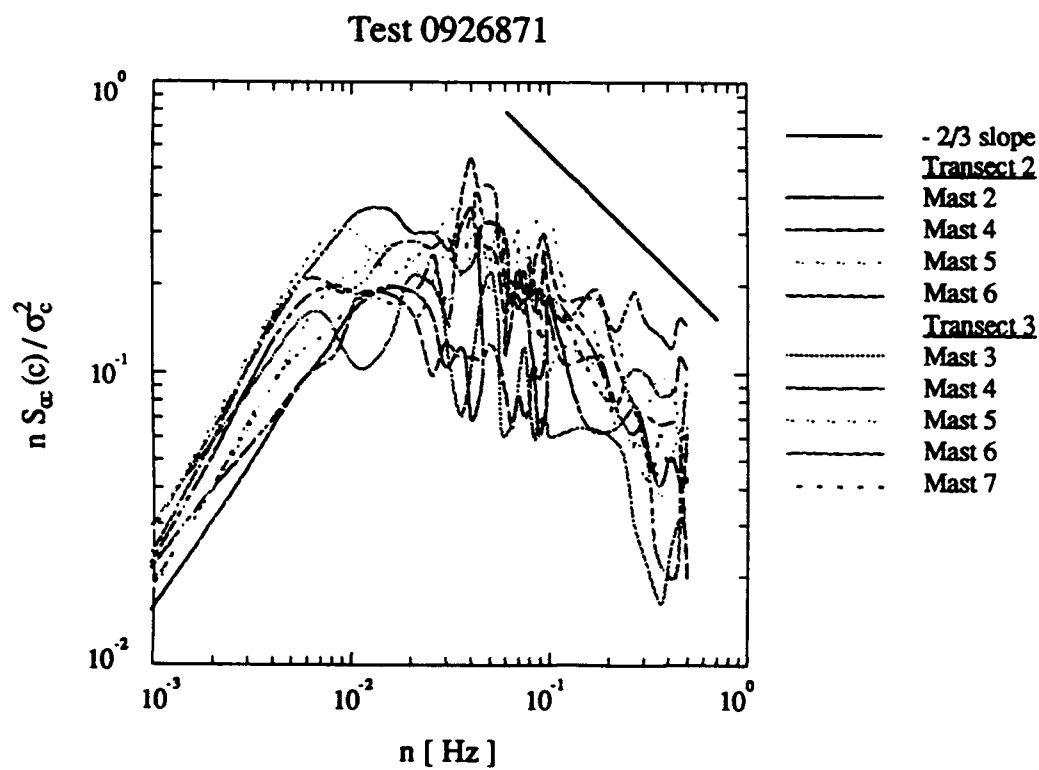


Figure 6.46 (continued) Spectra of the concentration variance. This plot includes data from all samplers in Test 0926871 for which the mean signal exceeded five times the background noise of the instrument. The spectra were normalized by the calculated variance for each data record.

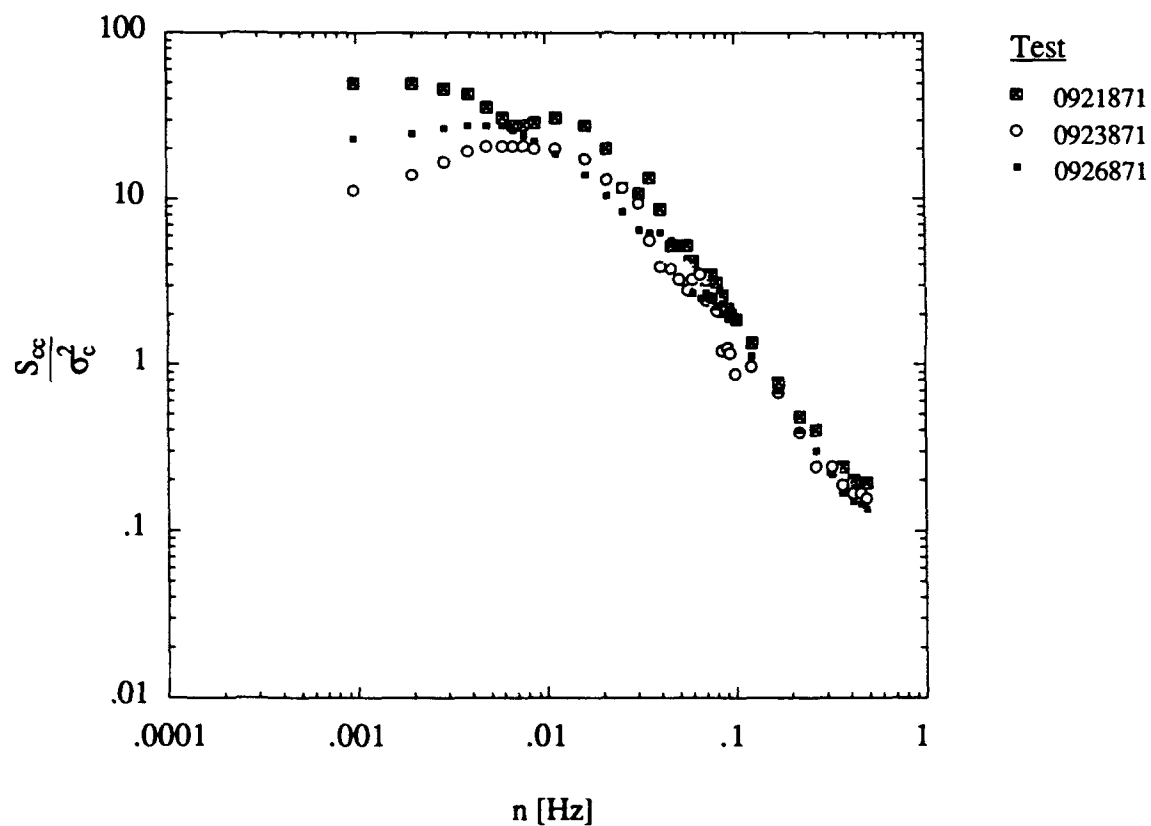


Figure 6.47 Ensemble averaged spectra of the concentration fluctuations measured in the unstable Meadowbrook dispersion tests. These data are the ensemble average of all the spectra from a given test for which the mean signal level exceeded the background noise by a factor of 4.

Table 6.3 Integral scales of concentration for the unstable Meadowbrook dispersion tests.

Test	$\tau_c$	$\tau_c/(z_i/w_*)$
0921871	11.2	0.036
0923871	8.4	0.054
0926871	10.3	0.026

#### 6.3.4 Concentration Exceedance

We find that averages of the mean continuous period of time for which  $c > 0$  at an individual sampler is approximately equal to the integral scale of the concentration fluctuations at the same sampler. This behavior is shown in Figure 6.48, where  $1/\lambda_u(0)$  is the mean duration of a continuous burst with  $c > 0$ . We note that the range of values in this plot within a given test is not large and no spatial dependence of  $1/\lambda_u(0)$  is found.

The probability distribution of continuous events of duration  $t$  with  $c > 0$  is shown in Figure 6.49. For all of these tests, the distribution is nearly exponential and follows Eq. 6.21. The hyperexponential behavior seen in the Camp Atterbury plots of the same type of data (Figure 6.19) is not seen in these plots. One possible explanation is that the mean burst durations  $1/\lambda_u(0)$  in the Meadowbrook tests are smaller than those found in the Camp Atterbury tests. This reduces the bias in sampling of individual long duration bursts in the Meadowbrook tests as compared to the Atterbury tests.

The mean rate of occurrence of bursts  $\lambda(0)$  with  $c > 0$  shows a spatial dependence. This is related to the mean burst duration  $1/\lambda(0)$  through  $\lambda(0) = 1/\lambda_u(0)$ , and  $\lambda(0)$  shows no spatial dependence. The crosswind dependence of  $\lambda_u(0)$  is shown in Figure 6.50. In this figure we use the convective time scale  $(z_i/w_*)$  to form dimensionless ratios. This plot shows the rate of bursts is greater near the center of the mean plume, and is less near the mean plume edges. A model of this distribution is also shown.

### 6.4 Stable Meadowbrook Data

For the nighttime experiments at Meadowbrook, the data are more site specific than any of our other data, being considerably influenced by the local terrain and meteorology. Maps of the entire test site were shown in Figures 4.8 to 4.10. Referring to these maps, the surface-layer wind follows the downhill slope of the land from east to west.

A map of the samplers in this test is shown in Figure 6.51. For all of the stable tests, the fog-oil source was located in the Plum Creek valley near UTM coordinates 4461750 N, 589500 E.

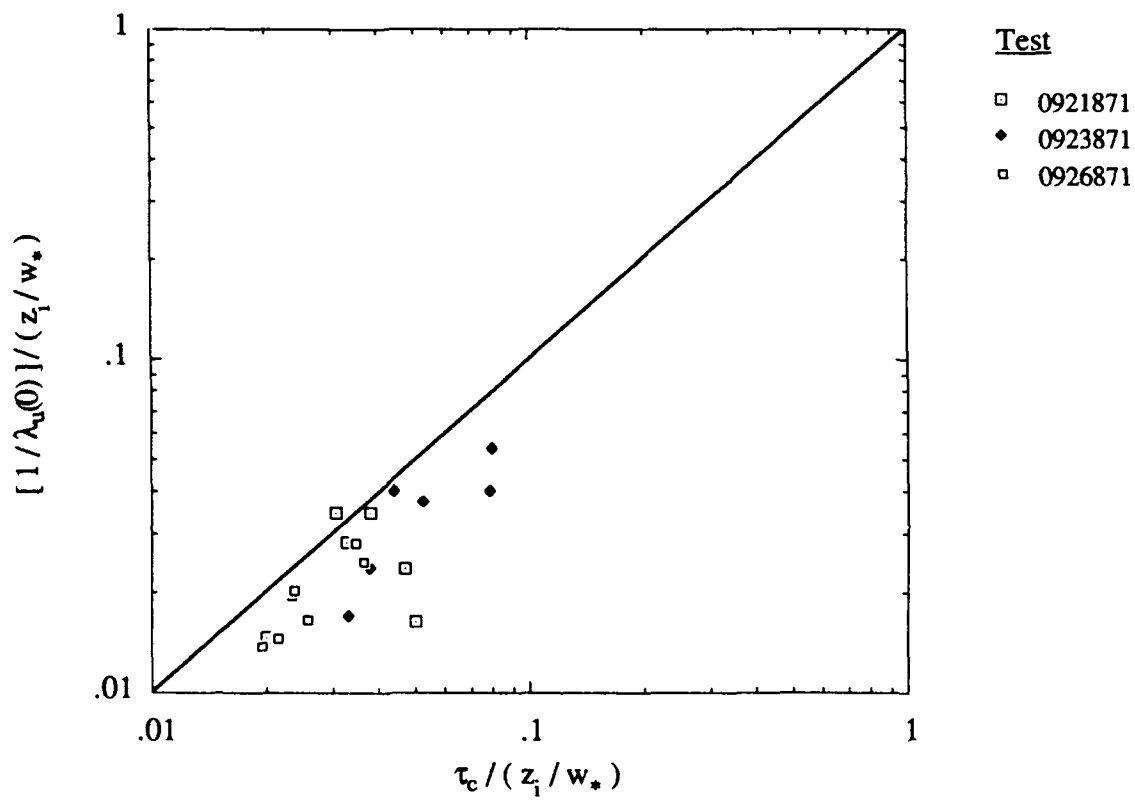


Figure 6.48 Duration of bursts in concentration with  $c > 0$ , versus the integral scale in concentration for the unstable Meadowbrook smoke dispersion tests.

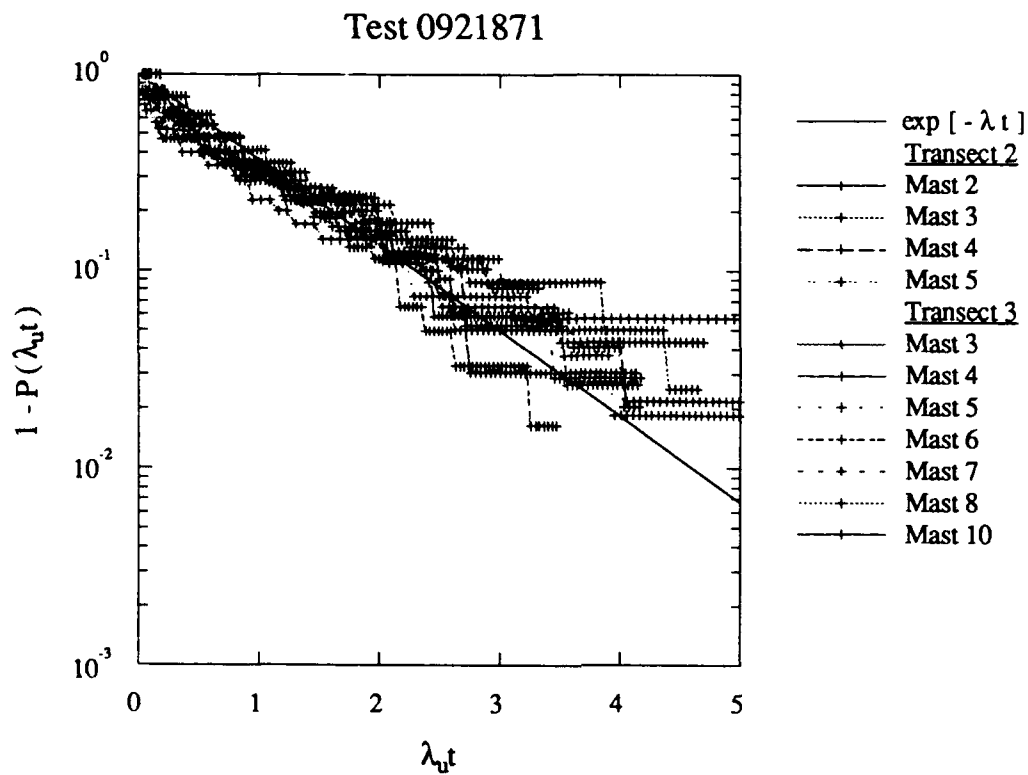


Figure 6.49 Histogram of time intervals for which the concentration exceeds zero for Test 0921871. The data from all records for which  $I > 0.1$  are included in the above plot.



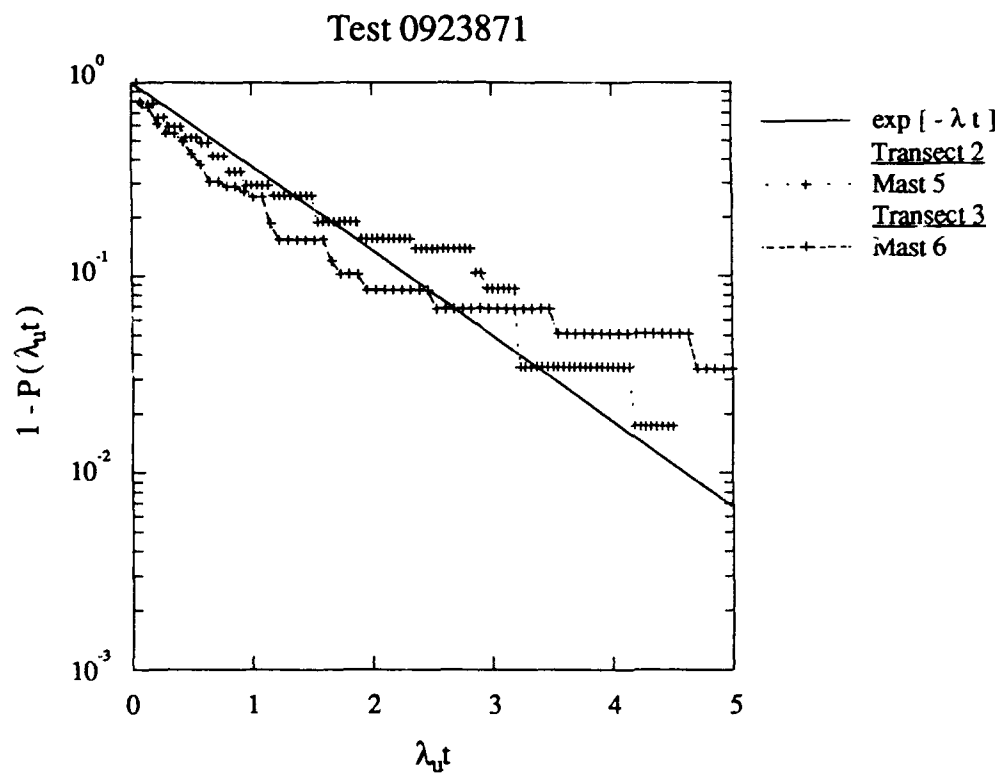


Figure 6.49 (continued) Histogram of time intervals for which the concentration exceeds zero for Test 0923871. The data from all records for which  $I > 0.1$  are included in the above plot.

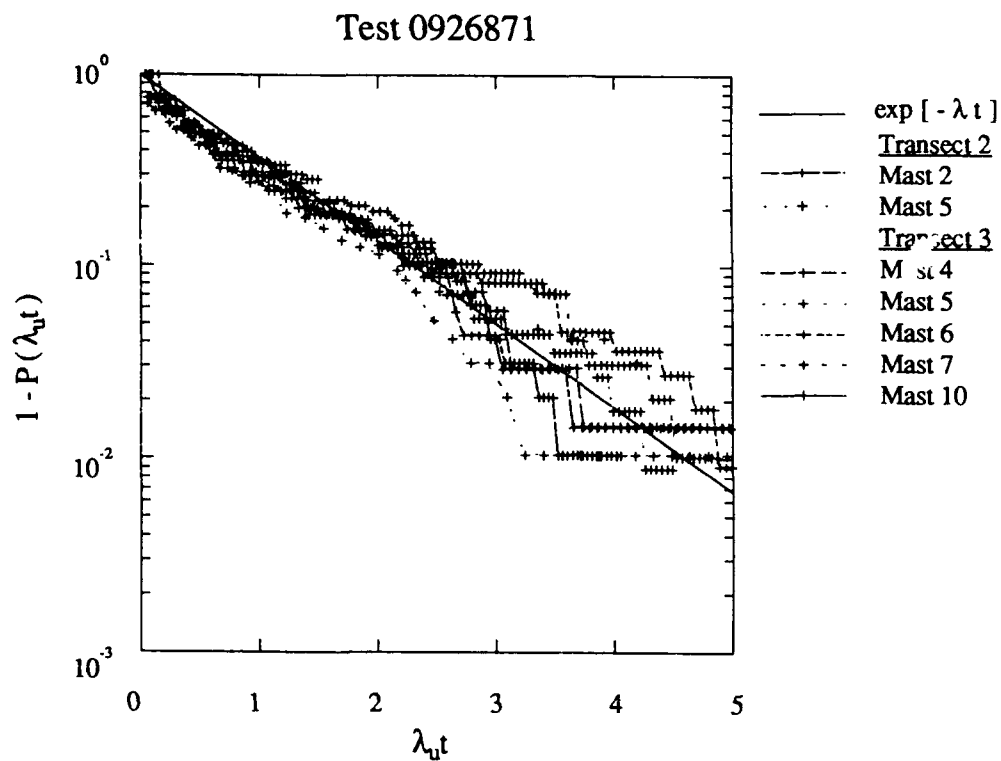


Figure 6.49 (continued) Histogram of time intervals for which the concentration exceeds zero for Test 0926871. The data from all records for which  $I > 0.1$  are included in the above plot.

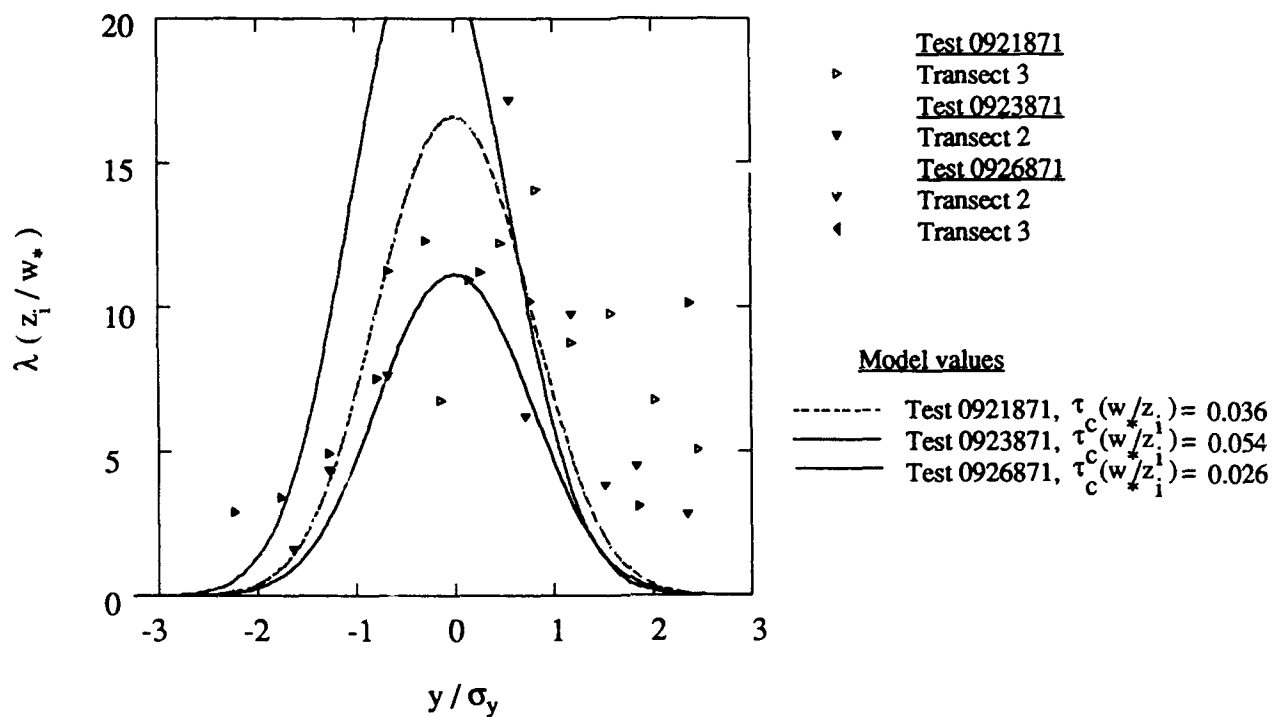


Figure 6.50 The crosswind distribution of intervals between smoke event starts for the unstable Meadowbrook smoke dispersion tests.. These data are nondimensionalized by the mean plume width and the convective time scale and are compared with model given by Equation 6.22.

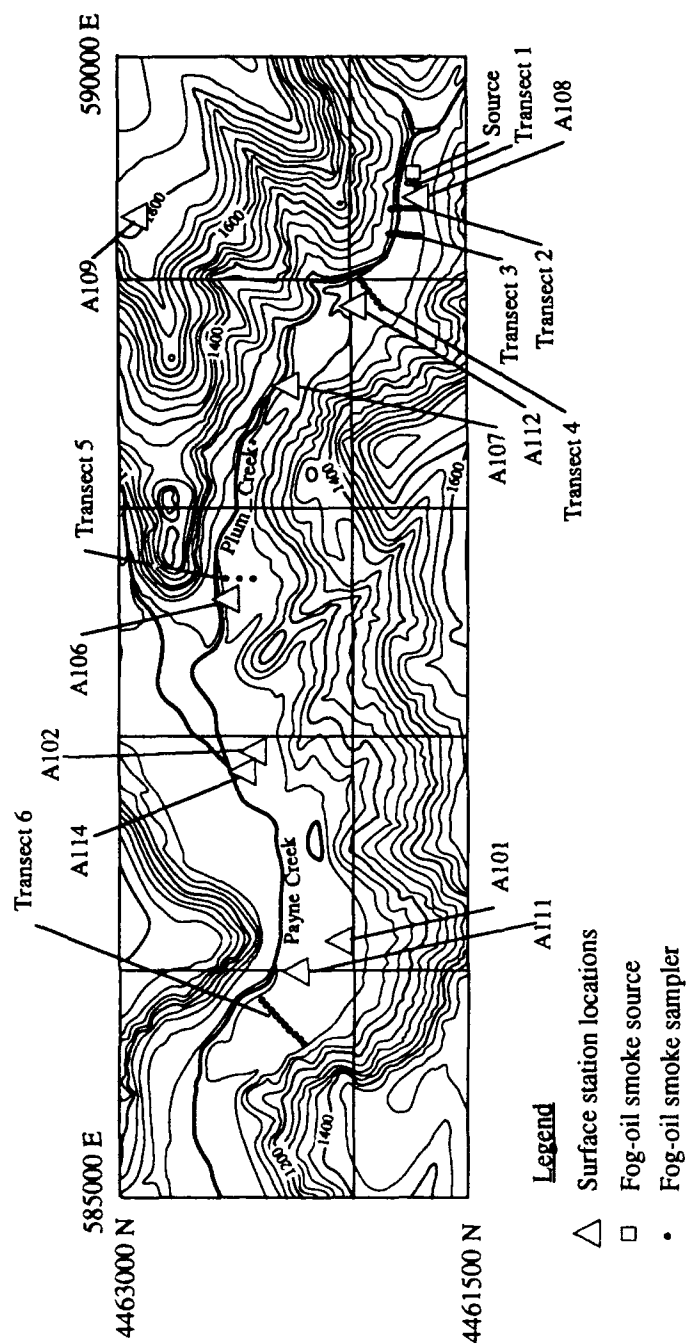


Figure 6.51 Map of the sampler locations for the stable dispersion tests. The sampling transects, meteorological towers, and source location are shown. Elevations are in ft above sea level with contour lines at increments of 40 ft. The horizontal scale is in Universal Transverse Mercator coordinates, with the grid marked in km. The topographical information is from a USGS map of Inskip Hill, California.

The six transects of samplers used in these tests were located at approximate geometrically increasing downwind distances from the source of 25, 125, 250, 550, 1800, and 3500 m. A map of the source and first three sampling transects is shown in Figure 6.52. This map shows the varying vegetation for the near-field grid. Some of the samplers are located in relatively open areas, whereas others are within a moderately dense forest canopy. A plot of the mean wind vector measured at a 2-m height near the source is shown in Figure 6.53. This vector plot shows the approximate mean direction of the plume near the source in each of the dispersion tests. Surveyed elevations of the first three transects are shown in Figure 6.54. This figure shows the overall west-northwest fetch of the ground for the near-source samplers in somewhat more detail than is presented in the topological maps. Mast 7 on Transect 3 was located in a gully near Plum Creek which was somewhat lower than the surrounding terrain.

#### 6.4.1 Mean Concentration Data

Crosswind profiles of the mean and fluctuating data taken in these tests are shown in Figure 6.55. The profiles of data in these plots is shown looking from the source downwind. The initial plume profile show a Gaussian-like shape. For the further transects the plume often fills the entire valley and the mean concentration measurements show a uniform distribution across the transect. Concentrations measured at Mast 7 on Transect 3 are lower than those measured on the adjacent masts because of its location in a low canopy covered area not penetrated by the bulk of the fog-oil smoke. Transect 6 was used only in the later tests, after observers reported smoke at this far downwind position. It is the same row of samplers used as Transect 3 for the unstable daytime dispersion tests. All of these data sets contain useful results, although the Test 0927872 is not analyzed in detail because the test was only 10 minutes in duration. For Test 1003871 the closer sampling transects were missed by the plume and therefore could not be examined.

The decay of the mean concentration levels with distance from the source occurs at a slower rate for these stable atmospheric conditions than for any of our other sets of data. For Transects 2 and 3 the highest mean concentration levels measured along the transect are often very close in magnitude, due to the buoyancy and momentum of the source which carried it partially over the closer samplers.

Further study of the dispersion may be accomplished using crosswind integrated concentrations. For Transects 2 and 3, a profile fit is used, similar to that previously discussed for determining plume width and crosswind integrated concentration in our other dispersion tests. At the further transects, an average concentration is found, then multiplied by the approximate width of the valley at that transect position, which is taken as 160 m, 120 m, and 260 m for Transect 4 through Transect 6, respectively. The value of  $\bar{c}_y$  is scaled by the local mean wind speed and the

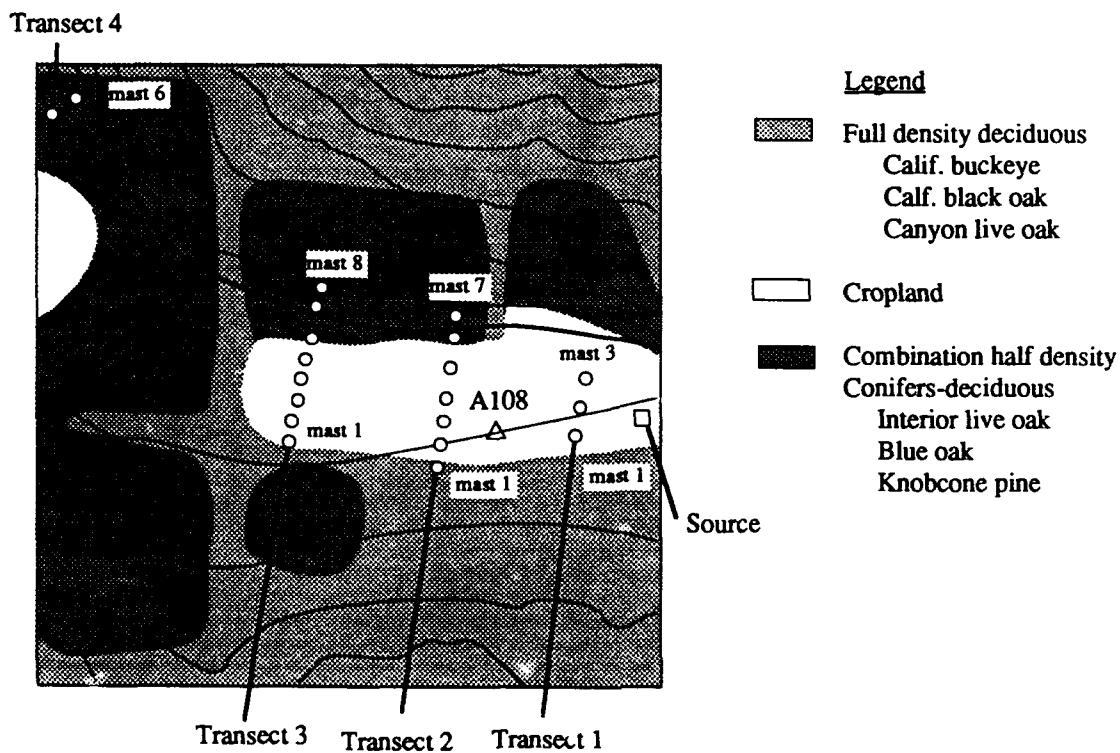


Figure 6.52 The near-source sampling transects for the stable Meadowbrook dispersion tests. Transects 2 and 3 are partially within an open field and a forest canopy. The total area shown above is 500 by 500 m with the lower left corner located at 4461500 N, 590000 E in UTM coordinates. The contour intervals in this map are 40 ft.

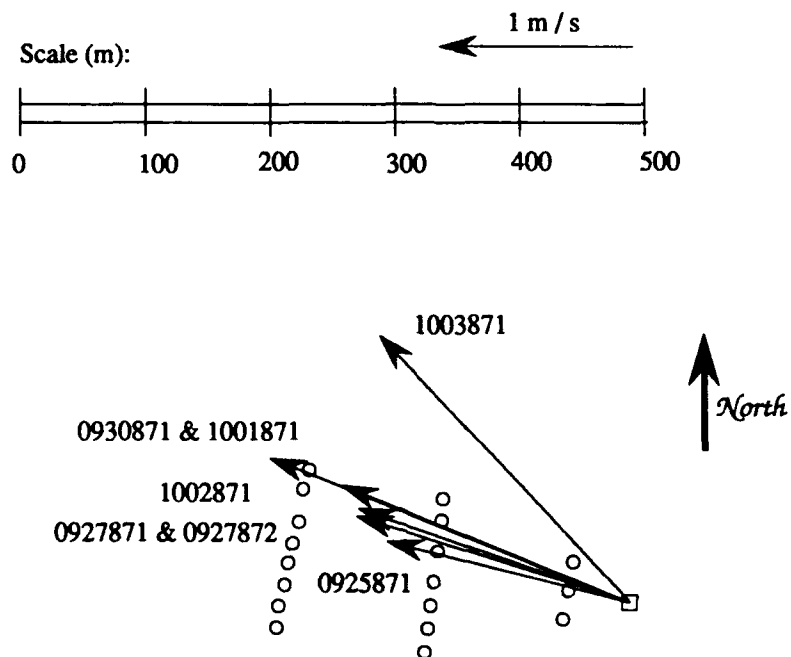


Figure 6.53 Source wind vectors for the stable dispersion tests at Meadowbrook. These were measured at a height of 2 m and are average values over the smoke release period.

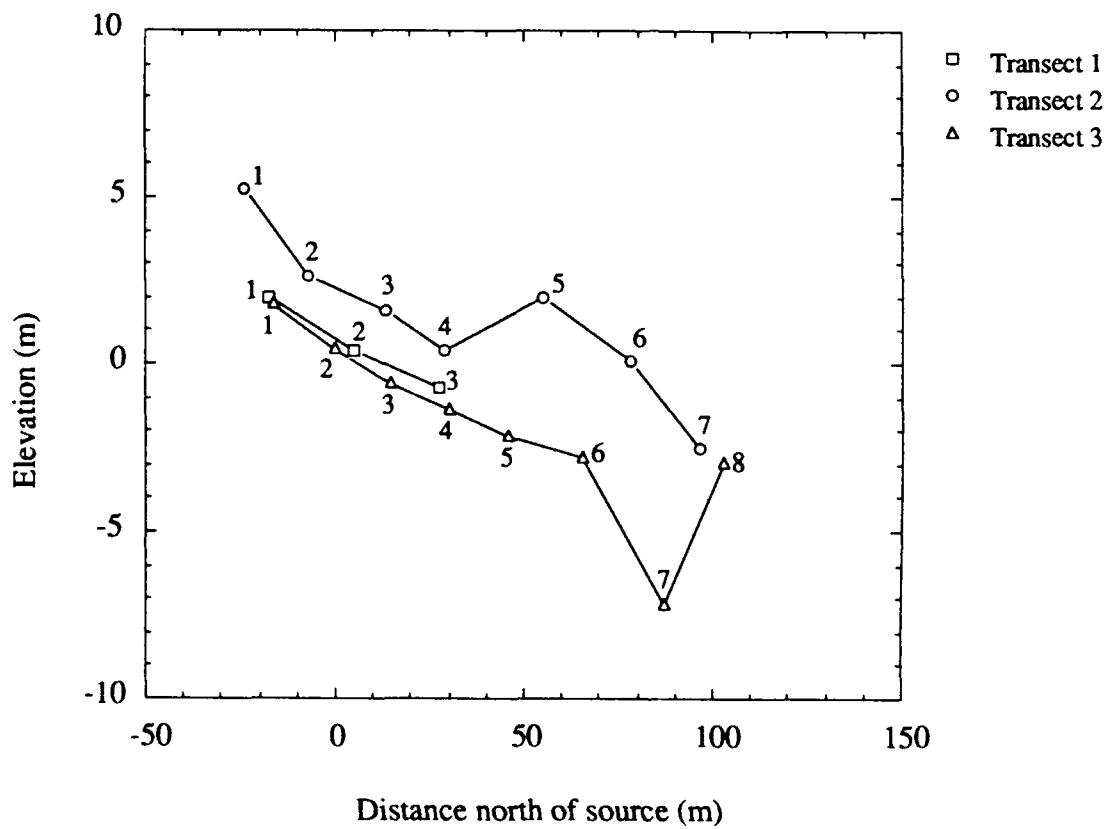


Figure 6.54 Elevation of samplers along the given transects for the stable dispersion grid at Meadowbrook. The crosswind view shown is from the source looking west and downwind.



Concentration data  
Meadowbrook site  
Test 0925871  
September 25, 1987  
0:18:00 to 1:03:00

—○— 1 m mean  
—○— 2 m mean  
—○— 8 m mean  
—●— 2 m std. dev.

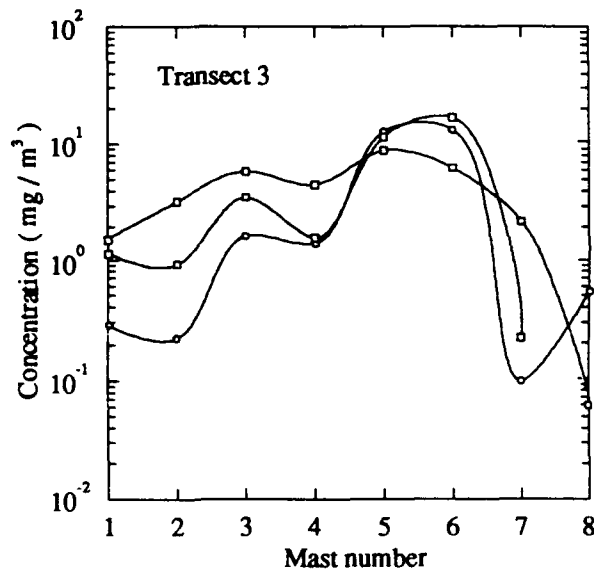
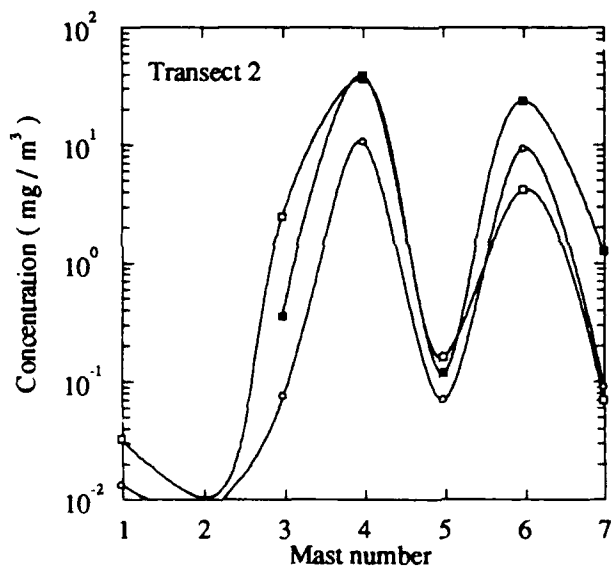
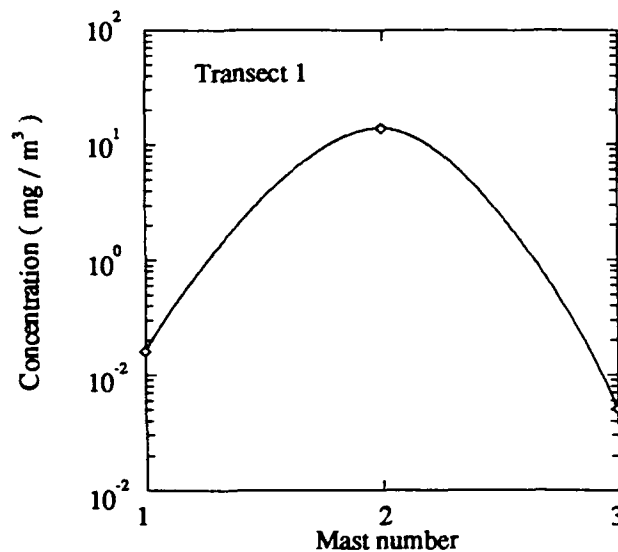


Figure 6.55 Profiles of fog-oil concentration measured along the sampling transects for the stable Meadowbrook dispersion tests. These plots are for Test 0925871 and the crosswind view in these graphs is looking downwind from the source. In addition to the mean concentrations, the standard deviation in concentration from the aerosol photometers is also shown in these plots.

Concentration data  
Meadowbrook site  
Test 0925871  
September 25, 1987  
0:18:00 to 1:03:00

—○— 1 m mean  
—○— 2 m mean  
—○— 8 m mean  
—■— 2 m std. dev.

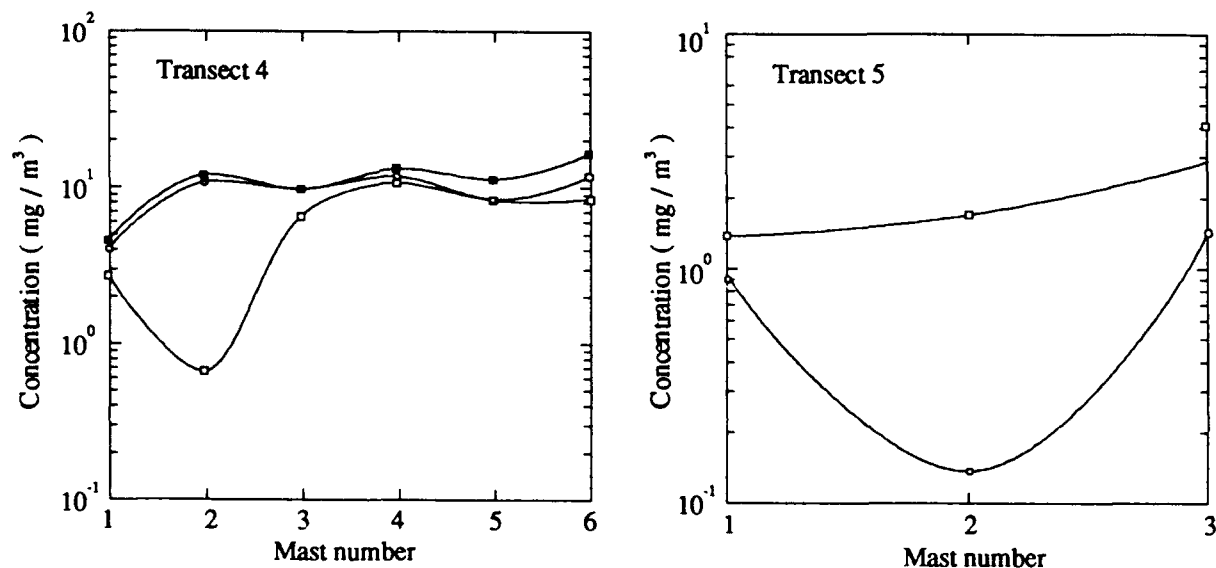


Figure 6.55 (continued) Profiles of fog-oil concentration measured along the sampling transects for the stable Meadowbrook dispersion tests. These plots are for Test 0925871 and the crosswind view in these graphs is looking downwind from the source. In addition to the mean concentrations, the standard deviation in concentration from the aerosol photometers is also shown in these plots.

Concentration data  
Meadowbrook site  
Test 0927871  
September 27, 1987  
3:19:00 to 3:39:00

—○— 1 m mean  
—●— 2 m mean  
—■— 8 m mean  
—■— 2 m std. dev.

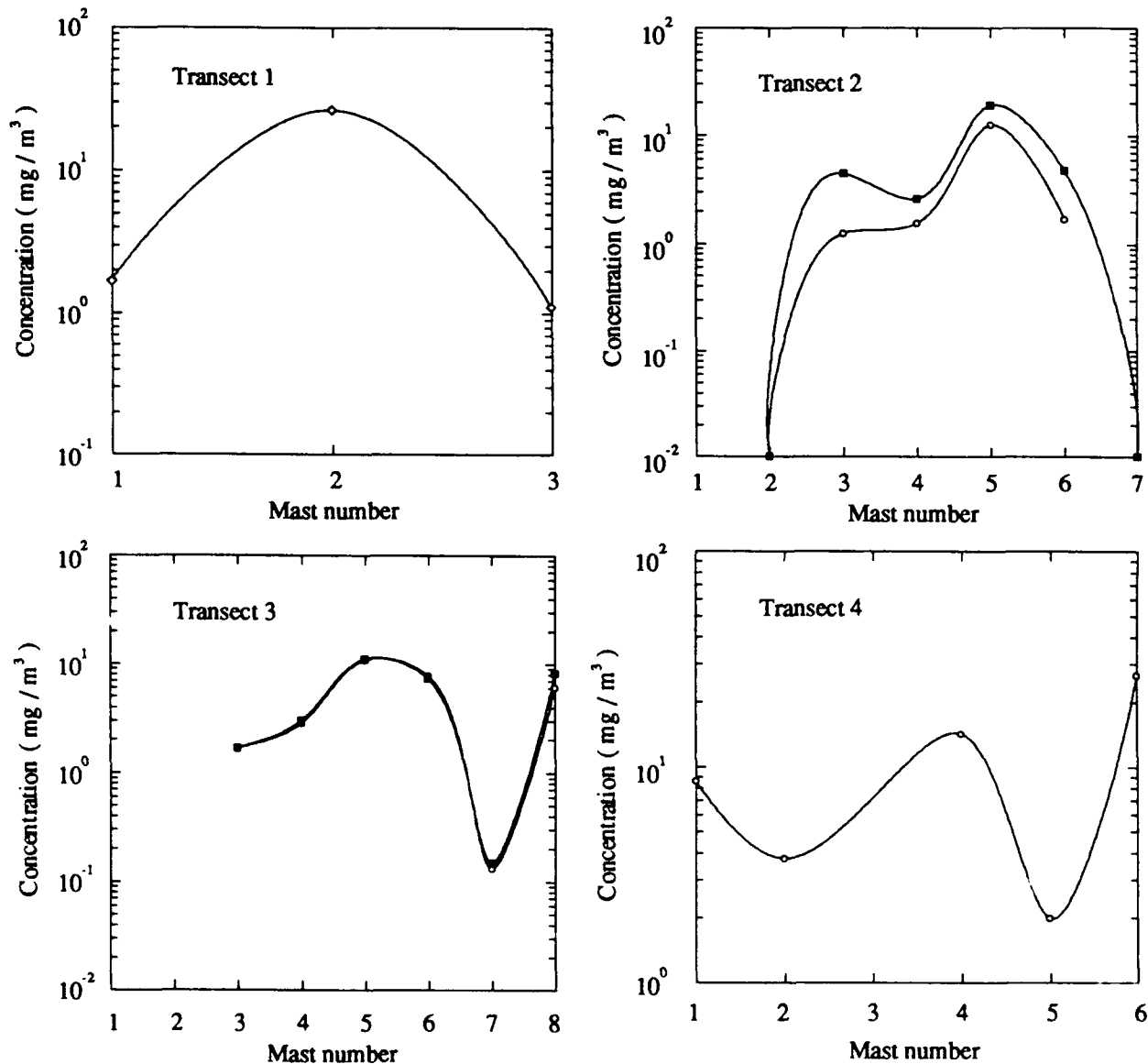


Figure 6.55 (continued) Profiles of fog-oil concentration measured along the sampling transects for the stable Meadowbrook dispersion tests. These plots are for Test 0927871 and the crosswind view in these graphs is looking downwind from the source. In addition to the mean concentrations, the standard deviation in concentration from the aerosol photometers is also shown in these plots.

Concentration data  
Meadowbrook site  
Test 0927872  
September 27, 1987  
6:44:00 to 6:54:00

—○— 1 m mean  
—○— 2 m mean  
—■— 8 m mean  
—■— 2 m std. dev.

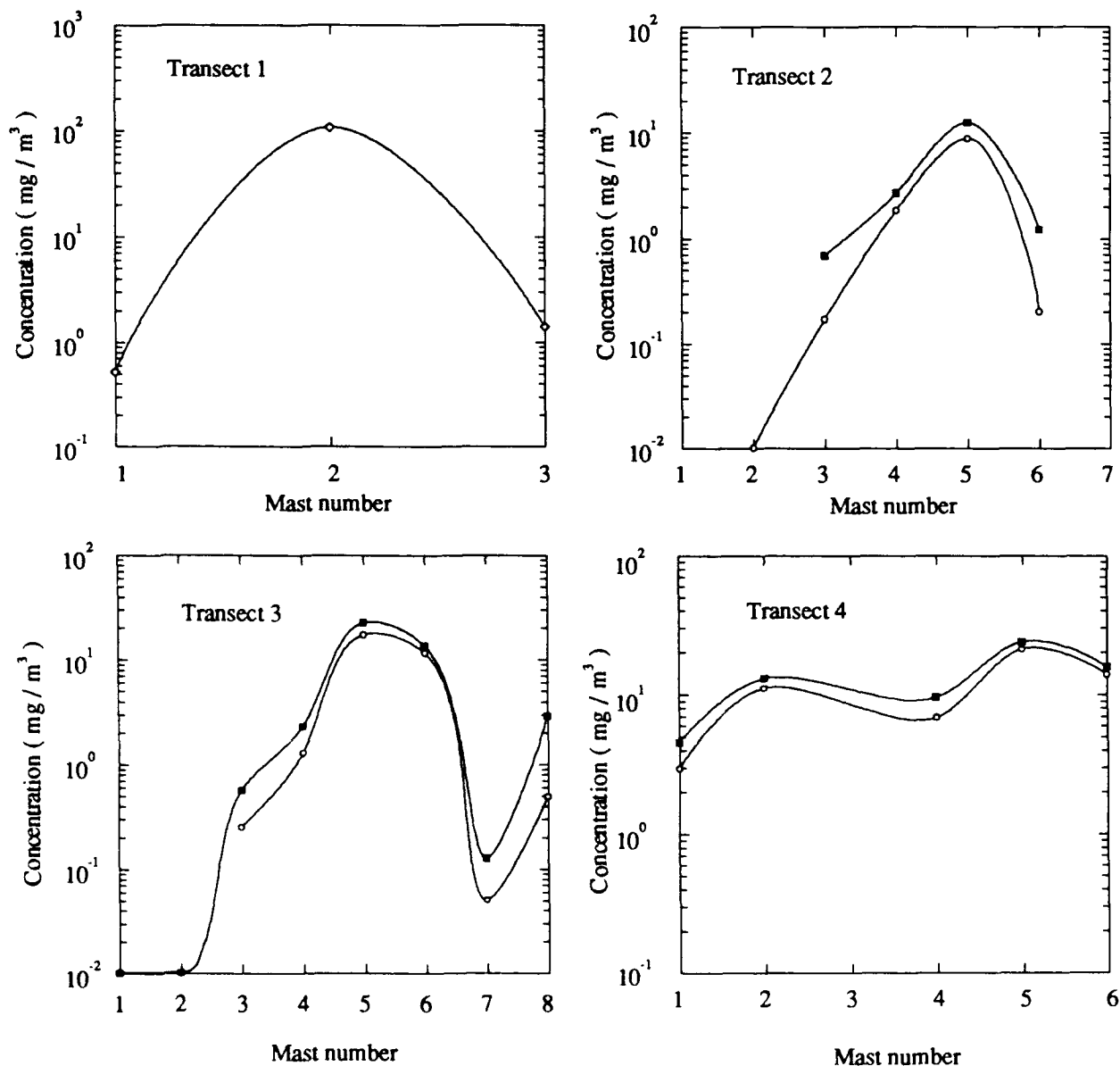


Figure 6.55 (continued) Profiles of fog-oil concentration measured along the sampling transects for the stable Meadowbrook dispersion tests. These plots are for Test 0927872 and the crosswind view in these graphs is looking downwind from the source. In addition to the mean concentrations, the standard deviation in concentration from the aerosol photometers is also shown in these plots.

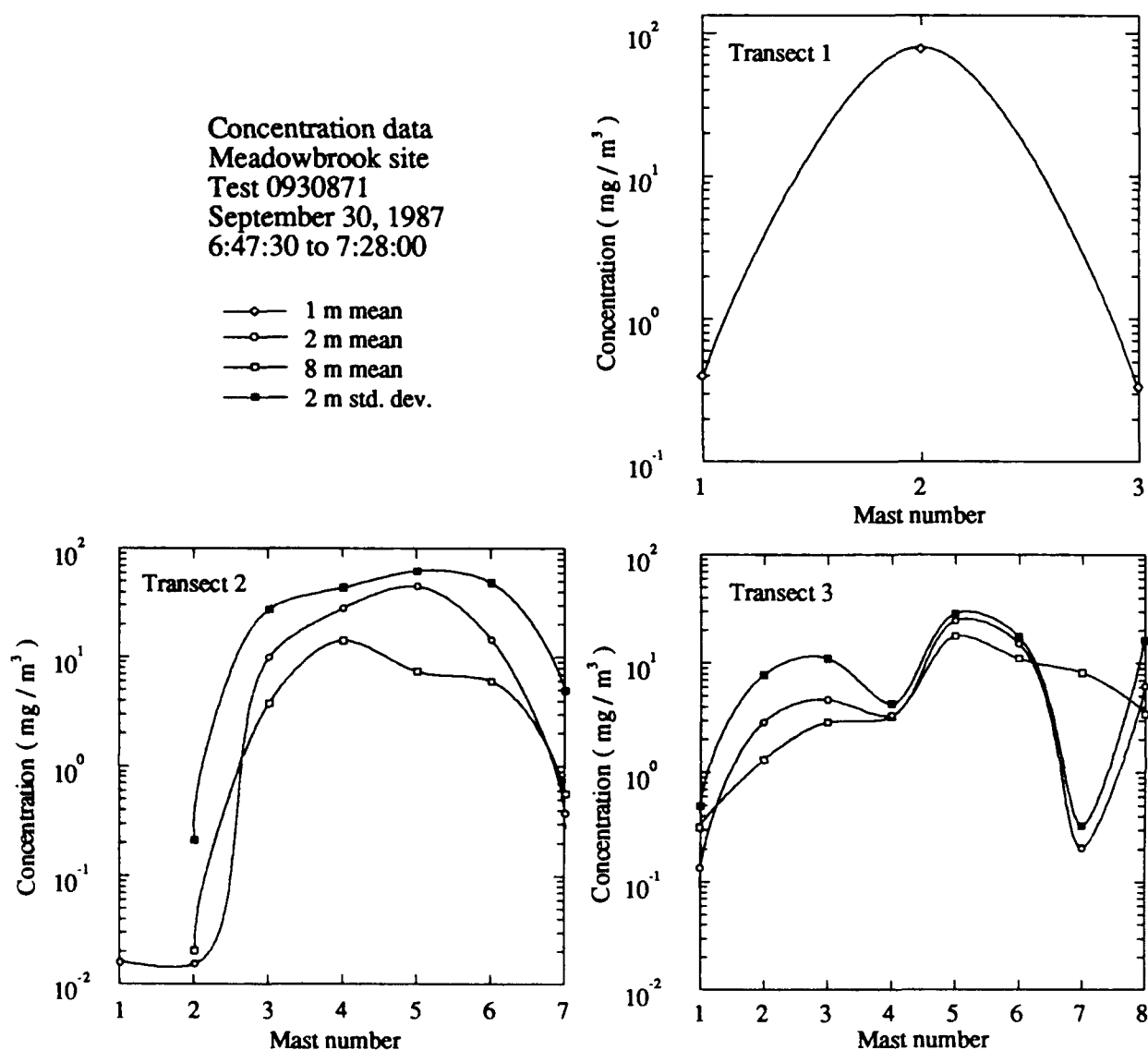


Figure 6.55 (continued) Profiles of fog-oil concentration measured along the sampling transects for the stable Meadowbrook dispersion tests. These plots are for Test 0930871 and the crosswind view in these graphs is looking downwind from the source. In addition to the mean concentrations, the standard deviation in concentration from the aerosol photometers is also shown in these plots.

Concentration data  
Meadowbrook site  
Test 0930871  
September 30, 1987  
6:47:30 to 7:28:00

—○— 1 m mean  
—○— 2 m mean  
—○— 8 m mean  
—■— 2 m std. dev.

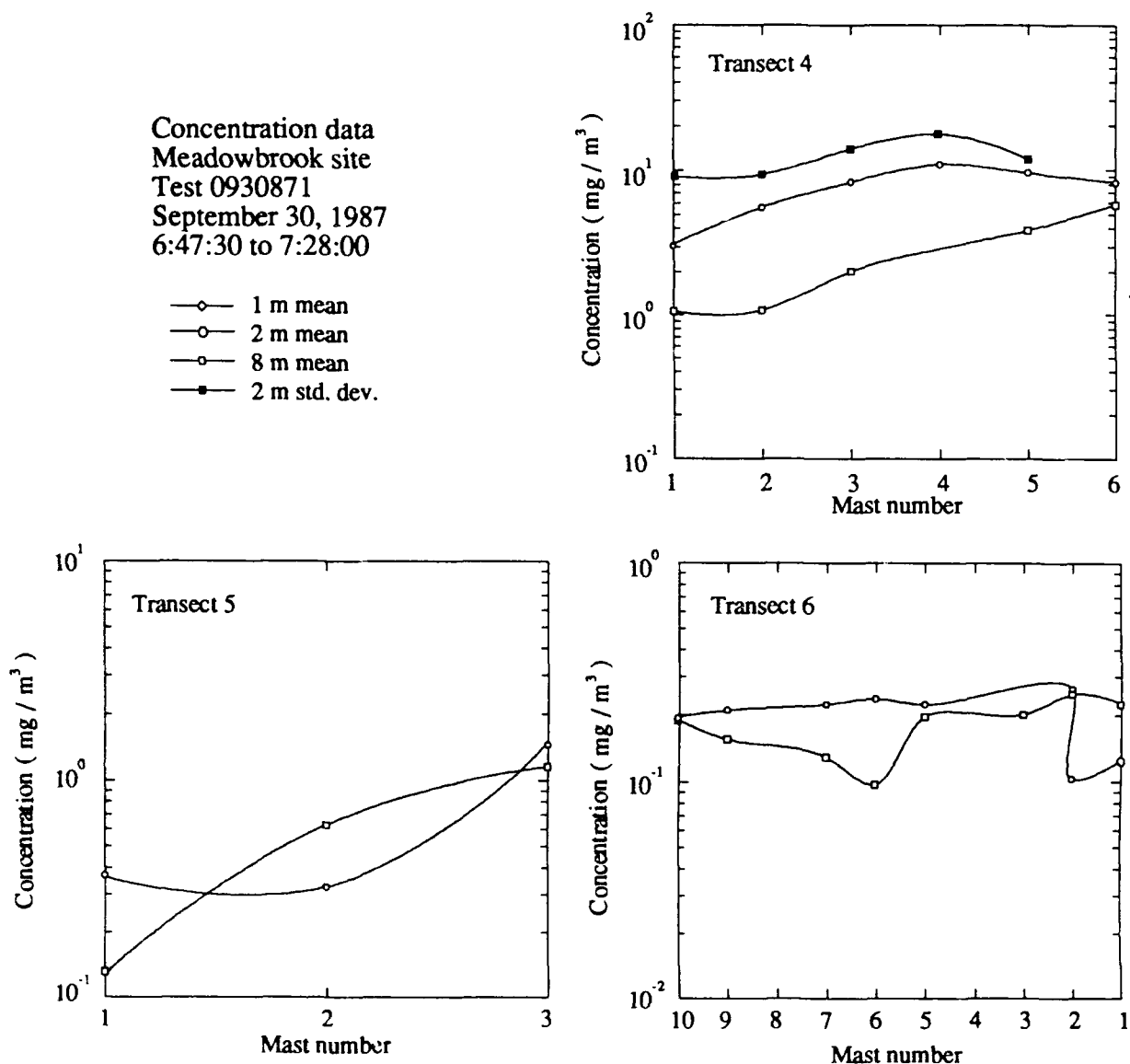


Figure 6.55 (continued) Profiles of fog-oil concentration measured along the sampling transects for the stable Meadowbrook dispersion tests. These plots are for Test 0930871 and the crosswind view in these graphs is looking downwind from the source. In addition to the mean concentrations, the standard deviation in concentration from the aerosol photometers is also shown in these plots.

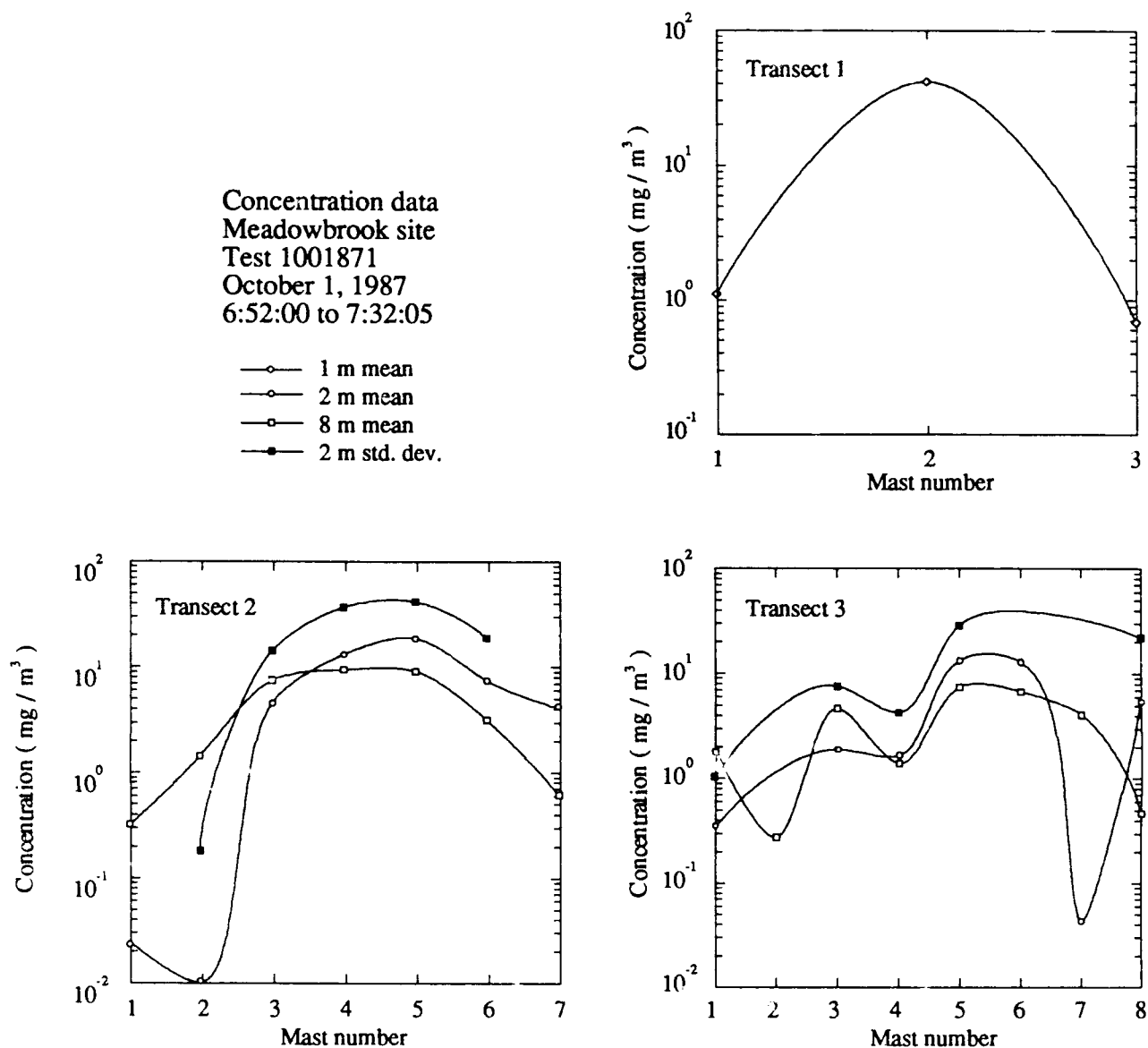


Figure 6.55 (continued) Profiles of fog-oil concentration measured along the sampling transects for the stable Meadowbrook dispersion tests. These plots are for Test 1001871 and the crosswind view in these graphs is looking downwind from the source. In addition to the mean concentrations, the standard deviation in concentration from the aerosol photometers is also shown in these plots.

Concentration data  
Meadowbrook site  
Test 1001871  
October 1, 1987  
6:52:00 to 7:32:05

—○— 1 m mean  
—○— 2 m mean  
—○— 8 m mean  
—●— 2 m std. dev.

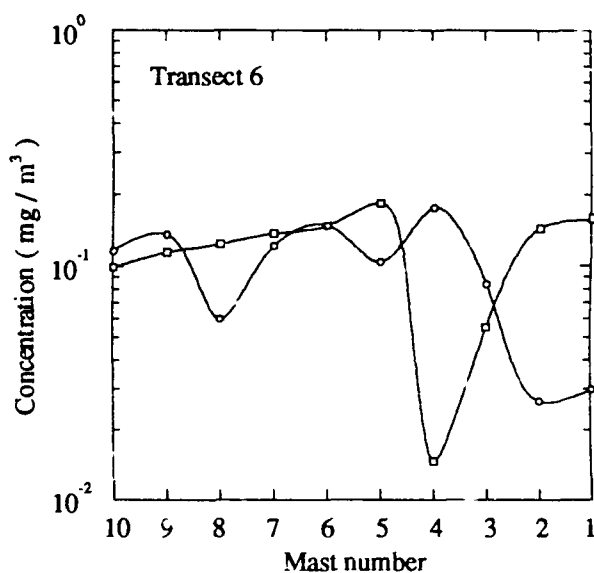
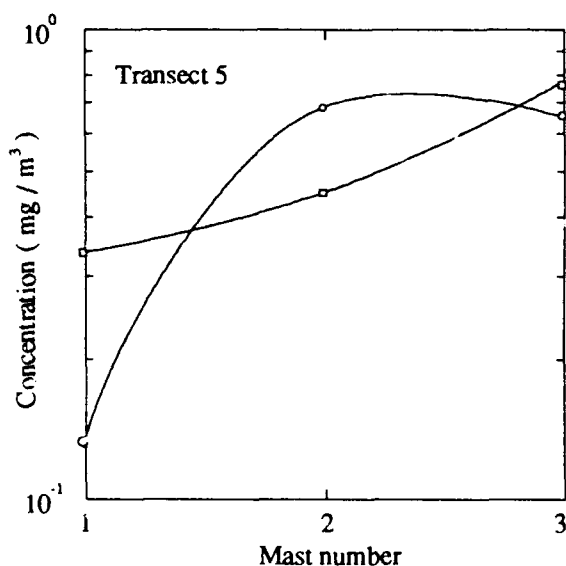
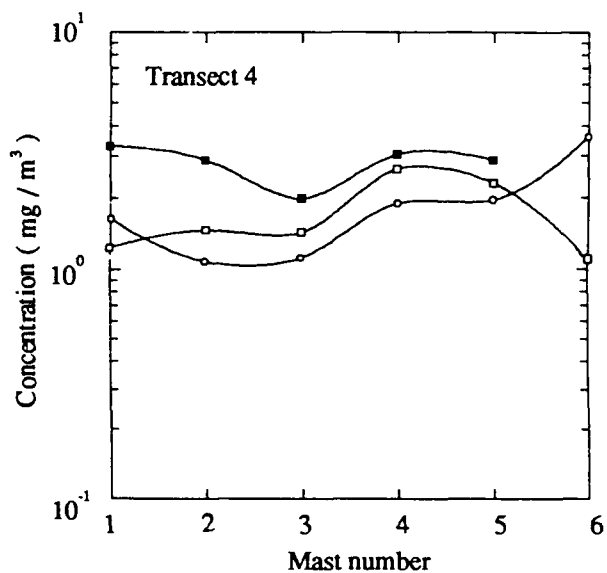


Figure 6.55 (continued) Profiles of fog-oil concentration measured along the sampling transects for the stable Meadowbrook dispersion tests. These plots are for Test 1001871 and the crosswind view in these graphs is looking downwind from the source. In addition to the mean concentrations, the standard deviation in concentration from the aerosol photometers is also shown in these plots.



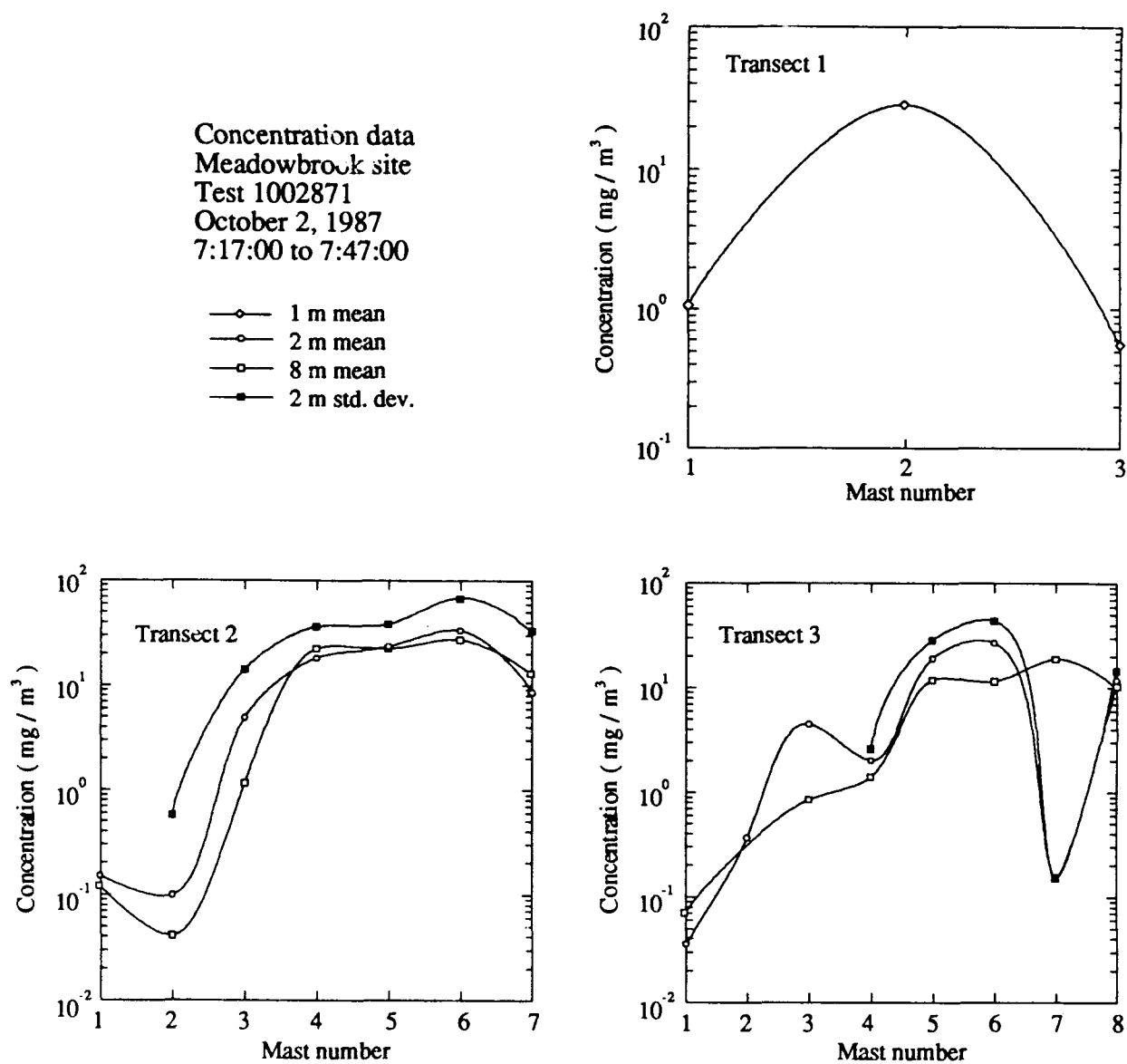


Figure 6.55 (continued) Profiles of fog-oil concentration measured along the sampling transects for the stable Meadowbrook dispersion tests. These plots are for Test 1002871 and the crosswind view in these graphs is looking downwind from the source. In addition to the mean concentrations, the standard deviation in concentration from the aerosol photometers is also shown in these plots.

Concentration data  
Meadowbrook site  
Test 1002871  
October 2, 1987  
7:17:00 to 7:47:00

—○— 1 m mean  
—○— 2 m mean  
—○— 8 m mean  
—■— 2 m std. dev.

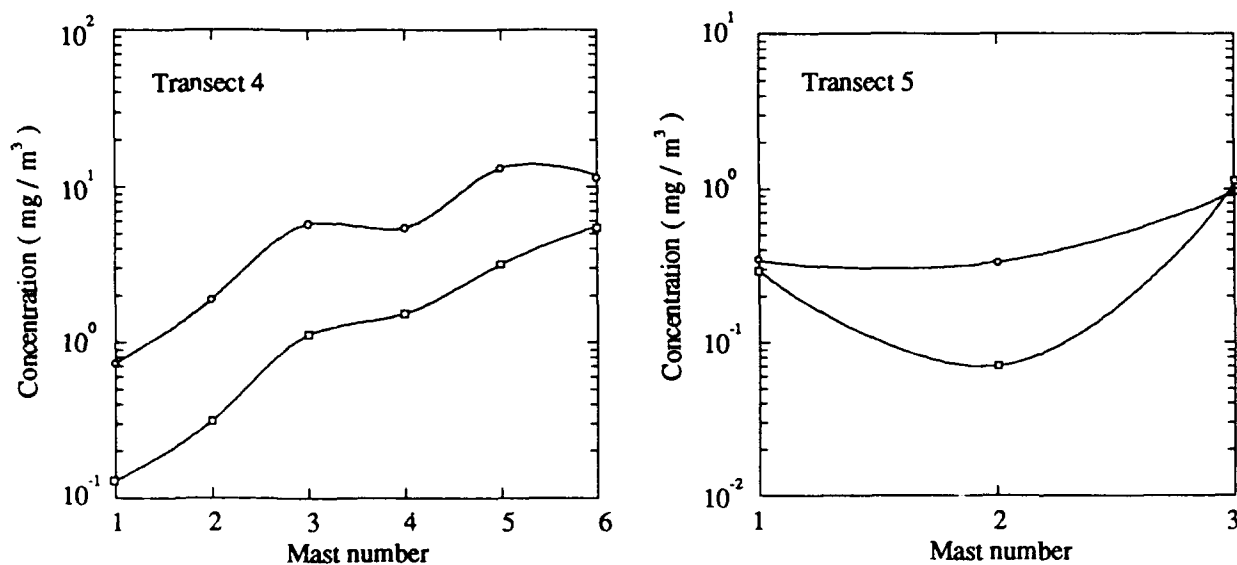


Figure 6.55 (continued) Profiles of fog-oil concentration measured along the sampling transects for the stable Meadowbrook dispersion tests. These plots are for Test 1002871 and the crosswind view in these graphs is looking downwind from the source. In addition to the mean concentrations, the standard deviation in concentration from the aerosol photometers is also shown in these plots.

Concentration data  
Meadowbrook site  
Test 1003871  
October 3, 1987  
6:56:00 to 7:27:00

—○— 1 m mean  
—○— 2 m mean  
—□— 8 m mean  
—■— 2 m std. dev.

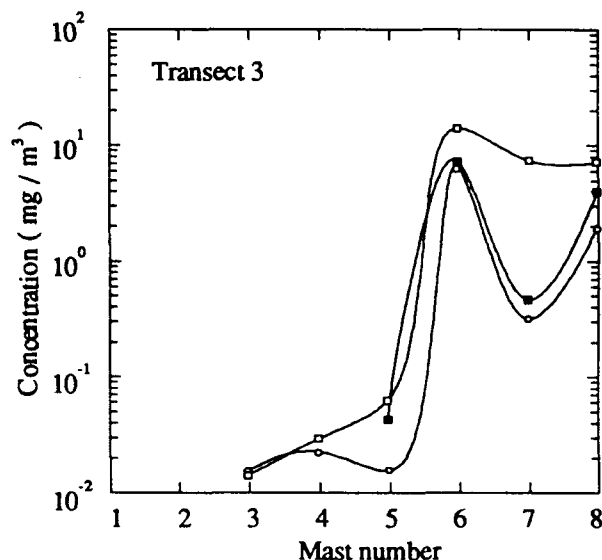
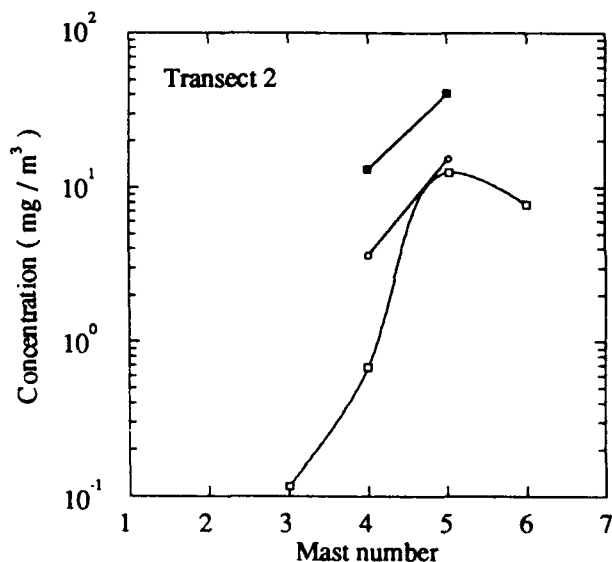
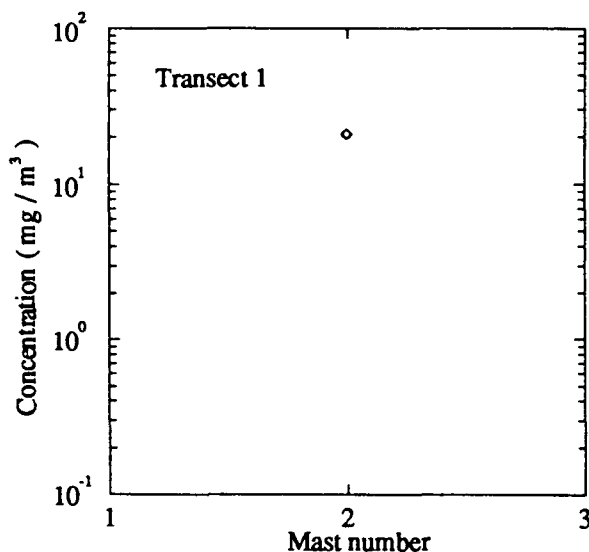


Figure 6.55 (continued) Profiles of fog-oil concentration measured along the sampling transects for the stable Meadowbrook dispersion tests. These plots are for Test 1003871 and the crosswind view in these graphs is looking downwind from the source. In addition to the mean concentrations, the standard deviation in concentration from the aerosol photometers is also shown in these plots.

Concentration data  
Meadowbrook site  
Test 1003871  
October 3, 1987  
6:56:00 to 7:27:00

—○— 1 m mean  
—○— 2 m mean  
—□— 8 m mean  
—●— 2 m std. dev.

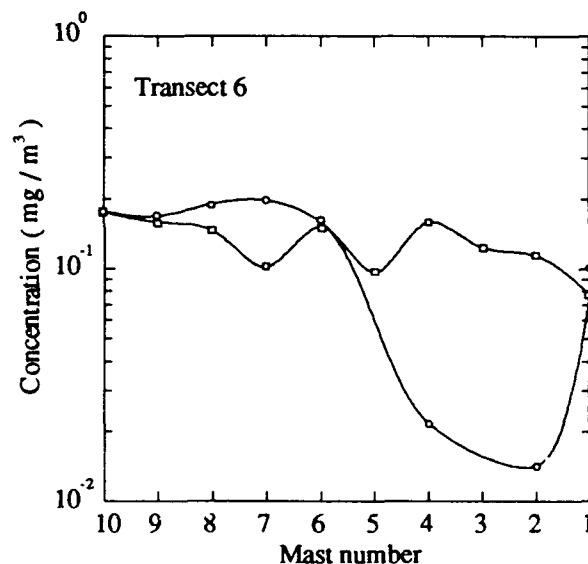
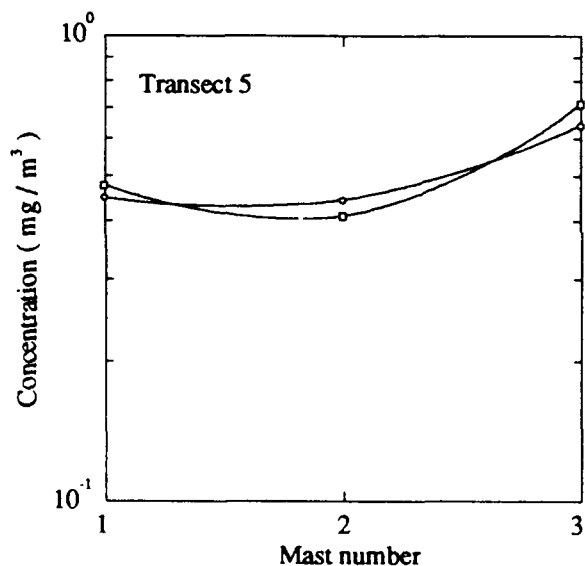
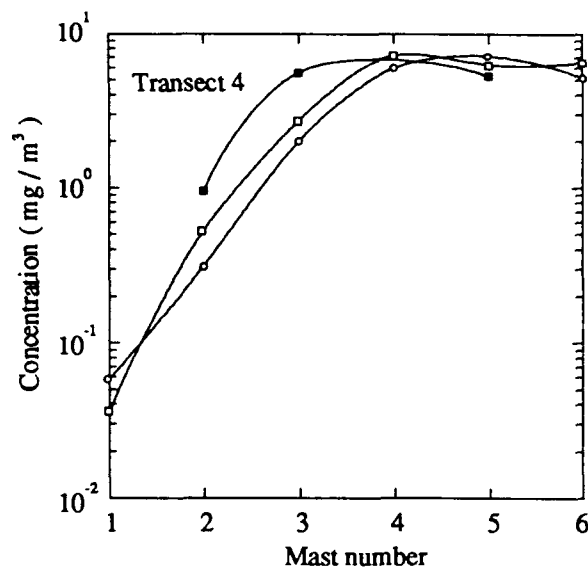


Figure 6.55 (continued) Profiles of fog-oil concentration measured along the sampling transects for the stable Meadowbrook dispersion tests. These plots are for Test 1003871 and the crosswind view in these graphs is looking downwind from the source. In addition to the mean concentrations, the standard deviation in concentration from the aerosol photometers is also shown in these plots.

source strength, where winds at tower positions along the smoke plume path are shown in the chart of Figure 6.56. These winds are predominantly in the downslope direction.

Results of the crosswind integrated concentration calculations are shown in Figure 6.57. There is reasonable collapse of the data using this scaling at further downwind distances. Part of the spread between the tests, or even increase in crosswind integrated concentration with distance for the near-source samplers, is due to the finite buoyancy, upward momentum, and release height at the source. These effects allow the smoke to travel over the near-field samplers on Transects 2 and 3. In conditions of higher turbulence, such as our in our daytime tests, these source effects are negligible.

The dilution of the smoke as seen in this plot is not a simple power-law function of distance. Physical effects responsible for this behavior, other than the source effects, can be found in examining the topography of the site. Terrain effects change the rate of decrease of crosswind integrated concentration as side canyons join with the plume, adding their mass of cool drainage flow air to the mixing plume.

Profile analysis of the data for the concentration fluctuations is limited to the early stages of the plume evolution, at Transects 2 and 3 before the plume fills the entire valley. The plume width is shown in Figure 6.58 as a function of travel time. For this data set the plume growth is linear with travel time. At further distances the growth of  $\sigma_y$  is strongly influenced by the terrain and resembles mixing in a closed channel. A nondimensionalized profile of the mean data for Transects 2 and 3 is shown in Figure 6.59, where we have neglected data from Mast 7 on Transect 3 because of its sheltered position.

Considering the complex terrain and variable vegetation, the data follow the Gaussian profile very well. The data in this plot are shown looking from the source downwind and most of the data shown in this plot are confined to the open area of the dispersion site, rather than the forested area on the north side of the sampling grid. Most of the deviation from this profile is due to a single data set from Transect 2 in Test 0925871.

#### 6.4.2 Fluctuating Concentration Data

Using the aerosol photometer data from Transects 2 and 3, plots of  $\sigma_c(x,y)/\bar{c}(x,0)$  versus  $\sigma_y/y$  in Figure 6.60 and  $\sigma_c(x,y)/\bar{c}(x,y)$  versus  $\sigma_y/y$  in Figure 6.61 are compared with the profiles given in Eqs. 6.10 and 6.11. The value of  $\alpha = \sigma_c(x,0)/\bar{c}(x,0)$  used here is 1.5, which is smaller than that found in the daytime Meadowbrook tests or the Camp Atterbury tests. Agreement between the model and data is reasonable in all cases.

The probability distribution of concentration at points in the flow field is seen to follow the probability distribution given by Eq. 6.12 in Figure 6.62 for all of the aerosol photometer data at

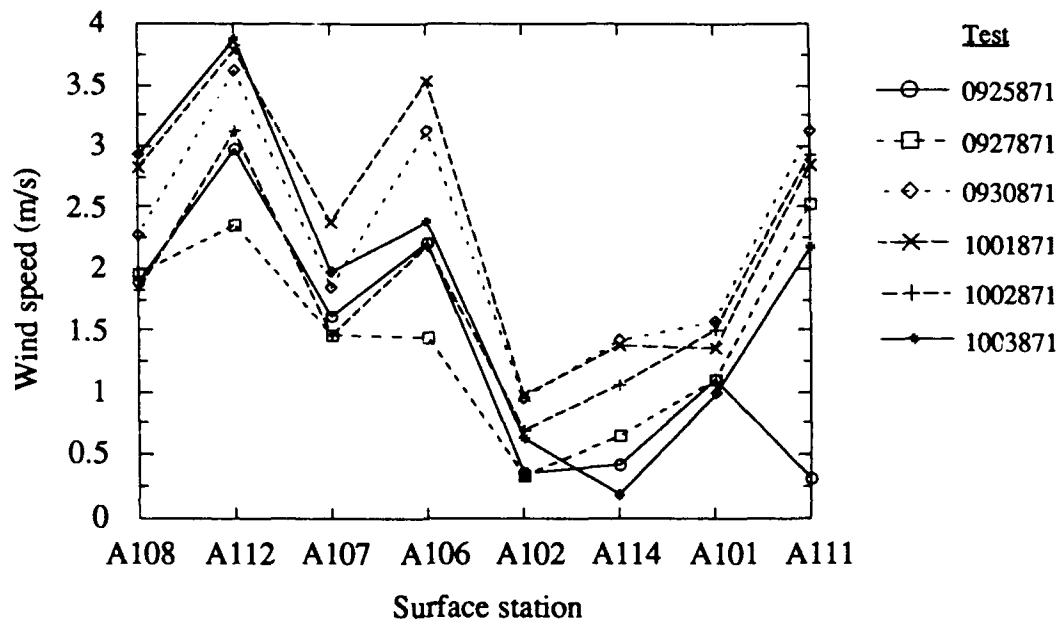


Figure 6.56 Wind speeds along the smoke plume path for the fog-oil dispersion tests at Meadowbrook. These data are from the 10-m surface stations and are averaged over the test period.

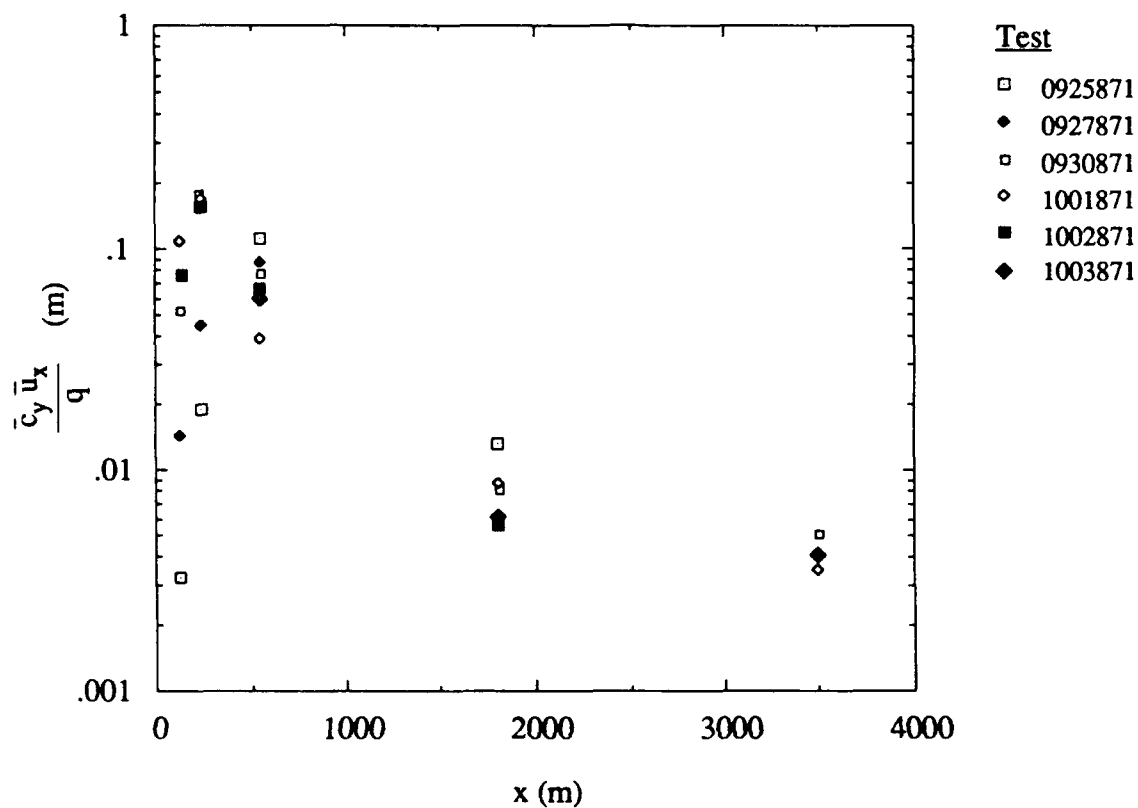


Figure 6.57 Cross wind integrated concentrations versus downwind distance for the stable dispersion tests at Meadowbrook. The cross wind integrated concentration for Transect 2 and 3 is found through a profile fit of the data. For Transects 4, 5, and 6 a mean concentration is found for the transect and is multiplied by the valley width for that transect. A local wind speed is used in the scaling. For Transect 2 and 3 this is the measurement at surface station A108. For Transect 4 we use the average of wind measurements at A112 and A107. For transect 6 we use the wind measurement at A111.

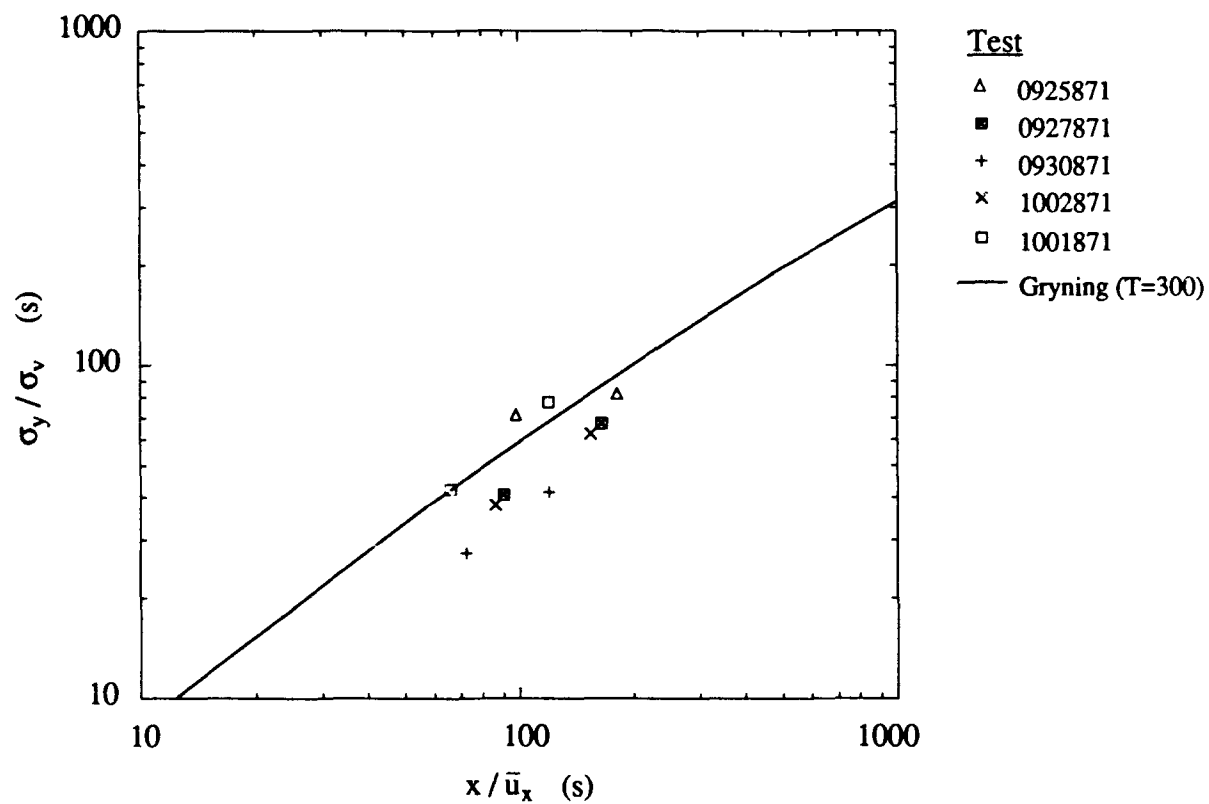


Figure 6.58 Estimated horizontal plume widths for the stable dispersion tests at Meadowbrook as compared with Gryning's adaptation of Draxler's model. This plot includes data from the second and third transects.



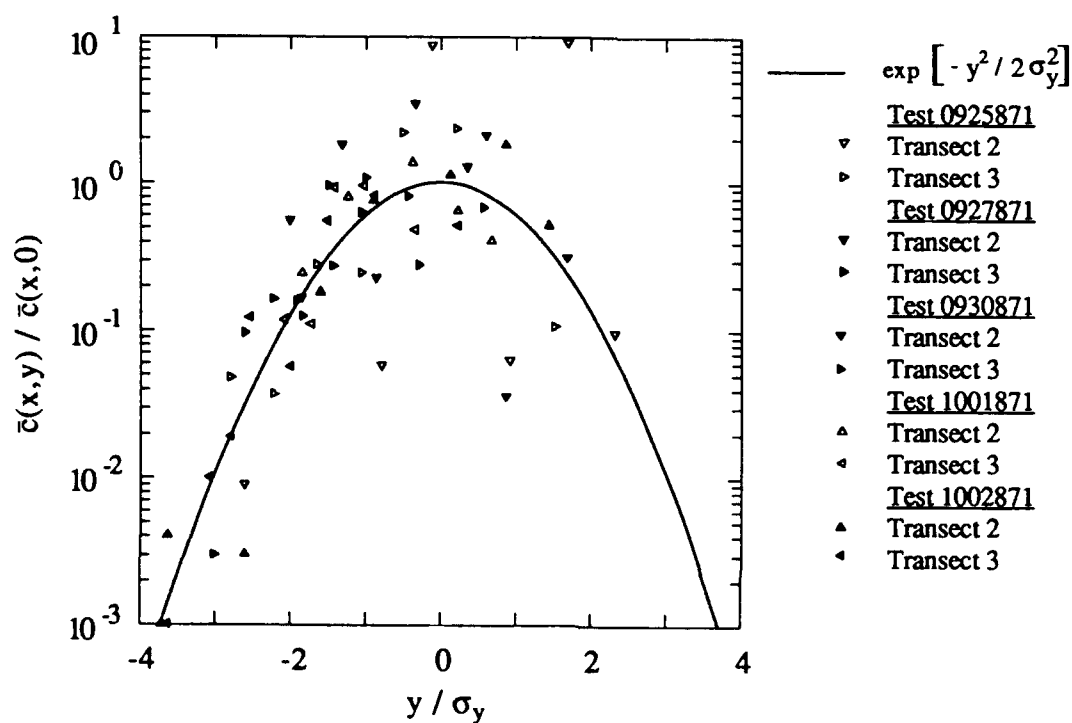


Figure 6.59 Normalized crosswind profile of mean concentration for the stable fog-oil dispersion tests at Meadowbrook. Lateral plume spread versus a ratio of actual concentration to the fitted centerline concentration is given in this plot. Comparison of the data with a Gaussian profile is also shown.

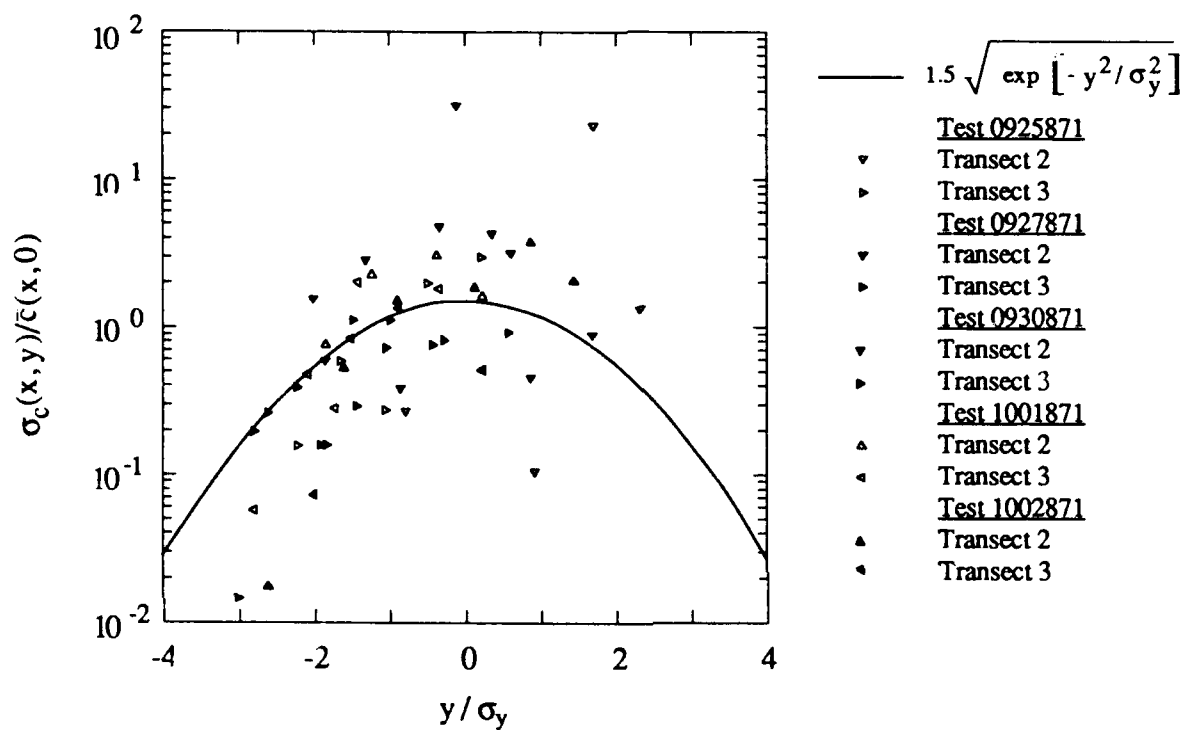


Figure 6.60 Crosswind profile of the standard deviation in concentration normalized by the centerline mean concentration for the stable Meadowbrook dispersion tests. The square root of a Gaussian profile is also plotted, with a constant coefficient of 1.5.

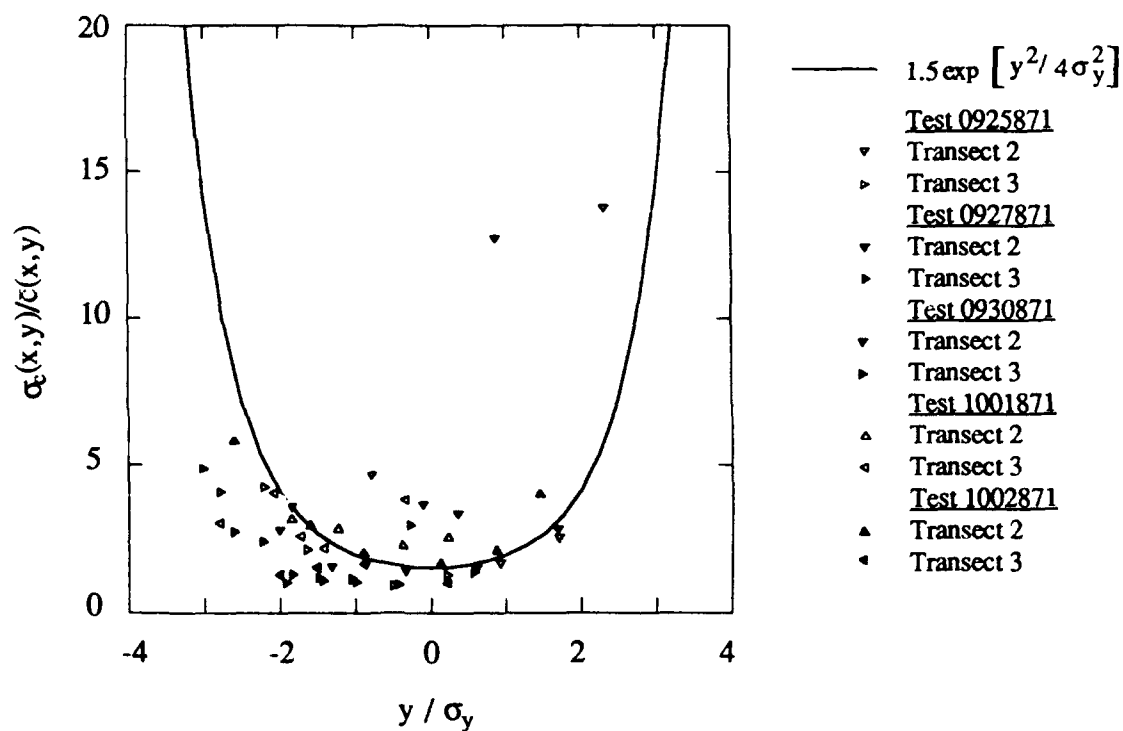


Figure 6.61 Crosswind profile of fluctuation intensity of concentration for the stable Meadowbrook dispersion tests. The data are plotted as a dimensionless profile of the local values of the standard deviation in concentration and mean concentration. The model profile is plotted with a coefficient of 1.5.

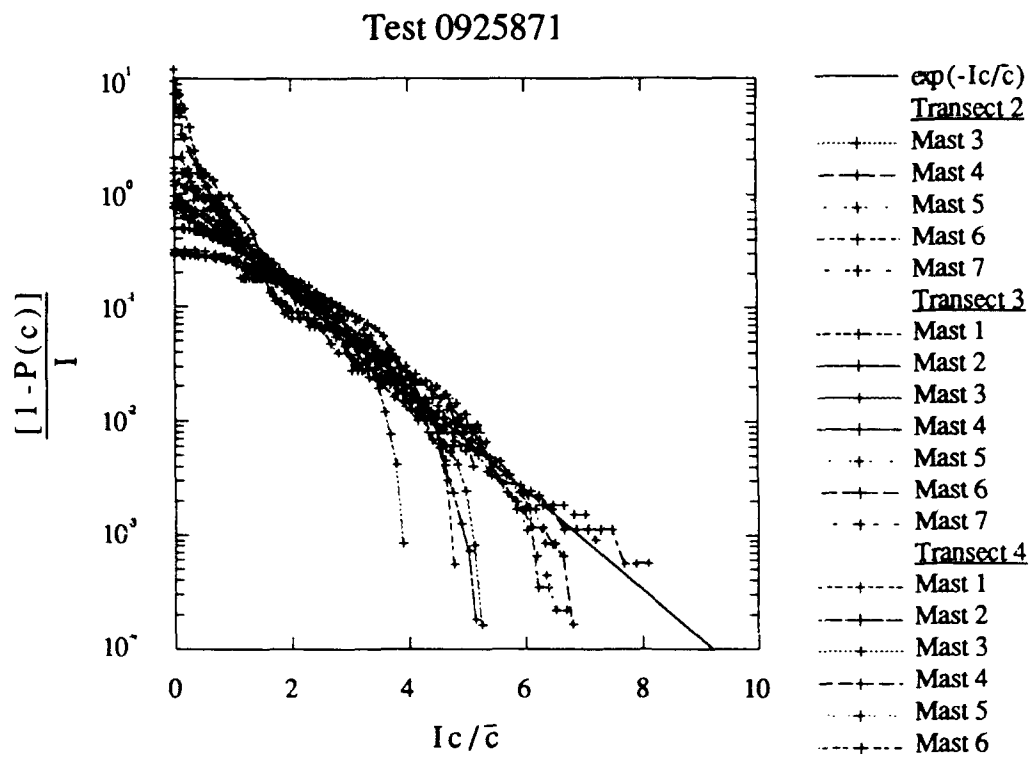


Figure 6.62 A comparison of the histograms in concentration with the exponential distribution. This plot is for Test 0925871. The mast numbers refer to the location along a given transect.

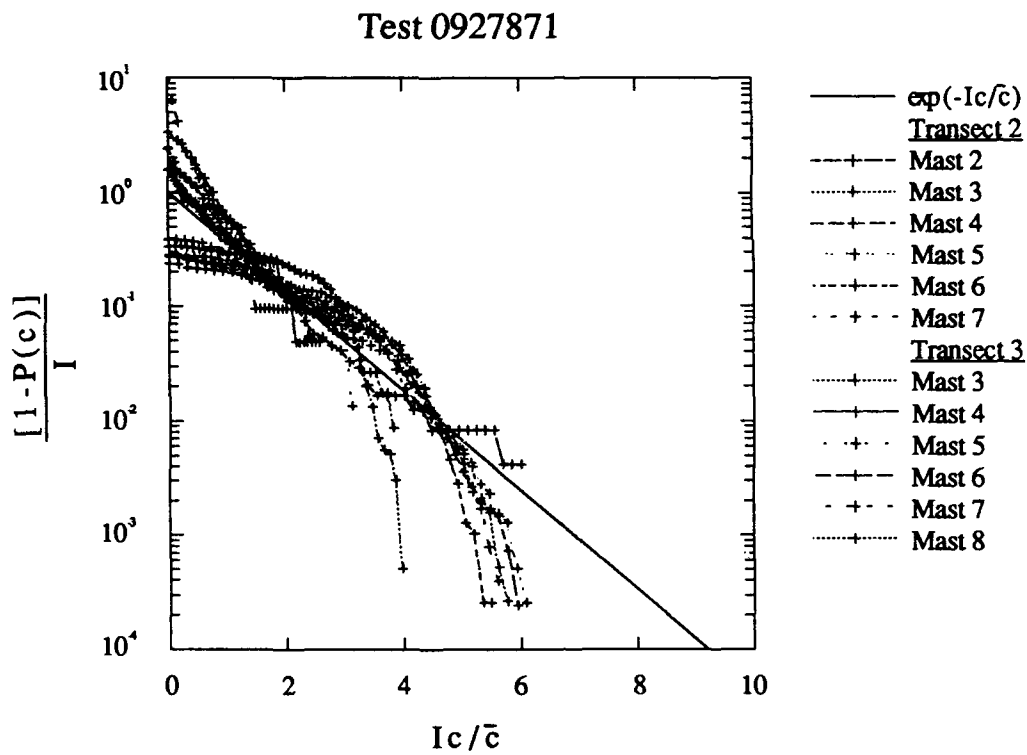


Figure 6.62 (continued) A comparison of the histograms in concentration with the exponential distribution. This plot is for Test 0927871. The mast numbers refer to the location along a given transect.

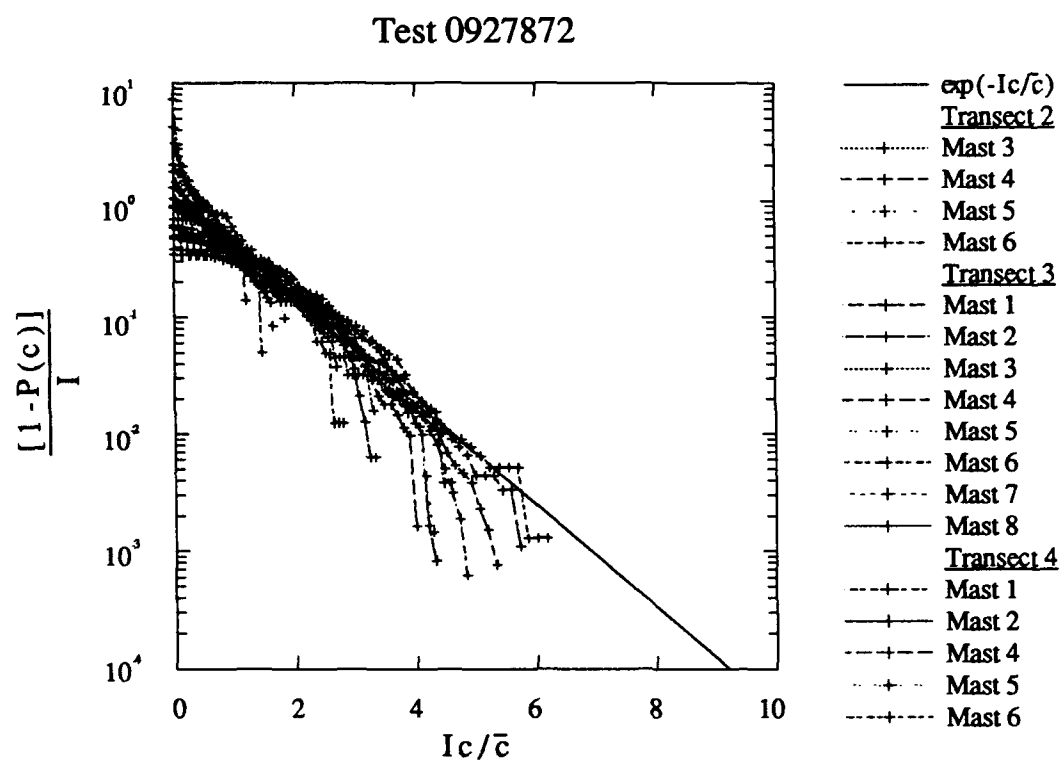


Figure 6.62 (continued) A comparison of the histograms in concentration with the exponential distribution. This plot is for Test 0927872. The mast numbers refer to the location along a given transect.

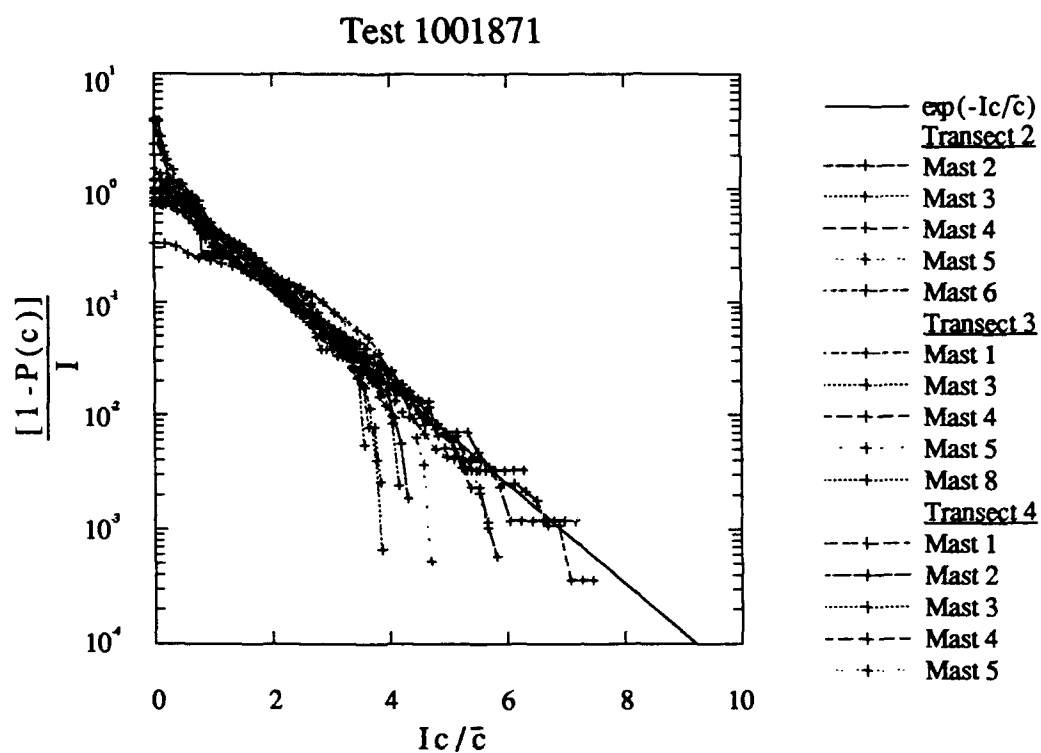


Figure 6.62 (continued) A comparison of the histograms in concentration with the exponential distribution. This plot is for Test 1001871. The mast numbers refer to the location along a given transect.

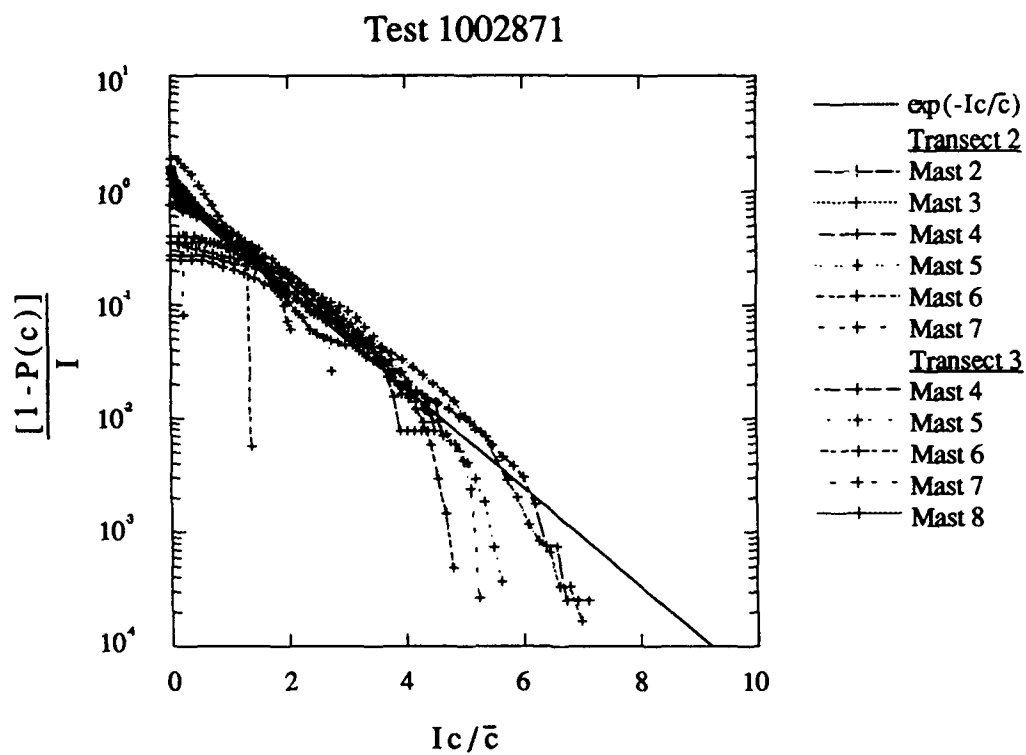


Figure 6.62 (continued) A comparison of the histograms in concentration with the exponential distribution. This plot is for Test 1002871. The mast numbers refer to the location along a given transect.



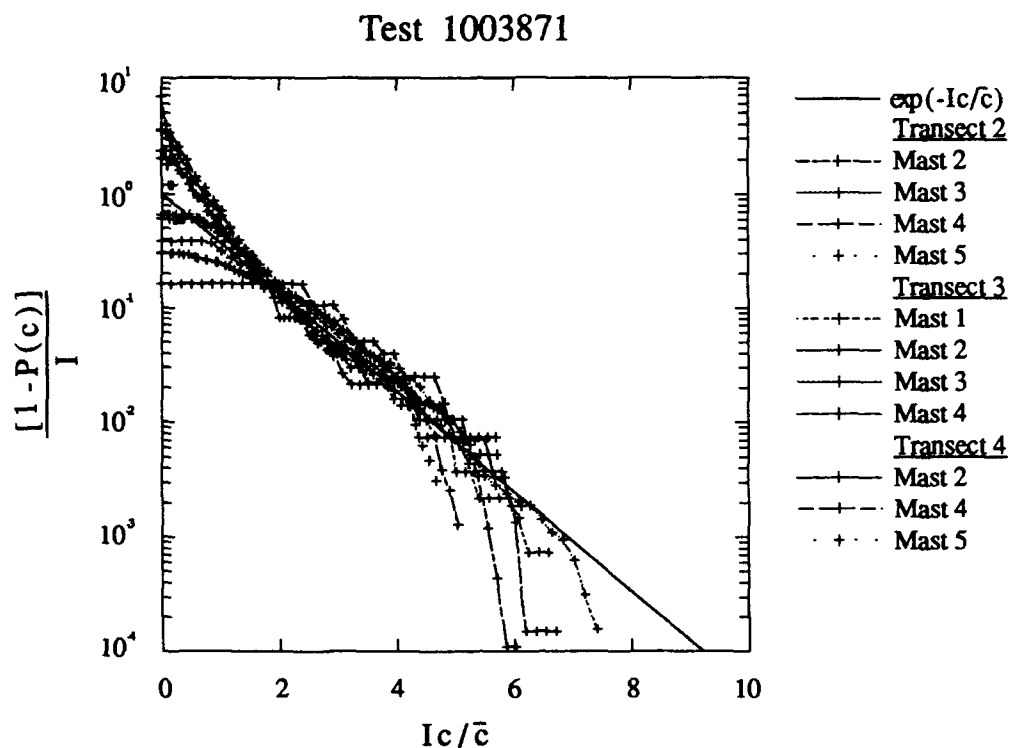


Figure 6.62 (continued) A comparison of the histograms in concentration with the exponential distribution. This plot is for Test 1003871. The mast numbers refer to the location along a given transect.

Transects 2 through 4. The signal is clipped from some of these samplers, mainly due to the higher than expected concentrations at the sampling locations. There is also scatter near zero concentration which is reflected in the measured value of the intermittency. Part of this scatter in intermittency is due to the noise of the instruments, while part is due to the short duration of the dispersion tests. The crosswind distribution of intermittency is given by Eq. 6.15. The data values of intermittency versus the crosswind length scale is shown in Figure 6.63 along with Eq. 6.15. There is considerable scatter in this plot, most likely due to the complicated nature of the flow for this test site and the relatively short duration of the tests. The approximate magnitude of the intermittency shows poor agreement with the model prediction, but we see that for all samplers the intermittency is less than unity.

#### 6.4.3 Spectra of the Concentration Fluctuations

Spectra of the concentration fluctuations are shown in Figure 6.64 for the stable dispersion tests. Unlike our other tests, these spectra do not all have a similar shape. They are divided into several groups for each test. For the samplers which are further from the source, there is a wide range of frequencies showing a  $-2/3$  power law scaling for  $nS_{cc}(n)$ . For samplers which are closer to the source in the open areas of the field, a peak in the spectra is found at much higher frequencies with no evidence of a clear  $-2/3$  scaling. For some of the tests, there was sufficient data collected at Transect 2, Mast 3 for analysis. This sampler was located within the dense forest canopy. At higher frequencies it showed lower values of  $nS_{cc}(n)/\sigma_c^2$  than the other samplers. The differences in the spectra at different locations can be attributed to the slower mixing rate in the low turbulence stable conditions. Closer samplers may be influenced by a core region of the plume.

Integral scales for this data set cover a wide range of values within a given test. They tend to be shorter closer to the source and in open areas of the field, but become much longer at further distances or in areas with a larger roughness height. No self-similar scaling is evident for the data.

#### 6.4.4 Concentration Exceedance

In examining the behavior of time intervals for which the concentration at a given sampler is greater than zero, as in previous experiments, we find that the mean duration  $1/\lambda_u(0)$  is approximately equal to the integral scale of the turbulence. This is shown in Figure 6.65 for the data in a dimensional form. In these stable tests, values of  $1/\lambda_u(0)$  cover a very broad range, from several seconds to over five minutes.

The probability distribution of the burst durations for individual samplers is shown for some of the samplers in Figure 6.66. Also shown is the curve for an exponential distribution given by

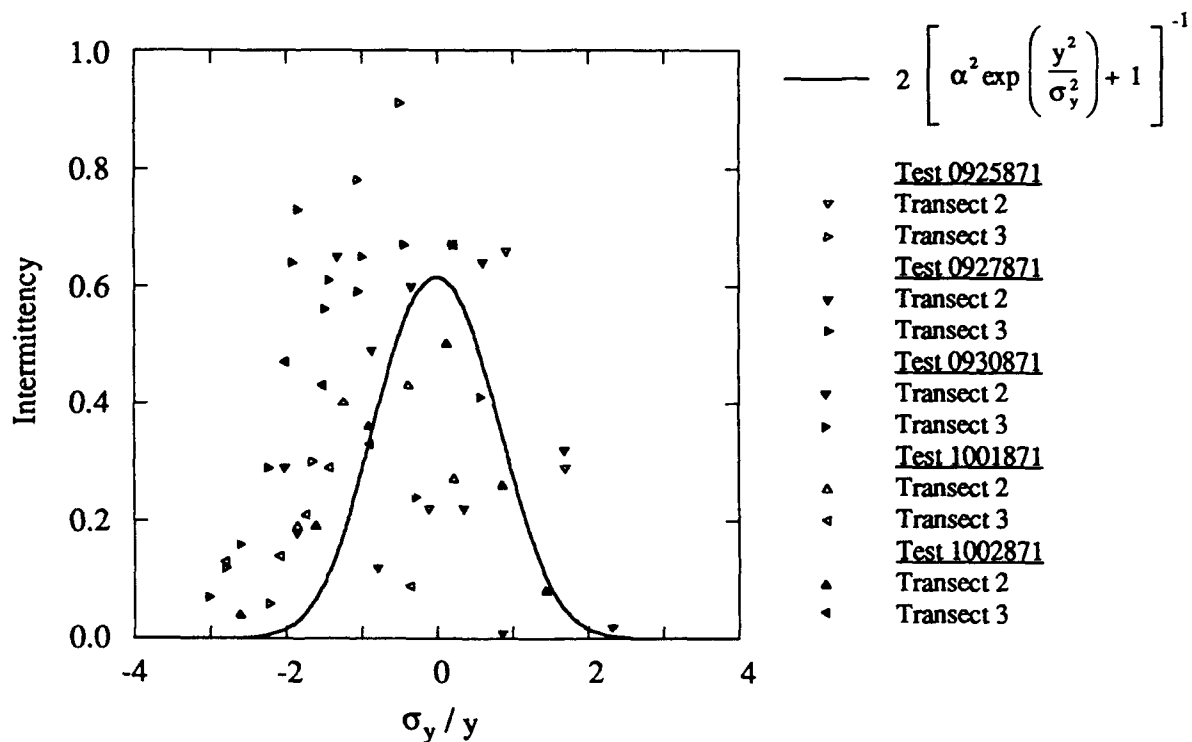


Figure 6.63 Crosswind intermittency for the stable Meadowbrook dispersion tests. The analytical solution uses a value of  $\alpha = 1.5$  in the expression shown.

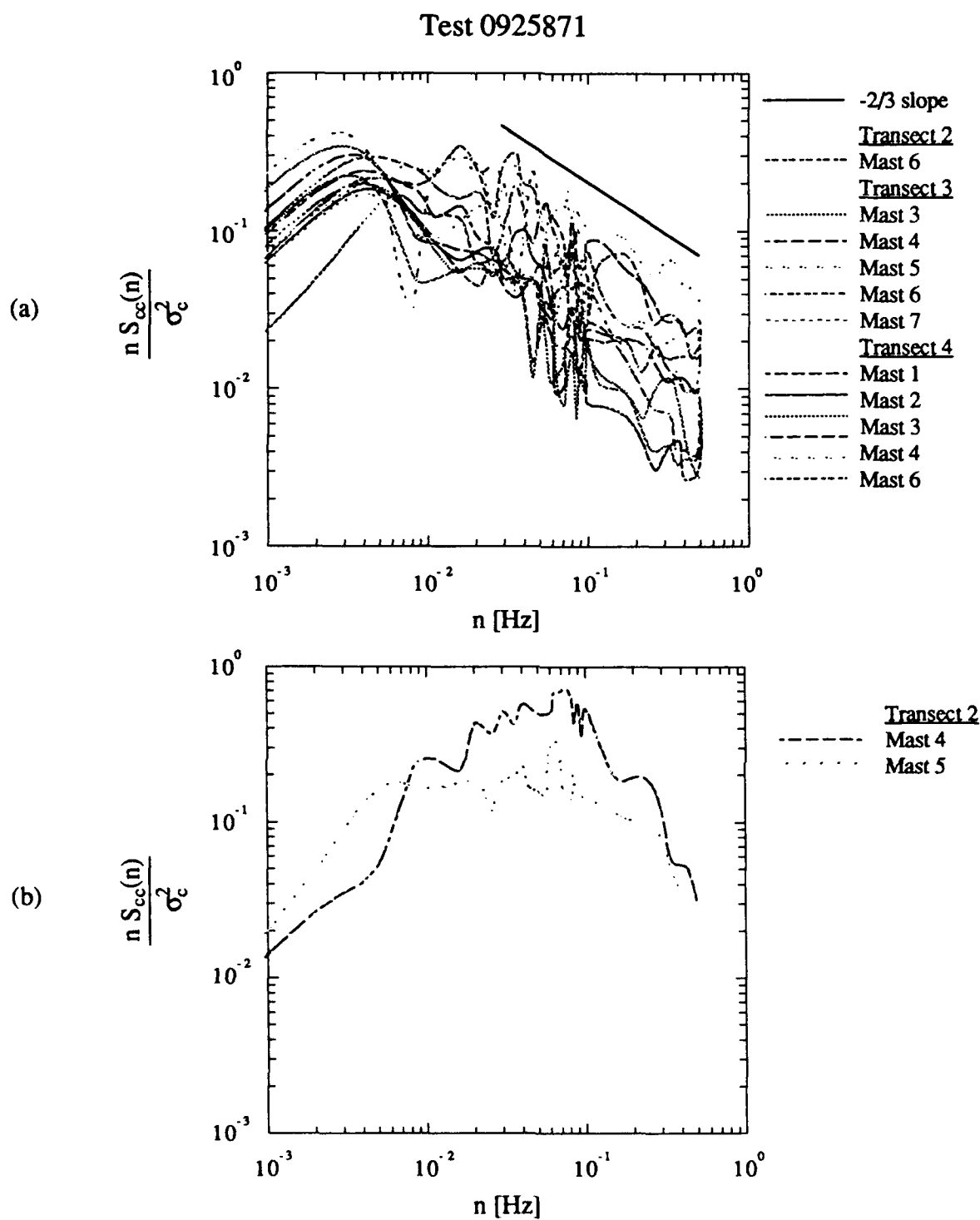


Figure 6.64 Spectra of the concentration variance for samplers located (a) near the source and (b) further downwind. This plot includes data from all samplers in Test 0925871 for which the mean signal exceeded five times the background noise of the instrument. The spectra were normalized by the calculated variance for each data record.

# Test 0927871

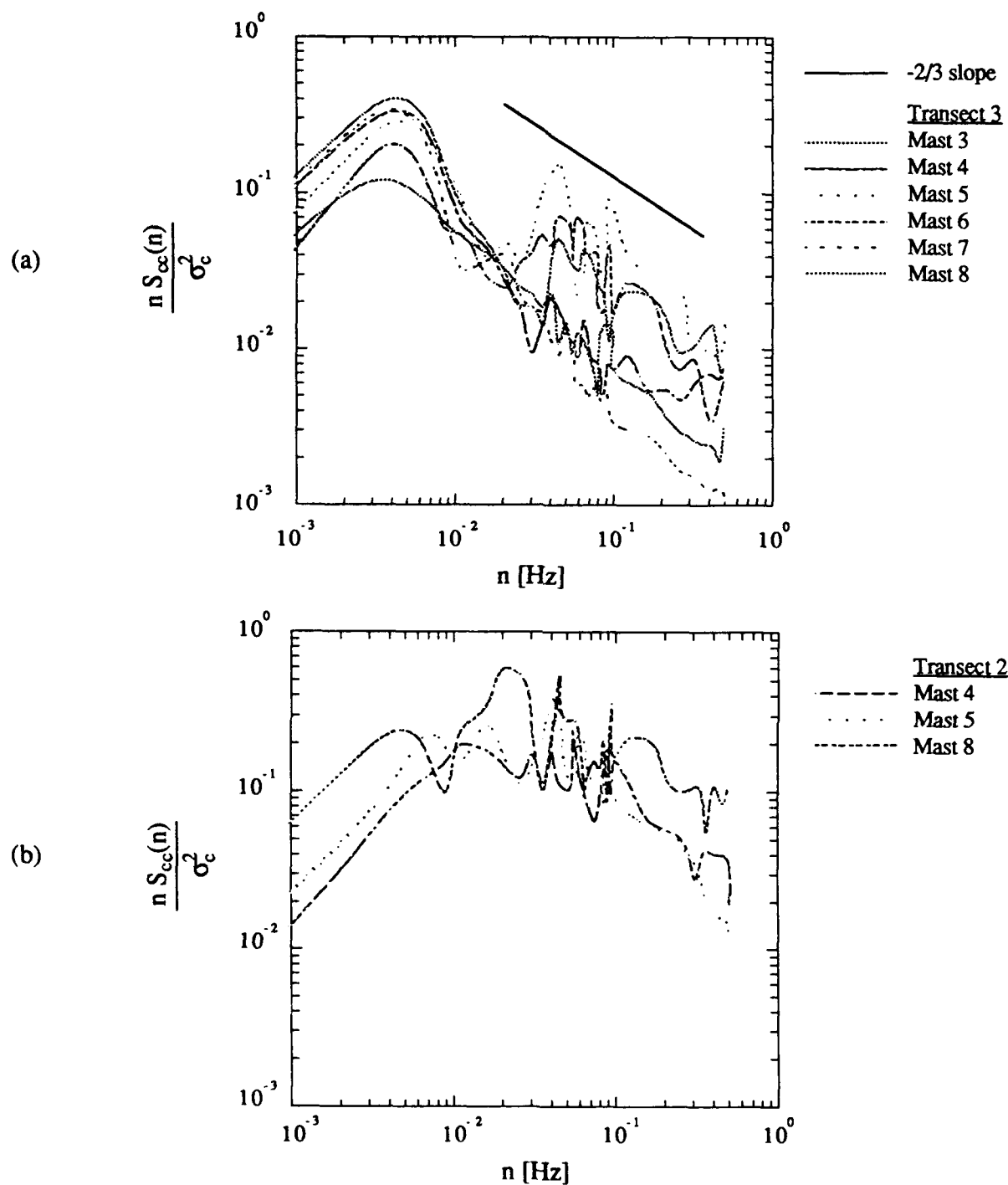


Figure 6.64 (continued) Spectra of the concentration variance for samplers located (a) near the source and (b) further downwind. This plot includes data from all samplers in Test 0927871 for which the mean signal exceeded five times the background noise of the instrument. The spectra were normalized by the calculated variance for each data record.

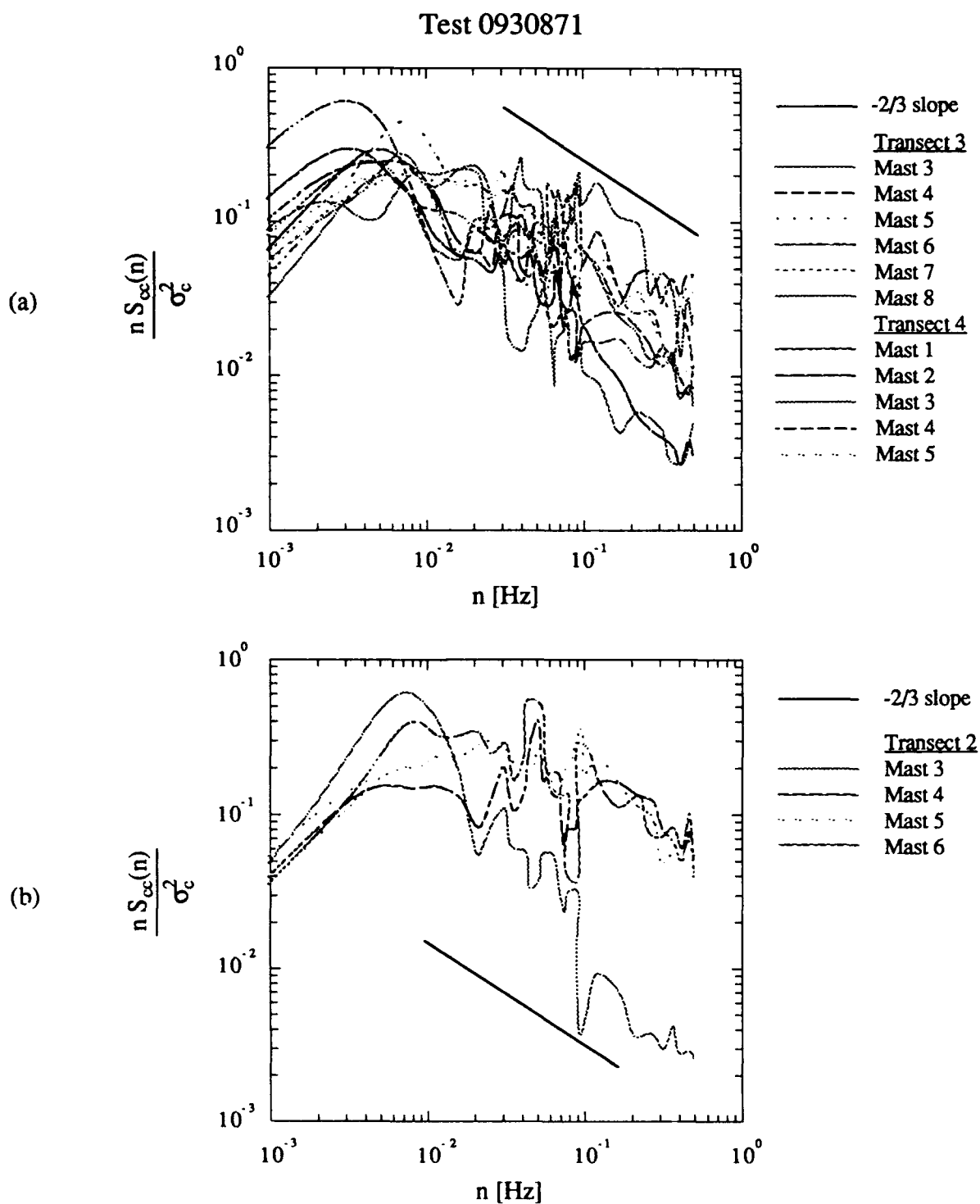


Figure 6.64 (continued) Spectra of the concentration variance for samplers located (a) near the source and (b) further downwind. This plot includes data from all samplers in Test 0930871 for which the mean signal exceeded five times the background noise of the instrument. The spectra were normalized by the calculated variance for each data record.

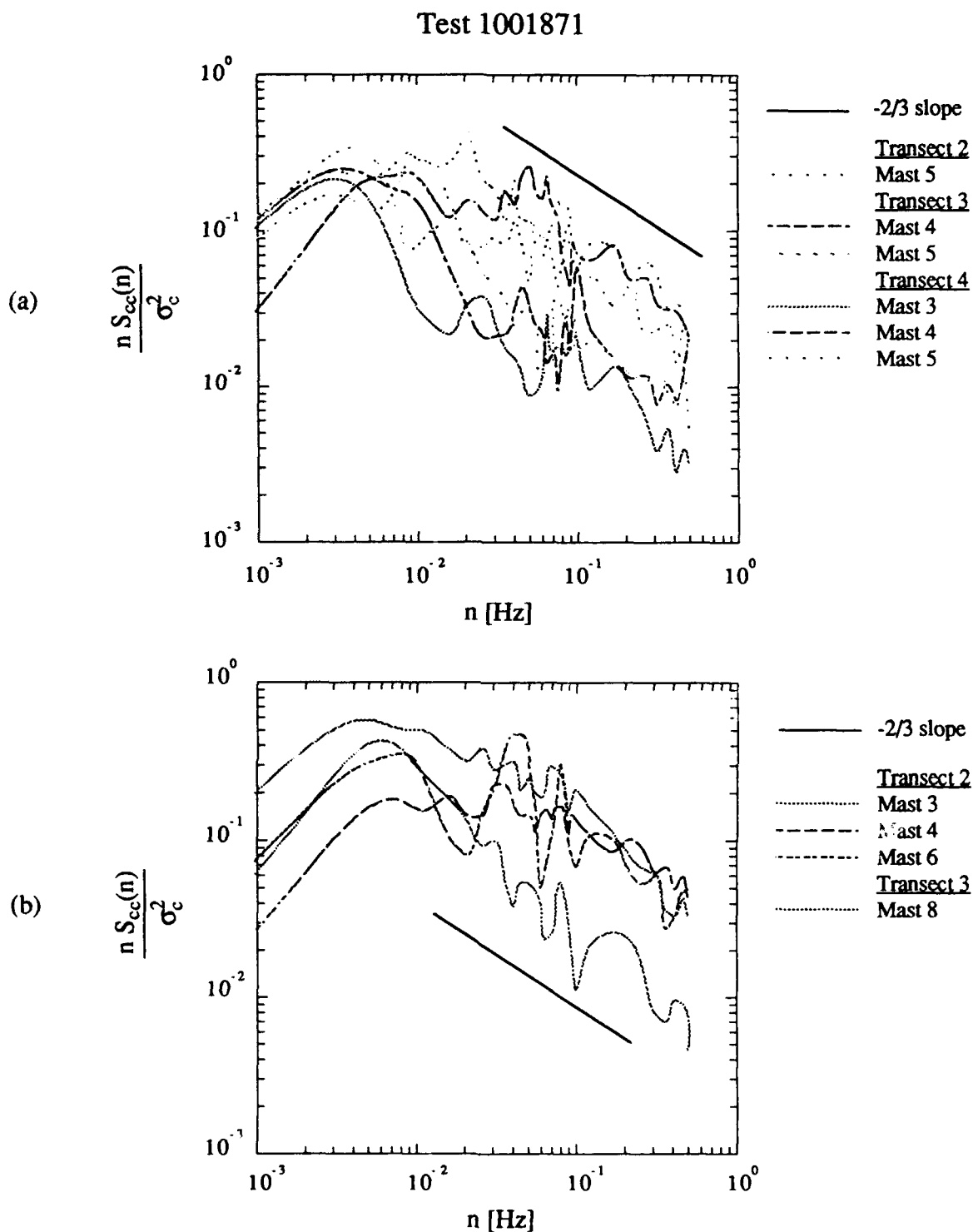


Figure 6.64 (continued) Spectra of the concentration variance for samplers located (a) near the source and (b) further downwind. This plot includes data from all samplers in Test 1001871 for which the mean signal exceeded five times the background noise of the instrument. The spectra were normalized by the calculated variance for each data record.

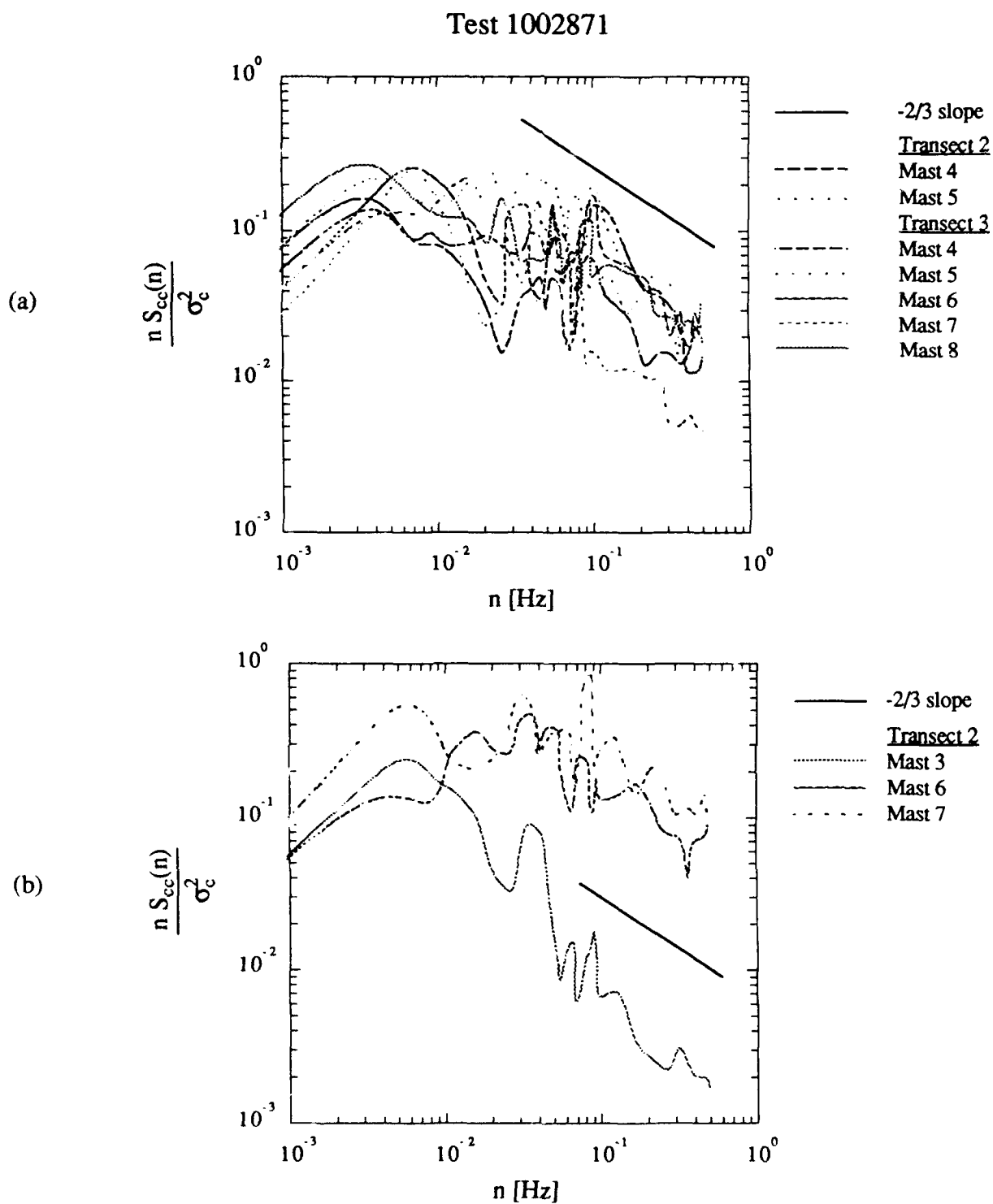


Figure 6.64 (continued) Spectra of the concentration variance for samplers located (a) near the source and (b) further downwind. This plot includes data from all samplers in Test 1002871 for which the mean signal exceeded five times the background noise of the instrument. The spectra were normalized by the calculated variance for each data record.



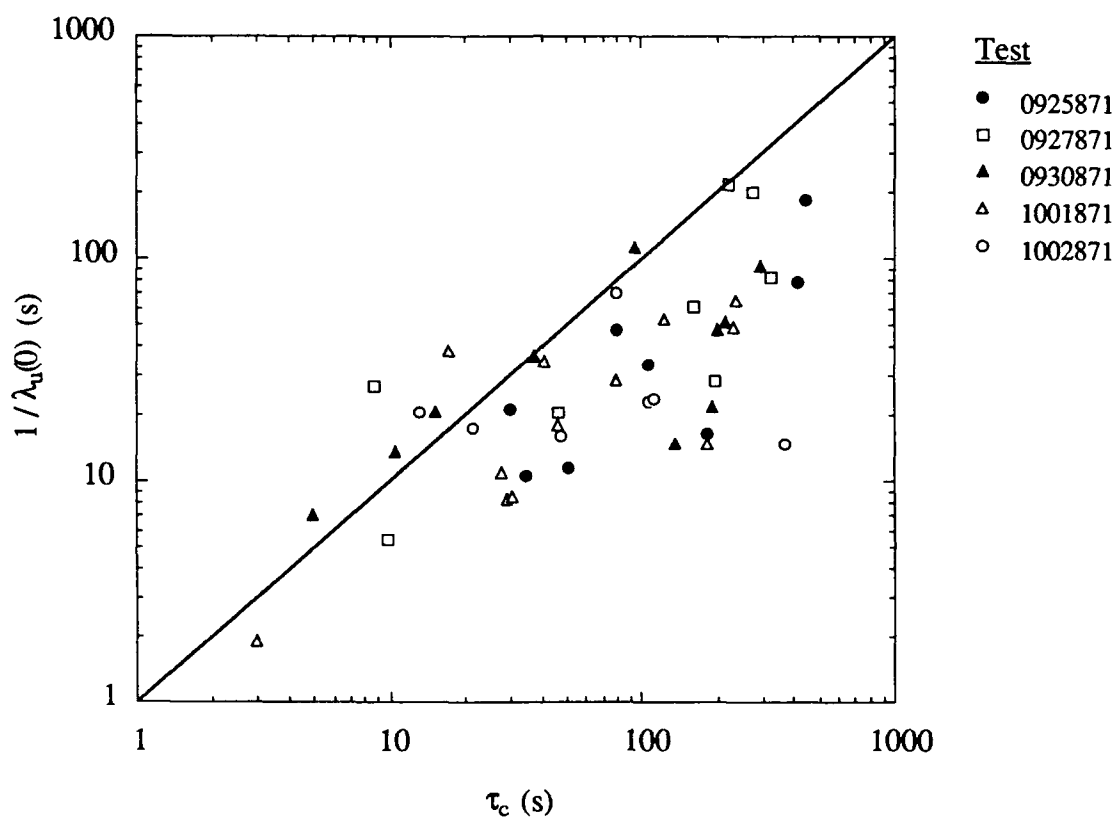


Figure 6.65 Duration of bursts in concentration with  $c > 0$ , versus the integral scale in concentration for the stable Meadowbrook smoke dispersion tests. This graph shows data from all samplers for which a reasonable integral scale could be found.

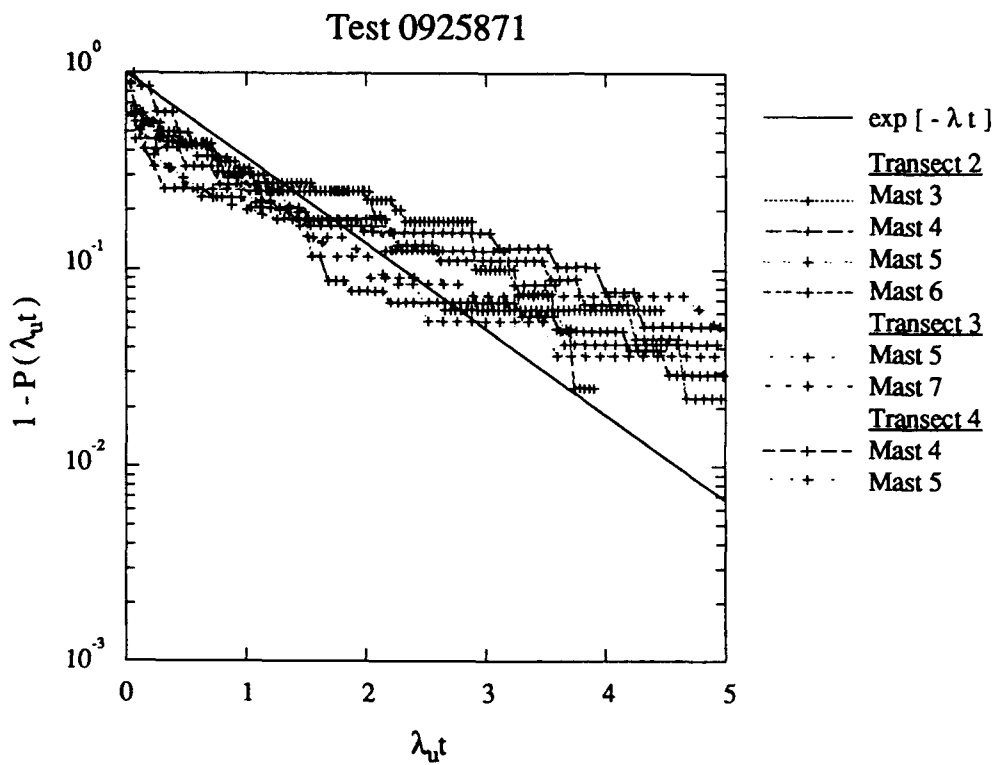


Figure 6.66 Histogram of time intervals for which the concentration exceeds zero for Test 0925871. Only data for which the average time interval is not biased by the sampling rate are included in the above plot.

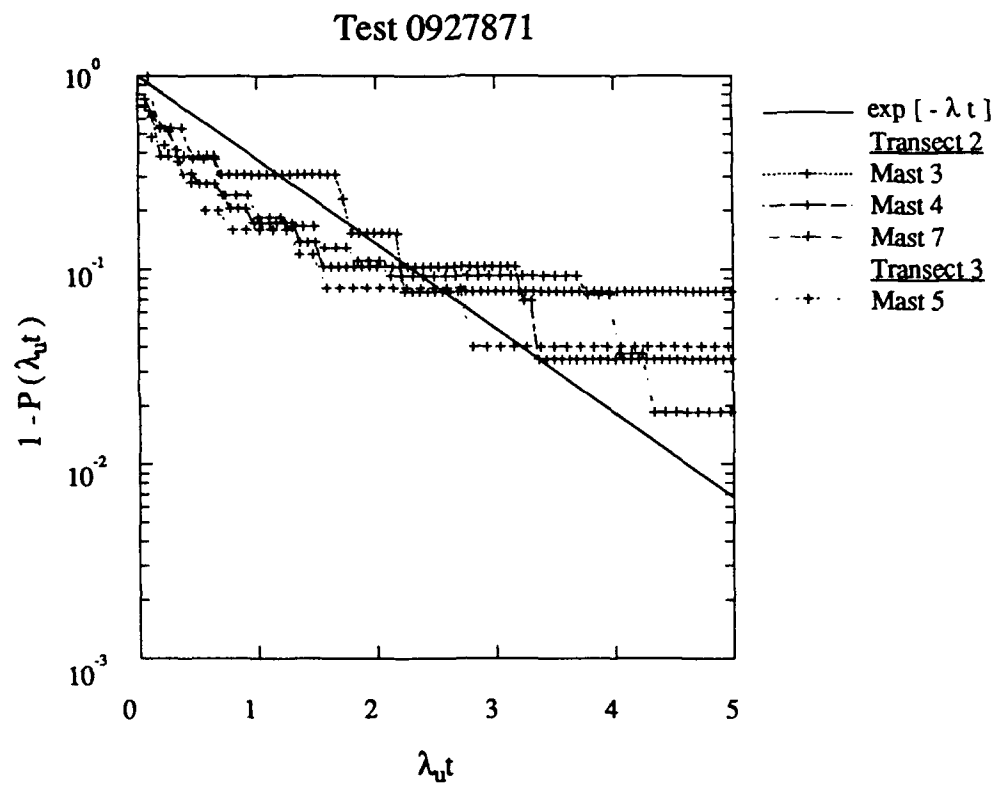


Figure 6.66 (continued) Histogram of time intervals for which the concentration exceeds zero for Test 0927871. Only data for which the average time interval is not biased by the sampling rate are included in the above plot.

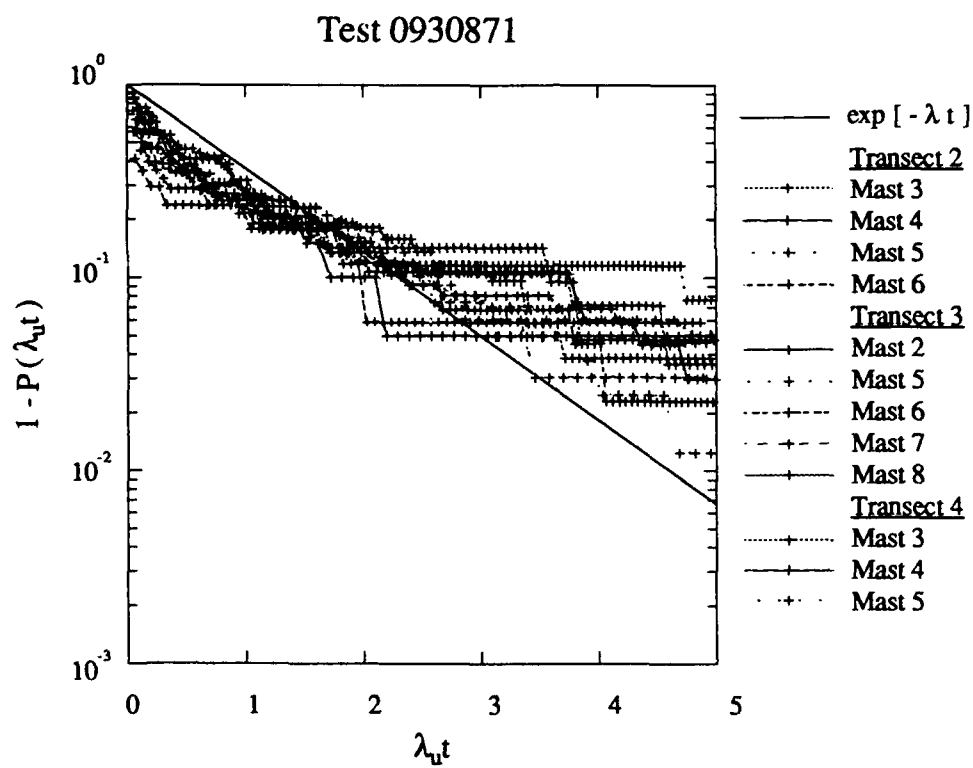


Figure 6.66 (continued) Histogram of time intervals for which the concentration exceeds zero for Test 0930871. Only data for which the average time interval is not biased by the sampling rate are included in the above plot.

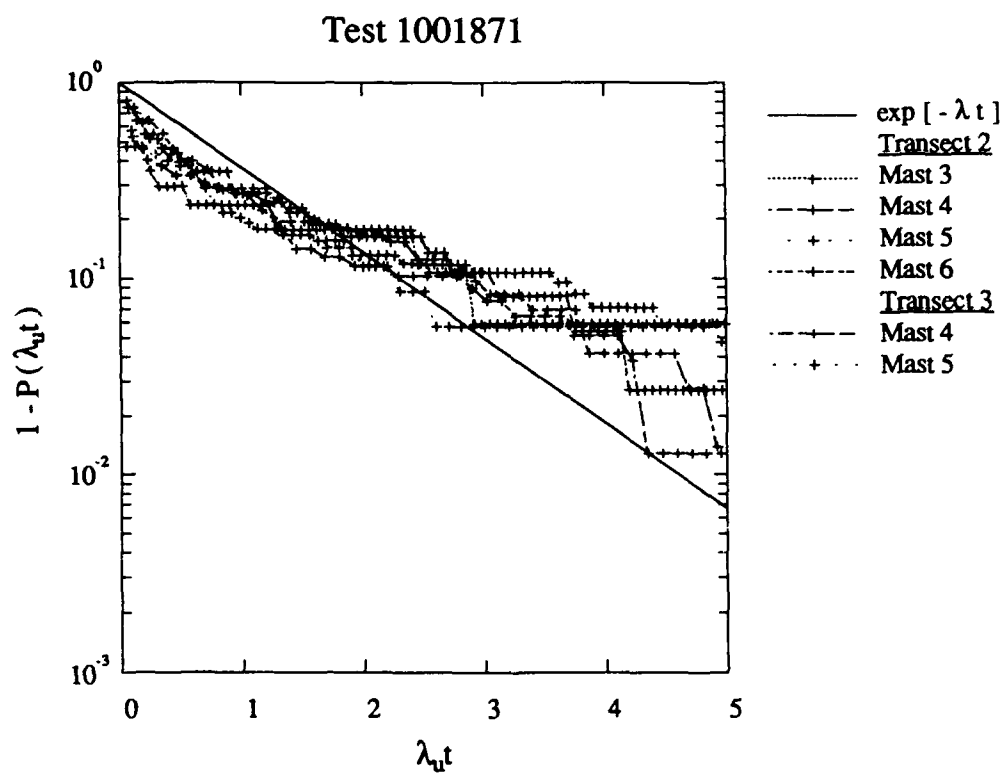


Figure 6.66 (continued) Histogram of time intervals for which the concentration exceeds zero for Test 1001871. Only data for which the average time interval is not biased by the sampling rate are included in the above plot.

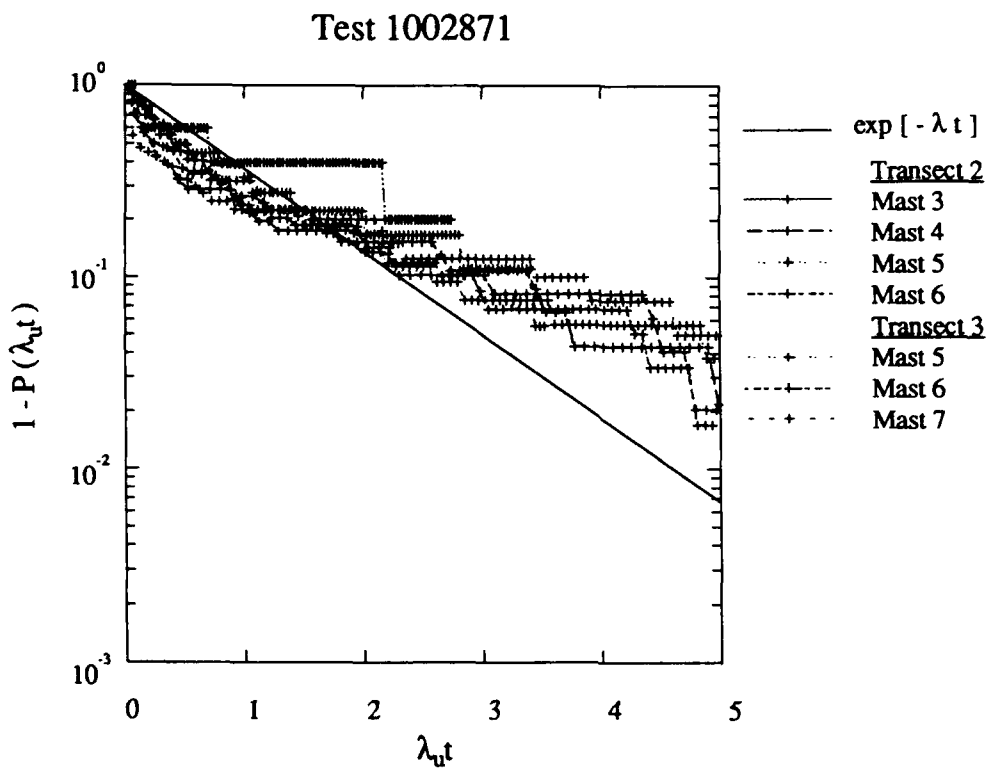


Figure 6.66 (continued) Histogram of time intervals for which the concentration exceeds zero for Test 1002871. Only data for which the average time interval is not biased by the sampling rate are included in the above plot.

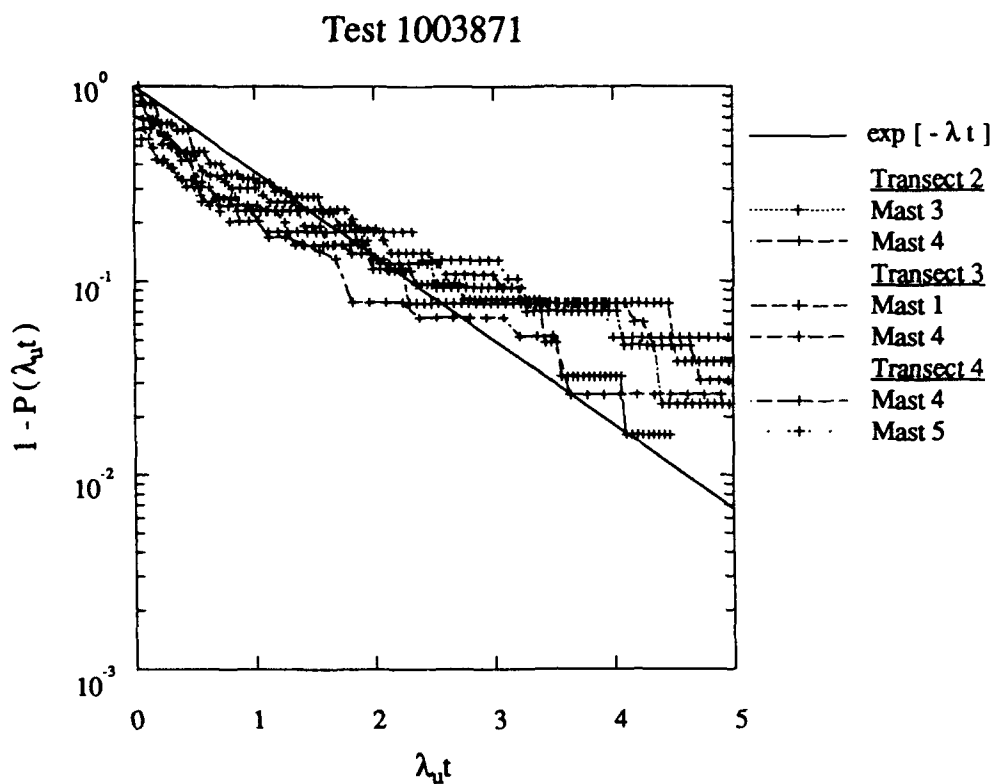


Figure 6.66 (continued) Histogram of time intervals for which the concentration exceeds zero for Test 1003871. Only data for which the average time interval is not biased by the sampling rate are included in the above plot.

Eq. 6.21. The data distributions in these plots are hyperexponential. This may be because of the limited bandwidth of the concentration data. Distributions which varied greatly from Eq. 6.21 are not shown in Figure 6.66. These distributions all had either very large values of  $1/\lambda_u(0)$ , so that the test duration was not long enough to collect sufficient data, or values of  $1/\lambda_u(0)$  of only several seconds, so that the 1-Hz sampling rate severely biased the data set.



## 7. EXAMINATION OF THE PRECISION IN THE DATA-MODEL COMPARISONS

We need to define confidence intervals for model-data comparisons and summarize the effective models for microscale atmospheric dispersion. In the analysis of many parameters we may examine the ratios of predicted values to measured values. For others a more detailed examination of the data is necessary. We first examine errors between the measured mean concentrations in comparison with several simple dispersion models. Parameters associated with the fluctuating concentration data are then compared with empirical models developed in this report. Finally, errors in the measured mean concentrations are examined along with predictions of expected maximum levels in concentration.

For this comparison we have sets of data from Camp Atterbury and the Meadowbrook site as analyzed in Chapter 6. The Atterbury tests used a fog-oil and HC smoke sources in unstable atmospheric conditions. The Meadowbrook tests were undertaken in both stable and unstable meteorological conditions using only the fog-oil smoke source.

### 7.1 Mean Concentrations

#### 7.1.1 The Field of Mean Concentration

The most direct comparison of the mean concentration data with models is on a point-by-point basis. For the data taken in our daytime tests we have two basic models. These are repeated here for convenience. The first is a Gaussian-plume model given by

$$\bar{c}(x,y) = \frac{q}{\pi \sigma_y \sigma_z \bar{u}_x} \exp\left(-\frac{y^2}{2 \sigma_y^2}\right) \quad (7.1)$$

with

$$\sigma_y = \frac{\sigma_v x}{\bar{u}_x} \left[ \frac{1}{1 + \sqrt{x / \bar{u}_x t_{L,y}}} \right] \quad (7.2)$$

and

$$\sigma_z = \frac{\sigma_w x}{\bar{u}_x} \left[ \frac{1}{1 + \sqrt{x / \bar{u}_x t_{L,z}}} \right] \quad (7.3)$$

with  $t_{L,y}$  and  $t_{L,z}$  both assumed to be 300 s from Gryning et al. (1987) and meteorological data taken over the test period. The second is a mixed-layer scaling model from Nieuwstadt (1980b) which may be written as

$$\bar{c}(x,y) = 0.9 \frac{q \sqrt{z_i}}{\sqrt{2\pi} \sigma_y \bar{u}_x} \left( \frac{\bar{u}_x}{w_* x} \right)^{3/2} \exp \left( -\frac{y^2}{2 \sigma_y^2} \right) \quad (7.4)$$

with  $\sigma_y$  given by Eq. 7.2.

We may calculate the correlation coefficient between each of the models and the data points for the mean concentration. This yields the information shown in Table 7.1. The overall average value is 0.82 for both models, indicating a strong relation between the model and data values. If the results of Test 1113871 are neglected, the average correlation coefficient rises to .87 for both model-data comparisons. The poor result for Test 1113871 was mostly due to the models' inaccurate prediction of the concentration on the first transect, which was caused by the use of the 10-m wind direction from the micrometeorological tower in the center of the sampling grid.

Table 7.1 Model-data correlation coefficients for mean concentrations in the unstable dispersion tests. The comparison is for data with  $-2\sigma_y < y < +2\sigma_y$  and  $\bar{c} > 0.01 \text{ mg/m}^3$ . The number of points which meet this criteria is indicated in the table. Each data value is compared with the model prediction for the same point and an average correlation coefficient is calculated for each test.

Test	Gaussian	Mixed	Number of points
1103871	0.81	0.81	19
1104872	0.82	0.81	26
1106871	0.96	0.96	25
1112871	0.89	0.90	19
1113871	0.46	0.47	18
0921871	0.80	0.80	12
0923871	0.91	0.90	18
0926871	0.90	0.89	15
Average/total	0.82	0.82	152

We may also compare the ratio of the model prediction to the measured mean value, which follows a lognormal distribution. The geometric mean  $\mu$  of the set of ratios is the average bias between the model and the data set. The width of the distribution of ratios is given by the geometric standard deviation  $\sigma_g$  which is always greater than one. On average, 68% of the data values will be within  $+\mu\sigma_g$  to  $-\mu/\sigma_g$  of  $\mu$ . This is an asymmetrical confidence interval. Since the average bias  $\mu$  is not always one, we find that 68% of the data points will be within a multiplier of  $\sigma_g \exp\{1$

$\ln(\mu) \pm 1\sigma_g$  of the model prediction and 95% of the data points will be within a factor of  $2\sigma_g \exp\{\pm \ln(\mu) \pm 1\sigma_g\}$  of the model prediction.

Calculated values of the geometric mean and the geometric standard deviation for this data set are given in Table 7.2. Also shown are factors for the model-data agreement using a confidence interval of 68%.

Table 7.2 Comparison of models to mean concentration data on a point by point basis. The geometric average ratio  $\bar{c}_{\text{model}}/\bar{c}_{\text{data}}$  between the model and data is given along with the geometric standard deviation of the distribution. The 68% confidence interval is a multiplicative factor.

Test	Gaussian model			Mixed-layer model		
	$\mu$	$\sigma_g$	68% C.I.	$\mu$	$\sigma_g$	68% C. I.
1103871	0.926	4.40	4.75	1.31	3.93	5.15
1104872	1.14	3.11	3.50	4.50	2.86	12.87
1106871	1.77	2.88	4.92	1.38	2.50	3.38
1112871	0.523	5.04	9.64	.874	3.62	4.14
1113871	0.796	4.29	5.38	1.02	4.20	4.28
0921871	1.64	2.77	4.54	1.26	1.98	2.49
0923871	3.87	3.81	14.65	1.42	3.19	4.53
0926871	1.43	3.39	4.85	0.645	3.33	5.16

Both models compare favorably with the data. Overall, the mixed-layer model yields slightly better predictions, especially when considering that the poor mixed-layer result for Test 1104871 is most likely a consequence of the near neutral conditions at the time of the test (see Table 4.1). Additional discrepancies between model predictions and data measurements may be due to inherent bias in the models, the stochastic nature of the data, or errors in the measurement of meteorological parameters. From a practical application standpoint the latter can be the most troubling, especially in complex terrain settings such as those for Tests 0921871, 0923871 and 0926871, where wind direction, roughness length, and surface-layer scaling parameters are rarely homogeneous. The method of analysis itself may contribute to apparently poor model performance when all data points are equally weighed. To improve the comparison we use other methods to predict a subset of the concentration distribution. In many cases the average dimensions of the plume, spatially averaged concentrations within the cloud, or centerline concentrations are of more interest than the absolute position of the field of mean concentration.

For the stable dispersion results we have no straightforward models of mean concentration for point-by-point comparisons because of the complex terrain-influenced flow in the winding valleys of the Meadowbrook test site. Some aspects of the dispersion in the stable tests is investigated in the following sections.

### 7.1.2 Mean Plume Dimensions and Parameters

#### Plume Width

For the crosswind plume width, we have several methods for prediction. The first is

$$\sigma_y = \sigma_v (x / \bar{u}_x) \quad (7.5)$$

which is the asymptotic limit for small travel times found by Taylor (1921). Gryning et al. (1987) gives an equation of the form

$$\sigma_y = \sigma_v (x/\bar{u}_x) \left[ 1 + \sqrt{\frac{(x/\bar{u}_x)}{2 t_{L,y}}} \right] \quad (7.6)$$

which asymptotically matches Taylor's theory for both small and large travel times. Using a ratio of measured to predicted values we have the geometric mean  $\mu$ , the geometric standard deviation  $\sigma_g$ , and multipliers for a 68% confidence interval as shown in Table 7.3.

These are quite reasonable predictions and confidence intervals. The average error factor is 1.37 using  $\sigma_v(x/\bar{u})$  and 1.62 using the more complicated expression from Gryning et al. (1987). We note that the stable test comparisons only includes data at distances less than 250 m, which is before the plume is significantly influenced by the winding valley.

#### Crosswind-Integrated Concentration

For our daytime dispersion tests, we examine a ratio of model predictions to measured crosswind integrated ground level concentrations. The Gaussian plume model is given by

$$\frac{\bar{c}_y \bar{u}_x}{q} = \sqrt{\frac{2}{\pi}} \frac{1 + \sqrt{(x/\bar{u}_x) / t_{L,z}}}{\sigma_w} \quad (7.7)$$

whereas the mixed-layer scaling is given by

$$\frac{\bar{c}_y \bar{u}_x}{q} = 0.9 \sqrt{z_i} \left( \frac{1}{w_*(x/\bar{u}_x)} \right)^{3/2} \quad (7.8)$$

The model-data ratios are shown in Figures 7.1 and 7.2 for our unstable tests as a function of a dimensionless mixed-layer travel time. The Gaussian plume model exhibits a trend with distance from the source which does not agree with the data. The mixed-layer model is in much better overall agreement with the data. Table 7.4 shows the errors calculated in each test for the mixed-

Table 7.3 Plume width model-data comparison. Agreement is close for all of our dispersion tests, including both stable and unstable cases.

Test	$\sigma_y / \sigma_v(x/\bar{u})$			Gryning data-model ratio		
	$\mu$	$\sigma_g$	68% C.I.	$\mu$	$\sigma_g$	68% C.I.
1103871	1.01	1.18	1.20	1.26	1.09	1.38
1104872	1.03	1.19	1.23	1.37	1.22	1.68
1106871	0.74	1.31	1.75	1.07	1.25	1.35
1112871	0.98	1.98	1.65	1.40	1.63	1.67
1113871	1.40	1.91	1.48	1.65	1.73	1.88
0921871	1.19	1.37	1.64	1.65	1.34	2.22
0925871	0.96	1.23	1.28	1.28	1.18	1.52
0927871	0.80	1.37	1.71	1.19	1.28	1.53
0930871	0.86	1.30	1.51	1.30	1.29	1.68
1001871	1.03	1.04	1.07	1.52	1.10	1.68
1002871	0.96	1.05	1.09	1.38	1.11	1.53
1003871	0.97	1.16	1.19	1.44	1.12	1.62

Table 7.4 Mixed-layer scaling comparison of model and data values.

Test	$\bar{c}_{y,mixed} / \bar{c}_y$	$\sigma_g$	68% C.I.
1103871	1.84	1.34	2.46
1104872	3.29	1.56	5.15
1106871	1.51	1.92	2.90
0921871	1.42	—	—
0923871	1.36	—	—
0926871	0.71	1.21	1.71
Averages			
Fog-oil tests	1.73	1.84	3.18
Nieuwstadt data	1.24	1.48	1.84

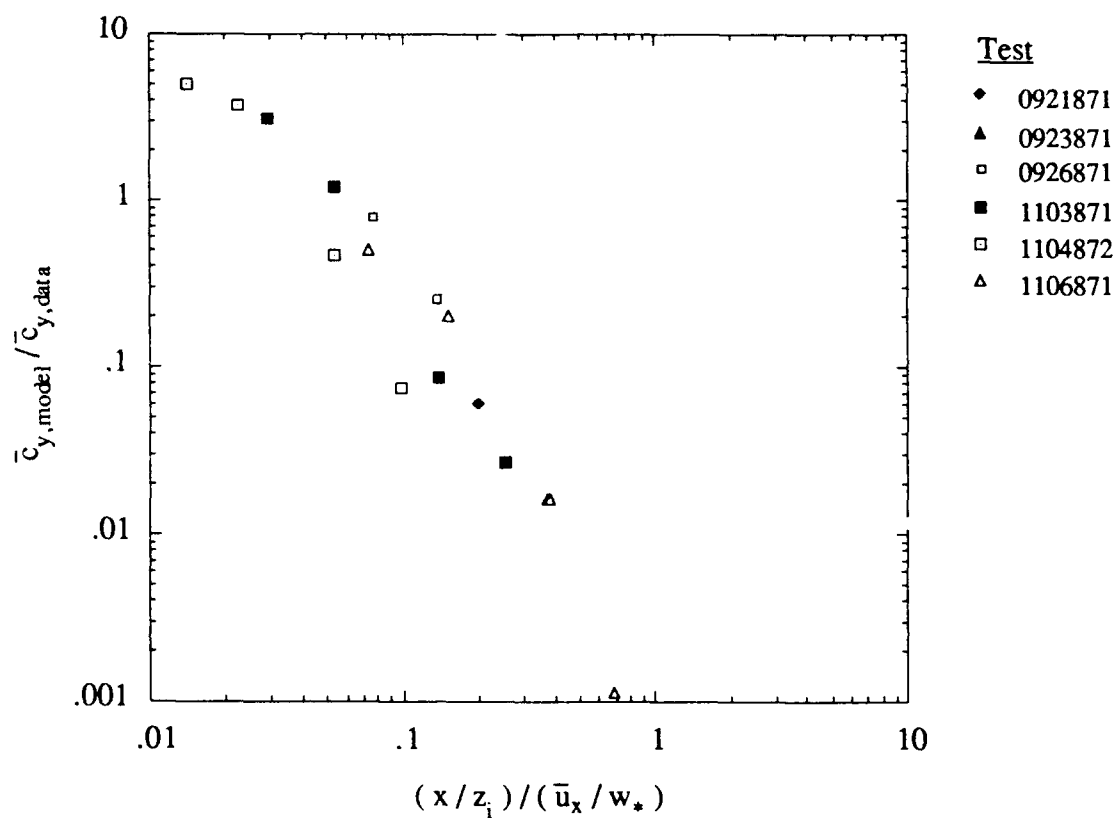


Figure 7.1 The ratio of predicted to measured crosswind integrated concentration using the Gaussian plume model. The values are presented as a function of a dimensionless downwind distance using mixed-layer scaling variables.

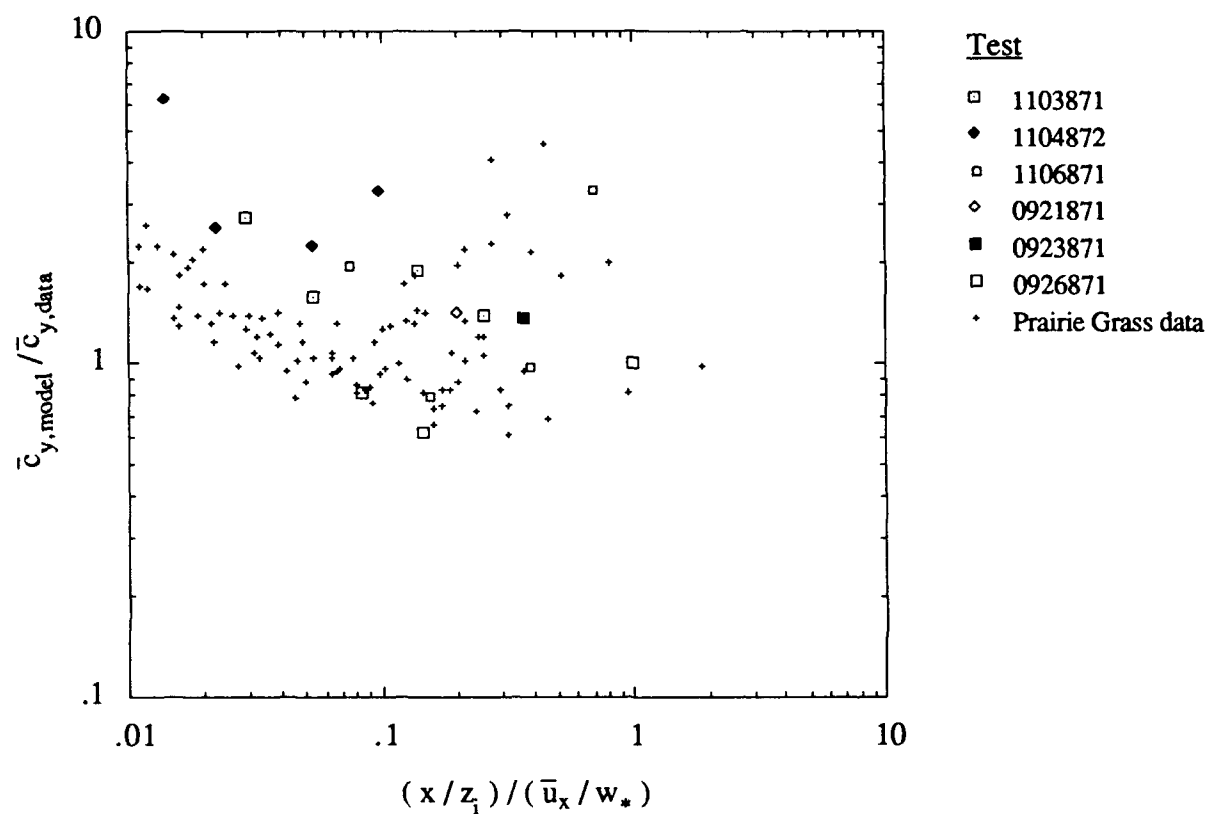


Figure 7.2 The ratio of predicted to measured crosswind integrated concentration using the mixed-layer scaling model from Nieuwstadt (1980b). The values are presented as a function of a dimensionless downwind distance.

layer model along with the same calculations for the Prairie Grass data used by Nieuwstadt (1980b) in developing the model. This comparison extends the applicability of the mixed-layer scaling to  $-z_i/L > 4.5$  from  $-z_i/L > 10$  for the data set used by Nieuwstadt.

The good agreement for the flat-terrain, mixed-layer model in the gently rolling terrain of the Meadowbrook dispersion site is encouraging. This may not be a general result, but instead could be due to the locally flat terrain near the unstable release point.

For our stable tests, no simple model is applicable because of the dominant terrain effects. By scaling these data with the expression  $\bar{u}_x c_y / q$  and using local values of the wind speed,  $\bar{u}_x c_y / q$  appears to be only a function of downwind distance. All measured values of  $\bar{u}_x c_y / q$  are within a factor of 3 of the overall average value at each downwind distance to 3000 m from the source. This average data fit is given by  $\bar{u}_x c_y / q = 3.4 x^{-3/4}$ , with  $x$  as the distance along the plume path.

### **Gaussian Mean Concentration Profile**

Also of interest is the shape of the crosswind profile. For crosswind scaling of the unstable dispersion tests within  $\pm 2y/\sigma_y$ , we find no bias in assuming a Gaussian shape. Measured values of  $\bar{c}(x, y/\sigma_y) / \bar{c}(x, y/\sigma_y = 0)$  are compared with

$$\frac{\bar{c}(x, y)}{\bar{c}(x, 0)} = \exp \left( -\frac{y^2}{2\sigma_y^2} \right) \quad (7.9)$$

in Table 7.5 for the individual dispersion tests. These values for the unstable tests are within a factor of 3.9 of the Gaussian profile for a 68% confidence interval. This indicates considerable random scatter in the data values but no bias in the Gaussian profile is evident.

For the tests conducted under stable conditions, a Gaussian profile is compared with measurements near the source for Transects 2 and 3. This is also shown in Table 7.5. We find considerable random error and bias in assuming a Gaussian profile for the data. This is most likely due to the change in surface character over the test grid.

## **7.2 Fluctuating Concentrations**

### **7.2.1 Intermittency and the Standard Deviation in Concentration**

We have examined our data set for factors such as the intermittency in concentration  $I$ , and the concentration fluctuation intensity  $\sigma_c / \bar{c}$ . In terms of the crosswind scaling  $y/\sigma_y$ , these values are given by



Table 7.5 Gaussian-plume shape scaling.

Test	$\mu$	$\sigma_g$	68% C.I.
Unstable			
1103871	1.164	2.99	3.48
1104872	1.181	1.96	2.32
1106871	1.327	2.69	3.58
0921871	1.089	2.38	2.60
0923871	1.846	1.77	3.28
0926871	1.343	2.06	2.77
Stable			
0925871	0.532	3.48	6.54
0927871	0.285	3.33	11.64
0930871	0.272	11.05	40.53
1001871	0.199	8.95	44.80
1002871	0.111	5.74	51.30

$$\frac{\sigma_c}{\bar{c}} = \alpha \exp \left( \frac{y^2}{4 \sigma_y^2} \right) \quad (7.10)$$

and

$$I = \left[ \alpha^2 \exp \left( \frac{y^2}{2 \sigma_y^2} \right) + 1 \right]^{-1} \quad (7.11)$$

with  $\alpha$  as an empirical parameter.

For  $\sigma_c/\bar{c}$  and  $I$ , measured values are compared with the model predictions in Table 7.6. For all tests the  $\sigma_c/\bar{c}$  data is within a factor of 3.3 of the predicted value and  $I$  is within a factor of 3.8. This includes the HC tests because both  $\sigma_c/\bar{c}$  and  $I$  are completely characterized by the aerosol photometer measurements. This is an optimization of the  $\alpha$  parameter in each test for both Eqs. 7.10 and 7.11.

The intermittency can also be estimated as a function of the fluctuation intensity  $\sigma_c/\bar{c}$  through

$$I = \frac{2}{\left( \frac{\sigma_c}{\bar{c}} \right)^2 + 1} \quad (7.12)$$

Table 7.6 Concentration fluctuation intensity. All data are for  $y < \pm 2\sigma_y$ .

Test	$[\sigma_c/\bar{c}]_{\text{measured}} / [\sigma_c/\bar{c}]_{\text{model}}$			$I_{\text{model}}/I_{\text{data}}$		
	$\mu$	$\sigma_g$	68% C.I.	$\mu$	$\sigma_g$	68% C.I.
Unstable						
0921871	0.73	1.47	2.00	0.72	2.01	2.78
0923871	0.42	1.95	4.66	0.54	3.80	7.02
0926871	0.55	1.99	3.62	0.50	2.50	5.04
1103871	0.72	1.94	2.70	0.45	1.76	3.89
1104872	0.58	1.86	3.20	0.91	2.03	2.23
1106871	0.53	1.84	3.45	1.00	1.76	1.76
1112871	0.59	2.20	3.76	0.80	2.18	2.73
1113871	0.49	2.16	4.39	1.53	2.74	4.19
Stable						
0925871	0.59	1.97	3.32	0.62	3.08	4.99
0927871	0.67	2.02	3.01	0.32	3.12	9.88
0930871	0.52	2.11	4.08	0.75	7.69	10.22
1001871	0.39	1.49	3.86	0.72	3.86	5.37
1002871	0.58	1.85	3.18	0.77	2.00	2.59
Average for all tests	0.57	1.91	3.34	0.74	2.79	3.76

The error in the ratio of predicted to measured values of  $I$  are given in Table 7.7. This error is much less than predictions of  $I$  based on  $y/\sigma_y$  and results in an average 68% confidence interval factor of only 1.41. This agreement is a test of the validity of the probability distribution for concentration on which Eq. 7.12 is based.

We may also test the model of the concentration probability distribution by examining the ratio of conditional standard deviation concentration  $\sigma_{c,s}$  to the conditional mean concentration  $\bar{c}_s$ . Both measures include only data for which  $c > 0$ . For each test the average value of this ratio, which should be unity, is given in Table 7.7. This value, however, is always smaller because of the underestimate in  $\sigma_{c,s}$  caused by the finite bandwidth of the instrument and clipping of the concentration signal. A Chi-square test on the fit of the data histogram to the exponential distribution given by

$$P(c) = 1 - I \exp\left(-\frac{Ic}{\bar{c}}\right) \quad (7.13)$$

Table 7.7 Intermittency errors and conditionally averaged data ratios.

Tests	$I(\sigma_c/c)_{\text{model}}/I_{\text{data}}$			$\sigma_{c,s}/\bar{c}_s$		
	$\mu$	$\sigma_g$	68% C.I.	$\mu$	$\sigma_g$	68% C.I.
Unstable						
0921871	0.99	1.32	1.34	0.88	1.66	1.89
0923871	1.44	1.18	1.69	0.73	1.48	2.02
0926871	1.18	1.16	1.37	0.86	1.27	1.48
1103871	1.09	1.30	1.41	0.87	1.38	1.58
1104872	1.18	1.23	1.44	0.76	1.48	1.95
1106871	0.98	1.21	1.24	0.93	1.30	1.39
1112871	1.04	1.20	1.25	0.98	1.23	1.26
1113871	1.14	1.25	1.42	0.83	1.40	1.70
Stable						
0925871	0.95	1.29	1.36	0.83	1.49	1.81
0927871	1.21	1.41	1.70	0.80	1.66	2.09
0930871	1.05	1.28	1.35	0.79	1.42	1.81
1001871	1.00	1.39	1.39	0.89	1.32	1.49
1002871	1.34	1.18	1.58	0.65	1.27	1.96

always yields a greater than 95% confidence interval for each record of concentration when the clipped region of the distribution for large  $c/\bar{c}$  is neglected.

### 7.2.2 Temporal Measures of the Concentration Fluctuations

We have assumed the integral scale of concentration measured at a point is a constant in a given dispersion test. In examining the set of values found within a test, no correlation between the concentration integral scale and spatial position is evident. The individual values do show considerable scatter. For the unstable dispersion tests, using the ratio of  $(\tau_{c,i} - \tau_c)/\tau_c$  with the test average given by  $\tau_c$  and individual sampler values indicated by  $\tau_{c,i}$  gives a standard deviation for the entire unstable data set of 0.51. Our limited duration experiments and the high fluctuation intensity in the concentration records are partly responsible for the scatter in the set of integral scale values. Determining the true spatial variation in the integral scale requires a more complete and precise data set than we have acquired.

The variation in  $\tau_c$  with differing, unstable atmospheric conditions is shown in Figure 7.3. This shows that  $\tau_c$  increases with increasing instability. This increase is consistent with the shift in the velocity spectra to lower frequencies as shown by Højstrup (1982). The error bars in this graph indicate the scatter in the set of  $\tau_{c,i}$  values in each test.

The integral scales of concentration found in our stable dispersion tests are inhomogeneous in individual tests. Variation in  $\tau_{c,i}$  is likely due in part to the changing surface character of the dispersion site. For samplers located in the open area of the test grid, the integral scale is relatively constant. For the samplers located within an area of forest canopy, the integral scale is considerably greater.

We have shown that the concentration integral scale  $\tau_{c,i}$  is approximately equal to the average burst duration  $1/\lambda_u(0)$  for the same sampler. This is a relation between two different measured quantities. The integral scale is derived from the autocorrelation of the signal. The average burst duration is found from a conditional analysis of the concentration record for the duration of events with  $c > 0$ . Both quantities are only a weak function of spatial position. The error in this approximation is shown in Table 7.8 for all of our dispersion tests.

We also have the relation  $1/\lambda_u(0) = I [1/\lambda]$ . This equates the average burst duration  $1/\lambda_u(0)$  to the product of concentration intermittency  $I$  and the duration between burst events  $1/\lambda$ . Both  $1/\lambda$  and  $I$  are functions of the crosswind position  $y/\sigma_y$ . The error in this ratio is given in Table 7.8 for each dispersion test.

Although we cannot easily calculate the expected error in the integral scale  $\tau_{c,i}$ , we know  $\tau_{c,i} \sim 1/\lambda_u(0)$ , and we can estimate errors in  $1/\lambda_u(0)$ . This value indicates the average of a set of time intervals for which  $c > 0$ . The probability density function of these intervals is given by

$$p(t) = \lambda_u(0) \exp [-\lambda_u(0) t] \quad (7.14)$$

which has a mean of  $1/\lambda_u(0)$  and a variance  $(1/\lambda_u(0))^2$ . If each of these time intervals is uncorrelated with other intervals, estimates of the mean value  $1/\lambda_u(0)$  taken over a long time period should be normally distributed. The error in this mean is given by

$$\sigma_{\frac{1}{\lambda_u}}^2 = \frac{1}{N} \sigma_{(1/\lambda_u)}^2 \quad (7.15)$$

with  $N$  as the number of events in the sampling period  $T$ . This is given by

$$N = \frac{T}{(1/\lambda)} = \frac{T}{(1/\lambda_u(0))/I} \quad (7.16)$$

where  $(1/\lambda)$  is the average duration between events and  $(1/\lambda_u(0))$  is the event duration.

Substituting the mean, variance and Eq. 7.16 into Eq. 7.15 gives

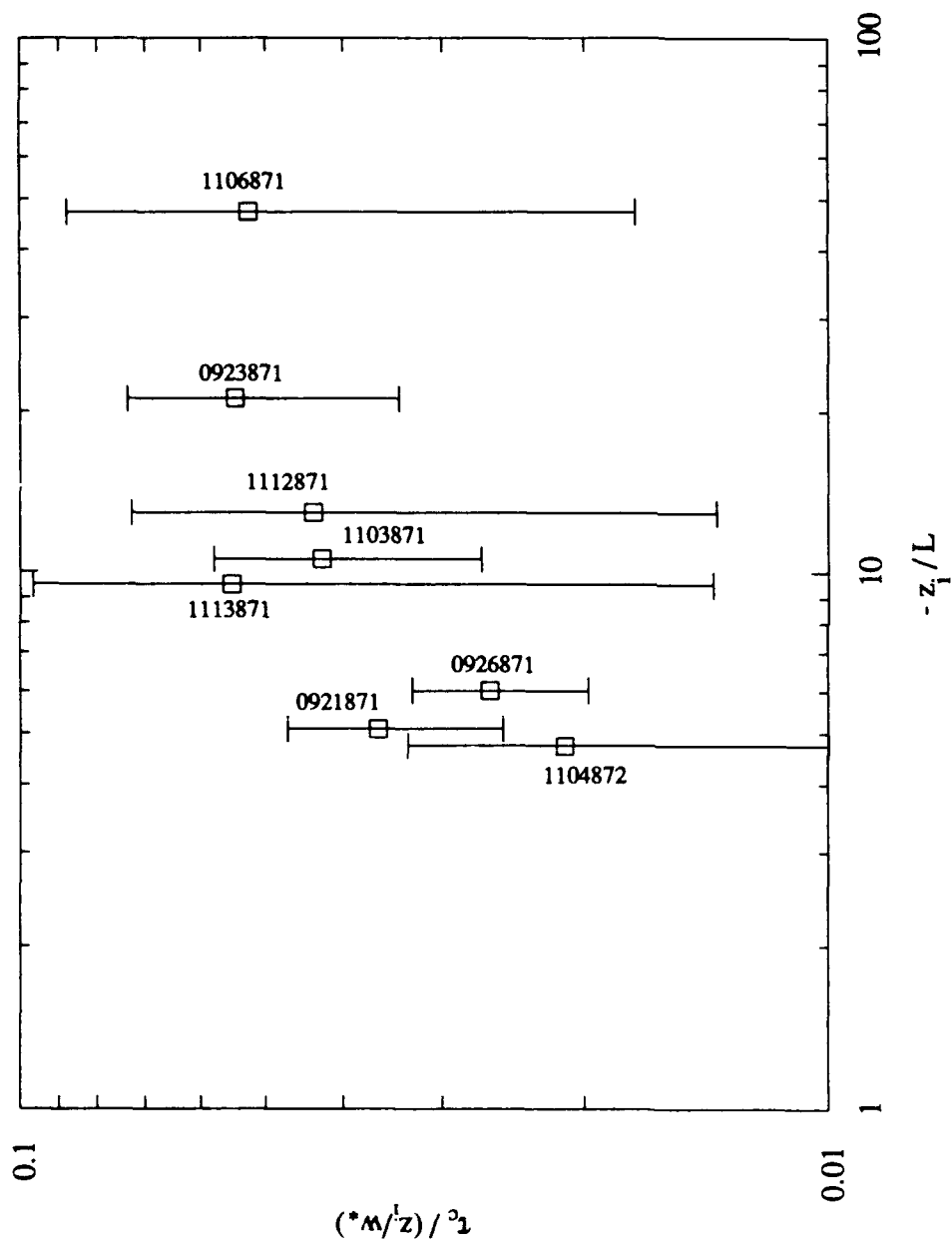


Figure 7.3 Stability parameter versus the integral scale of concentration. An average value of the integral scale is taken for each test. The error bars show one standard deviation in the set of integral scales measured in each test.

Table 7.8 Comparison of the integral scale and the mean burst durations.  $I > 0.1$  and  $|y| < 2\sigma_y$  for all data in this table. The first comparison is the ratio of the integral scale of concentration to the average duration of periods of time for which  $c > 0$ . The second comparison examines the relationship between the average duration of the periods of time for which  $c > 0$ , the period between these events, and the intermittency.

Test	$\tau_{c,i} / (1/\lambda_u(0))$			$[1/\lambda] I / [1/\lambda_u(0)]$		
	$\mu$	$\sigma_g$	68% C.I.	$\mu$	$\sigma_g$	68% C.I.
Unstable						
0921871	1.44	1.57	2.26	0.74	1.10	1.49
0923871	1.55	1.24	1.93	0.79	1.11	1.39
0926871	1.33	1.12	1.50	0.84	1.06	1.27
1104872	1.47	1.47	2.15	0.71	1.34	1.89
1106871	1.50	1.67	2.51	0.82	1.23	1.51
1112871	1.22	1.71	2.08	0.82	1.18	1.44
1113871	1.75	2.44	4.27	0.80	1.05	1.30
Unstable average	1.41	1.57	2.21	0.79	1.19	1.51
Stable						
0925871	0.51	2.70	5.26	0.70	1.22	1.74
0927871	0.70	2.50	3.60	0.25	3.44	13.65
0930871	0.46	2.45	5.37	0.56	1.43	2.56
1001871	0.43	2.40	5.58	0.58	1.28	2.22
1002871	0.39	3.03	7.85	0.60	1.29	2.14
1103871	1.18	1.67	1.96	0.85	1.08	1.27
Stable average	0.47	2.57	5.52	0.53	1.84	3.47

$$\frac{\sigma_{(1/\lambda_u(0))}}{[1/\lambda_u(0)]} = \sqrt{\frac{(1/\lambda_u(0))}{T I}} \quad (7.17)$$

for the relative error. Calculations using the measured experimental data gives an average value for this relative error of  $0.13 \pm 0.04$  for data within  $\pm 2y/sy$ . This error is consistent throughout each of the tests. It is also smaller than the spatial variation in average burst durations found in a given test.

### 7.3 Standard Deviation in Time Averaged Mean Concentrations

There is an inherent error between a true mean and a measured or predicted mean. With the information just presented, we are able to estimate the confidence interval for our own measured mean concentrations using

$$\frac{\sigma_{\bar{c}}}{\bar{c}} = \frac{\sigma_c}{\bar{c}} \left( \frac{T}{2 \tau_c} \right)^{-1/2} \quad (7.18)$$

from Bendat and Piersol (1971) with the total sampling time  $T > \tau_c$ . Results of these calculations are given in Table 7.9. These resulting values of  $\sigma_{\bar{c}}/\bar{c} \sim 1$  the presence of significant errors in a mean value measurements. Because of the approximately one hour limitation for our quasi-stationary microscale analysis, and the consistently large values of  $\tau_c/T$  and  $\sigma_{\bar{c}}/\bar{c}$ , we will always have a severe constraint on the precision of both mean concentration data and models predictions.

Table 7.9 Errors in the mean concentrations measured in the dispersion tests. Actual values of the test duration, fluctuation intensity, and integral scales are used to find  $\sigma_{\bar{c}}/\bar{c}$ .

Test	Maximum	Mean	$\sigma$ of $\sigma_{\bar{c}}/\bar{c}$
Unstable			
0921871	1.78	1.01	0.55
0923871	2.52	1.08	0.80
0926871	2.24	0.93	0.74
1103871	0.33	0.21	0.08
1104872	1.17	0.44	0.24
1106871	0.67	0.37	0.15
1112871	0.95	0.39	0.28
1113871	1.13	0.59	0.40
Stable			
0925871	5.48	1.07	1.36
0927871	1.08	0.52	0.40
0930871	4.89	0.89	1.09
1001871	1.27	0.72	0.29
1002871	2.10	0.75	0.59

## 7.4 Confidence Level Predictions

In hazard estimates it is desirable to predict a concentration level which has a given probability of being exceeded rather than just the mean concentration. In practical applications these particular concentration levels may be threshold levels for biological damage or explosive limits for combustible gases. Using the exponential probability distribution given by

$$P(c) = 1 - I \exp\left(-\frac{Ic}{\bar{c}}\right) \quad (7.19)$$

and the model for I given by

$$I = 2 \left[ \alpha^2 \exp\left(\frac{y^2}{2\sigma_y^2}\right) + 1 \right]^{-1} \quad (7.20)$$

we find

$$\frac{c_\xi(x,y)}{\bar{c}(x,y)} = \ln \left[ \frac{1}{2} (P(c_\xi) - 1) \left\{ \alpha^2 \exp\left(\frac{y^2}{2\sigma_y^2}\right) + 1 \right\} \right] \left[ \frac{\alpha^2}{2} \exp\left(\frac{y^2}{2\sigma_y^2}\right) + \frac{1}{2} \right] \quad (7.21)$$

Using a value for  $P(c_\xi) = \xi$  in the range of  $1-I < P(c_\xi) < 1$ , and a valid model for the mean concentration  $\bar{c}(x,y)$ , we can find the field of concentration  $c_\xi(x,y)$  which has a given probability of being exceeded.

For  $\xi = 0.99$ , experimentally measured values of  $c_{99}(x,y)/\bar{c}(x,y)$  in our dispersion tests are plotted with the model of Equation 7.21 in Figure 7.4. Two plots are given, one each for the unstable and stable dispersion tests. In these plots, the parameter  $\alpha$  is estimated from a fit of the concentration fluctuation intensity data. Errors in the values of  $c_{99}(x,y)/\bar{c}(x,y)$  found in this comparison are summarized in Table 7.10. On average, the data taken under unstable conditions is within a factor of 2.5 of the model value. The stable test values are within a factor of 3.2 of the predicted values. We note that the overall average value of  $c_{99}(x,y)/\bar{c}(x,y)$  from the data is 15. This shows there is a significant difference between mean concentrations and expected maximum concentrations.



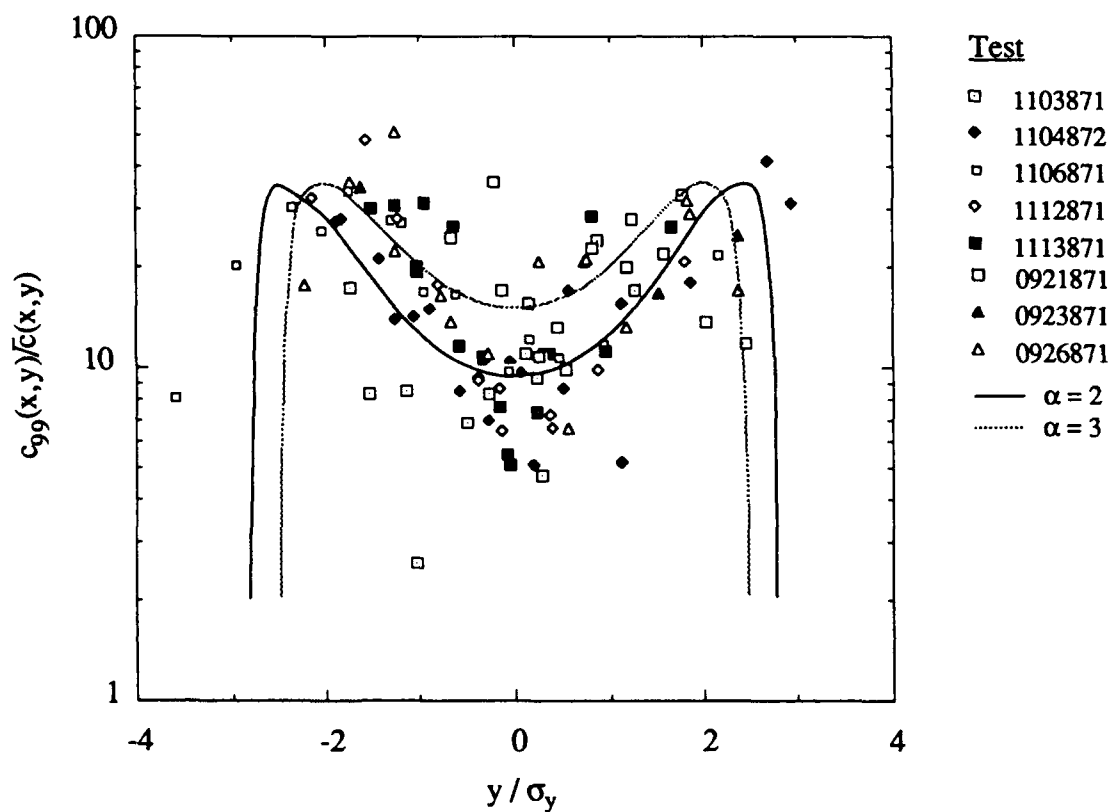


Figure 7.4 Comparison of concentration levels for which  $P(c) = 0.99$  with model predictions given in Eq. 7.21 for the unstable dispersion data. The 99th percentile concentrations are scaled by the mean concentrations.

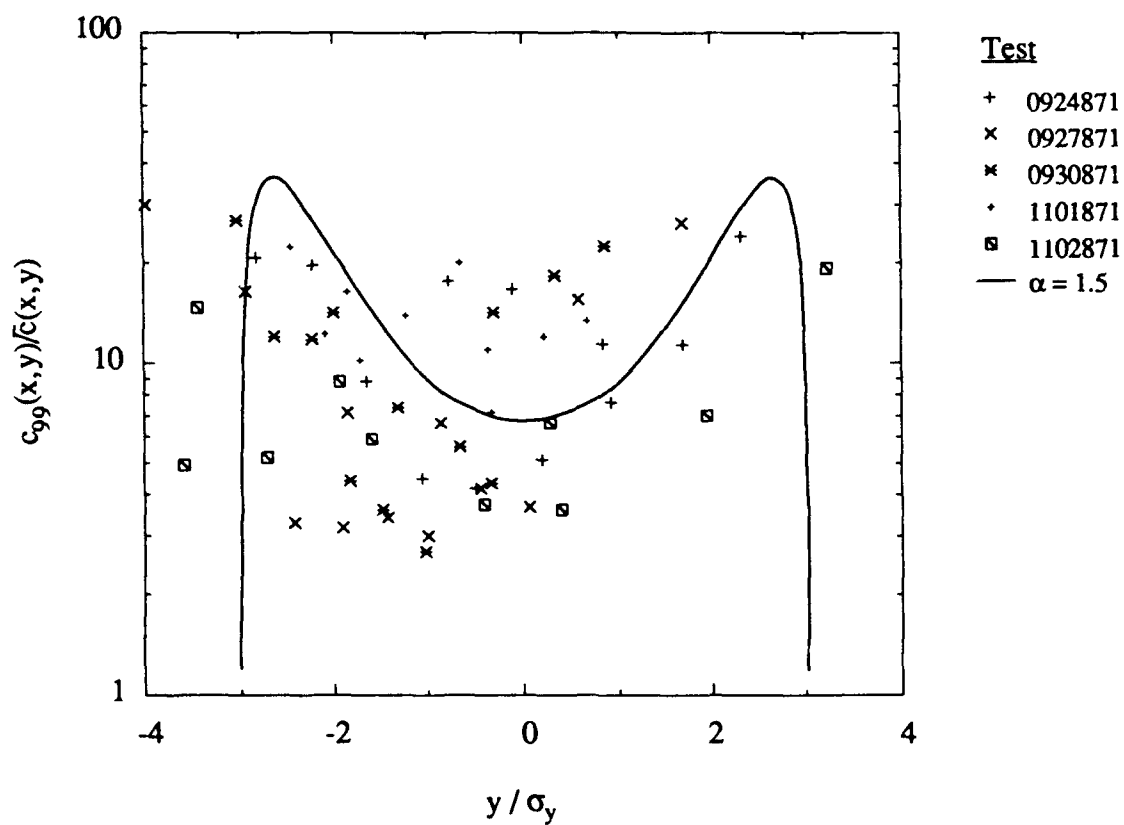


Figure 7.4 (continued) Comparison of concentration levels for which  $P(c) = 0.99$  with model predictions given in Eq. 7.21 for Transects 2 and 3 in the Meadowbrook stable dispersion tests. The 99th percentile concentrations are scaled by the mean concentrations.

Table 7.10 Errors in the ratio of measured to predicted  $c_{99}$  for the dispersion tests.

Test	$c_{99}(x,y)/\bar{c}(x,y)$		
	$\mu$	$\sigma_g$	68% C.I.
1103871	0.46	1.83	3.97
1104872	0.57	1.45	2.56
1106871	0.76	1.23	1.62
1112871	0.55	1.30	2.36
1113871	0.59	1.43	2.41
0921871	1.19	1.73	2.06
0926871	1.13	1.70	1.92
Unstable average	0.69	1.70	2.48
0925871	0.92	1.77	1.93
0927871	0.50	2.55	5.06
0930871	0.59	2.20	3.71
1001871	1.04	1.60	1.66
1002871	0.42	1.77	4.18
Stable average	0.66	2.13	3.22

## 7.5 Empirical Concentration Model Summary

For our unstable dispersion tests, we have found mean crosswind-integrated concentrations to agree with the mixed-layer model given by Nieuwstadt (1980b). This is given by

$$\frac{\bar{c}_y \bar{u}_x}{q} = 0.9 \sqrt{z_i} \left( \frac{1}{w_*(x/\bar{u}_x)} \right)^{3/2} \quad (7.22)$$

Our data cover a range in stability of  $-4.5 > z_i/L > -45$  and  $(x/z_i)/(\bar{u}_x/w_*) < 1$ . The source in these tests was between 1 to 2 m above the surface. Mean concentration measurements were made at heights of 1 to 8 m above the surface. No definite gradient in mean concentration is seen over this

range in sampling heights. Model values of  $\bar{c}_y$  are within a factor of 3.2 of the measured concentrations for a 68% confidence interval. Plume widths are best represented by

$$\sigma_y = \sigma_v (x / \bar{u}_x) \quad (7.23)$$

with  $\sigma_v/\bar{u}_x$  taken as an average over the test. Model values are within a factor of 1.4 of the data values using this equation with a 68% confidence interval. The plume centerline concentration is given by

$$\bar{c}(x, y=0) = \frac{\bar{c}_y(x)}{\sqrt{2\pi} \sigma_y} \quad (7.24)$$

If small errors in the absolute position of the centerline are accepted, measured centerline concentrations will be within a factor of  $3.2 \times 1.4 = 4.5$  of the measured value for a 68% confidence interval, or within a factor of 9 for a 95% confidence interval.

Our stable dispersion tests were strongly influenced by the local terrain. It is unlikely that the mean concentration values in these tests have general applicability to other dispersion sites. We have, however, found that the near-field plume width at distances less than 250 m is adequately represented by  $\sigma_y = \sigma_v (x/\bar{u}_x)$ , and the crosswind-integrated concentration is fitted by  $\bar{u}_x c_y/q = 3.4 x^{-3/4}$  within a factor of 3 for a 68% confidence interval over the entire 3000 m of plume travel. Other results for fluctuating data in the stable tests which are normalized by the mean concentration values may have a more general application than the mean concentration field alone.

The large scatter between mean concentration values and model predictions is due to the error inherent in mean concentration measurements and predictions, where we have found  $\sigma_y/\bar{c} \sim 1$  for one hour dispersion tests. This poses limitations on using mean concentrations for hazard estimates from accidental releases of toxic materials or pollutants. Predictions of a concentration field with a set probability  $P(c_\xi) = \xi$  of being exceeded may be made using

$$c_\xi = \ln \left[ \frac{1}{2} (P(c_\xi) - 1) \left\{ \alpha^2 \exp \left( \frac{y^2}{2\sigma_y^2} \right) + 1 \right\} \right] \frac{\bar{c}(x,0)}{2} \left[ \alpha^2 + \exp \left( -\frac{y^2}{2\sigma_y^2} \right) \right] \quad (7.25)$$

for the distribution of  $c_\xi$ . The centerline concentration  $\bar{c}(x,0)$  and plume width  $\sigma_y$  are found from the above model equations. The parameter  $\alpha = \sigma_c(x,0)/\bar{c}(x,0)$  was found to vary between 1.5 to 3 for our tests, with the larger value applying in more unstable conditions and the smallest value applying in stable conditions. For relative ratios of  $c_\xi(x,y)/\bar{c}(x,y)$  this model has agreed with the data within a factor of 3.2 for a 68% confidence interval at the  $\xi = 99\%$  level. Since this is a smaller margin of error than for the mean concentration itself, this equation may be used directly, with a safety factor applied only to the mean centerline concentration  $\bar{c}(x,0)$ .

Another possible significant error in the exceedance level model is added through the variability in the direction of the mean wind. This variability should be included in the estimate of the hazardous area, rather than just including the isopleths in  $c_\xi$  predicted by Eq. 7.25. Based on

information from the Federal Emergency Management Agency (1989) and Hanna et al. (1982) we have a 90% confidence interval that a plume will remain within a  $120^\circ$  arc for unstable cases, or within a  $40^\circ$  arc for stable conditions. This criteria, along with centerline predictions of  $c_x$  from Eq. 7.25 can be used in a hazard prediction model. Longer term releases should include even greater arc widths, determined through a study of the site meteorology. For light and variable winds, it may be necessary to include a circumferential area about the source location.

## 8. CONCLUSIONS

A great number of microscale atmospheric dispersion measurements and models have focused on the behavior of mean concentrations. With the use of proper modeling techniques unbiased estimates of mean concentration can be made, but a large variability is always seen between predicted and observed values.

We have carried out a number of atmospheric dispersion measurements which included measurements of the instantaneous concentration field. Reduction of these data has shown values of concentration fluctuation intensity of  $\sigma_c/\bar{c}$  in the range of 1.5 to 3 near the plume centerline over a wide range of atmospheric conditions. Near the plume edge we find values which range as high as 15. Estimates of the variability in mean concentrations give  $\sigma_c/\bar{c} \sim 1$  for averages taken over an hour. This is a significant error in a mean value measurement and shows a fundamental limit in the precision of both model predictions and experimental concentration measurements in the atmosphere. This result also raises questions on the validity of using mean concentration values for hazard assessments.

### 8.1 Meteorology and Mean Concentration Measurements

Our experimental measurements were taken in the period from September through November in 1987 at two different sites. One site was at Camp Atterbury, Indiana. The other site was near Red Bluff, California in the foothills of the Sierra Nevada mountains.

#### 8.1.1 Camp Atterbury Dispersion Measurements

The Camp Atterbury site provides nearly flat terrain. The roughness height at this site was 0.1 m and reflected contributions from surface vegetation, trees, and small hills. All tests were conducted in the daytime under unstable meteorological conditions. The meteorological measurements at this site conformed to flat-terrain boundary-layer scaling. Values of the stability parameter  $z_i/L$  were in the range of -4.5 to -45. More unstable values of  $z_i/L$  are not found at this site by virtue of both the late fall test period and the large roughness height.

Two different smoke types were used in the Camp Atterbury tests: fog-oil and hexachloroethane (HC). Samplers were located on five crosswind lines at distances of 100 m, 200 m, 300 m, 500 m, and 800 m from the source. Due to overloading of the filters during the tests, many of the raw data required adjustment to account for the reduced flowrates caused by filter clogging. This correction assumed an exponential drop in the collection efficiency after a threshold loading was reached. When the corrected results are employed the data agree well with mixed-

layer scaling models. The data acquired using fog-oil smoke conformed to mixed-layer scaling within the range of experimental uncertainty.

### **8.1.2 Meadowbrook Dispersion Measurements**

The Meadowbrook site is located in gently rolling terrain in the foothills of the Sierra Nevada mountains. The dominant terrain feature at this site is a bifurcating valley running the length of the test site in an east-west direction. Both the elevation and vegetation varied throughout the 5-km  $\times$  5-km site. The terrain strongly influenced the diurnal change in meteorology. During nighttime hours the gravity-driven winds follow the downward slope of the valley. Daytime winds reverse to the upslope direction. All dispersion tests at this site were conducted using the fog-oil smoke.

The unstable dispersion tests were conducted during the period from midmorning to midafternoon. The 1-km<sup>2</sup> unstable test site was relatively flat and open with a uniform ground cover. Meteorological data from the towers, sonic anemometers, and soundings conformed fairly well to flat-terrain boundary-layer scaling. For the dispersion tests in which good results were obtained the stability parameter  $z_i/L$  were in the range of -4.0 to -20. Concentration data were taken on crosswind transects at distances of 25 m, 150 m, and 250 m from the source. These dispersion data follow mixed-layer scaling in good agreement with flat terrain data.

The stable tests were conducted in a period from late evening to just after dawn. The winds during the night followed the downward slope of the terrain in the canyons and valleys. It is likely that the surface-layer winds were uncoupled from the upper-level winds during this period. Concentration measurements were made in lines perpendicular to the valley centerline at downwind distances of 25 m, 150 m, 250 m, 500 m, 1800 m, and 4000 m. Crosswind-integrated concentration measurements of the smoke plume were very consistent throughout all the tests. Although it is beyond the scope of this report to offer a detailed model of the stable dispersion, we have analyzed the near-field concentration data which may not be influenced by the valley width. A more general model of mean dispersion could be based on the wind field through each of the valleys in the bifurcating canyon which comprises the test site.

## **8.2 Fluctuating Concentration Measurements**

From analysis of the fluctuating concentration measurements we have found a suitable form for the probability density function in concentration. Intermittency at points within the plume is defined as the fraction of time that smoke is present at the location. Near the plume centerline the intermittency varies between 0.3 to 0.6. At the plume edges, this intermittency can be smaller than 0.01. For the fraction of time that smoke is present, the concentration follows an exponential distribution. This overall probability distribution means that concentrations are likely to be lower

than the mean concentration or zero for a significant fraction of time during any release. There is also a significant probability that concentrations may be 10 to 20 times greater than the mean value when material is present at a given sampling position.

In this report, a model is presented for estimating concentration fields  $c_{\xi}(x,y)$  which have a specified probability of being exceeded  $P(c) = \xi$  in any given release period. This method is directly applicable to continuous release plumes and is useful in predicting areas for which tolerance levels will be exceeded. From basic probability theory, we can extend these models from a constant source strength  $q$ , to cases in which  $q$  is a stochastic variable. This approach is applicable to instantaneous or short term releases of pollutants or toxic materials and is especially useful in cases for which the release rate is not well characterized.

In investigating the standard deviation in concentration we have found a self-preserving scaling in the crosswind direction and a constant centerline ratio of  $\alpha = \sigma_c(x,0)/\bar{c}$  within a given test. Both results are consistent with models presented by Durbin (1980) and Csanady (1973). The conservative nature of the concentration variance field is due to the very high mass Péclet numbers in our atmospheric dispersion tests. The range of  $\alpha$  values we have measured are in the range of 1.5 to 3.0. The smaller values are for the stable dispersion tests, whereas the largest values are for the unstable tests at the Meadowbrook site.

The invariance of  $\alpha$  within a test is probably a result of the limited downwind range of our measurements. Our sampling distances always are less than the Lagrangian integral scale  $l_{L,y}$  and are also removed from source effects. Laboratory measurements by Fackrell and Robins (1982a) and a model given by Kaplin and Dinar (1988) both show that  $\alpha$  is nearly constant within our sampling range but is more generally a function of distance from the source. Further investigation of the behavior of  $\alpha$  as a function of turbulent integral scale, source size, and downwind distance in atmospheric dispersion is a valid direction for future research.

Spectral investigation of the concentration fluctuations has shown a  $-5/3$  power-law behavior for  $S_{cc}(n)$  versus  $n$  in most of our measurements. We should have only small errors in estimates of  $\sigma_c^2$  due to the limited high-frequency response of our instruments. This  $-5/3$  spectral range extends to lower frequencies than the inertial subrange measured for velocity.

The only cases for which a  $-5/3$  spectral scaling range for concentration did not occur was for isolated samplers in the stable dispersion tests. These samplers were located either near the source or within the forest canopy. The samplers near the source may have been influenced by a core region of the plume or regions of non-turbulent fluid. Within the forest, the inertial-convective subrange occurs at frequencies higher than can be measured with our instruments.

Integral scales of the concentration records are relatively independent of position for the unstable tests. Average values increase with increasing instability, but are always less than the



convective velocity time scale. We would expect that the integral scale of concentration is greater at the further downwind distances. This result is not found in our tests, probably because of the limited sampling distances and noise in the experimental measurements.

To further investigate the temporal behavior of the concentration records, we examined the distribution of bursts for which  $c > 0$ . The mean duration of these bursts  $1/\lambda_u(0)$  at a given location is approximately equal to the integral scale of the concentration fluctuations. Like the integral scales, values of  $1/\lambda_u(0)$  are not a strong function of position.

The probability distribution of bursts for which  $c > 0$  is nearly exponential. In combination with the point probability distribution of concentration levels, this suggests that the mechanics of atmospheric dispersion are more closely associated with a Poisson-like process than the diffusive behavior often associated with time-averaged concentrations.

In the overall plume structure we find that correlated puffs of material are carried downwind from the source and dispersed by the instantaneous wind field. At a given downwind distance, the average time that it takes for an individual puff of smoke to pass over a sampler is nearly constant and not a function of crosswind position. The average time between puffs of smoke is longer at the plume edge than at the plume centerline. Over the long term we have a Gaussian crosswind profile of mean concentration.

## REFERENCES

- Adrian, R., 1983a: "Conditional Eddies in Isotropic Turbulence", Physics of Fluids, 22, 2065-2070.
- Adrian, R., 1983b: "Laser Velocimetry", in Fluid Mechanics Measurements, R.J. Goldstein, ed., (Hemisphere Publishing Corporation, Washington).
- Agarwal, J. K., and B. Y. H. Liu, 1980: "A Criterion for Accurate Aerosol Sampling in Calm Air", American Industrial Hygiene Association Journal, 41, 191-197.
- American Society for Testing and Materials, 1982: Annual Book of ASTM Standards, (ASTM, Philadelphia, Pa.).
- Ariessohn, Peter C., and James C. F. Wang, 1985: "Recent Development of a Real-Time Particulate Mass Sampling System for High Temperature Applications", Combustion and Flame, 59, 81-91.
- Barad, M.L., 1958: "Project Prairie Grass: A Field Program in Diffusion", Volumes 1 and 2, Geophysical Research Papers No. 59, Air Force Cambridge Research Center, AD-152572 and AD-152573.
- Barad, M.L., and B. Shorr, 1954: "Field Studies of the Diffusion of Aerosols", Industrial Hygiene Quarterly, June, 136-140.
- Barry, P. J., 1971: "A Note on Peak-to-Mean Concentration Ratios", Boundary-Layer Meteorology, 2, 122-126.
- Batchelor, G.K., 1949: "Diffusion in a Field of Homogeneous Turbulence, I. Eulerian Analysis", Australian Journal of Science Research, 2, 437-450.
- Batchelor, G.K., 1952: "Diffusion in a Field of Homogeneous Turbulence, II. The Relative Motion of Particles", Proceedings of the Cambridge Philosophical Society, 48, 345-362.
- Batchelor, G. K., 1953: The Theory of Homogeneous Turbulence, (Cambridge University Press, Cambridge).
- Batchelor, G. K., 1959: "Small-scale Variation of Convected Quantities Like Temperature in Turbulent Fluid", Journal of Fluid Mechanics, 5, 113-133.
- Becker, H. A., H.C. Hottel and G.C. Williams, 1967: "The Nozzle-Fluid Concentration Field of the Round, Turbulent, Free Jet", Journal of Fluid Mechanics, 30, 285-304.
- Becker, H. A., H.C. Hottel and G.C. Williams, 1967: "On the Light-Scatter Technique for the Study of Turbulence and Mixing", Journal of Fluid Mechanics, 30, 259-284.
- Becker, H A., R.E. Rosensweig, J.R. Gwozdz, 1966: "Turbulent Dispersion in a Pipe Flow", A.I.Ch.E. Journal, 12, 964-972.

- Belyaev, S. P., and L. M. Levin, 1974: "Techniques for Collection of Representative Aerosol Samples", Aerosol Science, 5, 325-338.
- Bendat, J.S. and A.G. Piersol, 1971: Random Data: Analysis and Measurement Procedures, (Wiley-Interscience, New York).
- Benkley, Carl W. and Lloyd L. Schulman, 1979: "Estimating Hourly Mixing Depths from Historical Meteorological Data", Journal of Applied Meteorology, 18, 772-780.
- Benoit, Robert, 1977: "On the Integral of the Surface Layer Profile-Gradient Functions", Journal of Applied Meteorology, 16, 859-860.
- Bertsch, Wolfgang, Ray C. Chang, and Albert Zlatkis, 1974: "The Determination of Organic Volatiles in Air Pollution Studies: Characterization of Profiles", Journal of Chromatographic Science, 12, 175-182.
- Birch, D. R., D.R. Brown, M.G. Dodson, and J.R. Thomas, 1978: "The Turbulent Concentration Field of a Methane Jet", Journal of Fluid Mechanics, 88, 431-449.
- Bohren, Craig F., and Donald R. Huffman, 1983: Absorption and Scattering of Light by Small Particles, (John Wiley and Sons, New York).
- Briggs, Gary A., 1985: "Analytical Parameterizations of Diffusion: The Convective Boundary Layer", Journal of Climate and Applied Meteorology, 24, 1167-1186.
- Brown, D. F., and W. E. Dunn, 1990: Analysis of Meteorological Data from the AMADEUS Smoke Dispersion Experiments, work completed under contract no. 90PP0819, University of Illinois, Urbana, IL
- Businger, J.A., J.C. Wyngaard, Y. Izumi, and E.F. Bradley, 1971: "Flux-Profile Relationships in the Atmospheric Surface Layer", Journal of the Atmospheric Sciences, 28, 181-189.
- Calder, K. L., 1966: "The Criterion of Turbulence in a Fluid of Variable Density, with Particular Reference to Conditions in the Atmosphere", Quarterly Journal of the Royal Meteorological Society, 75, 71-88.
- Carras, J. N. and D. J. Williams, 1986: "Experimental Studies of Plume Dispersion in Convective Conditions - II. Horizontal Plume Dispersion", Atmospheric Environment, 20, 2307-2314.
- Cess, R.D., G.L. Potter, J.P. Blanchet, G.J. Boer, S.J. Ghan, J.T. Kiehl, H. Le Treut, Z.-X. Li, X.-Z. Liang, J.F.B. Mitchell, J.-J. Morcrette, D.A. Randall, M.R. Riches, E. Roeckner, U. Schlese, A. Slingo, K.E. Taylor, W.M. Washington, R.T. Wetherald, and I. Yagai, 1989: "Interpretation of Cloud-Climate Feedback as Produced by 14 Atmospheric General Circulation Models", Science, 245, 513-516.
- Chandrasekhar, S., 1943: "Stochastic Problems in Physics and Astronomy", Reviews of Modern Physics, 15, 1-89.

- Cohen, J.J., and D.N. Montan, 1967: "Theoretical Considerations, Design, and Evaluation of a Cascade Impactor", American Industrial Hygiene Association Journal, 28, 95-104.
- Cooke, Derry D., and Milton Kerker, 1975: "Response Calculations for Light-Scattering Aerosol Particle Counters", Applied Optics, 14, 734-739.
- Corrsin, S. 1951: "On the Spectrum of Isotropic Temperature Fluctuations in an Isotropic Turbulence", Journal of Applied Physics, 22, 469-473.
- Courtney, William J., Robert W. Shaw, and Thomas G. Dzubay, 1982: "Precision and Accuracy of a  $\beta$  Gauge for Aerosol Mass Determinations", Environmental Science and Technology, 16, 236-239.
- Cropper, F. R., and Simon Kaminsky, 1963: "Determination of Toxic Organic Compounds in Admixture in the Atmosphere by Gas Chromatography", Analytical Chemistry, 35, 735-743.
- Csanady, G. T., 1973: Turbulent Diffusion in the Environment, (D. Reidel Publishing Company, Boston).
- Csanady, G. T., 1967: "Concentration Fluctuations in Turbulent Diffusion", Journal of Atmospheric Science, 24, 21-28.
- Davies, C. N., 1968: "The Sampling of Aerosols - The Entry of Aerosols into Sampling Tubes and Heads", Staub - Reinhalt Luft, 28, 6, 1-9.
- Deardorff, James W., 1970a: "Convective Velocity and Temperature Scales for the Unstable Planetary Boundary Layer and for Rayleigh Convection", Journal of the Atmospheric Sciences, 27, 1211-1213.
- Deardorff, James W., 1970b: "Preliminary Results from Numerical Integration of the Unstable Planetary Boundary Layer", Journal of the Atmospheric Sciences, 27, 1209-1211.
- Deardorff, James W., 1972: "Numerical Investigation of Neutral and Unstable Planetary Boundary Layers", Journal of the Atmospheric Sciences, 29, 91-115.
- Deardorff, J. W., and G. E. Willis, 1975: "A Parameterization of Diffusion into the Mixed Layer", Journal of Applied Meteorology, 14, 1451-1458.
- DeVaull, G., 1985: Development and Evaluation of a Sampling and Analysis Method for Fog Oil Smoke, M.S. Thesis, University of Illinois, Urbana.
- DeVaull, G., W. E. Dunn, and J. C. Liljegren, 1989: Analysis Methods and Results of Hexachloroethane smoke Dispersion Experiments Conducted as Part of Atterbury-87 Field Studies, work completed under contract no. 84PP4822, University of Illinois, Urbana, IL
- Draxler, R. R., 1976: "Determination of Atmospheric Diffusion Parameters", Atmospheric Environment, 10, 99-105.

- Durbin, P. A., 1980: "A Stochastic Model of Two-Particle Dispersion and Concentration Fluctuations in Homogeneous Turbulence", Journal of Fluid Mechanics, 100, 279-302.
- Durbin, Paul A., 1983: "Stochastic Differential Equations and Turbulent Dispersion", NASA Reference Publication 1103, Scientific and Technical Information Branch.
- Durham, Michael D., and Dale A. Lundgren, 1980: "Evaluation of Aerosol Aspiration Efficiency as a Function of Stokes Number, Velocity Ratio, and Nozzle Angle", Journal of Aerosol Science, 11, 179-188.
- Dyer, A.J., 1974: "A Review of Flux-Profile Relationships", Boundary Layer Meteorology, 3, 47-58.
- Dyer, A.J. and B.B. Hicks, 1970: "Flux-Gradient Relationships in the Constant Flux Layer", Quarterly Journal of the Royal Meteorological Society, 96, 715-721.
- Eggleton, A.E.J., and N. Thompson, 1961: "Loss of Fluorescent Particles in Atmospheric Diffusion Experiments by Comparison with Radioxenon Tracer", Nature, 192, 935-936.
- Fackrell, J. E., 1980: "A Flame Ionization Detector for Measuring Fluctuating Concentration", Journal of Physics E: Scientific Instrumentation, 80, 888-893.
- Fackrell, J.E., and A.G. Robins, 1982a: "Concentration Fluctuations and Fluxes in Plumes from Point Sources in a Turbulent Boundary Layer", Journal of Fluid Mechanics, 117, 1-26.
- Fackrell, J.E. and A.G. Robins, 1982b: "The Effects of Source Size on Concentration Fluctuations in Plumes", Boundary-Layer Meteorology, 22, 335-350.
- Federal Emergency Management Agency, 1989: Handbook of Chemical Hazard Analysis Procedures, (Federal Emergency Management Agency, Washington, D.C.).
- Fraust, Charles L. and Edward R. Hermann, 1966: "Charcoal Sampling Tubes for Organic Vapor Analysis by Gas Chromatography", American Industrial Hygiene Association Journal, 27, 68-74.
- Freymuth, Peter and Mahinder S. Uberoi, 1973: "Temperature Fluctuations in the Turbulent Wake behind an Optically Heated Sphere", The Physics of Fluids, 16, 161-168.
- Fuchs, N.A., 1975: "Sampling of Aerosols", Atmospheric Environment, 9, 697-707.
- Gad-el-Hak, Mohamed and J.B. Morton, 1979: "Experiments on the Diffusion of Smoke in Isotropic Turbulence", AIAA Journal, 17, 558-562.
- Garrett, A. J., 1981: "Comparison of Observed Mixed - Layer Depths to Model Estimates Using Observed Temperatures and Winds, and MOS Forecasts", Journal of Applied Meteorology, 20, 1277-1283.

- Gelbicova-Ruzickova, J., J. Novak, and J. Janak, 1972: "Application of the Method of Chromatographic Equilibrium to Air Pollution Studies; The Determination of Minute Amounts of Halothane in the Atmosphere of an Operating Theatre", Journal of Chromatography, 64, 15-23.
- Gibson, C. H. and W. H. Schwarz, 1963: "The Universal Spectra of Turbulent Velocity and Scalar Fields", Journal of Fluid Mechanics, 16, 366-384.
- Gifford, F.A., 1955: "A Simultaneous Lagrangian-Eulerian Turbulence Experiment", Monthly Weather Review, 83, 293-301.
- Gifford Jr., Frank, 1959: "Statistical Properties of a Fluctuating Plume Dispersion Model", Advances in Geophysics, 6, 117-137.
- Gifford Jr., Frank, 1960: "Peak to Average Concentration Ratios According to a Fluctuating Plume Dispersion Model", International Journal of Air Pollution, 3, 253-260.
- Golder, D., 1972: "Relations Among Stability Parameters in the Surface Layer", Boundary Layer Meteorology, 3, 47-58.
- Gryning, S.E., A.A.M. Holtslag, J.S. Irwin, and B. Sivertsen, 1987: "Applied Dispersion Modeling Based on Meteorological Scaling Parameters", Atmospheric Environment, 21, 79-81.
- Gryning, S.E., A.P. van Ulden, and S.E. Larsen, 1983: "Dispersion from a Continuous Ground-Level Source Investigated by a K-model", Quarterly Journal of the Royal Meteorological Society, 109, 355-364.
- Gucker Jr., F.T., C.T. O'Konski, H.B. Pickard, and J.N. Pitts, Jr., 1947: "A Photoelectric Counter for Colloidal Particles", Journal of the American Chemical Society, 69, 2422-2431.
- Hanna, Stephen R., 1984a: "Concentration Fluctuations in a Smoke Plume", Atmospheric Environment, 18, 1091-1106.
- Hanna, Steven R., 1984b: "The Exponential PDF and Concentration Fluctuations in Smoke Plumes", Lecture Notes, IFAORS Short Course No. 480, Atmospheric Transport and Diffusion, (Institute for Atmospheric Optics and Remote Sensing, Hampton, Virginia).
- Hanna, Steven R., Gary A. Briggs, and Rayford P. Hosker, Jr., 1982: Handbook on Atmospheric Dispersion, (U.S. Department of Energy, Technical Information Center, DOE/TIC-11223).
- Haugen, D.A., 1959: "Project Prairie Grass: A Field Program in Diffusion", Volume 3, Geophysical Research Papers No. 59, Air Force Cambridge Research Center, AD-217076.
- Heftman, E., ed., 1983: Chromatography, Fundamentals and Applications of Chromatographic and Electrophoretic Methods: Part B: Applications, (Journal of Chromatography Library - vol.22B, Elsevier Scientific Publishing Company, Amsterdam).

- Heintzenburg, J. and L. Bäcklin, 1983: "A High Sensitivity Integrating Nephelometer for Airborne Air Pollution Studies", Atmospheric Environment, 17, 433-436.
- Hinds, W.C., 1982: Aerosol Technology - Properties, Behavior, and Measurement of Airborne Particles, (John Wiley and Sons, New York).
- Højstrup, J., 1982: "Velocity Spectra in the Unstable Planetary Boundary Layer", Journal of Atmospheric Science, 39, 2239-2248.
- Holmburg, R. W., J. H. Moneyhun, and T. M. Gayle, 1982: Generating, Monitoring and Controlling Petroleum Aerosols for Inhalation Chamber Studies, ORNL/TM-8903, (Oak Ridge National Laboratory, Oak Ridge, TN).
- Holtstag, A. A. M., and F. T. M. Nieuwstadt, 1986: "Scaling the Atmospheric Boundary Layer", Boundary-Layer Meteorology, 36, 201-209.
- Holzworth, George C., 1967: "Mixing Depths, Wind Speeds and Air Pollution Potential for Selected Locations in the United States", Journal of Applied Meteorology, 6, 1039-1044.
- Houghton, J. A., and G. Lee, 1960: "Data on Ultraviolet Absorption and Fluorescence Emission", American Industrial Hygiene Association Journal, 21, 219-230.
- Hunt Jr., William F., 1972: "The Precision Associated with the Sampling Frequency of Log-Normally Distributed Air Pollutant Measurements", Journal of the Air Pollution Control Association, 22, 687-691.
- Irwin, J.S., and F. C. Binkowski, 1981: "Estimation of the Monin-Obukhov Scaling Length Using On-Site Instrumentation", Atmospheric Environment, 15, 1091-1094.
- Jakeman, A.K., J.A. Taylor, and R.W. Simpson, 1986: "Modeling Distributions of Air Pollutant Concentrations - II. Estimation of One and Two Parameter Statistical Distributions", Atmospheric Environment, 20, 2435-2447.
- Jakeman, A.J., R.W. Simpson, and J.A. Taylor, 1988: "Modeling Distributions of Air Pollutant Concentrations - III. The Hybrid Deterministic-Statistical Distribution Approach", Atmospheric Environment, 22, 163-174.
- Jenkins, R. A., T. M. Gayle, J. S. Wike, and D. L. Manning, 1982: "Sampling and Chemical Characterization of Concentrated Smokes", Toxic Materials in the Atmosphere, ASTM STP 786, American Society for Testing and Materials, 153-156.
- Jenkins, R. A., D. L. Manning, M. P. Maskarinec, J. H. Moneyhun, W. Dalbey, and S. Lock, 1983: Diesel Fuel Smoke Particulate Dosimetry in Sprague-Dawley Rats, ORNL/TM-9195, (Oak Ridge National Laboratory, Oak Ridge, TN).
- Jones, C. D., 1983: "On the Structure of Instantaneous Plumes in the Atmosphere", Journal of Hazardous Materials, 7, 87-112.

- Jones, C. D., 1979: "Statistics of the Concentration Fluctuations in Short Range Atmospheric Diffusion" in Mathematical Modeling of Turbulent Diffusion in the Environment, C. J. Harris, ed., Academic Press, 277-295.
- Kaimal, J. C., J. C. Wyngaard, D. A. Haugen, O. R. Coté, and Y. Izumi, 1976: "Turbulence Structure in the Convective Boundary Layer", Journal of the Atmospheric Sciences, 33, 2152-2169.
- Kaimal, J.C., J.C. Wyngaard, Y. Izumi, O.R. Cote, 1972: "Spectral Characteristics of Surface-Layer Turbulence", Quarterly Journal of the Royal Meteorological Society, 98, 563-389.
- Kaimal, J.C., 1978: "Horizontal Velocity Spectra in an Unstable Surface Layer", Journal of Atmospheric Science, 35, 18-23.
- Kampé De Fériet, J., 1974: "Turbulent Atmospheric Diffusion: The First Twenty-Five Years, 1920-1945", Advances in Geophysics, 18A, 1-23.
- Kao, S.K., 1984: "Theories of Amospheric Transport and Diffusion", in Atmospheric Science and Power Production, D. Randerson, ed., Weather Service Nuclear Support Office, National Oceanic and Atmospheric Administration, United States Department of Commerce, (Technical Information Center, Office of Scientific and Technical Information, United States Department of Energy).
- Kaplan, H. and N. Dinar, 1988: "A Stochastic Model for Dispersion and Concentration Distribution in Homogeneous Turbulence", Journal of Fluid Mechanics, 190, 121-140.
- Katz, Sidney, Alan Snelson, Ronald Butler, Raleigh Farlow, Roger Welker, Stephen Mainer, and Narayanan Rajendran, 1980a: Physical and Chemical Characterization of Military Smokes: Part II - Fog Oils and Oil Fogs Final Report, Contract No. DAMD17-78-C-8085, (IIT Research Institute, Chicago, Illinois).
- Katz, Sidney, Alan Snelson, Raleigh Farlow, Roger Welker, and Stephen Mainer, 1980b: Physical and Chemical Characterization of Fog Oil Smoke and Hexachloroethane Smoke - Final Report on Hexachloroethane Smoke, Contract No. DAMD17-78-C-8085, (IIT Research Institute, Chicago, Illinois).
- Kerker, M., 1969: "The Scattering of Light and Other Electromagnetic Radiation", (Academic Press, New York).
- Lamb, Robert G., 1984: "Air Pollution Models as Descriptors of Cause-Effect Relationships", Atmospheric Environment, 18, 591-606.
- Larsen, Ralph I., 1974: "An Air Quality Data Analysis System for Interrelating Effects, Standards, and Needed Source Reductions - Part 2", Journal of the Air Pollution Control Association, 24, 551-558.
- Larsen, R. I., 1969: "A New Mathematical Model Of Air Pollutant Concentration Averaging Time and Frequency", Journal of the Air Pollution Control Association, 19, 24-30.



- Lee, J. T., and G. L. Stone, 1983: "Eulerian - Lagrangian Relationships in Monte Carlo Simulations of Turbulent Diffusion", Atmospheric Environment, 17, 2483-2487.
- Lee, J.T., and G.L. Stone, 1986: "Monte Carlo Simulation of Two-Particle Relative Diffusion using Eulerian Statistics", Atmospheric Environment, 20, 2185-2197.
- Leighton, Philip A., William A. Perkins, Stuart W. Grinnell, and Francis X. Webster, 1965: "The Fluorescent Particle Atmospheric Tracer", Journal of Applied Meteorology, 4, 334-348.
- Liljegren, J.C., 1989: "A Stochastic Model of Turbulent Dispersion in the Convective Planetary Boundary Layer Compared with the Results of the Atterbury-87 Field Study", Ph.D. Thesis, University of Illinois, Urbana, IL.
- Liu, Mei-Kao and Gary E. Moore, 1984: "On the Evaluation of Predictions from a Gaussian Plume Model", Journal of the Air Pollution Control Association, 34, 1044-1050.
- Ludwick, J. D., J. J. Lashock, R. E. Connally, and P. W. Nickola, 1968: "Automatic Real Time Monitoring of  $^{85}\text{Kr}$  Utilizing the 4096 Memory of a Multiparameter Analyzer", The Review of Scientific Instruments, 39, 853-859.
- MacCready, P.B., 1966: "Mean Wind Speed Measurements in Turbulence", Journal of Applied Meteorology, 5, 219-224.
- Marple, V. A., and B.Y.H. Liu, 1974: "Characteristics of Laminar Jet Impactors", Environmental Science and Technology, 8, 648-654.
- Mercer, T.T., 1963: "On the Calibration of Cascade Impactors", Annals of Occupational Hygiene, 6, 1.
- McFarland, A.R., and H.W. Zeller, 1963: Study of a Large Volume Impactor for High Altitude Aerosol Collection, TID-18624, (United States Atomic Energy Commission, Division of Technical Information Extension, Oak Ridge, Tennessee).
- Michelson, Torbin, 1983: "The Borris Field Experiment: Observations of Smoke Diffusion in the Surface Layer over Homogeneous Terrain", Risø-R-479, Risø National Laboratory, Roskilde, Denmark.
- Miller, R. W., 1983: Flow Measurement Engineering Handbook, (McGraw-Hill Book Company, New York).
- Monin, A. S., and A. M. Yaglom, 1971: Statistical Fluid Mechanics: Mechanics of Turbulence, (MIT Press, Cambridge, Massachusetts).
- Monin, A. S., and A. M. Obhukov, 1954: "Basic Laws of Turbulent Mixing in the Ground Layer of the Atmosphere", translated from Akademiia Nauk SSSR, Leningrad, Geofizicheskii Institut, Trudy, 151, 163-187, in AIAA Selected Reprint Series, vol IX, Aerophysics of Air Pollution, (American Institute of Aeronautics and Astronautics, New York).

- Murthy, C.R., and G.T. Csanady, 1971: "Experimental Studies of Relative Diffusion in Lake Huron", Journal of Physical Oceanography, 1, 17-24.
- National Institute for Occupational Safety and Health, 1977: Manual of Analytical Methods, Second Edition, (U. S. Department of Health, Education, and Welfare, Public Health Service, Center for Disease Control, NIOSH, Cincinnati, Ohio).
- Nickerson, Everett C. and Virginia E. Smiley, 1975: "Surface Layer and Energy Budget Parameterizations for Mesoscale Models", Journal of Applied Meteorology, 14, 297-300.
- Nickola, P. W., 1971: "Measurements of the Movement, Concentration and Dimensions of Clouds Resulting from Instantaneous Point Sources", Journal of Applied Meteorology, 10, 962-973.
- Nieuwstadt, F. T. M., 1984: "The Turbulent Structure of the Stable, Nocturnal Boundary Layer", Journal of the Atmospheric Sciences, 41, 2202-2216.
- Nieuwstadt, F.T.M., 1980a: "Prediction of Air Pollution Frequency Distribution - Part II. The Gaussian Plume Model", Atmospheric Environment, 14, 259-265.
- Nieuwstadt, F.T.M., 1980b: "Application of Mixed-Layer Similarity to the Observed Dispersion from a Ground Level Source", Journal of Applied Meteorology, 19, 157-162.
- Nieuwstadt, F.T.M., and A.P. van Ulden, 1978: "A Numerical Study on the Vertical Dispersion of Passive Contaminants from a Continuous Source in the Atmospheric Surface Layer", Atmospheric Environment, 12, 2119-2124.
- North, M., E. Hernandez, and R. Garcia, 1984: "Frequency Analysis of High CO Concentrations in Madrid by Stochastic Process Modelling", Atmospheric Environment, 18, 2049-2054.
- Novak, Josef, Vladimir Vasak, and Jaroslav Janak, 1965: "Chromatographic Method for the Concentration of Trace Impurities in the Atmosphere and Other Gases", Analytical Chemistry, 37, 660-666.
- Olesen, H.R., S.E. Larsen, and J. Højstrup, 1984: "Modeling Velocity Spectra in the Lower Part of the Planetary Boundary Layer", Boundary-Layer Meteorology, 29, 285-312.
- Panofsky, Hans A., and John A. Dutton, 1984: Atmospheric Turbulence - Models and Methods for Engineering Applications, (John Wiley and Sons, New York).
- Panofsky, H. A., and B. Prasad, 1965: "Similarity Theories and Diffusion", International Journal of Air and Water Pollution, 9, 419-430.
- Panofsky, H.A., H. Tennekes, D.H. Lenschow, and J.C. Wyngaard, 1977: "The Characteristics of Turbulent Velocity Components in the Surface Layer Under Convective Conditions", Boundary-Layer Meteorology, 11, 355-361.
- Papoulis, L., 1965: Probability, Random Variables, and Stochastic Processes, (McGraw-Hill, New York).

- Pasquill, F. and F. B. Smith, 1983: Atmospheric Diffusion, third edition, (John Wiley and Sons, New York).
- Pasquill, F., 1974: Atmospheric Diffusion, second edition, (John Wiley and Sons, New York).
- Patashnick, Harvey and Georg Rupprecht, (1986): "Advances in Microweighing Technology", American Laboratory, July, 59-64.
- Paulson, C.A., 1970: "The Mathematical Representation of Wind Speed and Temperature Profiles in the Unstable Atmospheric Surface Layer", Journal of Applied Meteorology, 9, 857-861.
- Phinney, Dale E., and James E. Newman, 1972: "The Precision Associated with the Sampling Frequencies of Total Particulate at Indianapolis, Indiana", Journal of the Air Pollution Control Association, 22, 692-695.
- Ramsdell, J.V. and W.T. Hinds, 1971: "Concentration Fluctuations and Peak-to-Mean Concentration Ratios in Plumes from a Ground-Level Continuous Point Source", Atmospheric Environment, 5, 483-495.
- Ramsdell, J. V., C. S. Glantz, and R. E. Kerns, 1985: "Hanford Atmospheric Data: 1959 - 1974", Atmospheric Environment, 19, 83-86.
- Randerson, D., (Ed.), 1984: Atmospheric Science and Power Production, Weather Service Nuclear Support Office, National Oceanic and Atmospheric Administration, United States Department of Commerce (Technical Information Center, Office of Scientific and Technical Information, United States Department of Energy).
- Rao, A.K., and K.T. Whitby, 1978: "Non-Ideal Collection Characteristics of Inertial Impactors - I, Single-Stage Impactors and Solid Particles", Journal of Aerosol Science, 9, 77-86.
- Ray, Eugene M., 1970: "Sampling and Determination by Ultraviolet Absorption of Oil Mists and Solvent Vapors", American Industrial Hygiene Association Journal, 31, 472-478.
- Reid, John D., 1979: "Markov Chain Simulations of Vertical Dispersion in the Neutral Surface Layer for Surface and Elevated Releases", Boundary-Layer Meteorology, 16, 3-32.
- Reid, Frank H. and Walter R. Halpin, 1968: "Determination of Halogenated and Aromatic Hydrocarbons in Air by Charcoal Tube and Gas Chromatography", American Industrial Hygiene Association Journal, 29, 390-396.
- Richardson, L.F., 1926: "Atmospheric Diffusion Shown on a Distance-Neighbour Graph", Proceedings of the Royal Society of London, Series A, 15, 709-737.
- Robins, A. G., and J. E. Fackrell, 1979: "Continuous Plumes - Their Structure and Prediction", in Mathematical Modeling of Turbulent Diffusion in the Environment, C. J. Harris, ed., Academic Press, 55-114.

- Russell, John W., 1975: "Analysis of Air Pollutants Using Sampling Tubes and Gas Chromatography", Environmental Science and Technology, 9, 1175-1178.
- Russell, John W. and Lewis A. Shadoff, 1977: "The Sampling and Determination of Halocarbons in Ambient Air Using Concentration on Porous Polymer", Journal of Chromatography, 134, 375-384.
- Sawford, B.L., 1986: "Generalized and Random Forcing in Random-Walk Turbulent Dispersion Models", Physics of Fluids, 29, 3582-3585.
- Sawford, B.L., 1982: "Comparison of Some Different Approximations in the Statistical Theory of Relative Dispersion", Quarterly Journal of the Royal Meteorological Society, 108, 191-206.
- Sawford, B.L., 1982: "Lagrangian Monte Carlo Simulation of the Turbulent Motion of a Pair of Particles", Quarterly Journal of the Royal Meteorological Society, 108, 207-213.
- Shaughnessy, E. J., and J. B. Morton, 1977: "Laser Light-Scattering Measurements of Particle Concentration in a Turbulent Jet", Journal of Fluid Mechanics, 80, 129-148.
- Smith, F.B., and J.S. Hay, 1961: "The Expansion of Clusters of Particles in the Atmosphere", Quarterly Journal of the Royal Meteorological Society, 87, 82-101.
- Sutton, O. G., 1932, "A Theory of Eddy Diffusion in the Atmosphere", Proceedings of the Royal Society, A, 135, 143-165.
- Sutton, O. G., 1947a: "The Problem of Diffusion in the Lower Atmosphere", Quarterly Journal of the Royal Meteorological Society, 73, 257-281.
- Sutton, O. G., 1947b: "The Theoretical Distribution of Airborne Pollution from Factory Chimneys", Quarterly Journal of the Royal Meteorological Society, 73, 426-436.
- Stern, Arthur C., Henry C. Wohlers, Richard W. Boubel, and William P. Lowry, 1973: Fundamentals of Air Pollution, (Academic Press, New York).
- Stratton, J.A., 1941: Electromagnetic Theory, (McGraw-Hill, New York).
- Taylor, G. I., 1921: "Diffusion by Continuous Movements", Proceedings of the London Mathematical Society, 20, 196-212.
- Taylor, J.A., A.J. Jakeman, and R.W. Simpson, 1986: "Modeling Distributions of Air Pollutant Concentrations - I. Identification of Statistical Models", Atmospheric Environment, 20, 1781-1789.
- Tennekes, H. and J. L. Lumley, 1972: A First Course in Turbulence, (The MIT Press, Cambridge, Massachusetts).
- Thomson, D. J. 1984: "Random Walk Modeling of Diffusion in Inhomogeneous Turbulence", Quarterly Journal of the Royal Meteorological Society, 110, 1107-1120.

- Tufto, Pål Å, and Klaus Willeke, 1982: "Dependence of Particulate Sampling Efficiency on Inlet Orientation and Flow Velocities", American Industrial Hygiene Association, 43, 436-443.
- Van der Hoven, Isaac, 1957: "Power Spectrum of Horizontal Wind Speed in the Frequency Range from 0.0007 to 900 Cycles per Hour", Journal of Meteorology, 14, 160-164.
- van de Hulst, H. C., 1957: Light Scattering by Small Particles, (John Wiley and Sons, New York).
- van Dop, H., F.T.M. Nieuwstadt, and J.C.R. Hunt, 1985: "Random Walk Models for Particle Displacements in Inhomogeneous Unsteady Flows", Physics of Fluids, 28, 1639-1653.
- van Ulden, A.P., 1978: "Simple Estimates for Vertical Diffusion from Sources Near the Ground", Atmospheric Environment, 12, 2125-2129.
- van Kampen, N.G., 1981: Stochastic Processes in Physics and Chemistry, (North-Holland Publishing Company, Amsterdam).
- Venkatram, A., 1988: "An Interpretation of Taylor's Statistical Analysis of Particle Dispersion", Atmospheric Environment, 22, 865-868.
- Walker, E.R., 1965: "A Particulate Diffusion Experiment", Journal of Applied Meteorology, 4, 614-621.
- Wang, James C. F., Harvey Patashnick and George Rupprecht, 1980: "A New Real-Time Isokinetic Dust Mass Monitoring System", Air Pollution Control Association Journal, 30, 1018-1021.
- Wang, Ming Chen and G.E. Uhlenbeck, 1945: "On the Theory of the Brownian Motion II", Reviews of Modern Physics, 17, 323-342. reprinted in Selected Papers on Noise and Stochastic Processes, 1954, N. Wax ed., (Dover Publications, New York).
- Wax, N., 1954: Selected Papers on Noise and Stochastic Processes, (Dover Publications, New York).
- White, Lowell D., David G. Taylor, Patricia A. Mauer, and Ricard E. Kupel, 1970: "A Convenient Optimized Method for the Analysis of Selected Solvent Vapors in the Industrial Atmosphere", American Industrial Hygiene Association Journal, 31, 225-232.
- Wilson, D. J., A. G. Robins, J. E. Fackrell, 1982: "Predicting the Spatial Distribution of Concentration Fluctuations from a Ground Level Source", Atmospheric Environment, 16, 497-504.
- Wilson, D. J., A. G. Robins, J. E. Fackrell, 1985: "Intermittency and Conditionally - Averaged Concentration Fluctuation Statistics in Plumes", Atmospheric Environment, 19, 1053-1064.
- Yu, Tsann-Wang, 1978: "Determining Height of the Nocturnal Boundary Layer", Journal of Applied Meteorology, 17, 28-33.

Zeman, Otto, 1979: "Parameterization of the Dynamics of Stable Boundary Layers and Nocturnal Jets, Journal of the Atmospheric Sciences, 36, 792-804.

Zlatkis, Albert, Wolfgang Bertsch, H. A. Lichtenstein, Arye Tishbee, Farid Shunbo, A. M. Coscia, and N. Fleischer, 1973: "Profile of Volatile Metabolites in Urine by Gas Chromatography-Mass Spectrometry", Analytical Chemistry, 45, 763-767.

## DOCUMENT DISTRIBUTION LIST

### No. of Copies

6	Commander U.S. Army Biomedical Research and Development Laboratory ATTN: SGRD-UBZ-RA Fort Detrick Frederick, MD 21702-5010
2	Commander U.S. Army Medical Research and Development Command ATTN: SGRD-RMI-S (Ms. Mary Frances Bostian) Fort Detrick Frederick, MD 21702-5012
1	Commander U.S. Army Laboratory Command Army Research Office ATTN: SLCRO-GS (Dr. Walter Bach, Jr.) P.O. Box 12211 Research Triangle Park, NC 27709-2211
1	Battelle-Pacific Northwest Laboratory ATTN: Dr. Peter Van Voris P.O. Box 999 Richland, WA 99352
1	Commander U.S. Army Environmental Hygiene Agency ATTN: HSHB-ME-AA (Mr. Jeff Kirkpatrick) Aberdeen Proving Ground, MD 21010-5423
1	Commander Chemical Research, Development and Engineering Center ATTN: SMCCR-ST (Mr. Ron O. Pennsyle) Aberdeen Proving Ground, MD 21020